

Diagnostic and Prognostic Profiling of Infectious Diseases Through Multiplexed Protein Assays

by

Krista Meserve

A dissertation submitted in partial fulfillment
of the requirements for the degree of
Doctor of Philosophy
(Chemistry)
in the University of Michigan
2024

Doctoral Committee:

Professor Ryan C. Bailey, Chair
Professor Julie Biteen
Associate Professor Robert Dickson
Associate Professor Kristin Koutmou

Krista Meserve

kmeserve@umich.edu

ORCID iD: [0000-0002-9398-9158](https://orcid.org/0000-0002-9398-9158)

© Krista Meserve 2024

Dedication

To my mom and dad, and my fiancé, TJ.

Acknowledgements

I would like to start by thanking my dissertation committee, Dr. Ryan C. Bailey, Dr. Julie Biteen, Dr. Robert Dickson, and Dr. Kristin Koutmou, for their guidance and feedback during each of my milestone meetings, all of which have significantly ($p < 0.05$) helped me achieve this goal. Thank you to the funding sources that have supported me in various ways: NIH project number R01AI141591 for funding this research, Rackham Graduate School for funding conference travel, and the chemistry department for funded teaching opportunities. Additionally, thank you to the staff in Chem1500, the chemistry building facilities team, and the procurement team (especially Jess Fitzgerald) for their dedication to the department, as well as to Dr. Kathleen Nolte for providing me mentorship and administrative opportunities as a GSI.

All the projects I worked on in the Bailey Lab were *highly* collaborative. I never envisioned having the opportunity to work with such a broad range of teams, but I learned several transferable skills from each unique collaboration. Project collaborators are acknowledged at the start of each pertinent chapter, but I would like to deeply thank all the teams I worked with from Mayo Clinic, Washington University, Mott Children's Hospital, University of Illinois-Urbana Champaign, Hospital de Tijuana, and the chemistry education research team here at Michigan. Specifically, I'd like to thank Dr. Patricio Escalante from the Mayo Clinic for his leadership in the tuberculosis project and providing me the opportunity to lead various parts of our collaboration. A big thank you to Dr. Rafael Laniado-Laborin from Tijuana for his quick correspondence and dedication to setting up our tuberculosis study in his lab.

Thank you to the team at Genalyte, Inc. for their helpful resources through my time in the Bailey Lab. Specifically, I would like to thank Nick Tilden for being my go-to contact for everything Genalyte related and for helping me solve many problems over the years.

For the majority of my time in graduate school I had a sticker on my laptop that said: “Just a kid from Maine.” On some days, it humbled me; on some days, it reminded me of how far I have come; and on some days, it reminded me of my family in Maine rooting for me to keep going. Thank you, dearly, to my mom and dad. My parents have been my biggest supporters (even if they have no idea what I actually do) and have provided me with relief from grad school stress during our weekly facetimes. To my mom- thank you for fostering a love of reading and learning, instilling the importance of accountability, and reminding me (many times) to take a breath when school was overwhelming. To my dad- thank you for watching CSI with me at a young, impressionable, age because my interest in science stemmed from those Sunday mornings. Thank you for always making me laugh and (in a roundabout way) for my passion to develop better diagnostics.

I have been extremely fortunate to go through this journey alongside my fiancé, TJ. Having a partner who understands the stresses and intricacies of graduate school has been invaluable. The late nights, work-weekends, and unexpected hurdles were paralleled with (many) trips to breweries, treasure hunting at yard sales, and adventures through Howell. Thank you for all your support and encouragement through the years. Thank you for bringing light to my darkest days, as Ed Sheeran says, “In this chaos, you're my calm; And I will find my feet again; 'Cause even the worst days of my life will always end; At midnight in your arms.” You have made me a better scientist and person, thank you.

Going back to my roots in rural Maine was the best reminder to slow down. For an only child, I have a pretty big family so it may be easier just to thank the small town of Hollis. I'd like to thank Faith (aka Aunnie) for her constant support through college and grad school because it really means the world to me. I've watched my cousins Amelia and Lulu grow up through facetime and I'd like to thank them (and I guess Chad by association) for always keeping me entertained. These girls are the reason I keep going on hard days. How lucky am I to have been able to share this journey with my grandparents! To my Nana and Papa, thank you for your constant encouragement ("you'll get through it") and for our shared excitement to hang out whenever I come home. To my Grammie, thank you for calling to check in and keeping me updated with the Hollis happenings. To my great grandfather, thanks for suggesting we venture to the Upper Peninsula! To my aunts and uncles: Faith, Chet, Chad, Geoff, Diane, Mike, Kelly, Robbie, Sonny, and Sam, thank you for the encouraging messages through the years and for letting me talk science every now and then. Don't worry, that's not stopping anytime soon. To my cousins: Mikey, Zac, Jared, Tayte, Gabe, Amelia, Lulu, Lydia, and Sammy, thanks for the laughs when I'm home, hopefully you think this is cool or something. I would also like to thank my future family, the Delano clan, for supporting TJ and I through the entirety of grad school.

I would like to take a moment to thank the mentors I have been fortunate to have advise me through college, industry, and graduate school. Dr. Aren Gerdon served as my research advisor at Emmanuel College and has, more importantly, been one of the greatest influences in my career. I may not have realized my passion for analytical science without such a supportive undergraduate research experience and I truly believe being invited to join the GRAB Lab team meetings in my sophomore year was the most pivotal point in my journey to where I am today. Dr. Gerdon's unwavering support has been incredibly important, and I cannot thank him enough

for instilling in me that *there is no such thing as a failed experiment*. Thank you to my professors and faculty mentors at Emmanuel College who helped me succeed as a first-generation college student. My bosses at Matrivax, Dr. Rob Cartee and Dr. Christian Tooley, really helped grow my confidence as a bioanalytical scientist by allowing me to take ownership of so many projects in my brief year at the company. I am so thankful for their support as I applied to grad school.

Dr. Ryan C. Bailey (a real doctor, btw) has served as my research advisor for these wildly unpredictable past five years. I'd like to thank him for his support, and for genuinely being a real human and a caring boss. He allowed me to take ownership of several projects early on and develop as a leader in the lab and in our collaborations. Graduate school was a wild journey, but I'm forever grateful that I went on the wild journey as part of the Bailey Lab. My first graduate student mentor, Dr. Cole Chapman, was the reason I joined the Bailey Lab (really it was the clinical applications but don't tell him that). Cole taught me many important things in the lab, like how to use the Matchbox instrument and work up the data, but even more important things out of the lab, like to have a healthy work-life balance and that you can't trust him when he says he's from a 'small town'. Thank you for being a great mentor and friend. I was very fortunate to have Bailey Lab alum, Dr. Abraham Qavi, serve as a collaborator-turned-mentor-turned-friend. Abe pushed me to think about my future even when I didn't want to and always has a great answer to any question I have. Sorry I'm not moving to California; guess you'll have to find a conference on the east coast!

To my lab mates- what a ride! To the six senior students when I joined to lab- Cole, Sarah, John, Emily, Shannon, and Colleen, thank you for teaching me the ways of lab and providing (often unsolicited) grad school advice. Once that crew graduated, we were left as a group of six. To the five I spent the most time with- Gloria, Nico, Marina, Claire, and Nick, I

would not have made it through without you guys. I credit these people with getting me through the hardest parts of graduate school. Watching them all graduate and move into their careers was so rewarding. Gloria- our GRC roomie adventure through Boston is a top memory. Thank you for being true to yourself and allowing me into your journey through grad school and life beyond. Nico- thank you for being the best proponent of enjoying life outside of work, our coffee walks pulled me together on many occasions. I'm grateful for your levelheaded perspective (and fancy engineering tape measure) you brought anytime I asked you for help troubleshooting problems. Marina- my days were better when they began with our hour-long recap of the previous day's activities. Thank you for being a listening ear, validating my frustrations, and making me a better scientist. I'm excited for our future adventures in New England and Indy- as long as there is Dunks involved. Claire- thank you for bringing your positive energy anytime I needed to work out a problem. Driving from Howell was way more fun with you and I'm grateful for all of our shared driving and life adventures. And also, thanks for Thomas, he's pretty cool and is super good at relieving stress! Nick- thank you for teaching me the importance of not taking grad school too seriously. I envy your ability to portray a sense of calm in stressful situations. To my favorite undergrad, Sam, thanks for bringing your young energy (and pantone color of the year) into lab. You are going to do great things.

To the new generation of Bailey Lab members- Ayush, Manik, Hanyu, and Lindsay, thank you for being an absolutely fantastic group of lab mates over the past year. Your positive encouragement has been instrumental to getting through this dissertation. The directions you are taking these projects is exciting and I wish you all continued success. Thank you all for the work you put into my defense (S/O Ayush and Manik for being tech support and putting up with a very stressed me) and the celebration after. I appreciated it more than you know! I'd like to thank

Manik for his help this past year and wish him the best of luck in the continuation (or not) of these projects. Finally, to the newest members of the lab- Anusha, Antigone, Camilla, and Hannah, your positive energy this past semester made coming into lab so fun and I'm so excited to see all the work you accomplish here.

I would like to thank my friends outside of lab who I could not have done this without. To my cohort friends- Hayley, Judy, Rebecca, Ina, Laura, Rosie, Danielle, Betsy, and Natalie by proxy, thank you for the many happy hours during pre-pandemic days. Hayley- our weekly lunches are the only reason I've gotten through this year, honestly. Judy- your random gossip texts and bagel Wednesday updates kept me going. To my college friends- Kellie, Vicky, Tanner, Jenn, Kat, Steph, Islam, and Dave, thanks for keeping it real, getting me through p chem, and sending me funny videos. Kellie, Vicky, and Tanner, thank you guys for being lights in my life and always making sure I know I'm supported. I can't wait until we are reunited! To my high school friends- Katie, Anna, Kristen, Hilary, Z, and Corey, thanks for staying connected through the many moves we have made. Your excitement for any of my accomplishments meant the world to me. You are all fantastic humans.

I'd like to end with a list of random things that brought me joy through these five years. Shoutout to Ed Sheeran, skinny pop popcorn, NCAA gymnastics, Bones, my houseplants, the smell of the ocean, holiday festivities, Dunkin Donuts, the Hamilton soundtrack, Block Brewing Company, the Group-X workout classes, Criminal Minds, my heating pad, Friends, sunshine in February, hot chocolate, sports, commutes without traffic, Armchair Expert podcast, Saturdays, sunflowers, our pet fish, the Today show, and my air fryer.

Finally, shoutout to all the first-generation college kids: it's hard but it's worth it.

Table of Contents

Dedication	ii
Acknowledgements	iii
List of Tables	xii
List of Figures.....	xiv
List of Abbreviations and Acronyms	xviii
List of Appendices.....	xxiii
Abstract.....	xxiv
Chapter 1 An Introduction to Inflammatory Protein Biomarkers and Multiplexed Detection Methods	1
1.1 Author Contributions and Acknowledgements.....	1
1.2 Why are we studying biomarkers? The economic and industrial impacts of biomarkers. .	1
1.3 What are biomarkers? A summary of application-based classifications.	3
1.4 Overlapping applications of biomarkers.....	10
1.5 Non-specific biomarker signatures	12
1.6 Inflammatory protein signatures as diagnostic biomarkers	14
1.7 Cytokines as non-specific biomarkers in infectious diseases	20
1.8 Multiplexed assays for cytokine detection.....	21
1.9 Silicon photonic microring resonators as a sensing platform	28
1.10 Dissertation Summary.....	36
1.11 Figures.....	40
1.12 References.....	47
Chapter 2 Detection of Biomarkers for Filoviral Infection with a Silicon Photonic Resonator Platform.....	56
2.1 Author Contributions and Acknowledgements.....	56
2.2 Abstract.....	57
2.3 Before You Begin	57
2.4 Step-By-Step Method Details	60
2.5 Expected Outcomes	70
2.6 Quantification and Statistical Analysis.....	71

2.7 Limitations	76
2.8 Troubleshooting	76
2.9 Figures.....	80
2.10 Tables.....	84
2.11 References.....	89
Chapter 3 Rapid Detection of an Ebola Biomarker with Optical Microring Resonators.....	90
3.1 Author Contributions and Acknowledgements.....	90
3.2 Abstract.....	91
3.3 Introduction.....	91
3.4 Methods.....	94
3.5 Results.....	97
3.6 Discussion	102
3.7 Conclusion	106
3.8 Figures.....	107
3.9 Tables.....	114
3.10 References.....	118
Chapter 4 Chorioamnionitis-Exposure Alters Serum Cytokine Trends in Premature Neonates.....	123
4.1 Author Contributions and Acknowledgements.....	123
4.2 Abstract.....	124
4.3 Introduction.....	124
4.4 Methods.....	126
4.5 Results.....	132
4.6 Discussion.....	135
4.7 Conclusion	142
4.8 Figures.....	144
4.9 Tables.....	153
4.10 References.....	162
Chapter 5 Comparison of Two Subject Cohorts Towards Development of a Multi-Biomarker Approach to Latent Tuberculosis Infection and Risk Assessment.....	166
5.1 Author Contributions Acknowledgements	166
5.2 Abstract.....	167
5.3 Introduction.....	168
5.4 Methods.....	174
5.5 Results and Discussion	186
5.6 Study Limitations.....	205

5.7 Conclusion	207
5.8 Figures.....	209
5.9 Tables.....	221
5.10 References.....	225
Chapter 6 Multiplexed Protein Detection Platform for Diagnosing Latent Tuberculosis and Stratifying Risk of Reactivation	233
6.1 Author Contributions and Acknowledgements.....	233
6.2 Introduction.....	234
6.3 Methods.....	238
6.4 Results.....	247
6.5 Discussion.....	252
6.6 Conclusion	259
6.7 Figures.....	260
6.8 Tables.....	268
6.9 References.....	276
Chapter 7 Analytical Considerations for Future Development of Longitudinal, Multi-Biomarker Assays: Dilution Effects, Combination Assays, and Stability Studies.....	283
7.1 Author Contributions and Acknowledgements.....	283
7.2 Introduction.....	283
7.3 Methods.....	293
7.4 Results and Discussion	303
7.5 Limitations and Future Directions	329
7.6 Conclusion	330
7.7 Figures.....	332
7.8 Tables.....	344
7.9 References.....	347
Chapter 8 Dissertation Summary, Side Projects, and Future Directions (oh my!)	350
8.1 Author Contributions and Acknowledgements.....	350
8.2 Dissertation Summary.....	351
8.3 Short-lived side projects	353
8.4 Future Directions	362
8.5 Concluding Remarks.....	385
8.6 Figures.....	387
8.7 References.....	390
Appendices.....	395

List of Tables

Table 2.1 Key resources table with materials and equipment used in this protocol.	84
Table 2.2 Calibration standard preparation for EBOV sGP and SUDV sGP in a serum matrix. .	86
Table 2.3 96-well plate set up for immunoassay on Matchbox instrument.	87
Table 2.4 Example recipe for immunoassay on Matchbox instrument.	88
Table 3.1 Fitting parameters used in generating calibration curves in Figure 3.5 for EBOV and SUDV sGP with a logistic function, Eq.1.....	114
Table 3.2 Matrix blank parameters from the calibration curves in Figure 3.5 for EBOV and SUDV sGP to determine the limit-of-detection (LOD).	115
Table 3.3 EBOV sGP concentrations in NHP samples shown in Figure 3.6, percent error in comparison to ELISA data, and days post infection at time of sample collection.	116
Table 4.1 Functions of the selected cytokine panel markers.	153
Table 4.2 Reagents used in the multiplexed assay.....	154
Table 4.3 Limits of detection (LODs) of the 7-plex panel calculated as the concentration corresponding to the signal from the blank sample plus three times the standard deviation of the blank, using data from the two respective matrix calibrations.	155
Table 4.4 Subject characteristics.....	156
Table 4.5 Comparison of chorioamnionitis-exposed and unexposed preterm neonatal cytokine and chemokine levels over the first month of life using Generalized Estimating Equations.	158
Table 5.1 Patient demographics by pertinent clinical categories for cohort 1.....	221
Table 5.2 Patient demographics by pertinent clinical categories for cohort 2.....	223
Table 6.1 Demographic data of the patients enrolled in the LTBI study.....	268
Table 6.2 Median values of absolute and normalized cytokine levels between LTBI negative and LTBI positive patients.....	270
Table 6.3 Median values of absolute and normalized cytokine levels between low-risk and high-risk designated patients within the LTBI+ patient population.	273

Table 7.1 Average and standard deviation (pg/mL) in the x_0 value of the calibration curves for 50% plasma and 10% plasma calibrations.....	344
Table 7.2 Average and standard deviation of the maximum value (A) and minimum value (B) in picometers of the calibration curves for 50% plasma and 10% plasma calibrations.....	345
Appendix Table A-1 Recruitment of Coaches and Coachees.....	419
Appendix Table A-2 Summary of Coachee’s goals by program year and retrospective theme categorization.....	420
Appendix Table A-3 Recommended coaching schedule throughout the semester.....	421
Appendix Table A-4 Timeline of coaching training and description of content discussed in each session.....	422
Appendix Table A-5 Recruitment of coaches and coachees by year.....	423
Appendix Table B-1 Documented information for the antibody and standard reagents used in this thesis.....	427
Appendix Table B-2 Documented information for the assay reagents used in this thesis.	430

List of Figures

Figure 1.1 Summary of biomarker classifications by application.	40
Figure 1.2 Diagram of cytokine cascade involving interferons, tumor necrosis factors, and interferon cytokine biomarkers.	41
Figure 1.3 Conventional sandwich style ELISA.....	42
Figure 1.4 Simple-Plex Ella Platform.....	43
Figure 1.5 Luminex multiplexed bead-based assay workflow.	44
Figure 1.6 Quanterix Simoa bead and planar array technologies.	45
Figure 1.7 Microring resonator multiplexed assay.	46
Figure 2.1 Sensor chip silanization diagram.....	80
Figure 2.2 24-well plate set up during sensor chip functionalization.	81
Figure 2.3 Diagram of sensor array on microring chips.	82
Figure 2.4 Example data post-work up.....	83
Figure 3.1 Ebola virus genome, generation of sGP, and comparison of EBOV RT-PCR versus sGP values during infection.	107
Figure 3.2 Microring resonator diagram.....	108
Figure 3.3 Sensor traces and calibration curves for EBOV sGP for both primary binding of sGP and enzymatic amplification.	109
Figure 3.4 Schematic of sGP detection assay.....	110
Figure 3.5 Cross reactivity of microring resonators and calibration curves.	111
Figure 3.6 Detection of sGP from EBOV infected non-human primate (NHP) samples.	112
Figure 3.7 Comparison of ELISA and microring resonator platform performance.	113

Figure 4.1 Comparison of cytokine and chemokine levels by chronologic age in chorioamnionitis only (black circles) and chorioamnionitis plus funisitis (white circles) exposed preterm neonates.	144
Figure 4.2 Overview of multiplexed immunoassay method and calibration.	145
Figure 4.3 Comparison of cytokines and chemokines obtained in the first and second weeks of life in preterm neonates.	146
Figure 4.4 Longitudinal cytokine and chemokine trends over time in chorioamnionitis-exposed and unexposed preterm neonates.	147
Figure 4.5 Longitudinal cytokine and chemokine trajectories over time in chorioamnionitis-exposed and unexposed preterm neonates.	148
Figure 4.6 Comparison of serum cytokine and chemokine levels at the time of diagnosis of bacterial sepsis or necrotizing enterocolitis in preterm neonates.	149
Figure 4.7 Longitudinal profiles of cytokine and chemokine levels for subjects with necrotizing enterocolitis diagnosis and treatment.	150
Figure 4.8 Longitudinal profiles of cytokine and chemokine levels for subjects with sepsis diagnosis and treatment.	151
Figure 4.9 Longitudinal profiles of cytokine and chemokine levels for subjects with urinary tract infection diagnosis and treatment.	152
Figure 5.1 Random forest model results for Cohort 1: 42 patients with 45 subject sets.	209
Figure 5.2 Random forest model results for Cohort 2: 72 patients with 87 subject sets.	210
Figure 5.3 Comparison of models across the two subject cohorts.	211
Figure 5.4 Comparison of biomarkers across cohorts, stratified by LTBI status, for the NIL condition.	212
Figure 5.5 Comparison of biomarkers across cohorts, stratified by LTBI status, for the TB1 condition.	213
Figure 5.6 Comparison of biomarkers across cohorts, stratified by LTBI status, for the MIT condition.	214
Figure 5.7 Comparison of biomarkers across cohorts, stratified by LTBI status, for the TB1-NIL normalized condition.	215
Figure 5.8 Comparison of biomarkers across cohorts, stratified by LTBI status, for the TB1-MIT normalized condition.	216

Figure 5.9 Comparison of biomarkers across cohorts, stratified by LTBI status, for the MIT-NIL normalized condition.....	217
Figure 5.10 Paired comparisons of cytokine values within TB1 and TB2 stimulations, stratified by LTBI status.....	218
Figure 5.11 Paired comparisons of cytokine values within TB1 and TB2 stimulations, stratified by high-risk status.....	219
Figure 5.12 Random forest model results for secondary cohort including the QFT TB2 stimulation.....	220
Figure 6.1 LTBI classification using absolute cytokine levels.....	260
Figure 6.2 Absolute cytokine concentration distribution between LTBI positive and negative populations.....	261
Figure 6.3 LTBI classification using normalized cytokine levels.....	262
Figure 6.4 Normalized cytokine concentration distribution between LTBI positive and negative populations.....	263
Figure 6.5 High and low reactivation risk stratification.....	264
Figure 6.6 Cytokine concentration distribution between high risk and not high-risk populations within LTBI positive subjects.....	265
Figure 6.7 Cytokine concentration distribution between low risk and not low-risk populations within LTBI positive subjects.....	266
Figure 6.8 Significantly different absolute concentration distributions between high-risk and low-risk LTBI positive patients.....	267
Figure 7.1 Diagram of a data collection workflow relevant to LTBI sample processing.....	332
Figure 7.2 Variation in the 10% plasma calibration between sensor chip decks.....	333
Figure 7.3 Variation in the 50% plasma calibration between sensor chip decks.....	334
Figure 7.4 Comparing calibrations for both matrix calibrations.....	335
Figure 7.5 Alluvial diagram to visualize dilution selection across the LTBI patient sample set.....	336
Figure 7.6 Intra-chip batch stability.....	337
Figure 7.7 Example of shifted calibration curve.....	338
Figure 7.8 Diagrams of different assay designs tested to shift the IL-8 calibration curve.....	339

Figure 7.9 Shifting IL-8 calibration using the non-biotinylated tracer assay design.....	340
Figure 7.10 Shifting IL-8 calibration by altering spotting concentration of capture Ab.	341
Figure 7.11 Shifting IL-8 calibration by altering the assay format with streptavidin (SA) coated beads.	342
Figure 7.12 Shifting IL-8 calibration by altering the assay design with HRP-conjugated tracer antibodies.	343
Figure 8.1 COVID-19 immunoprofiling project summary.....	387
Figure 8.2 Tango monobody project summary.....	388
Figure 8.3 Ring-drops project summary.	389
Appendix Figure A-1 Coaching Cycle.	416
Appendix Figure A-2 Example recruitment materials.....	417
Appendix Figure A-3 Examples of team developed resources.....	418

List of Abbreviations and Acronyms

4-CN	4-chloro-1-naphthol
AAALAC	Association of Assessment and Accreditation of Laboratory Animal Care
Ab	Antibody
AIC	Akaike information criteria
APTES	(3-Aminopropyl)triethoxysilane
AUC	Area under the curve
BDBV	Bundibugyo ebolavirus
BS3	Bis(sulfosuccinimidyl)suberate
BSA	Bovine Serum Albumin
BSL	Biosafety Level
Bt	Biotin
Bt-Ab	Biotinylated antibody
CCL2	C-C motif chemokine ligand 2, monocyte chemoattractant protein 1, MCP-1
CCL3	C-C motif chemokine ligand 3, macrophage inflammatory protein 1- α , MIP-1 α
CCL4	C-C motif chemokine ligand 4, macrophage inflammatory protein 1- β , MIP-1 β
CCL8	C-C motif chemokine ligand 8, monocyte chemoattractant protein 2, MCP-2
CDC	Center for Disease Control
CFP-10	Culture filtrate protein 10
COVID-19	Coronavirus disease 2019

DE	Double emulsion
DNA	Deoxyribonucleic acid
EBOV	Zaire ebolavirus
ED	Emergency department
ELISA	Enzyme linked immunosorbent assay
ESAT-6	Early secretory antigenic target protein 6
EVD	Ebola virus disease
GM-CSF	Granulocyte-macrophage colony-stimulating factor, colony-stimulating factor 2
GP	Glycoprotein
HRP	Horse radish peroxidase
IACUC	International animal care and use committee
IFN- γ	Interferon gamma
IgG	Immunoglobulin G
IGRA	Interferon gamma release assay
IL-1 β	Interleukin 1 β
IL-1Ra	Interleukin 1 receptor antagonist protein
IL-2	Interleukin 2
IL-3	Interleukin 3
IL-6	Interleukin 6
IL-8	Interleukin 8, C-X-C motif chemokine ligand 8, CXCL8
IL-10	Interleukin 10, human cytokine synthesis inhibitory factor
IL-12(p40)	Interleukin 12 subunit p40, natural killer cell stimulatory factor 2
IL-13	Interleukin 13

IL-15	Interleukin 15
IL-17	Interleukin 17, IL-17A
IP-10	Interferon gamma-inducible protein 10, C-X-C motif chemokine ligand 10, small inducible cytokine B10, CXCL10
LOD	Limit of detection
LOQ	Limit of quantitation
LPS	Lipopolysaccharide
LTBI	Latent tuberculosis infection
mAb	Monoclonal antibody
MARV	Marburg virus
Mb	Monobody
MCSF	Macrophage Colony Stimulating Factor 1
MDR-TB	Multi drug resistant tuberculosis
µg	Microgram
µL	Microliter
mg	Milligram
min	Minute
MIT	Mitogen, positive control in QuantiFERON test
mL	Milliliter
mM	Millimolar
Ms IgG	Mouse immunoglobulin G
Mtb	Mycobacterium tuberculosis
NaCl	Sodium chloride

ng	Nanogram
NHP	Non-human primate
NICU	Neonatal Intensive Care Unit
NIL	Negative control in QuantiFERON test
nm	nanometer
non-Bt-Ab	non-biotinylated antibody
PBMC	Peripheral blood mononuclear cell
PBS	1X Phosphate buffered saline
PBS-BSA	1X Phosphate buffered saline with 0.05% bovine serum albumin, running buffer
PBS-T	1X Phosphate buffered saline with 0.05% tween 20
PCR	Polymerase chain reaction
PDMS	Polydimethylsiloxane
PFU	plaque-forming unit
pg	Picogram
pm	Picometer
pM	Picomolar
PTB	Preterm birth
QFT	QuantiFERON Gold In-tube test
QFT-Plus	QuantiFERON Gold In-tube Plus test
qRT-PCR	Quantitative reverse transcription polymerase chain reaction
RBD	Receptor binding domain
rcf	relative centrifugal force
RI	refractive index

RNA	Ribonucleic acid
ROC	Receiver Operator Characteristic
SA	Streptavidin
SA-HRP	Streptavidin horse radish peroxidase
SARS-CoV-2	Severe acute respiratory syndrome Coronavirus 2
SDOH	Social determinants of health
SE	Single emulsion
sGP	soluble glycoprotein
SUDV	Sudan ebolavirus
TAT	Turn Around Time
TB	Tuberculosis
TB1/AG	TB specific stimulation 1 in QuantiFERON test
TB2	TB specific stimulation 2 in QuantiFERON test
TMB	3,3',5,5'- Tetramethylbenzidine
TNF- α	Tumor necrosis factor α
TST	Tuberculin skin test
USARMIID	United States Army Medical Research Institute of Infectious Diseases
VEGF	Vascular endothelial growth factor, vascular permeability factor
WGM	Whispering-gallery mode
WHO	World Health Organization
WMW	Whicoxon-Mann-Whitney test, two-sample Wilcoxon rank-sum test, Mann-Whitney U test

List of Appendices

Appendix A: Chemistry Instructional Coaching: Adapting a Peer-Led Professional Development Program for Chemistry Graduate Teaching Assistants	396
Appendix B: Record of Sandwich-Style Microring Assay Reagents Used in this Thesis.....	427

Abstract

Laboratory-based biomarkers can indicate that normal biologic functions, pathogenic processes, or immunologic responses have occurred. Diagnostic biomarkers are used to diagnose patients with a specific disease or condition, while prognostic biomarkers provide information on disease progression, recurrence, or adverse outcome. Host inflammatory proteins, such as cytokines, can be employed as diagnostic and prognostic biomarkers; however, due to the complex nature of an inflammatory response, multi-biomarker signatures increase clinical utility. The need to identify and validate protein signatures for specific diseases is driving a need for analytical techniques amenable to multiplexed protein detection.

This thesis applies silicon photonic microring resonators as a biomolecular sensing platform. The instrument and assay method are amenable for multiplexed detection of sixteen analytes in two samples simultaneously, using automated reagent handling and featuring a time-to-result of 45 minutes. Herein, I describe the development and application of multiplexed protein biomarker assays to diagnose and identify biomarker signatures for various infections. To improve rapid diagnostic approaches in the field of filoviral infection, we developed a two-plex biomarker assay for diagnosis of Zaire ebolavirus and Sudan ebolavirus infections using the pathogen-specific soluble glycoprotein (sGP). The sGP is a potential early diagnostic and prognostic biomarker of infection and, when coupled with the microring resonator assay, provides a fast, sensitive method for early Ebola infection diagnosis. The assay achieved limits of

detection in the ng/mL range, exhibited no cross-reactivity, and successfully detected sGP in clinically relevant specimens (Chapter 2 and 3).

Exploration of host inflammatory biomarker signatures was applied to expand the diagnostic and prognostic toolbox of neonatal conditions (Chapter 4) and tuberculosis infections (Chapters 5 and 6). We employed a seven-plex panel to temporally measure cytokine profiles in over sixty preterm neonates and identified altered cytokine trends in neonates exposed to inflammation *in utero*. Our work highlights the potential of longitudinal profiling studies to identify prognostic or monitoring biomarkers associated with infection status. Extending this multiplexed profiling approach to an infectious disease, we applied a fourteen-plex cytokine panel to profile over 500 QuantiFERON stimulated plasma samples from patients with latent tuberculosis infection (LTBI) with the goal of generating multi-biomarker signatures for LTBI diagnosis and disease reactivation prognosis. In comparing two independent patient cohorts, we showed a high overlap in important biomarkers, mainly IP-10, IL-2, and CCL8, towards classifying LTBI and high-risk of reactivation status. After merging cohorts to increase sample size, we uncovered a set of biomarkers capable of classifying LTBI status with 87% accuracy. Importantly, we identified a panel of biomarkers that can be used to stratify low versus high risk of reactivation and conclude that a group of eight host inflammatory protein biomarkers should be considered for future LTBI diagnostic platform development. Further analysis of multiplexed assay calibrations yielded insight into expected analyte- and sensor batch-related variability (Chapter 7). Targets IL-6, CCL3, and CCL8 were the most robust assays and should be used as comparisons for newly generated calibration curves.

Taken together, the work presented in this thesis applies analytical techniques to clinically relevant challenges through rapidly detecting an early biomarker of Ebola virus

infection, monitoring immunological changes in preterm neonates, and identifying host immune biomarkers correlated to disease phase and reactivation risk in LTBI. The assays and biomarker signatures presented here have the potential to impact diagnosis, prognosis, and clinical management of infections and infectious diseases.

Chapter 1 An Introduction to Inflammatory Protein Biomarkers and Multiplexed Detection Methods

1.1 Author Contributions and Acknowledgements

The content of this chapter was conceived, and all figures were designed by the thesis author, Krista Meserve. Section 1.9 is adapted from a subsection of the published review: Yu, D.; Humar, M.; **Meserve, K.**; Bailey, R. C.; Chormaic, S. N.; Vollmer, F. [Whispering-Gallery-Mode Sensors for Biological and Physical Sensing](#). *Nat Rev Methods Primers* **2021**, 1 (1), 83. I would like to thank Dr. Deshui Yu, Dr. Matjaž Humar, Dr. Síle Nic Chormaic, and Dr. Frank Vollmer for including our microring resonator sensing subsections in the review, and Dr. Ryan Bailey for his feedback and edits on that section prior to publication. I would additionally like to thank Dr. Claire Cook and Dr. Gloria Diaz for their feedback on this chapter.

1.2 Why are we studying biomarkers? The economic and industrial impacts of biomarkers.

Biomarker research is a rapidly growing area of profit and investment. The term initially gained traction in 2005 and has increasingly garnered interest.¹ In 2022, the global biomarker market was valued at 66.97 billion dollars and is expected to continue to grow at a compounded annual growth rate of 13.3% over the next seven years to over 180 billion dollars in 2030.² The increase in biomarker discovery research has been linked to the growing interest in personalized medicine, the increased prevalence of cancer and cardiovascular diseases — which both require biomarkers for early detection, prognosis, and treatment efficacy — and a rise in safety biomarkers for more effective clinical trials.

The key players aiming to increase their biomarker industry share include Abbott, Roche, Thermo Fisher Scientific, Qiagen, and Bio-Rad. Abbott's biomarker discovery work in traumatic brain injury (TBI) blood tests has led to FDA clearance of the first commercially available blood-based TBI test which is compatible with their Alinity i instrument found in many hospital laboratories.³ The semi-quantitative test measures two proteins with chemiluminescent microparticle immunoassays and provides information on TBI severity with 96.7% sensitivity in 18 minutes.^{4,5} Abbott's TBI assay possesses the potential to rapidly triage patients, reduce reliance on subjective clinical assessments, and eliminate unnecessary CT scans. Combined, these implications can cut healthcare costs and time spent in the emergency department.

In late 2022, Qiagen announced FDA approval of their *therascreen* KRAS kit for identifying non-small cell lung cancer (NSCLC) patients eligible for treatment with KRAZATI.⁶ Mutations in the KRAS oncogene are predictive biomarkers of a patient's responsiveness to the treatment. Qiagen has repurposed their existing assay technology to be a leader in rapidly developing predictive and diagnostic biomarker assays across multiple cancer therapy studies. Quanterix, developers of the ultrasensitive single molecule array (Simoa) bead-based immunoassay technology, have been granted a Breakthrough Device designation from the FDA for a semiquantitative Simoa immunoassay for P-Tau 181 to aid in diagnostic evaluation of Alzheimer's Disease.⁷ The assay detects the biomarker in blood samples using their commercialized HD-X instrument. Furthermore, Quanterix has developed multiplexed assays, such as the three-plex assay of total tau, amyloid β 1-42 and amyloid β 1-40, currently being used in development of blood-based Alzheimer's diagnostics.⁸⁻¹⁰

These few examples highlight the important role biomarkers have in improving diagnostics and patient care, expanding business plans, and impacting the overall economy.

Considering the far-reaching impact of biomarkers in clinical settings, it is important to understand how biomarkers are defined, classified, and detected within clinically relevant contexts.

1.3 What are biomarkers? A summary of application-based classifications.

The FDA-NIH Biomarker Working Group officially defines a biomarker as “a defined characteristic that is measured as an indicator of normal biological processes, pathogenic processes, or biological responses to an exposure or intervention.”¹¹ With this definition, there is a wide range of interpretations of what constitutes a biomarker. Biomarkers can include molecular, histologic, radiographic, or physiologic characteristics. They can be classified by the type of measurement: extrinsic markers, such as cigarette or drug use, intrinsic markers, such as physical evaluation (signs and symptoms), psychological evaluation (Likert scales or lifestyle questionnaires), or laboratory evaluation.¹ We classically associate molecular clinical diagnostics with biomarkers categorized under laboratory evaluation. These types of biomarkers include biochemical, hematological, immunological, microbiological, histological, radiographic, and genetic.¹

Biomarkers can additionally be defined and categorized into subtypes based on their specific use or application.¹² Many of the subtypes are mentioned through this thesis within the context of a specific purpose. It is important to note that the same biomarkers can serve cross functional purposes, as a single biomarker can meet criteria for different uses. The application-based biomarker subtypes are diagnostic, monitoring, response, predictive, prognostic, safety, and susceptibility/risk.^{11,12} Here, we will define and provide examples of each of these biomarker classifications. The work presented throughout this dissertation provides applications of almost

all subclasses: diagnostic (chapters 3, 5 and 6), monitoring (chapter 4), response (chapter 4), prognostic (chapters 3, 5, and 6), and susceptibility (chapters 5 and 6).

1.3.1 Diagnostic biomarkers

A diagnostic biomarker is used to confirm disease, subtype of disease, or a specific condition.¹² Diagnostic biomarkers must be specific to the disease of interest and should provide clinical utility. Establishing cut-off values of these biomarkers is a critical step in developing diagnostic tests and is highly dependent on the disease or condition. A test with a high false positive rate might be allowable for diseases with easy or non-invasive follow up tests or for extremely infectious disease, as a low false negative rate should be minimized. Conversely, a low false positive rate is more critical for rare disease, as they should not be over diagnosed in the general population, or for diseases with physically or mentally intense repercussions, as diagnosis or treatment after a false positive can be life altering. Receiver-operator characteristic (ROC) curves are used to quantify the ability of a biomarker to classify subjects in disease categories.¹³ ROC curves plot the sensitivity and specificity at various cut-off values of the biomarker(s) and the area under the ROC curve (AUC) is representative of the diagnostic marker's overall accuracy to distinguish disease positive from disease negative populations.

Examples of diagnostic biomarkers specific to an infection or condition include the spike and nucleocapsid proteins of SARS-CoV-2 infection,^{14,15} cardiac troponin T and cardiac troponin I for myocardial infarction,¹⁶ and the soluble glycoprotein of filoviruses for filoviral infection.¹⁷ Detection of these biomarkers is specific to the associated disease. Similarly, a combination of microRNAs miR-141-3p, miR-375-3p, and let-7a can differentiate prostate cancer patients who are in remission, those with advanced localized disease, and those with advanced metastatic cancer.¹⁸ These are classified as diagnostic biomarkers due to their association with a specific

phase of disease. **Figure 1.1A** depicts a diagnostic biomarker that confirms disease, as the concentration of analyte is statistically different between a non-disease population compared to a population with the disease. The analyte additionally separates disease populations by stage or phase of disease, adding further utility to the diagnostic biomarker.

1.3.2 Monitoring biomarkers

Monitoring biomarkers measure the effects of disease, treatment, or exposure over time.^{11,12} Gaining clinically relevant information for patient status through serial measurements of the marker qualifies biomarkers to the monitoring designation. Repeated measurements give clinicians information about the rate or magnitude of biomarker change in addition to absolute concentration. Patients are commonly monitored for a change in status of their condition during a clinical treatment course, effects of treatments on overall organ function, and overall health.

Figure 1.1B depicts a monitoring biomarker that decreased in concentration at disease onset but increased with treatment. This example biomarker could be used to follow disease progression, as well as a patient's response to treatment.

Glucose is a monitoring biomarker for patients with diabetes. Detection technology has been employed in wearable devices with user-friendly, mobile device readouts.¹⁹ Continuous glucose monitoring alerts patients to changes in blood sugar levels to make decisions in day-to-day activities and the compiled data can be shared with a medical doctor to monitor and prevent diabetes-associated complications. Other examples of monitoring biomarkers include evaluating protein changes in mice following a TBI to understand pathological rebuilding processes and long-term effects,²⁰ or measuring microRNA-371a-3p in patients with testicular germ cell tumors over the course of chemotherapy.²¹

1.3.3 Response biomarkers

Response biomarkers can be used to confirm a biological response has occurred following a specific exposure.^{11,12} Exposures of interest may be a new medical device, environmental antigen, or treatment course. Two further subclasses fall within the response category: pharmacodynamic biomarkers and surrogate endpoint biomarkers. In pharmacodynamic studies, response biomarkers indicate that there is biologic activity after exposure, but the biomarker does not provide information towards clinical utility of the exposure. **Figure 1.1C** depicts a pharmacodynamic response biomarker. The biomarker concentration in the treatment group significantly changed from before and after treatment, while that in the placebo group remained constant. The biomarker change does not mean the treatment or exposure is clinically relevant but indicates there is some biologic response. As an example, the response to warfarin therapy is measured via the prothrombin test time and concentration of coagulation biomarkers.^{22,23}

The other classification of response biomarkers, surrogate endpoint biomarkers, are short-term biomarkers associated with long-term clinical outcomes based on previous scientific evidence and are imperative to conducting clinical trials for therapeutics. An example is a study by Meyvisch et al. that compared sputum culture conversion at weeks 8 and 24 in a drug trial for multidrug resistant- tuberculosis.²⁴ The true endpoint was the patient outcome after the 120-week drug administration, but they concluded the culture conversion results at week 24 was a sufficient surrogate endpoint to evaluate the drug treatment in a patient. This would allow for treatment adjustment before the full 120-week course is completed to increase treatment efficacy. Response biomarkers can additionally be used as biomarkers of potential harm, which are short-term biomarkers that can measure the early effects of exposures and potential health risks in the absence of long-term, epidemiologic-based, definitive endpoints.²⁵ A prominent

example is in tobacco use research. The true endpoints in this research population are severe (lung cancer, cardiovascular disease, chronic obstructive pulmonary disease), but surrogate endpoints related to the severe disease states can be measured when evaluating new tobacco products for the market.²⁶

1.3.4 Predictive biomarkers

Predictive biomarkers are those whose presence, or change in, indicate whether patients will respond (favorably or unfavorably) to an exposure or treatment.^{11,12} These biomarkers can be used to guide treatment decisions, select patient populations to enroll in clinical trials, or identify groups most likely to benefit from lifestyle interventions. Predictive biomarkers are commonly validated through randomized trials of those with and without the biomarker to compare effects of an experimental treatment in both groups. If one group has a more favorable response to the therapy, then that group would be targeted for clinical trials.

In addition to identifying patients *who will respond* to a treatment, predictive biomarkers can also be used to understand *how they will respond*. In patients with advanced melanoma, sCD163 levels in serum was associated with adverse events in patients receiving nivolumab and baseline IL-6 serum concentrations greater than 2.5 ng/L was associated with greater toxicity during ipilimumab treatment.^{27,28} **Figure 1.1D** highlights how the presence of these biomarkers in a disease population can tailor treatment dosage or options to individual patients, leading to better personalization of medicine.²⁹ To note, predictive biomarkers are markers whose presence can be used to identify factors associated with efficacy or treatment responses in patients already classified as having a disease (opposed to susceptibility biomarkers) and are not predictive of disease progression or outcome (opposed to prognostic biomarkers).

1.3.5 Prognostic biomarkers

Prognostic biomarkers provide information on disease progression or recurrence, the likelihood of a clinical event occurring, and disease outcome.^{11,12} Prostate specific antigen (PSA) kinetics are used in prognosis, relapse prediction, and as a mortality indicator in men with prostate cancer. A short doubling time indicates a relapse and faster rates have been associated with lower five-year survival rates.³⁰ In some cases, such as in Ebola virus disease, prognostic biomarkers at a specific concentration can be used to stratify patients by mortality risk, allowing for more efficient resource allocation.

In treated patients, prognostic biomarkers can be indicative of recurrence risk. Lower expression of miRNA biomarkers miR-135a and miR-409-3p have been associated with a higher risk of recurrence in an acute myeloid leukemia patient population.³¹ Combinations of other miRNAs provided value to prognosis of overall survival, relapse-free survival, or complete recovery.³² Validation of prognostic biomarkers requires association of the biomarker level at a certain threshold with the outcome of interest. **Figure 1.1E** demonstrates this type of study to associate a biomarker above and below a certain threshold with the percent of patients that did not have disease progression. The patients with the higher biomarker concentration did not progress to disease as readily as those with lower biomarker concentrations, indicating this specific biomarker should be studied in a larger cohort for its efficacy as a prognostic biomarker.

1.3.6 Safety biomarkers

Safety biomarkers are measured before or after an exposure and provide information regarding toxicity of the exposure. Similar to surrogate endpoint response biomarkers, the safety biomarker is unlikely to provide information on clinical efficacy of the treatment or exposure. Common safety biomarkers include those specific to liver or kidney function to determine hepatotoxicity or nephrotoxicity of the therapy over the course of a clinical trial.^{33,34} From a

regulation standpoint, safety biomarkers can be used to evaluate the risk-benefit ratios of drugs or therapies. A therapy that treats an aggressive disease but leads to slight cardiovascular toxicity might be approved as long as the safety biomarker is monitored over the course of treatment.

However, a therapy that treats a common cold but induces kidney failure would not be approved.

The example safety biomarker in **Figure 1.1F** is measured before, during, and after drug removal. There are no significant differences at any time point between the test groups; however, the slight decrease in the treatment group during drug administration should be investigated for potential adverse events that may persist even after the concentration rebounds post-treatment. In addition to drug toxicity and risk-benefit analysis, safety biomarkers can be used like a predictive biomarker to identify which patients are at greater risk of toxic adverse events or who will be most affected by an environmental exposure so appropriate mitigation and intervention strategies can be employed.

1.3.7 Susceptibility biomarkers

A susceptibility biomarker is one that provides information on the potential of a healthy, non-diseased population to develop a condition or illness. These biomarkers are crucial for starting preventative therapies or treatments, changing lifestyle factors, or increasing disease surveillance tests. Many susceptibility, or risk, biomarkers are commonly known. The breast cancer genes 1 and 2 (BRCA1/2) mutations increase the risk of developing breast cancer.

Clinical treatments, such as a mastectomy, or frequent surveillance testing, such as mammograms, can be offered to reduce risk or improve early detection. High LDL cholesterol levels are known to increase risk of coronary artery disease, and patients with high levels can be advised to make lifestyle and nutrition changes or qualified for certain treatments. While not a laboratory biomarker, familial history of certain types of cancer, such as colorectal cancers, can

be susceptibility biomarkers that warrant more aggressive surveillance through colonoscopies.

The example susceptibility biomarker in **Figure 1.1G** would be one whose presence indicates the patient is at high risk of disease onset but does not yet have the disease.

Quantification of a patient's risk of disease was discussed as a function of prognostic biomarkers. The difference between prognostic and susceptibility biomarkers is the target population: those with disease for prognostic and those without disease for susceptibility. Of these two populations, the population who can benefit from susceptibility biomarkers (the general healthy, non-disease population) is much larger than the population of those with a specific disease and may be why the susceptibility biomarker examples are more familiar to a general audience. Identification of general susceptibility or risk biomarkers can lead to public health campaigns in hopes of people being able to prospectively act on their health, rather than retrospectively after progressing to disease.

1.4 Overlapping applications of biomarkers

The seven use-based classifications are not independent of each other, and the same biomarker can be classified under many subtypes. If a biomarker is to be used for multiple purposes, it is imperative that evidence is collected, and validation is completed for each individual use. A biomarker can be both diagnostic and prognostic if it is specific to the disease state and the concentration or rate of change is correlated to outcome or disease progression. A monitoring biomarker within a disease population whose temporal change is indicative of how a patient will respond to a potential treatment would also be a predictive biomarker. Similarly, if the temporal change of a monitoring biomarker can be used as a measure of biologic response to a treatment, that biomarker would also be classified as a response biomarker.

Examples of multi-application biomarkers include the BRCA1/2 mutation, PSA, and P-tau181. As described above, the BRCA1/2 mutation is a susceptibility biomarker among a non-disease population as a factor of increased risk of developing breast cancer. BRCA1/2 can also be a prognostic biomarker, with overexpression related to lower survival rates,^{35,36} and a predictive biomarker for effectiveness of chemotherapy additives³⁶ and treatment^{37,38} options. PSA was discussed above as a prognostic biomarker of prostate cancer relapse and survival, but it is also commonly used as a diagnostic biomarker and is used to monitor patients post-treatment.^{39,40} Alzheimer's disease biomarker discovery research has demonstrated serum levels of P-tau181 can be a diagnostic biomarker to distinguish those with cognitive impairment from cognitive unimpaired populations, as well as a monitoring biomarker for clinical trials and a prognostic biomarker for cognitive decline from cognitive impairment to Alzheimer's disease.^{41,42}

A biomarker validated for one classification can be used to identify biomarkers in other classifications. For example, evaluating various monitoring biomarkers over the course of a treatment administration could lead to identification of biomarkers that correlate to treatment efficacy (predictive biomarkers) or indicate a biological response occurred during treatment (response biomarkers). Quantitation of known diagnostic biomarkers correlated to disease outcome could result in prognostic status. Additionally, biomarkers from distinct classifications are used in tandem. Prognostic biomarkers could be used to identify patients with poor prognosis, and a separate predictive biomarker could qualify them as a candidate for an exploratory treatment specifically for those with aggressive diseases. Similarly, a prognostic biomarker could classify a patient at high risk of disease progression, and a diagnostic biomarker could then be analyzed at frequent time points to monitor changes that could indicate disease

onset, with subsequent treatment to follow. Clinical trials use many biomarkers in tandem, such as measuring response biomarkers to ensure a biologic response, safety biomarkers to ensure low toxicity in the drug, and monitoring biomarkers associated with the drug or disease to measure drug efficacy.

1.5 Non-specific biomarker signatures

A handful of biomarker examples presented in the previous section were directly associated with the condition or infection, such as the spike protein of SARS-CoV-2, soluble glycoprotein in filoviral infection, and BRCA 1/2 mutations of breast cancer. Most biomarkers that have been mentioned were non-specific to the disease state. Instead, they were biologic changes in non-specific patient, or host, biomarkers that can be associated with a condition or infection through large cohort studies. While singular biomarkers can be useful for some applications, specifically in diagnostic and prognostic functions, combinations of specific and non-specific biomarkers can lead to greater diagnostic accuracy and provide actionable items over the course of the disease to improve patient outcomes.⁴³ Combinations of non-specific biomarkers, referred to herein as biomarker signatures, are commonly found across all biomarker use-based classifications. To develop, validate, and employ laboratory tests using biomarker signatures, collaborations between academia, industry, health care providers, funding sources, and insurance agencies are needed. Identifying clinically useful biomarker signatures that can detect disease faster or more accurately monitor treatment efficacy will be beneficial for all stakeholders.

Research into identifying biomarker signatures can include investigation of proteins, nucleic acids, and multi-omic analyses. Signatures may be measured as single time points, changes over time, or comparisons before and after an exposure or disease onset. Tanaka et al.

followed a large cohort of patients over eighteen years and profiled their proteomes to identify 193 protein biomarkers associated with all-cause mortality after covariate adjustment.⁴⁴ Onset of co-morbidities was associated with enrichment of non-specific inflammatory proteins that could be used to develop prognostic models for aging related conditions. They reported a group of 76 proteins that can estimate the rate of aging to compare how quickly a patient is aging with respect to their chronologic age. In a separate study, a 39-marker signature including cellular, microbiome, and genetic biomarkers comprised a prognostic biomarker signature with a 94% accuracy in predicting overall survival in breast cancer patients and 77% accuracy in predicting a progression free survival.⁴⁵ Transcriptomic data has provided multi-biomarker signatures for differential diagnosis of diabetes, demonstrating a diagnostic approach for various disease phases.⁴⁶ Various biomarkers, many overlapping, successfully differentiated diabetes mellitus from non-diabetic patients, those with diabetes mellitus who are at a high risk of diabetic kidney disease, and those without diabetes but are at a high risk of chronic kidney disease.

Furthermore, researchers studying disease states that currently apply single biomarkers for analysis or rely on pathology-based biomarkers have been replacing these methods with multi-biomarker signatures. The single biomarker sepsis diagnostic kits are limited in clinical utility, but diagnostic or prognostic signatures complicate data interpretation, as cutoffs are needed for each biomarker in the signature.⁴⁷ Ware et al. compared 11 plasma biomarkers in sepsis patients with and without acute respiratory distress syndrome (ARDS) and determined a group of five biomarkers that could potentially prognose severe ARDS in sepsis patients with 82% accuracy.⁴⁸ When evaluated individually, each of the five biomarkers resulted in accuracies of 63%-72%. The work showed an increase in positive and negative predictive values and prognostic accuracies with the biomarker signature. Similarly, preeclampsia is classically

diagnosed through clinical signs and symptoms, which lacks sensitivity and specificity, leading to poor diagnosis and prognosis. To replace clinical symptom markers, a group of 11 serum protein biomarkers was identified using a multi-omic workflow. Through a longitudinal profiling study over the course of pregnancy, the biomarkers showed different trends in patients who developed preeclampsia versus those who did not. These findings indicate that the biomarker panel has potential to prognose disease onset, but a large cohort study is needed for validation.⁴⁹

The presented examples have focused on prognostic and diagnostic biomarker discovery, but biomarker signatures can be found in all biomarker classifications. Examples include continuous monitoring biomarkers in patients treated with chimeric antigen receptor T-cell therapy after cytokine release syndrome,⁵⁰ monitoring of predictive biomarkers for cancer treatment efficacy,⁵¹ and using combinations of non-molecular markers (blood pressure, heart rate, internal temperature, etc.) as response or safety biomarkers. Employing non-specific biomarker signatures — rather than a single specific biomarker— can improve diagnosis and prognosis of many conditions, leading to improved patient care, decreased costs, increased value of molecular testing, and updated precision medicine techniques.

1.6 Inflammatory protein signatures as diagnostic biomarkers

As mentioned previously, diagnostic biomarkers are specific to the disease or condition of interest. However, in the discussion of biomarker signatures, many serve a diagnostic purpose but are developed with non-specific biomarkers. Inflammatory proteins, specifically cytokines and chemokines, are a specific subclass of protein biomarkers used in diagnostic development research. They are ideal biomarker candidates for many reasons, including that they are found in detectable concentrations in many bodily fluids that are non-invasive to collect, such as serum, plasma, saliva, and tears. Additionally, they are more stable than nucleic acids, do not require

RNA free environments, and can provide information regarding complex pathology in various cellular networks.⁵²

1.6.1 Cytokines and chemokines

Cytokines are small, signaling proteins that communicate within the immune system and play central roles in any inflammatory response.^{52,53} The upregulation or downregulation of cytokines alerts the immune system to mount a response, which triggers the release of other cytokines that recruit more cells and activates downstream cascades and processes. The cascade continues until the damage is repaired and can be clinically presented as fever, pain, or redness. However, if the cascade becomes unregulated it can lead to a cytokine storm and adverse health outcomes, such as sepsis, organ failure, and death.

Various cells secrete cytokines in response to a stimulus, and the specific subclass of cytokine depends on their origin.⁵⁴ Cytokines secreted, or produced and released into the bloodstream, by lymphocytes are called lymphokines. Those secreted by monocytes are monokines, and those made by leukocytes and signal other leukocytes are called interleukins (IL); however, ILs have been found to be produced by many other cells. Cytokines are not uniquely made or associated with a single cell type and the same cytokine can be secreted by multiple cell types simultaneously. Many are pleiotropic, meaning the same cytokine can elicit multiple different responses from various cell types, and cytokine activities can be synergistic or agonistic with other cytokines. The interplay of some cells and cytokines is depicted in **Figure 1.2**. Importantly, the messenger RNA for ILs is unstable, resulting in transient synthesis, rapid secretion once synthesized, and temporal variation in concentrations.⁵⁵ While mechanisms and inherent characteristics of cytokines control the secretion of the signaling proteins, dysregulation in one cytokine can affect the whole cascade.

An example cytokine to highlight the complexity and multi-functional roles of cytokines in the inflammatory response is IL-6. IL-6 is a prominent cytokine that increases during an acute phase inflammatory response and is produced by activated T-helper 2 cells, antigen-presenting cells (macrophages, dendritic cells, B cells), and other somatic cells. When cells of the innate immune system (neutrophils, monocytes, macrophages) encounter foreign microorganisms, the Toll-like receptors are stimulated, and IL-6 is secreted to activate the immune system.⁵⁶ General secretion of IL-6 promotes secretion of other acute-phase inflammatory proteins from somatic cells during viral, bacterial, and parasitic infections. IL-6 secretion induced by the interleukin IL-12 leads to proliferation of T-helper 1 cells; IL-6 secretion induced by IL-4 leads to proliferation of T-helper 2 cells, and local IL-6 secretion induced by IL-1 in the brain endothelial cells results in a fever.⁵⁷ Simply speaking, IL-6 is one of the main warning signals that indicates an emergency in the body has occurred (foreign microorganism in a cut, tissue damage, burn, trauma, or other stimuli) and begins to promote inflammation and healing by inducing several, interwoven, downstream functions.⁵⁸ IL-6 is a great first line of defense to activate the immune system, but IL-6 dysregulation can become fatal. There are several other cytokines with important functions that work synergistically and antagonistically to cultivate an appropriate and balanced immune response.

Chemokines are a subclass of cytokines that exhibit chemotactic activity.^{53,54} Chemotaxis is when cells or other organisms move due to a chemical concentration gradient or stimulus. The most studied role of chemokines is to stimulate and migrate leukocytes to local sites of infection; however, they can also induce cellular proliferation, survival, and differentiation and stimulate secretion of other cytokines.⁵⁹ Various structural differences in chemokines determine which cell types they recruit. The migration and recruitment of immune cells, specifically leukocytes, is of

great importance to a successful immunological response in various disease states, but dysregulation or unchecked secretion of chemokines can contribute to a cytokine storm and adverse health events.

A cytokine storm refers to the abnormal production of cytokines and inflammatory proteins.^{60,61} Moderate cytokine storms are typical in patients with chronic neurodegeneration, leading to unresolved inflammation in the brain and changes in mood and executive function.⁶² A major, unchecked inflammatory reaction can lead to systemic inflammation, multi-organ failure, septic shock, and a life-threatening health emergency. Detrimental cytokine storms were of interest during the COVID-19 pandemic, as a handful of infected individuals were severely affected by the host inflammatory response. Concentrations of key cytokines and chemokines, such as IL-6, TNF- α , IFN- γ , IP-10, CCL2, and IL-10, were severely altered and the dysregulation, especially in immunocompromised, elderly, and predisposed patients, led to pneumonia, ARDS, and multi-organ damage.⁶³ Cytokines were associated with disease severity,⁶⁴ allowing their profiles to be used in diagnostic, prognostic, response, and monitoring applications. Additionally, cytokines were targets for therapeutics with their concentrations evaluated for treatment efficacy.⁶⁵ A cytokine storm is not specific to coronavirus infection and can occur due to excessive immune responses brought on by infectious diseases, autoimmune diseases, immunotherapies, or organ transplants.^{66,67} Sepsis results from the dysregulated host response of a cytokine storm and is a severe clinical syndrome.⁶⁸ The detection of cytokine responses to various diseases and conditions is of increasing importance for disease diagnosis, prognosis, and management.

1.6.2 Cytokines in this dissertation by function

Pro-inflammatory cytokines are involved in the upregulation of an inflammatory response and are mainly secreted by macrophages but can be produced by several cell types.⁵⁴ Pro-inflammatory cytokines employed in this thesis include interleukins IL-1 β , IL-6, and IL-17, tumor necrosis factor TNF- α , and chemokines CCL2, CCL3, CCL4, CCL8, IL-8, and IP-10. Anti-inflammatory cytokines are immunoregulatory molecules that inhibit cytokine production and other functions aimed at avoiding adverse events associated with the extreme or sustained pro-inflammatory response.⁶⁹ Anti-inflammatory cytokines employed in this thesis include interleukins IL-6 and IL-10 and tumor necrosis factor TNF- α . Not all cytokines are classified as pro- or anti-inflammatory and have other functions, such as antiviral activity, signaling, or inducing cellular maturation. In this thesis, these cytokines include interleukins IL-2 and IL-15 and interferon IFN- γ . A short, global description of the main functions for each cytokine follows.

1.6.2.1 Pro-inflammatory cytokines

Interleukin IL-1 β is a fundamental, initial upregulator of the acute phase response. It stimulates T cell activation through induction of cytokines, chemokines, and their receptors, plays a role in B cell proliferation, increases natural killer cell cytotoxicity, and induces fever.⁵³ Interleukin IL-17, specifically IL-17A, is expressed only by activated T cells. Its functional role is to increase the expression of other cytokines, such as IL-6 and IL-8, and it has been linked to airway inflammation in allergic responses.^{53,70} The chemokines in our studies are inflammatory chemokines which guide cells to sites of active infection, rather than homeostatic chemokines which deploy cells to their correct locations in the body. CCL2, CCL3, CCL4, and CCL8 attract T cells, natural killer cells, dendritic cells, and monocytes. CCL2, CCL3, and CCL8 additionally attract basophils. IL-8 attracts neutrophils and naïve T cells, and IP-10 attracts T cells, natural killer cells, and monocytes.⁵³

1.6.2.2 Anti-inflammatory cytokines

The only stand-alone anti-inflammatory cytokine in our studies is IL-10. IL-10 is secreted by several cell types with a primary role of inhibiting the inflammatory response. It is known to inhibit cytokine production, including IL-2, IFN- γ , TNF- α , IL-6, IL-8, and CCL2, and suppress macrophage functions.^{53,69} Concentrations of IL-10 inhibit T-cell proliferation and disrupt cell surface expression. IL-10 is the most important anti-inflammatory cytokine, and, similar to IL-6 and TNF- α , dysregulation can lead to an unbalanced immune response and the onset of adverse events.

1.6.2.3 Pro- and anti-inflammatory cytokines

Two of the most important cytokines in the acute phase response are IL-6 and TNF- α , as they initiate a pro-inflammatory response and regulate that response through anti-inflammatory functions. The role of IL-6 is integral to the pro-inflammatory acute phase response and cellular differentiation, as discussed above, but it also has anti-inflammatory functions through downregulation of TNF and inhibition of proinflammatory cytokines GM-CSF, MIP-2, and IFN- γ . TNF- α is secreted by several cell types, and along with IL-1 β and IL-6, plays a central role in acute phase pro-inflammatory response through induction of cytokine secretion and activation of macrophages for phagocytosis; it also has antiviral, tumor cytotoxic, and chemotactic functions.⁵³ TNF- α aids in regulation of the cytokines and other proteins during the acute phase response, giving it anti-inflammatory functions.

1.6.2.4 Uncategorized cytokines

IFN- γ is secreted by T-cells and natural killer cells. It increases the efficiency of the pro-inflammatory response through activation of macrophages and plays a critical role in viral clearance through inhibition of viral replication.⁷¹ IFN- γ is the primary cytokine for

differentiation of type 1 T helper cells through a positive feedback loop, while suppressing type 2 T helper cells.⁵³ Interleukin IL-2 is secreted by type 1 T helper cells and plays a partner role to increase the efficiency of cellular function. It is a fundamental upregulator of the adaptive immune system, increases proliferation of both T- and B-cells, amplifies natural killer cell toxicity, and enhances anti-tumor and antimicrobial responses by monocytes and macrophages.⁵³ Interleukin IL-15 is secreted by several cell types and acts similar to IL-2 by mainly inducing proliferation of B and T-cells and cytokine production.⁵³ It enhances cytotoxic functions of natural killer cells, localizes T-cells, and stimulates growth of the intestinal epithelium.

1.7 Cytokines as non-specific biomarkers in infectious diseases

Infectious diseases are illnesses caused by pathogens outside of the body; they can be viral, bacterial, fungal, or parasitic.⁷² Viral infectious disease examples include COVID-19, influenza, the common cold, norovirus, and viral hemorrhagic fevers, such as Ebola virus and Marburg virus. Examples of bacterial infectious diseases include strep throat, tuberculosis, urinary tract infections, pneumonia, and *Clostridioides difficile*. Fungal infectious diseases include ringworm, vaginal yeast infections, thrush, and candidiasis, and parasitic infectious diseases include hookworms, giardiasis, Chagas disease, and malaria. Infectious diseases can be spread through bodily fluids, surfaces, food, water, or animal bites, among other modes of transmission. Symptoms of these infections vary, and treatment can range from rest and over-the-counter anti-inflammatory drugs to hospitalization and multi-month antibiotic treatment regimes. Vaccinations targeting infectious disease reduce the recipient's risk of getting severely ill by priming the immune system.

As described in the previous section, cytokines and chemokines possess critical roles in the inflammatory responses to infections, tissue damage, and other events; therefore, they have

been studied as biomarkers in many infectious and non-infectious disease states. Many challenges block the development and implementation of cytokine measurement assays. One of the more difficult aspects harkens back to their identity as host inflammatory proteins. They are inherently nonspecific to an individual infection and vary from person to person based on the functionality of their baseline immune system. Validating cytokines as biomarkers requires large populations of diverse patients to confidently state that the concentrations, rates of change, or signatures are specific to the disease state and not due to other inflammatory-based confounders. The transient nature of cytokine concentrations can be advantageous for capturing an inflammatory event at a specific timepoint but unfavorable in that those concentrations can be specific to the individual's immune response or change drastically before sample can be collected.⁷³ The generally low concentration (picogram/milliliter, pg/mL) of cytokines in plasma and serum requires sensitive analytical techniques to detect a difference between baseline and elevated levels. Additionally, cytokine detection assays have a lack of standardization across different platforms and often provide relative quantification instead of the absolute values; this makes cross-platform comparisons difficult.⁷³ The cytokine network is complex, and multiple cytokines need to be measured simultaneously to afford a broad picture of a patient's immune system for personalized management of infections. Therefore, development and deployment of multiplexed cytokine detection assays for infectious disease management is an ongoing area of research and development.

1.8 Multiplexed assays for cytokine detection

The conventional enzyme-linked immunosorbent assay (ELISA) has been used for protein biomarker detection and quantitation for decades.^{74,75} In a common, sandwich-style ELISA, capture antibodies specific to the target of interest are covalently bound to the surface of

individual wells in a 96-well plate (**Figure 1.3A**). The plates are incubated overnight and blocked to prevent non-specific binding. The sample of interest is incubated in the well for 90 minutes, and the wells are manually washed to remove unbound material. The wash is followed by introduction of a detection antibody specific to the analyte of interest, which is incubated for two hours and then manually washed away. The next step includes a secondary antibody conjugated to an enzyme that binds the detection antibody while incubating for one to two hours. Another manual wash is followed by detection substrate, and the absorbance of the well is correlated to analyte concentration using on-plate standards (**Figure 1.3B**).

While a useful technique for quantitation of protein analytes, an ELISA method takes over 18 hours to complete, relies on many manual pipetting steps, and requires on-plate standards for each analyte. Plate-based ELISAs are an endpoint only technique, meaning usable information is produced only after 18 hours pass. Additionally, they are inherently single-plex, as there would be no way to determine how much absorbance signal resulted from each target if multiple captures were linked in one well. For analysis of multiple analytes in one sample, multiple wells will need to be used, which increases the required sample volume, increases the number of wells needed for on-plate standards, and decreases sample throughput. The detection principles of sandwich ELISAs have been heavily utilized in assays with multiplexing capabilities.

1.8.1 Ella Simple Plex automated ELISA platform

Bio-Techne has developed Ella, an automated “Simple Plex” ELISA platform, that uses microfluidic circuits patterned into cartridges to create multiplexed cartridges (**Figure 1.4A**).⁷⁶ The samples need to be manually loaded on the cartridge, but after insertion into the benchtop instrument (**Figure 1.4B**), the remaining steps are fully automated. The sample flows through

glass nanoreactor segments that are coated with the capture antibody of interest. Buffer rinses remove unbound material, and a labeled detection antibody is flowed through, followed by a conjugated fluorescent molecule that elicits a signal for each sandwich complex. The nanoreactor is imaged at three different spots for technical replicates. Parallel channels are patterned into the device to analyze up to eight biomarkers in one cartridge, and calibration standards are pre-loaded into each cartridge. Current panels include two 8-plex cytokine and chemokine panels and a 4-plex cytokine storm specific panel. The Ella platform requires a sample volume of 25 microliters (μL), takes 75 minutes from sample introduction to readout, requires minimal manual work, accommodates multiple cartridges at one time, and offers customization. This system mitigates many of the plate-based ELISA problems, but it is still an endpoint only technique, and the spatial multiplexing layout limits high-plexity possibilities.

1.8.2 Luminex bead-based barcoding platform

A widely used, commercialized multiplexed cytokine assay is the Luminex bead-based assay.⁷⁷ Magnetic microparticle beads are fabricated with various ratios of red dye and infrared dye in up to 50 unique combinations that each fall in a unique area on the fluorescent spectrum. Each different bead is coated with unique antibodies for a specific analyte and multiplexed with all targets in a panel for a multiplexed assay (**Figure 1.5A**). The antibody-coated bead mixture is incubated for three hours with just 50 μL of the sample in a 96-well plate. The wells are manually washed, and a cocktail of biotinylated detection antibodies is incubated in the wells for an hour to form a sandwich complex with the antibody-coated bead and analyte (**Figure 1.5B**). After another manual wash step, the wells are incubated with phycoerythrin conjugated streptavidin for 30 minutes. A final wash step is performed, the beads are resuspended, and the well plate is placed into the Luminex instrument.

The beads from each well are analyzed using a dual-laser flow-based detection scheme where the beads are flowed past two lasers (**Figure 1.5B**).⁷⁸ One laser uses the unique dye combination to identify which target is associated with that specific bead, while the second laser measures signal from the phycoerythrin, which correlates through the standard curve to the analyte concentration. The Luminex technology is highly multiplexable, as the current cytokine panel measures 46 targets with limits of detection in the pg/mL range. The Luminex instrumentation is compatible with any bead-based detection kit. Thus, many companies produce multiplexed detection kits for use on the Luminex platform with analytes ranging from cytokines and growth factors to cancer specific biomarkers and kidney function markers with the option to build custom panels. Each sample and standard are suggested to be analyzed in duplicate, allowing for 30-40 unique samples at one dilution or 15-20 samples at two dilutions to be assessed per plate.

While there are many advantages for using the Luminex platform for multiplexed cytokine detection, there are drawbacks of this plate-based technique. The assay steps all the way until readout are still prone to the drawbacks of a traditional ELISA, including sample loss from manual wash steps, over five hours of incubation and hands-on time, weak off-target interactions produced during stagnant incubations, requirement of on-plate standards for every plate and instrument run, and it is an endpoint only technique with no information gleaned until after at least five hours.

1.8.3 Quanterix array- and bead-based assays

Quanterix digital ELISA platform uses single molecule array (Simoa) bead-based assays to achieve ultra-sensitive detection in the femtogram range and multiplexing capabilities of up to four targets simultaneously in the commercialized kits.⁷⁹ Magnetic beads coated with antibodies

specific to the target of interest are incubated for 30 minutes with the sample and biotinylated detection antibodies to form the sandwich motif in solution (**Figure 1.6A**). At low concentrations, a ratio of one protein per bead is a possibility, with some beads containing no bound protein. At high concentrations, multiple sandwich motifs are formed per bead and most beads will have one or more proteins bound. Beta-galactosidase conjugated streptavidin is incubated in solution for five minutes to enzymatically tag each sandwich motif. The sample is loaded into a disc-shaped array containing over 200,000 microwells. Each microwell has a capacity of around one femtoliter, which is just large enough for a single magnetic bead. A fluorescent substrate is added to catalyze an enzymatic reaction at each tagged sandwich motif. The spatial separation and fluorescent readout allow for ultra-sensitive detection of one protein per bead in a high-throughput manor.

The current menus of commercialized tests from Quanterix are primarily single-plex and include cytokines, HIV-specific proteins, SARS-CoV-2 specific targets, and neurological based target panels. The fully automated instrumentation increases consistency between samples and allows for a laboratory technician to simply add the samples into the sample holder, input reagent kits, select the method, and return when the full assay is completed. Approximately 55 μL of sample are required per replicate, with at least duplicate measurements suggested. Multiple replicates of the same sample can be taken from the same well, given approximately 55 μL is present per desired replicate, which still allows for up to 88 samples to be analyzed at one dilution, or 44 samples to be analyzed at two dilutions, per 96-well plate. Quantitation through fluorescence signal can be completed for some commercialized kits, as 8-point calibration standards are suggested to be run with each sample analyses. Some kits are non-quantitative, and results are only focused on the presence of the biomarker.

Similar to Luminex, the beads can be dyed to encode bead identity to a specific target and then decoded during multiplexed analysis. The extremely low limit of detection is the mainstay of this technique, but the ultra-sensitivity leads to high chances of signal cross-over when multiplexing different beads. Thus, a maximum of four target multiplexed panels are currently commercialized, and none of them include cytokines. Another drawback of the Quanterix technology is that it is still an endpoint only technique, so information from individual steps cannot be used and errors in the reagents or protocols may not be known until analysis is complete.

Quanterix has more recently developed a planar array technology that is more reminiscent of a multiplexed plate-based ELISA, but it is amenable to multiplexing up to twelve analytes.⁷⁹ Nano deposition technology precisely places capture antibodies in twelve discrete spots on the surface of a single well (**Figure 1.6B**). Fifty microliters of sample are added to each well, and the plate is shaken for two hours. The plate movement creates a vortex to increase the interactions of target analytes and the surface deposited capture antibodies as opposed to stagnant techniques. After a manual wash, biotinylated detection antibodies are added and incubated with shaking for 30 minutes. The plate is again manually washed, followed by addition of horse-radish peroxidase conjugated streptavidin and incubation with shaking for 30 minutes. After a final manual wash, a signal substrate is added to generate a chemiluminescent signal, and the wells are imaged through the bottom of the plate within 10 minutes. The imaging process on the Quanterix instrument takes approximately 2 minutes and is guided by machine learning and artificial intelligence. It includes analysis of multiple exposures to ensure a broad dynamic range and low limits of detection across all analytes in the multiplexed system.

The current commercialized kits include a 10-plex cytokine panel and 4-plex chemokine panel. The use of different exposures is a great way to ensure appropriate dynamic ranges are achieved for each of the multiplexed cytokines, and the shaking protocol increases desired interactions and minimizes weak, non-specific interactions. However, the method requires manual wash and sample administration steps, the multiplexed plate kits and imager are specific to Quanterix, and it is an endpoint only technique. With on-plate standards required for every plate and duplicates using double the number of wells, 30-40 unique samples at one dilution or 15-20 samples at two dilutions can be assessed per plate.

ALPCO has also been developing these multiplexed, plate-based ELISA platform with patterned spots of different capture antibodies within a single well.⁸⁰ The ALPCO multiplexed biomarker kits are designed to be used with the DYNEX fully automated ELISA instrument. This takes advantage of the multiplexed capabilities of the Quanterix method with a similar throughput while eliminating the disadvantages associated with manual plate and reagent handling. Currently, ALPCO produces a 5-plex assay with gastrointestinal biomarkers but has no cytokine-based kits.

1.8.4 Comparing Ella Simple Plex automated ELISA, Luminex bead-based assays, and Quanterix Simoa and planar array assays

Each of these three commercialized assay platforms aims to improve the conventional plate based ELISAs in regard to speed, reagent handling, plexity and/or sample volume. All four decrease the time to result (two to five hours), decrease sample volume (all less than 100 μ L), and increase the multiplexing capabilities. The Luminex instrument comes out on top in multiplexing capabilities, with current commercialized assays of 46 cytokines dramatically higher than 8-plex in Ella, single-plex Quanterix Simoa assays, and 10-plex in Quanterix planar

array assays. However, the two highest plexity assays, Luminex and Quanterix planar assays, still require manual handling for washing the well plate and introducing new reagents. The Ella platform and Quanterix Simoa assays are nearly fully automated, outside of sample preparation. Each method has calibration standards engineered into the workflow, but the plate-based techniques require on-plate standards in duplicate wells. All methods are still endpoint only techniques, leading to unnoticed intra assay errors and ignorance regarding assay successes until method completion.

A drawback of all multiplexed or non-ELISA assays in cytokine profiling is that the quantitation of absolute biomarker concentrations can be substantially different from the ‘gold standard’ ELISA, but they can still demonstrate good correlation or relative concentrations from analyte to analyte.⁸¹ The differences in absolute concentrations can be attributed to variations in liquid handling leading to different interaction efficiencies, variations in what antibodies or other reagents are used, or variation in sample dilution schemas for analysis. Therefore, comparing absolute cytokine concentrations across platforms can be difficult. This can be mitigated by using a single technique and platform across studies. Furthermore, focusing on trends and comparisons rather than absolute values and establishing systemic bias when comparing cross-vendor assay results can help lessen the expected variation.

1.9 Silicon photonic microring resonators as a sensing platform

The microring resonator sensing platform employed in this thesis was developed by Genalyte, Inc., a biotechnology company co-founded by Professor Ryan Bailey that uses optical whispering-gallery-mode (WGM) microcavity technology in a biomarker sensing platform. WGM microcavities confine light within precision fabricated microstructures. Near-total internal reflection of the light occurs between the microcavity structure and the surroundings and, in

tandem with an appropriate optical coupler, an evanescent field extends from the excited microcavity into the surrounding area. Disturbance or perturbations to the evanescent field results in a change in how the light interacts with the microstructure. Different WGM geometries include microrings, microbubbles, microspheres, and microtoroids.

1.9.1 Evanescent field sensing in microring resonators

Chip-integrated, silicon photonic microring resonators have emerged as the most promising WGM sensing format for biosensing applications due to advantages in scalability, multiplexing potential, and standardized fabrication.⁸³ This technology has been commercialized by Genalyte, Inc. using a 4x6 mm silicon-on-insulator substrate with 128, 30 μm diameter sensors per chip (**Figure 1.7A**).⁸⁴⁻⁸⁶ An additional advantage of silicon photonic microrings is the ability to easily optically interrogate sensors using chip-integrated grating couplers positioned in a critical coupling condition to access waveguides adjacent to the microrings.

Light from a tunable, external cavity laser propagates through linear waveguides under total internal reflection (TIR) and wavelengths that satisfy the resonance condition couple into the microring. The TIR creates an evanescent field that extends from the sensor surface into the adjacent sensing region, with an intensity that decays exponentially from the sensor surface.^{87,88} The resulting evanescent field is sensitive to local changes in the refractive index of the exposed cavity in which it propagates, causing the resonant wavelength to shift in response to biomolecular binding-induced changes in refractive index (**Figure 1.7B**), according to the following equation:

$$\lambda = \frac{2\pi r}{m} n_{eff}$$

where r is the microring radius, m is an integer, and n_{eff} is the effective refractive index.^{89,90}

The commercial system enables the resonance wavelength of each ring on the chip to be read out

quickly by rastering the laser across different input grating couplers.^{85,86} One key element of these chips is that thermal control rings, which are covered by an inert cladding material and unexposed to the sensing solution, allow for correction of resonance drifts due to temperature fluctuations.⁹¹

1.9.2 Biomarker detection on microring resonators using sandwich ELISA-style methods

Refractive index sensors have the attribute that they are “universal” and can detect any change in local refractive index irrespective of molecular structure. The downside to universality is that the sensors inherently lack specificity. Therefore, in order to detect specific biomarkers of interest, resonators must be modified with analyte-specific capture agents, such as antibodies,^{92,93} antibody fragments,⁹⁴ or complementary nucleic acids through straightforward silane and bioconjugate linking chemistries.^{95,96} Our lab has used microring resonators for label-free detection of targets, including nucleic acids,^{97,98} viruses,⁹⁹ proteins,^{92,100} nanodiscs,¹⁰¹ and telomerase activity.¹⁰² While label-free detection has upsides of simplicity and rapidity, there is a lack of specificity due to non-specific adsorption of molecules from complex matrices and bulk refractive index changes from biologic samples. Label-free detection is also limited by the binding affinity of the capture agent, which can sometimes result in limits of detection above what is required to be of analytical utility.

As an alternative to label-free detection, additional assay reagents may be incorporated to increase the per-analyte refractive index change, providing increased analyte selectivity and improved limits of detection and sensitivity. Such reagents include secondary (tracer) antibodies,^{100,103,104} and (sub-)micron-scale beads.^{93,105} Furthermore, secondary reagents can include enzymatic tags that can create extremely large per-analyte resonance shifts, allowing sub-pg/mL limits of detection for proteins.^{100,106}

The assays employed in this thesis use sandwich ELISA sensing principles for protein quantitation (**Figure 1.7C**). Microring fabricated sensor chips functionalized with analyte-specific capture antibodies localize the target molecule in a sample or standard mixture to the microring surface. A biotinylated tracer, or detection, antibody is then introduced to form the sandwich complex. Importantly, this second antibody provides high specificity for the targeted analyte because two high affinity interactions are now localized near the microring surface. A tertiary recognition molecule of horse-radish peroxidase conjugated streptavidin binds to the biotin. Finally, 4-chloro-1-naphthol is used as an amplification reagent, as its reaction with the localized horse-radish peroxidase results in biocatalytic precipitation. The insoluble precipitate that is deposited at the microring surface leads to extremely large resonance wavelength shifts that are proportional to the amount of target in the sample.^{75,107} The instrument used in this thesis uses fully automated microfluidic handling of the reagents across the chips surface and an automated buffer washing step is programmed between each reagent to ensure removal of weak, non-specific interactions to decrease background noise and off-target responses.

1.9.3 Multiplexed analyte detection and calibration

For multiplexed analyses, each capture agent-analyte-biotinylated antibody sandwich complex must be optimized individually for the described assay. The concentration of analyte and tracer reagent that results in a saturating signal must be determined and then titrated down to levels below the limit of detection to ensure a calibration can be constructed. The target must then be validated in the complex biologic matrix (serum, plasma, whole blood, urine, etc.) to ensure a similar response as in buffer. Once each target in a proposed panel is individually optimized, cross-reactivity experiments are imperative to ensure no false positive results. Cross-reactivity experiments are conducted by analyzing each individual analyte-biotinylated antibody

pair across all capture antibodies in the panel to ensure only the capture antibodies specific to the analyte-biotinylated antibody pair result in a significant response.

Once targets are individually calibrated and there is deemed to be no cross-reactivity in the panel, a cocktail of proteins and a cocktail of biotinylated tracers for all targets in the panel can be used to generate a simultaneous multiplexed calibration. Since antibody affinities and susceptibility to non-specific responses can be antibody- and target-specific, calibrations for each specific analyte must be used to quantify that analyte. Additionally, for our work, calibrations must be conducted for each batch of spotted sensor decks to account for any minute variability in the spotting procedure or reagent lots.

1.9.4 Quantitation of microring resonator responses

For the sandwich-style method with biocatalytic amplification described above, the net shift in resonance wavelength is typically recorded before and after the signal enhancement step to provide quantitation. An eight-point series of analyte standards are analyzed to characterize the concentration-versus-response relationship within each sensor chip batch. Data is then fit using a four parametric curve, akin to a traditional ELISA:

$$y = \frac{A_1 - A_2}{1 + \left(\frac{x}{x_0}\right)^p} + A_2$$

where y (pm) is the response at concentration x (pM), A_1 is the initial value (Δ pm), A_2 is the final value (Δ pm), x_0 is the inflection point of the curve (pM), and p is the power parameter affecting the slope fit of the linear portion of the curve.⁹⁵ The resulting fit values for A_1 , A_2 , x_0 , and p can be used in conjunction with the net shift in an unknown sample to calculate the concentration of analyte present, as well as statistically establishing limits of detection and quantification.

1.9.5 Limitations of microring resonators as a sensing platform

There are three major sources of measurement noise when dealing with WGM sensors.¹⁰⁸ The first is noise associated with non-optimized optical coupling from the interrogation waveguide into the resonator, though this can be solved through engineering controls, which includes physically anchoring the linear waveguide onto the resonator-containing chip. Another significant potential source of noise is thermal fluctuations. The materials systems of the resonator and surrounding environment have different thermo-optical coefficients, so their refractive indices do not move in unison when the temperature across the chip varies even by very small amounts. Genalyte, Inc.'s silicon chips integrate thermal control sensors that are irresponsive to biochemical binding events yet are exposed to the same temperature fluctuations. Finally, the most challenging source of noise for biosensing is biological. When flowing solutions containing biomolecular targets of interest, other biochemicals are present and produce an inherent background of resonance wavelength fluctuation due to either bulk refractive index changes or non-specifically bound molecules. The levels of these non-specific responses can vary widely among samples—particularly patient-derived samples. Therefore, in many practical applications, the ability to determine resonance wavelength shifts is limited by thermal and biological noise considerations compared to optical performance, which means that higher Q-factors, while theoretically providing better sensitivity, often do not yield enhanced performance for biological assays.

Non-specific adsorption refers to the adhesion of non-targeted proteins to the surface of the sensor, regardless of surface functionalization. This can cause resonance shifts and lead to a false positive result. To mitigate these issues, the surface should be blocked prior to sensing with buffer containing an agent such as bovine serum albumin to reach an equilibrium on the surface of the sensor and prevent the non-specific interactions from exogenous proteins. Additives to the

buffer, such as the detergent Tween, can further aid in preparing the surface. Furthermore, the sensor itself can be functionalized with antifouling elements, such as polymeric scaffolds.¹⁰⁹ It has been reported that surface modification with zwitterionic polymer conjugates¹¹⁰ can reduce the bulk shift caused by the complex matrices, allowing for label-free assays in human samples; however, it is unclear if even the best surface modification can minimize non-specific binding to the point that its contribution to signal can be ignored relative to the targeted biomolecule.¹¹¹

An additional consideration for performing sensing with evanescent wave-based technologies is to understand the nature of the chemical and biological moieties necessary to bind analytes to the sensor surface. For example, the $1/e$ decay length for silicon photonic sensors is 63 nm,⁸⁷ which means that the biochemical binding events must be confined within this most sensitive region of the device.

1.9.6 Genalyte, Inc. microring resonator technology provides real time results of up to 16 biomarkers in 45 minutes.

The cytokine detection assays employed through this thesis have not been commercialized and have been developed and used to achieve pg/mL range detection limits within the Bailey Lab. The current commercialized assay panels are focused on multiplexed general clinical chemistry, lipid, metabolic, and serology panels.⁸⁴ The assay method described above was employed in many chapters of this thesis and is detailed for the respective assay within the chapters. The assay time on the Genalyte Matchbox instrument was 45 minutes per sample, which included five minutes of a pre-assay buffer rinse to equilibrate the chip surface and 40 minutes of the assay steps with buffer washes between each.

In comparison to the Ella Simple Plex automated ELISA, Luminex bead-based assays, and Quanterix Simoa and planar array assays, the microring resonator technology minimizes

many of the downfalls. The assay is fully automated for all sample steps including buffer washes, unlike the Luminex and Quanterix planar array assays. The possibility of 16-plex cytokine assays, each with four technical replicates, outcompetes the Ella automated ELISA and both Quanterix cytokine assays. The throughput in the Luminex and Quanterix platforms is greater than the microring Matchbox platform. Multiple patient samples (range of 20-80) can be analyzed per plate (range 3-5 hours) in those platforms compared to two samples, or one sample at two dilutions, every 45 minutes using our platform. This would equate to approximately 5-6 patients at two dilutions in the 3-5 hours. Newer instrumentation models from Genalyte, Inc. incorporate more sensing and optical elements to simultaneously measure multiple chips at once, increasing the throughput.

Unique to the microring resonator platform is that it is the only method of these commercialized instruments that is not an endpoint only technique. The resonant wavelength is tracked over the course of the assay in near real time, allowing a constant monitoring of the refractive index change. It is advantageous to monitor the expected profiles of each assay step to ensure the reagents are of proper quality and identify unexpected errors in the assay that may not be identified with the endpoint result. For example, a clogged microfluidic line in one channel can reduce the amount of sample or reagent that reaches the capture antibodies on the microrings. However, if the clog dislodges mid-sample run, the remaining reagents can still flow across the chip and a signal will result. Without knowing that a clog was present during a part of the assay, the signal would be taken as the unobstructed result even though the signal is likely artificially low. Additionally, the profiles of the individual assay steps have been used to identify which reagent (standards, tracer antibodies, streptavidin conjugate, amplification reagent) had

gone bad when the expected profiles in a standard curve did not match prior data. Endpoint only techniques cannot provide this level of insight into the individual assay steps and reagent quality.

1.10 Dissertation Summary

The themes presented in this introduction include biomarker subclasses, cytokines and chemokines, and multiplexed protein assays. These topics that span across the multiple projects and disease states explored through this thesis. Chapter two is an in-depth protocol of how to optimize, validate, and employ multiplexed biomarker assays on the Genalyte, Inc. Matchbox platform. The protocol describes the procedures for functionalizing the sensor chips with multiple capture antibodies, the sample and calibration preparation process, and how to run the Matchbox instrument. Additionally, the chapter covers step-by-step instructions on analyzing data, the reasoning behind each step in the data work-up process, and common pitfalls and associated solutions. While this chapter was written within the context of building an Ebola virus diagnostic assay that was employed in the following chapter, the processes and procedures were followed for development and employment of the cytokine assays used in later chapters. Chapter three focuses on the successful development of a two-plex assay using diagnostic and prognostic biomarkers of the infectious diseases caused by Ebola and Sudan viruses. The two-plex sandwich-style protein detection assay was optimized and validated for cross-reactivity and detection in serum matrices. The assay was then applied in non-human primate serum specimen, in which the ebolavirus biomarker was successfully detected in a clinically relevant population.

Chapter four forays into identifying potential monitoring and response biomarkers for preterm neonates exposed to a maternal inflammation. A seven-plex cytokine and chemokine protein biomarker assay was employed in nearly 400 samples collected from 61 preterm neonates over their stay in the neonatal intensive care unit. The data presented provides insight

into the variation in the innate immune systems of preterm neonates in general and identifies differences in trends between an exposed group and an unexposed group, leading to potential response biomarkers. The chapter includes examples of longitudinal biomarker profiles that show the promise of cytokines and chemokines as monitoring biomarkers, and even potentially prognostic biomarkers.

Chapters five and six switch focus to development and validation of a multiplexed cytokine and chemokine biomarker panel to diagnose a bacterial infectious disease, latent tuberculosis infection, and classify a patient's risk of reactivation from latent to active disease. A 13-plex cytokine and chemokine biomarker assay was employed in over 550 patient samples. The measured concentrations were coupled with random forest machine learning algorithms to build diagnostic biomarker signatures to classify latency status and prognostic biomarker signatures to classify risk of reactivation. Chapter five specifically explores similarities and differences between two patient cohorts that were analyzed by different teams under the same procedures. We report that the two cohorts produce similar diagnostic accuracies for classification of latently infected patients and high overlap between the most important biomarkers for classification. Additionally, we discuss the statistically similar cytokine and chemokine concentrations across two tuberculosis-specific antigen stimulations in the QuantiFERON diagnostic test kit. Chapter six focuses on results from a large cohort of over 550 plasma samples, which includes merged data from the two cohorts discussed in chapter five. We have achieved an accuracy of 87% to classify latently infected individuals from non-infected individuals and identified IP-10, IL-2, and CCL8 as important cytokines for this differentiation. Within the latently infected population, we aimed to classify the patients as high risk or low risk of reactivation from latent to active disease phase and achieved accuracies of 81% for both

classification models. Important biomarkers for risk discrimination included IL-10 and IL-2. Results from these projects demonstrate successful incorporation of the microring resonator platform into a clinically relevant tuberculosis detection workflow. This work aims to improve latent tuberculosis diagnostics, treatment of patients at a high risk of reactivation, and multiplexed biomarker discovery methods.

Chapter seven summarizes the analytical considerations that have been noted over the course of using several multiplexed cytokine and chemokine sensor chip batches. Calibration parameter variation across and within multiple sensor chip batches is analyzed and discussed, as well as important considerations surrounding sample dilutions. Data from an ongoing sensor chip deck stability study is presented, and conclusions highlight that calibration variation and stability is more associated with biologic variation than sensor chip deficiencies. Finally, alternate assay methods on the microring resonator platform are explored to tailor the dynamic range of a specific chemokine, IL-8, towards developing methods that can measure cytokines and chemokines in clinically relevant ranges. Chapter eight concludes this thesis with a summary of three, short-term side projects and a discussion into proposed future work for all projects discussed in previous chapters. Future research directions that this thesis builds a strong foundation for including cytokine and chemokine biomarker profiling to identify host diagnostic, prognostic, or predictive biomarkers for viral hemorrhagic fevers and an expanded clinical study or incorporation of social determinants of health in latent tuberculosis diagnostic projects.

Taken together, the work presented in the chapters of this thesis have potential impacts in diagnosis, prognosis, and clinical management of infectious diseases and in improving reproducibility and robustness of our assays. The quantitation of assay and target-specific variability will be important to the long-term clinical projects within our lab and have the

potential to impact decisions regarding target selection and sensor chip batch qualification to ensure robust sample processing. The Ebola virus project has shown the ability to detect an early biomarker of infection in clinically relevant matrices that could be used in an outbreak setting to both diagnose and prognose infection. Clinicians can use the levels of the biomarker to quarantine positive patients and allocate resources based on disease prognosis, armed with the information from this one assay. The results from the LTBI project have been justified across two individual cohorts and, when combined, have led to a method with high accuracy in LTBI diagnosis and stratification of risk of disease reactivation. Specifically, the risk assessment at time of initial evaluation can impact monitoring and treatment of LTBI positive individuals. Those at a high-risk can be monitored closely for symptoms and reactivation events can be captured sooner, effectively reducing the spread of TB through reactivation events. Those at a low-risk can be treated effectively, with a potential to reduce unnecessary antibiotic regimens and reduce prevalence of drug-resistant TB strains. The public health impacts from these diagnostic development projects are clear, and achieving the future directions presented in this thesis will bring these projects closer to implementation in relevant clinical settings.

1.11 Figures

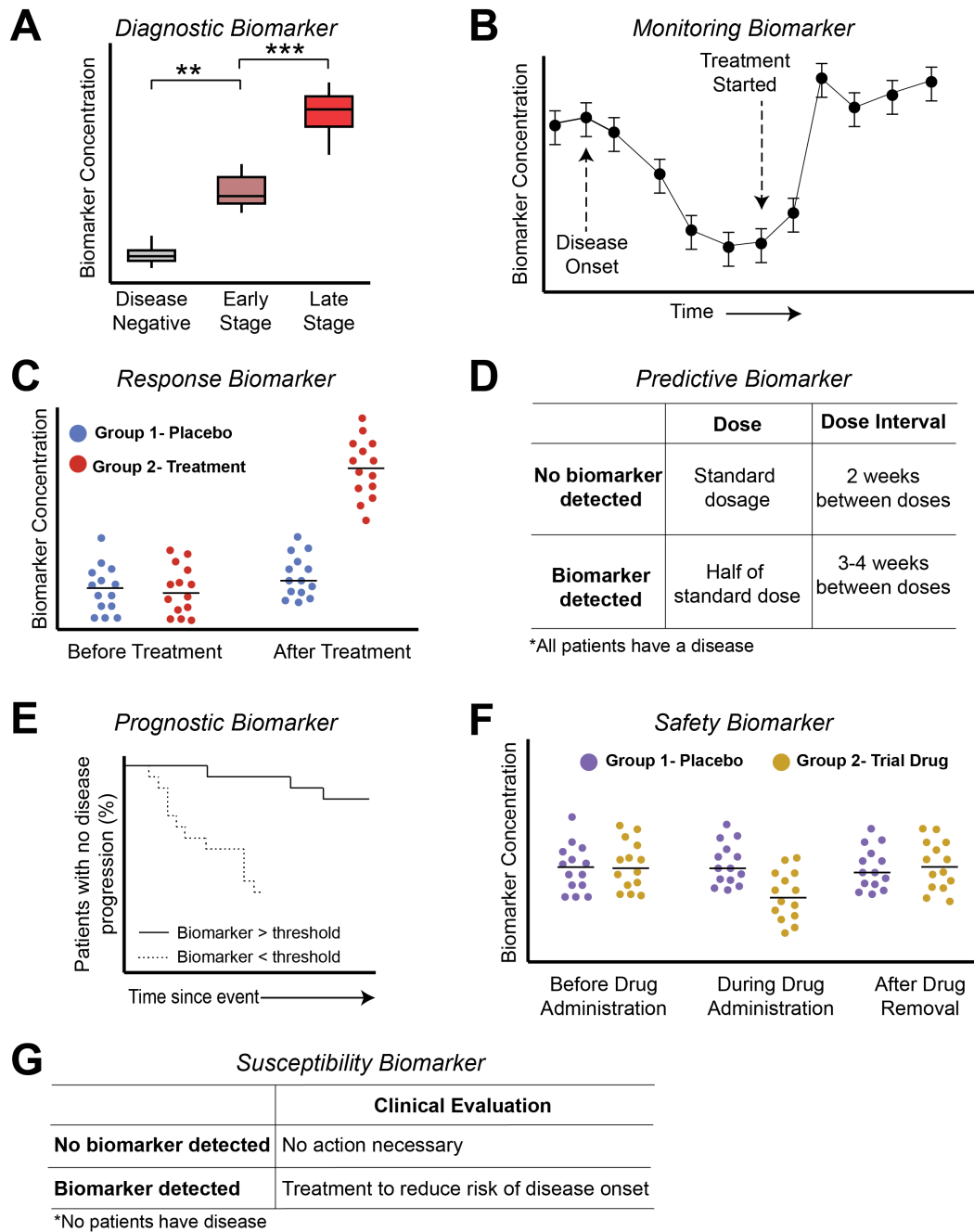


Figure 1.1 Summary of biomarker classifications by application. Diagnostic biomarkers (A) indicate specific diseases or distinguish disease states. Monitoring biomarkers (B) temporally measure the effects of disease, treatment, or exposure through repeated measurements to monitor status changes. Response biomarkers (C) measure a biologic response after an exposure or treatment. Predictive biomarkers (D) are indicative of an individual patient's response to specific treatment or exposure. Prognostic biomarkers (E) provide information about the likelihood of an event or disease progression. Safety biomarkers (F) are a measurement of adverse effects before and after an exposure. Susceptibility biomarkers (G) indicate a healthy patient's potential to progress to a disease.

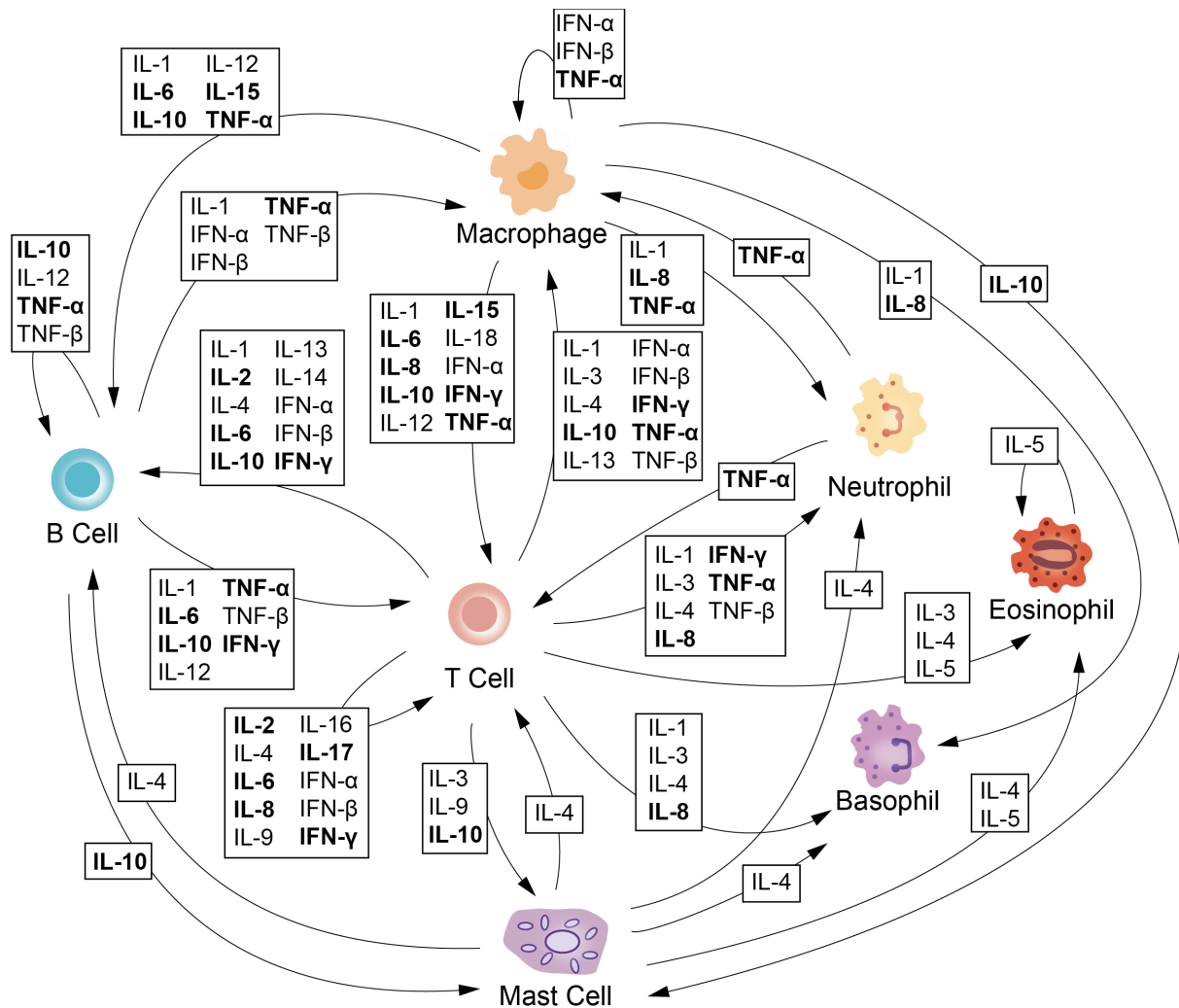


Figure 1.2 Diagram of cytokine cascade involving interferons, tumor necrosis factors, and interferon cytokine biomarkers. This diagram highlights the multi-functional aspects of many cytokines and how they can act upon the cells they are secreted from, as well as others. The bolded cytokines are ones used in this dissertation. This figure is adapted from Zhang and Ann and other cytokine cascade images, with cell color schemes based on Nature style.⁵⁴

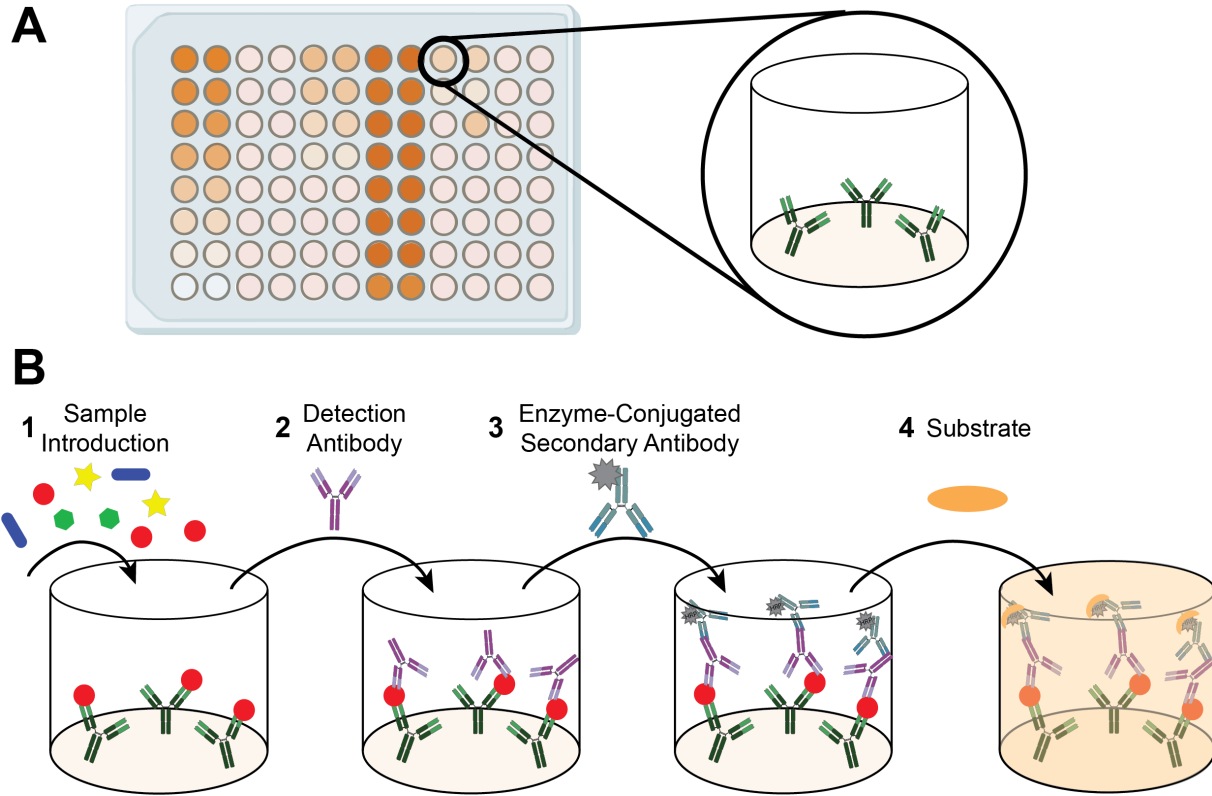


Figure 1.3 Conventional sandwich style ELISA. Each well of a 96-well plate is coated with an antibody specific to the target of interest (A). Reagents for each individual assay step are added into the wells, with buffer washes between each step (B). The resulting absorbance signal after substrate addition is converted to concentration using on-plate standards. Only one analyte can be surveyed per well. Figure not drawn to scale.

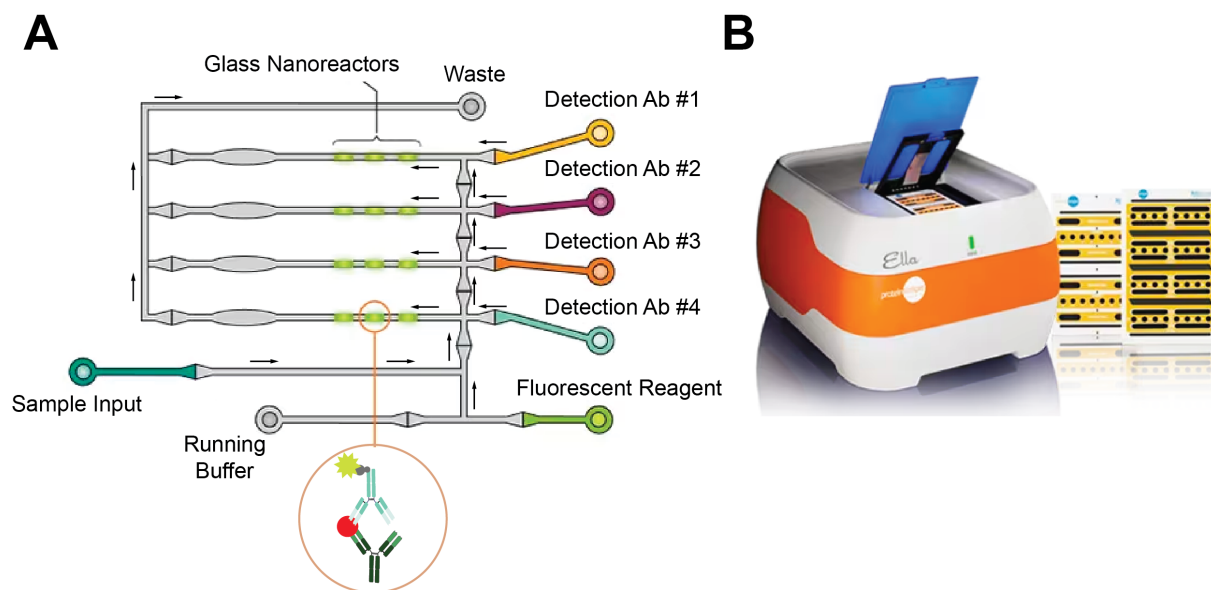


Figure 1.4 Simple-Plex Ella Platform. This commercialized sandwich ELISA platform uses microfluidic cartridges pre-loaded with assay reagents and standard reagents to complete an ELISA assay on up to eight targets in one cartridge. The sample is distributed into different channels for each unique target analyte, captured in the antibody-coated glass nanoreactor, and detected with fluorescent signal (A). Black arrows indicate flow direction. The cartridge is loaded into a benchtop instrument, with multiple cartridges able to be analyzed in one run (B). Figure not drawn to scale. Figure reproduced and adapted from Bio-Techne website and instrument documents.⁷⁶

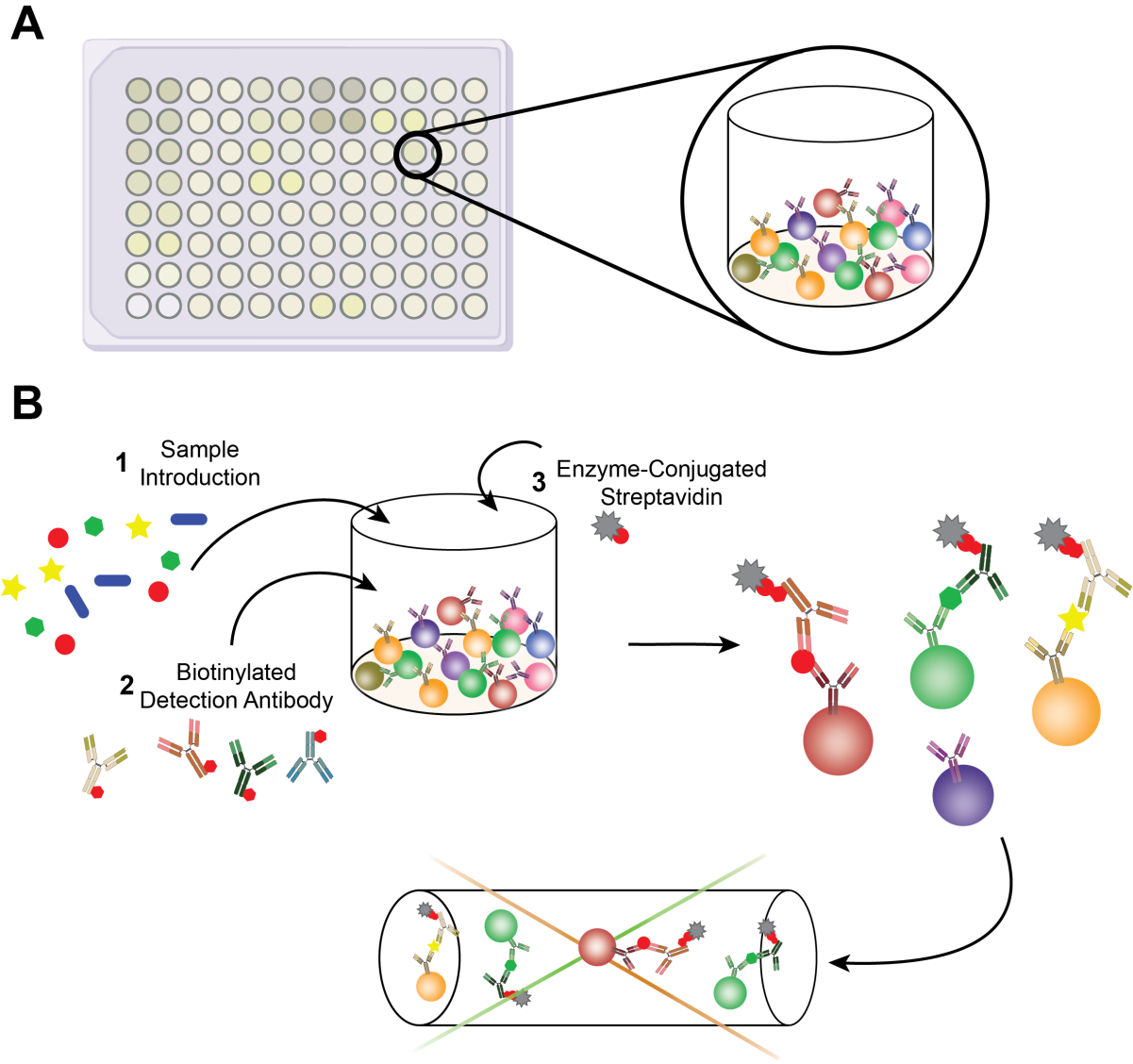


Figure 1.5 Luminex multiplexed bead-based assay workflow. Wells of a 96-well plate are filled with a mixture of dyed magnetic beads each with a different antibody coated on the surface (A). Sandwich-style ELISA assay reagents are added consecutively and manually, with washes in between each step, similar to the conventional ELISA (B). The sandwich complexes are formed on the beads, which are then interrogated with two lasers, one for bead identification and one for signal magnitude, in the instrument. On-plate standards are used to convert signal to concentration for each of the up to 50 analytes. Figure not drawn to scale. Figure adapted from Luminex assay principles website through R&D.⁷⁸

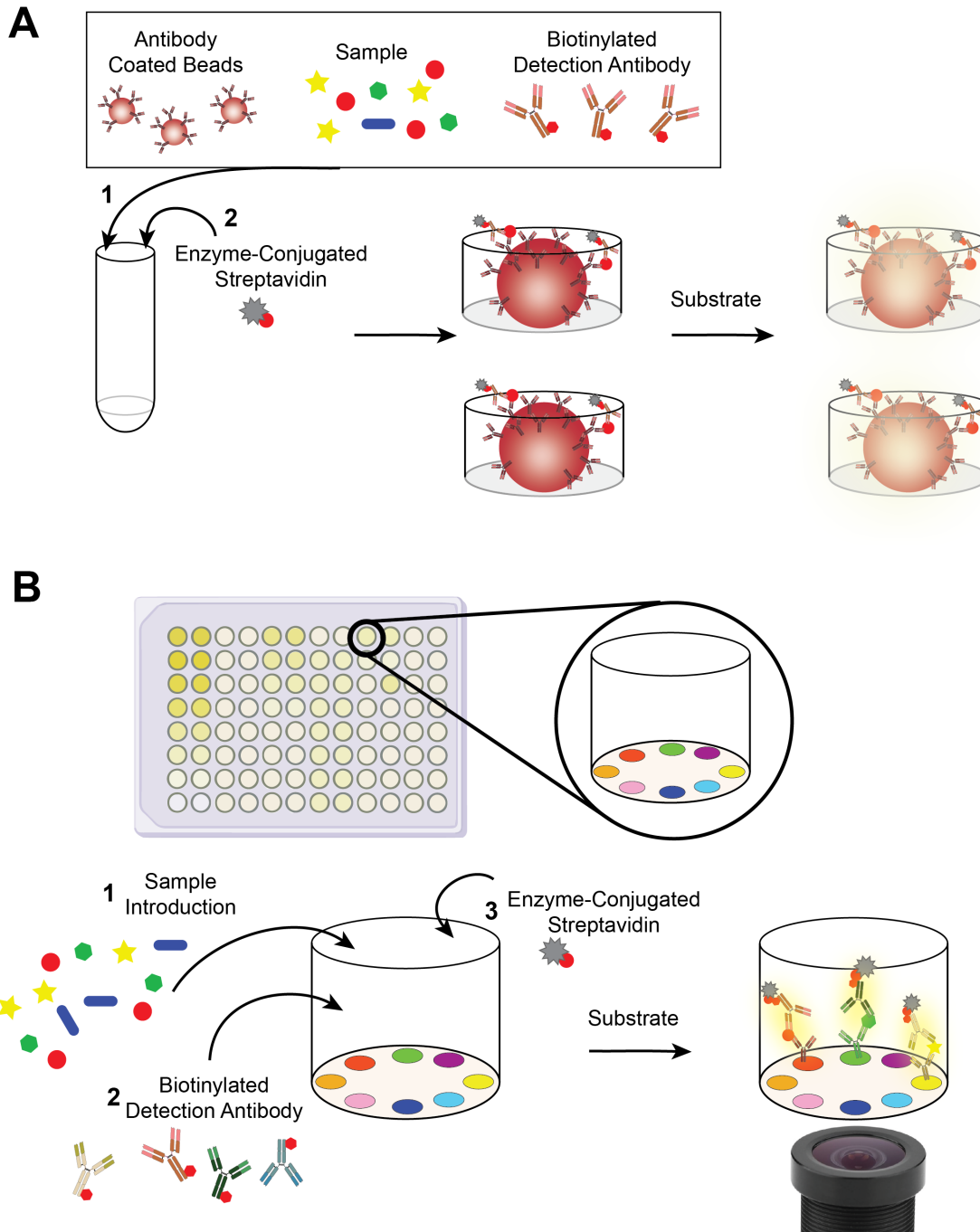


Figure 1.6 Quanterix Simoa bead and planar array technologies. In the fully automated Simoa assay, a cocktail of antibody coated beads, sample, and biotinylated detection antibodies are incubated in solution (A). After a buffer wash, a detection reagent is added, and the solution is deposited onto a microarray disc containing over 200,000 fL volume reaction wells. A single bead fits into a well and after substrate addition, fluorescence signal is detected. In the planar arrays, up to twelve capture antibodies are spatially deposited onto the surface of a single well (B). Sandwich-style ELISA assay reagents are added consecutively and manually, with washes in between each step, similar to the conventional ELISA. Chemiluminescent signal is detected in each individual antibody spot through the bottom of the well plate and converted to analyte concentration through on-plate standards. Figure not drawn to scale. Figure adapted from the Simoa technology webpage through Quanterix.⁷⁹

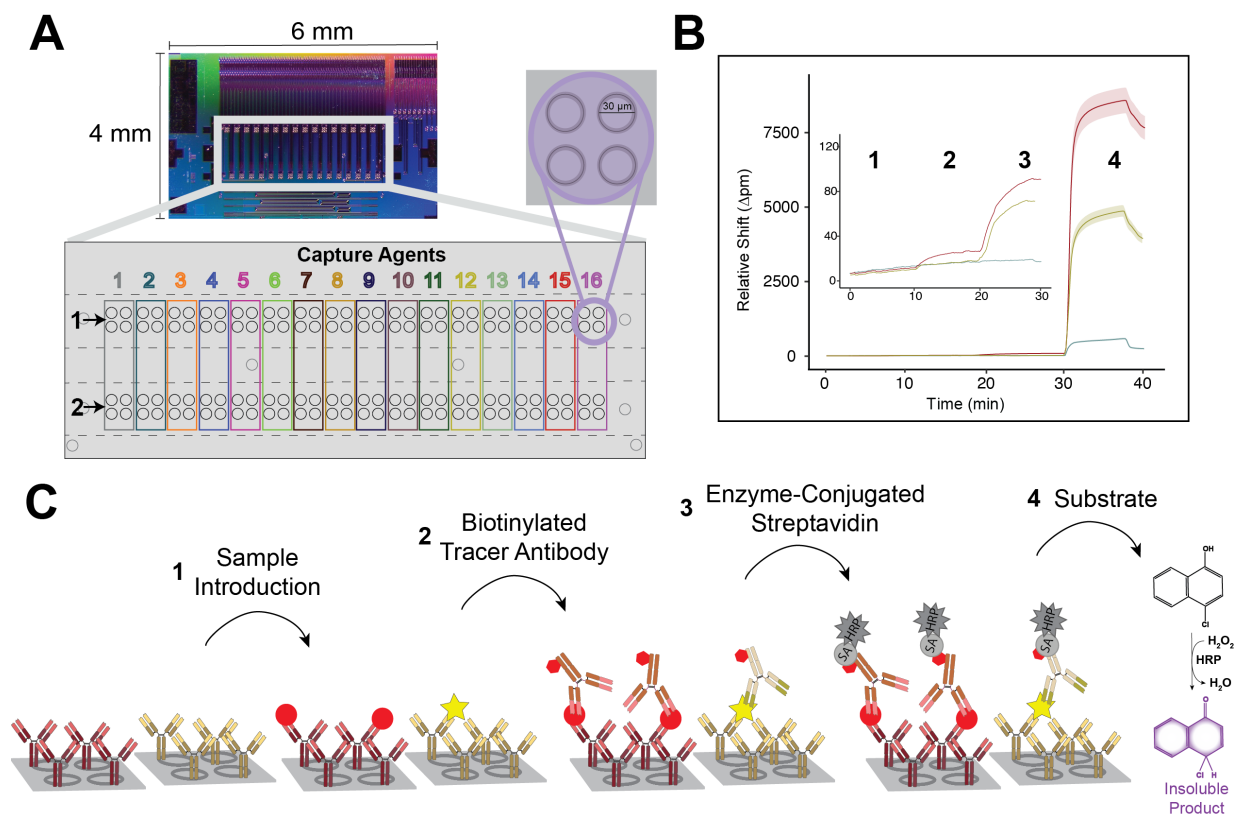


Figure 1.7 Microring resonator multiplexed assay. The 128 individually addressable microring resonator sensors are arrayed over two microfluidic channels on a silicon chip (A). The rings are arranged in clusters of four, allowing measurement of up to sixteen different targets with four technical replicates each, per channel. The resonant shift is reported in near real-time, allowing for inter-step data to be assessed (B). The fully automated reagent handling uses microfluidics to sequentially flow sandwich-style ELISA reagents, with buffer rinses between each step, over the microrings (C). The final step (4) is an amplification reaction that drastically shifts the resonant wavelength. Figure not drawn to scale. Figure adapted from original files submitted for Yu, D. et al.⁸²

1.12 References

- (1) Aronson, J. K.; Ferner, R. E. Biomarkers—A General Review. *Curr. Protoc. Pharmacol.* **2017**, 76 (1). <https://doi.org/10.1002/cpph.19>.
- (2) *Biomarkers Market Size, Share And Growth Report, 2030*. <https://www.grandviewresearch.com/industry-analysis/biomarkers-industry> (accessed 2024-02-20).
- (3) *Abbott Receives FDA Clearance for First Commercially Available Lab-based Blood Test to Help Evaluate Concussion*. Abbott MediaRoom. <https://abbott.mediaroom.com/2023-03-07-Abbott-Receives-FDA-Clearance-for-First-Commercially-Available-Lab-based-Blood-Test-to-Help-Evaluate-Concussion> (accessed 2024-02-20).
- (4) Bazarian, J. J.; Biberthaler, P.; Welch, R. D.; Lewis, L. M.; Barzo, P.; Bogner-Flatz, V.; Brolinson, P. G.; Büki, A.; Chen, J. Y.; Christenson, R. H.; Hack, D.; Huff, J. S.; Johar, S.; Jordan, J. D.; Leidel, B. A.; Lindner, T.; Ludington, E.; Okonkwo, D. O.; Ornato, J.; Peacock, W. F.; Schmidt, K.; Tyndall, J. A.; Vossough, A.; Jagoda, A. S. Serum GFAP and UCH-L1 for Prediction of Absence of Intracranial Injuries on Head CT (ALERT-TBI): A Multicentre Observational Study. *Lancet Neurol.* **2018**, 17 (9), 782–789. [https://doi.org/10.1016/S1474-4422\(18\)30231-X](https://doi.org/10.1016/S1474-4422(18)30231-X).
- (5) Bazarian, J. J.; Welch, R. D.; Caudle, K.; Jeffrey, C. A.; Chen, J. Y.; Chandran, R.; McCaw, T.; Datwyler, S. A.; Zhang, H.; McQuiston, B. Accuracy of a Rapid Glial Fibrillary Acidic Protein/Ubiquitin Carboxyl-Terminal Hydrolase L1 Test for the Prediction of Intracranial Injuries on Head Computed Tomography after Mild Traumatic Brain Injury. *Acad. Emerg. Med.* **2021**, 28 (11), 1308–1317. <https://doi.org/10.1111/acem.14366>.
- (6) *QIAGEN receives FDA approval for companion diagnostic to Mirati Therapeutics' KRAZATI in non-small cell lung cancer*. <https://corporate.qiagen.com/English/newsroom/press-releases/press-release-details/2022/QIAGEN-receives-FDA-approval-for-companion-diagnostic-to-Mirati-Therapeutics-KRAZATI-in-non-small-cell-lung-cancer/default.aspx> (accessed 2024-02-20).
- (7) *Quanterix Granted Breakthrough Device Designation from U.S. FDA for Blood-Based pTau-181 Assay for Alzheimer's Disease*. Quanterix. <https://www.quanterix.com/press-releases/quanterix-granted-breakthrough-device-designation-from-u-s-fda-for-blood-based-ptau-181-assay-for-alzheimers-disease/> (accessed 2024-02-20).
- (8) Chen, X.; Wang, M.; Niu, J.; Ma, J.; Qian, J.; Ni, L.; Cheng, P.; You, H.; Chen, J. Plasma A β 42/A β 40 Ratio as a Biomarker for Cognitive Impairment in Patients Undergoing Hemodialysis: A Multi-Center Study. *Clin. Kidney J.* **2023**, sfad173. <https://doi.org/10.1093/ckj/sfad173>.
- (9) Huber, H.; Ashton, N. J.; Schieren, A.; Montoliu-Gaya, L.; Molfetta, G. D.; Brum, W. S.; Lantero-Rodriguez, J.; Grötschel, L.; Stoffel-Wagner, B.; Coenen, M.; Weinhold, L.; Schmid, M.; Blennow, K.; Stehle, P.; Zetterberg, H.; Simon, M.-C. Levels of Alzheimer's Disease Blood Biomarkers Are Altered after Food Intake—A Pilot Intervention Study in Healthy Adults. *Alzheimers Dement.* **2023**, 19 (12), 5531–5540. <https://doi.org/10.1002/alz.13163>.
- (10) Pais, M. V.; Forlenza, O. V.; Diniz, B. S. Plasma Biomarkers of Alzheimer's Disease: A Review of Available Assays, Recent Developments, and Implications for Clinical Practice. *J. Alzheimers Dis. Rep.* **2023**, 7 (1), 355–380. <https://doi.org/10.3233/ADR-230029>.
- (11) BEST (Biomarkers, EndpointS, and Other Tools) Resource.

- (12) Califf, R. M. Biomarker Definitions and Their Applications. *Exp. Biol. Med.* **2018**, *243* (3), 213–221. <https://doi.org/10.1177/1535370217750088>.
- (13) Bradley, A. P. The Use of the Area under the ROC Curve in the Evaluation of Machine Learning Algorithms. *Pattern Recognit.* **1997**, *30* (7), 1145–1159. [https://doi.org/10.1016/S0031-3203\(96\)00142-2](https://doi.org/10.1016/S0031-3203(96)00142-2).
- (14) Diao, B.; Wen, K.; Zhang, J.; Chen, J.; Han, C.; Chen, Y.; Wang, S.; Deng, G.; Zhou, H.; Wu, Y. Accuracy of a Nucleocapsid Protein Antigen Rapid Test in the Diagnosis of SARS-CoV-2 Infection. *Clin. Microbiol. Infect.* **2021**, *27* (2), 289.e1-289.e4. <https://doi.org/10.1016/j.cmi.2020.09.057>.
- (15) Barlev-Gross, M.; Weiss, S.; Ben-Shmuel, A.; Sittner, A.; Eden, K.; Mazuz, N.; Glinert, I.; Bar-David, E.; Puni, R.; Amit, S.; Kriger, O.; Schuster, O.; Alcalay, R.; Makdasi, E.; Epstein, E.; Noy-Porat, T.; Rosenfeld, R.; Achdout, H.; Mazor, O.; Israely, T.; Levy, H.; Mechaly, A. Spike vs Nucleocapsid SARS-CoV-2 Antigen Detection: Application in Nasopharyngeal Swab Specimens. *Anal. Bioanal. Chem.* **2021**, *413* (13), 3501–3510. <https://doi.org/10.1007/s00216-021-03298-4>.
- (16) Fathil, M. F. M.; Md Arshad, M. K.; Gopinath, S. C. B.; Hashim, U.; Adzhri, R.; Ayub, R. M.; Ruslinda, A. R.; Nuzaihan M.N., M.; Azman, A. H.; Zaki, M.; Tang, T.-H. Diagnostics on Acute Myocardial Infarction: Cardiac Troponin Biomarkers. *Biosens. Bioelectron.* **2015**, *70*, 209–220. <https://doi.org/10.1016/j.bios.2015.03.037>.
- (17) Qavi, A. J. Rapid Detection of an Ebola Biomarker with Optical Microring Resonators. *OPEN ACCESS* **2022**, *22*.
- (18) Cai, S.; Pataillot-Meakin, T.; Shibakawa, A.; Ren, R.; Bevan, C. L.; Ladame, S.; Ivanov, A. P.; Edel, J. B. Single-Molecule Amplification-Free Multiplexed Detection of Circulating microRNA Cancer Biomarkers from Serum. *Nat. Commun.* **2021**, *12* (1), 3515. <https://doi.org/10.1038/s41467-021-23497-y>.
- (19) CDC. *Monitoring Your Blood Sugar*. Centers for Disease Control and Prevention. <https://www.cdc.gov/diabetes/managing/managing-blood-sugar/bloodglucosemonitoring.html> (accessed 2024-02-20).
- (20) Ahmed, F.; Plantman, S.; Cernak, I.; Agoston, D. V. The Temporal Pattern of Changes in Serum Biomarker Levels Reveals Complex and Dynamically Changing Pathologies after Exposure to a Single Low-Intensity Blast in Mice. *Front. Neurol.* **2015**, *6*.
- (21) Dieckmann, K.-P.; Radtke, A.; Geczi, L.; Matthies, C.; Anheuser, P.; Eckardt, U.; Sommer, J.; Zengerling, F.; Trenti, E.; Pichler, R.; Belz, H.; Zastrow, S.; Winter, A.; Melchior, S.; Hammel, J.; Kranz, J.; Bolten, M.; Krege, S.; Haben, B.; Loidl, W.; Ruf, C. G.; Heinzlbecker, J.; Heidenreich, A.; Cremers, J. F.; Oing, C.; Hermanns, T.; Fankhauser, C. D.; Gillessen, S.; Reichegger, H.; Cathomas, R.; Pichler, M.; Hentrich, M.; Eredics, K.; Lorch, A.; Wülfing, C.; Peine, S.; Wosniok, W.; Bokemeyer, C.; Belge, G. Serum Levels of MicroRNA-371a-3p (M371 Test) as a New Biomarker of Testicular Germ Cell Tumors: Results of a Prospective Multicentric Study. *J. Clin. Oncol.* **2019**, *37* (16), 1412–1423. <https://doi.org/10.1200/JCO.18.01480>.
- (22) Stohl, W.; Hilbert, D. M. The Discovery and Development of Belimumab: The Anti-BLyS–Lupus Connection. *Nat. Biotechnol.* **2012**, *30* (1), 69–77. <https://doi.org/10.1038/nbt.2076>.
- (23) Costa, I. M.; Soares, P. J.; Afonso, M.; Ratado, P.; Lanao, J. M.; Falcão, A. C. Therapeutic Monitoring of Warfarin: The Appropriate Response Marker. *J. Pharm. Pharmacol.* **2010**, *52* (11), 1405–1410. <https://doi.org/10.1211/0022357001777405>.

- (24) Meyvisch, P.; Kambili, C.; Andries, K.; Lounis, N.; Theeuwes, M.; Dannemann, B.; Vandebosch, A.; Van Der Elst, W.; Molenberghs, G.; Alonso, A. Evaluation of Six Months Sputum Culture Conversion as a Surrogate Endpoint in a Multidrug Resistant-Tuberculosis Trial. *PLOS ONE* **2018**, *13* (7), e0200539. <https://doi.org/10.1371/journal.pone.0200539>.
- (25) Chang, C. M.; Cheng, Y.-C.; Cho, T. M.; Mishina, E. V.; Del Valle-Pinero, A. Y.; van Bommel, D. M.; Hatsukami, D. K. Biomarkers of Potential Harm: Summary of an FDA-Sponsored Public Workshop. *Nicotine Tob. Res.* **2019**, *21* (1), 3–13. <https://doi.org/10.1093/ntr/ntx273>.
- (26) Makena, P.; Scott, E.; Chen, P.; Liu, H.-P.; Jones, B. A.; Prasad, G. L. Biomarkers of Exposure and Potential Harm in Two Weeks of Smoking Abstinence: Changes in Biomarkers of Platelet Function, Oxidative Stress, and Inflammation. *Int. J. Mol. Sci.* **2023**, *24* (7), 6286. <https://doi.org/10.3390/ijms24076286>.
- (27) Xu, Y.; Fu, Y.; Zhu, B.; Wang, J.; Zhang, B. Predictive Biomarkers of Immune Checkpoint Inhibitors-Related Toxicities. *Front. Immunol.* **2020**, *11*.
- (28) Fujimura, T.; Sato, Y.; Tanita, K.; Kambayashi, Y.; Otsuka, A.; Fujisawa, Y.; Yoshino, K.; Matsushita, S.; Funakoshi, T.; Hata, H.; Yamamoto, Y.; Uchi, H.; Nonomura, Y.; Tanaka, R.; Aoki, M.; Imafuku, K.; Okuhira, H.; Furudate, S.; Hidaka, T.; Aiba, S. Serum Levels of Soluble CD163 and CXCL5 May Be Predictive Markers for Immune-Related Adverse Events in Patients with Advanced Melanoma Treated with Nivolumab: A Pilot Study. *Oncotarget* **2018**, *9* (21), 15542–15551. <https://doi.org/10.18632/oncotarget.24509>.
- (29) Valpione, S.; Pasquali, S.; Campana, L. G.; Piccin, L.; Mocellin, S.; Pigozzo, J.; Chiarion-Sileni, V. Sex and Interleukin-6 Are Prognostic Factors for Autoimmune Toxicity Following Treatment with Anti-CTLA4 Blockade. *J. Transl. Med.* **2018**, *16* (1), 94. <https://doi.org/10.1186/s12967-018-1467-x>.
- (30) Vickers, A. J.; Brewster, S. F. PSA Velocity and Doubling Time in Diagnosis and Prognosis of Prostate Cancer. *Br. J. Med. Surg. Urol.* **2012**, *5* (4), 162–168. <https://doi.org/10.1016/j.bjmsu.2011.08.006>.
- (31) Díaz-Beyá, M.; Brunet, S.; Nomdedéu, J.; Tejero, R.; Díaz, T.; Pratcorona, M.; Tormo, M.; Ribera, J. M.; Escoda, L.; Duarte, R.; Gallardo, D.; Heras, I.; Queipo de Llano, M. P.; Bargay, J.; Monzo, M.; Sierra, J.; Navarro, A.; Esteve, J. MicroRNA Expression at Diagnosis Adds Relevant Prognostic Information to Molecular Categorization in Patients with Intermediate-Risk Cytogenetic Acute Myeloid Leukemia. *Leukemia* **2014**, *28* (4), 804–812. <https://doi.org/10.1038/leu.2013.281>.
- (32) Hajizamani, S.; Shahjahani, M.; Shahrabi, S.; Saki, N. MicroRNAs as Prognostic Biomarker and Relapse Indicator in Leukemia. *Clin. Transl. Oncol.* **2017**, *19* (8), 951–960. <https://doi.org/10.1007/s12094-017-1638-x>.
- (33) Senior, J. R. Evolution of the Food and Drug Administration Approach to Liver Safety Assessment for New Drugs: Current Status and Challenges. *Drug Saf.* **2014**, *37* (Suppl 1), 9–17. <https://doi.org/10.1007/s40264-014-0182-7>.
- (34) Wasung, M. E.; Chawla, L. S.; Madero, M. Biomarkers of Renal Function, Which and When? *Clin. Chim. Acta Int. J. Clin. Chem.* **2015**, *438*, 350–357. <https://doi.org/10.1016/j.cca.2014.08.039>.
- (35) Jin, T. Y.; Park, K. S.; Nam, S. E.; Yoo, Y. B.; Park, W. S.; Yun, I. J. BRCA1/2 Serves as a Biomarker for Poor Prognosis in Breast Carcinoma. *Int. J. Mol. Sci.* **2022**, *23* (7), 3754. <https://doi.org/10.3390/ijms23073754>.

- (36) Carser, J. E.; Quinn, J. E.; Michie, C. O.; O'Brien, E. J.; McCluggage, W. G.; Maxwell, P.; Lamers, E.; Lioe, T. F.; Williams, A. R. W.; Kennedy, R. D.; Gourley, C.; Harkin, D. P. BRCA1 Is Both a Prognostic and Predictive Biomarker of Response to Chemotherapy in Sporadic Epithelial Ovarian Cancer. *Gynecol. Oncol.* **2011**, *123* (3), 492–498. <https://doi.org/10.1016/j.ygyno.2011.08.017>.
- (37) Jin, J.; Zhang, W.; Ji, W.; Yang, F.; Guan, X. Predictive Biomarkers for Triple Negative Breast Cancer Treated with Platinum-Based Chemotherapy. *Cancer Biol. Ther.* **2017**, *18* (6), 369–378. <https://doi.org/10.1080/15384047.2017.1323582>.
- (38) James, C. R.; Quinn, J. E.; Mullan, P. B.; Johnston, P. G.; Harkin, D. P. BRCA1, a Potential Predictive Biomarker in the Treatment of Breast Cancer. *The Oncologist* **2007**, *12* (2), 142–150. <https://doi.org/10.1634/theoncologist.12-2-142>.
- (39) Hernández, J.; Thompson, I. M. Prostate-Specific Antigen: A Review of the Validation of the Most Commonly Used Cancer Biomarker. *Cancer* **2004**, *101* (5), 894–904. <https://doi.org/10.1002/cncr.20480>.
- (40) Payne, H.; Cornford, P. Prostate-Specific Antigen: An Evolving Role in Diagnosis, Monitoring, and Treatment Evaluation in Prostate Cancer. *Urol. Oncol. Semin. Orig. Investig.* **2011**, *29* (6), 593–601. <https://doi.org/10.1016/j.urolonc.2009.11.003>.
- (41) Simrén, J.; Leuzy, A.; Karikari, T. K.; Hye, A.; Benedet, A. L.; Lantero-Rodriguez, J.; Mattsson-Carlgren, N.; Schöll, M.; Mecocci, P.; Vellas, B.; Tsolaki, M.; Kloszewska, I.; Soininen, H.; Lovestone, S.; Aarsland, D.; Consortium, for the A.; Hansson, O.; Rosa-Neto, P.; Westman, E.; Blennow, K.; Zetterberg, H.; Ashton, N. J. The Diagnostic and Prognostic Capabilities of Plasma Biomarkers in Alzheimer's Disease. *Alzheimers Dement.* **2021**, *17* (7), 1145–1156. <https://doi.org/10.1002/alz.12283>.
- (42) Janelidze, S.; Mattsson, N.; Palmqvist, S.; Smith, R.; Beach, T. G.; Serrano, G. E.; Chai, X.; Proctor, N. K.; Eichenlaub, U.; Zetterberg, H.; Blennow, K.; Reiman, E. M.; Stomrud, E.; Dage, J. L.; Hansson, O. Plasma P-Tau181 in Alzheimer's Disease: Relationship to Other Biomarkers, Differential Diagnosis, Neuropathology and Longitudinal Progression to Alzheimer's Dementia. *Nat. Med.* **2020**, *26* (3), 379–386. <https://doi.org/10.1038/s41591-020-0755-1>.
- (43) Borrebaeck, C. A. K. Precision Diagnostics: Moving towards Protein Biomarker Signatures of Clinical Utility in Cancer. *Nat. Rev. Cancer* **2017**, *17* (3), 199–204. <https://doi.org/10.1038/nrc.2016.153>.
- (44) Tanaka, T.; Basisty, N.; Fantoni, G.; Candia, J.; Moore, A. Z.; Biancotto, A.; Schilling, B.; Bandinelli, S.; Ferrucci, L. Plasma Proteomic Biomarker Signature of Age Predicts Health and Life Span. *eLife* **2020**, *9*, e61073. <https://doi.org/10.7554/eLife.61073>.
- (45) Mao, X.-Y.; Perez-Losada, J.; Abad, M.; Rodríguez-González, M.; Rodríguez, C. A.; Mao, J.-H.; Chang, H. iCEMIGE: Integration of CELL-Morphometrics, Microbiome, and GENE Biomarker Signatures for Risk Stratification in Breast Cancers. *World J. Clin. Oncol.* **2022**, *13* (7), 616–629. <https://doi.org/10.5306/wjco.v13.i7.616>.
- (46) Wu, I.-W.; Tsai, T.-H.; Lo, C.-J.; Chou, Y.-J.; Yeh, C.-H.; Chan, Y.-H.; Chen, J.-H.; Hsu, P. W.-C.; Pan, H.-C.; Hsu, H.-J.; Chen, C.-Y.; Lee, C.-C.; Shyu, Y.-C.; Lin, C.-L.; Cheng, M.-L.; Lai, C.-C.; Sytwu, H.-K.; Tsai, T.-F. Discovering a Trans-Omics Biomarker Signature That Predisposes High Risk Diabetic Patients to Diabetic Kidney Disease. *Npj Digit. Med.* **2022**, *5* (1), 1–10. <https://doi.org/10.1038/s41746-022-00713-7>.
- (47) Silman, N. J. Rapid Diagnosis of Sepsis Using Biomarker Signatures. *Crit. Care* **2013**, *17* (6), 1020. <https://doi.org/10.1186/cc13137>.

- (48) Ware, L. B.; Koyama, T.; Zhao, Z.; Janz, D. R.; Wickersham, N.; Bernard, G. R.; May, A. K.; Calfee, C. S.; Matthay, M. A. Biomarkers of Lung Epithelial Injury and Inflammation Distinguish Severe Sepsis Patients with Acute Respiratory Distress Syndrome. *Crit. Care* **2013**, *17* (5), R253. <https://doi.org/10.1186/cc13080>.
- (49) Liu, L. Y.; Yang, T.; Ji, J.; Wen, Q.; Morgan, A. A.; Jin, B.; Chen, G.; Lyell, D. J.; Stevenson, D. K.; Ling, X. B.; Butte, A. J. Integrating Multiple ‘Omics’ Analyses Identifies Serological Protein Biomarkers for Preeclampsia. *BMC Med.* **2013**, *11* (1), 236. <https://doi.org/10.1186/1741-7015-11-236>.
- (50) Song, Y.; Sandford, E.; Tian, Y.; Yin, Q.; Kozminski, A. G.; Su, S.-H.; Cai, T.; Ye, Y.; Chung, M. T.; Lindstrom, R.; Goicochea, A.; Barabas, J.; Olesnavich, M.; Rozwadowski, M.; Li, Y.; Alam, H. B.; Singer, B. H.; Ghosh, M.; Choi, S. W.; Tewari, M.; Kurabayashi, K. Rapid Single-Molecule Digital Detection of Protein Biomarkers for Continuous Monitoring of Systemic Immune Disorders. *Blood* **2021**, *137* (12), 1591–1602. <https://doi.org/10.1182/blood.2019004399>.
- (51) Zhou, S.; Yang, Y.; Wu, Y.; Liu, S. Review: Multiplexed Profiling of Biomarkers in Extracellular Vesicles for Cancer Diagnosis and Therapy Monitoring. *Anal. Chim. Acta* **2021**, *1175*, 338633. <https://doi.org/10.1016/j.aca.2021.338633>.
- (52) Liu, C.; Chu, D.; Kalantar-Zadeh, K.; George, J.; Young, H. A.; Liu, G. Cytokines: From Clinical Significance to Quantification. *Adv. Sci.* **2021**, *8* (15), 2004433. <https://doi.org/10.1002/advs.202004433>.
- (53) Janeway, C.; Travers, P.; Walport, M.; Shlomchik, M. Chapter 2: Innate Immunity. In *Immunobiology: the immune system in health and disease*; Garland Science; pp 37–103.
- (54) Zhang, J.-M.; An, J. Cytokines, Inflammation and Pain. *Int. Anesthesiol. Clin.* **2007**, *45* (2), 27–37. <https://doi.org/10.1097/AIA.0b013e318034194e>.
- (55) Justiz Vaillant, A. A.; Qurie, A. Interleukin. In *StatPearls*; StatPearls Publishing: Treasure Island (FL), 2024.
- (56) Calabrese, L. H.; Rose-John, S. IL-6 Biology: Implications for Clinical Targeting in Rheumatic Disease. *Nat. Rev. Rheumatol.* **2014**, *10* (12), 720–727. <https://doi.org/10.1038/nrrheum.2014.127>.
- (57) Rose-John, S.; Winthrop, K.; Calabrese, L. The Role of IL-6 in Host Defence against Infections: Immunobiology and Clinical Implications. *Nat. Rev. Rheumatol.* **2017**, *13* (7), 399–409. <https://doi.org/10.1038/nrrheum.2017.83>.
- (58) Tanaka, T.; Narazaki, M.; Kishimoto, T. IL-6 in Inflammation, Immunity, and Disease. *Cold Spring Harb. Perspect. Biol.* **2014**, *6* (10), a016295. <https://doi.org/10.1101/cshperspect.a016295>.
- (59) Hughes, C. E.; Nibbs, R. J. B. A Guide to Chemokines and Their Receptors. *Febs J.* **2018**, *285* (16), 2944–2971. <https://doi.org/10.1111/febs.14466>.
- (60) Canna, S. W.; Cron, R. Q. Highways to Hell: Mechanism-Based Management of Cytokine Storm Syndromes. *J. Allergy Clin. Immunol.* **2020**, *146* (5), 949–959. <https://doi.org/10.1016/j.jaci.2020.09.016>.
- (61) Teijaro, J. R. Cytokine Storms in Infectious Diseases. *Semin. Immunopathol.* **2017**, *39* (5), 501–503. <https://doi.org/10.1007/s00281-017-0640-2>.
- (62) Clark, I. A.; Vissel, B. The Meteorology of Cytokine Storms, and the Clinical Usefulness of This Knowledge. *Semin. Immunopathol.* **2017**, *39* (5), 505–516. <https://doi.org/10.1007/s00281-017-0628-y>.

- (63) Zanza, C.; Romenskaya, T.; Manetti, A. C.; Franceschi, F.; La Russa, R.; Bertozzi, G.; Maiese, A.; Savioli, G.; Volonnino, G.; Longhitano, Y. Cytokine Storm in COVID-19: Immunopathogenesis and Therapy. *Medicina (Mex.)* **2022**, *58* (2), 144. <https://doi.org/10.3390/medicina58020144>.
- (64) Hu, B.; Huang, S.; Yin, L. The Cytokine Storm and COVID-19. *J. Med. Virol.* **2021**, *93* (1), 250–256. <https://doi.org/10.1002/jmv.26232>.
- (65) Han, H.; Ma, Q.; Li, C.; Liu, R.; Zhao, L.; Wang, W.; Zhang, P.; Liu, X.; Gao, G.; Liu, F.; Jiang, Y.; Cheng, X.; Zhu, C.; Xia, Y. Profiling Serum Cytokines in COVID-19 Patients Reveals IL-6 and IL-10 Are Disease Severity Predictors. *Emerg. Microbes Infect.* **2020**, *9* (1), 1123–1130. <https://doi.org/10.1080/22221751.2020.1770129>.
- (66) Guo, X. J.; Thomas, P. G. New Fronts Emerge in the Influenza Cytokine Storm. *Semin. Immunopathol.* **2017**, *39* (5), 541–550. <https://doi.org/10.1007/s00281-017-0636-y>.
- (67) Srikiatkachorn, A.; Mathew, A.; Rothman, A. L. Immune-Mediated Cytokine Storm and Its Role in Severe Dengue. *Semin. Immunopathol.* **2017**, *39* (5), 563–574. <https://doi.org/10.1007/s00281-017-0625-1>.
- (68) Chousterman, B. G.; Swirski, F. K.; Weber, G. F. Cytokine Storm and Sepsis Disease Pathogenesis. *Semin. Immunopathol.* **2017**, *39* (5), 517–528. <https://doi.org/10.1007/s00281-017-0639-8>.
- (69) Opal, S. M.; DePalo, V. A. Anti-Inflammatory Cytokines. *Chest* **2000**, *117* (4), 1162–1172. <https://doi.org/10.1378/chest.117.4.1162>.
- (70) Kawaguchi, M.; Adachi, M.; Oda, N.; Kokubu, F.; Huang, S.-K. IL-17 Cytokine Family. *J. Allergy Clin. Immunol.* **2004**, *114* (6), 1265–1273. <https://doi.org/10.1016/j.jaci.2004.10.019>.
- (71) Kopitar-Jerala, N. The Role of Interferons in Inflammation and Inflammasome Activation. *Front. Immunol.* **2017**, *8*, 873. <https://doi.org/10.3389/fimmu.2017.00873>.
- (72) *Infectious Disease: Types, Causes & Treatments*. Cleveland Clinic. <https://my.clevelandclinic.org/health/diseases/17724-infectious-diseases> (accessed 2024-02-20).
- (73) Tarrant, J. M. Blood Cytokines as Biomarkers of In Vivo Toxicity in Preclinical Safety Assessment: Considerations for Their Use. *Toxicol. Sci.* **2010**, *117* (1), 4–16. <https://doi.org/10.1093/toxsci/kfq134>.
- (74) Aydin, S. A Short History, Principles, and Types of ELISA, and Our Laboratory Experience with Peptide/Protein Analyses Using ELISA. *Peptides* **2015**, *72*, 4–15. <https://doi.org/10.1016/j.peptides.2015.04.012>.
- (75) The Enzyme-Linked Immunosorbent Assay (ELISA). *Bull. World Health Organ.* **1976**, *54* (2), 129–139.
- (76) *Ella Instrument - Automated Immunoassay* | ProteinSimple. Bio-Techne. <https://www.bio-techne.com/> (accessed 2024-02-20).
- (77) *What is a Luminex® Assay?*. www.rndsystems.com. <https://www.rndsystems.com/what-luminex-assay> (accessed 2024-02-20).
- (78) *Luminex Assay Principle*. www.rndsystems.com. <https://www.rndsystems.com/resources/technical/luminex-assay-principle> (accessed 2024-02-20).
- (79) *Simoa® Technology*. Quanterix. <https://www.quanterix.com/simoa-technology/> (accessed 2024-02-20).

- (80) *AutoPlex Automated Multiplex Biomarker Analysis*.
<https://www.alpco.com/resources/automated-multiplex-assay> (accessed 2024-02-20).
- (81) Elshal, M. F.; McCoy, J. P. Multiplex Bead Array Assays: Performance Evaluation and Comparison of Sensitivity to ELISA. *Methods San Diego Calif* **2006**, *38* (4), 317–323.
<https://doi.org/10.1016/j.ymeth.2005.11.010>.
- (82) Yu, D.; Humar, M.; Meserve, K.; Bailey, R. C.; Chormaic, S. N.; Vollmer, F. Whispering-Gallery-Mode Sensors for Biological and Physical Sensing. *Nat. Rev. Methods Primer* **2021**, *1* (1), 83. <https://doi.org/10.1038/s43586-021-00079-2>.
- (83) Vos, K. D.; Bartolozzi, I.; Schacht, E.; Bienstman, P.; Baets, R. Silicon-on-Insulator Microring Resonator for Sensitive and Label-Free Biosensing. *Opt. Express* **2007**, *15* (12), 7610–7615. <https://doi.org/10.1364/OE.15.007610>.
- (84) *Move Data, not Blood - 30 Minutes Results - Onsite Lab Automation*.
<https://www.genalyte.com/> (accessed 2024-02-19).
- (85) Iqbal, M.; Gleeson, M. A.; Spaugh, B.; Tybor, F.; Gunn, W. G.; Hochberg, M.; Baehr-Jones, T.; Bailey, R. C.; Gunn, L. C. Label-Free Biosensor Arrays Based on Silicon Ring Resonators and High-Speed Optical Scanning Instrumentation. *IEEE J. Sel. Top. Quantum Electron.* **2010**, *16* (3), 654–661. <https://doi.org/10.1109/JSTQE.2009.2032510>.
- (86) Bailey, R. C.; Washburn, A. L.; Qavi, A. J.; Iqbal, M.; Gleeson, M.; Tybor, F.; Gunn, L. C. A Robust Silicon Photonic Platform for Multiparameter Biological Analysis; Kubby, J. A., Reed, G. T., Eds.; San Jose, CA, 2009; p 72200N. <https://doi.org/10.1117/12.809819>.
- (87) Luchansky, M. S.; Washburn, A. L.; Martin, T. A.; Iqbal, M.; Gunn, L. C.; Bailey, R. C. Characterization of the Evanescent Field Profile and Bound Mass Sensitivity of a Label-Free Silicon Photonic Microring Resonator Biosensing Platform. *Biosens. Bioelectron.* **2010**, *26* (4), 1283–1291. <https://doi.org/10.1016/j.bios.2010.07.010>.
- (88) Tsai, D. P.; Jackson, H. E.; Reddick, R. C.; Sharp, S. H.; Warmack, R. J. Photon Scanning Tunneling Microscope Study of Optical Waveguides. *Appl. Phys. Lett.* **1990**, *56* (16), 1515–1517. <https://doi.org/10.1063/1.103160>.
- (89) Hutchinson, A. M. Evanescent Wave Biosensors. *Mol. Biotechnol.* **1995**, *3* (1), 47–54.
<https://doi.org/10.1007/BF02821334>.
- (90) Ramachandran, A.; Wang, S.; Clarke, J.; Ja, S. J.; Goad, D.; Wald, L.; Flood, E. M.; Knobbe, E.; Hryniewicz, J. V.; Chu, S. T.; Gill, D.; Chen, W.; King, O.; Little, B. E. A Universal Biosensing Platform Based on Optical Micro-Ring Resonators. *Biosens. Bioelectron.* **2008**, *23* (7), 939–944. <https://doi.org/10.1016/j.bios.2007.09.007>.
- (91) Wu, S.; Guo, Y.; Wang, W.; Zhou, J.; Zhang, Q. Label-Free Biosensing Using a Microring Resonator Integrated with Poly-(Dimethylsiloxane) Microfluidic Channels. *Rev. Sci. Instrum.* **2019**, *90* (3), 035004. <https://doi.org/10.1063/1.5074134>.
- (92) Washburn, A. L.; Gunn, L. C.; Bailey, R. C. Label-Free Quantitation of a Cancer Biomarker in Complex Media Using Silicon Photonic Microring Resonators. *Anal. Chem.* **2009**, *81* (22), 9499–9506. <https://doi.org/10.1021/ac902006p>.
- (93) Luchansky, M. S.; Washburn, A. L.; McClellan, M. S.; Bailey, R. C. Sensitive On-Chip Detection of a Protein Biomarker in Human Serum and Plasma over an Extended Dynamic Range Using Silicon Photonic Microring Resonators and Sub-Micron Beads. *Lab. Chip* **2011**, *11* (12), 2042. <https://doi.org/10.1039/c1lc20231f>.
- (94) Shia, W. W.; Bailey, R. C. Single Domain Antibodies for the Detection of Ricin Using Silicon Photonic Microring Resonator Arrays. *Anal. Chem.* **2013**, *85* (2), 805–810.
<https://doi.org/10.1021/ac3030416>.

- (95) Robison, H. M.; Bailey, R. C. A Guide to Quantitative Biomarker Assay Development Using Whispering Gallery Mode Biosensors: Whispering Gallery Mode Biosensors. *Curr. Protoc. Chem. Biol.* **2017**, *9* (3), 158–173. <https://doi.org/10.1002/cpch.23>.
- (96) Arnfinnsdottir, N. B.; Chapman, C. A.; Bailey, R. C.; Aksnes, A.; Stokke, B. T. Impact of Silanization Parameters and Antibody Immobilization Strategy on Binding Capacity of Photonic Ring Resonators. *Sensors* **2020**, *20* (11), 3163. <https://doi.org/10.3390/s20113163>.
- (97) Scheler, O.; Kindt, J. T.; Qavi, A. J.; Kaplinski, L.; Glynn, B.; Barry, T.; Kurg, A.; Bailey, R. C. Label-Free, Multiplexed Detection of Bacterial tmRNA Using Silicon Photonic Microring Resonators. *Biosens. Bioelectron.* **2012**, *36* (1), 56–61. <https://doi.org/10.1016/j.bios.2012.03.037>.
- (98) Qavi, A. J.; Bailey, R. C. Multiplexed Detection and Label-Free Quantitation of MicroRNAs Using Arrays of Silicon Photonic Microring Resonators. *Angew. Chem. Int. Ed.* **2010**, *49* (27), 4608–4611. <https://doi.org/10.1002/anie.201001712>.
- (99) McClellan, M. S.; Domier, L. L.; Bailey, R. C. Label-Free Virus Detection Using Silicon Photonic Microring Resonators. *Biosens. Bioelectron.* **2012**, *31* (1), 388–392. <https://doi.org/10.1016/j.bios.2011.10.056>.
- (100) Kindt, J. T.; Luchansky, M. S.; Qavi, A. J.; Lee, S.-H.; Bailey, R. C. Subpicogram Per Milliliter Detection of Interleukins Using Silicon Photonic Microring Resonators and an Enzymatic Signal Enhancement Strategy. *Anal. Chem.* **2013**, *85* (22), 10653–10657. <https://doi.org/10.1021/ac402972d>.
- (101) Medfisch, S. M.; Muehl, E. M.; Morrissey, J. H.; Bailey, R. C. Phosphatidylethanolamine-Phosphatidylserine Binding Synergy of Seven Coagulation Factors Revealed Using Nanodisc Arrays on Silicon Photonic Sensors. *Sci. Rep.* **2020**, *10* (1), 17407. <https://doi.org/10.1038/s41598-020-73647-3>.
- (102) Woo Kim, K.; Shin, Y.; Promoda Perera, A.; Liu, Q.; Sheng Kee, J.; Han, K.; Yoon, Y.-J.; Kyoung Park, M. Label-Free, PCR-Free Chip-Based Detection of Telomerase Activity in Bladder Cancer Cells. *Biosens. Bioelectron.* **2013**, *45*, 152–157. <https://doi.org/10.1016/j.bios.2013.02.001>.
- (103) Qavi, A. J.; Kindt, J. T.; Gleeson, M. A.; Bailey, R. C. Anti-DNA:RNA Antibodies and Silicon Photonic Microring Resonators: Increased Sensitivity for Multiplexed microRNA Detection. *Anal. Chem.* **2011**, *83* (15), 5949–5956. <https://doi.org/10.1021/ac201340s>.
- (104) Luchansky, M. S.; Bailey, R. C. Silicon Photonic Microring Resonators for Quantitative Cytokine Detection and T-Cell Secretion Analysis. *Anal. Chem.* **2010**, *82* (5), 1975–1981. <https://doi.org/10.1021/ac902725q>.
- (105) Valera, E.; McClellan, M. S.; Bailey, R. C. Magnetically-Actuated, Bead-Enhanced Silicon Photonic Immunosensor. *Anal. Methods* **2015**, *7* (20), 8539–8544. <https://doi.org/10.1039/C5AY01477H>.
- (106) Robison, H. M.; Escalante, P.; Valera, E.; Erskine, C. L.; Auvil, L.; Sasieta, H. C.; Bushell, C.; Welge, M.; Bailey, R. C. Precision Immunoprofiling to Reveal Diagnostic Signatures for Latent Tuberculosis Infection and Reactivation Risk Stratification. *Integr. Biol.* **2019**, *11* (1), 16–25. <https://doi.org/10.1093/intbio/zyz001>.
- (107) Wu, C.; Maley, A. M.; Walt, D. R. Single-Molecule Measurements in Microwells for Clinical Applications. *Crit. Rev. Clin. Lab. Sci.* **2020**, *57* (4), 270–290. <https://doi.org/10.1080/10408363.2019.1700903>.

- (108) Wade, J. H.; Bailey, R. C. Applications of Optical Microcavity Resonators in Analytical Chemistry. *Annu. Rev. Anal. Chem.* **2016**, *9* (1), 1–25. <https://doi.org/10.1146/annurev-anchem-071015-041742>.
- (109) Wang, F.; Anderson, M.; Bernards, M. T.; Hunt, H. K. PEG Functionalization of Whispering Gallery Mode Optical Microresonator Biosensors to Minimize Non-Specific Adsorption during Targeted, Label-Free Sensing. *Sensors* **2015**, *15* (8), 18040–18060. <https://doi.org/10.3390/s150818040>.
- (110) Kirk, J. T.; Brault, N. D.; Baehr-Jones, T.; Hochberg, M.; Jiang, S.; Ratner, D. M. Zwitterionic Polymer-Modified Silicon Microring Resonators for Label-Free Biosensing in Undiluted Human Plasma. *Biosens. Bioelectron.* **2013**, *42*, 10.1016/j.bios.2012.10.079. <https://doi.org/10.1016/j.bios.2012.10.079>.
- (111) Limpoco, F. T.; Bailey, R. C. Real-Time Monitoring of Surface-Initiated Atom Transfer Radical Polymerization Using Silicon Photonic Microring Resonators: Implications for Combinatorial Screening of Polymer Brush Growth Conditions. *J. Am. Chem. Soc.* **2011**, *133* (38), 14864–14867. <https://doi.org/10.1021/ja205358g>.

Chapter 2 Detection of Biomarkers for Filoviral Infection with a Silicon Photonic Resonator Platform

2.1 Author Contributions and Acknowledgements

This chapter has been published as a detailed protocol paper: **Meserve, K.***, Qavi, A.* , Aman, M.J., Vu, H., Zeitlin, L., Dye, J.M., Froude, J.W., Leung, D.W., Yang, L., Holtsberg, F.W., Bailey, R.C., Amarasinghe, G.K. [Detection of biomarkers for filoviral infection with a silicon photonic resonator platform](#). *STAR Protocols* 3, 2022, [* co-first authors]. The thesis author, Krista Meserve, was the primary writer of this manuscript, completed the method and assay development for the project, and designed and generated all figures within the manuscript. Dr. Abe Qavi aided in manuscript editing and wrote sections related to the *in-vivo* studies.

I would like to thank Dr. Abe Qavi and Dr. Gaya Amarasinghe from Washington University School of Medicine (WashU) for their mentorship through the course of this project. I acknowledge Dr. Fredrick Holtzberg, Dr. M. Javad Aman, and Hong Vu from Integrated Biotherapeutics for providing the specific antibodies and standards; Dr. Larry Zeitlin from Mapp Biopharmaceuticals, Dr. John M. Dye from the United States Army Medical Research Institute of Infectious Diseases, and Dr. Jeffrey W. Froude from the United States Army Nuclear and Countering Weapons of Mass Destruction Agency for providing the non-human primate samples; Dr. Daisy Leung and Dr. Lan Yang from WashU for manuscript editing; and Dr. Ryan Bailey for project guidance. Additionally, I would like to thank Genalyte, Inc. for providing the raw chips I spotted for this project.

2.2 Abstract

This protocol describes the use of silicon photonic microring resonator sensors for detection of Ebola virus (EBOV) and Sudan virus (SUDV) soluble glycoprotein (sGP). This protocol encompasses biosensor functionalization of silicon microring resonator chips, detection of protein biomarkers in sera, preparing calibration standards for analytical validation, and quantification of the results from these experiments. This protocol is readily adaptable toward other analytes, including cytokines, chemokines, nucleic acids, and viruses. For complete details on the use and execution of this protocol, please refer to Qavi and Meserve, *et al.* (2022).¹

2.3 Before You Begin

The protocol below describes the specific steps for detection of EBOV sGP and SUDV sGP using the microring resonator sensing platform. However, we have used this protocol for detection of varying cytokines,² chemokines,³ nucleic acids,⁴ and viruses.⁵ Additionally, we have used this protocol for detection of cytokines and chemokines in clinical samples for precision medicine applications.^{6,7}

2.3.1 Institutional Permissions.

All animal studies were performed under approval of the local IACUC committees. All work was performed in compliance with the Animal Welfare Act and other federal statutes and regulations relating to animals. The USARMIID is accredited by the Association for Assessment and Accreditation of Laboratory Animal Care, International (AAALAC) and adhere to principles stated in the Guide for the Care and Use of Laboratory Animals, National Research Council.

2.3.2 Non-Human Primate Samples.

The collection of serum samples must be approved through appropriate Institutional Review Boards prior to any studies and be collected in accordance with local laws and regulations.

2.3.3 Critical Point.

Patient plasma samples carry risk of pathogens, not limited to hepatitis B (HBV), hepatitis C (HCV), and human immunodeficiency virus (HIV). Therefore, proper PPE must be utilized when handling any samples.⁸

2.3.4 Antibody Desalting and Dilution

Timing: 30 mins

1. Desalt the stock capture antibody solutions to remove azide from the formulation. The [Buffer Exchange Procedure](#) in the package insert from Thermo Scientific was followed.
 - a. Remove columns' bottom closure and loosen cap.
 - b. Place column in 1.5 mL collection tube and centrifuge at 1500 g for 1 min.
Discard filtrate.
 - c. Mark side of column where resin is slanted upward, place column in same orientation for each following spin.
 - d. Add 300 μ L of 1X PBS on top of resin bed, place back into 1.5 mL collection tube and centrifuge at 1500 g for 1 min. Discard filtrate. Repeat for a total of 3 resin washes.
 - e. Place column in new collection tube, pipette 50-100 μ L of antibody on top of resin bed.
 - f. Centrifuge at 1500 g for 2 mins and collect filtrate.

2. Measure the absorbance of the resulting filtrate from Step 1 at 280 nm using the Nanodrop1000 Spectrophotometer (Thermo Fisher Scientific) or equivalent.
 - a. In the software panel, select Protein A280.
 - b. Initialize the instrument by pipetting 1 μL of ultrapure water onto the measurement pedestal and initialize the software.
 - c. Clean the pedestal with DI water and blank by pipetting 1 μL of 1X PBS onto the measurement pedestal. Click 'Blank' on the software.
 - d. Clean the pedestal with DI water and pipette 1 μL of antibody sample onto the pedestal. Click 'Measure Sample' on the software.
 - e. Record the mg/mL output. Repeat step 2d twice more and then calculate the average mg/mL.
 - f. Dilute the filtered antibody solution to 0.5 mg/mL using 1X PBS, aliquot into 5 μL aliquots and store at $-80\text{ }^{\circ}\text{C}$ until use.

2.3.5 Key Resources Table

Please see the key resources table (**Table 2.1**) for a complete list of the materials, reagents, and equipment used in this protocol. Any version of Rstudio or other data processing software, such as excel, will work for this purpose. Any nanodrop or spectrophotometer that measures samples at 280 nm will work for this purpose.

2.3.6 Materials and Equipment

2.3.6.1 1X PBS

To make 1000 mL of a 137 mM NaCl and 10 mM phosphate solution, 9.6 grams of solid phosphate buffered saline was dissolved in 1000 mL of ultrapure water. The solution was filtered

through a 0.2 μm filter and stored at room temperature, 18°C to 22°C, for no longer than 12 months. Alternatively, solid sodium chloride and sodium phosphate can be substituted for phosphate buffered saline with final concentrations matched to above.

2.3.6.2 1X PBS-BSA

To make 1000 mL of a 137 mM NaCl, 10 mM phosphate, and 0.5% bovine serum albumin solution, 9.6 grams of solid phosphate buffered saline and 5 grams of solid bovine serum albumin were dissolved in 1000 mL of ultrapure water. The solution was filtered through a 0.2 μm filter and stored at 4°C for up to 6 months. Alternatively, solid sodium chloride and sodium phosphate can be substituted for phosphate buffered saline with final concentrations matched to above.

2.3.6.3 50% glycerol

To make 1 mL of a 50% glycerol solution, 500 μL of glycerol stock was added to 500 μL of ultrapure water. The solution was stored at room temperature, 18°C to 22°C, for up to 12 months.

2.4 Step-By-Step Method Details

2.4.1 Functionalization of Sensor Chip

Timing: 3-4 hours

This section describes the method to functionalize the silicon photonic microring sensor chips through silanization of the chip surface and use of a homo-bifunctional linker molecule to covalently attach the antibodies to the microring sensors. This step requires about 1-2 hours of active work and two 1-hour incubations.

1. Capture Antibody Preparation

This should be completed prior to the following steps to mitigate time restraints later in the protocol.

- a. In a 0.6 mL microcentrifuge tube, add 4 μ L of 1X PBS, 1 μ L of 50% glycerol and 5 μ L of anti-EBOV antibody at 0.5 mg/mL.
 - b. In a second 0.6 mL microcentrifuge tube, add 4 μ L of 1X PBS, 1 μ L of 50% glycerol and 5 μ L of anti-SUDV stored at 0.5 mg/mL.
 - c. In a third 0.6 mL microcentrifuge tube, add 25.7 μ L of 1X PBS, 3 μ L of 50% glycerol and 1.3 μ L of Ms IgG control antibody stored at 5 mg/mL.
 - i. The final concentration of capture antibodies is 0.25 mg/mL in 5% glycerol.
 - d. Store the diluted antibodies at 4° C until use. It is best to make fresh the day of spotting.
2. Silanization of Sensor Chip
- a. Collect five 20-mL scintillation vials and label them 1-5 (**Figure 2.1**).
 - b. Fill with the following:
 - i. Vials #1, #2, and #4: 2 mL acetone
 - ii. Vial #3: 1.9 mL acetone.
 - iii. Vial #5: 2 mL isopropanol.
 - c. Using clean tweezers, immerse up to six silicon photonic chips in scintillation vial #1. Secure vial onto orbital shaker and gently agitate for 2 mins.
 - d. Using tweezers, transfer the chips to Vial #2. Secure vial onto orbital shaker and gently agitate for 2 mins.
 - e. While chips are in Vial #2, prepare 5% APTES solution.

- i. Remove APTES from desiccated storage area.
 - ii. Use a syringe fitted with a needle tip to remove 100 μL of APTES from the bottle.
 - iii. Dispense APTES into scintillation vial #3 and recap vial.
 - iv. Return APTES to desiccated storage.
- f. Transfer the chips to scintillation Vial #3. Secure vial onto orbital shaker and gently agitate for 4 mins.
- g. Transfer the chips to scintillation Vial #4. Secure vial onto orbital shaker and gently agitate for 2 mins.
- h. Transfer the chips to scintillation Vial #5. Secure vial onto orbital shaker and gently agitate for 2 mins.
- i. While chips are in Vial #5, fill the top row (A) of 6 wells in the 24-well plate with deionized water (**Figure 2.2**).
- j. Transfer the chips to the water filled wells, with one chip per well.
- k. Remove chips from water and place onto a DURX 670 cleanroom wipe.
- l. Dry surface with N_2 gas line while holding the chip securely with tweezers. Place the dried chips in the second row (B) of wells in the 24 well plate.
- m. Prepare the BS3 reagent to 5 mM by adding 700 μL acetic acid to a 2 mg no weigh format vial of BS3. Vortex to fully dissolve solid.
 - i. The BS3 solution should be prepared fresh and added to the chip shortly after, as once prepared it is a limited active time (1 hr.) before hydrolysis of the NHS-ester moieties occur.

- n. Immediately pipette 20 μL of dissolved BS3 onto the sensor surface. Be sure to fully cover the microring sensor portion of the chip.
- o. Incubate for 3 mins. Briefly dip chips into the water in the first row (A) of the 24 well plate to rinse off BS3 and dry with N_2 gas. Place dried chips into third row (C) of 24-well plate.
- p. Cut a strip of a DURX 670 cleanroom wipe that is the length and width of the last row (D) of the 24 well plate. Dampen the strip with water and press onto the lid of the 24-well plate over the bottom row. This will create a humidity chamber to house the spotted chips.

3. Antibody Spotting

- a. Prepare chip spotting station at microscope by collecting the prepared chips, the 0.25 mg/mL antibodies, tweezers, 2.5 μL pipette set from 0.2-0.4 μL , pipette tips, and sensor layout map to annotate (**Figure 2.3a**).
- b. Place the first chip under the microscope, adjust the settings to 25X magnification and adjust focus on the sensor chip.
- c. Deposit 0.2-0.4 μL of the first antibody over 2-5 ring clusters in each of the two channels of rings. The exact volume can vary, lower volumes will cover fewer clusters and higher volumes will cover more clusters.
- d. Repeat with the remaining antibodies moving across the chip.
 - i. Take care to avoid any merging of drops of different antibodies, as this will result in cross reactivity (**Problem 1: Spill-over of capture agents while spotting**).

- ii. Using this hand spotting method, it is reasonable to deposit 2-4 antibodies in each channel, with each antibody spanning 2-4 clusters of microrings. For higher plexity, this spotting process would need to be completed through microspotting procedures. However, for this protocol, only three antibodies (anti-EBOV sGP, anti-SUDV sGP and anti-Ms IgG control) were needed in each channel.

For this work, the spotting generally looked like **Figure 2.3b-d**.

- e. Once all antibodies have been spotted, note down which clusters of rings are covered by each antibody (**Problem 2: Uneven spotting of ring clusters**). Label this as chip #1.
- f. Carefully transfer the completed chip to the final row (D) of the 24-well plate in the first position. Cover with well plate lid to create humidity chamber.
- g. Repeat steps 2-6 with remaining chips. It is important to know which spotting map layout corresponds to which chip.
- h. Leave chips at room temperature in the humidity chamber for 1 hour.
- i. Pipette 1 mL of starting block into each of the wells. Incubate chips in the starting block at room temperature under the humidity chamber for 1 hour.
- j. Remove chips from the 24-well plate and place on the DURX 670 cleanroom wipe. Take care to keep them in the same order. Dry with N₂ gas.
- k. Pipette 20 µL of dry coat solution over the surface of each chip. Gently tap the sides of the chip with the tweezers to wick off excess dry coat onto the DURX 670 cleanroom wipe. There should remain a thin layer of dry coat over the chip to stabilize the antibodies.

1. Place the chips into a gel pack. Place gel pack in a desiccator in a 4 °C refrigerator.

CRITICAL: Hold chips by the shorter sides to avoid damaging important chip features. Be gentle with the chips, do not drag the tweezers over the surface. Any chips or scratches can damage optical waveguides on the chip. If this occurs, discard of the chip as it is no longer reliable to use.

Pause point: Once the dry coat has been placed on the chip and they are stored, the chips will be stable for 1-6 months depending on antibody stability.

Note: BS3 solution should be made as close to use as possible to avoid hydrolysis. In this procedure, it is recommended that there are no stopping points once silanization begins to avoid loss of chip functionality.

Note: Before moving to calibration and analysis of the target in samples, it is important to validate that the antibody sandwich works on the assay platform. This includes optimizing the concentration of standard protein that elicits a saturated response and optimization of the biotinylated tracer antibody to ensure high response with minimal off-target binding.

Additionally, the control rings should demonstrate minimal wavelength shift from addition of target antigen in comparison to a blank with no target present.

Optional: This protocol has been optimized for the intended use with our specific instrumentation and experimental needs. However, there are varying options that could be

explored for other applications, such as choice of silane, linker molecule, and concentration of capture reagent. Additionally, other biorecognition molecules, such as DNA, can be used in place of antibodies.

2.4.2 Preparing Calibration Standards and Samples

Timing: 30-60 min

This section sets up the reagents for the immunoassay, including how to construct calibration standards, how to prepare biological samples, and how to prepare the amplification assay reagents.

4. Serial Dilutions for Calibration Standards

- a. Prepare 3,600 μL of stock pooled healthy human serum at concentration of interest by adding PBS-BSA buffer and pooled healthy serum to a labeled 5 mL Eppendorf tube.
 - i. 1% serum: 36 μL serum + 3,594 μL PBS-BSA
 - ii. 10% serum: 360 μL serum + 3,240 μL PBS-BSA
- b. Invert the Eppendorf tube five times to mix.
- c. Prepare eight 1.5 mL microcentrifuge tubes labeled 1-8.
- d. In tube 2, add 300 μL of diluted serum made in step 4a. In tubes 3-8, add 480 μL of diluted serum.
- e. In tube 1, add 16.8 μL each of thawed EBOV sGP standard and SUDV sGP standard (both standards stored at 100 $\mu\text{g}/\text{mL}$ in -80°C), pooled healthy serum and PBS-BSA buffer. The amount of serum and buffer varies for each calibration, as follows, for a total of 700 μL with each protein at 2.4 $\mu\text{g}/\text{mL}$.
 - i. 1% serum: 7 μL healthy serum + 659.4 μL PBS-BSA

- ii. 10% serum: 70 μL healthy serum + 596.4 μL PBS-BSA
- f. Close tube 1 and invert five times to mix. Remove 300 μL from tube 1 by pipetting up and down three times in tube 1 and then dispense by pipetting up and down three times into tube 2. Change pipette tip.
- g. Close tube 2 and invert five times to mix. Remove 120 μL from tube 2 by pipetting up and down three times in tube 2 and then dispense by pipetting up and down three times into tube 3. Change pipette tip.
- h. Repeat step 4g with the next chronological tube until tube 7 is reached. Do not add protein standard into tube 8, as this will serve as the matrix blank. Steps 4c-h are summarized in **Table 2.2**.

5. Sample Preparation

- a. Thaw the frozen sample to room temperature (18°C to 22°C).
- b. In a microcentrifuge tube, add PBS-BSA and thawed sample depending on which dilution is being prepared. In the corresponding study (Qavi, et al.), each sample was prepared at 10 \times and 100 \times in a total volume of 350 μL . A minimum of 330 μL is required on the Maverick Matchbox instrument.
 - i. 100 \times dilution: 3.5 μL sample + 346.5 μL PBS-BSA buffer
 - ii. 10 \times dilution: 35 μL sample + 315 μL PBS-BSA buffer

6. Prepare Detection Reagents

- a. In a 5 mL Eppendorf tube, make a tracer antibody solution at 2 $\mu\text{g}/\text{mL}$ by adding 2889.2 μL of PBS-BSA and 10.8 μL of the pan-EBOV/SUDV biotinylated tracer stored at 0.5 mg/mL. This is enough tracer for two channels on four chips, which is one full 8-point calibration, or four samples analyzed at two dilutions.

- b. Close the tube and invert five times to mix.
- c. In a 5 mL Eppendorf tube, make SAHRP solution at 3 $\mu\text{g}/\text{mL}$ by adding 2891.3 μL and 8.7 μL of SAHRP stored at 1 mg/mL . This is enough SAHRP for two channels on four chips, which is one full 8-point calibration, or four samples analyzed at two dilutions.
- d. Close the tube and invert five times to mix.

Note: Store all prepared reagents at 4°C until ready for use. Reagents (calibration standards, SAHRP, tracer) should be prepared the day of the experiment. The samples should be diluted and analyzed within eight hours of thawing. It is best to prepare smaller batches (enough for 2-4 chips at a time) to avoid any potential degradation or wasting of reagents.

Optional: The concentration of standard protein to reach the saturating condition and the concentration of the biotinylated tracer antibody were previously optimized for our experimental parameters. When optimizing new targets, a range of 300-500 ng/mL for the protein standard and 2 $\mu\text{g}/\text{mL}$ for the tracer are appropriate starting points. Adjustments can be made based on initial optimization experiments.

2.4.3 Running Calibration Standards and Samples on Microring Instrument

Timing: 10 mins prep work, 40 mins of assay run time per sample

This section explains how to plate the reagents prepared above for loading into the Genalyte Maverick Matchbox, as well as how to run the instrument interface.

7. Preparation of Reagents in 96-Well Plate

- a. Collect all reagents: PBS-BSA, calibration standards or diluted samples, diluted tracer antibody, diluted SAHRP, and 4-chloro-1-naphthol (4CN).
 - b. Fill a 96-well plate according to the diagram in **Table 2.3**. This diagram corresponds to the reagent positions in the instrument method in **Table 2.4**. With this configuration, the pumps draw liquid for channel 1 in the left well (columns 1 or 3) as it draws liquid for channel 2 in the right well (columns 2 or 4). It then moves from row A to row B and so forth.
 - c. Calibrations were analyzed as follows:
 - i. Experiment #1- channel 1: calibration tube 1, channel 2: calibration tube 8
 - ii. Experiment #2- channel 1: calibration tube 7, channel 2: calibration tube 2
 - iii. Experiment #3- channel 1: calibration tube 3, channel 2: calibration tube 6
 - iv. Experiment #4- channel 1: calibration tube 5, channel 2: calibration tube 4
 - d. Samples were analyzed as follows:
 - i. Day #1 of experiments- channel 1: 10× dilution, channel 2: 100× dilution
 - ii. Day #2 of experiments- channel 1: 100× dilution, channel 2: 10× dilution
 - e. Return reagents to 4 °C until next assay set up.
 - f. Bring filled 96 well plate to instrument and slide into well-plate holder.
8. Preparation of Microring Chip
- a. Remove one of the spotted chips from the storage gel pack.
 - b. Rinse chip with deionized water and dry with compressed air.
 - c. Insert the chip into the cartridge holder using the chip holder tool.
 - d. Use tweezers to push the chip into cartridge to ensure snug fit. Blow compressed air into the channels to free any remaining debris or liquid.

- e. Put cartridge/chip into instrument with the tubes towards the front of the holder.
9. Preparation of Instrument
- a. Open the instrument software interface.
 - b. In 'Register & Batch Run' tab, select recipe file (see **Table 2.4** for example recipe). The recipe file needs to be in .csv format.
 - c. Select data path (where data is to be stored after the experiment ends).
 - d. Enter chip name/identifier.
 - e. Click execute, close the door of the instrument as the chip registers.
 - f. After registration, the pumps will engage, which starts the fluid flow across the chip. Once this happens, it is helpful to reopen the instrument and observe the liquid flowing through the cartridge across both channels. Close the door before the scan starts and avoid opening it until the end of the experiment (**Problem 3: Clogging of microfluidic lines during experiment**).
 - g. Clean up area and prepare for next experiment.
 - i. Remove next sample from the freezer and put with the other reagents in the 4 °C to thaw slowly.
 - ii. The microring chip, cartridge holder, and any other disposable materials that touched the serum should be discarded as biohazardous waste.
10. Repeat steps 7-9 for all calibration standards and samples.

2.5 Expected Outcomes

For an immunoassay with both standards, an example trace post work-up of data is seen in **Figure 2.4a**. This is an example of tube 2 (1,200 ng/mL) for both EBOV sGP and SUDV sGP in 10% serum. Both sets of spotted rings respond to their corresponding antigen standard, and the

control rings have very low response. The bulk shift seen between 2 and 9 minutes corresponds to the analyte in the complex matrix flowing across the sensors. Once the extraneous component of the complex matrix is washed away in the buffer step, the response returns to baseline. The bulk shift between 30 and 37 minutes is due to the 4CN amplification reagent flowing across the surface. This solution has a different refractive index in comparison to the previous immunoassay steps, which are mainly composed of PBS-BSA. This causes a shift in resonant wavelength in all the rings. However, once the surface is rinsed with buffer, a new baseline is reached, and binding is identified in the rings spotted with the anti-EBOV sGP and anti-SUDV sGP antibodies.

An example 8-point calibration curve for EBOV sGP and SUDV sGP in a 10% serum matrix is seen in **Figure 2.4b**. The antigen concentration tested should span from a saturating range to a concentration at or below the limit of detection. Additionally, it is important to have points within the curve region and close to the center of the curve, as that region is where the assay is the most sensitive.

An example immunoassay of a sample containing EBOV sGP analyzed at a 10× dilution is seen in **Figure 2.4c**. While similar in profile to the standards example curve, only the rings spotted with anti-EBOV sGP respond. The anti-SUDV sGP rings result in bulk shifts and a final shift indistinguishable from the control spotted rings.

2.6 Quantification and Statistical Analysis

Timing: 5 mins per sample, 20-30 mins for final conversation to analyte concentration

This section starts with description of data output and then the data analysis for this specific project. The data was analyzed using R code modified from in-house developed code that is in a

GitHub repository. The general usage of the code can be found in BaileyLabUM/biosensor on GitHub.

1. Data Output and Work-up for Individual Experiments
 - a. The data output from the instrument is .csv files for each individual sensor ring. They contain the resonant wavelength (nm) at a specific time point, along with the time stamp.
 - b. To work up this data, the information in BaileyLabUM/biosensor GitHub repository is followed. First, create a ‘groupnames_allclusters’ file (found in BaileyLabUM/MRR repository) that correlates ring numbers with capture antibody spotted on them. Name each ring using the annotated spotting map from **Figure 2.3a** (from step 3e). For partially spotted clusters or for empty rings, they can be named “Ignore” in the file names and the code skips them.
 - c. For calibration data, input the concentration of target standard run in each channel in the ‘Concentration’ column in this file. Leave this value as ‘1’ for unknown concentrations.
 - d. Analyze each individual experiment using “analyzebiosensor” code (found in BaileyLabUM/biosensor repository).
 - i. This code first aggregates all the individual .csv files from an experiment, names each ring based on the manually annotated ‘groupnames_allclusters’ file, subtracts the thermal control sensor ring response from all rings, and then calculates the net shifts (**Problem 4: Malfunctioning microring sensors**).

- ii. The net shifts are calculated by subtracting the resonant wavelength prior to the amplification step from the resonant wavelength after the post-amplification buffer rinse. Using the recipe in **Table 2.4**, the net shift is calculated as the difference in resonant wavelength between minute 28 and minute 41.
- iii. The average and standard deviation of net shifts across the identically named rings is then calculated. The code outputs this set of net shift data for each channel in .csv files. Additionally, the code outputs multiple plots for data visualization, such as a trace plotting the resonant wavelength over time of assay (**Figure 2.4 a, c**) and bar graphs of the net shift for each individual ring (**Problem 5: High control ring response**).

2. Calibration Data Work-up

- a. Once each individual experiment is analyzed following step 1 and all 8 points of the calibration curve are done, complete the following to construct the calibration curve and calculate limits of detection and quantitation.
- b. Modify the ‘calibrationstation’ code (from BaileyLabUM/biosensor) for each specific target. Here, we specified EBOV sGP and SUDV sGP were the targets for calibration.
 - i. The code aggregates the net shifts and manually entered concentrations for all the calibration standards.
 - ii. The net shifts and concentration data for each target are fit to the following logistic function as previously described.⁹

$$y = \frac{A_1 - A_2}{1 + \left(\frac{x}{x_0}\right)^p} + A_2, \text{ where } y \text{ is the net shift } (\Delta\text{pm}) \text{ of the sample of}$$

concentration x (pM), A_1 is the minimum net shift (Δpm), A_2 is the maximum net shift (Δpm), x_0 is the center value (pM), and p is the power parameter affecting the slope around the inflection point.

- iii. After fitting the data to this function, the code outputs the fit parameters (A_1 , A_2 , x_0 and p) in a .csv file and plots the fit, along with each data point in the calibration curve on a log scale (**Figure 2.4b**).
 - iv. A four parametric logistic fit is chosen for direct comparison to traditional plate-based ELISA assays. Bioassays dependent on protein-protein interaction equilibriums result in non-linear responses upon analyte/ligand binding.¹⁰ The lower asymptote results from concentrations below the method's limit of detection in which no net shift response is seen over a range of concentrations. The upper horizontal asymptote results from concentrations above the saturating point of the capture antibodies where any additional antigen will not affect the response and may even decrease the response due to the hook effect. The ideal working range is the linear dynamic range of the curve, with mid-point of the curve providing the area of highest sensitivity.
- c. Calculate the limit of detection (LOD) and limit of quantitation (LOQ) from the fit parameters, the average net shifts, and standard deviations from the matrix blank (tube 8 in the calibration).
 - i. For LOD calculations, add the net shift from the matrix blank to 3 times the standard deviation. Using this calculated net shift as 'y', the fit

parameters, and the equation in step 2b, the concentration 'x' can be calculated. This concentration is the LOD.

ii. Similarly, for LOQ, take the same steps, but multiply the standard deviation of the blank by 10. Continue through to calculate the concentration 'x' based on this higher net shift 'y'. This concentration is the LOQ.

d. Repeat this calculation for each target in each calibration.

3. Conversion of Net Shift to Target Concentration

a. Once all samples have been analyzed and worked up as described in step 1, use the 'aggdata' code in BaileyLabUM/biosensor repository to complete the following tasks. This analysis could also be done manually using basic excel functions.

b. **Aggregation of data for each sample:** the average net shifts files that were created in step 1d are extracted for both channels per experiment. A new file is created that binds this aggregated net shift data with sample information including experiment number, subject ID, and dilution ID (10× or 100×) based on the name of the data file.

c. **Aggregation of all sample data:** this new file that was created for every experiment in 3b is then extracted and aggregated with the files from all samples.

d. **Conversion to concentration:** the fit parameters from step 2b iii need to be manually input into the 'aggdata' code for each target in both serum matrices. The four parametric logistic fit is used to convert each net shift to concentration (ng/mL).

- e. **Selection of dilution:** the data is sorted by experiment and by target. If two dilutions are present, the net shift closest to the inflection point of the calibration curve (where the assay is most sensitive) is kept, while the other dilution is removed from the data file.
- f. **Consider dilution factor:** depending on which dilution was chosen, the concentration is multiplied by the dilution factor (10× or 100×). At this point, each target in each sample has one final concentration associated with it.
- g. **Analysis:** Further analysis can be conducted on these final concentrations depending on what is necessary for the study.

2.7 Limitations

There are several limitations for this protocol. Assay response will vary based on the antibodies used and their respective affinities. This protocol also uses BS3 as a linker to covalently attach antibodies to the silanized sensor surface. As BS3 reacts with primary amines, this results in attachment of antibodies to the sensor surface in random orientations. This protocol also is designed for a two-step sandwich assay - primary detection of analytes in complex media may prove difficult given that the Maverick Matchbox platform is sensitive to changes in refractive index. While this assay has the potential to be used within a BSL3 or BSL4 facility, this protocol has currently only been performed in a BSL2 facility which necessitates irradiation of the samples, as well as significant precautions for user safety.

2.8 Troubleshooting

2.8.1 Problem 1: Spill-over of capture agents while spotting

This occurs when the drop of antibody capture agent of one antigen merges with that of a second antigen (step 3d). This can cause cross-reactivity and cannot be used reliably. This merging of spots is visualized in **Figure 2.3e**, channel 1.

Potential solution

If this occurs, do not use that chip, as it is not reliable. Practice spotting using water/glycerol solutions before using valuable reagents to understand the mechanics and pipette tip placement.

If this continues to occur, additional steps would be to decrease the volume of reagent being spotted (ie down to 0.2 μ L) or increasing the glycerol content from 5% to 10% in the spotting solution.

2.8.2 Problem 2: Uneven spotting of ring clusters

This occurs when the drop of antibody capture agent does not encapsulate entire ring clusters or rings themselves (step 3e). Even spotting looks like **Figure 2.3b-d**, while uneven spotting looks like **Figure 2.3e**, channel 2.

Potential solution

In the groupnames_allclusters file, type “Ignore” as the ring name for any clusters that are known to be partially spotted. This removes these rings from any data work up so if there is signal drop-off due to the variation in antibody coverage, it will not affect the results. Continue to use the chip, providing each capture antibody still spans at least 2-3 ring clusters.

2.8.3 Problem 3: Clogging of microfluidic lines during experiment

This occurs when a particle larger than the inner diameter of the instrument tubing gets stuck, causing a stoppage of flow of reagents across the chip and loss of data for that channel (step 9f).

Potential solution

Avoid using samples with particulates. If samples are particularly dirty, try briefly centrifuging them and only using the resulting supernatant. If clogging occurs, be sure to purge the lines of the instrument with water before starting the next sample. This would dislodge the blockage. It is good practice to purge the microfluidic lines with bleach and water after each day of running serum samples.

2.8.4 Problem 4: Malfunctioning microring sensors

Individual or clusters of microring sensors will sporadically malfunction. This could be due to a fabrication error with the specific sensor, a small alignment error, or other reasons (step 1d in Quantification and Statistical Analysis).

Potential solution

Continue letting the experiment run. During data work up, analyze all rings, then using one of the resulting csv files, identify which ring or ring cluster resulted in an abnormal trace or shift. In the groupnames_allclusters file, type “Ignore” for the ring(s) and reanalyze the data. This will remove the rogue ring(s) and results will not be affected.

2.8.5 Problem 5: High control ring response

If the control spotted rings are higher than they typically are (~500 pm net shift), the antibodies on the chip might have gone bad or there could have been capture reagent merging during spotting ((step 1d in Quantification and Statistical Analysis).

Potential solution

The data from this experiment should not be used, as the validity of the chip will be in question. If sample remains, rerun it on a different chip. If problem persists, re-spot and use fresher chips.

If this occurs during target validation, there could be some non-specific binding of target antigens or tracer antibodies and new reagent sets should be explored.

2.9 Figures

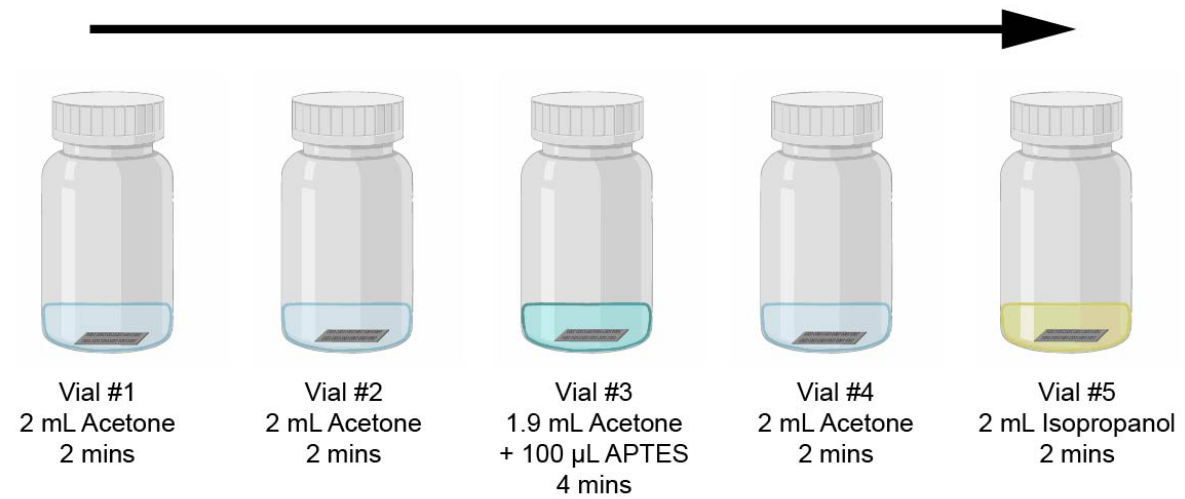


Figure 2.1 Sensor chip silanization diagram. The sensor chips should be moved through each vial after incubating on the orbital shaker for the specified amount of time (step 2). Created with BioRender.com.

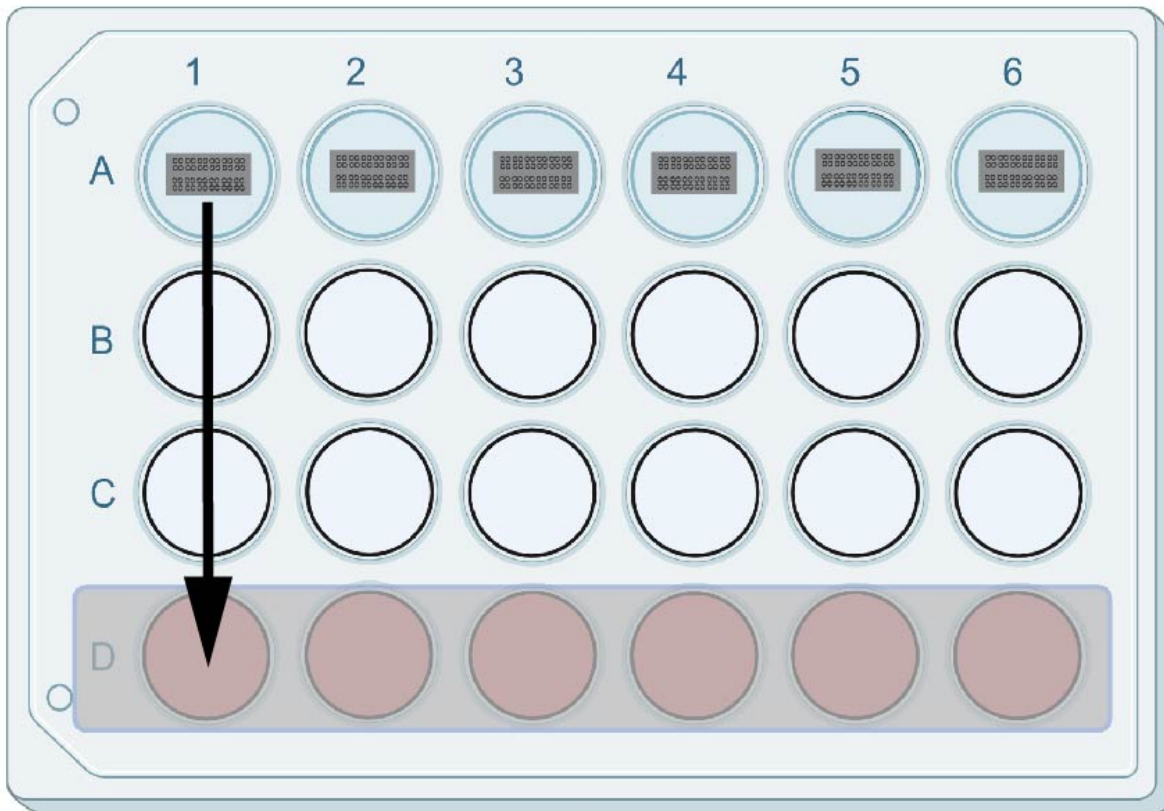


Figure 2.2 24-well plate set up during sensor chip functionalization. Row A contains DI water and houses the sensor chip after silanization (step 2j). The sensor chip moves to row B for BS3 applications (step 2l) and to row C after removing the excess BS3 (step 2o). Finally, the sensor chip is housed in the humidity chamber created in row D after the capture antibody has been applied (step 3f). Created with BioRender.com.

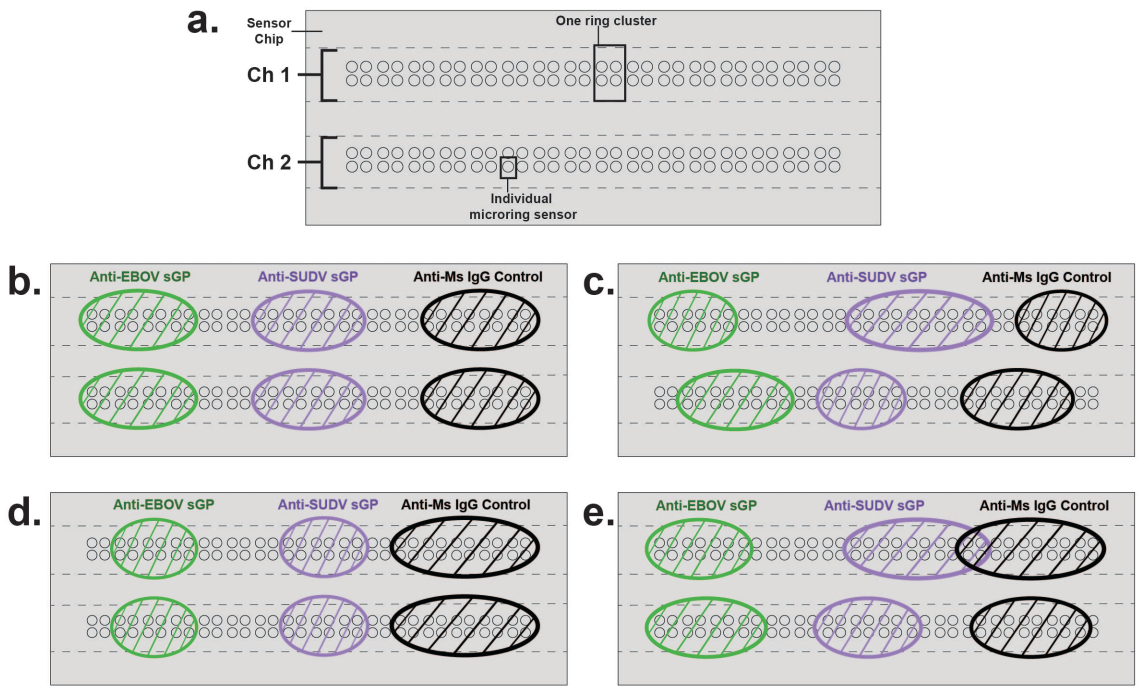


Figure 2.3 Diagram of sensor array on microring chips. Blank template (a) highlighting the 128 individual sensors in clusters of four and the two-channel arrangement. Examples of appropriate spotting maps (b-d), with each of the capture antibodies in the tr-plex assay encompassing at least two full chip clusters and none have merged. Example of errors in chip spotting (e). In channel 1, the SUDV sGP antibody has merged with the control antibody. IN channel 2, uneven spotting of clusters has occurred, with some clusters only have two of the four rings covered. This channel is still usable, as the unevenly spotted clusters can be ignored in the final data work-up while keeping the fully spotted clusters for analysis.

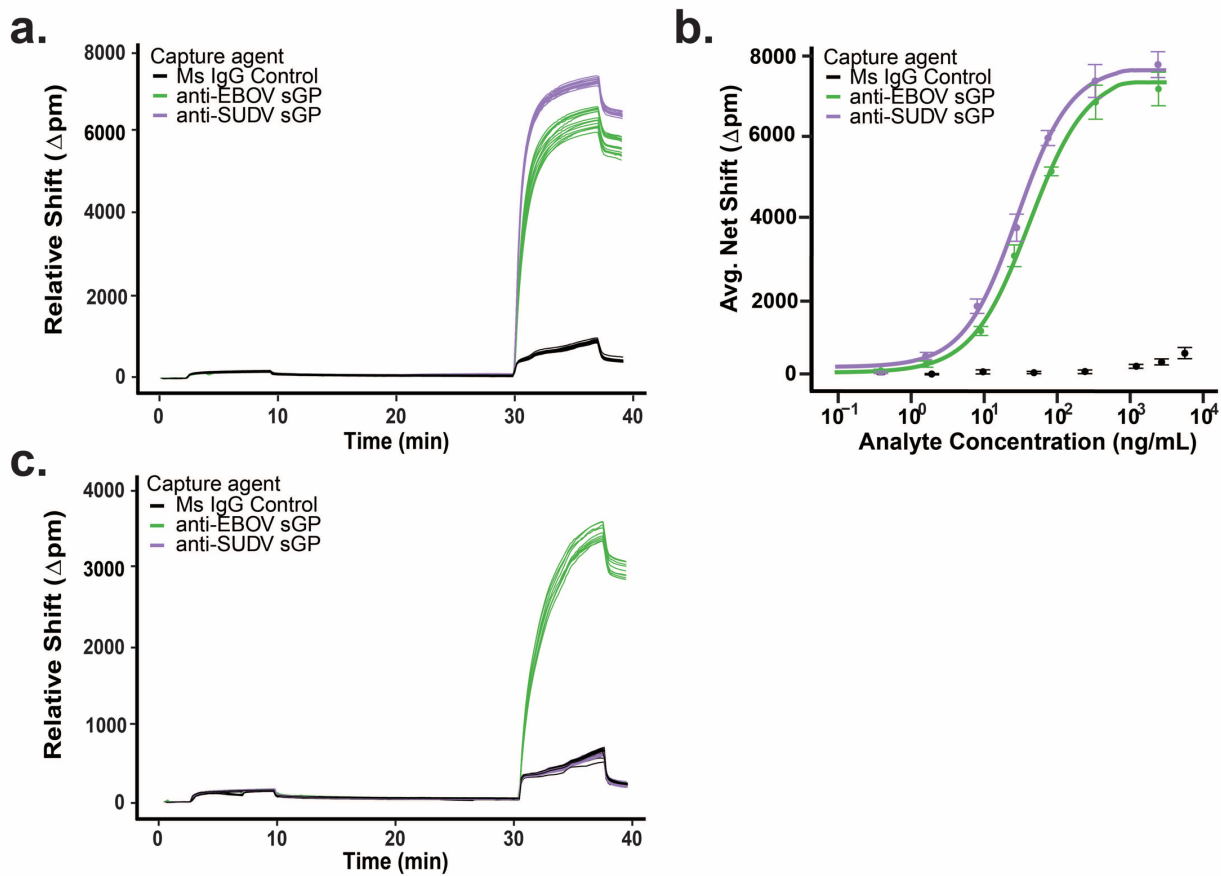


Figure 2.4 Example data post-work up. a) Trace of wavelength shifts over the course of an immunoassay experiment detecting 1,200 ng/mL of EBOV sGP and SUDV sGP. Each line represents the resonant wavelength of one sensor at the specific time of experiment. b) Calibration curve of the EBOV sGP and SUDV sGP spanning from 0 ng/mL to 2400 ng/mL in 10% serum. Error bars result from triplicate measurements. c) Trace of wavelength shift over the course of a sample containing EBOV sGP.

2.10 Tables

Table 2.1 Key resources table with materials and equipment used in this protocol.

REAGENT or RESOURCE	SOURCE	IDENTIFIER
Antibodies		
Anti-EBOV capture Ab, desalted, stored at 0.5 mg/mL	Integrated BioTherapeutics	Cat#: 0365-001
Anti-SUDV capture Ab, stored at 0.5 mg/mL	Integrated BioTherapeutics	Cat#: 0302-030
Biotinylated Anti-EBOV/SUDV pan Ab	Integrated BioTherapeutics	NA
Ms IgG control Ab, 5 mg/mL	Thermo Fisher Scientific	Cat #: 0031903
Biological samples		
NHP serum	N/A	N/A
Pooled healthy serum	Innovative Research, Novi, MI	Cat #: ISER50ML
Chemicals, peptides, and recombinant proteins		
Recombinant EBOV Soluble GP (sGP)	Integrated BioTherapeutics	Cat#: 0565-001
Recombinant SUDV Soluble GP (sGP)	Integrated BioTherapeutics	Cat#: 0570-001
Acetone (7.9 mL)	Fisher Chemical	Cat#: A184
Isopropanol (2 mL)	Fisher Chemical	Cat#: A4154
3-aminopropyltriethoxysilane (APTES, 100 μ L)	Sigma Aldrich	Cat#: 440140
Bis(sulfosuccinimidyl)suberate (BS3, 2 mg)	Thermo Fisher Scientific	Cat#: A39266
Acetic acid (2 mM)	Fisher Chemical	Cat#: A38-212
Glycerol (50% solution)	Sigma Aldrich	Cat#: G5516
DryCoat Assay Stabilizer	Virusys Corporation	Cat#: AG066-1
Starting Block Buffer	Thermo Fisher Scientific	Cat#: 37578
Streptavidin horse radish peroxidase	Thermo Fisher Scientific	Cat#: 21130
4-chloro-1-naphthol	Thermo Fisher Scientific	Cat#: 34012
Software and algorithms		
Genalyte Matchbox User Interface	Genalyte, Inc.	MavII Host 8.2
Rstudio: Integrated Development Environment for R	Rstudio, Inc.	Version 1.2.5001
Nanodrop1000 User Interface	Thermo Scientific	Version 3.8.1
Other		
Matchbox Instrument, Maverick Detection System	Genalyte Inc.	NA
Unstripped Silicon Photonic Chips	Genalyte, Inc.	NA
Chip Carriers with Back Door Adhesive	Genalyte Inc.	NA
Zeba Sip Desalting Columns, 7K MWCO	Thermo scientific	Cat#: 89882
Vortexer	Fisher Scientific	Cat#: 12-812
Microscope	Leica	Cat#: EZ4W
The Belly Dancer Orbital Shaker	IBI Scientific	Model#: BDRAA115S
Microcentrifuge tubes (0.6 mL)	Fisher Scientific	Cat#: 02-682-000
Microcentrifuge tubes (1.5 mL)	Fisher Scientific	Cat#: 02-682-002

Microcentrifuge tubes (5 mL)	Fisher Scientific	Cat#: 14-282-300
DURX 670 cleanroom wipe	Berkshire	Cat#: DR670.0909.20
24 well plate with lid	Thermo Scientific	Cat#: 142485
96 well V-bottom plate	Corning	Cat#: 3357
20 mL Glass Screw-Thread Scintillation Vials	Fisher Scientific	Cat#: 03-340-4L
Monoject 1 mL Tuberculin Syringe (Regular Tip)	Fisher Scientific	Cat#: 22-257-135
BD PrecisionGlide Needle, 26G x ½	Fisher Scientific	Cat#: 14-826-15
Nanodrop1000 Spectrophotometer	Thermo Scientific	Cat#: ND-1000(US\CAN)

Table 2.2 Calibration standard preparation for EBOV sGP and SUDV sGP in a serum matrix.

Tube #	Final Concentration	Buffer Dilution	Standard Protein
1	2,400 ng/mL	7 µL serum 659.4 µL PBS-BSA OR 70 µL serum 596.4 µL PBS-BSA	16.8 µL recombinant SUDV sGP (100 µg/mL) 16.8 µL recombinant EBOV sGP (100 µg/mL)
2	1200 ng/ml	300 µL of diluted serum at corresponding dilution	300 µl previous concentration
3	240 ng/mL	480 µL of diluted serum at corresponding dilution	120 µl previous concentration
4	48 ng/mL	480 µL of diluted serum at corresponding dilution	120 µl previous concentration
5	9.6 ng/mL	480 µL of diluted serum at corresponding dilution	120 µl previous concentration
6	1.92 ng/mL	480 µL of diluted serum at corresponding dilution	120 µl previous concentration
7	0.384 ng/mL	480 µL of diluted serum at corresponding dilution	120 µl previous concentration
8	Blank	330 µL Diluted serum at corresponding dilution	0

Table 2.3 96-well plate set up for immunoassay on Matchbox instrument.

	1	2	3	4	5...12
A	PBS-BSA	PBS-BSA	4CN	4CN	
B	PBS-BSA	PBS-BSA	PBS-BSA	PBS-BSA	
C	Sample #1	Sample #2			
D	PBS-BSA	PBS-BSA			
E	bt-Ab	bt-Ab			
F	PBS-BSA	PBS-BSA			
G	SAHRP	SAHRP			
H	PBS-BSA	PBS-BSA			

Table 2.4 Example recipe for immunoassay on Matchbox instrument.

96-well plate row	96-well plate column	Flow rate (μL/min)	Duration (min)	Back forth	comment
1	1	30	5	0	Pre-buffer rinse
Start_scan					
2	1	30	2	0	PBS-BSA
3	1	30	7	0	Analyte
4	1	30	2	0	PBS-BSA
5	1	30	7	0	Biotinylated Tracer Ab
6	1	30	2	0	PBS-BSA
7	1	30	7	0	SA-HRP
8	1	30	2	0	PBS-BSA
1	3	30	7	0	4CN
2	3	30	2	0	PBS-BSA
Stop_scan					
end_recipe					

2.11 References

- (1) Qavi, A. J. Rapid Detection of an Ebola Biomarker with Optical Microring Resonators. *OPEN ACCESS* **2022**, 13.
- (2) Kindt, J. T.; Luchansky, M. S.; Qavi, A. J.; Lee, S.-H.; Bailey, R. C. Subpicogram Per Milliliter Detection of Interleukins Using Silicon Photonic Microring Resonators and an Enzymatic Signal Enhancement Strategy. *Anal. Chem.* **2013**, *85* (22), 10653–10657. <https://doi.org/10.1021/ac402972d>.
- (3) Valera, E.; Shia, W. W.; Bailey, R. C. Development and Validation of an Immunosensor for Monocyte Chemotactic Protein 1 Using a Silicon Photonic Microring Resonator Biosensing Platform. *Clin. Biochem.* **2016**, *6*.
- (4) Qavi, A. J.; Kindt, J. T.; Gleeson, M. A.; Bailey, R. C. Anti-DNA:RNA Antibodies and Silicon Photonic Microring Resonators: Increased Sensitivity for Multiplexed microRNA Detection. *Anal. Chem.* **2011**, *83* (15), 5949–5956. <https://doi.org/10.1021/ac201340s>.
- (5) McClellan, M. S.; Domier, L. L.; Bailey, R. C. Label-Free Virus Detection Using Silicon Photonic Microring Resonators. *Biosens. Bioelectron.* **2012**, *31* (1), 388–392. <https://doi.org/10.1016/j.bios.2011.10.056>.
- (6) Robison, H. M.; Escalante, P.; Valera, E.; Erskine, C. L.; Auvil, L.; Sasieta, H. C.; Bushell, C.; Welge, M.; Bailey, R. C. Precision Immunoprofiling to Reveal Diagnostic Signatures for Latent Tuberculosis Infection and Reactivation Risk Stratification. *Integr. Biol.* **2019**, *11* (1), 16–25. <https://doi.org/10.1093/intbio/zyz001>.
- (7) Robison, H. M.; Chapman, C. A.; Zhou, H.; Erskine, C. L.; Theel, E.; Peikert, T.; Lindestam Arlehamn, C. S.; Sette, A.; Bushell, C.; Welge, M.; Zhu, R.; Bailey, R. C.; Escalante, P. Risk Assessment of Latent Tuberculosis Infection through a Multiplexed Cytokine Biosensor Assay and Machine Learning Feature Selection. *Sci. Rep.* **2021**, *11* (1), 20544. <https://doi.org/10.1038/s41598-021-99754-3>.
- (8) Twitchell, K. T. Bloodborne Pathogens. What You Need to Know--Part I. *AAOHN J. Off. J. Am. Assoc. Occup. Health Nurses* **2003**, *51* (1), 38–45; quiz 46–47.
- (9) Robison, H. M.; Bailey, R. C. A Guide to Quantitative Biomarker Assay Development Using Whispering Gallery Mode Biosensors: Whispering Gallery Mode Biosensors. *Curr. Protoc. Chem. Biol.* **2017**, *9* (3), 158–173. <https://doi.org/10.1002/cpch.23>.
- (10) Azadeh, M.; Gorovits, B.; Kamerud, J.; MacMannis, S.; Safavi, A.; Sailstad, J.; Sondag, P. Calibration Curves in Quantitative Ligand Binding Assays: Recommendations and Best Practices for Preparation, Design, and Editing of Calibration Curves. *AAPS J.* **2017**, *20* (1), 22. <https://doi.org/10.1208/s12248-017-0159-4>.

Chapter 3 Rapid Detection of an Ebola Biomarker with Optical Microring Resonators

3.1 Author Contributions and Acknowledgements

This chapter has been adapted from the published article: Qavi, A.*, Meserve, K.*, Aman, M.J., Vu, H., Zeitlin, L., Dye, J.M., Froude, J.W., Leung, D.W., Yang, L., Holtsberg, F.W., Bailey, R.C., Amarasinghe, G.K. [Rapid detection of an Ebola biomarker with optical microring resonators](#), *Cell Reports Methods* 2, 2022 [* co-first authors] and was highlighted in a [‘Meet the Authors’](#) article within the issue. Dr. Abraham Qavi conceived the project, completed the work presented in figures 3.1 and 3.7, generated those figures and table 3.3, and co-wrote and edited the manuscript. The thesis author, Krista Meserve, led project implementation on the microring resonators, conducted all optimization and validation experiments for assay development, completed cross reactivity, matrix compatibility, and calibration curves experiments, and analyzed the non-human primate samples. The thesis author completed data analysis, designed and generated the TOC figure, figures 3.2-3.6, tables 3.1 and 3.2, and co-wrote and edited the manuscript.

I would like to thank Dr. Abraham Qavi and Dr. Gaya Amarasinghe from Washington University School of Medicine (WashU) for their mentorship through the course of this project, allowing me full experimental freedom and providing great feedback on my presentations and writing. I acknowledge Dr. Fredrick Holtzberg, Dr. M. Javad Aman, and Hong Vu from Integrated Biotherapeutics for providing the specific antibodies and standards; Dr. Larry Zeitlin from Mapp Biopharmaceuticals, Dr. John M. Dye from the United States Army Medical

Research Institute of Infectious Diseases, and Dr. Jeffrey W. Froude from the United States Army Nuclear and Countering Weapons of Mass Destruction Agency for providing the non-human primate samples; Dr. Daisy Leung and Dr. Lan Yang from WashU for manuscript editing; and Dr. Ryan Bailey for project guidance. Additionally, I would like to thank Genalyte, Inc. for providing the raw chips I spotted for this project.

3.2 Abstract

Ebola virus (EBOV) is a highly infectious pathogen, with a case mortality rate as high as 89%. Rapid therapeutic treatments and supportive measures can drastically improve patient outcome; however, the symptoms of EBOV disease (EVD) lack specificity from other endemic diseases. Given the high mortality and significant symptom overlap, there is a critical need for sensitive, rapid diagnostics for EVD. Facile diagnosis of EVD remains a challenge. Here, we describe a rapid and sensitive diagnostic for EVD through microring resonator sensors in conjunction with a unique biomarker of EBOV infection, soluble glycoprotein (sGP). Microring resonator sensors detected sGP in under 40 minutes with a limit-of-detection (LOD) as low as 1.00 ng/mL in serum. Furthermore, we validated our assay with the detection of sGP in serum from EBOV infected non-human primates. Our results demonstrate the utility of a highly sensitivity diagnostic platform for detection of sGP for diagnosis of EVD.

3.3 Introduction

RNA viruses are an area of critical concern and a major threat to global health; between 25% to 44% of all emerging infectious diseases are caused by RNA viruses.¹⁻⁴ This is in part attributed to their ability to mutate rapidly, a consequence of low fidelity RNA-dependent RNA polymerases,⁵⁻⁹ as well as increased contact between both humans and zoonotic vectors.¹⁰

Filoviruses are among the most lethal human single-stranded, negative-sense RNA viruses, with high case fatality rates up to 89% during outbreaks.¹¹ Ebola virus (EBOV) is the causative agent of EBOV Disease (EVD), characterized by pathognomonic symptoms of internal and external bleeding, in addition to a constellation of non-specific symptoms including fever, fatigue, nausea, vomiting, diarrhea, and headache.¹²

Previous outbreaks of EBOV highlight the need for rapid diagnostics to accurately and rapidly detect disease. Access to diagnostic information is critical for disease management by enabling healthcare systems to initiate isolation protocols and begin supportive measures that drastically improve patient outcomes.¹³⁻¹⁵ In resource limited settings, accurate diagnosis also enables healthcare providers to utilize limited resources more efficiently to limit the outbreak spread. Current diagnostics for EBOV mainly rely on PCR-based techniques, ELISAs, or lateral flow assays with varying degrees of success.¹⁶⁻¹⁹ Each of these methods require additional electronics for sample processing and trained technicians to perform studies. Moreover, these techniques have several disadvantages, including low multiplexing capabilities, limited quantitative information, lengthy assay times, and/or the requirement of centralized laboratories or cold chain custody. Specific to EVD, these assays rely on either the glycoprotein (GP) of EBOV or nucleic acid-based testing, both of which are subject to a diagnostic window period during which infected patients will test negative. Therefore, new technologies that bypass traditional analytical limitations and technical requirements as well as informative actionable biomarkers of EVD are needed to enable effective triaging and treatment of infected individuals are needed.

The EBOV genome, consisting of 7 genes, is highlighted in **Figure 3.1a** EBOV GP, is expressed as two distinct transcriptional products. These two proteins are expressed through site-

specific transcriptional editing of the GP gene. The primary product of the GP gene is the soluble glycoprotein (sGP), a nonstructural secreted glycoprotein, which is expressed from the unedited RNA transcript. sGP is dimerized by two cysteine bridges and released from EBOV infected cells.^{20,21} The full-length GP, which coats the surface of mature viral particles, is expressed only following transcriptional editing of the GP gene, where an additional uridine residue is added to the genomic RNA. This editing adds an additional adenosine residue in the transcript, which results in an extended open reading frame. The majority of transcripts are non-edited and therefore sGP is the first and predominant product of GP gene transcription and translation.^{21,22} sGP shares the first 295 residues with GP but contains a unique C-terminal tail.

There are several roles sGP appears to play in EBOV pathogenesis. It has been proposed that the expression and secretion of sGP allows EBOV to evade the host immune response via immune decoy leading to increased virulence.^{23,24} Additionally, sGP has been shown to have immune modulatory functions. It inhibits pro-inflammatory cytokine production by macrophages, limits macrophage migration, and reduces CD16b receptors on human neutrophils.^{25,26} sGP has been reported to have a protective function in the context of endothelial layer integrity as well, which may support viral replication.²⁷ sGP also activates the MAP kinase signaling pathway, which is thought to increase the uptake and internalization of EBOV virions.¹⁷ Despite sGP's numerous functions, its role as a biomarker is only now being appreciated.

In this study, we address critical diagnostic gaps for EVD by adapting a silicon photon microring resonator platform to detect EBOV sGP. Microring resonators are a class of whispering gallery mode (WGM) devices in which light circulating within the microring interacts with biomolecules deposited on the ring surface, resulting in a shift in the ring's

resonant wavelength that is proportional to the amount of the surface-adsorbed material. WGM devices have been leveraged for sensing applications over the past decade due to their amenability to multiplexing, high analytical sensitivity, quick time-to-result, and ease of integration with microfluidics. This has enabled their use in a wide variety of applications, including the detection of nucleic acids,^{28–30} proteins,^{31–33} and viruses.³⁴ Recent work has integrated this sensing platform into clinical workflows to use varying biomarkers to profile disease states for diagnostic use.^{35–38} We demonstrate that microring resonators are an effective sensing platform for the rapid, multiplexed detection of filoviral infection using sGP. We also establish sGP as a sentinel biomarker and potential prognostic biomarker of EVD outcome with anticipated benefits in outbreak management.

3.4 Methods

Capture agents and Antigens. Antibodies and antigens used in this study were obtained from Integrated Biotherapeutics (Rockville, MD), except for Mouse IgG (ThermoFisher Scientific, Rockford, Illinois), which served as a binding control.

Photonic Microring Resonators. Measurements were performed with a Maverick Matchbox optical scanning instrument and silicon sensor chips fabricated by Genalyte, Inc. (San Diego, CA). Experiments were performed on 4 x 6 mm sensor chips containing 128 microring sensors, each 30 μm in diameter, arranged in clusters of four. The clusters are split between two microfluidic channels, with four additional unfunctionalized temperature control rings on each chip.

Chemical functionalization and immobilization of capture antibodies on sensor chips.

Antibodies were covalently attached to the microring sensor surfaces as previously described.³⁹ Briefly, the chips were silanized with 1% (3-Aminopropyl)triethoxysilane (APTES, Sigma) to

add primary amines to the sensor surfaces. The sensors were incubated with 5 mM bis(sulfosuccinimidyl)suberate (BS3, ThermoFisher Scientific), an amine-reactive, homobifunctional crosslinker, for 3 minutes. The sensor chips were dipped in H₂O to remove unreacted BS3 and dried with N₂. Approximately 0.2 µL of each primary capture antibody diluted to 0.25 mg/mL was spotted onto two to five ring clusters in each of the two channels and incubated for 1 hour. Primary capture antibodies were desalted on Zeba Spin Desalting Columns (7K MWCO, ThermoFisher Scientific) prior to covalent attachment to the ring surfaces to remove any residual amines that would cross-react with BS3. The sensor chips were blocked using starting block buffer (ThermoFisher Scientific) for 1 hour, dried with N₂ and coated with DryCoat Assay Stabilizer (Virusys Corporation) for storage in a 4°C humidity chamber until use.

Assay set-up. Functionalized chips were housed in a disposable, injection molded, two-channel microfluidic cartridge and inset into the instrument. All fluidic handling was controlled at a flow rate of 30 µL/min via a series of pumps. Due to the two-channel microfluidic design, two assays were simultaneously completed on one chip. For immunoassay analysis, running buffer (1X phosphate buffered saline, PBS, Sigma) with 0.5% bovine serum albumin (BSA, Sigma) was first flowed across the channel surface for at least 5 minutes to equilibrate the system prior to analysis. Assay steps for each experiment were as follows: running buffer (2 min), sample (7 min), running buffer (2 min), biotinylated tracer antibody (2 µg/mL, 7 min), running buffer (2 min), streptavidin- horse radish peroxidase (3 µg/mL, SAHRP, ThermoFisher Scientific) (7 min), running buffer (2 min), 4-chloro-1-naphthol (4-CN, ThermoFisher scientific) (7 min), running buffer (2 min).

Calibrations and Sample Analysis. Immunoassays for EBOV sGP and Sudan ebolavirus (SUDV) sGP were simultaneously calibrated in parallel. Serial dilutions of antigen from a

saturating concentration to an undetectable concentration resulted in an eight-point calibration curve for each target. Calibrations were constructed in 1%, 10%, and 50% serum matrices. Samples were diluted and analyzed at 10× or 100×, allowing the concentrations to remain in the quantitative regime of the calibration curves.

NHP Sera Samples. The kinetics of sGP production in vivo was tested in rhesus macaques challenged with 1,000 PFU of EBOV and treated post exposure with either a cocktail of three monoclonal antibodies (MB-03)⁴⁰ or vehicle control. Longitudinal serum samples on days 0-15, 21, and 28 from survivors and days 0 through the day of death for fatal cases were prepared and tested by our quantitative sGP ELISA content and by PCR for EBOV genome content.

ELISAs. A quantitative ELISA to detect sGP resulting from virus infection was developed in-house at Integrated Biotherapeutics. Critical reagents were generated to support the development of the ELISA. Specifically, a recombinant sGP was developed in-house at Integrated Biotherapeutics in order to standardize the quantitation of sGP levels in serum samples. A capture antibody was generated that specifically recognizes EBOV sGP and not the full-length GP. A number of secondary antibodies were evaluated, and one monoclonal antibody was selected for use in this assay. Using these reagents, an ELISA method was developed and optimized for reproducibility and robustness. sGP as early as day 3 post challenge was detected in NHPs. Also, the level of sGP in the serum appears to correlate with survival, similar to what is observed in the viremia results as determined by RT-PCR.

PCR. Blood samples were processed for qRT-PCR. USAMRIID standard procedure were used to process the serum samples and determine serum viremia levels.⁴¹

Microring Resonator Data analysis. Analysis of data was performed using an in-house developed R-script as previously described,³⁹ but could be completed using standard excel

software functions. Briefly, resonance shifts from each individual sensor were tracked over the course of the experiment and the net shift of resonant wavelength of each sensor ring before and after the 4-CN amplification step were analyzed. The net shift of all rings spotted with a specific antibody was averaged across each channel for each experiment. The average net shift was used to calculate the target concentration in each sample based on the appropriate calibration curve fit (e.g., 1% serum calibration for 100× dilution and 10% serum calibration for 10× dilutions). If two dilutions of the same sample were performed, the dilution that resulted in a net shift closest to the inflection point of the respective calibration curve was selected for use.

3.5 Results

The EBOV genome consists of seven genes, with sGP resulting from an unedited transcription of the glycoprotein (GP) gene (**Figure 3.1a**). This secreted protein was detected using an ELISA assay developed by Integrated Biotherapeutics and compared to RT-PCR in NHP infected with EBOV in **Figure 3.1b** and **Figure 3.1c**. Samples were obtained following infection with EBOV in both treated and untreated NHPs. In all cases, sGP levels increased earlier or at the same time as RT-PCR values. Furthermore, NHPs with EBOV levels greater than 1,000 ng/mL succumbed to disease regardless of treatment status. These results reinforce sGP as both a diagnostic and prognostic marker of EBOV infection.

We utilized a silicon photonic microring resonator platform for the detection of sGP. Microring resonators operate on the principle of whispering gallery mode sensing and continue to be a promising layout for biosensing applications due to ease of fabrication, chip integration, and high multiplexing potential (**Figure 3.2**).^{42,43} Light at a specific resonant wavelength is confined in small microring cavities. As changes in the local refractive index in the sensing region occur, the resonant wavelength within the microcavity shifts, which can be tracked in near real-time. As

each biomolecular binding event occurs over the course of the sandwich-style immunoassay, the resonant wavelength shifts relative to the initial wavelength. The extent of the final net shift is proportional to the amount of analyte bound on the microring resonator.

Initial assay methods were aimed at developing a label-free method to detect primary binding of the protein standard to the capture antibodies, eliminating the requirement of a secondary tracer antibody and other amplification reagents. Multiple concentrations of EBOV sGP were tested, in buffer, on the EBOV-sGP capture antibodies (**Figure 3.3a**). However, distinct responses were only identified at concentrations over 1 $\mu\text{g/mL}$, relative shifts ranged from 0-10 pm, and a calibration curve was unable to be constructed (**Figure 3.3b**). Additionally, the detectable concentrations were tested in a dilute serum matrix which consequently obscured the low relative shifts due to bulk effects from the higher viscosity serum matrix.

We moved towards employing a sandwich immunoassay, with expectations that a secondary tracer antibody and amplification reagents would result in lower limits of detection, higher relative shifts, and added specificity. Multiple concentrations of EBOV sGP were tested, in a serum matrix, on the EBOV-sGP capture antibodies with the additional assay reagents (described below) (**Figure 3.3c-d**). Results demonstrated an increase in relative shift with an increase in EBOV sGP concentration and a calibration curve was constructed, with relative shifts ranging from 0-6500 pm. This assay method was selected to be optimized for a two-plex panel to detect EBOV sGP and Sudan virus (SUDV) sGP.

We next sought to optimize and validate the sandwich immunoassay and assess antibody specificity. The steps of the finalized immunoassay, based on the above results, consist of sample introduction followed by secondary recognition and amplification steps, highlighted in **Figure 3.4a**. Antibodies for EBOV sGP and SUDV sGP were functionalized in a multiplex fashion on

the surface of the microrings, with each capture agent spanning 8-12 microrings to provide technical replicates. The sample of interest was introduced to the sensor surface through microfluidic fittings and automated with pumps as previously described (**Figure 3.4a, step 1**).^{36,39,44-47} As the antigen is flowed across the surface of the sensor, the primary binding occurred as EBOV sGP was captured by the anti-EBOV sGP antibodies on the sensor surface. After addition of sample, a buffer rinse washed away unbound material prior to introduction of the recognition molecule, a pan-EBOV-SUDV biotinylated tracer antibody produced by Integrated Biotherapeutics, (**Figure 3.4a, step 2**) to form a sandwich motif. This secondary tracer antibody recognizes multiple filovirus strains via conserved binding epitopes on the filoviral GP. These binding epitopes are different than those used with the primary antibody. Using a second antibody for this purpose increases the specificity of the assay, as any agent non-specifically adhered to the capture antibodies would not be recognized. After a buffer rinse, SA-HRP was flowed across the sensor surface, (**Figure 3.4a, step 3**). In the final amplification step, 4CN reacts with the HRP to form an insoluble product (**Figure 3.4a, step 4**). The precipitate is localized on the sensor surface, leading to a drastic change in refractive index proportional to EBOV-sGP concentration. Unbound reagent is washed away with a final buffer rinse and the net shift of resonant wavelength from the start of the 4CN amplification step to the end of the final buffer rinse is used for analysis. Incorporating these amplification steps leads to resonant wavelength shifts of ~6,000 pm for the highest concentrations, resulting in a larger dynamic range and lower limits of detection in comparison to using the primary antigen binding steps. An example trace of wavelength shift during the assay for detection of EBOV sGP with controls is highlighted in **Figure 3.4b**.

To address antibody specificity, cross-reactivity experiments were performed between EBOV and SUDV sGP. SUDV and EBOV are related species within the Ebolavirus genus, and SUDV also secretes sGP. The EBOV and SUDV sGPs were individually introduced to a sensor chip covalently functionalized with anti-EBOV sGP, anti-SUDV sGP, and Mouse IgG antibodies. Mouse IgG antibodies were used as negative controls to monitor non-specific adsorption interactions and resonant wavelength shifts due to bulk refractive index change. Only the sensor rings functionalized with the respective antibody responded to introduction of EBOV or SUDV sGPs (**Figure 3.5a-b**). When exposed to EBOV sGP, the anti-EBOV sGP functionalized rings (black) increase over the final amplification step, leading to a measurable net shift, while the anti-SUDV sGP functionalized rings (red) and control functionalized rings (blue) have low net shifts (<1,000 pm). The same trend is observed with a SUDV sGP target, where the anti-SUDV sGP functionalized rings result in a large net-shift, while the anti-EBOV sGP and control functionalized rings have comparable shifts. There was no evidence of cross-reactivity in these assays, which is attributed to the specificity of the primary capture antibodies.

Calibration of EBOV and SUDV sGP occurred simultaneously over a range of concentrations spanning from undetectable levels to saturation of the signal (**Figure 3.5c-e**). The net shifts for all concentrations were fit to a logistic function for calculation of unknown concentrations based on net shift,

$$y = \frac{A_1 - A_2}{1 + \left(\frac{x}{x_0}\right)^p} + A_2 \quad \text{Eq. 1}$$

Where y is the net shift of the sample, A_1 is the maximum net shift (Δpm), A_2 is the minimum net shift (Δpm), x is the sample analyte concentration (pM), x_0 is the center value (pM), and p is the power parameter affecting the slope around the inflection point (**Table 3.1**).^{37,39} The calibration curves shown in **Figure 3.5c-e** were constructed in the biologic matrices of 1%, 10% and 50% serum. The limit-of-detection (LOD) for EBOV sGP and SUDV sGP were determined to be 1.72 ng/mL and 1.00 ng/mL in 1% sera, respectively, and 4.20 ng/mL and 1.54 ng/mL in 10% sera, respectively, and 2.33 ng/mL and 7.76 ng/mL in 50% sera, respectively (**Table 3.2**). We calculated the LOD as the concentration correlating to the sensor response three standard deviations from the blank signal. Our calibration curves of spiked sGP into pooled human sera demonstrated a decreased LOD with increased percent of serum. However, given that the LOD from 1% serum to 50% serum decreased by ~ 2.5 -fold for EBOV and ~ 5 -fold for SUDV, we anticipated no difficulties in detecting sGP from the NHP samples.

Analysis of NHP samples were done at 10 \times or 100 \times dilutions due to limited sample volume (**Figure 3.6**). Each sample was analyzed using the same experimental and data extraction methods as the calibrations, with each sample taking just under 40 minutes to complete. The researchers were blinded to the subject number and outcome of subject but did know a relative range of concentrations of EBOV sGP in each sample to make appropriate dilutions for this preliminary work. For the samples analyzed at two dilutions, the dilution that resulted in the net shift closest to the calibration curve inflection point was used for concentration determination. The 10 \times dilution was the most generalizable, ultimately being used for 24 of the 30 samples. The remaining six samples were those of highest sGP concentrations, resulting in the 10 \times dilution falling in the saturating range of the calibrations. However, the 100 \times dilution resulted in quantifiable results for these remaining. Additionally, only one of the 30 samples contained sGP

below the LOD. Comparison of the microring resonators and ELISA assay are highlighted in **Figure 3.7** and **Table 3.3**. The microring platform had a positive correlation with the ELISAs ($R^2 = 0.94$), but error rates of the microring platform relative to ELISA varied between 2.5% and 88.7%.

3.6 Discussion

The ongoing COVID-19 pandemic highlights the need for sensitive diagnostic platforms and novel biomarkers. EBOV sGP represents a unique and powerful biomarker for the detection of EBOV infection and EVD prognosis for several reasons. The presence of sGP in the blood prior to, or simultaneously with, PCR based assays improves the diagnostic window. As previously noted, survival outcomes from EBOV infection depend critically on the initiation of supportive measures, which heavily rely on accurate diagnoses in resource limited settings. Rapid diagnosis facilitates faster treatment initiation, thereby improving patient outcomes.^{13,48,49} Quarantine of affected individuals has profound implications in infection and outbreak management and prevention. Alternatively, a confirmation of a negative test allows for healthcare providers to efficiently leverage their resources in treating patients. Because sGP is a protein biomarker, there is flexibility in the assay designs that can be used with the biomarker (e.g., lateral flow assays). The NHP study suggests that levels higher than 1,000 ng/mL of sGP may be a potential prognostic marker of EVD. Further studies are necessary to fully characterize the prognostic value of sGP.

The role of sGP as a diagnostic marker for infection has been previously explored by several groups. In one instance, researchers leveraged a modified D4 assay in combination with scFv-Fc antibodies generated from phage-display libraries for the highly sensitive detection of EBOV sGP.⁵⁰ Similar to our study, Fontes et al., confirmed the presence of sGP in EBOV

infected NHP with both a D4 assay and by RT-PCR. A critical difference is the use of fluorescence-based measurements, which requires a hand-held fluorescence reader. The D4 assay platform provides highly sensitive, multiplexed measurements, however, scalability of manufacturing may be challenging. In contrast, Chen and colleagues demonstrated the use of nanoparticles functionalized with nanobodies against EBOV sGP with a turn-around-time (TAT) of as little as 5 minutes.⁵¹ Through aggregation of nanoparticles and optimization of nanobody pairs, the researchers were able to detect both EBOV sGP and the receptor binding domain (RBD) of glycoprotein using a low-cost LED reader. The authors of this study only went up to 5% pooled sera and whole blood, due to the significant decrease in LOD seen due to matrix effects.

Initial development of the EBOV sGP assay using the microring resonators focused on the direct, label-free binding of sGP to the capture antibodies. Label-free detection of analytes has been demonstrated in the past with microring resonators; however, the LOD has typically remained in the low ng/mL level for proteins in neat, buffered solutions.^{28,30,33} Our results were consistent with these findings, as no reliable calibration curve could be constructed based on primary binding data in a neat-running buffer at low ng/mL concentrations. Even more challenging is the elimination of primary binding profiles due to bulk RI shift upon the addition of a complex matrix (e.g., serum). Given that the prognostic value of sGP rests around 1,000 ng/mL, and that direct detection of antigens in sera is significantly more difficult due to matrix effects, label-free detection was insufficient for our purposes. We subsequently employed a two-step sandwich assay with an amplification step.³¹ While the tracer antibody binding and amplification steps result in additional assay time, it provides drastically increased sensitivity and working dynamic range. Furthermore, because signal amplification is performed in neat,

buffered solutions in a separate step from sample introduction, there are no interfering matrix-effects that would be seen with direct binding in sera or plasma.⁵² An added benefit of the assay format is the use of a pan-Ebola mAb as a tracer antibody – that is, a single tracer antibody can be employed despite multiple primary capture antibodies and targets, simplifying the workflow of the assay.

An advantage of our sensor platform is the multiplexed capabilities, with 128 active sensors per chip. While our study highlights 3 targets on a single chip, the microring resonator platform has demonstrated up to 13-plex measurements on a single chip.³⁷ The total multiplexing of targets is limited in part by the spotting of the capture antibodies on chip, as well as the number of desired technical replicates per run. Nonetheless, the current assay design can be adapted towards a broad range of pathogens. Given the non-specific symptoms seen with EVD that overlap significantly with other endemic tropical diseases (e.g., malaria), there is potential to further improve the capabilities of this assay by including additional targets.⁵³ Another advantage is addition of unfunctionalized thermal control microrings, which negates any environmental fluxes that may influence measurements. Additionally, our covalent linkage chemistry utilizes BS3, a homobifunctional crosslinker that reacts agnostically with primary amines. This ability to use unmodified antibodies or other capture agents and swap components within the assay represents a significant benefit in flexibility of assay design.

One concern with the microring assay is the percent error from ELISAs. Despite higher analytical sensitivity as compared to the ELISAs, our results suggested variable error in sGP concentration from the ELISA samples (**Figure 3.7**). At higher concentrations, the error appears to approach ~60%. It is unclear whether this is due to degradation of the sample over time, as the NHP samples were originally obtained in 2013, or a fundamental limitation of mass diffusion of

the antigens. The microring platform leverages active fluidics in comparison to ELISAs relying on incubation steps. Further studies are necessary to resolve this discrepancy. Nonetheless, our platform was able to successfully detect EBOV sGP in 29 out of the 30 NHP samples. With the limited NHP samples available, we had to dilute samples to reach the minimum volume of ~300 μ L to run the assay. Given the assays ability to calibrate in 50% serum with limited decrease in the LOD, we anticipate no significant problems in the direct analysis of serum.

Another concern of the microring resonator platform is the expense of the instrument for an in-field assay. While the single-use disposable chips and cartridges are cost effective, the optical readout system itself can be cost-prohibitive, especially in resource-limited settings. There have been pushes to reduce the cost of these systems, either through Distributed Bragg Reflect (DRB) lasers⁵⁴ or alternate tuning mechanisms.⁵⁵ Additionally, this instrument is not portable but is well suited for a field hospital or lab.

An additional concern with the assay is biocontainment. While the need for biocontainment is a consideration for any assay running human samples, this is especially relevant in the context of BSL-4 work. One potential solution is pre-treatment of samples for EBOV inactivation. Current methods include the use of irradiation,^{56,57} alkylating agents,⁵⁸ acetic acid with heat,⁵⁹ or Triton X-100 with heat.⁶⁰ An alternative to inactivation would be a self-contained sensor unit. In the context of WGM sensors, optofluidic devices such as liquid core optical ring resonators (LCORR)^{61,62} or microbubble resonators⁶³ integrate the optical sensor component with fluidic handling.

While our study highlights a potential biomarker for EVD and a new utility of the sensor platform, there are some areas for future development. Our technique requires the use of an instrument capable of interrogating optical resonators, which requires a tunable laser source

within an optical readout instrument. While there have been pushes to miniaturize these instruments,⁵⁴ current devices are laboratory-based and one of the most expensive components of the assay. De novo detection of these antigens is not possible with our assay format. Further work is also required to fully characterize the diagnostic and prognostic value of sGP in EVD.

3.7 Conclusion

Together, our results indicate that microring resonators that detect sGP are an appealing diagnostic platform for the detection of EBOV infection. We demonstrate that sGP is a diagnostic and prognostic marker for EBOV infection, and when leveraged in conjunction with a sensitive diagnostic assay, can provide actionable clinical information. Our work provides proof-of-concept and a framework for further optimization and assay development. Multiplexed measurements enabled by our platform will allow for a broader range of pathogens to be assessed, as well as the potential to incorporate other biomarkers relevant towards infection.

3.8 Figures

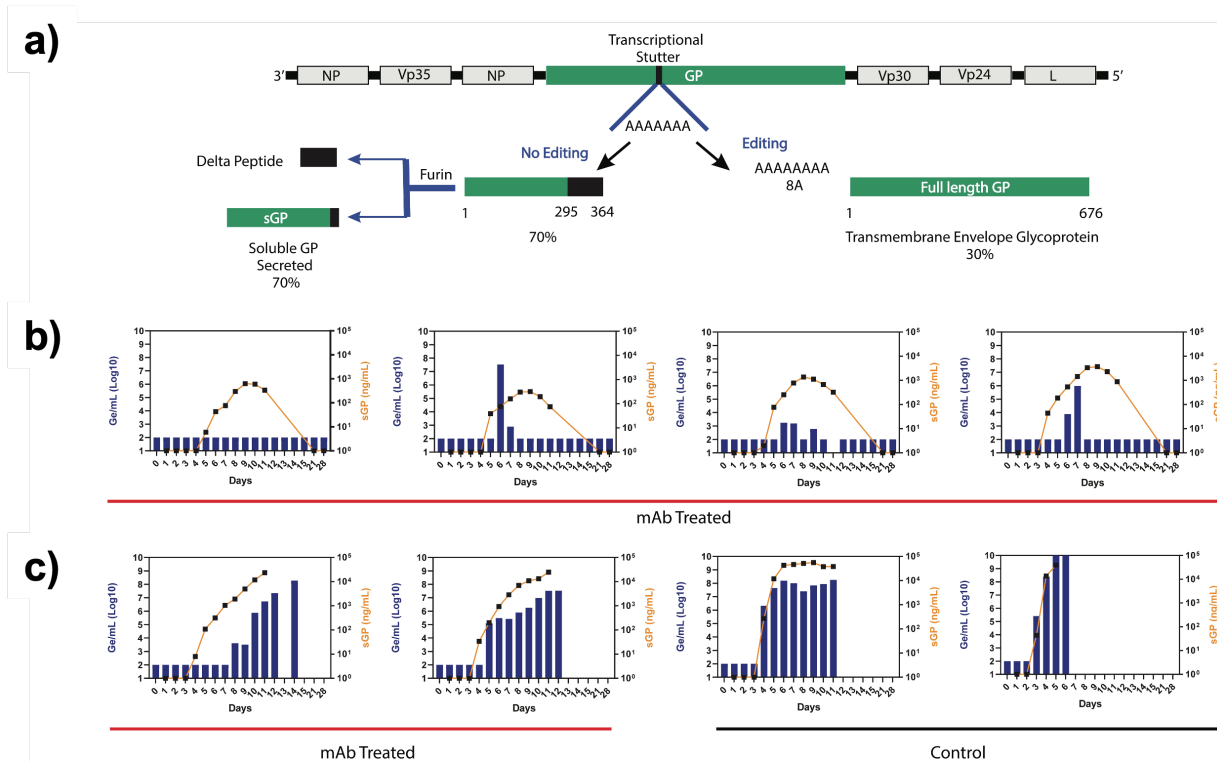


Figure 3.1 Ebola virus genome, generation of sGP, and comparison of EBOV RT-PCR versus sGP values during infection. (a) The Ebola genome contains 7 genes, including one encoding for glycoprotein (GP). A transcriptional stutter leads to the addition of 7 additional adenines, that are edited to result in the full length, transmembrane glycoprotein. In contrast, without editing, a soluble glycoprotein (sGP) is formed, which is secreted from the infected cell. (b) Comparison of RT-PCR values (blue bars) and an ELISA for sGP (orange lines) in non-human primates infected with EBOV who survived and (c) were deceased. Treatment either with mAb or control (no treatment) is reflected under the plots.

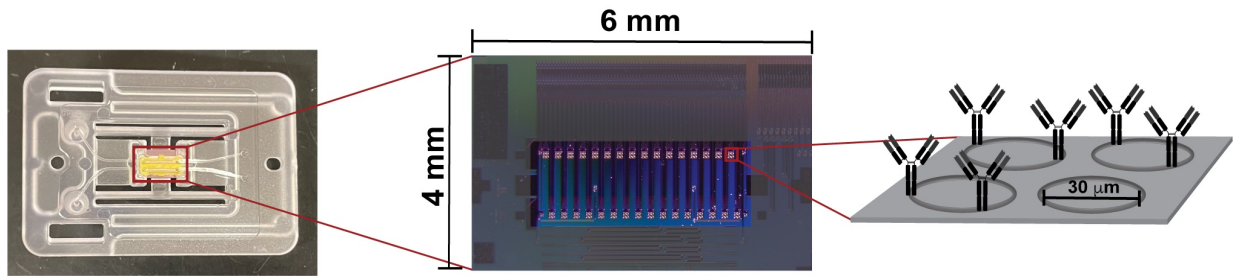


Figure 3.2 Microring resonator diagram. (a) (Left) A single 4 mm x 6 mm chip embedded into a two-channel, microfluidic cartridge. (Center) Optical micrograph of a single chip used with the Maverick M1 instrument, with 16 clusters of 4 sensors in both channels. (Right) Schematic of the cluster of four microring sensors. Microring sensors are fabricated in clusters of 4 sensors with a linear waveguide near the microring waveguide for coupling of light into the microcavity.

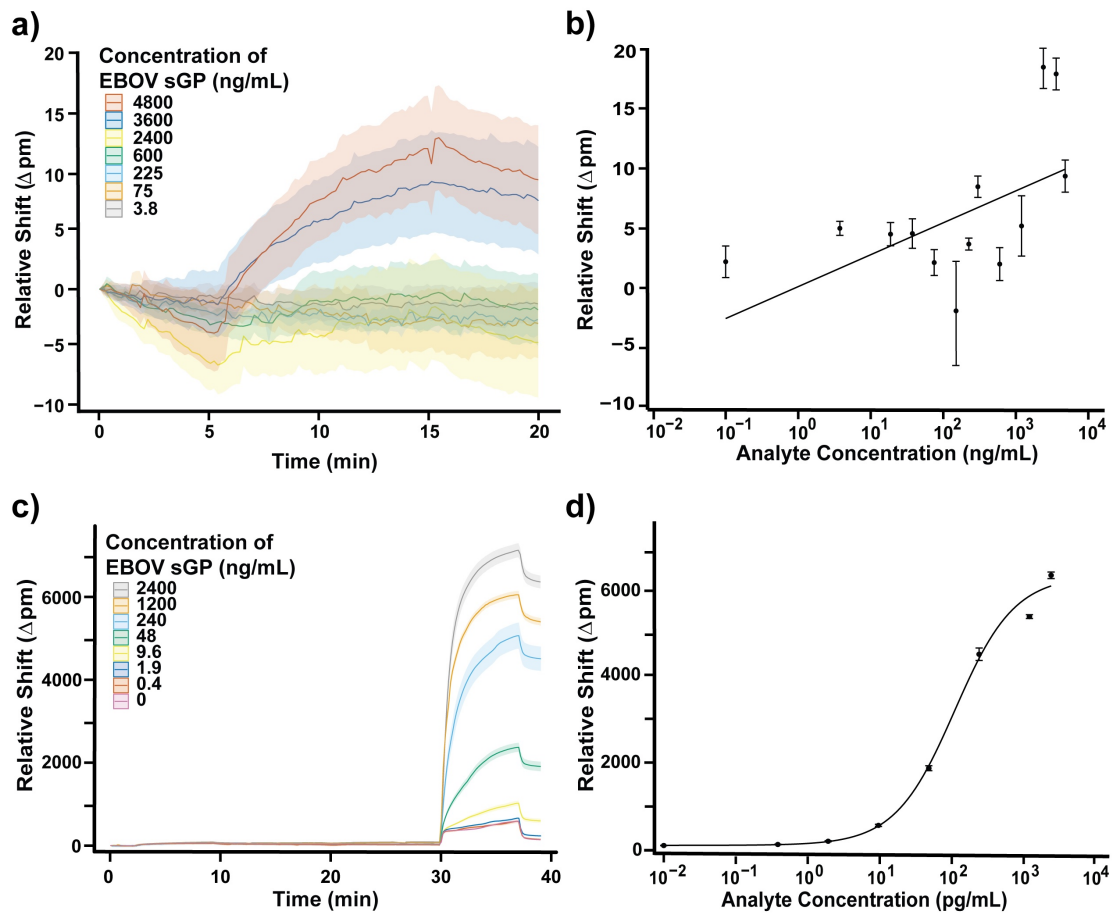


Figure 3.3 Sensor traces and calibration curves for EBOV sGP for both primary binding of sGP and enzymatic amplification. (a) Primary binding of sGP to the microring sensors with concentrations ranging from 3.8 ng/mL to 4,800 ng/mL in neat buffer. (b) Calibration curve for the primary binding responses. (c) Full sandwich immunoassay and amplification response for EBOV sGP concentrations ranging from 0.4 ng/mL to 2,400 ng/mL in a 1% serum matrix. (d) Calibration curve for the amplification responses. Error is from technical replicates of 8-12 microrings per concentration. Each solid line represents the average response from between 8-12 sensors, and the halo is the spread of signal.

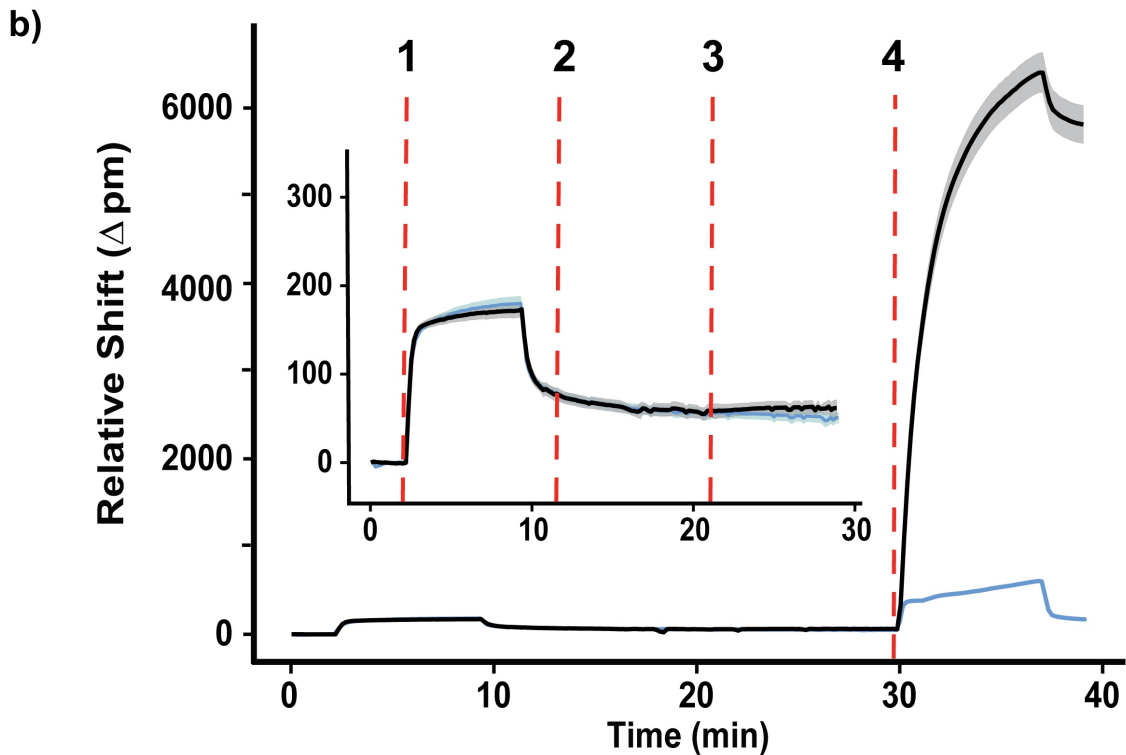
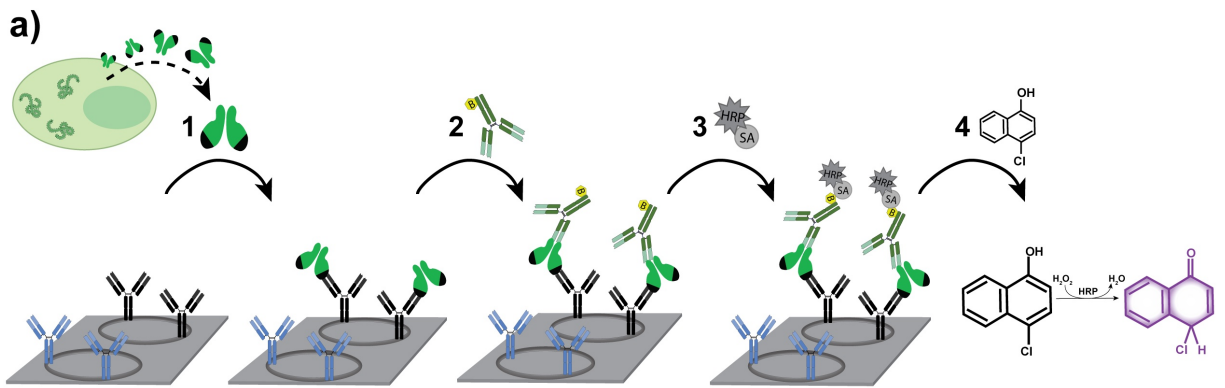


Figure 3.4 Schematic of sGP detection assay. (a) General workflow of sGP detection from infection to sample analysis. During infection, sGP is secreted from infected cells into the patient's circulation and is isolated in patient serum. The immunoassay begins by binding of the secreted sGP in serum (1) onto the functionalized microring surface using specific antibodies (black), while off-target antibodies serve as negative controls (blue). As a secondary recognition element, biotinylated pan-filoviral antibodies (2) detect the captured sGP. This sandwich complex is recognized by streptavidin horse radish peroxidase (3), which allows for enzymatic processing of solution-phase 4-chloro-1-naphthol (4). This final step leads to a large shift in resonant wavelength that is proportional to the amount of sGP bound by the capture antibodies. (b) Corresponding microring traces for each of the steps in part (a). The solid line reflects the average response of 8-12 technical replicates, while the surrounding halo reflects the spread of individual rings. Inset reflects the steps 1-3.

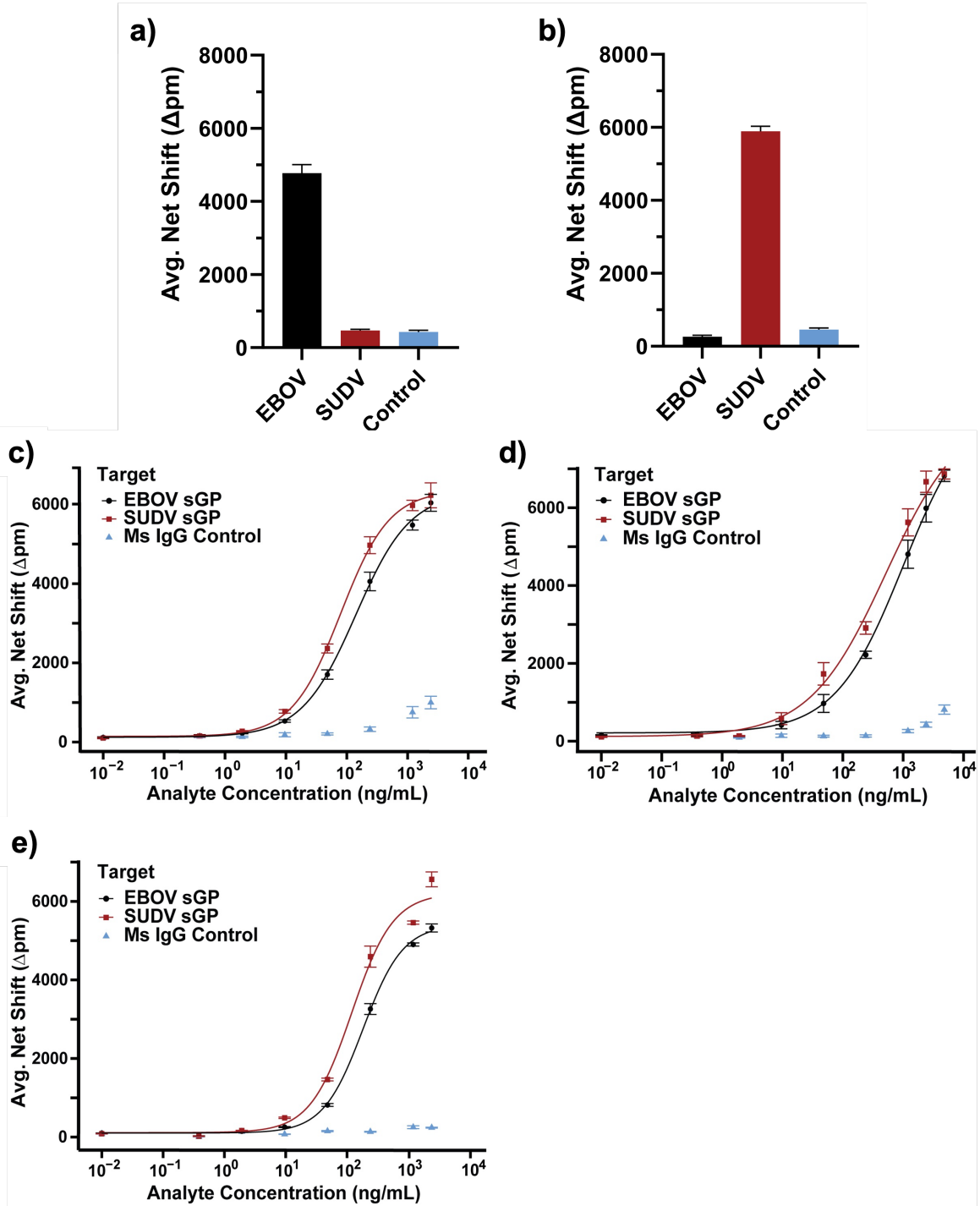


Figure 3.5 Cross reactivity of microring resonators and calibration curves. Chips functionalized with anti-EBOV sGP antibodies (black) and anti-SUDV sGP antibodies (red) show no cross reactivity, as only those rings functionalized with the specific antibody elicit a response in the presence of the respective protein standard, 600 ng/mL of EBOV sGP (a) or 600 ng/mL of SUDV sGP (b). Mouse IgG antibodies (blue) were functionalized on every chip as negative controls. Error bars represent $n=8-12$ technical replicates. (c-e) Calibration curves over a range of analyte concentrations in (c) 1%, (d) 10%, and (e) 50% serum. Each point represents 3 separate runs, with each run containing 8-12 technical replicates. Error bars reflect ± 1 standard deviation.

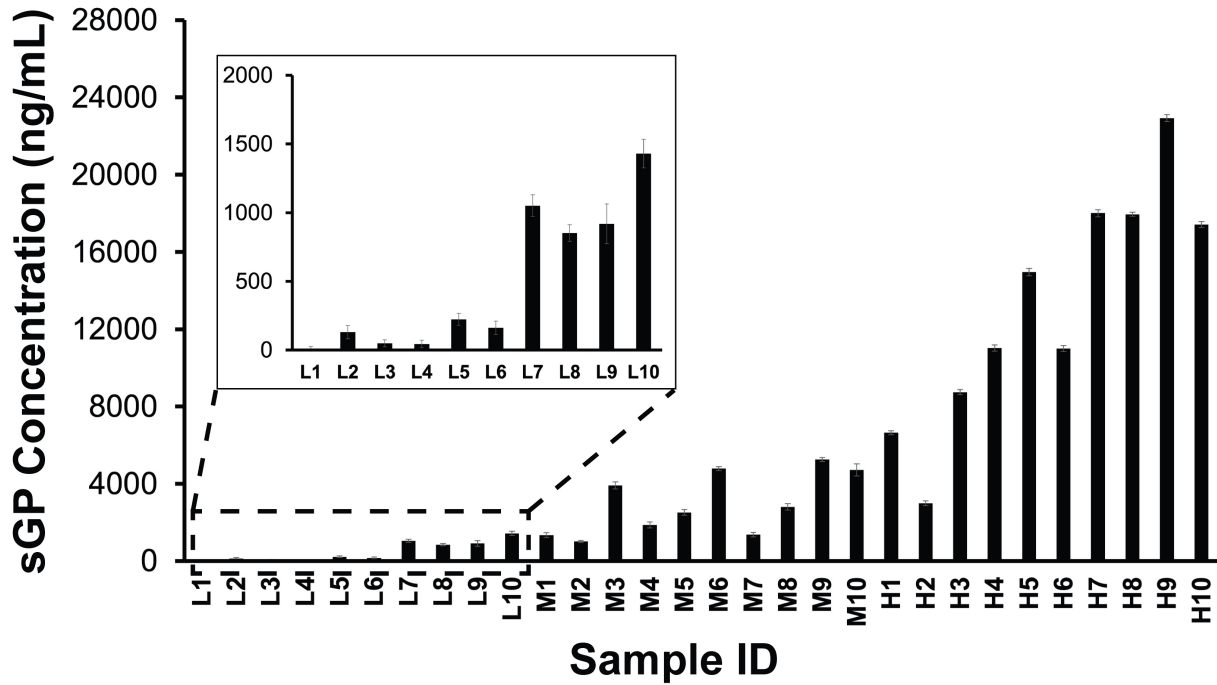


Figure 3.6 Detection of sGP from EBOV infected non-human primate (NHP) samples. Average net shift and standard deviation of microring resonators towards EBOV infected NHP samples. Error bars reflect ± 1 standard deviation. Samples designated with L refer to a sGP concentration range (confirmed via ELISA) between 100 – 1,000 ng/mL, M corresponding to 1,000 – 10,000 ng/mL, and H corresponding to 10,000 –60,000 ng/mL. A total of 8 to 12 technical replicates were performed for each sample.

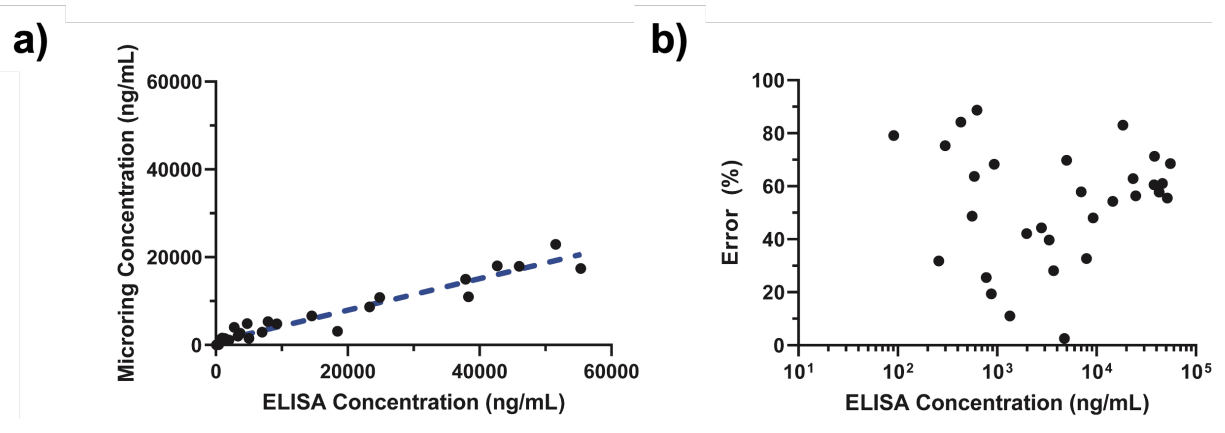


Figure 3.7 Comparison of ELISA and microring resonator platform performance. (a) Full range of concentrations for the NHP samples ($n = 30$). (b) Error (%) for the microring sensors relative to the ELISA standard.

3.9 Tables

Table 3.1 Fitting parameters used in generating calibration curves in Figure 3.5 for EBOV and SUDV sGP with a logistic function, Eq.1.

	1% Serum		10% Serum		50% Serum	
	EBOV	SUDV	EBOV	SUDV	EBOV	SUDV
A₁	123.6	144.6	134.4	80.4	102.4	112.6
A₂	6,307.8	6,356.8	8,642.9	8,409.3	5,404.9	6,210.9
x₀	141.0	79.6	933.7	484.0	182.4	119.1
P	0.97	1.08	0.81	0.73	1.34	1.28

Table 3.2 Matrix blank parameters from the calibration curves in Figure 3.5 for EBOV and SUDV sGP to determine the limit-of-detection (LOD).

Target	Matrix (% Serum)	Blank Net shift (Δpm)	Blank Std. Dev. (Δpm)	LOD (ng/mL)
EBOV	1	119.13	29.48	1.72
SUDV		102.32	31.89	1.00
EBOV	10	152.16	29.33	4.20
SUDV		113.72	29.69	1.54
EBOV	50	100.41	5.80	2.33
SUDV		146.60	47.69	7.76

Table 3.3 EBOV sGP concentrations in NHP samples shown in Figure 3.6, percent error in comparison to ELISA data, and days post infection at time of sample collection.

Sample Code	sGP Concentration by ELISA (ng/mL)	sGP Concentration by Microrings (ng/mL)	Error (%)	Days Post Infection
Low sGP Level Samples (100-1,000 ng/mL)				
L1	91	19	79.1	5
L2	258	176	31.8	7
L3	300	74	75.3	9
L4	431	68	84.2	9
L5	559	287	48.7	7
L6	590	214	63.7	7
L7	627	1,183	88.7	9
L8	777	975	25.5	7
L9	875	1,045	19.4	11
L10	935	1,574	68.3	6
Mid sGP Level Samples (1,000-10,000 ng/mL)				
M1	1,341	1,488	11.0	8
M2	1,984	1,148	42.1	8
M3	2,792	4,030	44.3	9
M4	3,343	2,017	39.7	8
M5	3,699	2,661	28.1	9
M6	4,749	4,870	2.5	10

M7	5,003	1,510	69.8	9
M8	7,001	2,946	57.9	8
M9	7,914	5,324	32.7	11
M10	9,246	4,807	48.0	10
High sGP Level Samples (10,000-60,000 ng/mL)				
H1	14,538	6,649	54.3	9
H2	18,446	3,137	83.0	10
H3	23,307	8,658	62.9	11
H4	24,861	10,845	56.4	11
H5	37,898	14,955	60.5	10
H6	38,311	10,997	71.3	11
H7	42,688	18,007	57.8	6
H8	46,016	17,947	61.0	7
H9	51,546	22,930	55.5	8
H10	55,356	17,411	68.5	9

3.10 References

- (1) Binder, S.; Levitt, A. M.; Sacks, J. J.; Hughes, J. M. Emerging Infectious Diseases: Public Health Issues for the 21st Century. *Science* **1999**, *284* (5418), 1311–1313. <https://doi.org/10.1126/science.284.5418.1311>.
- (2) Jones, K. E.; Patel, N. G.; Levy, M. A.; Storeygard, A.; Balk, D.; Gittleman, J. L.; Daszak, P. Global Trends in Emerging Infectious Diseases. *Nature* **2008**, *451* (7181), 990–993. <https://doi.org/10.1038/nature06536>.
- (3) Morens, D. M.; Folkers, G. K.; Fauci, A. S. The Challenge of Emerging and Re-Emerging Infectious Diseases. *Nature* **2004**, *430* (6996), 242–249. <https://doi.org/10.1038/nature02759>.
- (4) Woolhouse, M. E. J.; Gowtage-Sequeria, S. Host Range and Emerging and Reemerging Pathogens - Volume 11, Number 12—December 2005 - Emerging Infectious Diseases Journal - CDC. <https://doi.org/10.3201/eid1112.050997>.
- (5) Bishara, W.; Sikora, U.; Mudanyali, O.; Su, T.-W.; Yaglidere, O.; Luckhart, S.; Ozcan, A. Holographic Pixel Super-Resolution in Portable Lensless on-Chip Microscopy Using a Fiber-Optic Array. *Lab. Chip* **2011**, *11* (7), 1276–1279. <https://doi.org/10.1039/C0LC00684J>.
- (6) Greenbaum, A.; Akbari, N.; Feizi, A.; Luo, W.; Ozcan, A. Field-Portable Pixel Super-Resolution Colour Microscope. *PLOS ONE* **2013**, *8* (9), e76475. <https://doi.org/10.1371/journal.pone.0076475>.
- (7) Institute of Medicine (US) Committee on Emerging Microbial Threats to Health. *Emerging Infections: Microbial Threats to Health in the United States*; Lederberg, J., Shope, R. E., Oaks, S. C., Eds.; National Academies Press (US): Washington (DC), 1992.
- (8) McLeod, E.; Nguyen, C.; Huang, P.; Luo, W.; Veli, M.; Ozcan, A. Tunable Vapor-Condensed Nanolenses. *ACS Nano* **2014**, *8* (7), 7340–7349. <https://doi.org/10.1021/nn502453h>.
- (9) Mudanyali, O.; McLeod, E.; Luo, W.; Greenbaum, A.; Coskun, A. F.; Hennequin, Y.; Allier, C. P.; Ozcan, A. Wide-Field Optical Detection of Nanoparticles Using on-Chip Microscopy and Self-Assembled Nanolenses. *Nat. Photonics* **2013**, *7* (3), 247–254. <https://doi.org/10.1038/nphoton.2012.337>.
- (10) Carrasco-Hernandez, R.; Jácome, R.; López Vidal, Y.; Ponce de León, S. Are RNA Viruses Candidate Agents for the Next Global Pandemic? A Review. *ILAR J.* **2017**, *58* (3), 343–358. <https://doi.org/10.1093/ilar/ilx026>.
- (11) Rugarabamu, S.; Mboera, L.; Rweyemamu, M.; Mwanyika, G.; Lutwama, J.; Paweska, J.; Misinzo, G. Forty-Two Years of Responding to Ebola Virus Outbreaks in Sub-Saharan Africa: A Review. *BMJ Glob. Health* **2020**, *5* (3), e001955. <https://doi.org/10.1136/bmjgh-2019-001955>.
- (12) Beeching, N. J.; Fenech, M.; Houlihan, C. F. Ebola Virus Disease. *BMJ* **2014**, *349*, g7348. <https://doi.org/10.1136/bmj.g7348>.
- (13) Chertow, D. S.; Kleine, C.; Edwards, J. K.; Scaini, R.; Giuliani, R.; Sprecher, A. Ebola Virus Disease in West Africa — Clinical Manifestations and Management. *N. Engl. J. Med.* **2014**, *371* (22), 2054–2057. <https://doi.org/10.1056/NEJMp1413084>.
- (14) Khan, A. S.; Tshioko, F. K.; Heymann, D. L.; Le Guenno, B.; Nabeth, P.; Kerstiëns, B.; Fleerackers, Y.; Kilmarx, P. H.; Rodier, G. R.; Nkuku, O.; Rollin, P. E.; Sanchez, A.; Zaki, S. R.; Swanepoel, R.; Tomori, O.; Nichol, S. T.; Peters, C. J.; Muyembe-Tamfum, J. J.; Ksiazek, T. G.; for the Commission de Lutte contre les Epidémies à Kikwit. The Reemergence of Ebola

- Hemorrhagic Fever, Democratic Republic of the Congo, 1995. *J. Infect. Dis.* **1999**, *179* (Supplement_1), S76–S86. <https://doi.org/10.1086/514306>.
- (15) Lindblade, K. A.; Kateh, F.; Nagbe, T. K.; Neatherlin, J. C.; Pillai, S. K.; Attfield, K. R.; Dweh, E.; Barradas, D. T.; Williams, S. G.; Blackley, D. J.; Kirking, H. L.; Patel, M. R.; Dea, M.; Massoudi, M. S.; Wannemuehler, K.; Barskey, A. E.; Zarecki, S. L. M.; Fomba, M.; Grube, S.; Belcher, L.; Broyles, L. N.; Maxwell, T. N.; Hagan, J. E.; Yeoman, K.; Westercamp, M.; Forrester, J. D.; Mott, J.; Mahoney, F.; Slutsker, L.; DeCock, K. M.; Nyenswah, T. G. Decreased Ebola Transmission after Rapid Response to Outbreaks in Remote Areas, Liberia, 2014 - Volume 21, Number 10—October 2015 - Emerging Infectious Diseases Journal - CDC. <https://doi.org/10.3201/eid2110.150912>.
- (16) Broadhurst, M. J.; Brooks, T. J. G.; Pollock, N. R. Diagnosis of Ebola Virus Disease: Past, Present, and Future. *Clin. Microbiol. Rev.* **2016**, *29* (4), 773–793. <https://doi.org/10.1128/cmr.00003-16>.
- (17) Furuyama, W.; Marzi, A. Development of an Enzyme-Linked Immunosorbent Assay to Determine the Expression Dynamics of Ebola Virus Soluble Glycoprotein during Infection. *Microorganisms* **2020**, *8* (10), 1535. <https://doi.org/10.3390/microorganisms8101535>.
- (18) Kebenei, C. K.; Okoth, P. Ebola Virus Disease, Diagnostics and Therapeutics: Where Is the Consensus in Over Three Decades of Clinical Research? *Sci. Afr.* **2021**, *13*, e00862. <https://doi.org/10.1016/j.sciaf.2021.e00862>.
- (19) Moran, Z.; Rodriguez, W.; Ahmadou, D.; Soropogui, B.; Magassouba, N. F.; Kelly-Cirino, C.; Ben Amor, Y. Comparative Performance Study of Three Ebola Rapid Diagnostic Tests in Guinea. *BMC Infect. Dis.* **2020**, *20* (1), 670. <https://doi.org/10.1186/s12879-020-05339-2>.
- (20) Pallesen, J.; Murin, C. D.; de Val, N.; Cottrell, C. A.; Hastie, K. M.; Turner, H. L.; Fusco, M. L.; Flyak, A. I.; Zeitlin, L.; Crowe, J. E.; Andersen, K. G.; Saphire, E. O.; Ward, A. B. Structures of Ebola Virus GP and sGP in Complex with Therapeutic Antibodies. *Nat. Microbiol.* **2016**, *1* (9), 16128. <https://doi.org/10.1038/nmicrobiol.2016.128>.
- (21) Volchkova, V. A.; Feldmann, H.; Klenk, H.-D.; Volchkov, V. E. The Nonstructural Small Glycoprotein sGP of Ebola Virus Is Secreted as an Antiparallel-Orientated Homodimer. *Virology* **1998**, *250* (2), 408–414. <https://doi.org/10.1006/viro.1998.9389>.
- (22) Sanchez, A.; Yang, Z.-Y.; Xu, L.; Nabel, G. J.; Crews, T.; Peters, C. J. Biochemical Analysis of the Secreted and Virion Glycoproteins of Ebola Virus. *J. Virol.* **1998**, *72* (8), 6442–6447. <https://doi.org/10.1128/jvi.72.8.6442-6447.1998>.
- (23) de La Vega, M.-A.; Wong, G.; Kobinger, G. P.; Qiu, X. The Multiple Roles of sGP in Ebola Pathogenesis. *Viral Immunol.* **2015**, *28* (1), 3–9. <https://doi.org/10.1089/vim.2014.0068>.
- (24) Zhu, W.; Banadyga, L.; Emeterio, K.; Wong, G.; Qiu, X. The Roles of Ebola Virus Soluble Glycoprotein in Replication, Pathogenesis, and Countermeasure Development. *Viruses* **2019**, *11* (11). <https://doi.org/10.3390/v11110999>.
- (25) Bradley, J. H.; Harrison, A.; Corey, A.; Gentry, N.; Gregg, R. K. Ebola Virus Secreted Glycoprotein Decreases the Anti-Viral Immunity of Macrophages in Early Inflammatory Responses. *Cell. Immunol.* **2018**, *324*, 24–32. <https://doi.org/10.1016/j.cellimm.2017.11.009>.
- (26) Kindzelskii, A. L.; Yang, Z.; Nabel, G. J.; Todd, R. F., III; Petty, H. R. Ebola Virus Secretory Glycoprotein (sGP) Diminishes FcγRIIIB-to-CR3 Proximity on Neutrophils1. *J. Immunol.* **2000**, *164* (2), 953–958. <https://doi.org/10.4049/jimmunol.164.2.953>.
- (27) Wahl-Jensen, V. M.; Afanasieva, T. A.; Seebach, J.; Ströher, U.; Feldmann, H.; Schnittler, H.-J. Effects of Ebola Virus Glycoproteins on Endothelial Cell Activation and

- Barrier Function. *J. Virol.* **2005**, *79* (16), 10442–10450.
<https://doi.org/10.1128/jvi.79.16.10442-10450.2005>.
- (28) Qavi, A. J.; Bailey, R. C. Multiplexed Detection and Label-Free Quantitation of MicroRNAs Using Arrays of Silicon Photonic Microring Resonators. *Angew. Chem. Int. Ed.* **2010**, *49* (27), 4608–4611. <https://doi.org/10.1002/anie.201001712>.
- (29) Qavi, A. J.; Kindt, J. T.; Gleeson, M. A.; Bailey, R. C. Anti-DNA:RNA Antibodies and Silicon Photonic Microring Resonators: Increased Sensitivity for Multiplexed microRNA Detection. *Anal. Chem.* **2011**, *83* (15), 5949–5956. <https://doi.org/10.1021/ac201340s>.
- (30) Scheler, O.; Kindt, J. T.; Qavi, A. J.; Kaplinski, L.; Glynn, B.; Barry, T.; Kurg, A.; Bailey, R. C. Label-Free, Multiplexed Detection of Bacterial tmRNA Using Silicon Photonic Microring Resonators. *Biosens. Bioelectron.* **2012**, *36* (1), 56–61.
<https://doi.org/10.1016/j.bios.2012.03.037>.
- (31) Kindt, J. T.; Luchansky, M. S.; Qavi, A. J.; Lee, S.-H.; Bailey, R. C. Subpicogram Per Milliliter Detection of Interleukins Using Silicon Photonic Microring Resonators and an Enzymatic Signal Enhancement Strategy. *Anal. Chem.* **2013**, *85* (22), 10653–10657.
<https://doi.org/10.1021/ac402972d>.
- (32) Shia, W. W.; Bailey, R. C. Single Domain Antibodies for the Detection of Ricin Using Silicon Photonic Microring Resonator Arrays. *Anal. Chem.* **2013**, *85* (2), 805–810.
<https://doi.org/10.1021/ac3030416>.
- (33) Washburn, A. L.; Gunn, L. C.; Bailey, R. C. Label-Free Quantitation of a Cancer Biomarker in Complex Media Using Silicon Photonic Microring Resonators. *Anal. Chem.* **2009**, *81* (22), 9499–9506. <https://doi.org/10.1021/ac902006p>.
- (34) McClellan, M. S.; Domier, L. L.; Bailey, R. C. Label-Free Virus Detection Using Silicon Photonic Microring Resonators. *Biosens. Bioelectron.* **2012**, *31* (1), 388–392.
<https://doi.org/10.1016/j.bios.2011.10.056>.
- (35) Cardenosa-Rubio, M. C.; Robison, H. M.; Bailey, R. C. Recent Advances in Environmental and Clinical Analysis Using Microring Resonator-Based Sensors. *Curr. Opin. Environ. Sci. Health* **2019**, *10*, 38–46. <https://doi.org/10.1016/j.coesh.2019.09.001>.
- (36) Robison, H. M.; Escalante, P.; Valera, E.; Erskine, C. L.; Auvil, L.; Sasieta, H. C.; Bushell, C.; Welge, M.; Bailey, R. C. Precision Immunoprofiling to Reveal Diagnostic Signatures for Latent Tuberculosis Infection and Reactivation Risk Stratification. *Integr. Biol.* **2019**, *11* (1), 16–25. <https://doi.org/10.1093/intbio/zyz001>.
- (37) Robison, H. M.; Chapman, C. A.; Zhou, H.; Erskine, C. L.; Theel, E.; Peikert, T.; Lindestam Arlehamn, C. S.; Sette, A.; Bushell, C.; Welge, M.; Zhu, R.; Bailey, R. C.; Escalante, P. Risk Assessment of Latent Tuberculosis Infection through a Multiplexed Cytokine Biosensor Assay and Machine Learning Feature Selection. *Sci. Rep.* **2021**, *11* (1), 20544. <https://doi.org/10.1038/s41598-021-99754-3>.
- (38) Wade, J. H.; Alsop, A. T.; Vertin, N. R.; Yang, H.; Johnson, M. D.; Bailey, R. C. Rapid, Multiplexed Phosphoprotein Profiling Using Silicon Photonic Sensor Arrays. *ACS Cent. Sci.* **2015**, *1* (7), 374–382. <https://doi.org/10.1021/acscentsci.5b00250>.
- (39) Robison, H. M.; Bailey, R. C. A Guide to Quantitative Biomarker Assay Development Using Whispering Gallery Mode Biosensors: Whispering Gallery Mode Biosensors. *Curr. Protoc. Chem. Biol.* **2017**, *9* (3), 158–173. <https://doi.org/10.1002/cpch.23>.
- (40) Pettitt, J.; Zeitlin, L.; Kim, D. H.; Working, C.; Johnson, J. C.; Bohorov, O.; Bratcher, B.; Hiatt, E.; Hume, S. D.; Johnson, A. K.; Morton, J.; Pauly, M. H.; Whaley, K. J.; Ingram, M. F.; Zovanyi, A.; Heinrich, M.; Piper, A.; Zelko, J.; Olinger, G. G. Therapeutic Intervention of

- Ebola Virus Infection in Rhesus Macaques with the MB-003 Monoclonal Antibody Cocktail. *Sci. Transl. Med.* **2013**, *5* (199), 199ra113-199ra113. <https://doi.org/10.1126/scitranslmed.3006608>.
- (41) United States Army Medical Research Institute of Infectious Diseases Specimen Collection and Submission Manual. *USAMRIID* **2016**.
- (42) Jiang, X.; Qavi, A. J.; Huang, S. H.; Yang, L. Whispering-Gallery Sensors. *Matter* **2020**, *3* (2), 371–392. <https://doi.org/10.1016/j.matt.2020.07.008>.
- (43) Yu, D.; Humar, M.; Meserve, K.; Bailey, R. C.; Chormaic, S. N.; Vollmer, F. Whispering-Gallery-Mode Sensors for Biological and Physical Sensing. *Nat. Rev. Methods Primer* **2021**, *1* (1), 83. <https://doi.org/10.1038/s43586-021-00079-2>.
- (44) Arnfinnsdottir, N. B.; Chapman, C. A.; Bailey, R. C.; Aksnes, A.; Stokke, B. T. Impact of Silanization Parameters and Antibody Immobilization Strategy on Binding Capacity of Photonic Ring Resonators. *Sensors* **2020**, *20* (11), 3163. <https://doi.org/10.3390/s20113163>.
- (45) Medfisch, S. M.; Muehl, E. M.; Morrissey, J. H.; Bailey, R. C. Phosphatidylethanolamine-Phosphatidylserine Binding Synergy of Seven Coagulation Factors Revealed Using Nanodisc Arrays on Silicon Photonic Sensors. *Sci. Rep.* **2020**, *10* (1), 17407. <https://doi.org/10.1038/s41598-020-73647-3>.
- (46) Mordan, E. H.; Wade, J. H.; Pearce, E.; Meunier, D. M.; Bailey, R. C. A Linear Mass Concentration Detector for Solvent Gradient Polymer Separations. *The Analyst* **2020**, *145* (13), 4484–4493. <https://doi.org/10.1039/C9AN02533B>.
- (47) Wetzler, S. P.; Miller, K. A.; Kisley, L.; Stanton, A. L. D.; Braun, P. V.; Bailey, R. C. Real-Time Measurement of Polymer Brush Dynamics Using Silicon Photonic Microring Resonators: Analyte Partitioning and Interior Brush Kinetics. *Langmuir* **2020**, *36* (35), 10351–10360. <https://doi.org/10.1021/acs.langmuir.0c01336>.
- (48) Feldmann, H.; Geisbert, T. W. Ebola Haemorrhagic Fever. *The Lancet* **2011**, *377* (9768), 849–862. [https://doi.org/10.1016/S0140-6736\(10\)60667-8](https://doi.org/10.1016/S0140-6736(10)60667-8).
- (49) Fowler, R. A.; Fletcher, T.; Fischer, W. A.; Lamontagne, F.; Jacob, S.; Brett-Major, D.; Lawler, J. V.; Jacquerioz, F. A.; Houlihan, C.; O’Dempsey, T.; Ferri, M.; Adachi, T.; Lamah, M.-C.; Bah, E. I.; Mayet, T.; Schieffelin, J.; McLellan, S. L.; Senga, M.; Kato, Y.; Clement, C.; Mardel, S.; Vallenias Bejar De Villar, R. C.; Shindo, N.; Bausch, D. Caring for Critically Ill Patients with Ebola Virus Disease. Perspectives from West Africa. *Am. J. Respir. Crit. Care Med.* **2014**, *190* (7), 733–737. <https://doi.org/10.1164/rccm.201408-1514CP>.
- (50) Fontes, C. M.; Lipes, B. D.; Liu, J.; Agans, K. N.; Yan, A.; Shi, P.; Cruz, D. F.; Kelly, G.; Luginbuhl, K. M.; Joh, D. Y.; Foster, S. L.; Heggstad, J.; Hucknall, A.; Mikkelsen, M. H.; Pieper, C. F.; Horstmeyer, R. W.; Geisbert, T. W.; Gunn, M. D.; Chilkoti, A. Ultrasensitive Point-of-Care Immunoassay for Secreted Glycoprotein Detects Ebola Infection Earlier than PCR. *Sci. Transl. Med.* **2021**, *13* (588), eabd9696. <https://doi.org/10.1126/scitranslmed.abd9696>.
- (51) Chen, X.; Kang, S.; Ikbali, M. A.; Zhao, Z.; Pan, Y.; Zuo, J.; Gu, L.; Wang, C. Synthetic Nanobody-Functionalized Nanoparticles for Accelerated Development of Rapid, Accessible Detection of Viral Antigens. *Biosens. Bioelectron.* **2022**, *202*, 113971. <https://doi.org/10.1016/j.bios.2022.113971>.
- (52) Connell, E. Tietz Textbook of Clinical Chemistry and Molecular Diagnostics (5th Edn). *Ann. Clin. Biochem.* **2012**, *49* (6), 615–615. <https://doi.org/10.1258/acb.2012.201217>.
- (53) Wit, E. de; Falzarano, D.; Onyango, C.; Rosenke, K.; Marzi, A.; Ochieng, M.; Juma, B.; Fischer, R. J.; Prescott, J. B.; Safronetz, D.; Omballa, V.; Owuor, C.; Hoenen, T.; Groseth, A.;

- Doremalen, N. van; Zemtsova, G.; Self, J.; Bushmaker, T.; McNally, K.; Rowe, T.; Emery, S. L.; Feldmann, F.; Williamson, B.; Nyenswah, T. G.; Grolla, A.; Strong, J. E.; Kobinger, G.; Stroehrer, U.; Rayfield, M.; Bolay, F. K.; Zoon, K. C.; Stassijns, J.; Tampellini, L.; Smet, M. de; Nichol, S. T.; Fields, B.; Sprecher, A.; Feldmann, H.; Massaquoi, M.; Munster, V. J. The Merits of Malaria Diagnostics during an Ebola Virus Disease Outbreak - Volume 22, Number 2—February 2016 - Emerging Infectious Diseases Journal - CDC.
<https://doi.org/10.3201/eid2202.151656>.
- (54) Xu, X.; Jiang, X.; Zhao, G.; Yang, L. Phone-Sized Whispering-Gallery Microresonator Sensing System. *Opt. Express* **2016**, *24* (23), 25905–25910.
<https://doi.org/10.1364/OE.24.025905>.
- (55) Adolphson, M. R.; M.d, A. J. Q.; Shmuylovich, L.; Amarasinghe, G. K.; Yang, L. Reverse Tuning of Whispering Gallery Mode Microresonators. In *Optics and Biophotonics in Low-Resource Settings VIII*; SPIE, 2022; Vol. 11950, pp 10–15.
<https://doi.org/10.1117/12.2608720>.
- (56) Elliott, L. H.; McCormick, J. B.; Johnson, K. M. Inactivation of Lassa, Marburg, and Ebola Viruses by Gamma Irradiation. *J. Clin. Microbiol.* **1982**, *16* (4), 704–708.
<https://doi.org/10.1128/jcm.16.4.704-708.1982>.
- (57) Sagripanti, J.-L.; Lytle, C. D. Sensitivity to Ultraviolet Radiation of Lassa, Vaccinia, and Ebola Viruses Dried on Surfaces. *Arch. Virol.* **2011**, *156* (3), 489–494.
<https://doi.org/10.1007/s00705-010-0847-1>.
- (58) Warfield, K. L.; Swenson, D. L.; Olinger, G. G.; Kalina, W. V.; Viard, M.; Aitichou, M.; Chi, X.; Ibrahim, S.; Blumenthal, R.; Raviv, Y.; Bavari, S.; Aman, M. J. Ebola Virus Inactivation with Preservation of Antigenic and Structural Integrity by a Photoinducible Alkylating Agent. *J. Infect. Dis.* **2007**, *196* (Supplement_2), S276–S283.
<https://doi.org/10.1086/520605>.
- (59) Mitchell, S. W.; McCormick, J. B. Physicochemical Inactivation of Lassa, Ebola, and Marburg Viruses and Effect on Clinical Laboratory Analyses. *J. Clin. Microbiol.* **1984**, *20* (3), 486–489. <https://doi.org/10.1128/jcm.20.3.486-489.1984>.
- (60) Lau, R.; Wang, A.; Chong-Kit, A.; Ralevski, F.; Boggild, A. K. Evaluation of Ebola Virus Inactivation Procedures for Plasmodium Falciparum Malaria Diagnostics. *J. Clin. Microbiol.* **2015**, *53* (4), 1387–1390. <https://doi.org/10.1128/jcm.00165-15>.
- (61) Suter, J. D.; White, I. M.; Zhu, H.; Shi, H.; Caldwell, C. W.; Fan, X. Label-Free Quantitative DNA Detection Using the Liquid Core Optical Ring Resonator. *Biosens. Bioelectron.* **2008**, *23* (7), 1003–1009. <https://doi.org/10.1016/j.bios.2007.10.005>.
- (62) Zhu, H.; White, I. M.; Suter, J. D.; Dale, P. S.; Fan, X. Analysis of Biomolecule Detection with Optofluidic Ring Resonator Sensors. *Opt. Express* **2007**, *15* (15), 9139–9146.
<https://doi.org/10.1364/OE.15.009139>.
- (63) Giannetti, A.; Barucci, A.; Berneschi, S.; Cosci, A.; Cosi, F.; Farnesi, D.; Conti, G. N.; Pelli, S.; Soria, S.; Tombelli, S.; Trono, C.; Righini, G. C.; Baldini, F. Optical Micro-Bubble Resonators as Promising Biosensors. In *Optical Sensors 2015*; SPIE, 2015; Vol. 9506, pp 241–247. <https://doi.org/10.1117/12.2180242>

Chapter 4 Chorioamnionitis-Exposure Alters Serum Cytokine Trends in Premature Neonates

4.1 Author Contributions and Acknowledgements

This chapter is adapted from the published article: Stepanovich, G.E.*, Chapman, C.A.*, Meserve, K., Sturza, J.M., Ellsworth, L.A., Bailey, R.C., Bermick, J.R. [Chorioamnionitis-exposure alters serum cytokine trends in premature neonates](#), *Journal of Perinatology* 43(6), 2022. The seven-plex cytokine assay development and optimization, and the cytokine profiling of the approximately 425 patient serum samples was completed by Dr. Cole Chapman and the thesis author, Krista Meserve. The thesis author completed the final data work up of all samples in the study. Data analysis presented in figures 4.1, 4.3, 4.4, 4.5, and 4.6 and tables 4.1, 4.4, and 4.5 were completed by our project collaborators, Dr. Jennifer Bermick, Dr. Lindsay Ellsworth, and Dr. Julie Sturza. Figure 4.2, and tables 4.2-4.3 were designed by Dr. Cole Chapman, and figures 4.7-4.9 were designed by the thesis author. Dr. Cole Chapman and Dr. Jennifer Bermick were the main writing contributors to the manuscript. The thesis author provided content edits and added additional information regarding longitudinal profiling for the context of this thesis.

I acknowledge Dr. Gretchen Stepanovich from the UM Department of Pediatrics for completing the clinical side of the project (collecting informed consent from parents, saving the patient serum, and providing subject demographic data); Dr. Lindsay Ellsworth from the UM Department of Pediatrics for administrative and logistical work; Julie Sturza from UM Department of Pediatrics Biostatistics division for her work towards final analysis of the data set; Dr. Jennifer Bermick from the University of Iowa Department of Pediatrics (formerly of the UM

Department of Pediatrics) for her clinical knowledge, manuscript writing, and guidance of the project from start to finish; and Dr. Ryan Bailey for his project guidance.

4.2 Abstract

Objective: Determine if baseline serum cytokine and chemokine levels in preterm neonates differ by chronologic age and chorioamnionitis exposure.

Study Design: A 7-plex immunoassay measured levels of serum IL-1 β , IL-6, IL-8, IL-10, TNF- α , CCL2 and CCL3 longitudinally from chorioamnionitis-exposed and unexposed preterm neonates under 33 weeks' gestation.

Results: Chorioamnionitis-exposed and unexposed preterm neonates demonstrated differences in the trends of IL-1 β , IL-6, IL-8, IL-10, TNF- α , and CCL2 over the first month of life. The unexposed neonates demonstrated elevated levels of these inflammatory markers in the first two weeks of life with a decrease to baseline levels by the third week of life, while the chorioamnionitis-exposed neonates demonstrated differences over time without a predictable pattern. Chorioamnionitis-exposed and unexposed neonates demonstrated altered IL-10 and TNF- α , trajectories over the first twelve weeks of life.

Conclusion: Chorioamnionitis induces a state of immune dysregulation that persists for at least twelve weeks following delivery in preterm neonates.

4.3 Introduction

Preterm birth, defined as delivery that occurs prior to 37 weeks' gestation, complicates approximately 11% of births globally.¹ Preterm neonates are at risk for numerous morbidities during their initial hospitalization, including an increased risk for sepsis.² This infection risk is often attributed to immaturity of the preterm immune system, particularly the innate immune

system. Several studies have demonstrated differences in innate immune cytokine levels between term and preterm infants.^{3,4} These altered cytokine responses are thought to contribute to a preterm neonate's heightened susceptibility to infection as appropriate cytokine responses are necessary to guide the clearance of microorganisms.⁵ However, the natural evolution of innate immune responses in premature neonates is incompletely understood.

Preterm delivery is often complicated and may even be stimulated by intrauterine inflammation and/or infection, termed chorioamnionitis.¹ Chorioamnionitis is present in up to 70% of very preterm deliveries and leads to an initial fetal pro-inflammatory response, including increased expression of the pro-inflammatory cytokines IL-1 β , IL-6, IL-8 and TNF- α .^{6,7} This fetal inflammatory response alters the developing immune system, resulting in decreased pro-inflammatory cytokine expression when umbilical cord blood monocytes from chorioamnionitis-exposed neonates undergo a secondary challenge with either LPS or *Staphylococcus epidermidis*.^{8,9} Chorioamnionitis exposure is known to increase the risk of developing both early and late onset neonatal sepsis, which may be at least partially due to these dampened monocyte responses.^{10,11} It is currently unclear how long this chorioamnionitis-induced immune hypo-responsiveness persists, which could impact a preterm infant's already heightened susceptibility to infection beyond the immediate neonatal period.

The primary objective of this study was to determine if baseline serum cytokine and chemokine concentrations in preterm neonates differed based on chronologic age and/or chorioamnionitis-exposure. A secondary objective was to compare serum cytokine and chemokine levels between preterm infants with bacterial sepsis, necrotizing enterocolitis and healthy controls. To achieve these objectives, we performed longitudinal cytokine and chemokine profiling using a 7-plex cytokine and chemokine assay to measure concentrations of

CCL2, CCL3, IL-1 β , IL-6, IL-8, IL-10, and TNF- α in neonatal serum samples. These cytokines span pro- and anti-inflammatory classes and represent various functions of the innate immune system, including recruitment of cells to infection sites, signaling, and clearance of microorganisms (**Table 4.1**). Using less than 200 μ L of residual serum from clinically indicated routine blood tests, we compared cytokine and chemokine levels throughout a subject's entire NICU stay.

4.4 Methods

Patient Recruitment and Blood Collection. This study was approved by the University of Michigan IRB. This study was performed in accordance with the Declaration of Helsinki. This was a single-center study. The University of Michigan C.S. Mott Children's Hospital is a 348-bed tertiary care hospital. The Brandon NICU is a 52-bed level IV NICU and the Von Voigtlander Women's Hospital has 3,600 births yearly. After informed written parental consent was obtained, residual serum was collected prospectively from clinically indicated lab draws of neonates born at less than 33 weeks' gestational age. Serum samples were collected from 61 patients from birth through 42 weeks' postmenstrual age, death, or discharge, whichever occurred first. A power calculation was performed using our previously published data demonstrating decreased IL-8 protein expression in neonatal chorioamnionitis-exposed monocytes following stimulation with lipopolysaccharide compared to unexposed monocytes (1023 \pm 507.5 pg/mL vs 384.6 \pm 156.1 pg/mL).⁹ Using an alpha value of 0.05 and a power of 90%, a sample size of 13 subjects per exposure group was estimated to detect a statistically significant difference between groups. Our subject cohort included 27 chorioamnionitis-exposed and 34 unexposed preterm infants, exceeding this target sample size. The average number of blood

draws for enrolled subjects was 14 (range 2-37). Sample collection occurred from April 2019 through April 2021.

Histopathologic examination of the placenta was performed by qualified pathologists and the Amsterdam Placental Staging Criteria was used to diagnose chorioamnionitis.^{9,12,13} Ten of the chorioamnionitis-exposed subjects also had evidence of funisitis on placental histopathology. Subjects with placental pathology significant for acute chorioamnionitis ± funisitis were included in the chorioamnionitis group as we found no differences in serum cytokines or chemokines between chorioamnionitis only and chorioamnionitis with funisitis exposed preterm neonates, as evidenced in **Figure 4.1**. Subjects without inflammation on placental pathology, even if there was clinical suspicion for chorioamnionitis, were included in the unexposed group. The blood volume collected with each sample varied, as the serum available for testing was what remained after all clinically ordered testing was performed. As 200 µL was required for performance of the cytokine assay, samples were pooled if collected within three days of one another and the subject had no significant change in clinical status. A total of 397 residual serum samples were collected. Samples were frozen and stored in a -80° C freezer prior to use. As the main objective of this study was to evaluate if baseline serum cytokine values differed based on chronologic age and/or chorioamnionitis exposure and several previous studies demonstrated elevated levels of IL-6, IL-10, IL-8 and/or TNF- α around the time of sepsis or necrotizing enterocolitis diagnosis, we excluded samples from longitudinal data evaluation if the subject had a suspected or confirmed infection and was being treated with antibiotics at the time of sample collection to eliminate samples that may falsely elevate baseline cytokine and chemokine levels.¹⁴⁻¹⁷ This included treatment for sepsis, urinary tract infection, pneumonia, necrotizing enterocolitis, or spontaneous intestinal perforation, excluding 100 samples from analysis. Samples were excluded from 13

chorioamnionitis-exposed and 16 unexposed preterm neonates. A total of 297 serum samples were included in the final longitudinal analysis. Samples were again included from these subjects once the antibiotic treatment course had ended. Six subjects had culture-positive bacterial sepsis and seven subjects had Bell's stage 2 or greater necrotizing enterocolitis. Using previously published data, a power calculation using an alpha level of 0.05 and a power of 90% demonstrated that a sample size of six subjects per group was needed to detect a difference in cytokine levels between bacteremic and control infants (IL-6 in bacteremic infants 3.7 ± 1.8 ng/mL vs 0.4 ± 0.2 ng/mL in control infants) with four subjects per group needed to detect a difference in cytokine levels between infants with necrotizing enterocolitis and control infants (IL-6 in infants with necrotizing enterocolitis 2.1 ± 0.7 ng/mL vs 0.4 ± 0.2 ng/mL in control infants).¹⁶ We matched subjects with culture-positive bacterial sepsis or Bell's stage 2 or greater necrotizing enterocolitis with a healthy control infant based on sex, gestational age at birth (± 1 week) and chorioamnionitis-exposure. We then compared cytokine and chemokine values between these matched groups at the time of sepsis or necrotizing enterocolitis diagnosis and at a similar day of life in the healthy controls (± 5 days).

Reagents and Buffers. Dulbecco's phosphate buffered saline (PBS, catalog # D5573), bovine serum albumin (BSA, catalog # A2153), and (3-Aminopropyl) triethoxysilane (catalog # 440140) were purchased from Millipore Sigma (St. Louis, MO USA). Glycerol (catalog # BP229), bis(sulfosuccinimidyl)suberate (catalog # A39266), starting block blocking buffer (catalog # 37538), Pierce high sensitivity streptavidin-HRP (SA-HRP, catalog # 21130), and 4-chloronaphthol (4-CN, catalog # 34012) were purchased from Thermo Fisher Scientific (Waltham, MA USA). Drycoat assay stabilizer (catalog # AG066) was obtained from Virusys Corporation (Taneytown, MD USA). Vendors and catalog numbers for antibodies for all

multiplexed assay components are summarized in **Table 4.2**. Running buffer for all assays was 0.5% BSA in 1X PBS, pH 7.4.

Multiplexed Immunoassays. Microring resonator immunoassays were validated and performed on the Maverick M1 and Matchbox systems (San Diego, CA USA), respectively, as previously described.^{18–20} The Maverick instruments use microfluidic systems for automated reagent handling. The M1 uses reusable cartridge devices and the Matchbox uses disposable, injection-molded, plug-and-play devices.²⁰ Microring chips were functionalized with capture antibodies using an amine-reactive, homobifunctional crosslinker to create a 7-plex cytokine and chemokine capture array. Each capture antibody spanned two clusters of four microring sensors in each of the two microfluidic channels, giving n=8 technical replicates of each target cytokine or chemokine per channel. After introducing the sample to the chip surface, a mixture of all tracer antibodies was flowed across the chip, followed by streptavidin-tagged enzymes and a signal amplification reagent. Assays were performed at a 30 μ l/min flow rate for all steps. There was an initial rinse of 5 minutes with the running buffer to ensure equilibration of the chip prior to sample analysis. The assay included steps as follows: 1) running buffer (2 min); 2) sample (7 min); 3) running buffer rinse (2 min); 4) biotinylated tracer antibodies (7 min); 5) running buffer rinse (2 min); 6) SA-HRP (7 min); 7) running buffer rinse (2 min); 8) 4-CN (7 min); 9) running buffer rinse (2 min). The total assay time was 38 minutes (**Figure 4.2A**).

Immunoassay Calibrations. The 7-plex immunoassay was simultaneously calibrated for all analytes in a multiplexed format, as described previously.¹⁸ Serial dilutions from a mixed saturating analyte sample of all multiplexed targets were used to construct eight-point calibration curves correlating net sensor shifts to target concentrations. To quantify, the signal before the amplification step (t=29 min) was subtracted from the signal after the final assay rinse step (t=38

min). These net resonance wavelength shifts (Δpm) were plotted as a function of standard concentration and fit to a four-parametric logistic function (**Figure 4.2B**). Limits of detection (LOD) and quantification (LOQ) were defined as the blank signal plus 3 times and 10 times the standard deviation of the blank, respectively (**Table 4.3**). Each calibration was performed at least in triplicate for each sample dilution as measured with 8 sensors per technical replicate.

Sample Evaluation. All samples contained at least 200 μL of residual serum. Neonatal residual serum samples were analyzed at two dilutions (2X and 10X) in running buffer using the same steps highlighted in **Figure 4.2A**. To quantify, the net shift surrounding the amplification step for each target was correlated to concentration using the corresponding standard calibration curve, 50% serum or 10% serum, matching the serum content of the residual serum dilution. The most appropriate dilution to use for statistical analysis was selected by choosing the dilution that resulted in the relative shift closer to the inflection point of the respective calibration curve.

Statistical Analysis. Basic statistical analysis was performed in GraphPad Prism 8. Data normality was evaluated using the Shapiro-Wilk test. Study group characteristics were compared using the student's t-test for quantitative parametric data, the Mann-Whitney test for nonparametric data and the Chi-square test for categorical variables. p-values of <0.05 were considered significant. Cytokine and chemokine levels were compared between the first and second weeks of life in the same subject using the Wilcoxon matched pairs signed rank test. If there was more than one data point within these time frames, the data points were averaged to create a single mean level for each week. p-values < 0.05 was considered significant for this analysis method.

General Estimating Equations were used in SPSS 28.0.1.0 to evaluate for changes in cytokine trends over the first four weeks of life in the chorioamnionitis-exposed and unexposed

groups as the data was longitudinal, paired, and non-parametric with missing data points for some subjects. The General Estimating Equations used a robust covariance matrix, an unstructured working correlation matrix and a Tweedie with log link model. If there was more than one data point within each time frame, the data points were averaged to create a single mean level for each week. p-values < 0.05 was considered significant for the comparison of overall trends within each exposure group. However, when individual timepoints were compared within exposure groups, p-values < 0.01 were considered significant to correct for multiple comparisons. Cytokine and chemokine levels from each subject were then compared over time by week-of-life (chronologic age) through 12 weeks. When there was more than one data point in a week, all points within that week were averaged to create a single mean cytokine level. Univariate statistics showed that the cytokines were not normally distributed and were largely right skewed, with many zeros, representing cytokine levels below the limit of detection. To transform the data to approximate a normal distribution more appropriate for modeling, the natural log of (cytokine level + x, where x is a positive value that varies based on the cytokine in question) was used. SAS Proc Mixed was used to perform repeated measures regression to look at the effect of chorioamnionitis status on the trajectory of cytokines over time while controlling for gestational age, ethnicity, and birth via C-section, all of which were found to be statistically different between exposure groups. Analyses were restricted to the first twelve weeks of life as the chorioamnionitis-exposed group had no data points beyond the first twelve weeks of life. Autoregressive covariance structure was selected based upon a) a conceptual understanding of the data (measurements close in time would be expected to more strongly correlated than measurements which are farther away from one another) and b) lower Akaike information criteria (AIC) in comparison to other covariance structures. The interaction term between week

of life and chorioamnionitis status indicated whether or not the cytokine trajectories differed. Least square mean values from SAS Proc Mixed were graphed to allow for a clearer understanding of trajectory differences. p-values of < 0.05 were considered significant.

Comparisons between subjects with either culture-positive bacterial sepsis or necrotizing enterocolitis and healthy control subjects were made using the Friedman test with multiple comparisons correction. p-values of < 0.05 were considered significant.

4.5 Results

Characteristics of Study Subjects. A total of 61 preterm neonates were enrolled in this study, including 27 exposed to chorioamnionitis and 34 unexposed. Subjects ranged from 22 to 32 weeks' gestational age at birth and were followed to 42 weeks' postmenstrual age, discharge, or death, whichever came first. **Table 4.4** describes characteristics of the two study groups.

Chorioamnionitis-exposed preterm neonates were younger, more likely to be African American and more likely to be born by vaginal delivery than unexposed preterm neonates.

Cytokine and Chemokine Measurements During Initial Two Weeks of Life. Levels of 7 cytokines and chemokines known to be important in innate immunity were measured in residual neonatal serum (**Table 4.1**). We first sought to investigate the change in cytokine and chemokine levels from the first week of life to the second in all of the preterm neonates and separated subjects based on chorioamnionitis exposure. We directly compared all cytokine and chemokine levels from each infant averaged over the first week of life to its average levels in the second week of life using a matched comparison, with each infant compared to itself at two different points in time. Levels from the first week of life were significantly higher than those in week two for IL-6 and CCL2 in both chorioamnionitis-exposed and unexposed subjects but IL-8 only demonstrated this trend in unexposed subjects (**Figure 4.3**).

Cytokine and Chemokine Trends Over the First Month of Life. We then compared the levels of serum cytokines and chemokines in chorioamnionitis-exposed and unexposed subjects by time post birth. The following epochs were compared between the same subject: week 1 (day of life 1-7), week 2 (day of life 8-14), week 3 (day of life 15-21), week 4 (day of life 22-28) and beyond 4 weeks (29+ days of life). Unexposed and chorioamnionitis-exposed preterm neonates both demonstrated significant changes in IL-1 β , IL-6, IL-8, IL-10, TNF- α and CCL2 during the first month of life (**Figure 4.4A-F**). Chorioamnionitis-exposed preterm neonates demonstrated changes in CCL3 over the first month of life, but unexposed preterm neonates did not (**Figure 4.4G**). In general, unexposed preterm neonates demonstrated elevated levels of IL-1 β , IL-6, IL-8, IL-10, TNF- α and CCL2 in the first one to two weeks of life with a decrease to what appears to be baseline levels by the third week of life (**Figure 4.4**, black circles). This contrasts with chorioamnionitis-exposed preterm neonates, who demonstrated differences in cytokine levels over the first month of life but without a predictable pattern (**Figure 4.4**, white circles). Direct comparisons between the different time points are detailed in **Table 4.5**.

Cytokine and Chemokine Trajectories Between Chorioamnionitis-exposed and unexposed preterm neonates. Repeated measures of regression were then performed to look at the effect of chorioamnionitis status on the trajectory of cytokines over the 12 weeks following birth. This analysis controlled for gestational age, race/ethnicity, and mode of delivery, as all of these variables were found to differ between exposure groups on univariate analysis. The trajectories of IL-10 and TNF- α differed between chorioamnionitis-exposed and unexposed neonates, while there were no differences in the trajectories of IL-1 β , IL-6, IL-8, CCL2 or CCL3 between groups (**Figure 4.5**).

Cytokine and Chemokine Levels at the Time of Bacterial Sepsis or Necrotizing

Enterocolitis Diagnosis. For prior analysis, blood draws that correlated with clinically indicated adverse events or treatment courses were excluded. Here, we used those data points to compare cytokine and chemokine levels between healthy matched control preterm infants and infants with culture-positive bacterial sepsis (**Figure 4.6A**) or Bell's stage 2 or greater necrotizing enterocolitis (**Figure 4.6B**) at the time of diagnosis. Preterm neonates with bacterial sepsis or necrotizing enterocolitis had increased serum IL-6 at the time of diagnosis compared to healthy controls.

Longitudinal Multi-biomarker Profiling Towards Clinical Monitoring. Cytokine and chemokine levels were plotted for each subject that had two or more time points. All collected data points were included in longitudinal profiling plots for each individual subject and timepoints associated with clinically indicated adverse events were identified for observational investigation towards future monitoring or rapid diagnostic applications. In subjects with necrotizing enterocolitis diagnosis and treatment (**Figure 4.7 A-E**), there were consistent spikes observed in CCL2 during treatment. In those with both necrotizing enterocolitis and bacteremia ongoing treatment (**Figure 4.7 E-G**), there were consistent spikes observed in CCL2 and IL-8. Interestingly, the two chorioamnionitis exposed subjects with necrotizing enterocolitis (**Figure 4.7 A, E**) have very similar increases in CCL2, CCL3, TNF- α and IL-1 β across both subjects and within the same subject. In subjects with clinically indicated early onset sepsis diagnosis and treatment, there was little observed similarity in profiles (**Figure 4.8 A-D**). In those with late onset sepsis, there was an observed consistent increase in both CCL2 and IL-6, regardless of exposure group (**Figure 4.8 E-G**). There is, additionally, no observed pattern in gram-negative (**Figure 4.8 A, B, C, E**) or gram-positive (**Figure 4.8 C, D, F, G**) associated infections. The final

adverse event most common in this cohort was urinary tract infections. Among these subjects, there are consistently multiple biomarkers, CCL2, IL-1 β , TNF- α , IL-6 and CCL3, observed as peaking during the diagnosis and treatment time frame, regardless of exposure group or specific bacteria causing the infection (**Figure 4.9**). A similarity among these longitudinal plots with adverse events highlighted is that a large portion of subjects show an observable decrease in the cytokine concentrations at the end of the noted treatment period, or at the timepoint following treatment.

4.6 Discussion

Neonatal infections are a cause of significant morbidity and mortality in preterm neonates during their hospitalization in the NICU.² It is known that preterm neonates exposed to chorioamnionitis have an increased risk of developing early-onset sepsis (blood stream infection that occurs within the first 72 hours of life).^{8,11,21} It is unclear if this infection risk is due to a common pathogen causing both conditions or alterations in the neonatal immune response following chorioamnionitis exposure, or both. Multiple studies have shown that exposure to chorioamnionitis impacts the neonatal immune system by altering gene transcription and innate immune responses.⁷⁻⁹ These altered immune responses include dampened pro-inflammatory cytokine expression when a second pathogen is encountered.^{8,9} Appropriate pro-inflammatory cytokine expression is necessary for the clearance of microorganisms, so these chorioamnionitis-induced changes to neonatal immune responses are thought to be at least partially responsible for this increased risk of infection. However, it is unclear how long chorioamnionitis-induced dampened cytokine expression persists, as studies are conflicting about whether chorioamnionitis exposure protects against or increases the risk for developing late onset sepsis (blood stream infection that presents after 72 hours of life).^{11,22-24}

To assess the persistence of chorioamnionitis-induced dampened pro-inflammatory cytokine expression in preterm neonates, we performed longitudinal cytokine and chemokine profiling in very preterm neonates from birth to NICU discharge. We chose a panel of cytokines and chemokines known to be significant contributors to neonatal immune responses. Neonates primarily rely upon the innate immune system early in life to protect against infections due to limited antigen exposure in utero and major deficiencies in adaptive immune responses.^{25,26} Innate immune cells, including monocytes, macrophages and neutrophils, require signaling from cellular messengers such as cytokines and chemokines in order to mount a coordinated response to an infectious pathogen.²⁷ CCL2 and CCL3 are chemokines that recruits monocytes, macrophages and neutrophils to local sites of infection and are necessary for prominent signaling pathways in the neonatal immune system.²⁸ IL-8 shows similar chemotactic affinity for neutrophils and stimulates bacterial phagocytosis.²⁹ IL-6, IL-1 β and TNF- α are pro-inflammatory cytokines important to the acute phase response necessary to assist in the clearance of microorganisms.^{30,31} IL-10 is an immunoregulatory cytokine important for immune homeostasis that also suppresses autoinflammation.³² We believe this panel of cytokines and chemokines provides a broad overview of neonatal innate immune reactivity.

In this study, we used a novel method of cytokine and chemokine evaluation, using each preterm neonate as its own matched control to compare levels at different chronologic ages. While this method has previously been used to demonstrate a significant decline in IL-1 β , IL-6 and TNF- α from DOL 1 to DOL 40 in term neonates, we are the first to use it to evaluate changes in cytokine and chemokine levels over time in preterm neonates.^{33,34} We found that in our population of preterm neonates, levels of IL-6 and CCL2 decreased between the first and second weeks of life in both chorioamnionitis-exposed and unexposed groups while IL-8 only

decreased in the unexposed group. Non-chorioamnionitis exposed preterm neonates had a consistent decrease in levels of IL-1 β , IL-6, IL-8, IL-10, TNF- α and CCL2 over the first month of life, reaching what appeared to be baseline levels around three weeks after birth. This is in contrast to chorioamnionitis-exposed preterm neonates, whose cytokine and chemokine levels demonstrated differences over the first month of life without a consistent pattern based on chronologic age. We additionally found that the trajectory of IL-10 and TNF- α serum levels differed between chorioamnionitis-exposed and unexposed preterm neonates. These findings are important as most of these cytokines and chemokines have been proposed as biomarkers to diagnose or predict prematurity-based complications, including sepsis, necrotizing enterocolitis, and bronchopulmonary dysplasia.^{14,15,35-38} Our findings suggest that chronologic age and chorioamnionitis-exposure should be taken into consideration when using cytokines and chemokines as biomarkers in premature neonates.

The altered cytokine and chemokine responses seen in the chorioamnionitis-exposed preterm neonates is in line with previous reports demonstrating altered cytokine responses from chorioamnionitis-exposed umbilical cord blood monocytes following stimulation with either LPS or *Staphylococcus epidermidis*.^{8,9} The cytokines and chemokines measured in this study are primarily expressed by innate immune cells, which are not typically self-renewing immune populations. How then, can chorioamnionitis-exposure around the time of birth influence cytokine and chemokine expression up to 12 weeks of life when the originally exposed innate immune cells are no longer around? The answer likely involves the concept of trained immunity, which describes long-term functional reprogramming of innate immune cells through epigenetics. We previously showed that chorioamnionitis exposure alters the histone tail modification landscape and subsequent gene expression profile of neonatal monocytes, resulting

in a trained immunity phenotype.⁹ This phenotype resulted in dampened pro-inflammatory cytokine expression when chorioamnionitis-exposed monocytes encountered a secondary pathogenic stimulus.⁹ Based on these findings, it is possible that chorioamnionitis-induced histone modification changes in innate immune cells results in long-lasting “epigenetic memory” and altered immune responses well beyond the immediate neonatal period. It is also possible that chorioamnionitis exposure results in a trained immunity phenotype in bone marrow progenitor cells, which would repopulate the circulating innate immune cells with this altered “epigenetic memory”. Alterations in innate immune “epigenetic memory” may provide insight into immune-related complications experienced by chorioamnionitis-exposed neonates, including late onset sepsis, persistent wheezing and asthma.^{24,39}

Our 7-plex cytokine microring resonator assay was robustly validated for all targets simultaneously to ensure reproducible results across all samples analyzed. Each assay was 38 minutes to result, creating a quick method for analyzing important clinical samples. Using this multiplexed immunoassay, we were able to collect large amounts of immunological data quickly and with little starting sample volume. Early sepsis detection and prompt initiation of antibiotic therapy significantly improves outcomes in neonatal sepsis.⁴⁰ In practice, early sepsis detection is difficult as signs of infection in the neonatal population are often non-specific. The gold standard test to diagnose a blood stream infection is a blood culture that demonstrates growth of a pathogenic organism; however this often takes at least 24 hours to result.⁴¹ Several biomarkers are commonly used to support or refute the presence of infection, including C-reactive protein, procalcitonin and the presence of many immature forms of neutrophils.⁴² These biomarkers are non-specific and are often more useful to rule infection out rather than diagnose it. Several cytokines have been proposed as useful biomarkers to diagnose neonatal sepsis or necrotizing

enterocolitis, including IL-1 β , IL-6, IL-8, IL-10 and TNF- α .^{14,15,17,35,36} Our results support this, as we demonstrated that preterm neonates had elevated serum IL-6 at the time of bacterial sepsis or necrotizing enterocolitis diagnosis when compared to healthy preterm neonates. While cytokines hold great promise as biomarkers to diagnose neonatal sepsis, they often take days to result, so are unable to be used to promptly diagnose infection. Our microring resonator assay has the potential to provide cytokine values quickly for the most vulnerable patients, which could allow for the use of cytokine values in real time to accurately predict the risk of sepsis and impact bedside patient care.

Furthermore, with the large amounts of immunological data emanating from the same subjects over the course of their stay in the NICU, we demonstrated a rapid method for immunoprofiling neonates. Monitoring patients in near real time can decrease time to intervention and potentially trigger treatments prior to increased severity of disease, which has the potential to decrease time in the NICU and cost of treatments. The monitoring method can be further used in therapeutic approaches if increases or decreases of certain biomarkers can be correlated with treatment efficacy, giving clinicians a rapid method to identify if the treatment is working, if the treatment can be ended, or if the treatment needs to be continued longer. We retrospectively tracked increases in cytokine and chemokine concentrations before and during the diagnosis and treatment time points across three noted adverse events that occurred in multiple subjects over the course of this study: necrotizing enterocolitis, sepsis, and urinary tract infections. The concentrations then decreased in most cases at the final time point of treatment or after treatment has ended. These observed profiles show potential for this method to be used as a monitoring tool for evaluating treatment efficacy.

The relatively low occurrence of these adverse events inhibits our ability to make conclusions about statistically significant biomarkers towards infection diagnosis stratified by exposure groups. Instead, as discussed above, we looked at the infections as a whole to compare age, sex, and gestational age matched healthy vs adverse event affected subjects. We can also use the profiles to discuss trends that should be studied further, in larger cohorts of preterm neonates, for use in disease diagnosis or treatment efficacy. In the three disease states explored here (necrotizing enterocolitis, sepsis, and urinary tract infections), there was an observed increase in CCL2 before and during clinically designated time points of infection. CCL2 is a pro inflammatory cytokine that recruits monocytes, macrophages, and neutrophils to local sites of infection and play an important role in signaling pathways in the neonatal immune system.²⁸ Our results demonstrate the preterm neonate populations immune systems reliance on CCL2 for infection response, regardless of chorioamnionitis exposure status, gestational age, or infection.

Subjects with necrotizing enterocolitis diagnosis and treatment had observed increases in CCL2, CCL3, TNF- α , and IL-1 β during infection time points, with higher responses in those with the chorioamnionitis exposure (n=2 subjects with 3 events). When necrotizing enterocolitis treatment coincided with bacteremia treatments (n=3) there was an increase in only CCL2 and IL-6 concentrations. Our results indicate there was a difference in observed cytokine and chemokine response in subjects undergoing necrotizing enterocolitis alone versus those with combined necrotizing enterocolitis and bacteremia treatments.

Subjects with clinically indicated early onset sepsis or late onset sepsis did not have observable patterns in cytokine or chemokine responses, outside of increased CCL2. There was no observable pattern in regard to chorioamnionitis exposure or gram stain of the bacterial strain identified as cause of infection. Some subjects (n=3) had an increase of IL-6, while others (n=3)

had an increase of CCL3 and TNF- α . Our results demonstrate the difficult nature of sepsis prediction, as various inflammatory markers were present with no observable patterns within our data set.

Finally, in subjects with urinary tract infections, we observed a consistent trend of multi-biomarkers increasing during the treatment time points, including CCL2, IL-1 β , TNF- α , IL-6 and CCL3. The cytokines and chemokines that increased were similar across the subjects even though there were various bacterial causes of the urinary tract infection and none of the subjects in this study had the same strains of bacteria reported as a cause. Compared to the other adverse events, this infection resulted in the greatest number of observed targets increasing during infection and treatment time points. Our results show the importance of studying multi-biomarker panels for monitoring specific infections or treatments. Overall, our longitudinal profiling analysis allowed us to observe the importance of CCL2 in a neonatal immune system, that cytokines tend to decrease after clinically indicated adverse events and treatment time points, and that these infections induce a multi-cytokine response during infection and treatment. Further work to move from small sample observations towards statistical significance will require a larger cohort of subjects with targeted approaches to collect samples from subjects with specific adverse effects, rather than from a general population of preterm neonates.

This study has several limitations. All samples were collected from clinically indicated laboratory tests, so the timing of sample collection varied between patients and was not standardized. There were differences between the exposure groups, and chorioamnionitis-exposed subjects were more likely to be born earlier, African American and by vaginal delivery than unexposed subjects. It is unclear if these differences impacted cytokine and chemokine expression. Degree of prematurity and mode of delivery have been shown to impact immune

responses in prior studies, so these factors were accounted for in our statistical evaluation.^{43–45} Samples were excluded from subjects who had a suspected or confirmed infection and were receiving antibiotics at the time of sample collection. We excluded these samples as several previous studies have demonstrated elevated levels of IL-6, IL-10, IL-8 and/or TNF- α around the time of sepsis or necrotizing enterocolitis diagnosis, and we were concerned that these and similar conditions could falsely elevate baseline cytokine measurements and confound the study results.^{14–17} However, this should be taken into account when interpreting and attempting to generalize our results. We did include samples from these patients later during their NICU course once the infection was treated, however, as infectious/inflammatory conditions are common in preterm neonates and this population is likely to make up a large proportion of infants upon which normative values are based. Additionally, it is unclear if suspected or confirmed infections influence future cytokine and chemokine expression, but this would be an interesting and informative comparison to make in future studies. Furthermore, corrections were not made for clinical differences such as mode of respiratory support, presence of BPD, steroid administration, or PDA treatment. The numbers in this study are not large enough to directly address these potential confounding factors, but future studies containing more subjects would be of benefit.

4.7 Conclusion

This study demonstrated that healthy preterm neonates had a consistent decrease in levels of IL-1 β , IL-6, IL-8, IL-10, TNF- α and CCL2 over the first month of life, reaching what appeared to be baseline levels around three weeks after birth. This same pattern of changes was not present in chorioamnionitis-exposed preterm neonates, which may reflect immune system dysregulation beyond the immediate neonatal period. We demonstrated use for a multiplexed

biomarker panel to study preterm neonates' immune systems, with future applications in clinical monitoring and diagnostics.

4.8 Figures

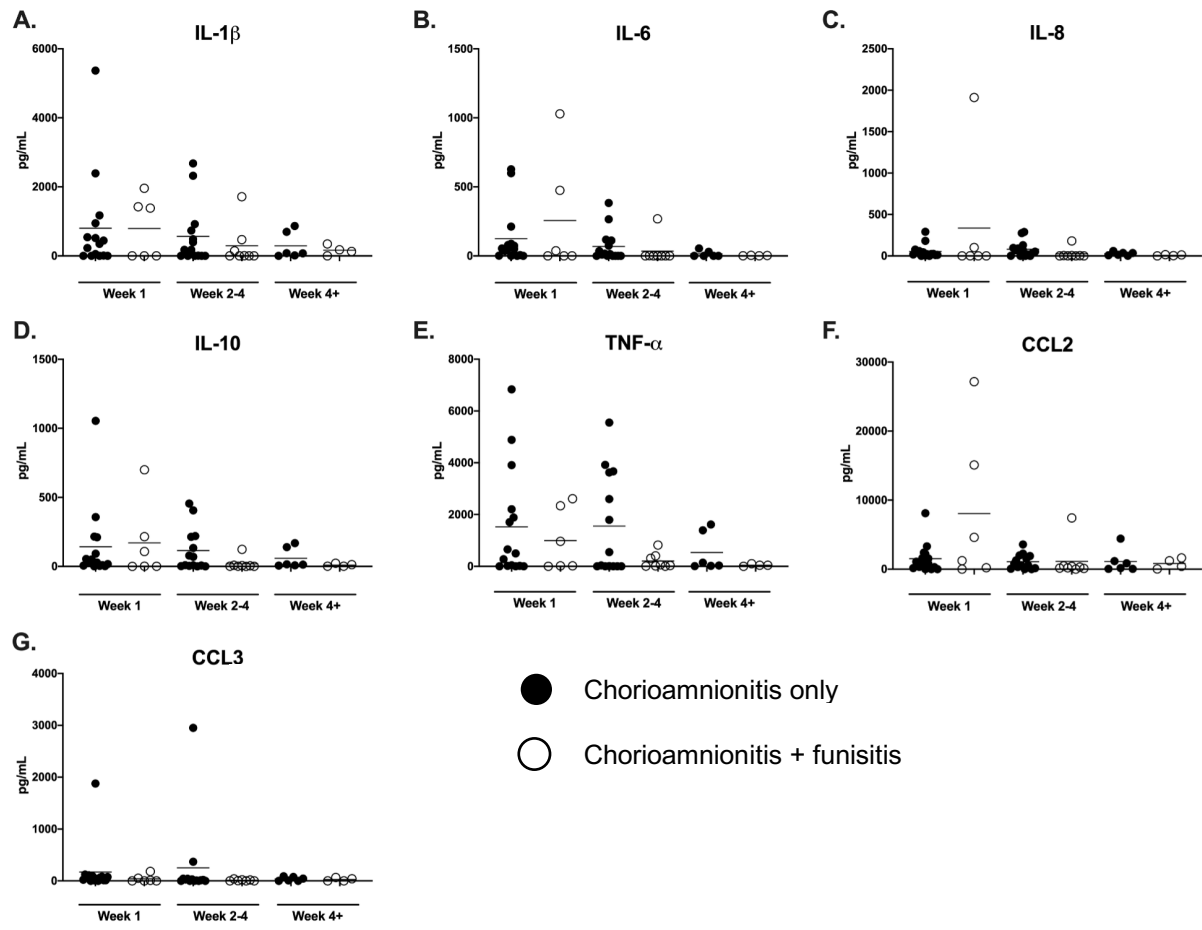


Figure 4.1 Comparison of cytokine and chemokine levels by chronologic age in chorioamnionitis only (black circles) and chorioamnionitis plus funisitis (white circles) exposed preterm neonates. Serum protein levels were measured during the first week of life (week 1), weeks 2-4 of life (week 2-4) and beyond 4 weeks of life (week 4+). If more than one serum level was obtained during each timeframe, then the average level was used for comparison. Serum protein levels were analyzed for A) IL-1 β , B) IL-6, C) IL-8, D) IL-10, E) TNF- α , F) CCL2, and G) CCL3. Chorioamnionitis only n=17, chorioamnionitis with funisitis n=10. Bars represent group mean. Differences between groups were evaluated using the Kruskal-Wallis test with correction for multiple comparisons. No statistically significant values were noted ($p < 0.05$).

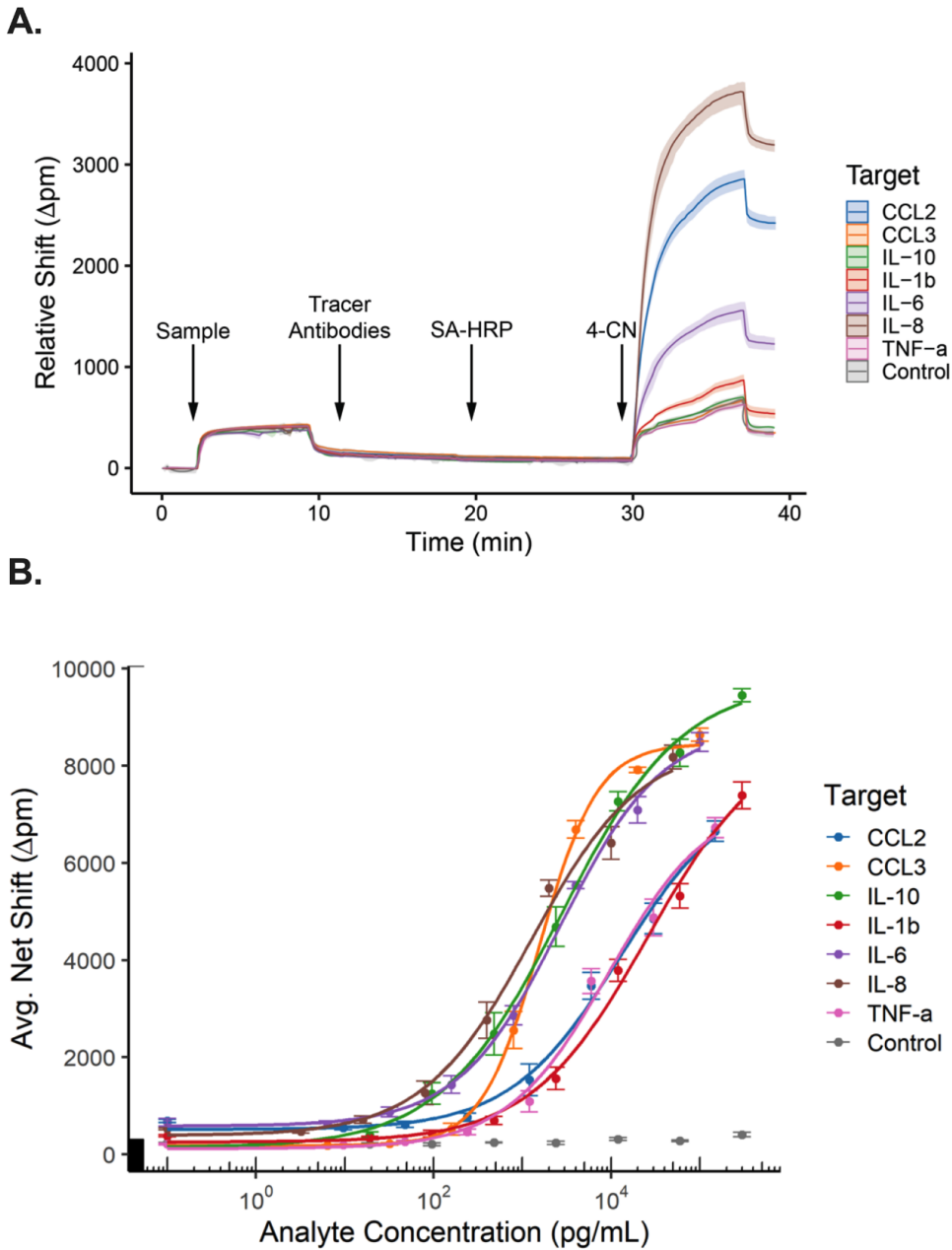


Figure 4.2 Overview of multiplexed immunoassay method and calibration. A) Example microring trace of a multiplexed immunoassay for neonatal residual serum. All liquid flow is automated and sequential with running buffer rinses between each reagent. Net shifts are calculated by subtracting the relative shift before the amplification step ($t=29$) from that after the final rinse step ($t=38$). The shading around the lines represent variation between the $n=8$ microrings for each target. B) Multiplexed serum calibrations in a 50% serum matrix. Error bars represent standard deviation from $n=4$ calibrations with $n=8$ ring replicates per target.

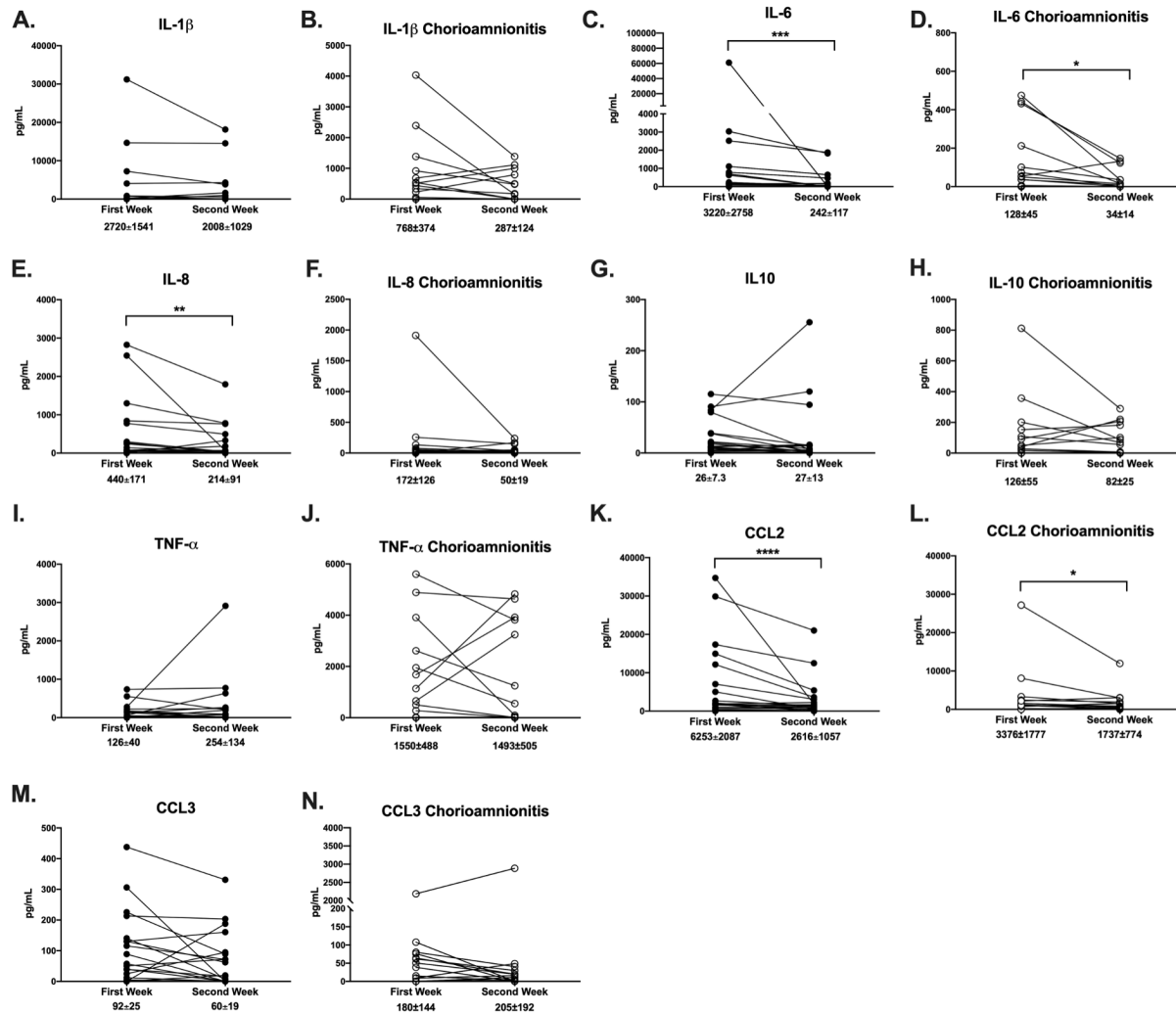


Figure 4.3 Comparison of cytokines and chemokines obtained in the first and second weeks of life in preterm neonates. Serum protein levels were measured and compared between the same subject during the first and second weeks of life. If more than one serum level was obtained during each week, then the average level was used for comparison. Serum protein levels are demonstrated for IL-1 β in unexposed (A) and chorioamnionitis-exposed (B) neonates, IL-6 in unexposed (C) and chorioamnionitis-exposed (D) neonates, IL-8 in unexposed (E) and chorioamnionitis-exposed (F) neonates, IL-10 in unexposed (G) and chorioamnionitis-exposed (H) neonates, TNF- α in unexposed (I) and chorioamnionitis-exposed (J) neonates, CCL2 in unexposed (K) and chorioamnionitis-exposed (L) neonates and CCL3 in unexposed (M) and chorioamnionitis-exposed (N) neonates. First week unexposed n=22, second week unexposed n=22, first week chorioamnionitis-exposed n=15, second week chorioamnionitis-exposed n=15. Wilcoxon test used to determine statistical significance. *p<0.05, **p<0.01, ***p<0.0001, ****p<0.0001. Mean \pm standard error of the mean for each protein level shown below each x-axis label.

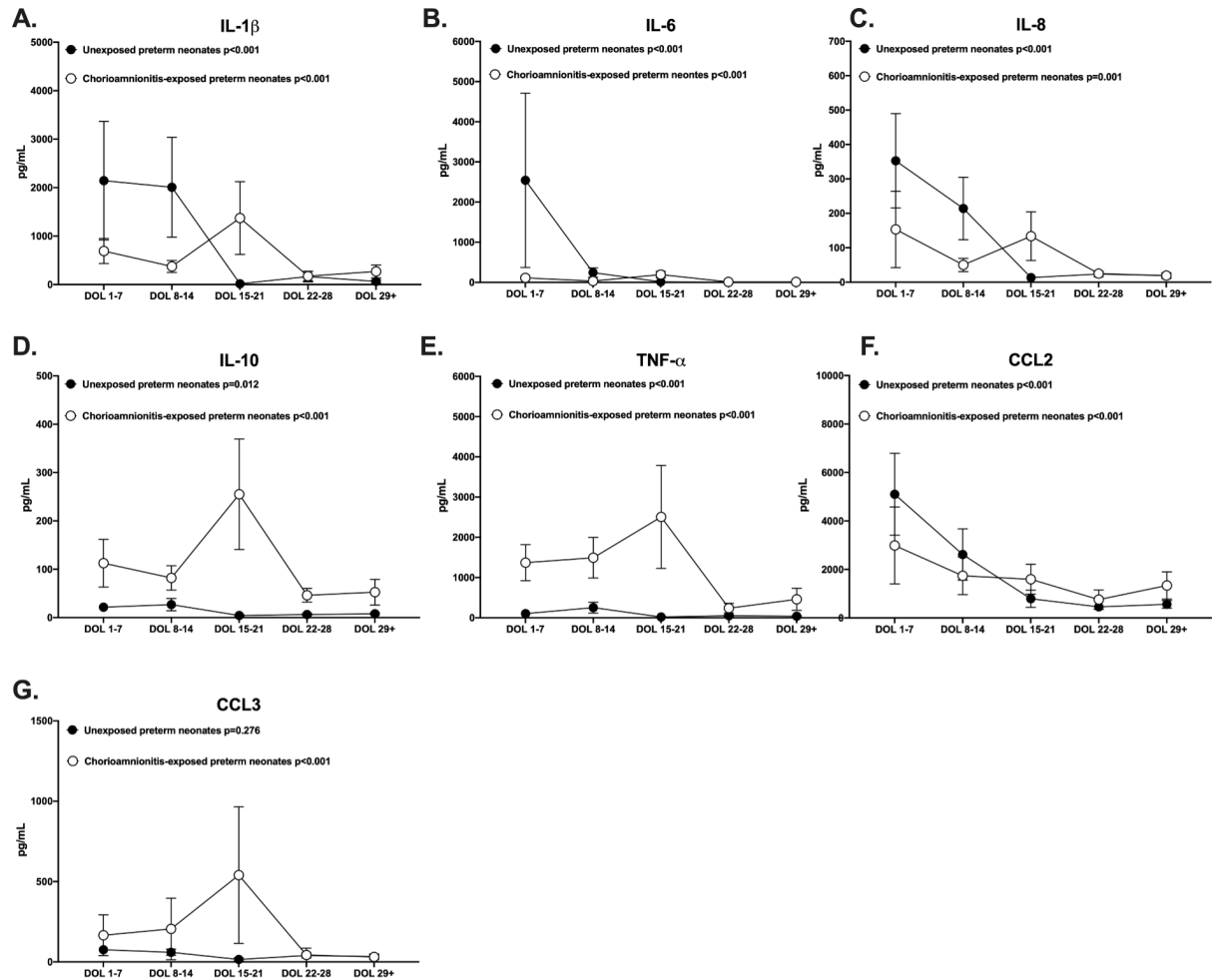


Figure 4.4 Longitudinal cytokine and chemokine trends over time in chorioamnionitis-exposed and unexposed preterm neonates. Serum protein levels were measured and compared between the same subject during day of life (DOL) 1-7, 8-14, 15-21, 22-28 and 29 and beyond. If more than one serum level was obtained during each timeframe, then the average level was used for comparison. Serum protein levels are demonstrated in chorioamnionitis-exposed (white circles) and unexposed (black circles) preterm neonates for A) IL-1 β , B) IL-6, C) IL-8, D) IL-10, E) TNF- α , F) CCL2 and G) CCL3. Unexposed n=28, chorioamnionitis-exposed n=17. General Estimating Equations were used to determine statistical significance. Circles represent mean levels and error bars represent standard error of the mean. p-values for differences in trends over time are shown.

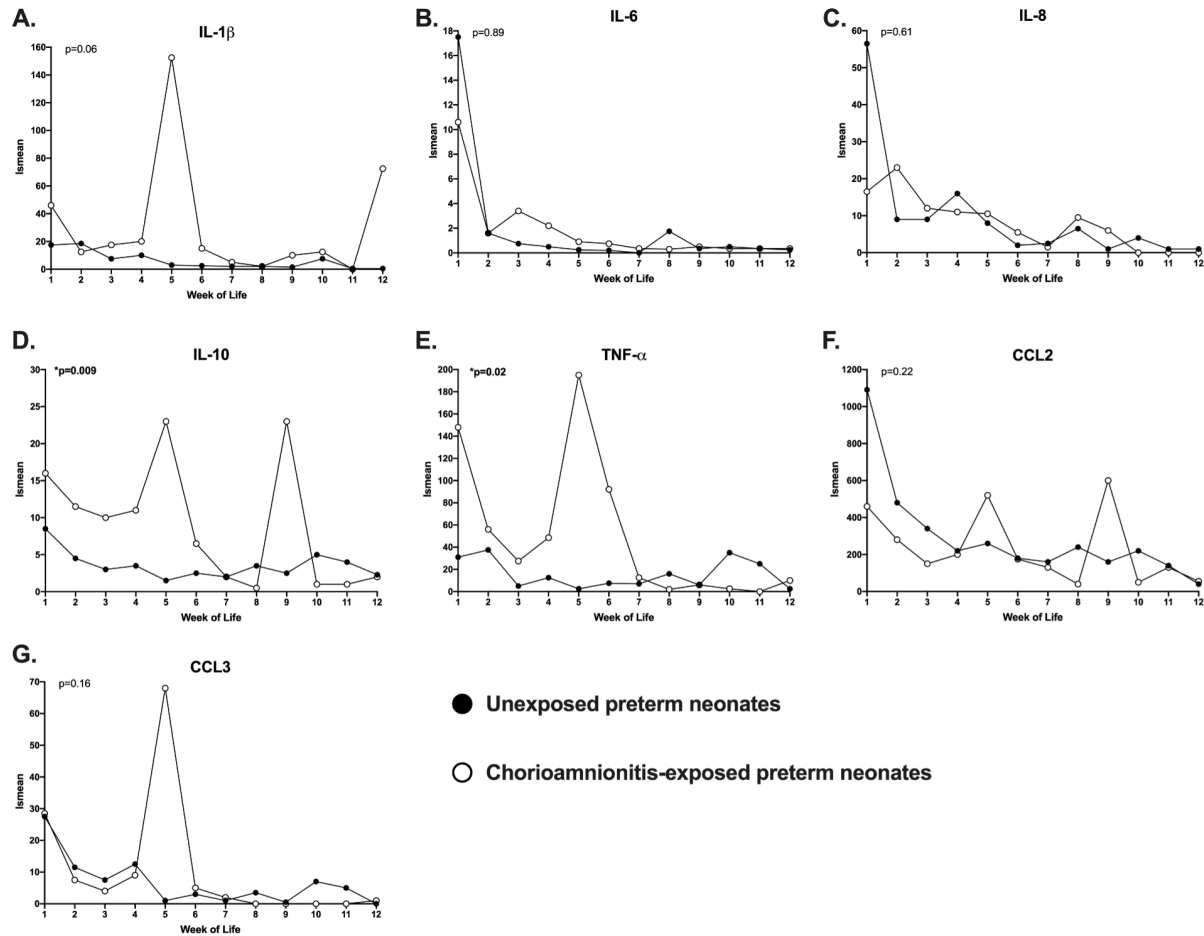


Figure 4.5 Longitudinal cytokine and chemokine trajectories over time in chorioamnionitis-exposed and unexposed preterm neonates. If more than one serum level was obtained for a patient during each timeframe, then the average level was used for comparison. The lsmean of serum protein levels are demonstrated in chorioamnionitis-exposed (white circles) and unexposed (black circles) preterm neonates for A) IL-1 β , B) IL-6, C) IL-8, D) IL-10, E) TNF- α , F) CCL2 and G) CCL3. Unexposed n=34, chorioamnionitis-exposed n=27. SAS Proc Mixed was used to perform repeated measures of regression to look at the effect of chorioamnionitis status on the trajectory of cytokines over time, while controlling for gestational age, ethnicity, and mode of delivery.

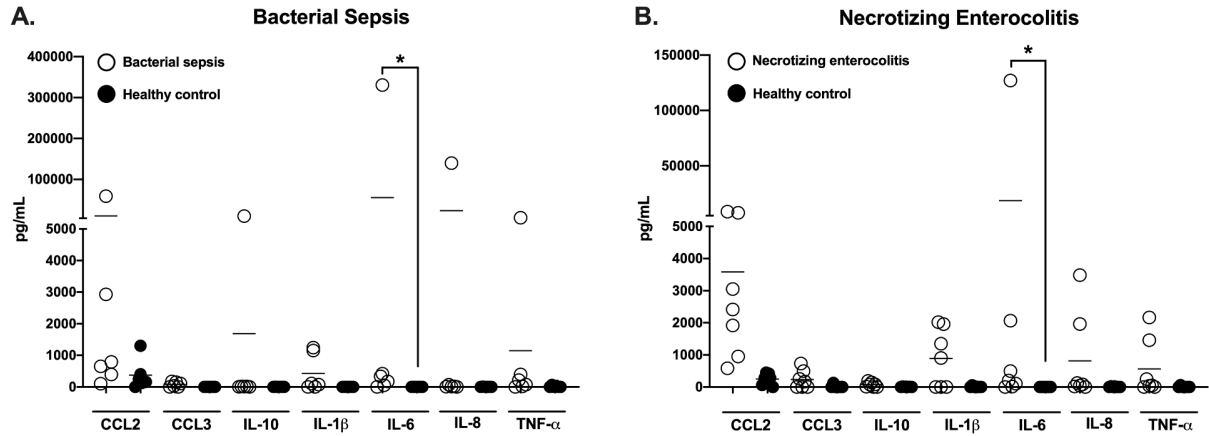


Figure 4.6 Comparison of serum cytokine and chemokine levels at the time of diagnosis of bacterial sepsis or necrotizing enterocolitis in preterm neonates. A) Subjects with blood culture-positive bacterial sepsis (white circles, n=6) were matched with healthy control subjects (black circles, n=6) based on sex, gestational age (± 1 week) and chorioamnionitis-exposure. Cytokine and chemokine levels were compared at the time of diagnosis in the septic infants and at a similar chronologic age (± 5 days) in the controls. B) Subjects with Bell's stage 2 or greater necrotizing enterocolitis (white circles, n=7) were matched with healthy control subjects (black circles, n=7) based on sex, gestational age (± 1 week) and chorioamnionitis-exposure. Cytokine and chemokine levels were compared at the time of diagnosis in the infants with necrotizing enterocolitis and at a similar chronologic age (± 5 days) in the controls. Bars demonstrate the mean. The Friedman test with correction for multiple comparisons was used to evaluate for differences between groups. * $p < 0.05$.

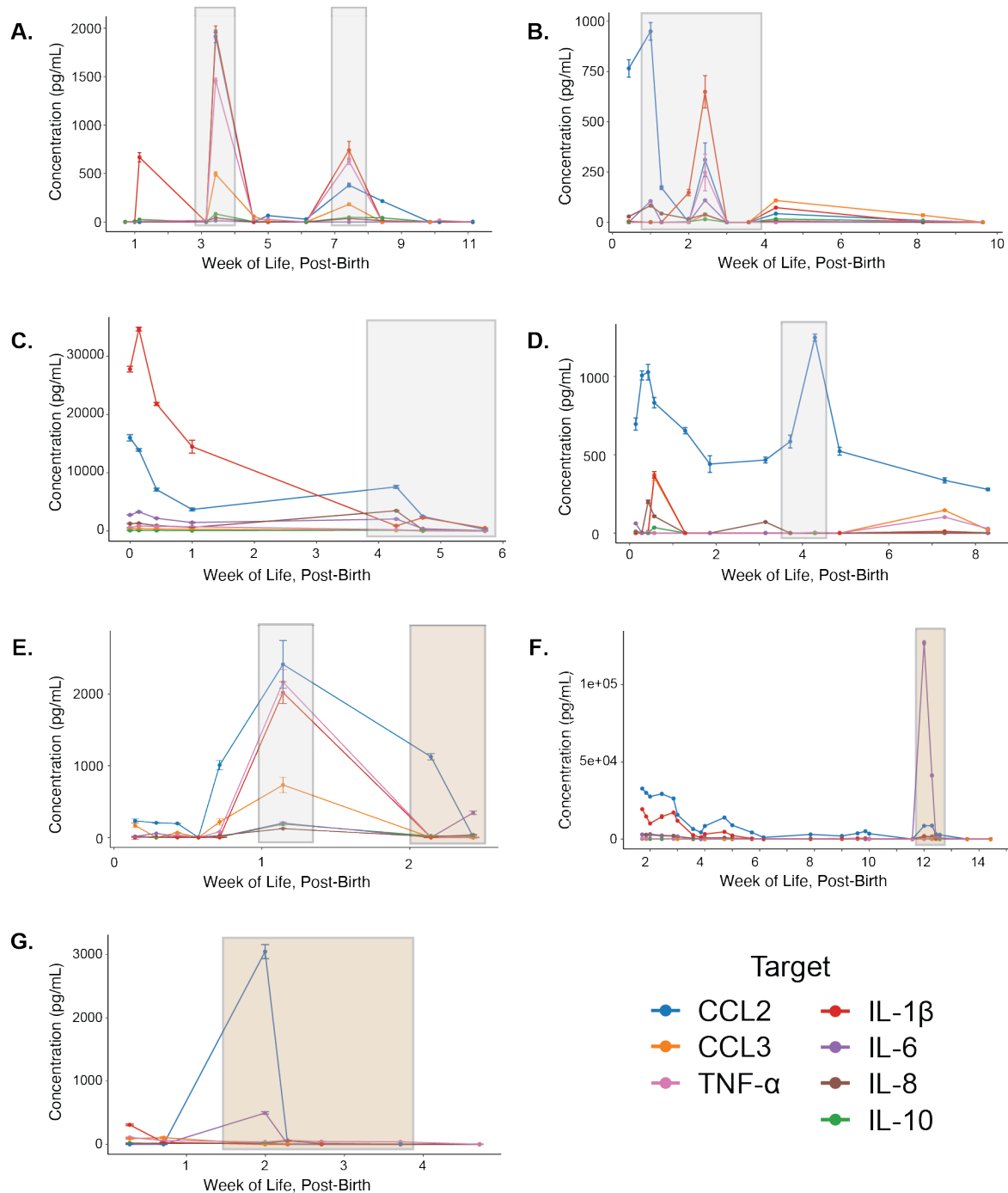


Figure 4.7 Longitudinal profiles of cytokine and chemokine levels for subjects with necrotizing enterocolitis diagnosis and treatment. The grey shaded boxes (A-E) indicate the timepoints designated as necrotizing enterocolitis treatment. The orange shaded boxes (E-G) indicate timepoints designated as both necrotizing enterocolitis treatment and bacteremia treatment. Each panel A-G represents a separate subject, with A and E having exposure to chorioamnionitis and B-D and F-G having no exposure. Error bars represent variation between the n=8 microrings for each target.

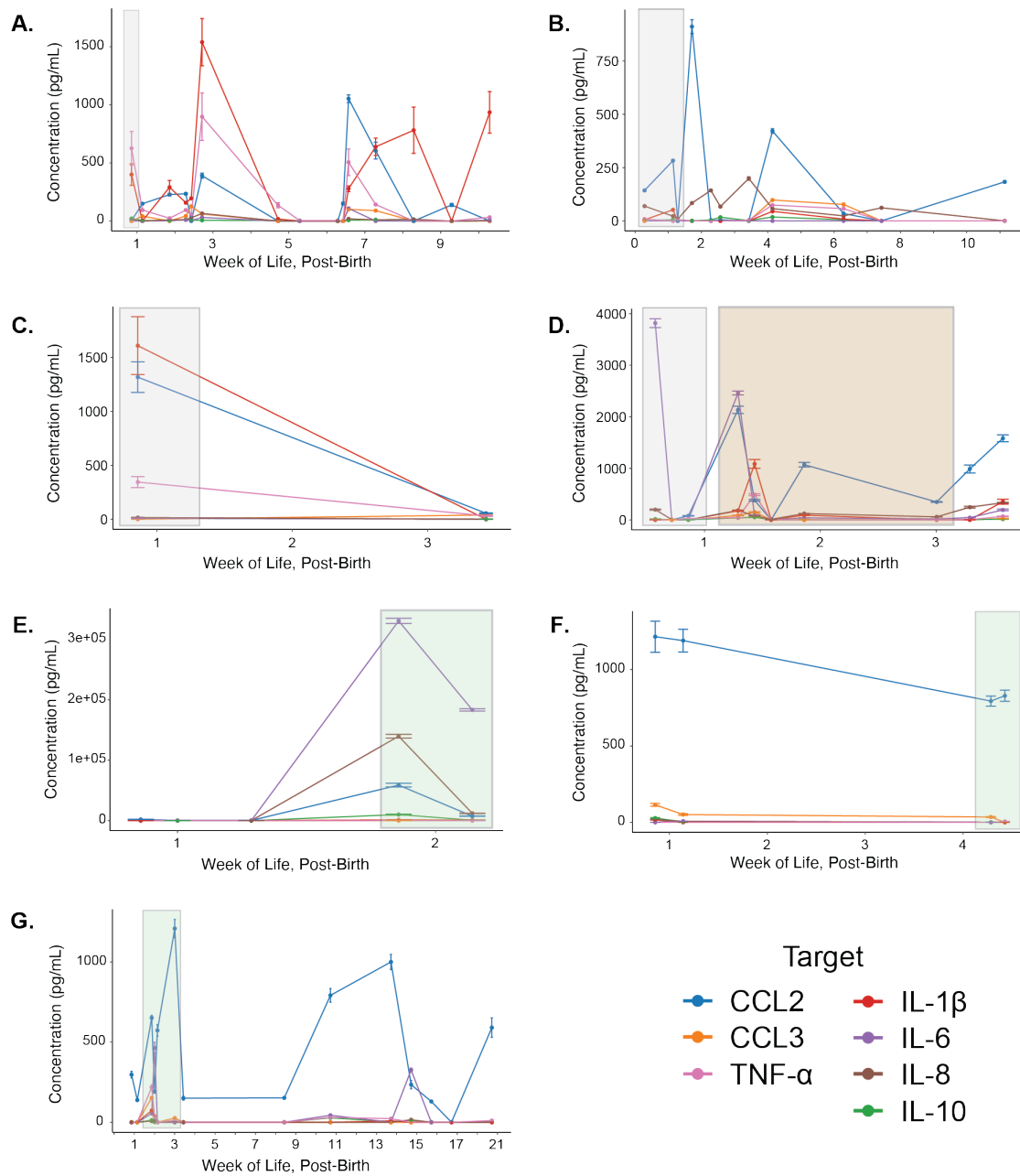


Figure 4.8 Longitudinal profiles of cytokine and chemokine levels for subjects with sepsis diagnosis and treatment. The grey shaded boxes (A-D) indicate the timepoints designated as early onset sepsis treatment. The orange shaded box (D) indicates a timepoint designated as both early onset sepsis treatment and spontaneous intestinal perforation. The green shaded boxes (E-F) indicate timepoints designated as late onset sepsis treatment. Each panel A-G represents a separate subject, with A-E all having exposure to chorioamnionitis and F-G having no exposure. Panels A, B and E represent infections with gram negative bacteria (*E-coli*, *Klebsiella Pneumoniae/Morganella Morganii*, and *Enterobacter*, respectively), D, F, and G represent infections with gram positive bacteria (*Enterococcus Faecium*, *Streptococcus Mitis*, and *Staphylococcus Capitis*, respectively) and C represents a dual infection with both gram negative (*E-coli*) and gram positive (*Enterococcus Faecium*) bacteria. The error bars represent variation between the n=8 microrings for each target.

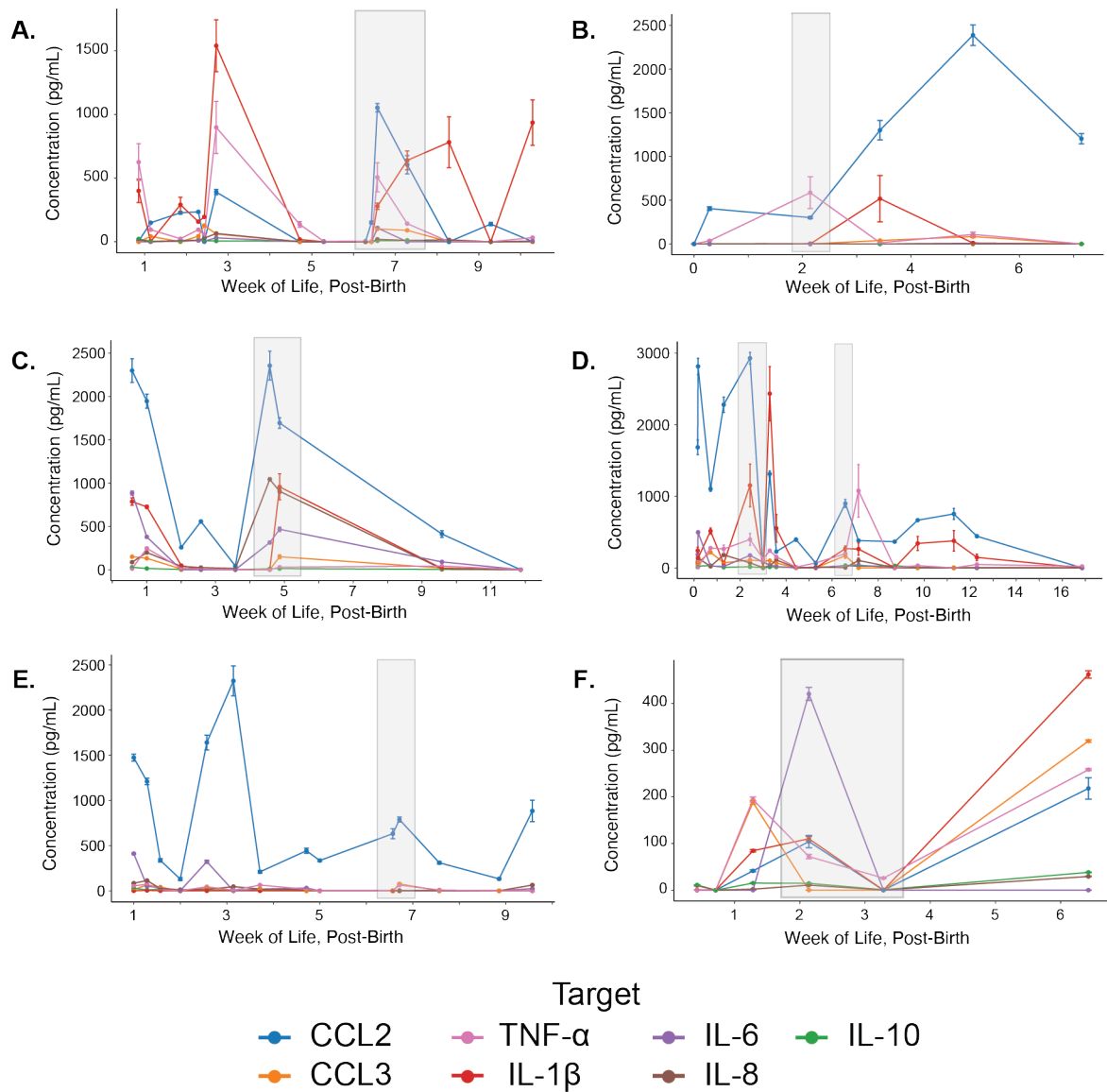


Figure 4.9 Longitudinal profiles of cytokine and chemokine levels for subjects with urinary tract infection diagnosis and treatment. The grey shaded boxes indicate the timepoints designated as urinary tract infection treatment. Each panel A-F represents a separate subject, with A-B having exposure to chorioamnionitis and C-F having no exposure. The error bars represent variation between the n=8 microrings for each target.

4.9 Tables

Table 4.1 Functions of the selected cytokine panel markers.

Cytokine/ Chemokine	Produced By	Pro- or Anti- Inflammatory	Function
IL-1β	Macrophages, fibroblasts, epithelial cells, endothelial cells	Pro	Involved in cell proliferation and differentiation; important to the acute phase response to assist in the clearance of microorganisms ³⁰
IL-6	Macrophages, T cells, B cells, fibroblasts, epithelial cells, endothelial cells	Both	Secreted by macrophages; important to the acute phase response to assist in the clearance of microorganisms ^{30,31}
IL-10	T regulatory cells, CD4 Th2 cells	Anti	A CD4+ regulatory cytokine; important for immune homeostasis, suppresses autoinflammation ³²
IL-8	Macrophages, endothelial cells, epithelial cells and airways smooth muscle cells	Pro	Induces chemotaxis in granulocytes, causing them to migrate toward the site of infection; stimulates bacterial phagocytosis ²⁹
TNF-α	Macrophages, Th1 cells, Th2 cells	Both	Involved in signaling via TNFR1 and TNFR2; has both pro- and anti-inflammatory effects; important to the acute phase response to assist in the clearance of microorganisms ³⁰
CCL2	Monocytes, dendritic cells, endothelial cells	Pro	Recruits monocytes macrophages and neutrophils to local sites of infection and are necessary for prominent signaling pathways in the neonatal immune system ²⁸
CCL3	Macrophages, osteoblasts	Pro	Recruits monocytes macrophages and neutrophils to local sites of infection and are necessary for prominent signaling pathways in the neonatal immune system ²⁸

Table 4.2 Reagents used in the multiplexed assay.

Target	Role	Source	Catalog Number	Saturating antigen (ng/mL)/Tracer Concentrations (µg/mL)
CCL2	Capture Ab	Thermo Fisher	14-7099	150/2
	Antigen	Thermo Fisher	14-8398	
	Bt-Tracer Ab	Thermo Fisher	13-7096	
CCL3	Capture Ab	R&D Systems	MAB670-100	100/1
	Antigen	R&D Systems	270-LD-010	
	Bt-Tracer Ab	R&D Systems	MAB270-100	
IL-1β	Capture Ab	Thermo Fisher	14-7018-85	300/2
	Antigen	Thermo Fisher	RIL-1BI	
	Bt-Tracer Ab	Thermo Fisher	13-7016-85	
IL-6	Capture Ab	Thermo Fisher	16-7069	100/2
	Antigen	Thermo Fisher	14-8069	
	Bt-Tracer Ab	Thermo Fisher	13-7068	
IL-8	Capture Ab	BD Biosciences	554716	50/2
	Antigen	BD Biosciences	554609	
	Bt-Tracer Ab	BD Biosciences	554718	
IL-10	Capture Ab	Thermo Fisher	16-7108	300/2
	Antigen	Thermo Fisher	14-8109-80	
	Bt-Tracer Ab	Thermo Fisher	13-7109	
TNF-α	Capture Ab	Biologend	502802	150/2
	Antigen	Biologend	570102	
	Bt-Tracer Ab	Biologend	502904	

All capture antibodies are spotted at 0.25 mg/mL. The saturating antigen concentration is the highest concentration of standard used to construct the calibration curve, with serial dilutions emanating from this highest point. Ab= antibody, Bt = biotinylated.

Table 4.3 Limits of detection (LODs) of the 7-plex panel calculated as the concentration corresponding to the signal from the blank sample plus three times the standard deviation of the blank, using data from the two respective matrix calibrations.

Target	50% Serum LODs	10% Serum LODs
CCL2	211.4 pg/mL	223.1 pg/mL
CCL3	64.5 pg/mL	41.8 pg/mL
IL-1 β	124.0 pg/mL	185.4 pg/mL
IL-6	83.2 pg/mL	37.1 pg/mL
IL-8	10.4 pg/mL	8.5 pg/mL
IL-10	4.0 pg/mL	6.8 pg/mL
TNF- α	86.2 pg/mL	73.7 pg/mL

Table 4.4 Subject characteristics.

	Chorioamnionitis-exposed Preterm Neonates (n=27)	Unexposed Preterm Neonates (n=34)	p-value
Birth gestational age in weeks (mean ± SD)	27.03 ± 2.7	28.69 ± 2.99	0.028*
Birth weight in grams (mean ± SD)	1051 ± 363	1181 ± 544	0.44
Male sex	10 (37%)	20 (59%)	0.09
Ethnicity			
- Caucasian	16 (59%)	27 (79%)	0.09
- African American	7 (26%)	1 (3%)	0.008*
- Other	4 (15%)	6 (18%)	0.77
C-section	19 (70%)	32 (94%)	0.01*
IUGR/SGA	2 (7%)	6 (18%)	0.24
Pregnancy-induced hypertension	1 (4%)	6 (26%)	0.09
Gestational diabetes	2 (7%)	6 (26%)	0.24
Prolonged rupture of membranes (>18 hours)	5 (19%)	3 (9%)	0.27
Antenatal steroids at least 12 hours prior to delivery	23 (85%)	23 (68%)	0.11
Multiple gestation	16 (59%)	20 (59%)	0.97
Early onset sepsis (blood culture positive within 72 hours of birth)	4 (15%)	1 (3%)	0.09
Late onset sepsis (blood culture positive after 72 hours of life)	4 (15%)	5 (15%)	0.99
Ventilator associated pneumonia	3 (11%)	4 (12%)	0.94
Urinary tract infection	2 (7%)	7 (21%)	0.15
Necrotizing enterocolitis (Bell's stage II or greater)	2 (7%)	5 (15%)	0.37

Spontaneous intestinal perforation	3 (11%)	2 (6%)	0.46
Supplemental oxygen at 28 days	12 (44%)	17 (50%)	0.67
Supplemental oxygen at 36 weeks' gestation	9 (33%)	13 (38%)	0.69
Death before discharge	4 (15%)	1 (3%)	0.09
*p<0.05. IUGR=intrauterine growth restriction, SGA=small for gestational age. Quantitative variables were compared using the student's t-test for parametric data, the Mann-Whitney test for nonparametric data and categorical variables were compared using the Chi-square test.			

Table 4.5 Comparison of chorioamnionitis-exposed and unexposed preterm neonatal cytokine and chemokine levels over the first month of life using Generalized Estimating Equations.

Cytokine	Time Point 1	Time Point 2	B-value	p-value	
IL-1 β Unexposed	DOL 1-7	DOL 8-14	-0.316	0.093	
	DOL 1-7	DOL 15-21	-4.381	<0.001*	
	DOL 1-7	DOL 22-28	-2.194	<0.001*	
	DOL 1-7	DOL 29+	-4.237	0.024	
	DOL 8-14	DOL 15-21	-4.066	<0.001*	
	DOL 8-14	DOL 22-28	-1.879	0.008*	
	DOL 8-14	DOL 29+	-3.922	0.027	
	DOL 15-21	DOL 22-28	2.187	0.003*	
	DOL 15-21	DOL 29+	0.144	0.922	
	DOL 22-28	DOL 29+	-2.043	0.214	
	IL-1 β Chorioamnionitis-exposed	DOL 1-7	DOL 8-14	-0.714	0.046
		DOL 1-7	DOL 15-21	0.214	0.623
DOL 1-7		DOL 22-28	-2.179	0.002*	
DOL 1-7		DOL 29+	-1.306	0.124	
DOL 8-14		DOL 15-21	0.928	0.17	
DOL 8-14		DOL 22-28	-1.465	0.011	
DOL 8-14		DOL 29+	-0.592	0.328	
DOL 15-21		DOL 22-28	-2.818	0.009*	
DOL 15-21		DOL 29+	-1.544	0.043	
DOL 22-28		DOL 29+	1.273	0.017	
IL-6 Unexposed		DOL 1-7	DOL 8-14	-2.332	0.015
		DOL 1-7	DOL 15-21	-5.192	<0.001*
	DOL 1-7	DOL 22-28	-6.508	<0.001*	
	DOL 1-7	DOL 29+	-5.195	<0.001*	
	DOL 8-14	DOL 15-21	-2.860	<0.001*	
	DOL 8-14	DOL 22-28	-4.177	<0.001*	
	DOL 8-14	DOL 29+	-2.863	<0.001*	
	DOL 15-21	DOL 22-28	-1.316	0.087	
	DOL 15-21	DOL 29+	-0.003	0.997	
	DOL 22-28	DOL 29+	1.313	0.083	
	IL-6 Chorioamnionitis-exposed	DOL 1-7	DOL 8-14	-1.303	<0.001*
		DOL 1-7	DOL 15-21	0.233	0.158
DOL 1-7		DOL 22-28	-3.102	<0.001*	
DOL 1-7		DOL 29+	-2.321	<0.001*	
DOL 8-14		DOL 15-21	1.536	<0.001*	
DOL 8-14		DOL 22-28	-1.800	<0.001*	
DOL 8-14		DOL 29+	-1.019	<0.001*	
DOL 15-21		DOL 22-28	-3.335	<0.001*	
DOL 15-21		DOL 29+	-2.554	<0.001*	

	DOL 22-28	DOL 29+	0.781	0.146
IL-8 Unexposed	DOL 1-7	DOL 8-14	-0.743	0.038
	DOL 1-7	DOL 15-21	-0.038	0.926
	DOL 1-7	DOL 22-28	-1.963	<0.001*
	DOL 1-7	DOL 29+	-2.785	<0.001*
	DOL 8-14	DOL 15-21	0.705	0.339
	DOL 8-14	DOL 22-28	-1.220	0.004*
	DOL 8-14	DOL 29+	-2.042	<0.001*
	DOL 15-21	DOL 22-28	-1.925	0.005*
	DOL 15-21	DOL 29+	-2.747	<0.001*
	DOL 22-28	DOL 29+	-0.822	0.043
IL-8 Chorioamnionitis-exposed	DOL 1-7	DOL 8-14	-1.222	0.028
	DOL 1-7	DOL 15-21	-0.377	0.728
	DOL 1-7	DOL 22-28	-3.406	0.109
	DOL 1-7	DOL 29+	-1.934	0.006*
	DOL 8-14	DOL 15-21	0.845	0.313
	DOL 8-14	DOL 22-28	-2.184	0.238
	DOL 8-14	DOL 29+	-0.712	0.045
	DOL 15-21	DOL 22-28	-3.026	0.076
	DOL 15-21	DOL 29+	-1.546	0.035
	DOL 22-28	DOL 29+	1.479	0.347
IL-10 Unexposed	DOL 1-7	DOL 8-14	0.012	0.975
	DOL 1-7	DOL 15-21	0.191	0.809
	DOL 1-7	DOL 22-28	-1.198	0.004*
	DOL 1-7	DOL 29+	-0.863	0.006*
	DOL 8-14	DOL 15-21	0.179	0.688
	DOL 8-14	DOL 22-28	-1.210	0.022
	DOL 8-14	DOL 29+	-0.875	0.045
	DOL 15-21	DOL 22-28	-1.389	0.101
	DOL 15-21	DOL 29+	-1.054	0.167
	DOL 22-28	DOL 29+	0.335	0.403
IL-10 Chorioamnionitis-exposed	DOL 1-7	DOL 8-14	-0.435	0.182
	DOL 1-7	DOL 15-21	0.384	0.347
	DOL 1-7	DOL 22-28	-0.662	0.532
	DOL 1-7	DOL 29+	-0.736	0.222
	DOL 8-14	DOL 15-21	0.819	0.056
	DOL 8-14	DOL 22-28	-0.227	0.822
	DOL 8-14	DOL 29+	-0.301	0.520
	DOL 15-21	DOL 22-28	-2.189	0.158
	DOL 15-21	DOL 29+	-1.208	0.069
	DOL 22-28	DOL 29+	0.981	0.310
TNF- α Unexposed	DOL 1-7	DOL 8-14	0.780	0.146
	DOL 1-7	DOL 15-21	-0.877	0.140
	DOL 1-7	DOL 22-28	-0.360	0.381
	DOL 1-7	DOL 29+	-0.902	0.046

	DOL 8-14	DOL 15-21	-1.657	<0.001*
	DOL 8-14	DOL 22-28	-1.140	0.002*
	DOL 8-14	DOL 29+	-1.682	0.003*
	DOL 15-21	DOL 22-28	0.517	0.179
	DOL 15-21	DOL 29+	-0.025	0.965
	DOL 22-28	DOL 29+	-0.542	0.117
TNF- α Chorioamnionitis-exposed	DOL 1-7	DOL 8-14	0.020	0.951
	DOL 1-7	DOL 15-21	0.096	0.830
	DOL 1-7	DOL 22-28	-2.976	<0.001*
	DOL 1-7	DOL 29+	-1.172	0.003*
	DOL 8-14	DOL 15-21	0.076	0.906
	DOL 8-14	DOL 22-28	-2.995	<0.001*
	DOL 8-14	DOL 29+	-1.192	<0.001*
	DOL 15-21	DOL 22-28	-3.072	<0.001*
	DOL 15-21	DOL 29+	-1.268	0.057
	DOL 22-28	DOL 29+	1.803	<0.001*
CCL2 Unexposed	DOL 1-7	DOL 8-14	-0.668	0.024
	DOL 1-7	DOL 15-21	-1.862	<0.001*
	DOL 1-7	DOL 22-28	-2.413	<0.001*
	DOL 1-7	DOL 29+	-2.207	<0.001*
	DOL 8-14	DOL 15-21	-1.194	0.037*
	DOL 8-14	DOL 22-28	-1.745	<0.001*
	DOL 8-14	DOL 29+	-1.539	<0.001*
	DOL 15-21	DOL 22-28	-0.727	0.297
	DOL 15-21	DOL 29+	0.170	0.890
	DOL 22-28	DOL 29+	0.898	0.515
CCL2 Chorioamnionitis-exposed	DOL 1-7	DOL 8-14	-0.686	<0.001*
	DOL 1-7	DOL 15-21	-1.028	0.167
	DOL 1-7	DOL 22-28	-1.937	0.077
	DOL 1-7	DOL 29+	-0.296	0.437
	DOL 8-14	DOL 15-21	-0.342	0.587
	DOL 8-14	DOL 22-28	-1.251	0.280
	DOL 8-14	DOL 29+	0.390	0.164
	DOL 15-21	DOL 22-28	-2.239	<0.001*
	DOL 15-21	DOL 29+	-2.276	0.003*
	DOL 22-28	DOL 29+	-0.038	0.938
CCL3 Unexposed	DOL 1-7	DOL 8-14	-0.321	0.341
	DOL 1-7	DOL 15-21	-2.106	0.098
	DOL 1-7	DOL 22-28	-1.875	0.190
	DOL 1-7	DOL 29+	-0.577	0.462
	DOL 8-14	DOL 15-21	-1.786	0.173
	DOL 8-14	DOL 22-28	-1.555	0.300
	DOL 8-14	DOL 29+	-0.257	0.744
	DOL 15-21	DOL 22-28	0.231	0.890
	DOL 15-21	DOL 29+	1.529	0.262

	DOL 22-28	DOL 29+	1.298	0.481
CCL3 Chorioamnionitis-exposed	DOL 1-7	DOL 8-14	0.111	0.542
	DOL 1-7	DOL 15-21	0.457	0.283
	DOL 1-7	DOL 22-28	-1.466	0.297
	DOL 1-7	DOL 29+	-1.719	0.073
	DOL 8-14	DOL 15-21	0.346	0.514
	DOL 8-14	DOL 22-28	-1.577	0.273
	DOL 8-14	DOL 29+	-1.830	0.102
	DOL 15-21	DOL 22-28	-1.842	0.241
	DOL 15-21	DOL 29+	-1.956	0.020
	DOL 22-28	DOL 29+	-0.113	0.929

4.10 References

- (1) Blencowe, H.; Cousens, S.; Oestergaard, M. Z.; Chou, D.; Moller, A.-B.; Narwal, R.; Adler, A.; Vera Garcia, C.; Rohde, S.; Say, L.; Lawn, J. E. National, Regional, and Worldwide Estimates of Preterm Birth Rates in the Year 2010 with Time Trends since 1990 for Selected Countries: A Systematic Analysis and Implications. *Lancet Lond. Engl.* **2012**, *379* (9832), 2162–2172. [https://doi.org/10.1016/S0140-6736\(12\)60820-4](https://doi.org/10.1016/S0140-6736(12)60820-4).
- (2) Simonsen, K. A.; Anderson-Berry, A. L.; Delair, S. F.; Davies, H. D. Early-Onset Neonatal Sepsis. *Clin. Microbiol. Rev.* **2014**, *27* (1), 21–47. <https://doi.org/10.1128/CMR.00031-13>.
- (3) Matoba, N.; Yu, Y.; Mestan, K.; Pearson, C.; Ortiz, K.; Porta, N.; Thorsen, P.; Skogstrand, K.; Hougaard, D. M.; Zuckerman, B.; Wang, X. Differential Patterns of 27 Cord Blood Immune Biomarkers across Gestational Age. *Pediatrics* **2009**, *123* (5), 1320–1328. <https://doi.org/10.1542/peds.2008-1222>.
- (4) Lusyati, S.; Hulzebos, C. V.; Zandvoort, J.; Sauer, P. J. Levels of 25 Cytokines in the First Seven Days of Life in Newborn Infants. *BMC Res. Notes* **2013**, *6* (1), 547. <https://doi.org/10.1186/1756-0500-6-547>.
- (5) Salio, M.; Speak, A. O.; Shepherd, D.; Polzella, P.; Illarionov, P. A.; Veerapen, N.; Besra, G. S.; Platt, F. M.; Cerundolo, V. Modulation of Human Natural Killer T Cell Ligands on TLR-Mediated Antigen-Presenting Cell Activation. *Proc. Natl. Acad. Sci. U. S. A.* **2007**, *104* (51), 20490–20495. <https://doi.org/10.1073/pnas.0710145104>.
- (6) Peng, C.-C.; Chang, J.-H.; Lin, H.-Y.; Cheng, P.-J.; Su, B.-H. Intrauterine Inflammation, Infection, or Both (Triple I): A New Concept for Chorioamnionitis. *Pediatr. Neonatol.* **2018**, *59* (3), 231–237. <https://doi.org/10.1016/j.pedneo.2017.09.001>.
- (7) Romero, R.; Chaemsaihong, P.; Docheva, N.; Korzeniewski, S. J.; Tarca, A. L.; Bhatti, G.; Xu, Z.; Kusanovic, J. P.; Dong, Z.; Yoon, B. H.; Hassan, S. S.; Chaiworapongsa, T.; Yeo, L.; Kim, Y. M. Clinical Chorioamnionitis at Term V: Umbilical Cord Plasma Cytokine Profile in the Context of a Systemic Maternal Inflammatory Response. *J. Perinat. Med.* **2016**, *44* (1), 53–76. <https://doi.org/10.1515/jpm-2015-0121>.
- (8) de Jong, E.; Hancock, D. G.; Wells, C.; Richmond, P.; Simmer, K.; Burgner, D.; Strunk, T.; Currie, A. J. Exposure to Chorioamnionitis Alters the Monocyte Transcriptional Response to the Neonatal Pathogen *Staphylococcus Epidermidis*. *Immunol. Cell Biol.* **2018**, *96* (8), 792–804. <https://doi.org/10.1111/imcb.12037>.
- (9) Bermick, J.; Gallagher, K.; denDekker, A.; Kunkel, S.; Lukacs, N.; Schaller, M. Chorioamnionitis Exposure Remodels the Unique Histone Modification Landscape of Neonatal Monocytes and Alters the Expression of Immune Pathway Genes. *FEBS J.* **2019**, *286* (1), 82–109. <https://doi.org/10.1111/febs.14728>.
- (10) Schrag, S. J.; Hadler, J. L.; Arnold, K. E.; Martell-Cleary, P.; Reingold, A.; Schuchat, A. Risk Factors for Invasive, Early-Onset *Escherichia Coli* Infections in the Era of Widespread Intrapartum Antibiotic Use. *Pediatrics* **2006**, *118* (2), 570–576. <https://doi.org/10.1542/peds.2005-3083>.
- (11) García-Muñoz Rodrigo, F.; Galán Henríquez, G.; Figueras Aloy, J.; García-Alix Pérez, A. Outcomes of Very-Low-Birth-Weight Infants Exposed to Maternal Clinical Chorioamnionitis: A Multicentre Study. *Neonatology* **2014**, *106* (3), 229–234. <https://doi.org/10.1159/000363127>.

- (12) Redline, R. W.; Faye-Petersen, O.; Heller, D.; Qureshi, F.; Savell, V.; Vogler, C.; Society for Pediatric Pathology, Perinatal Section, Amniotic Fluid Infection Nosology Committee. Amniotic Infection Syndrome: Nosology and Reproducibility of Placental Reaction Patterns. *Pediatr. Dev. Pathol. Off. J. Soc. Pediatr. Pathol. Paediatr. Pathol. Soc.* **2003**, *6* (5), 435–448. <https://doi.org/10.1007/s10024-003-7070-y>.
- (13) Khong, T. Y.; Mooney, E. E.; Ariel, I.; Balmus, N. C. M.; Boyd, T. K.; Brundler, M.-A.; Derricott, H.; Evans, M. J.; Faye-Petersen, O. M.; Gillan, J. E.; Heazell, A. E. P.; Heller, D. S.; Jacques, S. M.; Keating, S.; Kelehan, P.; Maes, A.; McKay, E. M.; Morgan, T. K.; Nikkels, P. G. J.; Parks, W. T.; Redline, R. W.; Scheimberg, I.; Schoots, M. H.; Sebire, N. J.; Timmer, A.; Turowski, G.; van der Voorn, J. P.; van Lijnschoten, I.; Gordijn, S. J. Sampling and Definitions of Placental Lesions: Amsterdam Placental Workshop Group Consensus Statement. *Arch. Pathol. Lab. Med.* **2016**, *140* (7), 698–713. <https://doi.org/10.5858/arpa.2015-0225-CC>.
- (14) Khaertynov, K. S.; Boichuk, S. V.; Khaiboullina, S. F.; Anokhin, V. A.; Andreeva, A. A.; Lombardi, V. C.; Satrutdinov, M. A.; Agafonova, E. A.; Rizvanov, A. A. Comparative Assessment of Cytokine Pattern in Early and Late Onset of Neonatal Sepsis. *J. Immunol. Res.* **2017**, *2017*, 8601063. <https://doi.org/10.1155/2017/8601063>.
- (15) Leviton, A.; O'Shea, T. M.; Bednarek, F. J.; Allred, E. N.; Fichorova, R. N.; Dammann, O.; ELGAN Study Investigators. Systemic Responses of Preterm Newborns with Presumed or Documented Bacteraemia. *Acta Paediatr. Oslo Nor. 1992* **2012**, *101* (4), 355–359. <https://doi.org/10.1111/j.1651-2227.2011.02527.x>.
- (16) Harris, M. C.; Costarino, A. T.; Sullivan, J. S.; Dulkerian, S.; McCawley, L.; Corcoran, L.; Butler, S.; Kilpatrick, L. Cytokine Elevations in Critically Ill Infants with Sepsis and Necrotizing Enterocolitis. *J. Pediatr.* **1994**, *124* (1), 105–111. [https://doi.org/10.1016/s0022-3476\(94\)70264-0](https://doi.org/10.1016/s0022-3476(94)70264-0).
- (17) Edelson, M. B.; Bagwell, C. E.; Rozycki, H. J. Circulating Pro- and Counterinflammatory Cytokine Levels and Severity in Necrotizing Enterocolitis. *Pediatrics* **1999**, *103* (4 Pt 1), 766–771. <https://doi.org/10.1542/peds.103.4.766>.
- (18) Robison, H. M.; Bailey, R. C. A Guide to Quantitative Biomarker Assay Development Using Whispering Gallery Mode Biosensors: Whispering Gallery Mode Biosensors. *Curr. Protoc. Chem. Biol.* **2017**, *9* (3), 158–173. <https://doi.org/10.1002/cpch.23>.
- (19) Robison, H. M.; Escalante, P.; Valera, E.; Erskine, C. L.; Auvil, L.; Sasieta, H. C.; Bushell, C.; Welge, M.; Bailey, R. C. Precision Immunoprofiling to Reveal Diagnostic Signatures for Latent Tuberculosis Infection and Reactivation Risk Stratification. *Integr. Biol.* **2019**, *11* (1), 16–25. <https://doi.org/10.1093/intbio/zyz001>.
- (20) Mudumba, S.; de Alba, S.; Romero, R.; Cherwien, C.; Wu, A.; Wang, J.; Gleeson, M. A.; Iqbal, M.; Burlingame, R. W. Photonic Ring Resonance Is a Versatile Platform for Performing Multiplex Immunoassays in Real Time. *J. Immunol. Methods* **2017**, *448*, 34–43. <https://doi.org/10.1016/j.jim.2017.05.005>.
- (21) Ofman, G.; Vasco, N.; Cantey, J. B. Risk of Early-Onset Sepsis Following Preterm, Prolonged Rupture of Membranes with or without Chorioamnionitis. *Am. J. Perinatol.* **2016**, *33* (4), 339–342. <https://doi.org/10.1055/s-0035-1556758>.
- (22) Strunk, T.; Doherty, D.; Jacques, A.; Simmer, K.; Richmond, P.; Kohan, R.; Charles, A.; Burgner, D. Histologic Chorioamnionitis Is Associated with Reduced Risk of Late-Onset Sepsis in Preterm Infants. *Pediatrics* **2012**, *129* (1), e134–141. <https://doi.org/10.1542/peds.2010-3493>.

- (23) Puri, K.; Taft, D. H.; Ambalavanan, N.; Schibler, K. R.; Morrow, A. L.; Kallapur, S. G. Association of Chorioamnionitis with Aberrant Neonatal Gut Colonization and Adverse Clinical Outcomes. *PLOS ONE* **2016**, *11* (9), e0162734. <https://doi.org/10.1371/journal.pone.0162734>.
- (24) Villamor-Martinez, E.; Lubach, G. A.; Rahim, O. M.; Degraeuwe, P.; Zimmermann, L. J.; Kramer, B. W.; Villamor, E. Association of Histological and Clinical Chorioamnionitis With Neonatal Sepsis Among Preterm Infants: A Systematic Review, Meta-Analysis, and Meta-Regression. *Front. Immunol.* **2020**, *11*. <https://doi.org/10.3389/fimmu.2020.00972>.
- (25) Cantó, E.; Rodriguez-Sanchez, J. L.; Vidal, S. Distinctive Response of Naïve Lymphocytes from Cord Blood to Primary Activation via TCR. *J. Leukoc. Biol.* **2003**, *74* (6), 998–1007. <https://doi.org/10.1189/jlb.0303098>.
- (26) Marodi, L. Down-Regulation of Th1 Responses in Human Neonates. *Clin. Exp. Immunol.* **2002**, *128* (1), 1–2. <https://doi.org/10.1046/j.1365-2249.2002.01873.x>.
- (27) Iroh Tam, P.-Y.; Bendel, C. M. Diagnostics for Neonatal Sepsis: Current Approaches and Future Directions. *Pediatr. Res.* **2017**, *82* (4), 574–583. <https://doi.org/10.1038/pr.2017.134>.
- (28) Kinjo, T.; Ohga, S.; Ochiai, M.; Honjo, S.; Tanaka, T.; Takahata, Y.; Ihara, K.; Hara, T. Serum Chemokine Levels and Developmental Outcome in Preterm Infants. *Early Hum. Dev.* **2011**, *87* (6), 439–443. <https://doi.org/10.1016/j.earlhumdev.2011.03.006>.
- (29) Franz, A. R.; Steinbach, G.; Kron, M.; Pohlandt, F. Interleukin-8: A Valuable Tool to Restrict Antibiotic Therapy in Newborn Infants. *Acta Paediatr. Oslo Nor.* **1992**, *90* (9), 1025–1032. <https://doi.org/10.1080/080352501316978110>.
- (30) de Bont, E. S.; Martens, A.; van Raan, J.; Samson, G.; Fetter, W. P.; Okken, A.; de Leij, L. H. Tumor Necrosis Factor-Alpha, Interleukin-1 Beta, and Interleukin-6 Plasma Levels in Neonatal Sepsis. *Pediatr. Res.* **1993**, *33* (4 Pt 1), 380–383. <https://doi.org/10.1203/00006450-199304000-00013>.
- (31) Dulay, A. T.; Buhimschi, I. A.; Zhao, G.; Bahtiyar, M. O.; Thung, S. F.; Cackovic, M.; Buhimschi, C. S. Compartmentalization of Acute Phase Reactants Interleukin-6, C-Reactive Protein and Procalcitonin as Biomarkers of Intra-Amniotic Infection and Chorioamnionitis. *Cytokine* **2015**, *76* (2), 236–243. <https://doi.org/10.1016/j.cyto.2015.04.014>.
- (32) Ye, Q.; Du, L.; Shao, W.-X.; Shang, S. Utility of Cytokines to Predict Neonatal Sepsis. *Pediatr. Res.* **2017**, *81* (4), 616–621. <https://doi.org/10.1038/pr.2016.267>.
- (33) Sarandakou, A.; Giannaki, G.; Malamitsi-Puchner, A.; Rizos, D.; Hourdaki, E.; Protonotariou, E.; Phocas, I. Inflammatory Cytokines in Newborn Infants. *Mediators Inflamm.* **1998**, *7* (5), 309–312.
- (34) Protonotariou, E.; Malamitsi-Puchner, A.; Giannaki, G.; Rizos, D.; Phocas, I.; Sarandakou, A. Patterns of Inflammatory Cytokine Serum Concentrations during the Perinatal Period. *Early Hum. Dev.* **1999**, *56* (1), 31–38. [https://doi.org/10.1016/s0378-3782\(99\)00029-8](https://doi.org/10.1016/s0378-3782(99)00029-8).
- (35) Reinhart, K.; Bauer, M.; Riedemann, N. C.; Hartog, C. S. New Approaches to Sepsis: Molecular Diagnostics and Biomarkers. *Clin. Microbiol. Rev.* **2012**, *25* (4), 609–634. <https://doi.org/10.1128/CMR.00016-12>.
- (36) Kocabaş, E.; Sarikçioğlu, A.; Aksaray, N.; Seydaoğlu, G.; Seyhun, Y.; Yaman, A. Role of Procalcitonin, C-Reactive Protein, Interleukin-6, Interleukin-8 and Tumor Necrosis Factor-Alpha in the Diagnosis of Neonatal Sepsis. *Turk. J. Pediatr.* **2007**, *49* (1), 7–20.
- (37) Maheshwari, A.; Schelonka, R. L.; Dimmitt, R. A.; Carlo, W. A.; Munoz-Hernandez, B.; Das, A.; McDonald, S. A.; Thorsen, P.; Skogstrand, K.; Hougaard, D. M.; Higgins, R. D.;

Eunice Kennedy Shriver National Institute of Child Health and Human Development Neonatal Research Network. Cytokines Associated with Necrotizing Enterocolitis in Extremely-Low-Birth-Weight Infants. *Pediatr. Res.* **2014**, 76 (1), 100–108. <https://doi.org/10.1038/pr.2014.48>.

- (38) Sahni, M.; Yeboah, B.; Das, P.; Shah, D.; Ponnalagu, D.; Singh, H.; Nelin, L. D.; Bhandari, V. NOVEL BIOMARKERS OF BRONCHOPULMONARY DYSPLASIA AND BRONCHOPULMONARY DYSPLASIA-ASSOCIATED PULMONARY HYPERTENSION. *J. Perinatol. Off. J. Calif. Perinat. Assoc.* **2020**, 40 (11), 1634–1643. <https://doi.org/10.1038/s41372-020-00788-8>.
- (39) Kumar, R.; Yu, Y.; Story, R. E.; Pongracic, J. A.; Gupta, R.; Pearson, C.; Ortiz, K.; Bauchner, H. C.; Wang, X. Prematurity, Chorioamnionitis, and the Development of Recurrent Wheezing: A Prospective Birth Cohort Study. *J. Allergy Clin. Immunol.* **2008**, 121 (4), 878–884.e6. <https://doi.org/10.1016/j.jaci.2008.01.030>.
- (40) Schmatz, M.; Srinivasan, L.; Grundmeier, R. W.; Elci, O. U.; Weiss, S. L.; Masino, A. J.; Tremoglie, M.; Ostapenko, S.; Harris, M. C. Surviving Sepsis in a Referral Neonatal Intensive Care Unit: Association between Time to Antibiotic Administration and In-Hospital Outcomes. *J. Pediatr.* **2020**, 217, 59–65.e1. <https://doi.org/10.1016/j.jpeds.2019.08.023>.
- (41) Venkatesh, M.; Flores, A.; Luna, R. A.; Versalovic, J. Molecular Microbiological Methods in the Diagnosis of Neonatal Sepsis. *Expert Rev. Anti Infect. Ther.* **2010**, 8 (9), 1037–1048. <https://doi.org/10.1586/eri.10.89>.
- (42) Sharma, D.; Farahbakhsh, N.; Shastri, S.; Sharma, P. Biomarkers for Diagnosis of Neonatal Sepsis: A Literature Review. *J. Matern.-Fetal Neonatal Med. Off. J. Eur. Assoc. Perinat. Med. Fed. Asia Ocean. Perinat. Soc. Int. Soc. Perinat. Obstet.* **2018**, 31 (12), 1646–1659. <https://doi.org/10.1080/14767058.2017.1322060>.
- (43) Sharma, A. A.; Jen, R.; Kan, B.; Sharma, A.; Marchant, E.; Tang, A.; Gadawski, I.; Senger, C.; Skoll, A.; Turvey, S. E.; Sly, L. M.; Côté, H. C. F.; Lavoie, P. M. Impaired NLRP3 Inflammasome Activity during Fetal Development Regulates IL-1 β Production in Human Monocytes. *Eur. J. Immunol.* **2015**, 45 (1), 238–249. <https://doi.org/10.1002/eji.201444707>.
- (44) Strunk, T.; Prosser, A.; Levy, O.; Philbin, V.; Simmer, K.; Doherty, D.; Charles, A.; Richmond, P.; Burgner, D.; Currie, A. Responsiveness of Human Monocytes to the Commensal Bacterium *Staphylococcus Epidermidis* Develops Late in Gestation. *Pediatr. Res.* **2012**, 72 (1), 10–18. <https://doi.org/10.1038/pr.2012.48>.
- (45) Jakobsson, H. E.; Abrahamsson, T. R.; Jenmalm, M. C.; Harris, K.; Quince, C.; Jernberg, C.; Björkstén, B.; Engstrand, L.; Andersson, A. F. Decreased Gut Microbiota Diversity, Delayed Bacteroidetes Colonisation and Reduced Th1 Responses in Infants Delivered by Caesarean Section. *Gut* **2014**, 63 (4), 559–566. <https://doi.org/10.1136/gutjnl-2012-303249>.

Chapter 5 Comparison of Two Subject Cohorts Towards Development of a Multi-Biomarker Approach to Latent Tuberculosis Infection and Risk Assessment

5.1 Author Contributions Acknowledgements

This chapter contains unpublished work. The thesis author, Krista Meserve, was the sole contributor to the writing, cytokine comparison analysis, and conclusions in this chapter and generated all figures and tables, except for table 5.1. The models in this chapter portrayed in figures 5.1-5.3 and 5.12 were developed by our bioinformatics collaborators, Dr. Ruoqing Zhu, Haowen Zhou, and Mingrui Xu. Dr. Cole Chapman and Dr. Heather Robison developed the 13-plex assay and analyzed the 135 QFT samples associated with ‘Cohort 1’. The thesis author analyzed the 348 QFT patient samples associated with ‘Cohort 2’ and managed the multi-site collaboration. Our clinical collaborators, led by Dr. Patricio Escalante, generated table 5.1.

I would like to thank the many people on the team who contributed to getting us the samples for analysis. Dr. Cole Chapman and Dr. Heather Robison for initial project conception and direction. I would like to thank Dr. Patricio Escalante from the Mayo Clinic for his leadership through this project and allowing me to lead the project at Michigan. I acknowledge Heather Hilgart for storing and sending the many LTBI samples collected over the years; Pedro Sanchez, Tom Cox, Kale Daniel, Mounika Vadiyala, Maleeha Shah, Snigdha Karnakoti, Dr. Paige Marty, Dr. Balaji Pathakumari, Courtney Erskine, Dr. Elitza Theel, and Virginia P. Van Keulen from the Mayo Clinic for their dedication to enrolling patients, collecting samples, and conducting additional testing; Dr. Ruoqing Zhu, Mingrui Xu, and Haowen Zhou from the University of Illinois at Urban-Champaign (UIUC) for their work on developing the

bioinformatic models used to analyze the data in this chapter; and Colleen Bushell, Michael Welge, Dr. Charles Blatti from UIUC and Dr. Rafael Laniado-Laborin from Hospital de Tijuana for their helpful discussions. Thank you to Ryan Bailey for his project guidance and to my Bailey Lab colleague, Manik Reddy, for editing this chapter and for all the fruitful conversations centered around this project.

5.2 Abstract

Tuberculosis (TB) infection is caused by *Mycobacterium tuberculosis* (Mtb) bacteria and affects around a quarter of the world's population. TB is characterized as a dynamic and immunological equilibrium between multiple phases of infection, leading to difficulty in diagnosing and treating infected individuals. Patients with the clinically silent, asymptomatic, latent phase of the infection, or LTBI, can reactivate to the active phase of infection following perturbation of the dynamic equilibrium and can contribute to the spread of the bacteria. Identifying individuals who are LTBI positive and those who are at a high risk of reactivation in one assay would be advantageous for improving treatment and monitoring of patients. We developed a microring resonator based multi-biomarker immunoprotein assay to profile thirteen cytokine biomarkers in two separate clinical cohorts. The analytical method was followed by precision normalization and random forest machine learning modeling to classify patients' LTBI and high-risk statuses. Across both cohorts, a predictive accuracy of almost 90% was achieved for LTBI positive versus LTBI negative patients and an accuracy of 91% to discriminate high-risk from not high-risk of reactivation was achieved in the second cohort. The random forest machine learning model identified similar biomarkers (IP-10, IL-2, CCL8, and CCL4) as important towards prediction of both LTBI and high-risk classifications across both clinical cohorts, indicating potential for development of a lower-plexity assay. Additionally, the effect of

including a secondary TB-specific stimulation, TB2, to the workflow was assessed and results indicated the TB2 stimulation associated data did not provide any improvements or new information relative to the classification model with only the TB1 stimulation associated data. Herein, we report on the application of our developed workflow to identify patients' LTBI and high-risk statuses in two clinical cohorts, followed by the comparison of results between cohorts. Using analytical tools and techniques combined with leftover QFT plasma samples and machine learning algorithms, we present a method easily integrated into the current TB diagnostic workflow that produced comparable results across two different clinical cohorts of subjects.

5.3 Introduction

Pulmonary tuberculosis (TB) is a complex condition resulting from infection with *Mycobacterium tuberculosis* (Mtb) bacteria. It is estimated that around 25% of the world's population has been infected with Mtb, resulting in 10.6 million new infections and 1.6 million deaths worldwide in 2021.^{1,2} Initiatives to reduce global TB mortality have been largely unsuccessful, as the 5.9% decrease in TB deaths from 2015-2020 failed to achieve the target goal of 35% reduction set by the World Health Organization's (WHO) End TB Strategy.³ Reductions in TB disease burden achieved during the late 2010s were reversed during the coronavirus disease 2019 (COVID-19) pandemic.⁴ Pandemic-induced impacts included reductions in spending on TB preventative services, an increase of infections through household contacts, and lower bacilli Calmette-Guérin (BCG) vaccination rates among children.⁴⁻⁶ Furthermore, diagnostic availability was impaired, leading to decreases in notification of TB infections. These adverse outcomes have only underlined the longstanding need for improved TB diagnostic platforms.

TB disease is currently regarded as a continuum or spectrum with various disease phases, from non-infectious TB to potentially infectious subclinical presentation and infectious TB disease.⁶⁻⁸ Each phase requires different methods of diagnosis and treatment regimes, adding to the complexity of TB disease. Mtb is concentrated in the lungs of actively infected individuals and transmitted to susceptible recipients through aerosolized respiratory droplets. The Mtb encountered upon inhalation of infectious droplets or aerosols can be cleared by the early innate immune system. However, if elimination is not achieved, pro-inflammatory cytokines continue to initiate a cellular response to the site of infection.^{9,10} Although delayed, initiation of the adaptive immune response recruits immune cells like lymphocytes and monocytes to the infection site and granulomas begin to form and calcify around the Mtb bacteria.¹¹ Granuloma development aids Mtb persistence by isolating the bacteria from the host's immune response, but also protects the host from continued bacterial growth and replication. The dynamic bacterial and immunological equilibrium induced by the granuloma environment results in latent TB infection (LTBI).^{9,11}

Patients diagnosed with LTBI can be treated with short-or long- course antibiotic regimens to prevent progression to active disease.^{12,13} Approximately 90% of LTBI patients who are immunocompetent will stay asymptomatic and non-contagious.⁷ However, in 5-10% of LTBI patients, factors such as inherent immune system characteristics, a co-infection, tumor necrosis factor (TNF) monoclonal antibody treatment, or other immunosuppressive factors will disrupt the dynamic equilibrium and result in granuloma rupture, deemed a reactivation event.⁹ The TB bacteria, no longer held in a quiescent state, will begin to replicate within the lungs of the host and be spread in respiratory droplets, facilitating further transmission of TB disease. Many

reactivation events occur within 24 months of initial infection, highlighting the importance of diagnosing the latent phase of infection.⁷

The current field of LTBI diagnostics lacks a gold standard and relies on detection of TB infection through the tuberculosis skin test (TST) and interferon- γ release assay (IGRA).^{8,14,15} TSTs are conducted by injecting purified protein derivatives from Mtb intradermally and measuring the resulting reactionary swelling. TSTs require a follow up visit within a very specific and regulated time frame to record the size of reaction and can result in false positives in individuals with a history of BCG vaccination or infection with nontuberculous mycobacterium.¹¹ IGRAs incorporate blood-based diagnostics into the TB testing field. The current standard IGRA is the commercialized QuantiFERON test (QFT).¹⁶ The QFT identifies those who have been infected by Mtb by measuring the interferon- γ (IFN- γ) response in blood samples stimulated with TB-specific and control antigens.¹⁵ The QFT controls consist of a negative (NIL) control, in which blood samples are stimulated with media, and a positive control (MIT) that stimulates blood samples with the bioactive protein mitogen. The TB-specific stimulation (termed AG) targets CD4⁺ T-cell responses via a peptide cocktail of culture filtrate protein 10 and early secretory antigenic target protein 6 (CFP-10/ESAT-6). An updated QFT kit, QFT-Plus, changed the name of the AG condition to TB1 and introduced a secondary TB-specific stimulation, TB2, that stimulates samples with a mixture of CFP-10/ESAT-6/additional proprietary peptides that are intended to simultaneously extract specific signals from CD4⁺ and CD8⁺ T-cells.

While the QFT-Plus test incorporates two controls, two sets of TB-specific peptide stimulations, and requires a single visit, the output response is reliant on only one biomarker, IFN- γ , and the assay to measure IFN- γ requires experienced lab technicians and can take many

hours. Thus, abnormal results and inconclusive tests can occur in IFN- γ dysregulated patients. The TST and IGRAs are suitable for identifying individuals with prior exposure to Mtb, but they are unable to accurately differentiate between LTBI and active disease and have less than 3% predictive value in determining risk of reactivation from latent to active TB.^{8,17,18} There is a current need to develop phase-specific TB diagnostics, particularly for LTBI, as well as identify patients at an increased risk of reactivation, since preventative antibiotic therapy would be most beneficial for these individuals. The ideal diagnostic would detect both LTBI status and reactivation risk simultaneously.

To facilitate the WHO's goal of decreasing TB incidence by 80% before 2030, our research team aims to expand the TB diagnostic toolbox with a multiplexed immunoassay tool that addresses both LTBI status and risk of reactivation. Multiplexed protein biomarker assays will identify host biomarkers, aside from IFN- γ , that could be potential indicators of disease or reactivation risk, effectively reducing false negatives from IFN- γ dysregulated patients.¹⁹

Multi-biomarker approaches have been studied to selectively distinguish active TB patients from healthy controls or those with other respiratory diseases.²⁰⁻²⁶ A systemic review of active TB biomarkers reported that many cytokines have been examined as standalone diagnostic markers, but that multi marker signatures would be more specific to disease state and provide greater diagnostic accuracy.²⁰ The authors suggested that multi biomarker TB signatures should be derived for clinically distinct populations within the TB space, such as populations with a high risk of reactivation, rather than focusing mainly on the active TB phase.

Efforts to uncover multiplexed protein signatures in active TB patients have been reported by Chegou and coworkers in the Stellenbosch University TB diagnostic biomarker research lab. In an analysis of untreated serum, this group identified a seven-biomarker signature

that resulted in a predictive accuracy of 90% for active TB infection, an improvement over the 79-86% accuracy obtained when assessing the biomarkers individually.²¹ Two follow up studies employed multiplexed biomarker analysis in the QFT stimulated plasma. Chegou et al quantified biomarker concentrations in the NIL and AG stimulated QFT plasma and concluded that no single, stand-alone marker was sufficient to discriminate active TB patients from other individuals, but a panel of four markers could complete this task with accuracy of 81% in 251 patients in Africa.²² Manngo et al further explored biomarkers in QFT stimulated plasma (NIL, TB1 and TB2 tubes), which resulted in accuracies of 56-77% using individual markers, but 91% using a six-signature combination, all under the NIL condition.²³

Additionally, studies have used multi-biomarker assays to classify patients as LTBI, active TB, or healthy controls.²⁷⁻³¹ Wang et al used the QFT stimulated plasma to identify a six-biomarker signature that could differentiate active TB (n=27), LTBI (n=32), and healthy controls (n=20) in a clinical validation cohort with 88.7% accuracy.²⁸ The cytokines included IFN- γ , IP-10, and IL-1Ra under TB1 stimulation and IP-10, VEGF, and IL-12 under NIL stimulation. Won et al used the QFT stimulated plasma to differentiate LTBI (n=15), healthy controls (n=13), active TB-QFT negative (n=12), and active TB-QFT positive (n=36) patient populations.²⁹ They identified the biomarkers IL-2, IL-1Ra, IFN- γ , IP-10, GM-CSF, and IL-3 as important for discriminating TB infected and healthy controls, biomarkers IL-15, IL-10, VEGF, IL-2/IFN- γ , and TNF- α as important for identifying active and latent TB, and VEGF, IP-10, IL-8, IL-2, and IL-13 as important for discerning between active TB and non-active (LTBI + healthy controls) TB. These studies demonstrate promise for using cytokine biomarkers to differentiate various phases of TB infection. However, they fail to account for immunological variation between

patients and do not include multi-biomarker signatures to identify individuals with the highest risk of reactivating from latent to active TB.

Most of the current research into quantifying reactivation risk is focused on RNA signatures.³²⁻³⁵ Previous work in our group has begun to explore using protein biomarkers for risk assessment signatures. Protein biomarkers are generally more stable than RNA, do not require RNase-free facilities, and would facilitate a more streamlined integration into and comparison to current protein-based TB diagnostics.³⁶ In two reports led by Bailey Lab alumni Dr. Heather Robison, peripheral blood mononuclear cells were stimulated with six antigens and the resulting supernatants were analyzed with our 13-plex cytokine and chemokine immunoassay.^{37,38} Initial work (n=15 LTBI subjects, n=35 controls, with n=5 high risk subjects) using machine learning feature selection identified IP-10, IL-2, and IFN- γ under normalized stimulation conditions as important for LTBI designation and IP-10 as most important for high-risk designation.³⁷ In a follow-up study (n=32 LTBI subjects, n=43 controls, with n=24 high risk subjects), they used random forest algorithms that selected various normalized conditions of IP-10, CCL8, IFN- γ , CCL2, and IL-2 in the stimulated cell supernatants to designate LTBI status with an accuracy of 87.4% and IP-10, IL-2, IFN- γ , TNF- α , and IL-15 to designate high-risk status with an accuracy of 85.5%.³⁸ This work demonstrated application of our 13-plex cytokine assay for designating both LTBI and high-risk status using precision normalized values. However, the process of incubating peripheral blood mononuclear cells with six stimulation antigens for 48 hours and collecting the resulting supernatant was a technically challenging and laborious process. Using more easily generated samples or patient samples collected as part of the current TB diagnostic workflow would increase the applicability of our 13-plex assay in developing a TB diagnostic panel.

Herein, we explore the use of QFT stimulated plasma as the sample source for analysis with our 13-plex microring resonator assay and random forest algorithms to differentiate LTBI positive from LTBI negative patients, as well as selectively identify patients at a high risk of reactivation. We report the results from two cohorts of subjects, collected at two different times and analyzed by two different teams. Both cohorts achieved predictive accuracies of ~90% for LTBI designation using a subset of measured, precision normalized, biomarkers. The second cohort achieved an accuracy of 91% for high-risk versus not high-risk designation. There was high overlap in the important biomarkers between the two cohorts and between the two designations, validating the findings within each cohort and indicating potential for a lower plexity, point-of-care focused assay. Furthermore, we tested the effect of adding the TB2 QFT-Plus stimulation to the workflow in the second cohort of subjects, ultimately determining no diagnostic advantage of this additional sample. The results presented in this chapter aim to compare the outcomes generated by two separate clinical cohorts, provide grounds for pooling the two cohorts together for greater sample size, and explain reasoning for excluding the TB2 QFT stimulation from future work.

5.4 Methods

5.4.1 Subject Enrollment and clinical designations

These two studies were approved by the Mayo Clinic Institutional Review Board and Olmsted County Public Health Services. All study participants signed an informed written consent. Cohort 1 subjects were enrolled in Rochester, MN between August 2017 and June 2018 and cohort demographics are tabulated in **Table 5.1**. Cohort 2 subjects were enrolled in Rochester, MN between November 2020 and February 2022 and cohort demographics are tabulated in **Table 5.2**. Risk factors for TB infection, TB progression, and/or TB reactivation

were obtained through a questionnaire and review of medical records as previously described.³⁹⁻
⁴¹ LTBI diagnoses were made based on the Center for Disease Control and Prevention (CDC) current guidelines criteria, TB risk factors, and prior TST and QuantiFERON®-TB Gold In-Tube or Gold In-Tube Plus results (Qiagen, Germantown, MD).⁴¹ LTBI-negative classified study subjects included unexposed individuals and subjects with non-tuberculosis mycobacterium infection. This study included subjects with varying risk for developing active TB infection, including untreated LTBI patients and patients who had LTBI therapy and, therefore, were at low risk of reactivation. A modified multifactorial predictive modeling platform (Online TST/IGRA interpreter), adjusted by LTBI treatment effect, was applied to estimate the cumulative risk of TB reactivation in all subjects.^{42,43}

The two clinical designations used in this study, LTBI and high-risk status, are both of interest to the TB diagnostic community and would, together, provide information relevant to treatment possibilities and infectious disease control. As described above, CDC guidelines for diagnosis of LTBI were used to classify subjects as LTBI positive or negative. Subjects were deemed high-risk of reactivation patients if they could be classified as either (1) having untreated LTBI with both TST+ and prior IGRA+ results, (2) having untreated LTBI with TST+ conversion, prior IGRA- results, and prior TB exposures, or (3) being immunosuppressed with prior TB exposure and prior IGRA+ results.

5.4.2 Sample collection and QuantiFERON testing

Three milliliters of blood were collected from each subject and sent for same-day QFT testing at the Mayo Clinic's clinical laboratories. Cohort 1 was overwhelmingly (39/45 samples) analyzed using the QuantiFERON®-TB Gold In-Tube IGRA kit (QFT, Qiagen). The QFT assay was performed as recommended by the manufacturer.^{42,44} The standard protocol includes three

in-tube stimulation conditions: a negative control (NIL), positive control (MIT), and the CFP-10/ESAT-6 peptide mixture for CD4+ cell stimulation (AG). The remaining six samples from cohort 1 and all samples collected for cohort 2 were analyzed using an updated IGRA assay, the QuantiFERON®-TB Gold Plus (QFT-Plus, Qiagen) kit, which includes four in-tube stimulation conditions.⁴⁵ The QFT-Plus kit contained the same stimulations: NIL, MIT, and CFP-10/ESAT-6 peptide mixture, now termed TB1 and shown to be akin to the AG stimulation in the original QFT assay.⁴⁶ The updated QFT-plus kit included an additional TB-specific stimulation, TB2. The TB2 stimulation included the same CFP-10/ESAT-6 peptide mixture as TB1, with additional proprietary peptides to illicit CD8+ T-cell responses. This TB2 tube was disregarded in the last six samples of cohort 1, but was analyzed for all samples in cohort 2, as is discussed in this chapter.

After patient blood was stimulated in-tube following protocol, the plasma was separated from the red blood cells and analyzed for IFN- γ concentration by an enzyme-linked immunosorbent assay (ELISA). In the original QFT assay, a positive QFT result was declared if measured levels of IFN- γ included $\text{NIL} \leq 8.0 \text{ IU/mL}$, the IFN- γ concentration difference between TB1 and NIL tubes ($\text{TB1-NIL} \geq 0.35 \text{ IU/mL}$), and $\text{TB1-NIL} \geq 25\%$ of the NIL IFN- γ value. In the updated QFT-Plus assay, a positive QFT result was declared if IFN- γ concentrations in $\text{NIL} \leq 8.0 \text{ IU/mL}$, TB1-NIL or $\text{TB2-NIL} \geq 0.35 \text{ IU/mL}$, and TB1-NIL or $\text{TB2-NIL} \geq 25\%$ of the NIL IFN- γ value. Leftover plasma samples from each QFT or QFT-Plus tube were frozen after ELISA testing, stored at -80°C , and thawed immediately before multiplexed cytokine analyses.

5.4.3 Silicon Photonic Microring Resonator Assays

5.4.3.1 Technology

Silicon photonic microring resonators are a type of whispering-gallery mode sensor in which light continually circulates within a microring waveguide microstructure, resulting in an evanescent field extending above the microring structure.⁴⁷⁻⁵⁰ Light from a laser travels down a linear waveguide and couples into the microring waveguide at a wavelength dependent on the effective refractive index (RI) in the evanescent field, according to the equation:

$$\lambda = \frac{2\pi r}{m} n_{eff}$$

where λ is the wavelength, m is an integer, r is the radius of the circular waveguide, and n_{eff} is the effective RI of the optical mode. The wavelength of light continues to resonate until the RI is altered. With the aid of standard recognition molecules (e.g., capture antibodies, nucleic acid aptamers) covalently linked to the microring sensor surface, biomolecules are deposited in the microring sensor evanescent field, which alters the effective RI.⁵¹⁻⁵³ The change in RI shifts the wavelength of light resonating within the microstructure, with the overall shift from start to end of an assay correlating to amount of material bound to the surface.^{50,54} The microring WGM structure is easily fabricated, results in low coefficient of variation, and is amenable to multiplexing microring sensors on one silicon chip.

5.4.3.2 Instrumentation

Our analysis was completed using the Genalyte Matchbox instrument (Genalyte, Inc., San Diego, CA) and silicon sensor chips (Genalyte, Inc. San Diego, CA).⁵⁵ The silicon sensor chips were 4X6 mm in size and fabricated with 128 individual microrings, including thermal control rings. The rings were arranged in clusters of four and were spatially separated into two channels of sixteen ring clusters each, allowing for sixteen analytes in two separate samples to be analyzed simultaneously. For experiments, the sensor chips were housed in injection molded

cartridges (Genalyte, Inc., San Diego, CA) to create two sealed microfluidic channels along the top of the microring channels. When inserted into the instrument, a fully automated microfluidic path is created that pulls all reagent liquid from a 96-well plate across the surface of the sensor chip at 30 $\mu\text{L}/\text{min}$ and then discarded into waste. The sensor chip and cartridge unit were discarded after each sample to eliminate potential carryover between samples.

5.4.3.3 Immunoassay

The assay deployed in this study is akin to a sandwich-style ELISA. This same method was employed for both cohorts, enabling comparison of biomarker concentrations between cohorts. Capture antibodies for each biomarker were spatially arrayed onto 13-plex sensor chips by Genalyte, Inc. using precision spotting techniques. As previously described in Chapter 2, the antibodies were covalently linked to clusters of four microring sensors through silanization chemistry and a homobifunctional linker.⁵⁴ The chips were dry coated and stored in a desiccator at 4°C until use. The antibody-functionalized chip was fitted into the cartridge and loaded into the instrument. The recipe programmed into the instrument was as follows: 1X phosphate buffered saline with 0.5% bovine serum albumin (PBS-BSA, buffer) buffer rinse to equilibrate the chip surface (5 mins), sample or standard solution (7 mins), buffer rinse (2 mins), mixture of all biotinylated tracer antibodies in the panel (7 mins), buffer rinse (2 mins), streptavidin horse radish peroxidase (SA-HRP, 7 mins, 4 $\mu\text{g}/\text{mL}$), buffer rinse (2 mins), and 4-chloro-1-naphthol (4-CN, 7 mins, stock concentration) with a final buffer rinse (3 mins). The frequent buffer rinses remove any unbound material before the next reagent is introduced. The final reagent, 4-CN, is the method's amplification reagent that reacts with the localized HRP to form an insoluble precipitate in the sensing region.⁵⁶ This crucial step increases the relative wavelength shift, thereby decreasing the limits of detection and expanding the dynamic sensing range. In total, the

13-plex assay is completed in under 45 minutes, uses less than 300 μ L of patient plasma, and analyzes two samples simultaneously. The immunoassays conducted in cohort 1 were completed by Dr. Cole Chapman and those in cohort 2 were completed by the author.

5.4.3.4 Assay Panel Optimization

The 13 plex cytokine and chemokine panel included IL-1 β , IL-2, IL-6, IL-10, IL-15, IL-17, CCL2, CCL3, CCL4, CCL8, IFN- γ , IP-10, and TNF- α . Each biomarker was individually optimized to determine optimal tracer antibody concentration and appropriate standard concentrations that allowed for construction of an eight-point, four-parametric calibration curve. Prior to multiplexing the biomarkers, each pair of capture antibody and standard/tracer antibody was tested for cross-reactivity. Using a checkerboard method, each individual standard/tracer antibody pair was flowed across each capture antibody to ensure that capture antibodies produce a response only to their respective standard/tracer antibody pair. Additionally, optimized sandwich assays were tested in the biologic matrix of interest to ensure minimal change in performance. New reagent lots introduced during the study were tested before use in sample analysis.

5.4.3.5 Assay Calibrations.

Multiplexed calibrations were completed by combining all protein standards at previously optimized saturating conditions into an Eppendorf tube and performing six five-fold serial dilutions into the matrix concentration of interest, as described previously (Chapter 2).^{54,57} Each standard solution and a matrix-only blank solution were analyzed following the assay method described above. The net shift at the end of each experiment was plotted against the standard concentration and a four parametric sigmoidal curve was fit to the data. New calibrations were constructed for each batch of sensor chips. At least three calibrations were completed and

averaged over the usage lifetime of each chip batch to account for temporal variation in the assay signal. Each calibration was constructed in a 10% and 50% plasma matrix, as patient plasma samples were analyzed at 10× and 2× dilutions.

5.4.3.6 Sample Analysis.

Each plasma sample (~300 µL) was removed from the -80°C and thawed at 4°C. The plasma was spun in a mini centrifuge for three seconds to aggregate any solid materials that may clog the microfluidic lines. The plasma was diluted two- and ten- fold in 1X PBS-BSA to a total volume of 350 µL. Standard biohazard safety level two precautions were exercised while handling the plasma samples. To make reagents for one chip (two assays), all biotinylated tracer antibodies were diluted together in 1X PBS-BSA to their running concentration at a total volume of 800 µL, SA-HRP was diluted in 1X PBS-BSA to 4 µg/mL at a total volume of 800 µL, and 4-CN was used at stock concentration. Two series of reagents were plated sequentially across a 96-well plate, with one series of reagents for each channel on the chip. The filled plate was inserted into the well-plate holder in the instrument. The sensor chip was secured into the disposable cartridge and inserted into the chip holder in the instrument. The instrument immunoassay recipe described above was selected in the Genalyte, Inc. software and executed using all automated microfluidic handling. This workflow has been previously used and described (Chapter 2).^{54,57}

5.4.3.7 Immunoassay Data Analysis.

The relative shift in resonant wavelength is monitored in near-real time from start to end of the experiment. The resulting data is a csv file for each individual microring sensor and data workup has been previously described in Chapter 2. Briefly, using in-house R programming code, the csv files were aggregated, thermal controls were subtracted, and ring clusters were named by capture antibody to determine which corresponding proteins were present in the

sample. The data was plotted as relative shift over time for each individual ring and then transformed to net shift by subtracting the relative shift immediately before the 4CN amplification step from the relative shift at the end of the final buffer rinse ($t=29$ to $t=41$). Using the calibration curve, the net shift for both analyzed dilutions (10 \times and 2 \times) was converted to analyte concentration using the corresponding calibration (10% plasma and 50% plasma, respectively). The technical replicates ($n=4$) were averaged within each dilution. For each target, the dilution that resulted in a concentration closest to the mid-point of the calibration curve was selected and used for the bioinformatic analysis. Data points that exceed the saturating point of the target were removed. Data points below the limit of detection were converted to zero.

5.4.4 Precision Normalization

Baseline immune responses exhibit significant variation across individuals and populations. Therefore, normalizing the biomarker levels measured in stimulated QFT samples from each individual can potentially account for patient-to-patient variation in baseline immunity and can result in development of more generalizable biomarker signatures. The QFT stimulations include a negative media control (NIL) to measure baseline response, a TB specific antigen cocktail stimulating CD4 $^+$ T-cells (TB1), a TB specific antigen cocktail stimulating CD4 $^+$ and CD8 $^+$ T-cell responses (TB2, only in QFT-Plus), and a positive antigen stimulation (mitogen, MIT) to provide insight into the individual's overall immune response. The normalization conditions for each biomarker target include a negative control subtraction to remove baseline immune response (TB1-NIL and TB2-NIL), a positive control subtraction to measure TB specific response against overall positive response (TB1-MIT and TB2-MIT), a TB specific subtraction to determine if there are differences between TB stimulations (TB1-TB2), and a

positive minus negative subtraction to account for the overall immune response of the subject (MIT-NIL) for each of the 13 targets measured per patient.

To compare both cohorts, we used the NIL, MIT and TB1 stimulation results from cohort 1 and cohort 2, which translated to normalized conditions of TB1-NIL, TB1-MIT, and MIT-NIL. Taken together, the three normalized conditions calculated for each of the 13 measured biomarker concentrations led to 39 features per patient for machine learning analysis. In cohort 2, we additionally analyzed the data with the TB2 tube added in, which translated to normalized conditions of TB1-NIL, TB2-NIL, TB1-MIT, TB2-MIT, TB1-TB2, and MIT-NIL. Taken together, the six normalized conditions calculated for each of the 13 biomarkers led to 78 features per patient for machine learning analysis.

5.4.5 Statistical tests for grouped comparisons

To compare the concentration of biomarkers across cohorts when stratified by stimulation condition and clinical status (inter-cohort comparison), two-sample Wilcoxon rank-sum tests, also known as Mann-Whitney U tests or Wilcoxon-Mann-Whitney (WMW) tests, were used. A WMW test is a non-parametric statistical hypothesis test that quantifies differences in the distribution of data between two populations.⁵⁸ This contrasts with a two-sample t-test, in that t-tests are measures of sample means between two populations. Compared to t-tests, WMW tests are more appropriate for data where intervals cannot be assumed constant, if outliers may be present, if the data is skewed, and/or if there are relatively low sample sizes ($n \leq 30$).⁵⁹ WMW tests were chosen for comparing the biomarkers between cohorts because the samples between groups meet the independent, ordinal, and continuous test assumptions, intervals may not be constant, outliers are present, and some classification bins contain just 20 samples. The null hypothesis is that the distribution of the groups being compared are identical, with the alternative

hypothesis being that the distribution of the groups is not identical. If distributions have the same shape, as is the common case in this chapter, significant results can be interpreted as a difference in medians between the groups.

To compare the concentration of biomarkers between the TB1 and TB2 tubes when stratified by stimulation condition and clinical status, paired Wilcoxon signed-rank tests were completed. The Wilcoxon signed-rank test is a non-parametric test used to compare the locations of matched pair populations.⁶⁰ This is similar to a paired t-test in that it is a paired difference test, or the difference between two paired samples is calculated, but differs from a paired t-test in that t-tests focus on population means rather than population distribution. The null hypothesis is that the difference between the pairs is symmetric around zero, while the alternative is that the difference symmetric around a value other than zero. The Wilcoxon signed rank test was selected for measuring differences in biomarker concentrations in the TB1 and TB2 tubes because the differences are independent from each other, both variables are measured on the same interval scale, and the distribution of differences are symmetrical, which are the test assumptions. A paired test was conducted because the samples being compared are obtained from the same patient and are, therefore, dependent.

5.4.6 Random Forest Machine Learning

Random forest is an ensemble learning method that constructs and aggregates a multitude of decision trees to determine a classification outcome.^{61,62} Single decision trees are prone to overfitting, leading to inaccuracy and low flexibility towards new observations.⁶³ Aggregating many trees n. However, random forest algorithms are unable to be easily interpreted in ways a single decision tree can be. The general machine learning method was previously described³⁸ and all work was completed using R programming.⁶⁴⁻⁶⁷

In the random forest supervised machine learning method, the rows of data corresponding to individual patients are the observations and the columns of the data containing normalized cytokine concentrations act as the input variables to the decision trees. This work applied bootstrap aggregating, or bagging, techniques, which reduces model variance due to the aggregation of multiple trees, and a leave-one-out cross validation, in which the trees are trained using a bootstrapped set of the data and the model is tested with the observation left out of the bootstrapped data set.⁶² Random forests do not require manually splitting the data into distinct testing and training sets, as the algorithm fundamentally uses a portion of the data to create a model and the remaining data to get an unbiased estimate of test error.

To create the random forest, a random sample of all but one of the observations were selected, or bootstrapped, to develop a model of many trees using random subsets of input variables at each node, or split point. The outcome classification using the observation not selected for forest development is determined for each individual tree and is then averaged across all the trees in the forest to determine the final designation of an observation, which is then compared to the known designation for accuracy. This is iterated through all observations, with model accuracy accumulated for each observation. Initially, all possible variables are options for the random forest to use to make the designations and is called the 'full' model. After model development, certain variables, or features, can be identified as not contributing to the predictive outcome. These unimportant variables are removed from the data set and new models are developed, which is called the 'reduced' model.

A unique bagging method was employed for the cohort 2 analysis. Cohort 2 included a high number (n=13 of 85) of repeat patient samples, meaning multiple samples were provided by an individual patient as part of the ongoing longitudinal profiling aspect of the project. This

raised the possibility that temporally distinct observations from the same patient could be used to both develop and then subsequently test a tree, introducing bias correlation bias into the classification model. To avoid this, our team developed a homogenous bagging method to ensure only one timepoint from a patient was included in the bootstrapped observations.

The visual representation of random forest outputs are receiver operator characteristic (ROC) curves. The ROC curve plots the sensitivity and specificity of the model at all possible classification thresholds.⁶⁸ ROC curves are compared using the area under the curve (AUC), a metric of sensitivity and specificity of the model that ranges from zero to one. An AUC of one indicates 100% accuracy and 100% specificity across all thresholds, or a perfect model, while an AUC of 0.5 is equivalent to a 50/50 guess. The AUC corresponds to overall predictive accuracy of the set of variables to predict a disease state.

Each node of a decision tree is an input variable (biomarker_normalized condition) that can potentially split the observations into the respective outcome bins, LTBI positive or negative and high-risk or not high-risk for our work. The ability of a variable to split data efficiently can be quantified using an impurity measurement. In cohort 1, purity was determined by the ROC curve generated by the variable at that specific node. The variable that resulted in the greatest AUC would be selected for that node. In cohort 2, purity was assessed using the Gini Impurity score, a quantitative value representing the probability of two binary classes at that node.⁶⁹ A score of 0 indicates a perfect classification (i.e., all LTBI positive classified as positive and none as negative) and a score of 1 indicates maximum impurity (i.e., all LTBI positive classified as negative). The different methods were due to differences in the number of samples in clinical bins, with Gini score being the more commonly used method.

Unlike single decision trees, random forests are unable to output specific thresholds of each variable used to make a decision, as a forest is the ensemble of multiple trees that use various thresholds of the variables. However, random forests can calculate the importance each specific variable has towards developing the most accurate data splits.⁷⁰ Each time a variable is used at a node, the impurity reduction is calculated and summed across every tree in the forest. The sum divided by the number of trees in the forest is the importance score for that variable.⁷¹ A greater reduction, or higher score, is desired. Across multiple forests, an average importance score is calculated, and all variables can be compared to each other to identify which variables are most important in making the classifications.

5.5 Results and Discussion

In this work, we implemented a 13-plex protein immunoassay to analyze cytokine and chemokine levels in two cohorts of patients at the Mayo Clinic and employed machine learning to build diagnostic models and identify biomarkers of interest in LTBI diagnostics. TB is a challenging disease to study due to the multiple, fluid phases and complex immune equilibrium. The clinical classification of LTBI was conducted according to QFT manufacturer protocols and high-risk classification was designated using current suggestions and clinical knowledge. We recognize that the lack of a gold standard for clinical classification can potentially hinder the accuracy of this method, as well as any other LTBI or risk related classification tool. However, all subjects across both studies were clinically assessed by a team of clinicians at the Mayo Clinic and final designations were thoroughly checked by the same doctor across both cohorts, aiming to reduce variation cohort to cohort and increase the compatibility. In this report, we will present and discuss the models created with each cohort of patients separately, we will compare

the biomarker concentrations and model results between cohorts, and finally we will compare cohort 2 models with and without the QFT-Plus addition of the TB2 tube.

5.5.1 Cohort 1 model reveals similar cytokines between the LTBI and high-risk designations

The first cohort of patients was enrolled at the Mayo Clinic between July 2017 and December 2018 and microring immunoassay work was completed by Dr. Cole Chapman using one chip batch.⁷² The concentration of each biomarker was normalized within each patient, resulting in a precision normalized method towards personalized medicine and diagnostics. Using the TB1-NIL, TB1-MIT, and MIT-NIL normalized conditions for the 13 biomarkers, 39 input variables per subject were used for the bioinformatics analysis. The random forest model resulted in ROC AUCs of 0.86 and 0.90 for the full and reduced data sets, respectively, with LTBI as the clinical outcome (**Figure 5.1A**) and of 0.76 and 0.83 for the full and reduced data sets, respectively, with high-risk as the clinical outcome (**Figure 5.1B**). The high-risk clinical outcome having a lower predictive accuracy is likely due to the low number of high-risk categorized subjects (13/42). As with most bioinformatics tools, a higher number of samples provide more power to the test and a data set with 13 observations in one bin may be underpowered. However, the LTBI designation had just 18 subjects and performed better. The relatively high performance for both of these models could be related to the alternate impurity measures required for the small sample set and could be lower if Gini impurity scores were able to be used.

The AUCs from full to reduced increased, as expected, by 4% for LTBI classification and 6% for high-risk classification. The reduced feature set consisted of 9 of the 39 variables, or about 25% of the input variables, for LTBI (**Figure 5.1C**) and 8 of the variables for high-risk (**Figure 5.1D**). Reducing the data set removes variables that create noise in the model, allowing

for the most important variables to account for more predictive weight, improving the accuracy of the overall model and decreasing complexity and speed. The input variables used for the reduced data set were selected by identifying the variables with ranges fully above zero in the variable importance metric. Reducing the data begins to identify which biomarkers and conditions are the highest predictors for the clinical designations and eliminates unnecessary input variables.

The most important variables between the two clinical designations of LTBI and high-risk have great overlap in biomarkers. Among the thirteen biomarkers in the panel, only five were used to distinguish the LTBI and high-risk classifications with the relatively high accuracies. The targets of CCL8, IP-10, IL-2, CCL4, and IL-17 were the only biomarkers among the reduced feature sets.

These targets have important implications in TB pathology and diagnostics.¹⁹ CCL8 is a proinflammatory chemokine induced by IFN- γ pathways and attracts immune cells, such as granulocytes and T-cells, to infection sites. CCL8 has been recently identified as an individual biomarker with the ability to discriminate LTBI and active TB with 89% accuracy and is produced at over ten-fold higher levels than IFN- γ .^{73,74} IP-10 is a cytokine associated with inflammation and is secreted from numerous immune cells in response to IFN- γ , among other cytokines.⁷⁵ In the past fifteen years, IP-10 has been extensively studied as an alternate TB biomarker to IFN- γ , with promise in both differentiating active TB and LTBI from healthy controls.^{19,27,31,76,77} IL-2 is an interleukin produced by T-cells, natural killer cells and dendritic cells through adaptive immune response. Similar to IP-10, IL-2 has been a recurring biomarker in TB studies, demonstrating comparable sensitivity as IFN- γ and IP10 for differentiating active TB, LTBI patients, and controls in small sample cohorts.^{78,79} CCL4 is a chemokine activated by

various immune cells, induced by TNF- α , IFN- γ , and IL-1, and was previously identified as an important marker for distinguishing TB cases and household contacts.⁸⁰ Interestingly, the study indicated that CCL4 was unable to discriminate between active and latent TB. IL-17 is an interleukin that has been linked to controlling bacterial growth and host defense in Mtb infection.⁸¹ In combination with TNF- α and IL-12(p40), IL-17 was able to differentiate TB from LTBI and healthy controls with 79% accuracy.⁸² All of the cytokines identified as important for differentiating LTBI and high-risk subjects in cohort 1 have been previously identified in some capacity as relevant in other small cohort diagnostic research, reinforcing the utility of our 13-plex immunoassay and machine learning workflow employed here.

The results from this pilot cohort of 45 samples demonstrated the ability to use the leftover QFT plasma samples and a 13-plex biomarker panel to distinguish LTBI negative and positive and high-risk and not high-risk patients with accuracies of 90% and 83%, respectively. We determined that only a set of five biomarkers under eight (LTBI) or nine (high-risk) conditions are needed to distinguish the clinical designations of interest. After these promising results, we employed the same method in a larger secondary cohort.

5.5.2 Cohort 2 model results in high AUCs and fewer important biomarkers

The second cohort of patients was enrolled at the Mayo Clinic and microring immunoassay work was completed using three chip decks between May 2021 and September 2022. Using the TB1-NIL, TB1-MIT, and MIT-NIL normalized conditions for the 13 biomarkers, 39 input variables per subject were used for the bioinformatics analysis, matching that of cohort 1. The random forest model with LTBI as the clinical outcome resulted in ROC AUCs of 0.85 and 0.88 for the full and reduced data sets, respectively (**Figure 5.2A**) and with high-risk as the clinical outcome resulted in ROC AUCs of 0.90 and 0.91 for the full and reduced

data sets, respectively (**Figure 5.2B**). As expected, the AUCs increased with the feature reduction, although by only 3% for the LTBI and 1% for the high-risk designations. The model developed with the full set of input variables generated relatively high AUCs for random forest models, so minimal increases were generally available. Particularly, the accuracy of 91% for high-risk designation is very promising for this diagnostic panel's ability to identify those at greatest risk of reactivation.

The variable importance metrics revealed that biomarker IP-10 was the main predictor for both LTBI (**Figure 5.2C**) and high-risk (**Figure 5.2D**) classifications. The IP-10 (TB1-NIL) condition is the only predictor in this data set that has the full variable importance metric range above zero, for both classifications. Therefore, the important variables presented in this figure are those with a mean variable importance metric 95% confidence interval that does not include zero. The overwhelming importance value for IP-10 (TB1-NIL) may also explain the low increase between the full and reduced data sets, as most other variables in the data set have no impact on the model, and hence, removing them has very little effect on the accuracy. The other biomarkers of importance in cohort 2 include IL-2, CCL8, CCL4, and TNF- α . Apart from TNF- α , the relevance of these biomarkers in TB infection and diagnostics was discussed within the context of cohort 1. TNF- α is a pro-inflammatory cytokine involved in several signaling events and, while it has not been deployed as a stand along biomarker for TB infection, it has been used successfully in conjunction with other targets to distinguish active from latent TB.^{8,26,82,83}

The results from this second cohort of 87 samples further demonstrated the ability of our workflow to accurately identify both LTBI positive and high-risk patients. These two separate cohorts analyzed in the same method by two study teams can now be compared to validate their results and trends.

5.5.3 Comparing the results across the two cohorts reveals similarities and differences

5.5.3.1 Random forest models vary in sensitivity and specificity

The random forest classification models performed exceptionally well, with the reduced models for both cohorts exhibiting approximately 90% accuracy while distinguishing LTBI positive individuals from the controls (**Figure 5.3A**). The most specific threshold (left vertical segment of the curve) reaches a higher sensitivity in cohort 1. The most sensitive threshold (top horizontal segment of the curve) model reaches a higher specificity in cohort 2, although the differences between the cohorts is marginal with many overlapping thresholds. Sensitivity and specificity are statistical trade-offs. Sensitivity is a measure of the true positive rate, is calculated as:

$$\frac{\textit{True Positives}}{\textit{True Positives} + \textit{False negatives}} = \frac{\textit{Test is positive}}{\textit{All who are positive}}$$

and is interpreted in a diagnostic context as the percentage of chance that the test will correctly identify those who actually have the disease.⁸⁴ Specificity is a measure of the true negative rate, is calculated as:

$$\frac{\textit{True Negatives}}{\textit{True Negatives} + \textit{False positives}} = \frac{\textit{Test is negative}}{\textit{All who are negative}}$$

and is interpreted in a diagnostic context as the percentage chance that the test will correctly determine who does not have the disease.⁸⁴ Conventionally, the true negative rate is converted and reported as a false positive rate by subtracting the calculated true negative proportion from 1. This new metric is interpreted as the chance that a test will incorrectly conclude an observation is positive when it should be categorized as a negative.

It is important to maximize the sensitivity and specificity (or minimize 1-specificity) of a diagnostic test. However, the inversely proportional relationship between these metrics results in

the prioritization of one in most cases. From a precautionary perspective, it is more acceptable to have false positives than false negatives in an LTBI diagnostic test. False positives will lead to additional screening (chest CT, cultures) that would likely rule out disease, whereas false negatives would leave LTBI patients untreated. The high-risk designation follows the same prioritization, in that false positives would lead to more frequent monitoring and urgent treatment, while false negatives would leave those most susceptible to reactivation with less frequent monitoring and less aggressive treatment. Therefore, if we are inclined towards prioritizing sensitivity at the expense of specificity and are more tolerant of a greater false positive rate than a false negative rate, the model with highest sensitivity at more thresholds is the cohort 2 model. However, the high sensitivity of >95% occurs at specificities of 50-60%. The best threshold that maximizes both sensitivity and specificity occur in cohort 1, at approximately 85% sensitivity and 84% specificity, which would be a favorable trade-off.

The cohort 2 model outperformed the cohort 1 model for high-risk classification by 8% in the reduced data sets (**Figure 5.3B**). This model improvement could have been a result of a higher sample size of those in the high-risk bin, which provided the model with more subjects in the bootstrapped data set to better optimize the outcome. Unlike the LTBI model, cohort 2 demonstrated both higher specificity at the most sensitive cutoffs (top horizontal segment of the curve) and higher sensitivity at the most specific cutoffs (left vertical segment of the curve). At all but one threshold, cohort 2 generated a better model, and would, therefore, be preferred for the high-risk classification.

A difference in the model classification does need to be noted, as we are comparing the two models as equivalents. In cohort 1, due to the limited sample numbers, each decision tree was assessed for purity using the AUC of the ROC curve generated by the data split at the end of

the tree. This is in opposition to conventional methods used in cohort 2 that assess decision trees based on the Gini impurity score, a measure of how groups of features split the data into the clinical bins, with zero indicating perfect splits and one indicating maximum impurity. The alternate method was required for completing the random forest analysis on the first cohort and this difference may be a reason for the variation in AUCs. However, we have thus far concluded that the model generated from cohort 2 using the conventional Gini impurity score for tree assessment performed better in high-risk designation and the sensitivities of both cohort models was comparable at moderately high specificity thresholds in the LTBI designation.

5.5.3.2 Comparing variable importance results identified important biomarkers for making both clinical designations

Notably, the most important variables for both LTBI and high-risk designation are highly similar between cohorts, especially when focusing specifically on the biomarkers (**Figure 5.3C-D**). For LTBI designation, the biomarkers of CCL8, IP-10, and IL-2 appeared in the top biomarkers for both cohorts. IL-17 and CCL4 were only in the list for cohort 1 and TNF- α for cohort 2. For high-risk designation, the overlap is more significant, with CCL8, IP-10, IL-2 and CCL4 appearing in the top biomarkers in both cohorts, TNF- α only in cohort 2 and no additional markers in cohort 1. Furthermore, the overlap between LTBI and high-risk biomarkers is extremely high, which may be due to the majority of LTBI subjects also being designated as high-risk. Future work will aim to include more not high-risk LTBI subjects.

These cohorts were led by different study teams, the samples were collected and analyzed by various clinical teams, cytokine concentrations were measured by separate graduate students and sensor chip decks. As discussed above, the method for measuring decision tree impurity, and therefore which biomarkers make a better split, also differed. However, it is clear that the same

biomarkers were important for the chosen clinical designations. This is a significant finding that showcases multiple cohorts yielded highly similar results. We measured concentrations of thirteen biomarkers, yet only six were important for making both clinical decisions in two cohorts of subjects. This reduction in targets would be highly beneficial for the development of a lower plexity assay for use in this workflow, which potentially decreases both the cost of reagents per sample and the inherent complexity of managing a 13-plex assay.

Two difference to note in the variable importance between cohort 1 (**Figure 5.1C-D**) and cohort 2 (**Figure 5.2C-D**) are the order of importance of the variables and a fewer number of important variables in cohort 2. These differences can be attributed to the increased number of patients in cohort 2. More patients result in an increased number of observations in the bootstrapped data sets for machine learning and the model can become more refined by identifying which biomarkers and conditions split the data efficiently using more observations. Furthermore, moving back to the classical machine learning method of using Gini impurity for tree classification assessment in cohort 2 could have resulted in better identification of the biomarkers and conditions that truly split the data. In cohort 1, important conditions were selected based on those that had the full range (min to max) above zero. In cohort 2, across both LTBI and high-risk designations, only one condition, IP-10 (TB1-NIL), had the full range above zero. Therefore, those with confidence intervals of the mean variable importance that do not contain zero were presented. This difference can again be attributed to higher sample count resulting in a convergence on the important conditions, as well as the alternate impurity classification method used in cohort 1.

The final comparison of variable importance results between cohorts also emphasizes the relative importance of each normalized stimulation condition. In general, the top markers are

associated with a normalized condition containing TB1, the TB-specific tube that stimulated patients' blood with the CFP-10/ESAT-6 peptides to elicit a CD4⁺ T-cell response. There is mix of TB1-NIL and TB1-MIT normalized conditions in cohort 1 and more of a reliance on TB1-NIL in the cohort 2. The association of the TB1 condition with the most important markers confirms that TB1 stimulated markers are the most significant contributors to the decisions regarding LTBI and high-risk outcomes. Interestingly, the variables deemed as important, but lower on the list, are generally under MIT-NIL normalized conditions across both cohorts and designations. This implies a reliance on a subject's overall, non-TB-specific, immune response to decide the outcome. In the cohort 1 high-risk designation, the important MIT-NIL biomarkers CCL8, CCL4, and IL-2, are all also identified as important biomarkers under other normalized simulation conditions prior in the list. This indicates that the overall model displays a greater reliance on these biomarkers. For the cohort 1 LTBI designation, two-thirds of the important biomarkers with the MIT-NIL condition, CCL8 and CCL4, are designated as more important on the list under other normalized conditions. However, IL-17 does not appear other than the MIT-NIL normalized condition. Similarly, in both of cohort 2's clinical designations, the MIT-NIL associated biomarker, TNF- α , does not appear under any other condition. These results imply that IL-17 and TNF- α play a role in the TB-related clinical designation outcomes solely based on the subject's overall immune response. This could mean that measuring dysregulation or variations in these cytokines between patients could contribute to the development of new diagnostic methods without TB-specific antigen stimulations.

While the order, weight, and number of conditions varies across cohorts, the general trend of important biomarkers and stimulations hold across them. The data presented here was collected from two temporally distinct cohorts and analyzed by different analysis teams.

Consequently, the strongly overlapping set of important predictive biomarkers between both clinical designations and cohorts highlights the robustness of the random forest models and multiplexed microring resonator immunoassay. These biomarkers should be noted as showing significant promise for developing future LTBI and high-risk diagnostic panels.

5.5.3.3 Cross validation between cohorts implies cohort 1 model is more robust

To understand how the models perform on samples that were not used to generate the model, each cohort of data acted as a clinical validation set for the opposing cohort (**Figure 5.3E**). The data from the opposing cohort was input into the random forest classification models and patients were classified and compared to their ‘true’ label for accuracy. Similar to the other models, the sensitivity and specificity at each threshold is plotted in a ROC curve and AUC is determined. The cohort 1 model cross-classifying cohort 2 patients had a higher AUC than the cohort 2 model cross-classifying the cohort 1 patients using the reduced data set, indicating the cohort 1 models are more robust to outside data in comparison to cohort 2 models.

Both of the LTBI cross-classifications models using the full data set achieved similar AUCs (0.85 for cohort 1 model and 0.83 for cohort 2 model). However, with the reduced set of variables, the AUCs dropped to 0.84 and 0.77, respectively, suggesting the variables removed between the full and reduced models contributed greatly to the classification of subjects. The greater drop for cohort 1 patients being analyzed by cohort 2’s developed model is likely due to the fewer important variables and varying sample sizes, indicating some of the variables removed while developing the reduced model were important for classifying the smaller bins of cohort 1 patients.

Moving into the high-risk model, the full and reduced cohort 1 models were both consistently more accurate than the cohort 2 models at classifying their counterpart data sets.

Cohort 1 models classified cohort 2 patients with AUCs of 0.83 and 0.89 for full and reduced models, respectively, while the cohort 2 models to classify cohort 2 patients resulted in AUCs of 0.77 and 0.78 for the full and reduced models, respectively. Unlike the LTBI cross-classification, the high-risk cross-classification AUC increased from the full to reduced data sets, suggesting the variables important for the opposite group's classification were not removed in the reduced model. However, cohort 1's model still significantly outperforms cohort 2's model overall. Using each cohort as a clinical validation group in the opposite cohort's model demonstrates that classification in both models is partially reliant on the specific conditions used to develop the model, rather than solely on general biomarkers. However, it is reassuring to achieve AUCs >78% for all cross-tested models, indicating that neither cohort's model exhibits excessive overfitting of the training data.

Taken together, the results and discussion in this subsection highlight the similarities in biomarkers and conditions that contribute to the random forest models across both cohorts, with six of the thirteen measured cytokines being the most important and TB1 specific normalized stimulations contributing most frequently. It was hypothesized that the increased sample numbers in cohort 2 allowed the model to focus in on the most important biomarkers, leading to fewer targets with variable importance metrics confidence intervals above zero. However, this decrease in important biomarkers has potentially lowered the model's capability to correctly classify the infection status of new subjects. Future model development should aim to identify fewer important conditions than the cohort 1 model but retain the elevated sensitivity and specificity for high-risk classification displayed by the cohort 2 model.

5.5.3.4 Some raw and normalized biomarker concentrations are different between cohorts when stratified by LTBI designation.

Wilcoxon-Mann-Whitney (WMW) analysis was completed to quantify the differences in distributions of the resulting biomarker concentrations between cohorts when stratified by LTBI status. Identifying differences in populations could reveal variation in assays or in sample populations between cohorts that could provide insight in the model differences highlighted above.

Initial analysis was completed on the log-transformed raw biomarker concentrations, stratified by cohort and LTBI status and binned by QFT stimulation, NIL (**Figure 5.4**), TB1 (**Figure 5.5**), and MIT (**Figure 5.6**). Two types of comparisons are displayed in the figures, intra-cohort comparisons to evaluate the biomarker concentrations between LTBI groupings within each cohort and inter-cohort comparisons to evaluate the biomarker concentrations between cohorts within LTBI groupings. As this chapter is focused on comparing data between cohorts, we will mainly focus on the inter-cohort comparisons. Therefore, there are a total of 26 comparisons per condition to evaluate (13 biomarkers under two clinical bins).

In the NIL condition, nine of these comparisons are statistically different, including CCL3 in LTBI positive ($p \leq 0.001$) and negative ($p \leq 0.0001$), IP10 in LTBI positive ($p \leq 0.05$), IFN- γ in LTBI positive ($p \leq 0.05$), IL-10 in LTBI positive and negative ($p \leq 0.0001$), IL-15 in LTBI positive and negative ($p \leq 0.0001$), and IL-17 in LTBI negative ($p \leq 0.0001$). The NIL condition represents the concentration of the biomarkers upon media stimulation, which would indicate the overall similarity in baseline immune response of the patients in each cohort. Of these listed biomarkers, IL-15 is the only biomarker quantified using different companies for the antibodies (both capture and tracer) between the two cohorts. All other antibodies across cohorts

were sourced from different production lots (both captures and tracers) from the same company, which could potentially contribute marginally towards the differences.

Notably, among the biomarkers with statistically significant differences in inter-cohort comparisons, the relationship of the biomarkers between clinical designations within each cohort, or the intra-cohort comparisons, is the same. For example, IL-10 is one of the three biomarkers with differences between cohorts for both LTBI positive and negative populations. However, within each cohort there is no significant difference in IL-10 concentrations between LTBI positive and negative groups, indicating that the typical biomarker levels are shifted between cohorts, but the overall relationship between the biomarker and LTBI status is cohort independent. This trend holds across all the biomarkers with significant differences in the inter-cohort comparisons. None of the intra-cohort comparisons achieve statistical significance, illustrating that the unstimulated patient samples are likely insufficient to identify LTBI signatures alone. These NIL population results suggest that we could potentially pool the results from the cohorts into one dataset, as the differences between cohorts are results from overall concentration shifts, rather than from differences in relationships of biomarker to disease state. It is promising for this cross-cohort study that the majority of baseline NIL stimulation levels are from statistically similar populations, meaning that variation in other stimulations could be attributed to patient differences.

Both the TB1 and MIT stimulation conditions contain more inter-cohort significant differences, 17 and 18, respectively. Similar to the NIL stimulation, many of the biomarkers with the inter-cohort significant differences have the same significance in intra-cohort comparisons. To show this point in TB1, we can look at two examples: TNF- α and IP-10, both biomarkers that were designated as important in LTBI-associated machine learning models. For TNF- α , there are

differences between cohorts within both clinical bins, but no significance between clinical bins within each cohort. Similarly, for IP-10 there are inter-cohort differences and there is the same level of significance ($p \leq 0.0001$) in the intra-cohort comparison. This trend persists in the MIT stimulation.

There are a few instances in which this trend does not hold, namely CCL2 in TB1 and CCL8, IFN- γ , TNF- α and IL-2 in MIT. These targets are some of the most important predictors in the previously presented models for both cohorts. Since these biomarkers, and therefore assays, were determined to be similar across cohorts using the baseline NIL stimulation, these variations are hypothesized to be true differences in the T-cell responses to stimulations across cohorts. The two cohorts differ in some demographics of patients within status bins (**Table 5.1** and **Table 5.2**). While the average age of patients is similar between cohorts, cohort 1 has a greater proportion of females in the LTBI positive classification than cohort 2 and the proportions of self-reported ethnicities vary between cohorts. These basic demographic differences could be a reason for the variation in stimulation responses, however, more data points within specific demographic groupings are needed to test this hypothesis.

While it was important to assess the variation in raw biomarker concentrations between cohorts to identify potential assay and population-specific effects, the random forest models described above do not use the raw concentrations in the models, rather they use the normalized conditions. Biomarker concentrations in the three normalization conditions were plotted and analyzed using the same method as the raw biomarkers, except that the absolute values after normalization were used for plotting as opposed to log transformed values, due to the presence of negative values generated by the normalization subtraction. The data tested were from the TB1-NIL (**Figure 5.7**), TB1-MIT (**Figure 5.8**), and MIT-NIL (**Figure 5.9**) conditions.

The TB1-NIL condition has 9 significant differences among the 26 inter-cohort combinations, while TB1-MIT has 19 differences, and MIT-NIL has 15 differences. However, the trend of differing inter-cohort levels paired with equivalent intra-cohort differences holds for the majority of these statistically significant differences, again indicating a shift among the normalized biomarkers overall between cohorts, not specific to clinical status. The exceptions include CCL2 in TB1-NIL, CCL8, TNF- α , and IFN- γ in TB1-MIT, and CCL8, TNF- α , IFN- γ , and IL-2 in MIT-NIL. These exceptions to the trends are also evident in the raw MIT concentrations mentioned above, and likely originate from the MIT stimulation.

The overall comparison of the raw and normalized biomarker levels between cohorts aims to provide helpful insight for pooling the two cohorts together. In further work (Chapter 6), the two cohorts of data will be pooled into one group, as the combined sample numbers will increase the power and implications for the random forest model relative to two smaller cohorts of subjects. A classification model derived from the pooled cohort is hypothesized to be more robust than models derived from individual cohorts due to the increased number of samples in clinical classification bins. However, the pooled data is subjected to inherent biological differences between cohorts. Literature surrounding pooling data when biomarkers are measured at multiple test sites or by different assays advises to use calibration parameters and interaction models to ensure homogeneity within the full sample set.^{85,86} In this study, two cohorts were recruited during two different windows of time and the samples were analyzed by different individuals. However, recruitment and clinical classifications were completed according to standardized procedures and samples were analyzed with the same assay and instrumentation. Additionally, the differences caused by changing analysis teams between the cohorts was minimized by thorough training on the assay and method. The baseline NIL biomarker

concentrations are similar across cohorts and the overall trend of the biomarkers with significant inter-cohort differences having the same intra-cohort significance is consistent across raw and normalized concentrations. Taken together, these findings do not present any evidence that a classification model derived from a pooled cohort would be biased by cohort-specific artifacts.

5.5.4 Inclusion of a secondary TB specific tube does not improve the model

The work described up until this section focused on three stimulation conditions, NIL, TB1, and MIT, from the QFT test that was used exclusively for cohort 1. Cohort 2 was analyzed with the QFT-Plus assay, which included a secondary TB specific stimulation condition, TB2. Until now, we have not included the data from this tube in analysis. However, the disregarded data represents 25% of the samples that were analyzed from cohort 2. To explore the effects of adding this stimulation condition to the method, we repeated the analysis of cohort 2 subjects with the biomarker concentrations resulting from the TB2 stimulation tube. The addition of this tube led to three new normalized conditions (TB2-NIL, TB2-MIT, and TB1-TB2) in addition to the original three. The six normalized conditions for the thirteen biomarkers resulted in 78 variables per subject for subsequent random forest model development.

5.5.4.1 Paired statistical analysis suggests very little difference in biomarker concentrations between TB1 and TB2

To first compare the impacts of each TB-specific stimulation tube on the biomarker concentrations, paired Wilcoxon signed-rank tests were completed for biomarker concentration between TB1 and TB2, stratified by LTBI (**Figure 5.10**) and high-risk (**Figure 5.11**) status. A paired test was selected because each patient provided both a TB1 and TB2 stimulation sample, so these observations in the data set are not independent. The 26 comparisons of interest

correspond to the concentration differences of 13 biomarkers between TB1 and TB2 conditions for both LTBI positive and LTBI negative individuals.

For LTBI status, there is one single statistical difference between TB1 and TB2 induced biomarker concentrations: CCL8 within LTBI negative subjects ($p \leq 0.05$). Similarly, when stratified by high-risk status, there are three statistical differences within the 26 possible tests: CCL8 within high-risk ($p \leq 0.05$), and TNF- α and IL-8 within not high-risk ($p \leq 0.05$) groups. Interestingly, all these statistical differences in biomarker concentrations are at the lowest level of significance. The very few significant conditions and no highly significant differences indicate there is very little difference in the biomarker profiles of the two different QFT stimulation conditions of TB1 and TB2.

5.5.4.2 Random forest model with TB2 tube does not increase predictive accuracy or identify different biomarkers compared to model without TB2 tube

The random forest model was constructed with the same method used on cohort 2 above, albeit now with double the number of input variables available to the model. The model with LTBI as the clinical outcome resulted in ROC AUCs of 0.85 and 0.87 for the full and reduced data sets, respectively (**Figure 5.12A**). With high-risk as the clinical outcome, ROC AUCs of 0.89 and 0.92 for the full and reduced data sets, respectively, were achieved (**Figure 5.12B**). These AUCs are heavily reminiscent of those produced from the cohort 2 model without the TB2 stimulation (0.88 and 0.91 for LTBI and high-risk reduced models, respectively). The addition of an additional TB stimulation tube, leading to three new normalized conditions, only changed the AUCs by 1%, which is within the noise threshold of the model. AUCs of such similarity to the first model without TB2 suggests the TB2 tube is of no greater importance than the TB1 tube results in either LTBI or high-risk classification using our method.

The variable importance metrics for the random forest model upon inclusion of the TB2 stimulation were constructed for LTBI classification (**Figure 5.12C**) and high-risk classification (**Figure 5.12D**). These results were compared to the results from the model without TB2 stimulation data for LTBI classification (**Figure 5.12E**) and high-risk classification (**Figure 5.12F**). No additional biomarkers were selected as important when TB2 was added into the model. In most cases across both clinical designations, important TB2-associated biomarkers were present as important TB1-associated biomarkers. For example, IP-10 (TB1-NIL) is the heavily favored top predictor for both LTBI and high-risk status in the initially reported cohort 2 models. When TB2 data was added, IP-10 (TB2-NIL) was selected as the second most important variable. This same TB2 redundancy occurs with IP-10 (TB1 and TB2 -MIT) in the reduced LTBI model and CCL8 and IL-2 (TB1 and TB2-MIT) in the reduced high-risk model. In the random forest algorithm, this translates to similar contributions towards the model by both TB1 and TB2 conditions. However, the results presented in **Figure 5.12** reaffirm that the TB2 condition is not necessarily needed when the TB1 condition is included.

A difference in the variable importance results presented here must be noted. In cohort 2, we presented and focused on the important variables that have 95% confidence intervals for the variable importance mean above zero. The same convention is applied for the high-risk classification presented here. However, for the LTBI classification, only two features (IP-10 TB1 and TB2- NIL) display confidence intervals greater than zero. To expand the important variables to allow for more thorough comparisons to the model lacking TB2, we included variables with a mean importance metric greater than 0.3% and have indicated these with lighter fill color in the figure. This threshold was selected since it correlated to a ten-fold reduction in the average importance of the top ranked variable.

In summary, the addition of the TB2 QFT-Plus stimulation condition does not significantly change the AUCs of either clinical designation. Additionally, TB2 fails to provide additional information into important biomarkers for clinical status prediction, and instead increased the predictive weight of a smaller set of biomarkers that were already associated with TB1 stimulation conditions. The TB2 QFT-Plus stimulation is a peptide concoction designed to elicit a CD4+ T-cell (same peptides as TB1 stimulation) and a CD8+ T-cell response. Previous work, albeit with small sample sizes, has reported that LTBI patients routinely exhibit a CD4+ T-cell response upon QFT-Plus antigen stimulation, but very few illicit a CD8+ T-cell response relative to active TB patients.⁸⁷ Furthermore, CD8+ T-cells have not been found to play a role in the host immune system during the latent TB phase.⁸⁸ The minimal differences between TB1 and TB2 stimulated biomarkers among LTBI patients observed here supports these findings. While TB2 may not be a useful addition to this current workflow, it may be important if the patients demonstrate low CD4+ T-cell responses, have active TB infection, or are immunocompromised.⁸⁹ Future work should consider the additional costs (personnel and assay reagents) and time associated with analyzing the TB2 stimulated samples and identify if the expected results are worth these additional costs.

5.6 Study Limitations

There are several limitations involved in these studies. One limitation not unique to our work is the lack of gold standards for LTBI and high-risk designations. We rely on current TB guidelines and clinical collaborator knowledge to make the clinical indications we use as the ‘true’ LTBI or risk-related status for the patients in our cohorts. This approach is particularly notable in the high-risk designation, since an online risk assessment tool is used that incorporates diagnostic test result, country of origin, recent travel, and occupation to classify reactivation risk

potential. Incorrectly categorized clinical designations may introduce inaccuracies and biases into the final model, minimizing optimal model performance. A second limitation is the cohort sizes, specifically for cohort 1. Relatively small numbers of samples within clinical bins can lead to suboptimal power to differentiate true differences between groups. However, the first cohort served as an initial proof of concept study to be followed with a larger secondary cohort, and many other studies mentioned through this chapter had similar sized patient cohorts. The third limitation is the use of non-specific, general inflammatory biomarkers for diagnosis. Many of these markers will change in response to any infection, including sepsis, pneumonia, or COVID-19. This could lead to low specificity in our diagnostic tool and future work will need to compare the ability of the models to differentiate LTBI from other respiratory infection groups. A fourth limitation is that our work does not include differentiation between multiple phases of TB infection, but rather focuses solely on the presence or absence of latent infection. More diagnostic value would be gained from parsing out unique signatures that could differentiate LTBI, subclinical TB, active TB, incipient TB, and patients who have cleared Mtb infection from each other and from healthy controls. Additionally, we can also consider the high-risk designation, in that our bins were those at a high reactivation risk vs all others, with high-risk subjects including LTBI positive and negative individuals with clinical indication of high risk based on previous exposures. Ideally, we could study a cohort of only LTBI positive patients to differentiate which individuals are at a high-risk, a low-risk, or indeterminate risk of reinfection. Deriving signatures that account for all these mentioned clinical groups would require access to a much larger cohort of subjects than our current study population. Future work will aim to address this limitation by introducing varying risk levels, TB case contacts, active TB disease, non-tuberculosis mycobacterium controls, and pneumonia controls. The work presented in this

chapter is focused on comparing results derived from two cohorts specifically focused on LTBI and high-risk designation, which does not require information about the additional phases of TB infection.

5.7 Conclusion

TB infection is characterized by multiple phases in a dynamic equilibrium that can result in a reactivation to active TB upon perturbation. Identifying individuals who are LTBI positive and those who are at a high risk of reactivation would be advantageous for improving treatment and monitoring of patients. We used a multi-biomarker immunoprotein assay to profile thirteen biomarkers in two separate cohorts of patient samples. Across both cohorts, a predictive accuracy of almost 90% was achieved for LTBI positive versus LTBI negative patients. The first cohort achieved 83% accuracy as discriminating individuals at a high risk of reactivation from non-high-risk individuals, while the second cohort improved the accuracy to 91%. There was high overlap in the important biomarker conditions for making the predictions between cohorts, which can facilitate the development of lower-plexity assays. When comparing the biomarker levels between the cohorts when stratified by stimulation condition and LTBI status, we found that while there were significant inter-cohort differences, the intra-cohort significance of these biomarkers was equivalent. These trends, in combination with the samples being analyzed using the same assay and the same instrument, indicate it would be appropriate to combine the two cohorts to derive an improved machine learning model. Finally, the effect of the TB2 tube from the QFT-Plus assay was assessed and did not provide any improvements or new information relative to the classification model without TB2. Consequently, the cost and time associated with running an additional sample for each patient may not warrant the continued analysis of the TB2 stimulated samples in this workflow. In conclusion, we developed a classification regime to

stratify patients by LTBI and high-risk status using analytical tools and techniques combined with machine learning algorithms and leftover QFT plasma samples that produced comparable results across two cohorts of subjects.

5.8 Figures

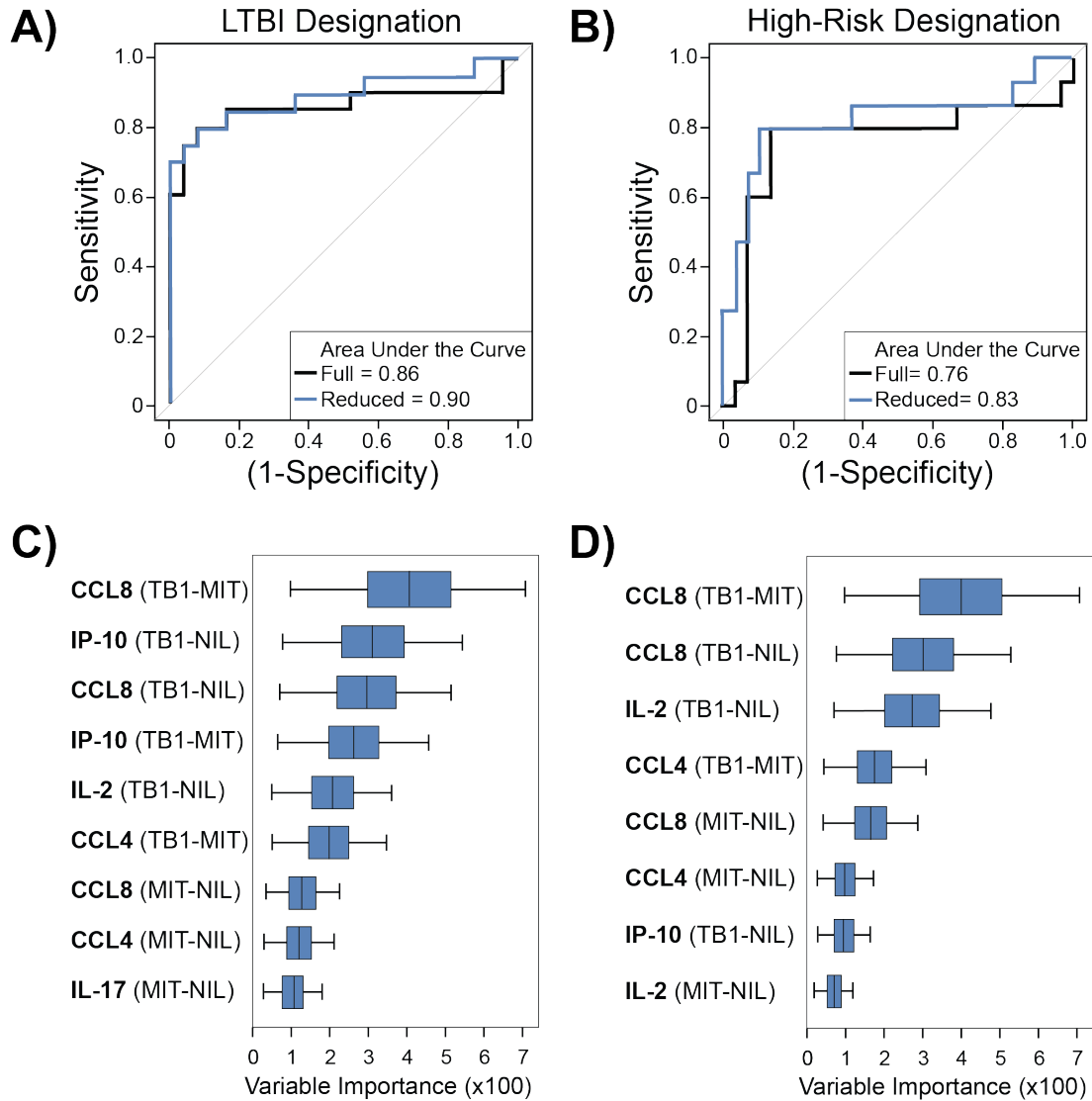


Figure 5.1 Random forest model results for Cohort 1: 42 patients with 45 subject sets. ROC curve for differentiating (A) LTBI positive and negative subjects and (B) high-risk vs not high-risk using normalized conditions. The full model uses all available features for prediction and the reduced model uses the top nine (LTBI) or eight (risk) features. Variable importance for (C) LBTI status and (D) high-risk status for the reduced data set identifies the features with full range above zero.

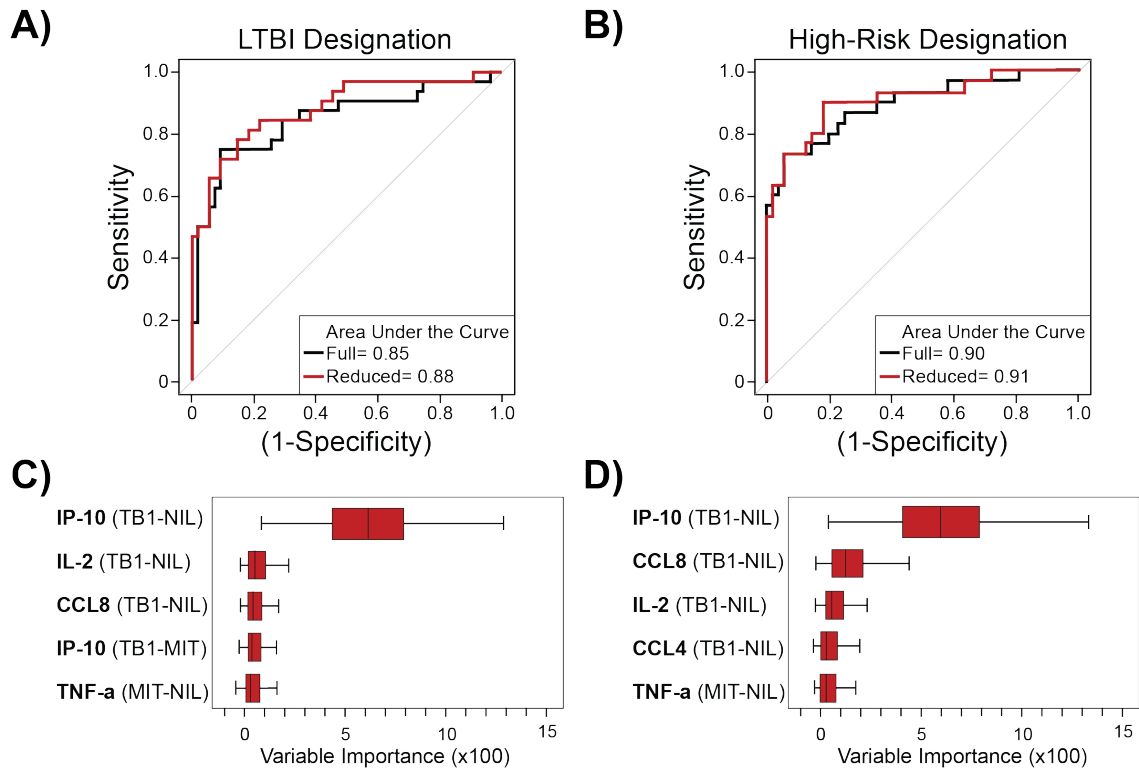


Figure 5.2 Random forest model results for Cohort 2: 72 patients with 87 subject sets. ROC curve for differentiating (A) LTBI positive and negative subjects and (B) high-risk vs not high-risk using normalized conditions. The full model uses all available features for prediction and the reduced model uses the top features. Variable importance for (C) LBTI status and (D) high-risk status for the reduced data set identifies the features with 95% confidence intervals above zero.

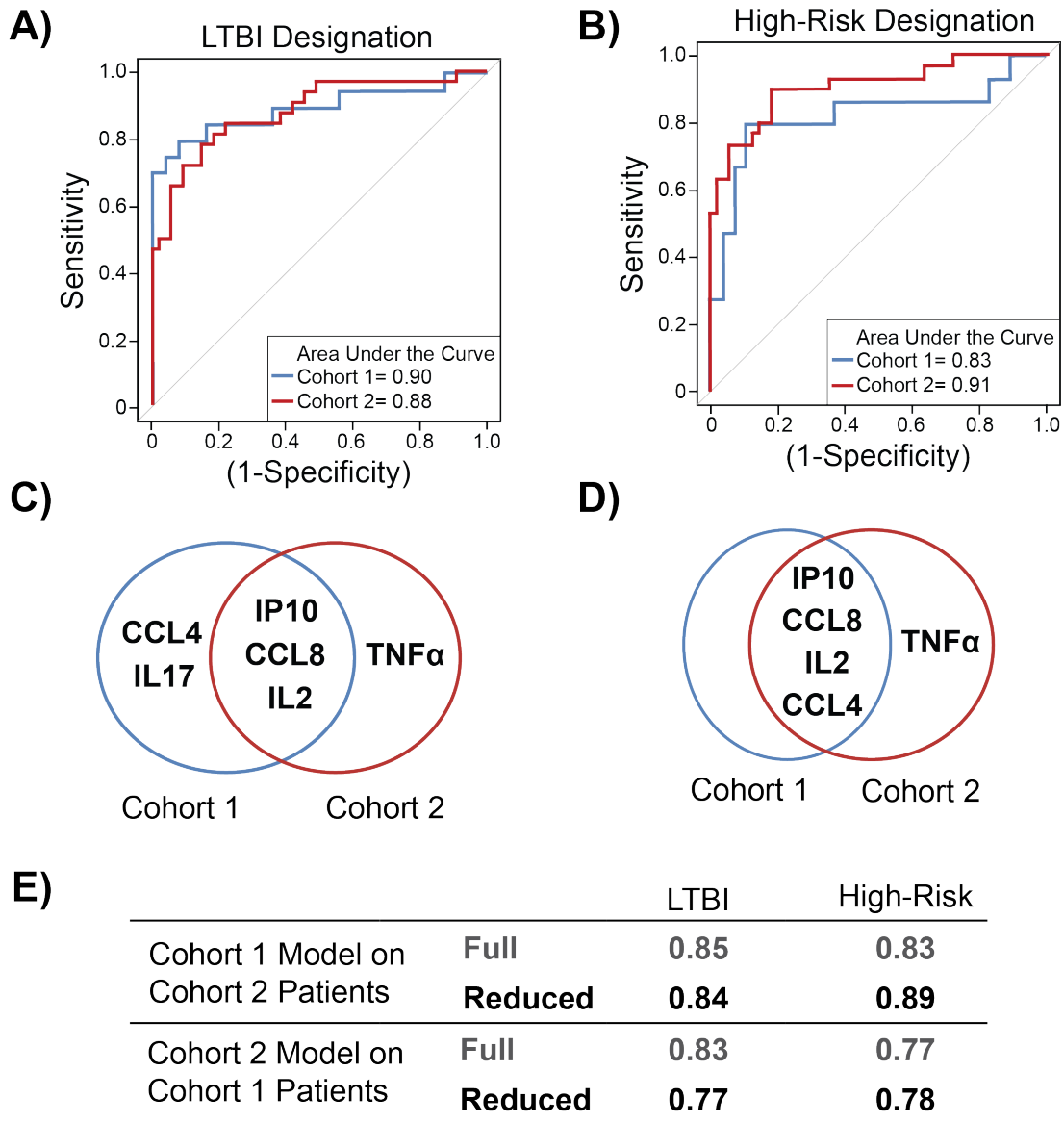


Figure 5.3 Comparison of models across the two subject cohorts. The reduced ROC curves for cohorts 1 and 2 are presented for both (A) LTBI and (B) high-risk designations, for visual comparison. Venn diagrams are presented to highlight the biomarkers present in the top predictive features for (C) LTBI and (D) high-risk designations across both cohorts. Cross validation of the models was completed by inputting the data from one cohort into the model constructed from the opposite cohort. The ROC AUCs (D) are a measure of how well the opposing model classified patients across all classification thresholds.

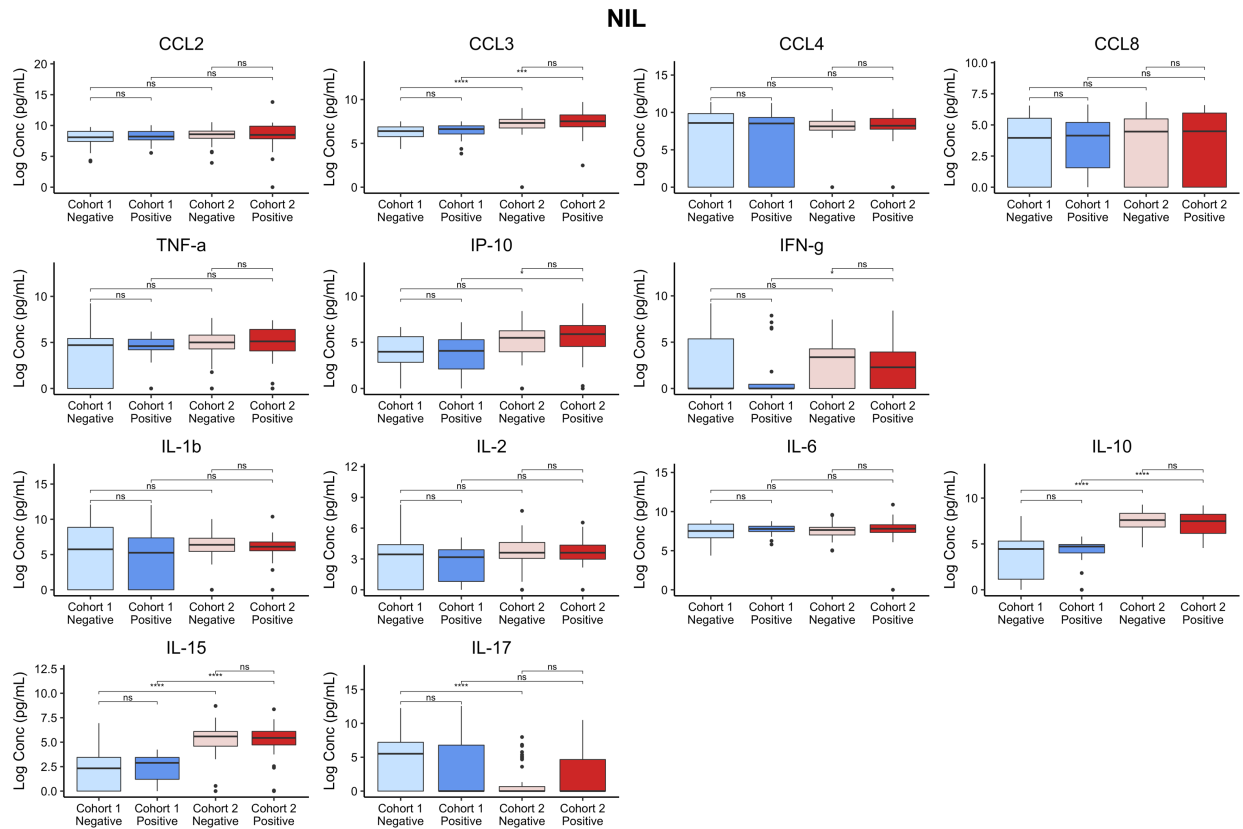


Figure 5.4 Comparison of biomarkers across cohorts, stratified by LTBI status, for the NIL condition. The plots show the statistical test results for comparing the concentrations of biomarkers between cohort 1 and 2 LTBI negative patients, between cohort 1 and 2 LTBI positive patients, and within cohort LTBI positive and negative using Wilcoxon-Mann-Whitney. The cohort 1 LTBI negative and positive bins contain 25 and 20 points, respectively, and the cohort 2 LTBI negative and positive bins contain 55 and 32 points, respectively. The data has been log transformed for visualization. (ns= $p > 0.05$, * = $p \leq 0.05$, ** = $p \leq 0.01$, *** = $p \leq 0.001$, **** = $p \leq 0.0001$)

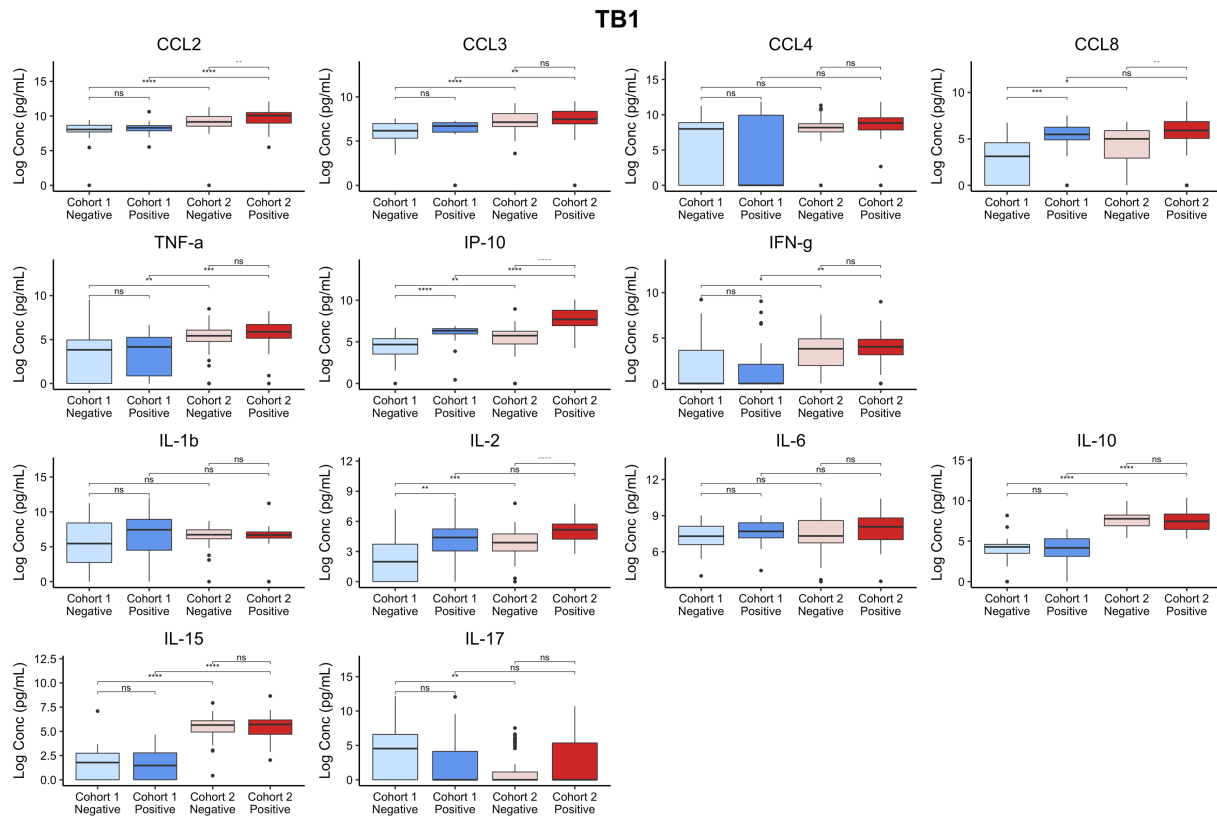


Figure 5.5 Comparison of biomarkers across cohorts, stratified by LTBI status, for the TB1 condition. The plots show the statistical test results for comparing the concentrations of biomarkers between cohort 1 and 2 LTBI negative patients, between cohort 1 and 2 LTBI positive patients, and within cohort LTBI positive and negative using Wilcoxon-Mann-Whitney. The cohort 1 LTBI negative and positive bins contain 25 and 20 points, respectively, and the cohort 2 LTBI negative and positive bins contain 55 and 32 points, respectively. The data has been log transformed for visualization. (ns= $p > 0.05$, * = $p \leq 0.05$, ** = $p \leq 0.01$, *** = $p \leq 0.001$, **** = $p \leq 0.0001$)

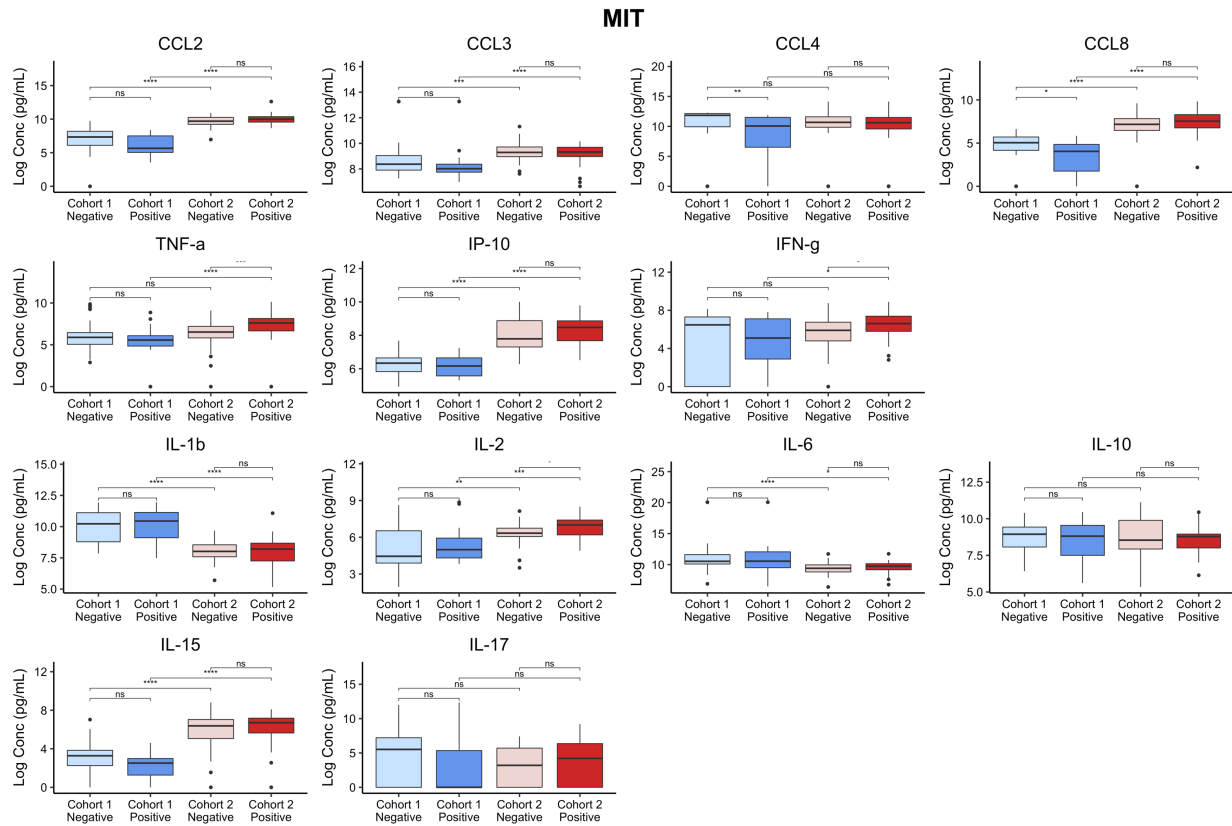


Figure 5.6 Comparison of biomarkers across cohorts, stratified by LTBI status, for the MIT condition. The plots show the statistical test results for comparing the concentrations of biomarkers between cohort 1 and 2 LTBI negative patients, between cohort 1 and 2 LTBI positive patients, and within cohort LTBI positive and negative using Wilcoxon-Mann-Whitney. The cohort 1 LTBI negative and positive bins contain 25 and 20 points, respectively, and the cohort 2 LTBI negative and positive bins contain 55 and 32 points, respectively. The data has been log transformed for visualization. (ns= $p > 0.05$, * = $p \leq 0.05$, ** = $p \leq 0.01$, *** = $p \leq 0.001$, **** = $p \leq 0.0001$)

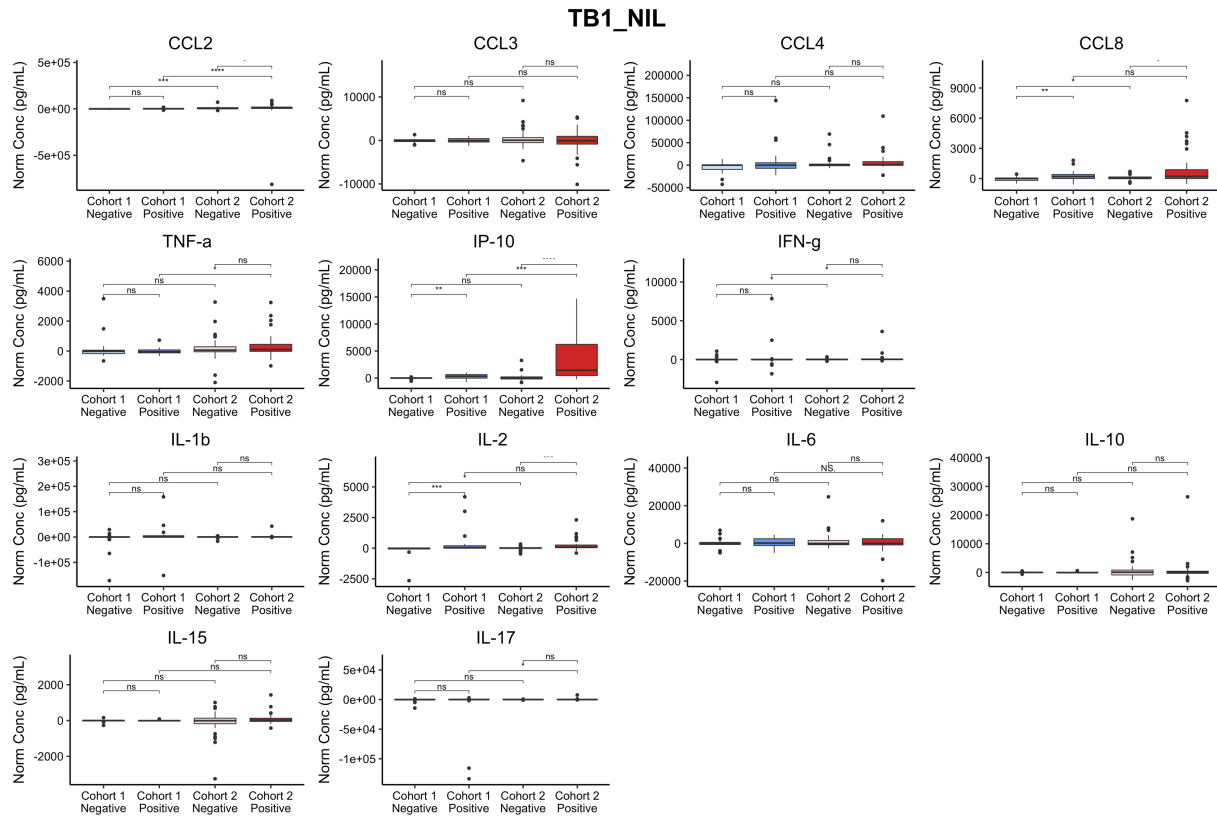


Figure 5.7 Comparison of biomarkers across cohorts, stratified by LTBI status, for the TB1-NIL normalized condition. The plots show the statistical test results for comparing the concentrations of biomarkers between cohort 1 and 2 LTBI negative patients, between cohort 1 and 2 LTBI positive patients, and within cohort LTBI positive and negative using Wilcoxon-Mann-Whitney. The cohort 1 LTBI negative and positive bins contain 25 and 20 points, respectively, and the cohort 2 LTBI negative and positive bins contain 55 and 32 points, respectively. (ns= $p > 0.05$, * = $p \leq 0.05$, ** = $p \leq 0.01$, *** = $p \leq 0.001$, **** = $p \leq 0.0001$)

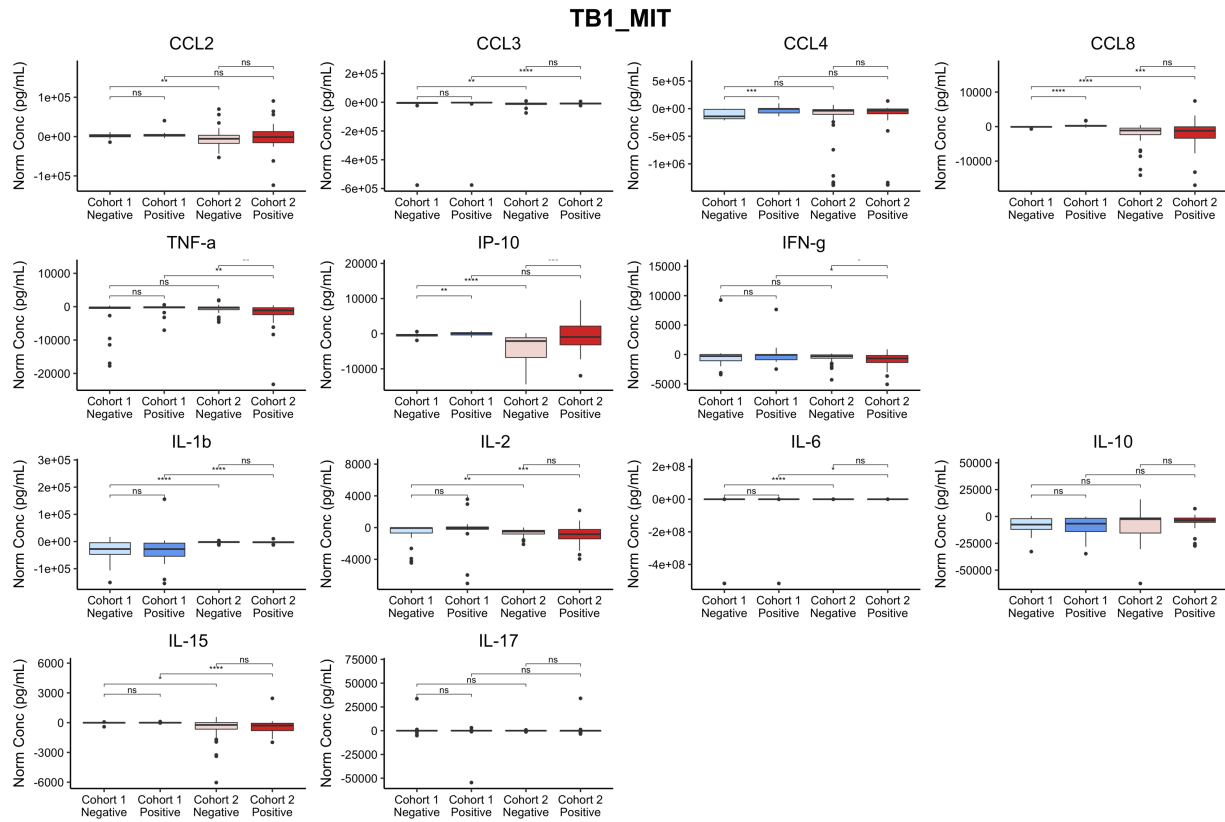


Figure 5.8 Comparison of biomarkers across cohorts, stratified by LTBI status, for the TB1-MIT normalized condition. The plots show the statistical test results for comparing the concentrations of biomarkers between cohort 1 and 2 LTBI negative patients, between cohort 1 and 2 LTBI positive patients, and within cohort LTBI positive and negative using Wilcoxon-Mann-Whitney. The cohort 1 LTBI negative and positive bins contain 25 and 20 points, respectively, and the cohort 2 LTBI negative and positive bins contain 55 and 32 points, respectively. (ns= p>0.05, *= p≤0.05, **= p≤0.01, ***= p≤0.001, ****= p≤0.0001)

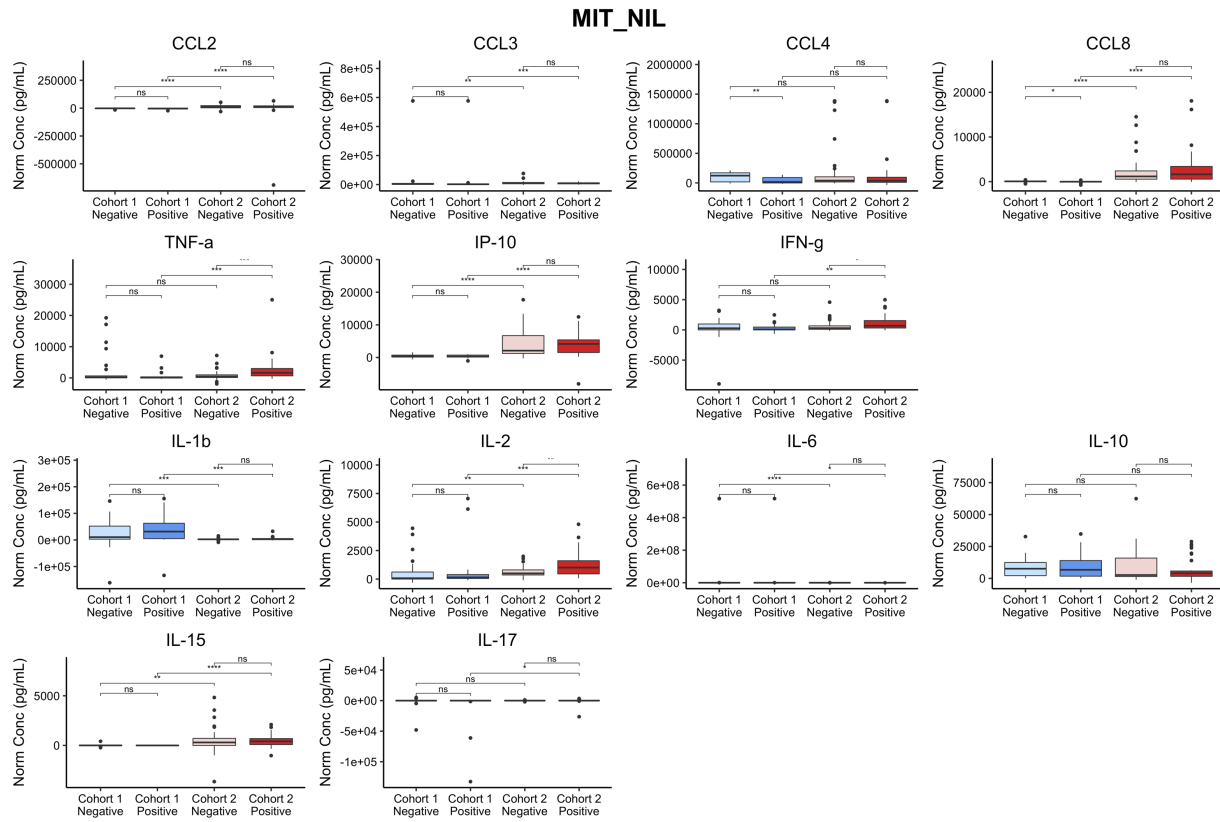


Figure 5.9 Comparison of biomarkers across cohorts, stratified by LTBI status, for the MIT-NIL normalized condition. The plots show the statistical test results for comparing the concentrations of biomarkers between cohort 1 and 2 LTBI negative patients, between cohort 1 and 2 LTBI positive patients, and within cohort LTBI positive and negative using Wilcoxon-Mann-Whitney. The cohort 1 LTBI negative and positive bins contain 25 and 20 points, respectively, and the cohort 2 LTBI negative and positive bins contain 55 and 32 points, respectively. (ns= p>0.05, *= p<0.05, **= p<0.01, ***= p<0.001, ****= p<0.0001)

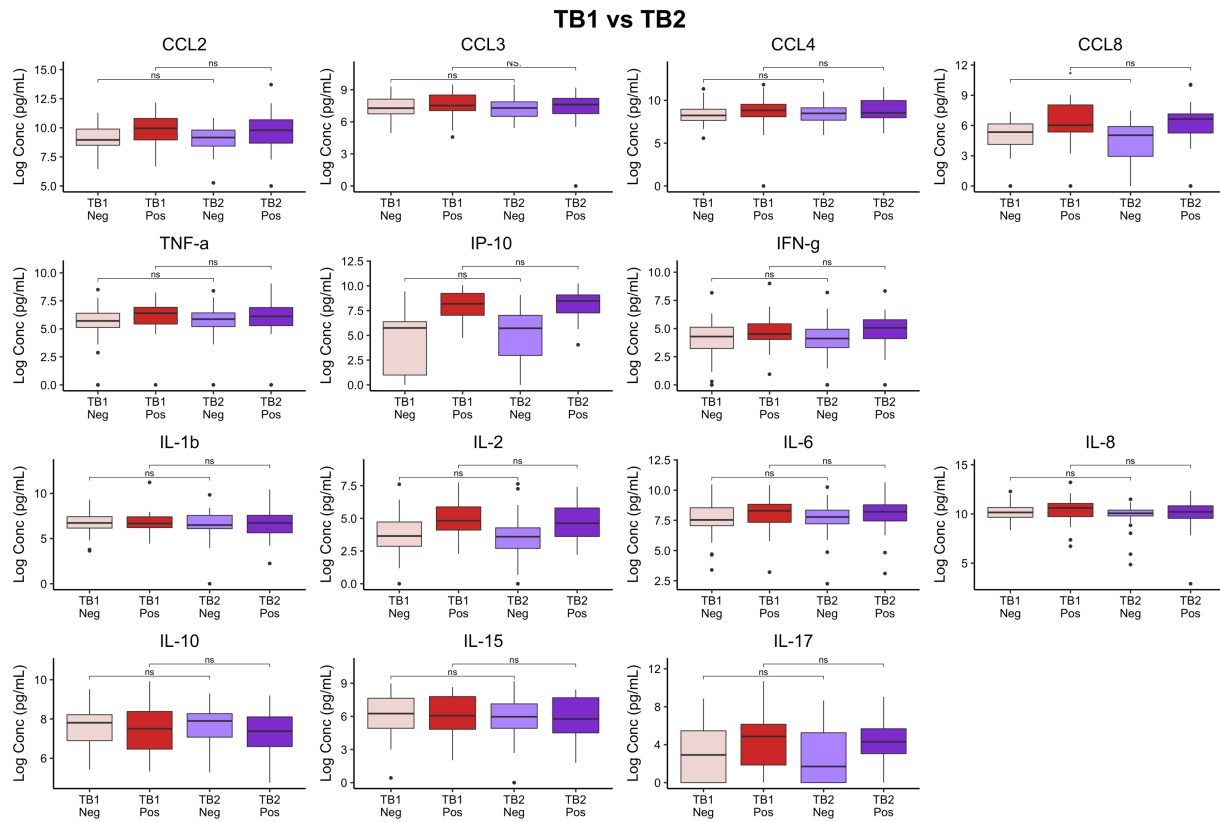


Figure 5.10 Paired comparisons of cytokine values within TB1 and TB2 stimulations, stratified by LTBI status. The TB1 and TB2 conditions are compared within LTBI negative subjects and within LTBI positive using the non-parametric paired Wilcoxon signed-rank test. The two LTBI negative bins contain 55 subject data points. The two LTBI positive bins contain 32 subject data points. (ns= $p > 0.05$, * = $p \leq 0.05$, ** = $p \leq 0.01$, *** = $p \leq 0.001$, **** = $p \leq 0.0001$)

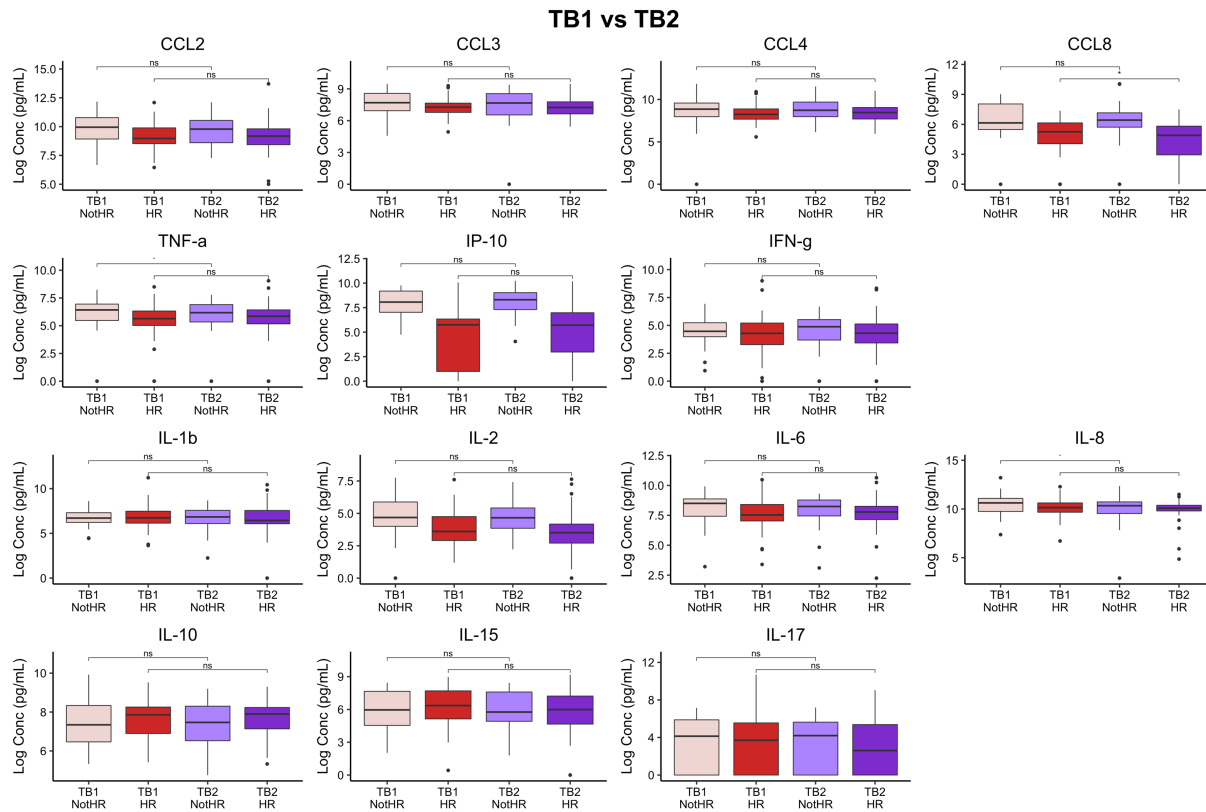


Figure 5.11 Paired comparisons of cytokine values within TB1 and TB2 stimulations, stratified by high-risk status. The TB1 and TB2 conditions are compared within high-risk (HR) designated subjects and within not high-risk (NotHR) designated subjects using the non-parametric paired Wilcoxon Test. The two High-Risk bins contain 55 subject data points. The two not high-risk bins contain 32 subject data points. (ns= $p > 0.05$, * = $p \leq 0.05$, ** = $p \leq 0.01$, *** = $p \leq 0.001$, **** = $p \leq 0.0001$)

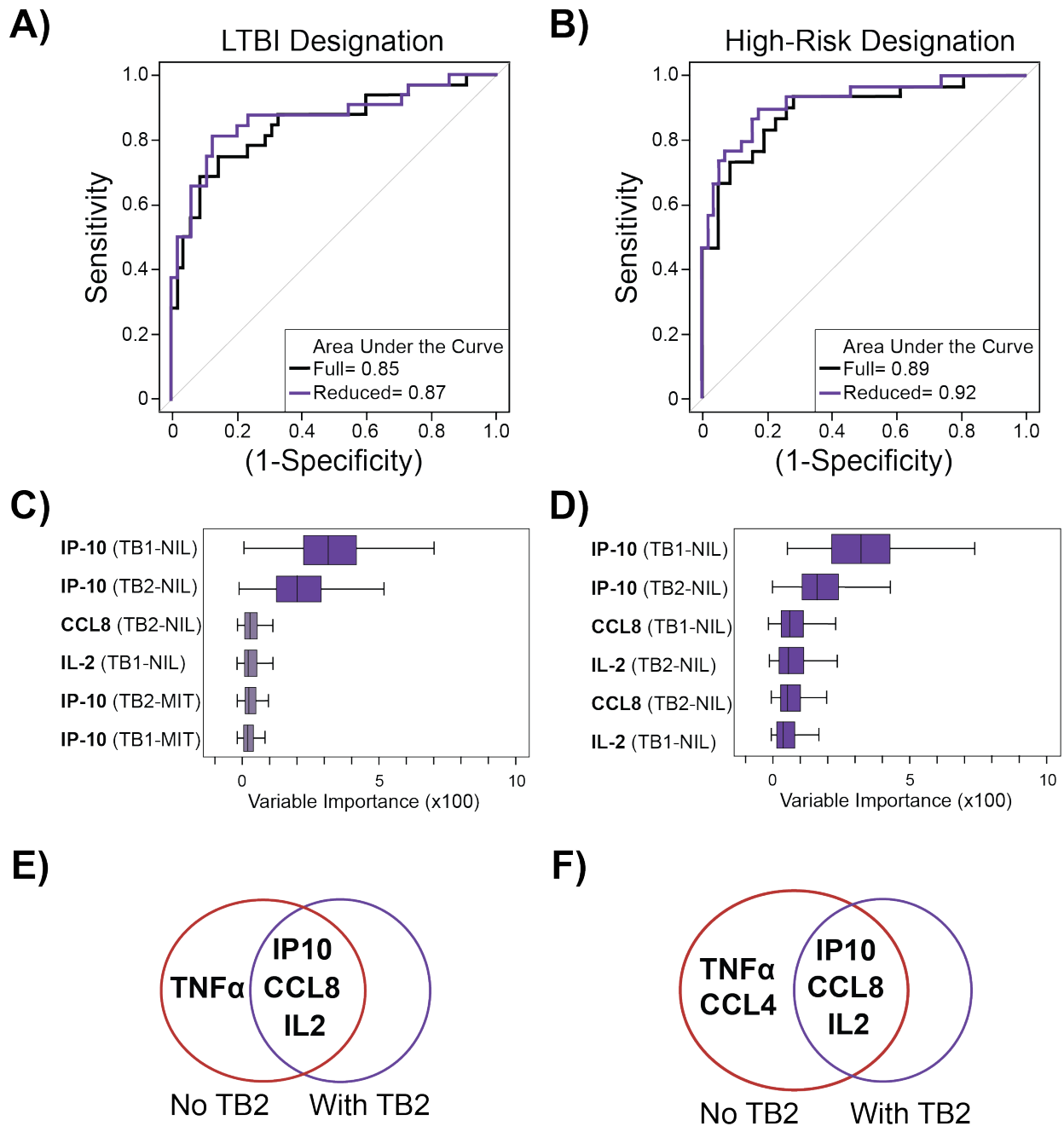


Figure 5.12 Random forest model results for secondary cohort including the QFT TB2 stimulation. ROC curve for differentiating (A) LTBI positive and negative subjects and (B) high-risk vs not high-risk subjects using all four QFT stimulation tubes. The full model uses all available features for prediction and the reduced model uses the top features. Variable importance from random forest algorithm for (C) LBTI status and (D) high-risk status for the reduced data set identifies the features with 95% confidence intervals above zero (dark purple). In C, only two features have 95% confidence intervals above zero. The light purple features indicate features with greater than 0.3% average importance. This cutoff corresponds to 10% of the average importance for the top variable. Venn diagram highlighting the biomarkers present in the top predictive features for (E) LTBI and (F) high-risk designations in models with and without the additional TB specific tube (TB2).

5.9 Tables

Table 5.1 Patient demographics by pertinent clinical categories for cohort 1.

	Subjects, no. (%) ^a				P value ^b
	All (n=42)	LTBI- (n= 24)	LTBI+ (n= 18)	High Risk+ (n=13)	
Sex (female)	28 (66.7)	17 (70.8)	11 (61.1)	6 (46.2)	0.529
Age, years					
Mean ± SD	53.3±17.6	59.4±14.7	45.4±18.3	46.3±20.1	0.016
Range	22-84	26-84	22-81	22-81	
Ethnicity					
Caucasian	32 (76.1)	22 (91.7)	10 (55.6)	6 (46.1)	<0.001
African American	2 (4.8)	0 (0)	2 (11.1)	2 (15.4)	
Asian Pacific	2 (4.8)	2 (8.3)	0 (0)	0 (0)	
Hispanic	1 (2.4)	0 (0)	1 (5.6)	0 (0)	
Others	5 (11.9)	0 (0)	5 (27.7)	5 (38.5)	
Place of Birth ^c					
US Born	30 (71.4)	20 (83.3)	10 (55.6)	6 (46.1)	0.033
Foreign Born (High TB)	1 (2.4)	3 (12.5)	8 (44.4)	7 (53.9)	
Foreign Born (Low TB)	11 (26.2)	1 (4.2)	0 (0)	0 (0)	
History of BCG vaccination					
Yes	7 (16.7)	3 (12.5)	4 (22.2)	3 (23.1)	0.583
No	30 (71.4)	19 (79.2)	11 (61.1)	7 (53.8)	
Unknown	5 (11.9)	2 (8.3)	3 (16.7)	3 (23.1)	
Occupation					
Health care worker, direct patient care	13 (30.9)	7 (29.2)	6 (33.3)	4 (30.7)	0.453
Health care worker, no direct patient care	18 (42.9)	9 (37.5)	9 (50.0)	6 (46.2)	
Other	11 (26.2)	8 (33.3)	3 (16.7)	3 (23.1)	
Adjusted predicted cumulative TB risk (%) ^d					
Mean ± SD	3.09±9.43	0.60±1.08	6.41±13.87	8.49±15.99	<0.001
Range	0 – 61.25	0 – 3.81	0.1 – 61.25	0.1 – 61.25	
History of immunosuppression ^e (yes)	6 (14.3)	5 (20.8)	1 (5.6)	1 (7.7)	0.371
Tuberculin skin test					
TST (+)	23 (54.8%)	10 (41.7)	13 (72.2)	9 (69.2)	0.103
TST mm induration (median; range)	14.5 (0-24)	0 (0-18)	17 (0-24)	20 (0-24)	
IGRA test					
QFT (+)	16 (39.0)	0 (0)	16 (88.9)	11 (84.6)	<0.001
QFT results (Mean ± SD; IU/mL) ^f	1.89±3.46	0 (0)	4.31±4.15	5.64±4.18	

Abbreviations: IGRA = Interferon-gamma release assay; SD = Standard deviation; High TB = High incidence of TB; Low TB = Low incidence of TB; QFT = QuantiFERON TB Gold In-Tube™ or QuantiFERON TB Gold Plus™; TST = Tuberculin skin test. HIV = Human immunodeficiency virus. HCW = healthcare worker.

^a Study included 42 subjects. The total sample set analyzed were 45 samples, encompassing 42 unique subjects and 3 additional time points separated by 5-7 months in testing, representing unique samples.

^b P value for comparison between subjects with LTBI diagnosis vs. no LTBI diagnosis by current diagnostic guidelines (Two-tailed Fisher's Exact test or r x c Exact contingency table, Wilcoxon rank sums when appropriate).

^c High incidence of TB was defined as a country with ≥20 cases per 100,000 population per year. 2020 WHO Global tuberculosis report (http://www.who.int/tb/publications/global_report/en/).

^d Adjusted estimates for the individual cumulative risk of TB reactivation are based on “The Online TST/IGRA interpreter” prediction modeling that includes TST and IGRA results, risk factors for LTBI and risk factors for progression to active TB (<http://www.tstin3d.com/en/calc.html>) as previously described.^{23,24}

^e Study subjects included 5 patients with non-HIV immunosuppressed conditions (a patient on methotrexate for rheumatoid arthritis, one on sirolimus for lymphangioleiomyomatosis, one with history of chemotherapy and stem-cell transplantation for angioimmunoblastic lymphoma, one on 50 mg daily of prednisone for bullous pemphigoid, and one on hydroxychloroquine and low-dose prednisone for lichenoid mucositis).

^f QFT results include Interferon-gamma levels (IU/mL) of antigen tube minus nil from QuantiFERON TB Gold In-Tube™ and TB1 tube from QuantiFERON TB Gold Plus™.

Table 5.2 Patient demographics by pertinent clinical categories for cohort 2.

	Subjects, no. (%) ^a				P value ^b
	All (n=74)	LTBI- (n= 47)	LTBI+ (n= 27)	High Risk+ (n=26)	
Sex (female)	48 (64.8)	35 (74.5)	13 (48.1)	13 (50)	0.02
Age, years					
Mean ± SD	54.2±17.8	58.0±17.5	47.5±16.6	47.8±16.0	0.02
Range	19-83	25-83	19-79	19-79	
Ethnicity					<0.001
Caucasian	54 (73.0)	43 (91.4)	11 (40.7)	12 (46.1)	
African American	6 (8.1)	2 (4.3)	4 (14.8)	4 (15.4)	
Asian Pacific	8 (10.8)	2 (4.3)	6 (22.2)	6 (23.0)	
Hispanic	4 (5.4)	0	4 (14.8)	3 (11.5)	
Others	2 (2.7)	0	2 (7.4)	1 (3.8)	
Place of Birth ^c					<0.001
US Born	55 (74.3)	42 (89.4)	13 (48.1)	13 (50)	
Foreign Born (High TB)	18 (24.3)	4 (8.5)	14 (51.9)	13 (50)	
Foreign Born (Low TB)	1 (1.4)	1 (2.1)	0		
History of BCG vaccination					0.0013
Yes	11 (14.9)	2 (4.3)	9 (33.3)	8 (30.8)	
No	52 (70.3)	39 (83)	13 (48.1)	13 (50)	
Unknown	11 (14.9)	6 (12.7)	5 (18.5)	5 (19.2)	
Occupation					0.48
Health care worker, direct patient care	12 (16.2)	6 (12.7)	6 (22.2)	4 (15.4)	
Health care worker, no direct patient care	7 (9.5)	4 (8.5)	3 (11.1)	4 (15.4)	
Other	55 (74.3)	37 (78.7)	18 (66.6)	18 (69.2)	
Adjusted predicted cumulative TB risk (%) ^d					<0.001
Mean ± SD	4.7±15.1	0.48±1.8	12.2±23.4	8.7±15.8	
Range	0-100	0-9	0-100	0-60	
History of immunosuppression ^e (yes)	19 (25.7)	9 (19.1)	10 (37.0)	8 (30.7)	0.10
Tuberculin skin test					
TST (+)	18 (24.3)	6 (12.7)	12 (44.4)	10 (38.5)	<0.001
TST mm induration (median; range)	17; 11-20	15; 15-15	17.5; 11-20	18; 11-20	
IGRA test					
QFT (+)	23 (31.1)	1 (2.1)	22 (81.5)	21 (80.7)	<0.001
QFT results, TB1 (Mean ± SD; IU/mL) ^f	3.15±2.8	2.86	3.17±2.8	3.4±2.7	
QFT results, TB2 (Mean ± SD; IU/mL) ^f	3.39±3.19	9.98	3.1±2.9	3.6±3.2	

Abbreviations: IGRA = Interferon-gamma release assay; SD = Standard deviation; High TB = High incidence of TB; Low TB = Low incidence of TB; QFT = QuantiFERON TB Gold In-Tube™ or QuantiFERON TB Gold Plus™; TST = Tuberculin skin test. HIV = Human immunodeficiency virus. HCW = healthcare worker.

^a Study included 42 subjects. The total sample set analyzed were 45 samples, encompassing 42 unique subjects and 3 additional time points separated by 5-7 months in testing, representing unique samples.

^b P value for comparison between subjects with LTBI diagnosis vs. no LTBI diagnosis by current diagnostic guidelines (Two-tailed Fisher's Exact test or r x c Exact contingency table, Wilcoxon rank sums when appropriate).

^c High incidence of TB was defined as a country with ≥20 cases per 100,000 population per year. 2020 WHO Global tuberculosis report (http://www.who.int/tb/publications/global_report/en/).

^d Adjusted estimates for the individual cumulative risk of TB reactivation are based on "The Online TST/IGRA interpreter" prediction modeling that includes TST and IGRA results, risk factors for LTBI and risk factors for progression to active TB (<http://www.tstin3d.com/en/calc.html>) as previously described. ^{23,24}

^e Study subjects included 5 patients with non-HIV immunosuppressed conditions (a patient on methotrexate for rheumatoid arthritis, one on sirolimus for lymphangioleiomyomatosis, one with history of chemotherapy and

stem-cell transplantation for angioimmunoblastic lymphoma, one on 50 mg daily of prednisone for bullous pemphigoid, and one on hydroxychloroquine and low-dose prednisone for lichenoid mucositis).
f QFT results include Interferon-gamma levels (IU/mL) of antigen tube minus nil from QuantiFERON TB Gold In-Tube™ and TB1 tube from QuantiFERON TB Gold Plus™.

5.10 References

- (1) *Tuberculosis (TB)*. <https://www.who.int/news-room/fact-sheets/detail/tuberculosis> (accessed 2023-09-25).
- (2) *2.2 TB mortality*. <https://www.who.int/teams/global-tuberculosis-programme/tb-reports/global-tuberculosis-report-2022/tb-disease-burden/2-2-tb-mortality> (accessed 2023-12-15).
- (3) *Global Tuberculosis Report 2022*. <https://www.who.int/teams/global-tuberculosis-programme/tb-reports/global-tuberculosis-report-2022> (accessed 2023-12-15).
- (4) *COVID-19 and TB*. <https://www.who.int/teams/global-tuberculosis-programme/tb-reports/global-tuberculosis-report-2022/covid-19-and-tb> (accessed 2023-12-15).
- (5) McQuaid, C. F.; Vassall, A.; Cohen, T.; Fiekert, K.; White, R. G. The Impact of COVID-19 on TB: A Review of the Data. *Int. J. Tuberc. Lung Dis.* **2021**, *25* (6), 436–446. <https://doi.org/10.5588/ijtld.21.0148>.
- (6) Migliori, G. B.; Thong, P. M.; Alffenaar, J.-W.; Denholm, J.; Tadolini, M.; Alyaquobi, F.; Blanc, F.-X.; Buonsenso, D.; Cho, J.-G.; Codecasa, L. R.; Danila, E.; Duarte, R.; García-García, J.-M.; Gualano, G.; Rendon, A.; Silva, D. R.; Souleymane, M. B.; Tham, S. M.; Thomas, T. A.; Tiberi, S.; Udwadia, Z. F.; Goletti, D.; Centis, R.; D’Ambrosio, L.; Sotgiu, G.; Ong, C. W. M.; Network, for the G. T. Gauging the Impact of the COVID-19 Pandemic on Tuberculosis Services: A Global Study. *Eur. Respir. J.* **2021**, *58* (5). <https://doi.org/10.1183/13993003.01786-2021>.
- (7) Escalante, P.; Vadiyala, M. R.; Pathakumari, B.; Marty, P. K.; Van Keulen, V. P.; Hilgart, H. R.; Meserve, K.; Theel, E. S.; Peikert, T.; Bailey, R. C.; Laniado-Laborin, R. New Diagnostics for the Spectrum of Asymptomatic TB: From Infection to Subclinical Disease. *Int. J. Tuberc. Lung Dis.* **2023**, *27* (7), 499–505. <https://doi.org/10.5588/ijtld.23.0032>.
- (8) Pai, M.; Behr, M. A.; Dowdy, D.; Dheda, K.; Divangahi, M.; Boehme, C. C.; Ginsberg, A.; Swaminathan, S.; Spigelman, M.; Getahun, H.; Menzies, D.; Raviglione, M. Tuberculosis. *Nat. Rev. Dis. Primer* **2016**, *2* (1), 1–23. <https://doi.org/10.1038/nrdp.2016.76>.
- (9) Ernst, J. D. The Immunological Life Cycle of Tuberculosis. *Nat. Rev. Immunol.* **2012**, *12* (8), 581–591. <https://doi.org/10.1038/nri3259>.
- (10) Flynn, J. L.; Chan, J. Immunology of Tuberculosis. *Annu. Rev. Immunol.* **2001**, *19* (1), 93–129. <https://doi.org/10.1146/annurev.immunol.19.1.93>.
- (11) Mukherjee, S.; Perveen, S.; Negi, A.; Sharma, R. Evolution of Tuberculosis Diagnostics: From Molecular Strategies to Nanodiagnosics. *Tuberculosis* **2023**, *140*, 102340. <https://doi.org/10.1016/j.tube.2023.102340>.
- (12) CDCTB. *Tuberculosis (TB) - Treatment Regimens for Latent TB Infection*. Centers for Disease Control and Prevention. <https://www.cdc.gov/tb/topic/treatment/ltbi.htm> (accessed 2023-12-15).
- (13) Huaman, M. A.; Sterling, T. R. Treatment of Latent Tuberculosis Infection – An Update. *Clin. Chest Med.* **2019**, *40* (4), 839–848. <https://doi.org/10.1016/j.ccm.2019.07.008>.
- (14) Organizat, W. H. WHO Consolidated Guidelines on Tuberculosis. Module 1: Prevention. Tuberculosis Preventive Treatment. *Tuberc. Lung Dis. HIV Infect.* **2021**, No. 2, 86–92. <https://doi.org/10.30978/TB2021-2-86>.
- (15) Pai, M.; Denkinger, C. M.; Kik, S. V.; Rangaka, M. X.; Zwerling, A.; Oxlade, O.; Metcalfe, J. Z.; Cattamanchi, A.; Dowdy, D. W.; Dheda, K.; Banaei, N. Gamma Interferon

- Release Assays for Detection of Mycobacterium Tuberculosis Infection. *Clin. Microbiol. Rev.* **2014**, *27* (1), 3–20. <https://doi.org/10.1128/CMR.00034-13>.
- (16) Qiagen QFT Home. <http://www.qiagen.com/us/> (accessed 2024-02-19).
- (17) Getahun, H.; Matteelli, A.; Chaisson, R. E.; Raviglione, M. Latent Mycobacterium Tuberculosis Infection. *N. Engl. J. Med.* **2015**, *372* (22), 2127–2135. <https://doi.org/10.1056/NEJMra1405427>.
- (18) Diel, R.; Loddenkemper, R.; Nienhaus, A. Predictive Value of Interferon- γ Release Assays and Tuberculin Skin Testing for Progression from Latent TB Infection to Disease State: A Meta-Analysis. *Chest* **2012**, *142* (1), 63–75. <https://doi.org/10.1378/chest.11-3157>.
- (19) Chegou, N. N.; Heyckendorf, J.; Walzl, G.; Lange, C.; Ruhwald, M. Beyond the IFN-Horizon: Biomarkers for Immunodiagnosis of Infection with Mycobacterium Tuberculosis. *Eur. Respir. J.* **2014**, *43* (5), 1472–1486. <https://doi.org/10.1183/09031936.00151413>.
- (20) MacLean, E.; Broger, T.; Yerlikaya, S.; Fernandez-Carballo, B. L.; Pai, M.; Denkinger, C. M. A Systematic Review of Biomarkers to Detect Active Tuberculosis. *Nat. Microbiol.* **2019**, *4* (5), 748–758. <https://doi.org/10.1038/s41564-019-0380-2>.
- (21) Chegou, N. N.; Sutherland, J. S.; Malherbe, S.; Crampin, A. C.; Corstjens, P. L. A. M.; Geluk, A.; Mayanja-Kizza, H.; Loxton, A. G.; Van Der Spuy, G.; Stanley, K.; Kotzé, L. A.; Van Der Vyver, M.; Rosenkrands, I.; Kidd, M.; Van Helden, P. D.; Dockrell, H. M.; Ottenhoff, T. H. M.; Kaufmann, S. H. E.; Walzl, G. Diagnostic Performance of a Seven-Marker Serum Protein Biosignature for the Diagnosis of Active TB Disease in African Primary Healthcare Clinic Attendees with Signs and Symptoms Suggestive of TB. *Thorax* **2016**, *71* (9), 785–794. <https://doi.org/10.1136/thoraxjnl-2015-207999>.
- (22) Chegou, N. N.; Sutherland, J. S.; Namuganga, A.-R.; Corstjens, P. L.; Geluk, A.; Gebremichael, G.; Mendy, J.; Malherbe, S.; Stanley, K.; van der Spuy, G. D.; Kriel, M.; Loxton, A. G.; Kriel, B.; Simukonda, F.; Bekele, Y.; Sheehama, J. A.; Nelongo, J.; van der Vyver, M.; Gebrexabher, A.; Hailu, H.; Esterhuyse, M. M.; Rosenkrands, I.; Aagard, C.; Kidd, M.; Kassa, D.; Mihret, A.; Howe, R.; Cliff, J. M.; Crampin, A. C.; Mayanja-Kizza, H.; Kaufmann, S. H. E.; Dockrell, H. M.; Ottenhoff, T. H. M.; Walzl, G. Africa-Wide Evaluation of Host Biomarkers in QuantiFERON Supernatants for the Diagnosis of Pulmonary Tuberculosis. *Sci. Rep.* **2018**, *8* (1), 2675. <https://doi.org/10.1038/s41598-018-20855-7>.
- (23) Manngo, P. M.; Gutschmidt, A.; Snyders, C. I.; Mutavhatsindi, H.; Manyelo, C. M.; Makhoba, N. S.; Ahlers, P.; Hiemstra, A.; Stanley, K.; McAnda, S.; Kidd, M.; Malherbe, S. T.; Walzl, G.; Chegou, N. N. Prospective Evaluation of Host Biomarkers Other than Interferon Gamma in QuantiFERON Plus Supernatants as Candidates for the Diagnosis of Tuberculosis in Symptomatic Individuals. *J. Infect.* **2019**, *79* (3), 228–235. <https://doi.org/10.1016/j.jinf.2019.07.007>.
- (24) Jacobs, R.; Malherbe, S.; Loxton, A. G.; Stanley, K.; van der Spuy, G.; Walzl, G.; Chegou, N. N. Identification of Novel Host Biomarkers in Plasma as Candidates for the Immunodiagnosis of Tuberculosis Disease and Monitoring of Tuberculosis Treatment Response. *Oncotarget* **2016**, *7* (36), 57581–57592. <https://doi.org/10.18632/oncotarget.11420>.
- (25) Nogueira, B. M. F.; Krishnan, S.; Barreto-Duarte, B.; Araújo-Pereira, M.; Queiroz, A. T. L.; Ellner, J. J.; Salgame, P.; Scriba, T. J.; Sterling, T. R.; Gupta, A.; Andrade, B. B. Diagnostic Biomarkers for Active Tuberculosis: Progress and Challenges. *EMBO Mol. Med.* **2022**, *14* (12), e14088. <https://doi.org/10.15252/emmm.202114088>.
- (26) Mihret, A.; Bekele, Y.; Bobosha, K.; Kidd, M.; Aseffa, A.; Howe, R.; Walzl, G. Plasma Cytokines and Chemokines Differentiate between Active Disease and Non-Active

- Tuberculosis Infection. *J. Infect.* **2013**, *66* (4), 357–365.
<https://doi.org/10.1016/j.jinf.2012.11.005>.
- (27) Qiu, B.; Liu, Q.; Li, Z.; Song, H.; Xu, D.; Ji, Y.; Jiang, Y.; Tian, D.; Wang, J. Evaluation of Cytokines as a Biomarker to Distinguish Active Tuberculosis from Latent Tuberculosis Infection: A Diagnostic Meta-Analysis. *BMJ Open* **2020**, *10* (10), e039501.
<https://doi.org/10.1136/bmjopen-2020-039501>.
- (28) Wang, S.; Li, Y.; Shen, Y.; Wu, J.; Gao, Y.; Zhang, S.; Shao, L.; Jin, J.; Zhang, Y.; Zhang, W. Screening and Identification of a Six-Cytokine Biosignature for Detecting TB Infection and Discriminating Active from Latent TB. *J. Transl. Med.* **2018**, *16* (1), 206.
<https://doi.org/10.1186/s12967-018-1572-x>.
- (29) Won, E.-J.; Choi, J.-H.; Cho, Y.-N.; Jin, H.-M.; Kee, H. J.; Park, Y.-W.; Kwon, Y.-S.; Kee, S.-J. Biomarkers for Discrimination between Latent Tuberculosis Infection and Active Tuberculosis Disease. *J. Infect.* **2017**, *74* (3), 281–293.
<https://doi.org/10.1016/j.jinf.2016.11.010>.
- (30) Manna, M. P. L.; Orlando, V.; Donni, P. L.; Sireci, G.; Carlo, P. D.; Cascio, A.; Dieli, F.; Caccamo, N. Identification of Plasma Biomarkers for Discrimination between Tuberculosis Infection/Disease and Pulmonary Non Tuberculosis Disease. *PLOS ONE* **2018**, *13* (3), e0192664. <https://doi.org/10.1371/journal.pone.0192664>.
- (31) Awoniyi, D. O.; Teuchert, A.; Sutherland, J. S.; Mayanja-Kizza, H.; Howe, R.; Mihret, A.; Loxton, A. G.; Sheehama, J.; Kassa, D.; Crampin, A. C.; Dockrell, H. M.; Kidd, M.; Rosenkrands, I.; Geluk, A.; Ottenhoff, T. H. M.; Corstjens, P. L. A. M.; Chegou, N. N.; Walzl, G.; Walzl, G.; Chegou, N. N.; Kriel, M.; van der Spuy, G.; Loxton, A. G.; Stanley, K.; Malherbe, S.; Mcanda, S.; Kriel, B.; Phalane, K. G.; Essone, P.; Sutherland, J. S.; Owolabi, O.; Sillah, A.; Mendy, J.; Gindeh, A.; Donkor, S.; Togun, T.; Ota, M.; Crampin, A. C.; Simukonda, F.; Amberbir, A.; Chilongo, F.; Houben, R.; Kassa, D.; Gebrezgabher, A.; Mesfin, G.; Belay, Y.; Gebremichael, G.; Alemayehu, Y.; van der Vyver, M.; Amutenya, F. N.; Nelongo, J. N.; Monye, L.; Sheehama, J. A.; Iiping, S.; Mayanja-Kizza, H.; Namuganga, A. R.; Muzanye, G.; Nsereko, M.; Peters, P.; Howe, R.; Mihret, A.; Bekele, Y.; Tessema, B.; Yamuah, L.; Ottenhoff, T. H. M.; Geluk, A.; Franken, K.; Corstjens, P. L. A. M.; Tjon Kon Fat, E. M.; de Dood, C. J.; van der Ploeg-van Schip, J. J.; Rosenkrands, I.; Aagaard, C.; Kaufmann, S. H. E.; Esterhuysen, M. M.; Cliff, J. M.; Dockrell, H. M. Evaluation of Cytokine Responses against Novel Mtb Antigens as Diagnostic Markers for TB Disease. *J. Infect.* **2016**, *73* (3), 219–230. <https://doi.org/10.1016/j.jinf.2016.04.036>.
- (32) Kaforou, M.; Broderick, C.; Vito, O.; Levin, M.; Scriba, T. J.; Seddon, J. A. Transcriptomics for Child and Adolescent Tuberculosis*. *Immunol. Rev.* **2022**, *309* (1), 97–122. <https://doi.org/10.1111/imr.13116>.
- (33) Suliman, S.; Thompson, E. G.; Sutherland, J.; Weiner, J.; Ota, M. O. C.; Shankar, S.; Penn-Nicholson, A.; Thiel, B.; Erasmus, M.; Maertzdorf, J.; Duffy, F. J.; Hill, P. C.; Hughes, E. J.; Stanley, K.; Downing, K.; Fisher, M. L.; Valvo, J.; Parida, S. K.; van der Spuy, G.; Tromp, G.; Adetifa, I. M. O.; Donkor, S.; Howe, R.; Mayanja-Kizza, H.; Boom, W. H.; Dockrell, H. M.; Ottenhoff, T. H. M.; Hatherill, M.; Aderem, A.; Hanekom, W. A.; Scriba, T. J.; Kaufmann, S. H. E.; Zak, D. E.; Walzl, G.; Walzl, G.; Black, G. F.; van der Spuy, G.; Stanley, K.; Kriel, M.; Du Plessis, N.; Nene, N.; Roberts, T.; Kleynhans, L.; Gutschmidt, A.; Smith, B.; Nene, N.; Loxton, A. G.; Chegou, N. N.; Tromp, G.; Tabb, D.; Ottenhoff, T. H. M.; Klein, M. R.; Haks, M. C.; Franken, K. L. M. C.; Geluk, A.; van Meijgaarden, K. E.; Joosten, S. A.; Boom, W. H.; Thiel, B.; Mayanja-Kizza, H.; Joloba, M.; Zalwango, S.; Nsereko, M.;

- Okwera, B.; Kisingo, H.; Kaufmann, S. H. E.; Parida, S. K.; Golinski, R.; Maertzdorf, J.; Weiner, J.; Jacobson, M.; Dockrell, H.; Smith, S.; Gorak-Stolinska, P.; Hur, Y.-G.; Lalor, M.; Lee, J.-S.; Crampin, A. C.; French, N.; Ngwira, B.; Ben-Smith, A.; Watkins, K.; Ambrose, L.; Simukonda, F.; Mvula, H.; Chilongo, F.; Saul, J.; Branson, K.; Suliman, S.; Scriba, T. J.; Mahomed, H.; Hughes, E. J.; Bilek, N.; Erasmus, M.; Xasa, O.; Veldsman, A.; Downing, K.; Fisher, M.; Penn-Nicholson, A.; Mulenga, H.; Abel, B.; Bowmaker, M.; Kagina, B.; Chung, W. K.; Hanekom, W. A.; Sadoff, J.; Sizemore, D.; Ramachandran, S.; Barker, L.; Brennan, M.; Weichold, F.; Muller, S.; Geiter, L.; Kassa, D.; Abebe, A.; Mesele, T.; Tegbaru, B.; Baarle, D. van; Miedema, F.; Howe, R.; Mihret, A.; Aseffa, A.; Bekele, Y.; Iwnetu, R.; Tafesse, M.; Yamuah, L.; Ota, M.; Sutherland, J.; Hill, P.; Adegbola, R.; Corrah, T.; Antonio, M.; Togun, T.; Adetifa, I.; Donkor, S.; Andersen, P.; Rosenkrands, I.; Doherty, M.; Weldingh, K.; Schoolnik, G.; Dolganov, G.; Van, T.; Kafaar, F.; Workman, L.; Mulenga, H.; Scriba, T. J.; Hughes, E. J.; Bilek, N.; Erasmus, M.; Xasa, O.; Veldsman, A.; Cloete, Y.; Abrahams, D.; Moyo, S.; Gelderbloem, S.; Tameris, M.; Geldenhuys, H.; Hanekom, W.; Hussey, G.; Ehrlich, R.; Verver, S.; Geiter, L. Four-Gene Pan-African Blood Signature Predicts Progression to Tuberculosis. *Am. J. Respir. Crit. Care Med.* **2018**, *197* (9), 1198–1208. <https://doi.org/10.1164/rccm.201711-2340OC>.
- (34) Leong, S.; Zhao, Y.; Ribeiro-Rodrigues, R.; Jones-López, E. C.; Acuña-Villaorduña, C.; Rodrigues, P. M.; Palaci, M.; Alland, D.; Dietze, R.; Ellner, J. J.; Johnson, W. E.; Salgame, P. Cross-Validation of Existing Signatures and Derivation of a Novel 29-Gene Transcriptomic Signature Predictive of Progression to TB in a Brazilian Cohort of Household Contacts of Pulmonary TB. *Tuberculosis* **2020**, *120*, 101898. <https://doi.org/10.1016/j.tube.2020.101898>.
- (35) Zak, D. E.; Penn-Nicholson, A.; Scriba, T. J.; Thompson, E.; Suliman, S.; Amon, L. M.; Mahomed, H.; Erasmus, M.; Whatney, W.; Hussey, G. D.; Abrahams, D.; Kafaar, F.; Hawkridge, T.; Verver, S.; Hughes, E. J.; Ota, M.; Sutherland, J.; Howe, R.; Dockrell, H. M.; Boom, W. H.; Thiel, B.; Ottenhoff, T. H. M.; Mayanja-Kizza, H.; Crampin, A. C.; Downing, K.; Hatherill, M.; Valvo, J.; Shankar, S.; Parida, S. K.; Kaufmann, S. H. E.; Walzl, G.; Aderem, A.; Hanekom, W. A. A Blood RNA Signature for Tuberculosis Disease Risk: A Prospective Cohort Study. *The Lancet* **2016**, *387* (10035), 2312–2322. [https://doi.org/10.1016/S0140-6736\(15\)01316-1](https://doi.org/10.1016/S0140-6736(15)01316-1).
- (36) Xi, X.; Li, T.; Huang, Y.; Sun, J.; Zhu, Y.; Yang, Y.; Lu, Z. J. RNA Biomarkers: Frontier of Precision Medicine for Cancer. *Non-Coding RNA* **2017**, *3* (1), 9. <https://doi.org/10.3390/ncrna3010009>.
- (37) Robison, H. M.; Escalante, P.; Valera, E.; Erskine, C. L.; Auvil, L.; Sasieta, H. C.; Bushell, C.; Welge, M.; Bailey, R. C. Precision Immunoprofiling to Reveal Diagnostic Signatures for Latent Tuberculosis Infection and Reactivation Risk Stratification. *Integr. Biol.* **2019**, *11* (1), 16–25. <https://doi.org/10.1093/intbio/zyz001>.
- (38) Robison, H. M.; Chapman, C. A.; Zhou, H.; Erskine, C. L.; Theel, E.; Peikert, T.; Lindestam Arlehamn, C. S.; Sette, A.; Bushell, C.; Welge, M.; Zhu, R.; Bailey, R. C.; Escalante, P. Risk Assessment of Latent Tuberculosis Infection through a Multiplexed Cytokine Biosensor Assay and Machine Learning Feature Selection. *Sci. Rep.* **2021**, *11* (1), 20544. <https://doi.org/10.1038/s41598-021-99754-3>.
- (39) Arlehamn, C. S. L.; McKinney, D. M.; Carpenter, C.; Paul, S.; Rozot, V.; Makgotlho, E.; Gregg, Y.; Rooyen, M. van; Ernst, J. D.; Hatherill, M.; Hanekom, W. A.; Peters, B.; Scriba, T. J.; Sette, A. A Quantitative Analysis of Complexity of Human Pathogen-Specific CD4 T Cell

- Responses in Healthy M. Tuberculosis Infected South Africans. *PLOS Pathog.* **2016**, *12* (7), e1005760. <https://doi.org/10.1371/journal.ppat.1005760>.
- (40) El Sahly, H. M.; Adams, G. J.; Soini, H.; Teeter, L.; Musser, J. M.; Graviss, E. A. Epidemiologic Differences between United States- and Foreign-Born Tuberculosis Patients in Houston, Texas. *J. Infect. Dis.* **2001**, *183* (3), 461–468. <https://doi.org/10.1086/318079>.
- (41) Lewinsohn, D. M.; Leonard, M. K.; LoBue, P. A.; Cohn, D. L.; Daley, C. L.; Desmond, E.; Keane, J.; Lewinsohn, D. A.; Loeffler, A. M.; Mazurek, G. H.; O'Brien, R. J.; Pai, M.; Richeldi, L.; Salfinger, M.; Shinnick, T. M.; Sterling, T. R.; Warshauer, D. M.; Woods, G. L. Official American Thoracic Society/Infectious Diseases Society of America/Centers for Disease Control and Prevention Clinical Practice Guidelines: Diagnosis of Tuberculosis in Adults and Children. *Clin. Infect. Dis. Off. Publ. Infect. Dis. Soc. Am.* **2017**, *64* (2), 111–115. <https://doi.org/10.1093/cid/ciw778>.
- (42) Escalante, P.; Peikert, T.; Van Keulen, V. P.; Erskine, C. L.; Bornhorst, C. L.; Andrist, B. R.; McCoy, K.; Pease, L. R.; Abraham, R. S.; Knutson, K. L.; Kita, H.; Schrum, A. G.; Limper, A. H. Combinatorial Immunoprofiling in Latent Tuberculosis Infection. Toward Better Risk Stratification. *Am. J. Respir. Crit. Care Med.* **2015**, *192* (5), 605–617. <https://doi.org/10.1164/rccm.201412-2141OC>.
- (43) Menzies, D.; Gardiner, G.; Farhat, M.; Greenaway, C.; Pai, M. Thinking in Three Dimensions: A Web-Based Algorithm to Aid the Interpretation of Tuberculin Skin Test Results. *Int. J. Tuberc. Lung Dis. Off. J. Int. Union Tuberc. Lung Dis.* **2008**, *12* (5), 498–505.
- (44) QuantiFERON-TB Gold (QFT) ELISA Package Insert. <https://www.quantiferon.com/us/wp-content/uploads/sites/13/2019/03/L1075116-Quantiferon-TB-Gold-ELISA-IFU-FDA-rev04.pdf> (accessed 2024-02-19)
- (45) *QuantiFERON-TB Gold Plus ELISA Kit Package Insert - QIAGEN.* <https://www.qiagen.com/us/resources/resourcedetail?id=ac068fc7-a994-4443-ac7c-dda43ce2bc5e&lang=en> (accessed 2024-02-19).
- (46) Theel, E. S.; Hilgart, H.; Breen-Lyles, M.; McCoy, K.; Flury, R.; Breeher, L. E.; Wilson, J.; Sia, I. G.; Whitaker, J. A.; Clain, J.; Aksamit, T. R.; Escalante, P. Comparison of the QuantiFERON-TB Gold Plus and QuantiFERON-TB Gold In-Tube Interferon Gamma Release Assays in Patients at Risk for Tuberculosis and in Health Care Workers. *J. Clin. Microbiol.* **2018**, *56* (7), e00614-18. <https://doi.org/10.1128/JCM.00614-18>.
- (47) Iqbal, M.; Gleeson, M. A.; Spaugh, B.; Tybor, F.; Gunn, W. G.; Hochberg, M.; Baehr-Jones, T.; Bailey, R. C.; Gunn, L. C. Label-Free Biosensor Arrays Based on Silicon Ring Resonators and High-Speed Optical Scanning Instrumentation. *IEEE J. Sel. Top. Quantum Electron.* **2010**, *16* (3), 654–661. <https://doi.org/10.1109/JSTQE.2009.2032510>.
- (48) Hutchinson, A. M. Evanescent Wave Biosensors. *Mol. Biotechnol.* **1995**, *3* (1), 47–54. <https://doi.org/10.1007/BF02821334>.
- (49) Cai, L.; Pan, J.; Zhao, Y.; Wang, J.; Xiao, S. Whispering Gallery Mode Optical Microresonators: Structures and Sensing Applications. *Phys. Status Solidi A* **2020**, *217* (6), 1900825. <https://doi.org/10.1002/pssa.201900825>.
- (50) Yu, D.; Humar, M.; Meserve, K.; Bailey, R. C.; Chormaic, S. N.; Vollmer, F. Whispering-Gallery-Mode Sensors for Biological and Physical Sensing. *Nat. Rev. Methods Primer* **2021**, *1* (1), 83. <https://doi.org/10.1038/s43586-021-00079-2>.
- (51) Luchansky, M. S.; Washburn, A. L.; Martin, T. A.; Iqbal, M.; Gunn, L. C.; Bailey, R. C. Characterization of the Evanescent Field Profile and Bound Mass Sensitivity of a Label-Free

- Silicon Photonic Microring Resonator Biosensing Platform. *Biosens. Bioelectron.* **2010**, *26* (4), 1283–1291. <https://doi.org/10.1016/j.bios.2010.07.010>.
- (52) Luchansky, M. S.; Washburn, A. L.; McClellan, M. S.; Bailey, R. C. Sensitive On-Chip Detection of a Protein Biomarker in Human Serum and Plasma over an Extended Dynamic Range Using Silicon Photonic Microring Resonators and Sub-Micron Beads. *Lab. Chip* **2011**, *11* (12), 2042. <https://doi.org/10.1039/c1lc20231f>.
- (53) Wade, J. H.; Bailey, R. C. Applications of Optical Microcavity Resonators in Analytical Chemistry. *Annu. Rev. Anal. Chem.* **2016**, *9* (1), 1–25. <https://doi.org/10.1146/annurev-anchem-071015-041742>.
- (54) Meserve, K.; Qavi, A. J.; Aman, M. J.; Vu, H.; Zeitlin, L.; Dye, J. M.; Froude, J. W.; Leung, D. W.; Yang, L.; Holtsberg, F. W.; Amarasinghe, G. K.; Bailey, R. C. Detection of Biomarkers for Filoviral Infection with a Silicon Photonic Resonator Platform. *STAR Protoc.* **2022**, *3* (4), 101719. <https://doi.org/10.1016/j.xpro.2022.101719>.
- (55) *Move Data, not Blood - 30 Minutes Results - Onsite Lab Automation.* <https://www.genalyte.com/> (accessed 2024-02-19).
- (56) Kindt, J. T.; Luchansky, M. S.; Qavi, A. J.; Lee, S.-H.; Bailey, R. C. Subpicogram Per Milliliter Detection of Interleukins Using Silicon Photonic Microring Resonators and an Enzymatic Signal Enhancement Strategy. *Anal. Chem.* **2013**, *85* (22), 10653–10657. <https://doi.org/10.1021/ac402972d>.
- (57) Robison, H. M.; Bailey, R. C. A Guide to Quantitative Biomarker Assay Development Using Whispering Gallery Mode Biosensors: Whispering Gallery Mode Biosensors. *Curr. Protoc. Chem. Biol.* **2017**, *9* (3), 158–173. <https://doi.org/10.1002/cpch.23>.
- (58) Mann, H. B.; Whitney, D. R. On a Test of Whether One of Two Random Variables Is Stochastically Larger than the Other. *Ann. Math. Stat.* **1947**, *18* (1), 50–60.
- (59) McKnight, P. E.; Najab, J. Mann-Whitney U Test. In *The Corsini Encyclopedia of Psychology*; John Wiley & Sons, Ltd, 2010; pp 1–1. <https://doi.org/10.1002/9780470479216.corpsy0524>.
- (60) Woolson, R. F. Wilcoxon Signed-Rank Test. In *Wiley Encyclopedia of Clinical Trials*; D'Agostino, R. B., Sullivan, L., Massaro, J., Eds.; Wiley, 2008; pp 1–3. <https://doi.org/10.1002/9780471462422.eoct979>.
- (61) Breiman, L. Random Forests. *Mach. Learn.* **2001**, *45* (1), 5–32. <https://doi.org/10.1023/A:1010933404324>.
- (62) Tibshirani, S.; Friedman, H. Valerie and Patrick Hastie. Random Forests. In *The Elements of Statistical Learning*, 2nd ed, Springer, 2016; pp 587–604.
- (63) Tibshirani, S.; Friedman, H. Valerie and Patrick Hastie. Boosting and Additive Trees. In *The Elements of Statistical Learning*, 2nd ed, Springer, 2016; pp 368.
- (64) R Core Team (2019) R: A Language and Environment for Statistical Computing. R Foundation for Statistical Computing, Vienna, Austria. <https://www.R-project.org/>.
- (65) Ishwaran, Hemant; Kogalur, U. B. Fast Unified Random Forests for Survival, Regression, and Classification (RF-SRC).
- (66) *vi function - RDocumentation.* <https://www.rdocumentation.org/packages/vip/versions/0.4.1/topics/vi> (accessed 2024-02-20).
- (67) *vi_model function - RDocumentation.* https://www.rdocumentation.org/packages/vip/versions/0.2.0/topics/vi_model (accessed 2024-02-20).

- (68) Bradley, A. P. The Use of the Area under the ROC Curve in the Evaluation of Machine Learning Algorithms. *Pattern Recognit.* **1997**, *30* (7), 1145–1159. [https://doi.org/10.1016/S0031-3203\(96\)00142-2](https://doi.org/10.1016/S0031-3203(96)00142-2).
- (69) Nembrini, S.; König, I. R.; Wright, M. N. The Revival of the Gini Importance? *Bioinformatics* **2018**, *34* (21), 3711–3718. <https://doi.org/10.1093/bioinformatics/bty373>.
- (70) Zhu, R.; Zeng, D.; Kosorok, M. R. Reinforcement Learning Trees. *J. Am. Stat. Assoc.* **2015**, *110* (512), 1770–1784. <https://doi.org/10.1080/01621459.2015.1036994>.
- (71) Archer, K. J.; Kimes, R. V. Empirical Characterization of Random Forest Variable Importance Measures. *Comput. Stat. Data Anal.* **2008**, *52* (4), 2249–2260. <https://doi.org/10.1016/j.csda.2007.08.015>.
- (72) Chapman, C. Clinical Diagnostics For Immune Response Assessment Through Multiplexed Biosensor Immunoassays In At-Risk Populations. Ph.D. Dissertation, University of Michigan, Ann Arbor, Michigan, 2021. <https://doi.org/10.7302/1556>.
- (73) Li, H.; Ren, W.; Liang, Q.; Zhang, X.; Li, Q.; Shang, Y.; Ma, L.; Li, S.; Pang, Y. A Novel Chemokine Biomarker to Distinguish Active Tuberculosis from Latent Tuberculosis: A Cohort Study. *QJM Int. J. Med.* **2023**, head214. <https://doi.org/10.1093/qjmed/head214>.
- (74) Ruhwald, M.; Bjerregaard-Andersen, M.; Rabna, P.; Eugen-Olsen, J.; Ravn, P. IP-10, MCP-1, MCP-2, MCP-3, and IL-1RA Hold Promise as Biomarkers for Infection with M. Tuberculosis in a Whole Blood Based T-Cell Assay. *BMC Res. Notes* **2009**, *2*, 19. <https://doi.org/10.1186/1756-0500-2-19>.
- (75) Liu, M.; Guo, S.; Hibbert, J. M.; Jain, V.; Singh, N.; Wilson, N. O.; Stiles, J. K. CXCL10/IP-10 in Infectious Diseases Pathogenesis and Potential Therapeutic Implications. *Cytokine Growth Factor Rev.* **2011**, *22* (3), 121–130. <https://doi.org/10.1016/j.cytogfr.2011.06.001>.
- (76) Petrone, L.; Cannas, A.; Vanini, V.; Cuzzi, G.; Aloï, F.; Nsubuga, M.; Sserunkuma, J.; Nazziwa, R. A.; Jugheli, L.; Lukindo, T.; Girardi, E.; Antinori, A.; Pucci, L.; Reither, K.; Goletti, D. Blood and Urine Inducible Protein 10 as Potential Markers of Disease Activity. *Int. J. Tuberc. Lung Dis.* **2016**, *20* (11), 1554–1561. <https://doi.org/10.5588/ijtld.16.0342>.
- (77) Corstjens, P. L. A. M.; Tjon Kon Fat, E. M.; De Dood, C. J.; Van Der Ploeg-van Schip, J. J.; Franken, K. L. M. C.; Chegou, N. N.; Sutherland, J. S.; Howe, R.; Mihret, A.; Kassa, D.; Van Der Vyver, M.; Sheehama, J.; Simukonda, F.; Mayanja-Kizza, H.; Ottenhoff, T. H. M.; Walzl, G.; Geluk, A. Multi-Center Evaluation of a User-Friendly Lateral Flow Assay to Determine IP-10 and CCL4 Levels in Blood of TB and Non-TB Cases in Africa. *Clin. Biochem.* **2016**, *49* (1–2), 22–31. <https://doi.org/10.1016/j.clinbiochem.2015.08.013>.
- (78) Borgström, E.; Andersen, P.; Atterfelt, F.; Julander, I.; Källenius, G.; Maeurer, M.; Rosenkrands, I.; Widfeldt, M.; Bruchfeld, J.; Gaines, H. Immune Responses to ESAT-6 and CFP-10 by FASCIA and Multiplex Technology for Diagnosis of M. Tuberculosis Infection; IP-10 Is a Promising Marker. *PLoS ONE* **2012**, *7* (11), e43438. <https://doi.org/10.1371/journal.pone.0043438>.
- (79) Biselli, R.; Mariotti, S.; Sargentini, V.; Sauzullo, I.; Lastilla, M.; Mengoni, F.; Vanini, V.; Girardi, E.; Goletti, D.; D' Amelio, R.; Nisini, R. Detection of Interleukin-2 in Addition to Interferon- γ Discriminates Active Tuberculosis Patients, Latently Infected Individuals, and Controls. *Clin. Microbiol. Infect.* **2010**, *16* (8), 1282–1284. <https://doi.org/10.1111/j.1469-0691.2009.03104.x>.

- (80) Chegou, N. N.; Black, G. F.; Kidd, M.; van Helden, P. D.; Walzl, G. Host Markers in Quantiferon Supernatants Differentiate Active TB from Latent TB Infection: Preliminary Report. *BMC Pulm. Med.* **2009**, *9* (1), 21. <https://doi.org/10.1186/1471-2466-9-21>.
- (81) Wozniak, T. M.; Ryan, A. A.; Britton, W. J. Interleukin-23 Restores Immunity to Mycobacterium Tuberculosis Infection in IL-12p40-Deficient Mice and Is Not Required for the Development of IL-17-Secreting T Cell Responses1. *J. Immunol.* **2006**, *177* (12), 8684–8692. <https://doi.org/10.4049/jimmunol.177.12.8684>.
- (82) Sutherland, J. S.; Jong, B. C. de; Jeffries, D. J.; Adetifa, I. M.; Ota, M. O. C. Production of TNF- α , IL-12(P40) and IL-17 Can Discriminate between Active TB Disease and Latent Infection in a West African Cohort. *PLOS ONE* **2010**, *5* (8), e12365. <https://doi.org/10.1371/journal.pone.0012365>.
- (83) Gourgouillon, N.; de Lauzanne, A.; Cottart, C.-H.; Curis, E.; Debord, C.; Guérin-El Khourouj, V.; Pédrón, B.; Faye, A.; Sterkers, G. TNF- α /IL-2 Ratio Discriminates Latent from Active Tuberculosis in Immunocompetent Children: A Pilot Study. *Pediatr. Res.* **2012**, *72* (4), 370–374. <https://doi.org/10.1038/pr.2012.89>.
- (84) Parikh, R.; Mathai, A.; Parikh, S.; Chandra Sekhar, G.; Thomas, R. Understanding and Using Sensitivity, Specificity and Predictive Values. *Indian J. Ophthalmol.* **2008**, *56* (1), 45–50. <https://doi.org/10.4103/0301-4738.37595>
- (85) Sloan, A.; Smith-Warner, S. A.; Ziegler, R. G.; Wang, M. Statistical Methods for Biomarker Data Pooled from Multiple Nested Case–Control Studies. *Biostat. Oxf. Engl.* **2019**, *22* (3), 541–557. <https://doi.org/10.1093/biostatistics/kxz051>.
- (86) Sloan, A.; Song, Y.; Gail, M. H.; Betensky, R.; Rosner, B.; Ziegler, R. G.; Smith-Warner, S. A.; Wang, M. Design and Analysis Considerations for Combining Data from Multiple Biomarker Studies. *Stat. Med.* **2019**, *38* (8), 1303–1320. <https://doi.org/10.1002/sim.8052>.
- (87) Petruccioli, E.; Chiacchio, T.; Pepponi, I.; Vanini, V.; Urso, R.; Cuzzi, G.; Barcellini, L.; Cirillo, D. M.; Palmieri, F.; Ippolito, G.; Goletti, D. First Characterization of the CD4 and CD8 T-Cell Responses to QuantiFERON-TB Plus. *J. Infect.* **2016**, *73* (6), 588–597. <https://doi.org/10.1016/j.jinf.2016.09.008>.
- (88) Barry, C. E.; Boshoff, H. I.; Dartois, V.; Dick, T.; Ehrt, S.; Flynn, J.; Schnappinger, D.; Wilkinson, R. J.; Young, D. The Spectrum of Latent Tuberculosis: Rethinking the Biology and Intervention Strategies. *Nat. Rev. Microbiol.* **2009**, *7* (12), 845–855. <https://doi.org/10.1038/nrmicro2236>.
- (89) Allen, N. PC.; Swarbrick, G.; Cansler, M.; Null, M.; Salim, H.; Miyamasu, M.; Howard, J.; Boyle, J.; Lewinsohn, D.; Lewinsohn, D. Characterization of Specific CD4 and CD8 T-Cell Responses in QuantiFERON TB Gold-Plus TB1 and TB2 Tubes. *Tuberculosis* **2018**, *113*, 239–241. <https://doi.org/10.1016/j.tube.2018.10.014>.

Chapter 6 Multiplexed Protein Detection Platform for Diagnosing Latent Tuberculosis and Stratifying Risk of Reactivation

6.1 Author Contributions and Acknowledgements

This chapter contains unpublished work intended for future publication. The thesis author, Krista Meserve, was the sole contributor to the writing and cytokine comparison analysis, and generated all figures and tables, except for table 6.1. The models in this chapter portrayed in figures 6.1, 6.3, and 6.5 and the machine learning methods section were developed and written by our bioinformatics collaborators, Dr. Ruoqing Zhu, Haowen Zhou, and Mingrui Xu. Dr. Cole Chapman and Dr. Heather Robison developed the 13-plex assay employed here and analyzed the first 135 patient QFT samples, while the thesis author analyzed the remaining 360 patient QFT samples, completed final cytokine comparison analysis, and managed the multi-site collaboration. Our clinical collaborators, led by Dr. Patricio Escalante, generated table 6.1. The working manuscript title is: Multiplexed Protein Detection Platform for Diagnosis Latent Tuberculosis and Stratifying Risk of Reactivation. The current authorship list is as follows: Krista Meserve, Cole Chapman, Haowen Zhou, Mingrui Xu, Heather Hilgart, Pedro Sanchez, Heather Robison, Balaji Pathakumari, Manik Reddy, Kale Daniel, Thomas Cox, Courtney L. Erskine, Paige K. Marty, Maleeha Shah, Mounika Vadiyala, Snigdha Karnakoti, Virginia Van Keulen, Elitza Theel, Tobias Peikert, Colleen Bushell, Micahel Welge, Rafael Laniado-Laborin, Ruoqing Zhu, Patricio Escalante, Ryan C. Bailey.

I would like to thank the many people on the team who contributed to getting us the samples for analysis. Dr. Cole Chapman and Dr. Heather Robison for initial project conception

and direction. I would like to thank Dr. Patricio Escalante from the Mayo Clinic for his leadership through this project. I acknowledge Heather Hilgart for storing and sending the many LTBI samples collected over the years; Pedro Sanchez, Tom Cox, Kale Daniel, Mounika Vadiyala, Maleeha Shah, Snigdha Karnakoti, Dr. Paige Marty, Dr. Balaji Pathakumari, Courtney Erskine, Dr. Elitza Theel, and Virginia P. Van Keulen from the Mayo Clinic for their dedication to enrolling patients, collecting samples, and conducting additional testing; Dr. Ruoqing Zhu, Mingrui Xu, and Haowen Zhou from the University of Illinois at Urban-Champaign (UIUC) for their work on developing the bioinformatic models used to analyze the data in this chapter; and Colleen Bushell, Michael Welge, Dr. Charles Blatti from UIUC and Dr. Rafael Laniado-Laborin from Hospital de Tijuana for their helpful discussions. Thank you to Ryan Bailey for his project guidance and to my Bailey Lab colleague, Manik Reddy, for all the fruitful conversations centered around this project.

6.2 Introduction

Pulmonary tuberculosis (TB) is a complex condition resulting from infection with *Mycobacterium tuberculosis* (Mtb) bacteria. TB is estimated to be present in around 25% of the world's population and continues to be a fatal disease, with an attributed 1.6 million deaths worldwide in 2021.^{1,2} TB disease is currently regarded as a continuum of various disease phases and each phase requires different methods of diagnosis and treatment regimes, adding to the complex task of TB eradication.³⁻⁵ Upon infection, the host immune response will attempt to contain and clear the Mtb, but under many circumstances only succeeds in sequestering the bacteria in calcified granulomas found primarily in the lungs and lymph nodes.⁶⁻⁸ Granuloma development aids Mtb persistence by isolating the bacteria from the host's immune response, but also protects the host from continued bacterial growth and replication. The dynamic bacterial and

immunological equilibrium induced by the granuloma environment results in a phase of TB infection called latent TB infection (LTBI).⁸ It is estimated that from all Mtb-infected individuals worldwide, 20% manifest clinically as TB disease and 80% persist as LTBI, totaling an estimated 1 billion people.^{6,9}

Approximately 90% of LTBI patients who are immunocompetent will stay asymptomatic and non-contagious.^{4,6} The remaining patients will eventually reactivate from LTBI to active TB through a disruption in the dynamic equilibrium resulting in rupture of the protective granuloma. The Mtb is no longer held in a quiescent state and will begin to replicate within the lungs of the host. This reactivation event facilitates further transmission of TB disease. Many reactivation events occur within 24 months of initial infection, highlighting the importance of diagnosing the latent phase.⁴ Therefore, a key to eradicating TB involves the identification of individuals with LTBI, as well as to stratify patients by risk of reactivation from LTBI to active TB, since preventative antibiotic therapy would be most beneficial for high-risk individuals.

To reach this ambitious goal, high performance diagnostics for accurate LTBI diagnosis and risk stratification are desperately needed. There is currently a lack of gold standard for stand-alone LTBI diagnostics and diagnosis relies on TB-specific blood-based interferon-gamma release assays (IGRAs) and additional testing. The current standard IGRA is the commercialized QuantiFERON test (QFT). The QFT assay stimulates monocytes in whole blood samples with Mtb-specific antigens and controls followed by detection of interferon-gamma (IFN- γ) using an enzyme-linked immunosorbent assay (ELISA) to identify those who have been infected by Mtb.^{10,11} While IGRAs are accurate in detecting prior exposure to Mtb, inconclusive tests can occur in IFN- γ dysregulated patients, IGRAs are unable to accurately differentiate between LTBI and active disease, and they have less than 3% predictive value in determining risk of

reactivation.^{5,12-14} Most of the current research into quantifying reactivation risk is focused on RNA signatures, which are generally less stable than protein biomarkers and require RNase-free facilities.¹⁵⁻¹⁹ To facilitate a more streamlined integration into current TB diagnostics, protein-based biomarker signatures for risk stratification need to be explored.

Our research aims to work towards the WHO's goal of decreasing TB incidence by 80% before 2030 by expanding the TB diagnostic toolbox with a multiplexed immunoassay tool that addresses both LTBI status and risk of reactivation using a sample input of stimulated QFT plasma. Multiplexed assays are an area of intense interest in clinical diagnostics, as the complex biological processes of the immune system are more informatively understood using multi-biomarker profiles, rather than single biomarkers.²⁰⁻²⁵ In a TB context, multiplexed assays can identify host biomarkers other than IFN- γ as potential indicators of disease or reactivation risk, effectively reducing false negatives from IFN- γ dysregulated or IFN- γ independent patients.^{24,26} There has been a heavy focus on developing multi-biomarker signatures for determining active TB status²⁷⁻³³ and some studies have incorporated multi-biomarker signatures for other phases of TB infection, such as LTBI.³⁴⁻³⁸ These studies demonstrate promise for using cytokine biomarkers to differentiate various phases of TB infection. However, many fail to account for immunological variation between patients and none provide a tandem approach to both LTBI and reactivation risk stratification.

This work applies a whispering gallery mode, silicon photonic microring resonator biosensor platform capable of multiplexing up to sixteen different biomarkers. The protein quantification in patient samples is followed by machine learning algorithms to classify patients into relevant clinical bins. The 40-minute assay with automated fluidic handling is faster and requires less manual manipulation than a traditional ELISA assay and, when coupled to machine

learning, provides a method to identify important diagnostic biomarkers for LTBI and risk classification. We have previously applied this multiplexed microring platform in various clinical capacities, including LTBI-relevant diagnostics.³⁹⁻⁴⁵ However, these earlier LTBI studies utilized peripheral blood mononuclear cells (PBMCs) that were cultured and stimulated with six different antigens or controls, which is technically laborious and time consuming. Notably, though, this work demonstrated the applicability of the platform coupled to machine learning methods to generate biomarker profiles that were not only biologically driven, but also led to predictive accuracies for LTBI and high-risk status that indicated the potential for clinical diagnostics. Employing this assay method with stimulated QFT plasma as the specimen would increase the applicability of our immunoassay platform and create a more rapid profiling approach that is directly amenable to the current clinical workflow for TB diagnostics.

Herein, we report a thirteen-plex immunoassay tool for LTBI diagnostics and risk assessment that uses QFT stimulated plasma as the sample input coupled with random forest machine learning to identify LTBI patients and classify their associated risk of reactivation. We report predictive accuracies for classifying LTBI positive (LTBI+) status from the population of patients who received QFT testing at the Mayo clinic using both absolute and precision normalized biomarker concentrations. We further divide the LTBI+ patient group into high or low risk of reactivation and report predictive accuracies for classifying both risk designations. Further, we report the top important variables for all the models and highlight a dependence on specific biomarkers in the panel for each classification. Through this implementation, we demonstrate how our microring resonator platform is applicable to the current TB-diagnostic pipeline and can increase clinical information gleaned from a single test to better inform further testing, treatment, and monitoring plans for individual patients.

6.3 Methods

6.3.1 Subject enrollment and clinical designations

This study approved by the Mayo Clinic Institutional Review Board and Olmsted County Public Health Services. All study participants signed an informed written consent. Subjects were enrolled in Rochester, Minnesota between August 2017 and December 2023. Risk factors for TB infection, TB progression, and/or TB reactivation were obtained through a questionnaire and review of medical records as previously described.⁴⁶⁻⁴⁸ LTBI diagnoses were made based on the Center for Disease Control and Prevention (CDC) current guidelines criteria, TB risk factors, and prior TST and QuantiFERON®-TB Gold In-Tube or Gold In-Tube Plus results (Qiagen, Germantown, MD).⁴⁸ The study subjects included TB unexposed individuals with negative IGRA testing results (LTBI negative-cases), and subjects with LTBI at varying risk for developing active TB infection, including untreated LTBI patients and patients who had LTBI therapy. A modified multifactorial predictive modeling platform (Online TST/IGRA interpreter), adjusted by LTBI treatment effect, was applied to estimate the cumulative risk of TB reactivation in all subjects.^{49,50}

Three clinical designations were used in this study: LTBI+, increased- or high-risk LTBI status, and low-risk LTBI status. Together, these designations will provide information relevant to TB risk assessment and, thus, individual treatment recommendations relevant for clinicians and public health providers who screen, diagnose, and manage subjects at risk of reactivation to active TB. As described above, CDC guidelines for diagnosis of LTBI were used to classify subjects as LTBI positive or negative. Subjects with a LTBI+ diagnosis were deemed high-risk of TB reactivation patients if they could be classified as either (1) having untreated LTBI with both TST+ and prior IGRA+ results, (2) having untreated LTBI with TST+ conversion, prior

IGRA- results, and prior TB exposures, (3) having prior close TB exposure and subsequent IGRA+ results, or (4) being immunosuppressed with untreated LTBI diagnosis as per current guidelines. Subjects with a LTBI+ diagnosis were classified as low-risk of TB reactivation if they had LTBI+ diagnosis and completed guidelines-based preventative treatment for LTBI and had low likelihood for subsequent TB exposures at the time of study enrollment, such as those living in Minnesota or other low TB endemic areas.

6.3.2 Sample Collection and QuantiFERON testing

Three milliliters of blood were collected from each subject and sent for same-day QFT testing at the Mayo Clinic's clinical laboratories. Initial study participants (39/165 patients) were analyzed using the QuantiFERON®-TB Gold In-Tube (QFT, Qiagen) IGRA kit. The QFT assay was performed as recommended by the manufacturer and the standard protocol included three in-tube stimulation conditions: a negative control (NIL), positive control (MIT), and the Mtb-specific peptide mixture for CD4+ cell stimulation (AG).^{49,51} During the study, the Mayo Clinic laboratory transitioned to the QuantiFERON®-TB Gold Plus (QFT-Plus, Qiagen) IGRA kit.⁵² The QFT-Plus kit contained the same stimulations of NIL, MIT, and Mtb-specific peptide mixture, now termed TB1 and shown to be akin to the AG stimulation in the original QFT assay. QFT-Plus included an additional Mtb-specific stimulation, TB2, that contained the same peptide cocktail as TB1 along with proprietary peptides to elicit both CD4+ and CD8+ T-cell responses.⁵³ For the algorithms developed in this work, data from the TB2 tube was excluded so that all data emanated from NIL, MIT, and AG/TB1 stimulations only.

After patient blood was stimulated in-tube, the plasma was separated from the red blood cells and analyzed for IFN- γ concentration by an enzyme-linked immunosorbent assay (ELISA). In the QFT assay, a positive result was declared if measured levels of IFN- γ included $NIL \leq 8.0$

IU/mL, the IFN- γ concentration difference between TB1 and NIL tubes (TB1-NIL) ≥ 0.35 IU/mL, and TB1-NIL $\geq 25\%$ of the NIL IFN- γ value. In the QFT-Plus assay, a positive result was declared if IFN- γ concentrations in NIL ≤ 8.0 IU/mL, TB1-NIL or TB2-NIL ≥ 0.35 IU/mL, and TB1-NIL or TB2-NIL $\geq 25\%$ of the NIL IFN- γ value. Leftover plasma from each QFT or QFT-Plus tube were frozen after ELISA testing, stored at -80°C , and thawed immediately before multiplexed cytokine analyses.

6.3.3 Silicon photonic microring resonator technology and instrumentation

Silicon photonic microring resonators are a type of whispering-gallery mode sensor in which light continually circulates within a microring waveguide microstructure, resulting in an evanescent field extending above the microring surface.⁵⁴ Light couples into the microring waveguide at a wavelength dependent on the effective refractive index (RI) in the evanescent field, according to the following equation:

$$\lambda = \frac{2\pi r}{m} n_{eff}$$

where λ is wavelength, m is an integer, r is radius of circular waveguide and n_{eff} is the effective RI of the optical mode.^{55,56} Capture probes (e.g., antibodies, nucleic acid aptamers) covalently attached to the microring resonator attract specific target biomolecules to the sensor surface, which alters the RI within the sensing region. The altered RI gives rise to a change the resonant wavelength and results in a measurable shift in non-transmitted wavelength. Using calibration curves, the overall wavelength shift over the course of an assay is correlated to amount of target biomolecule in a sample.^{57,58} The microring structure is easily fabricated, results in low coefficient of variation, and is amenable to multiplexing many microring sensors on one silicon chip.

The cytokine biomarker data in this report was collected using the Genalyte Matchbox instrument (Genalyte, Inc., San Diego, CA) and silicon sensor chips (Genalyte, Inc. San Diego, CA). The silicon sensor chips were 4X6 mm in size and fabricated with 128 individual microrings arranged in clusters of four rings spatially fabricated across two channels of sixteen ring clusters each. This sensor chip layout grants simultaneous analysis of up to sixteen different analytes, each with four technical replicates, in two samples. The multiplexed sensor chips were housed in injection molded cartridges (Genalyte, Inc., San Diego, CA) to create two sealed microfluidic channels along the top of the microring channels. When inserted into the instrument, a fully automated microfluidic path is created that pulls all reagent liquid from a 96-well plate across the surface of the sensor chip at 30 $\mu\text{L}/\text{min}$ and then discarded into waste. The sensor chip and cartridge unit were discarded after each sample to eliminate potential carryover between samples.

6.3.4 Multiplexed biomarker panel and assay design

The 13-plex cytokine and chemokine panel deployed in this study consisted of IL-1 β , IL-2, IL-6, IL-10, IL-15, IL-17, CCL2, CCL3, CCL4, CCL8, IFN- γ , IP-10, and TNF- α . As previously described, capture antibodies for each biomarker were covalently linked to clusters of four microring sensors through silanization with (3-aminopropyl)triethoxysilane (APTES), followed by introduction of a homo-bifunctional linker, bis(sulfosuccinimidyl)suberate (BS3), and the antibody of interest using precision spotting techniques by Genalyte, Inc.⁵⁷⁻⁵⁹ The sensor chips were blocked with bovine serum albumin (BSA) containing buffer, dry coated for antibody stability, and stored in a desiccator at 4°C until use.

The sensing scheme resembled a sandwich-style ELISA, with the immobilized capture antibody, protein, and biotinylated tracer antibody forming a highly specific sandwich complex

that is tagged with a streptavidin-linked recognition reagent through strong biotin-streptavidin interactions.⁶⁰⁻⁶² A functionalized chip was inserted into the instrument and running buffer, 1X phosphate buffered saline with 0.5% BSA (PBS-BSA), was flowed across the chip to equilibrate the surface for five minutes. The data collection then began with running buffer flowing consistently for two minutes to collect baseline signal. The following assay reagents were then flowed across sequentially: sample of interest (7 mins), buffer rinse (2 mins), mixture of biotinylated tracer antibodies (1-2 $\mu\text{g/mL}$, 7 mins), a buffer rinse (2 mins), streptavidin horse-radish peroxidase (SA-HRP, 4 $\mu\text{g/mL}$, 7 min), a buffer rinse (2 mins), 4-chloro-1-naphthol (4CN, stock concentration, 7 mins), and a final buffer rinse (3 mins), for a total assay time of 39 minutes. The frequent buffer rinses remove any unbound material before the next reagent is introduced. The final reagent, 4CN, reacts with the localized HRP to form an insoluble precipitate within the evanescent field, amplifying the resonant wavelength and resulting in lower detection limits and broader sensing regions. To quantify relative shifts in each sample, the signal immediately before the 4CN step ($t=29$ min) was subtracted from the signal at the end of the final buffer rinse ($t=39$ min) to obtain the net shift (Δpm) for each individual target.

6.3.5 Assay panel optimization and multiplexed calibrations

Each biomarker was individually optimized to determine optimal tracer antibody concentration and appropriate standard concentration that allowed for construction of an eight-point, four-parametric calibration curve that ranges from a saturating signal to baseline signal. Prior to multiplexing the biomarkers, each pair of capture antibody and standard/tracer antibody was tested for cross-reactivity. Using a checkerboard method, each individual standard/tracer antibody pair was flowed across each capture antibody to ensure that capture antibodies produce a response only to their respective standard/tracer antibody pair. Additionally, optimized

sandwich assays were tested in human plasma to ensure detection efficacy in the biologic matrix of interest. New reagent lots introduced during the study were tested before use in sample analysis.

Calibration of the 13-plex immunoassay was completed in a multiplexed format in two relevant background matrices (50% plasma and 10% plasma). Seven serial dilutions from a saturating analyte concentration and a matrix blank were analyzed in the assay format described above and yielded an eight-point calibration curve relating standard concentrations to relative resonance wavelength shift. Net resonance wavelengths (Δpm) were plotted as a function of standard concentration and fit to a four parametric logistic function, as described previously.⁵⁸ Limits of detection (LOD) and quantification (LOQ) were defined as the blank signal plus three times and ten times the standard deviation of the blank, respectively. New calibrations were constructed for each batch of sensor chips. At least three calibrations were completed per matrix and averaged over the usage lifetime of each chip batch to account for temporal variation in the assay signal. The averaged calibrations were used to construct a final four parametric calibration curve fit for each target that was subsequently used for converting net resonance wavelengths to analyte concentration in the patient samples.

6.3.6 Patient Sample Analysis

Each sample was analyzed at two dilutions, in parallel, in under forty minutes using a total of 210 μL of stimulated plasma leftover after QFT analysis. Sample dilutions of 10X and 2X were chosen to reduce sample volume requirements, while spanning necessary dynamic ranges for all cytokines in the multiplexed panel. Each plasma sample ($\sim 300 \mu\text{L}$) was removed from the -80°C , thawed at 4°C , and diluted two- and ten- fold in 1X PBS-BSA to a total volume of 350 μL . Standard biohazard safety level two precautions were exercised while handling the

plasma samples. The sample was analyzed with the method and reagents described above, with both dilutions of one sample being analyzed on a single sensor chip.

The resulting data for each immunoassay experiment is a csv file for each individual microring sensor. Using in-house R programming code, the csv files were aggregated, thermal controls were subtracted, and ring clusters were associated with their specific capture antibody. The data was plotted as relative shift over time for each individual ring and then transformed to net shift by subtracting the relative shift immediately before the 4CN amplification step from the relative shift at the end of the final buffer rinse. Using the calibration curves, the net shift for both analyzed dilutions (10X and 2X) was converted to analyte concentration using the corresponding calibration (10% plasma and 50% plasma, respectively). The technical replicates (n=4) were averaged within each dilution. The dilution that resulted in a concentration closest to the inflection point of the specific target's calibration curve was selected, corrected for dilution factor, and used for bioinformatic analysis, with the data from the other dilution being discarded. The inflection point is the midpoint of the calibration, and it is where the curve is most sensitive. Data points that exceed the saturating point of the target's specific calibration were removed and data points below the specific target's limit of detection were converted to zero.

6.3.7 Precision Normalization

Baseline immune responses exhibit significant variation across individuals and populations. Therefore, normalizing the biomarker levels measured in stimulated QFT samples from each individual can potentially account for patient-to-patient variation in baseline immunity and can result in development of more generalizable biomarker signatures. The normalization conditions for each biomarker target used in this report included a negative control subtraction to remove baseline immune response (TB1-NIL), a positive control subtraction to measure TB

specific response against overall positive response (TB1-MIT), and a positive minus negative subtraction to account for the overall immune response of the subject (MIT-NIL). Taken together, the three normalized conditions calculated for each of the 13 measured biomarker concentrations led to 39 features per patient for machine learning analysis.

6.3.8 Statistical testing

Comparing the cytokine concentrations between clinical designations, a two-sample Wilcoxon rank-sum tests, also known as Mann-Whitney U tests or Wilcoxon-Mann-Whitney (WMW) tests, was used. A WMW test is a non-parametric statistical hypothesis test that quantifies differences in the distribution of data between two populations.^{63,64} WMW tests were chosen for comparing the biomarkers between designations because the samples between groups meet the independent, ordinal, and continuous test assumptions, intervals may not be constant, outliers are present, and this test is suited for our sample sizes. The null hypothesis is that the distribution of the groups being compared are identical, with the alternative hypothesis being that the distribution of the groups is not identical.

6.3.9 Random forest machine learning

Random forest is an ensemble learning method that constructs and aggregates a multitude of decision trees to determine a classification outcome and can detect nonlinear effects of covariate features.⁶⁵ The aggregation of many trees increases the flexibility and improves accuracy when compared to using a single decision tree, while feature selection ranks a feature's effect on classification of a clinical designation, identifying the most important variables for classification.⁶⁶

In our random forest supervised machine learning method, the rows of data corresponding to individual patients are the observations and the columns of the data containing raw or normalized cytokine concentrations act as the input variables to the decision trees. The classification pipeline included biomarker feature importance evaluation and variable selection and model construction. Random forests can calculate the importance each specific variable has towards developing the most accurate data splits.⁶⁶ Each time a variable is used at a node, the impurity reduction is calculated and summed across every tree in the forest. The sum divided by the number of trees in the forest is the importance score for that variable.⁶⁷ A greater reduction, or higher variable importance score, is desired. Across multiple forests, an average importance score is calculated, and all variables can be compared to each other to identify which variables are most important in making the classifications. Variables with high importance rankings are used for training a refined, or variable reduced, model. Model performance evaluation was done using out-of-bag samples and leave-one-out cross validation. Random forests do not require manually splitting the data into distinct testing and training sets, as the algorithm fundamentally uses a portion of the data to create a model and the remaining data to get an unbiased estimate of test error.

A unique bagging method was developed specifically for this study due to a high number (n=21 of 165) of repeat patient samples, meaning multiple samples were provided by an individual patient as part of the ongoing longitudinal profiling aspect of the project. This raised the possibility that temporally distinct observations from the same patient could be used to both develop (in-bag) and then subsequently test (out-bag) a tree, introducing correlation bias into the classification model. To avoid this, our team developed a homogenous bagging method to ensure only one timepoint from a patient was included in the bootstrapped observations.

The visual representation of random forest outputs are receiver operator characteristic (ROC) curves. The ROC curve plots the sensitivity and specificity of the model at all possible classification thresholds. ROC curves are compared using the area under the curve (AUC), a metric of accuracy of the model to predict the disease state that ranges from zero to one. An AUC of one indicates 100% accuracy and 100% specificity across all thresholds, or a perfect model, while an AUC of 0.5 is equivalent to random chance. All informatics and data plotting were performed using R coding language.

6.4 Results

6.4.1 Patient Demographics

This study enrolled 144 individual patients who provided a blood draw for QFT testing at an initial timepoint (**Table 6.1**). Seventeen of the patients provided a later second time point and four provided a third time point as part of an ongoing longitudinal profiling project, leading to a total of 165 sample sets included in our analysis. Each set of QFT samples was analyzed independently and the machine learning algorithm accounted for repeat measurements to minimize correlation bias. Of the 165 samples, 78 came from LTBI+ patients. LTBI+ patients were younger, more likely to be male, more likely to be non-Caucasian, and more likely to be born outside of the US than the 84 LTBI- patients. Within the LTBI+ population, 50 were designated to be at a high-risk of reactivation and 25 were designated as being at a low risk of reactivation, with the remaining three being indeterminant risk. The high-risk patients were more likely to be male, but no other demographic data was significantly different between the populations.

6.4.2 Classification of LTBI positive subjects using absolute cytokine concentrations

Using the 165 sample sets in our study, we aimed to differentiate LTBI positive and negative subjects using random forest machine learning. Leave-one-out cross validation was completed to determine the ability of the cytokine profiles to diagnose LTBI from the study population. The absolute cytokine values of the QFT stimulated (TB1, NIL, MIT) plasma samples resulted in an accuracy of 84.1% using the full data set of 39 variables (**Figure 6.1A**). Variable reduction to remove variables contributing to model noise resulted in a reduced data set of twelve variables, but did not improve the accuracy, with a value of 84.8%. The variable importance metrics of the top ten most important variables demonstrates that IP-10 concentration from the TB1 stimulated plasma is the major predictor of LTBI status within the population (**Figure 6.1B**). Four of the top five variables are from the TB1 stimulated plasma, indicating reliance on TB-specific peptide stimulations for designation. Cytokines from the NIL and MIT stimulated plasmas are present later in the top ten list, indicating some contribution from a subject's functional immune response to classifying LTBI status. A key result to highlight in the top ten list is the dependence on a select few cytokines in the multiplexed profiling panel. The top ten variables are composed of six of the thirteen proteins, indicating a high reliance on few variables.

The comparison of cytokine distributions between LTBI positive and LTBI negative subjects in our population corroborates these selected important variables, with all the top six variables having statistically different cytokine distributions between LTBI positive and negative populations (**Figure 6.2, Table 6.2**). The greatest significance falls in the TB1 stimulated plasma, with IP-10, CCL8, and IL-2 showing greatest significance. IL-10 is the only target with significantly different distributions under all three QFT stimulated conditions.

6.4.3 Classification of LTBI positive subjects using normalized cytokine concentrations

Precision normalized biomarker concentrations (TB1-NIL, TB1-MIT, MIT-NIL) replaced the absolute cytokine concentrations as variables for the machine learning algorithm to determine if using intra-patient normalized values improves the accuracy of LTBI status designation. Using the normalized cytokine values resulted in an accuracy of 85.8% using the full data set of 39 variables (**Figure 6.3A**). Variable reduction to a data set of fourteen variables, improved the accuracy to 87.8%. The variable importance plot of the top ten most important variables demonstrates that IP-10 concentration from the TB1-NIL normalized condition is the major predictor of LTBI status within the population (**Figure 6.3B**). Eight of the top ten variables are under TB1-related normalized conditions, indicating heavy reliance on TB-specific peptide stimulation for designation. Cytokines from the MIT-NIL normalized condition are present later in the top ten list, indicating some contribution from a subjects overall immune response to classifying LTBI status. Similar to the absolute cytokine designation, a key result is the dependence on a select few cytokines in the multiplexed profiling panel. The top ten normalized condition variables are composed of five of the thirteen proteins, indicating a high reliance on few variables, specifically IP-10, CCL8, IL-2, and IL-10.

The comparison of cytokine distributions between LTBI positive and LTBI negative subjects in our population corroborates these selected important variables, with all the top five variables having statistically different cytokine distributions between LTBI positive and negative populations (**Figure 6.4, Table 6.2**). The greatest significance falls in the TB1-related normalized cytokine values, with IP-10, CCL8, and IL-2 showing greatest significance under TB1-NIL normalized conditions. IP-10 has the most distinction in population distributions between LTBI positive and negative for two normalized conditions, TB1-NIL and TB1-MIT. To note, IL-10 does not have significant differences in distributions, but all three normalized

conditions are important for the model to designate LTBI status, while CCL2 and IL-1 β are distinct between designations but are not in the top ten best variables for prediction.

6.4.4 Risk classification among LTBI positive subjects

Using the risk classification based on clinical variables at time of QFT sample collection, we aimed to differentiate high-risk and low-risk subjects within all LTBI positive patients. All variables, including absolute and normalized cytokine concentrations, were used as input variables for the model, meaning the full data set consisted of 78 input variables. The model resulted initially in 74.7% accuracy for differentiating high-risk from not-high risk individuals (**Figure 6.5A**). After data reduction to the most important variables, the accuracy increased to 81.3%. The variable importance metrics for high-risk classification revealed a heavy reliance on IL-10 for making the prediction, with five of the top ten variables being IL-10 concentration dependent (**Figure 6.5B**). Interestingly, half of the important variables are unrelated to the TB1 stimulation, meaning the high-risk classification is more dependent on the overall immune function of the LTBI positive patients. For this classification, the model mainly relied on six absolute concentrations and four normalized conditions from only four unique proteins, IL-10, IL-2, IL-6, and CCL3. Further work is currently being conducted to generate the model with just the absolute variables and just the normalized variables, as was described for the LTBI designation models. Early results suggest the model derived from absolute values only will be the best predictor for high-risk classification (full= 73.8%, reduced with six variables = 83%).

The full data set model resulted in 71.0% accuracy for differentiating low-risk from not low-risk subjects within the LTBI positive population (**Figure 6.5C**). Reducing the data set to the most important variables improved the accuracy greatly to 81.5%. The top ten important variables based on variable importance metrics reveals high reliance on IL-10, with five of the

ten variables being IL-10 concentration dependent (**Figure 6.5D**). Out of the ten variables, only three are from normalized cytokine concentrations and six are related to the TB1 variables, indicating a reliance on the absolute cytokine concentrations from TB-specific responses. Four of the thirteen profiled immune proteins comprise these top ten variables, including IL-10, IL-2, TNF- α , and CCL8. Further work is currently being conducted to generate the model with just the absolute variables and just the normalized variables, as was described for the LTBI designation models. Early results suggest the model derived from absolute values only will be the best predictor for low-risk classification (full= 70.1%, reduced with eight variables = 80.6%).

The cytokine distributions between high risk and not high-risk subjects are in **Figure 6.6** with MWM statistical test results. The highest number of targets with significant differences in cytokine distribution is from the NIL QFT stimulation, or the negative control; however, there are no significant differences under the TB1-NIL normalized condition. Across all stimulations and normalized conditions, IL-10 has the most significantly different distribution between groups, with the median concentration for the high-risk population being higher than the not high-risk population for TB1, NIL, MIT, and MIT-NIL. Eight of the ten important variables for high-risk classification are significantly different between populations. Interestingly, IFN- γ has a significantly lower median value in the high-risk group compared to the not-high risk group and is the only comparison that has this classically TB-related target as different between groups.

The cytokine distributions between low-risk and not low-risk subjects are in **Figure 6.7**. There are more significant differences in cytokine concentration distributions in the absolute concentrations in comparison to the normalized conditions, again indicating a classification reliance on the absolute cytokine concentrations. The highest number of targets with significant differences in cytokine distribution are from TB1-related stimulations, with variables across all

absolute and normalized conditions represented. The target with greatest significance is IL-10 and, opposite of high-risk, the median IL-10 concentration is lower for low-risk population in TB1, NIL, MIT, and MIT-NIL conditions compared to not low-risk populations. All variables in the top ten important variables for random forest classification of low-risk patients are significantly different in cytokine concentration distribution between low-risk and not low-risk populations.

Statistical testing was also completed within only LTBI+ patients classified as high or low risk, essentially removing the patients classified as indeterminant risk (n=3). Removing these subjects eliminates the need for “high versus not-high” and “low versus not-low” because all patients are either high- or low-risk classified. Early results confirm the dependence on IL-10 and IL-2 (**Figure 6.8, Table 6.3**). All ten absolute variables with significant differences have greater median concentrations in high-risk compared to low-risk LTBI+ patients. IL-10 is significantly different across all three QFT stimulations and IL-2 is significantly different in TB1 and MIT stimulated plasma samples. Only four normalized conditions resulted in significant differences between populations, with two associated with IL-10 and two with IL-2 (**Table 6.3**). This further supports the heavy reliance on these two cytokines for risk stratification and highlights why the absolute value-derived model is initially outperforming the normalized value-derived model for risk designation.

6.5 Discussion

The aim of this study was to employ microring resonators as a cytokine biomarker sensing platform, integrate the assay into the current TB diagnostic workflow through using QFT plasma as the specimen, and identify biomarker signatures for LTBI and TB reactivation risk-based classifications through machine learning. The 45-minute microring resonator multiplexed

biomarker assay required just 210 μ L of plasma to simultaneously analyze 13 cytokines at two sample dilutions. The multiplexed assay had been previously tested using cell stimulation supernatant samples, which are collected through technically laborious processes.^{44,45} Using QFT-stimulated plasma as the sample input places our method directly in the current TB diagnostic workflow and decreases the potential time between sample collection and analysis allowing for a faster turnaround time. Transitioning from the supernatant sample to the plasma sample matrix required re-optimization of each target biomarker to ensure appropriate responses in plasma and construction of multiplexed calibration curves in plasma for quantitation. We successfully transitioned the established assay into this new sample matrix and analyzed 495 QFT plasma samples.

The enrolled patient population consisted of 165 sample sets, which included 78 LTBI positive patients, of which 50 were classified as a high risk of reactivation and 25 were classified as low risk of reactivation patients. The patient population, which affects the target population of the study, are patients at the Mayo Clinic who underwent QFT testing to determine TB infection status. Each patient sample set consisted of three QFT stimulated plasma samples analyzed with our 13-plex cytokine panel assay, leading to 39 absolute cytokine concentration variables per patient. Precision normalized values led to an additional 39 normalized cytokine concentration variables per patient.

All data points in the study were used to construct random forest models to differentiate between LTBI positive and negative designated patients and reached an accuracy of 87.8% under normalized conditions. The normalized variables resulted in a better predictive accuracy and greater separation between clinical populations of LTBI positive and negative patients in comparison to the absolute variables. The cytokine concentration distributions under normalized

conditions had lower levels of significance for the same cytokines under absolute concentrations, indicating a better distinction between clinical groups. The normalization accounts for patient-to-patient variability by subtracting the cytokine concentrations resulting from negative and positive stimulations within each patient. Using normalized conditions can improve generalizability of the model and potentially reduce misclassification based on inherent variability in the basal immune response.

The important variables for making this classification are highly similar between the absolute cytokine concentration derived model and normalized condition derived model. The models both show TB-specific peptide stimulations are needed to distinguish LTBI positive patients because the top variables are derived from TB1-related stimulations. The main classification biomarker is IP-10 across both methods, with CCL8, IL-2, and IL-10 rounding out the top five in both models. IP-10 is a chemokine with high correlation to TB infection in previous studies. In the cytokine distributions, IP-10 repeatedly has the lowest significance levels between LTBI positive and negative populations which is correlating to the random forest results as the variable that has the greatest effect on differentiating populations. CCL8, IL-2, and IL-10 have also been associated with TB infection previously. The literature precedence of the important variables identified with our microring sensing workflow coupled to the random forest algorithm suggests our method is comparable to existing workflows. Our approach uses fully automated microfluidic reagent handling, has multiplexing capabilities of up to 16 targets, and has a time to result of 45-minutes for two simultaneous samples. These are improvements to current plate-based immunoassay methods that require manual washing, which can induce variability in each sample run.

Interestingly, IL-10 is a top important variable under all three normalized conditions but does not result in significant differences in cytokine distribution in any normalized condition. It is possible that the split value used for differentiating LTBI positive and negative populations is subtle and, therefore, does not result in a significant difference in cytokine distributions. Overall, the variable importance results across models derived from absolute and normalized cytokine concentrations reveal great importance for IP-10, CCL8, IL-2, and IL-10 under TB-specific peptide stimulations to identify LTBI positive subjects from the selected patient population.

The protein-based risk classification is an important aspect of this study, as most risk classifications are based on RNA signatures. Here, we integrate risk classification into the same workflow as QFT testing and LTBI classification using the multiplexed microring resonator sensing platform. The risk classification was completed within the LTBI positive population (n=78) with the goal of using the same data set to identify LTBI positive patients and then stratify them by high or low risk of reactivation. Compared to the LTBI classification model, the risk classification models are less accurate (~81% for both high and low risk classifications). This is likely due to both fewer patients in the population and a greater variability in patients who are clinically classified as a certain risk level. The classification of risk, especially low-risk criteria, has no current gold standard and relies on analysis of many lifestyle and medical factors by an experienced clinician. The LTBI status does not have a defined 'gold standard' diagnostic but can be more objectively defined based on QFT results and additional testing. The less defined clinical classification results in a higher variability of patients within a clinical bin, which contributes to lower predictive accuracies. Current work into developing separate absolute and normalized variable-derived models reveal a greater accuracy, similar to that of the combined model, when using just the absolute variables. This is opposed to the results from the

LTBI designation platform and suggests a reliance on the overall cytokine response to make the prediction in our population.

The high and low risk classifications are inversely related but unique in terms of the goal population of the respective classification. The high-risk classification aims to identify the biomarkers signature that makes the high-risk population stand out from all others (low risk and indeterminate) in the LTBI positive cohort. Conversely, the low-risk classification aims to identify biomarkers that can specifically select out the low-risk population from all others. Initially, we were interested to see if distinct variables or biomarkers would classify the different populations. The variable importance results revealed that very similar variables are important for both classifications. The high overlap in important variables implies the reactivation risk can be thought of as a linear spectrum, with concentrations of specific biomarker conditions responsible for separating out both high and low risk individuals, as opposed to different protein biomarkers altogether separating the risk populations.

Specifically, variables associated with absolute and normalized concentrations of IL-10 and IL-2 are responsible for the greatest variation reduction in the model. These variables account for seven of the ten top variables for high-risk and eight of the ten top variables for low-risk classifications. All the IL-10 and IL-2 associated important variables show significant differences in cytokine concentration distributions between respective clinical populations, further solidifying these variables can differentiate our LTBI positive subject population based on clinically designated reactivation risk. IL-10 is an anti-inflammatory cytokine whose primary function is inhibit cytokine production and the inflammatory response. IL-2 plays a role in increasing the efficiency of cellular function and upregulates the adaptive immune system. Since the concentrations of these cytokines are generally higher in high-risk patients, it may be a signal

that the patient's immune response is shifted from the dynamic equilibrium characteristic in LTBI infection. The IL-10 is working to reduce a possibly unbalanced inflammatory response and IL-2 is attempting to turn on the adaptive response to mitigate damage upon reactivation. However, further studies will be needed to confirm these hypotheses.

A highlight of the risk classification variable importance is the higher reliance on basal immune response (NIL and MIT associated variables) in comparison to the LTBI classification model. The top variable for both risk designations is the level of IL-10 in the negative control QFT stimulation. These results reveal that the general immune responses are more important than TB-specific stimulation responses in risk classification and should be investigated further as biomarkers of reactivation.

In comparing the identified important biomarkers across the normalized condition LTBI classification and both risk designations, a group of eight proteins comprise the top ten important variables: IP-10, CCL8, IL-2, IL-6, IL-10, CCL3, CCL4, and TNF- α . This biomarker reduction has implications in future work for reducing panel size towards developing smaller biomarker panels amenable across multiple cytokine detection platforms. All three QFT stimulations were in each of the top variable lists, so no sample reduction is amenable at this time.

A limitation of our study is our focus on distinguishing LTBI positive populations from an LTBI and active TB negative population. Developing diagnostics that can distinguish these groups is important, as those groups traditionally have similar results in molecular testing. However, by not including active TB populations as a cohort in our study we cannot conclude that the biomarker results are specific to LTBI rather than to general TB infections. Studies that neglect LTBI populations similarly cannot conclude whether the biomarkers are specific to active TB or to TB infection in general. Thus, future work should aim to include an active TB

population and models differentiating LTBI positive versus LTBI negative, LTBI positive versus active TB positive, or other combinations should be developed. Furthermore, based on our study population of individuals receiving QFT testing at the Mayo Clinic, very few were positive for active TB. This implies there is a greater need for our method in this population, as distinguishing LTBI positive patients from other QFT tested patients is more useful in this setting than distinguishing LTBI and active TB cases. A second limitation of this study is that there are currently no gold standards to define any of the clinical designations. The LTBI status is more objectively defined, but the risk classifications are still subjective. This can impart high variability in patient classification and lead to low predictive accuracies, but this limitation is true across all LTBI diagnostic and reactivation risk prediction work.

A goal of our study was to use QFT samples collected at an initial screen to classify a risk of reactivation from LTBI to active TB. Patients at a high risk have a greater potential to progress to active TB, while those at a low risk have lower potential to reactivate. Treatment and monitoring for the two populations can look different. Prognostic biomarkers of reactivation or disease progression have been identified through longitudinal studies that monitor biomarker profiles in patients before and after they progress to disease. These biomarkers are useful, but the act of reactivating to active TB over the course of the study can be related to lifestyle factors that are not captured with the biomarker profiles. Additionally, if treatments are provided to those identified as LTBI positive early in the study, the prognostic biomarkers are limited to a population of treated patients, rather than to all LTBI positive individuals. Furthermore, most work is focused on progression biomarkers and do not aim to find non-progression biomarkers. Our work was not focused on using progression to active TB as an endpoint, rather, we aimed to use biomarkers to classify patients by reactivation risk upon initial QFT sample collection. The

implications of identifying these biomarkers are that they can be generalized to all LTBI positive patients through larger, multi-center studies and they can be used to adjust patient monitoring schedules. Those identified as a high reactivation risk upon initial sample collection can receive specific treatment and increased monitoring schedules. Those identified as a low reactivation risk can receive specific treatment with less frequent monitoring, which can save time, resources, and money. Future work in this ongoing study includes increasing patient cohort size, increasing clinical bins to include more phases of TB infection, and applying the method to a patient population with a high-TB burden.

6.6 Conclusion

This work applied a microring resonator multiplexed sensing platform within a clinically relevant workflow to the TB diagnostic space. Our goals were to use the concentrations of thirteen cytokines in QFT stimulated plasma to identify biomarker signatures that could select LTBI positive subjects and classify their risk of reactivation to active TB. Within one 13-plex cytokine biomarker panel, we demonstrated an accuracy of 87.8% to differentiate LTBI positive patients and accuracies of 81% for stratifying those patients as high or low risk of reactivation. Variable importance metrics highlighted a significant reliance on various normalized conditions of IP-10, CCL8, and IL-2 for making the LTBI classification, while concentrations from various stimulation and normalized conditions of IL-10 and IL-2 were extremely important for both risk classifications. Our work employed a high-plexity, rapid technique to profile clinically relevant samples and identify biomarkers of importance consistent with literature. The inclusion of a low-risk designation in conjunction with high-risk designation provides a unique way to stratify LTBI positive patients with implications in monitoring and treatment.

6.7 Figures

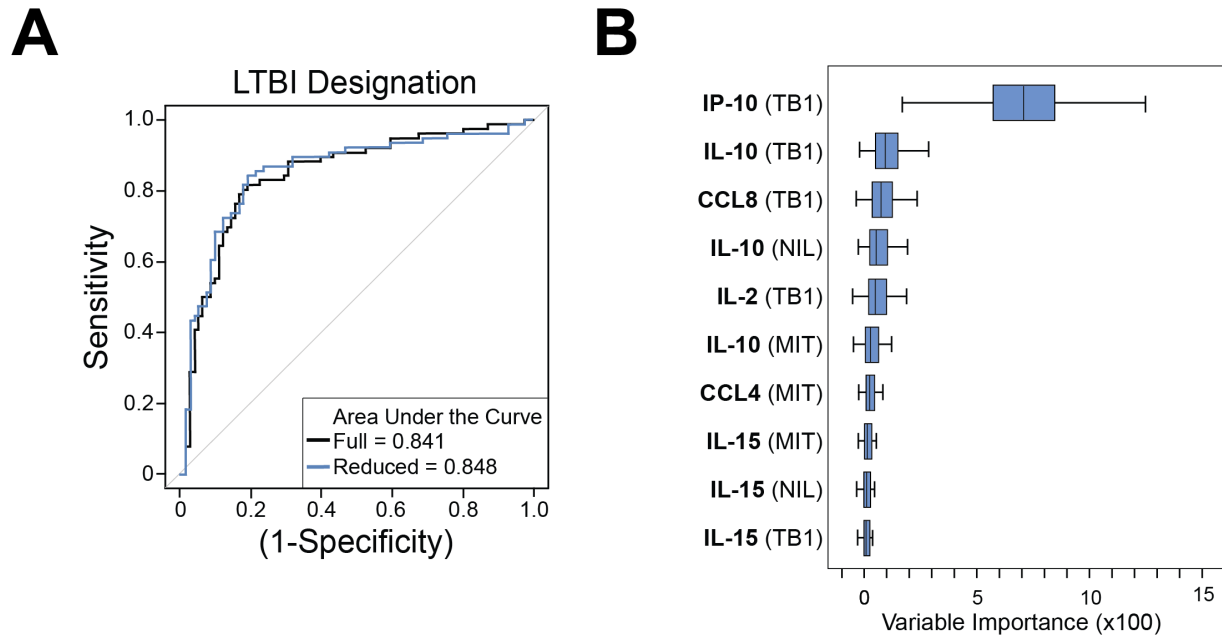


Figure 6.1 LTBI classification using absolute cytokine levels. Random forest classification (A) and the top ten important variables for classification (B) of LTBI positive patients from all others in the sample population.

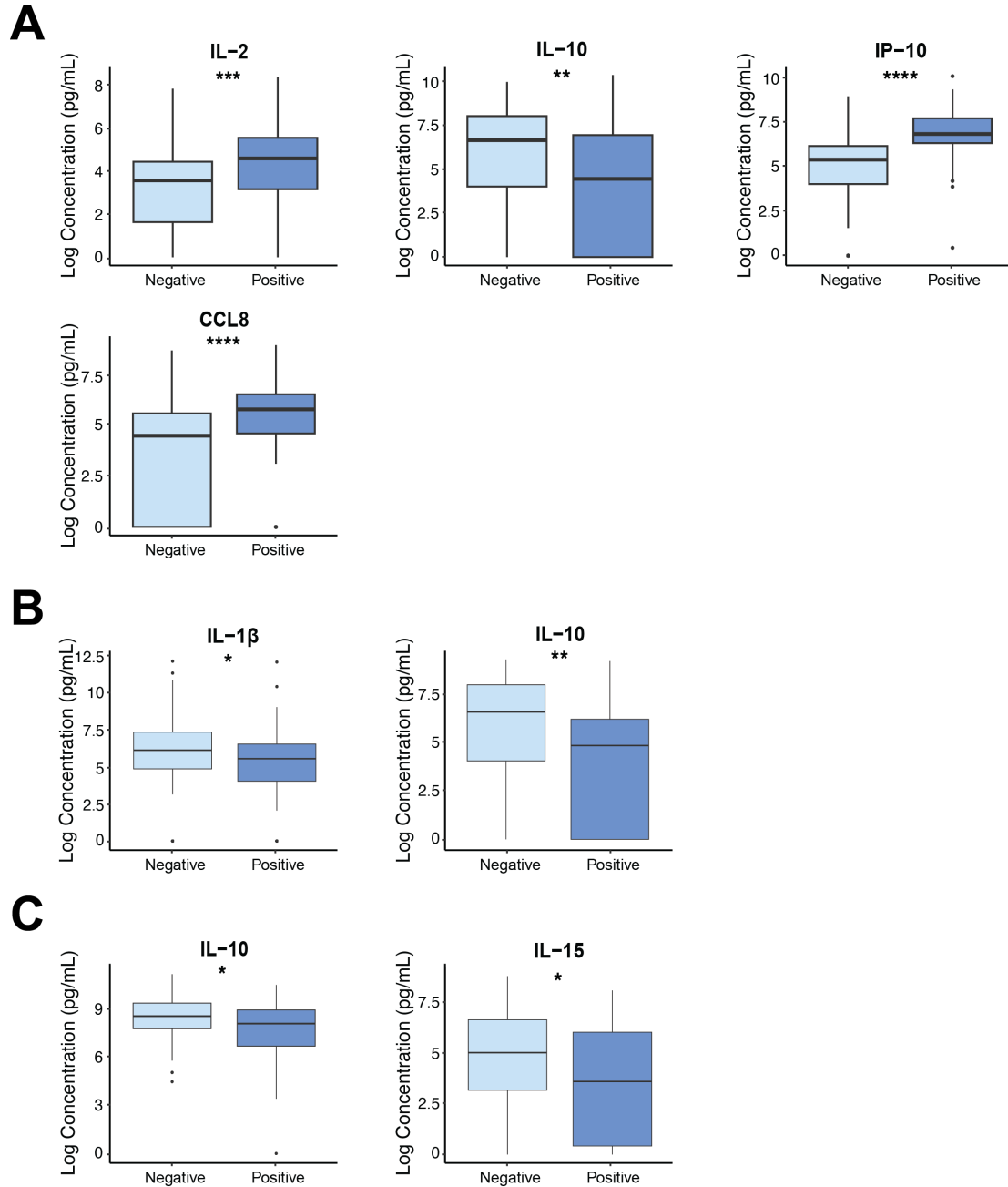


Figure 6.2 Absolute cytokine concentration distribution between LTBI positive and negative populations. The statistically significant differences between groups for the three QFT stimulations, TB1 (A), NIL (B), and MIT (C) are shown. All other cytokines did not show statistical differences between the LTBI positive and negative populations. Data presented on a log scale for visualization. Two-sample Mann-Whitney-Wilcox tests were used for comparing the cytokine distributions between clinical designations. * $p \leq 0.05$, ** $p \leq 0.01$, *** $p \leq 0.001$, **** $p \leq 0.0001$

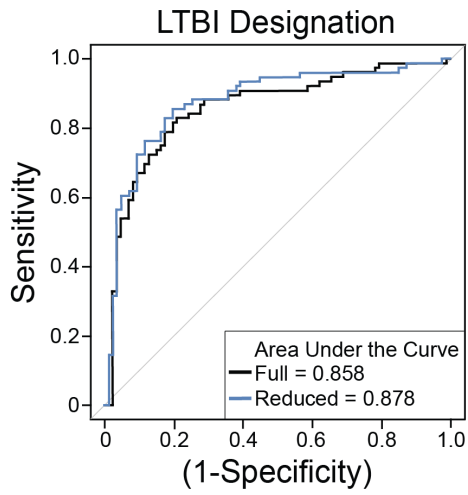
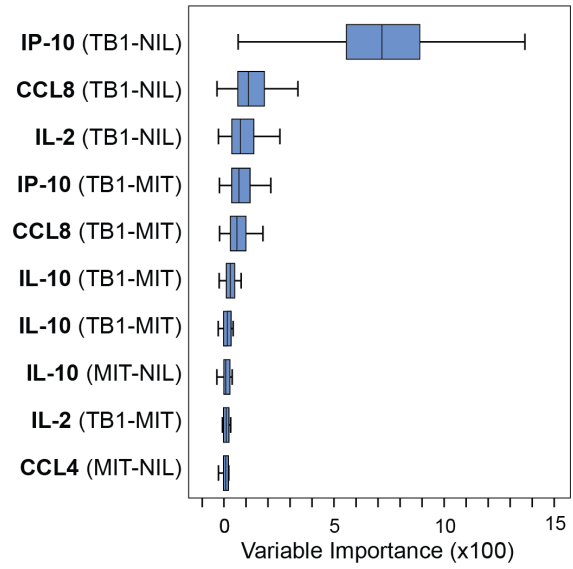
A**B**

Figure 6.3 LTBI classification using normalized cytokine levels. Random forest classification (A) and the top ten important variables for classification (B) of LTBI positive patients from all others in the sample population.

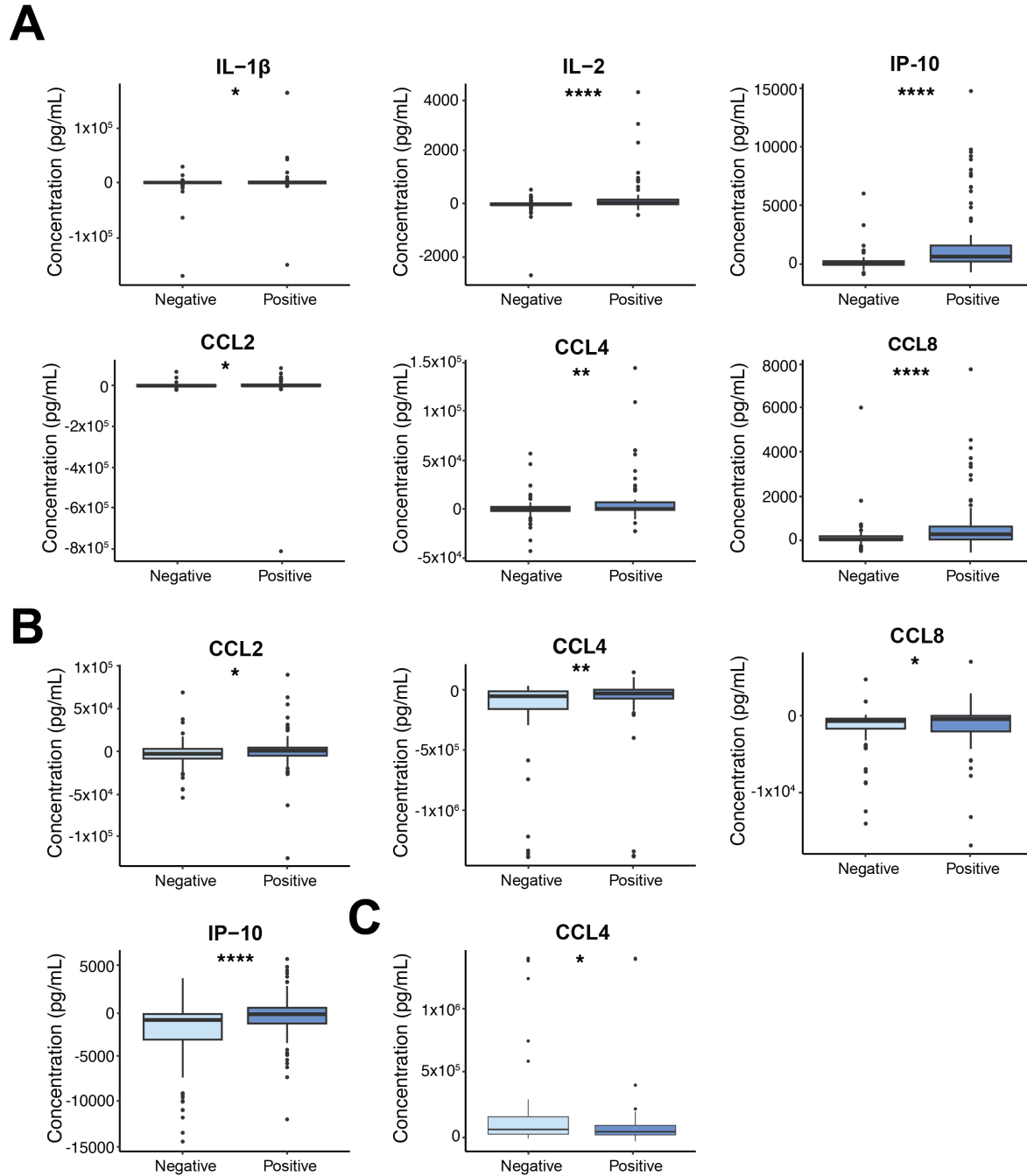


Figure 6.4 Normalized cytokine concentration distribution between LTBI positive and negative populations. The statistically significant differences between groups for the three normalized QFT stimulations, TB1-NIL (A), TB1-MIT (B), and MIT-NIL (C) are shown. All other cytokines did not show statistical differences between the LTBI positive and negative populations. Two-sample Mann-Whitney-Wilcoxon tests were used for comparing the cytokine distributions between clinical designations. * $p \leq 0.05$, ** $p \leq 0.01$, *** $p \leq 0.001$, **** $p \leq 0.0001$

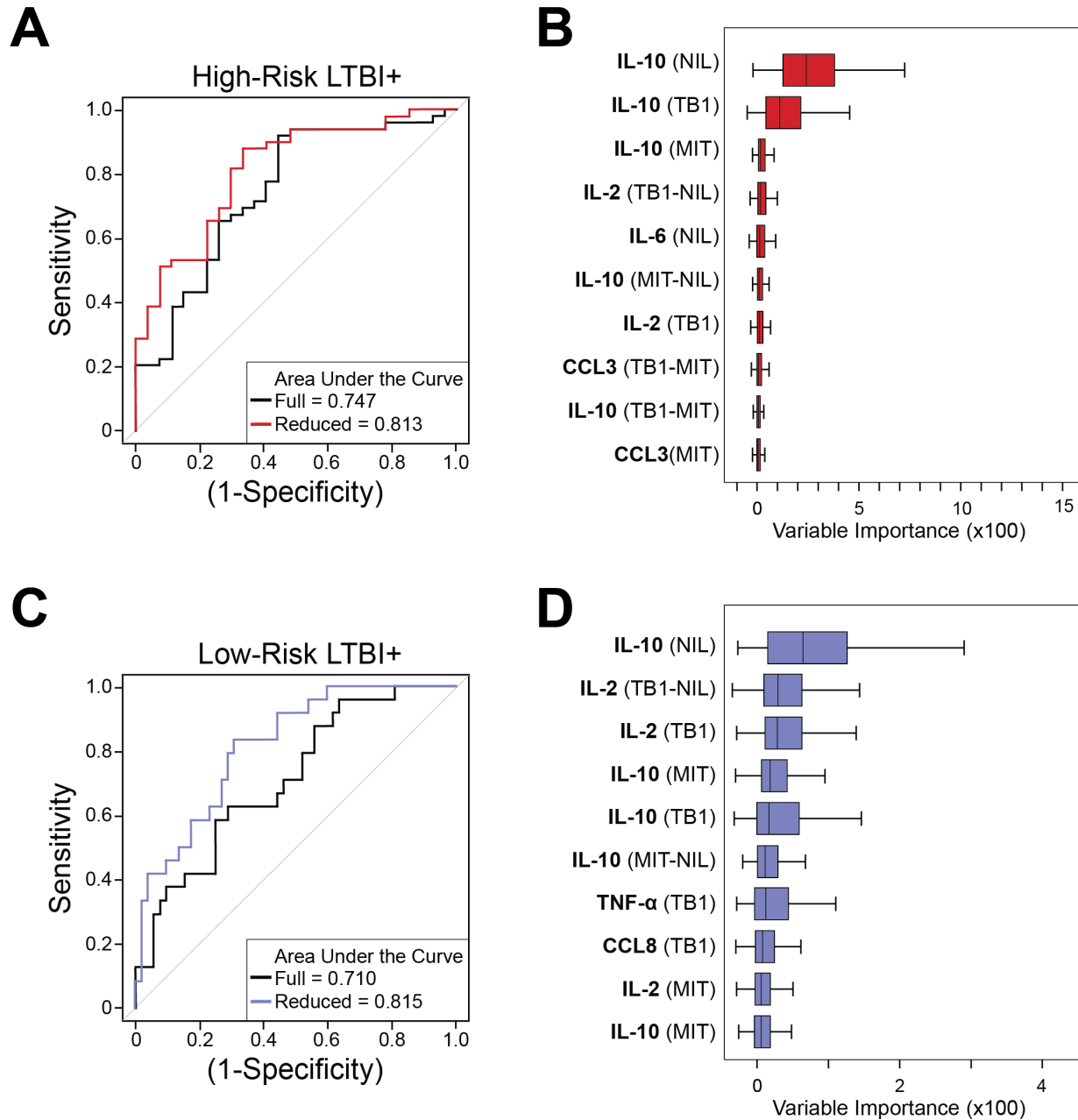


Figure 6.5 High and low reactivation risk stratification. Within the cohort of LTBI positive subjects, the random forest results for high-risk (A) and low-risk (C) designations. The top ten important variables for making the high risk (B) and low risk (D) designations. The variables used for the model was a mix of both absolute and normalized cytokine concentrations.

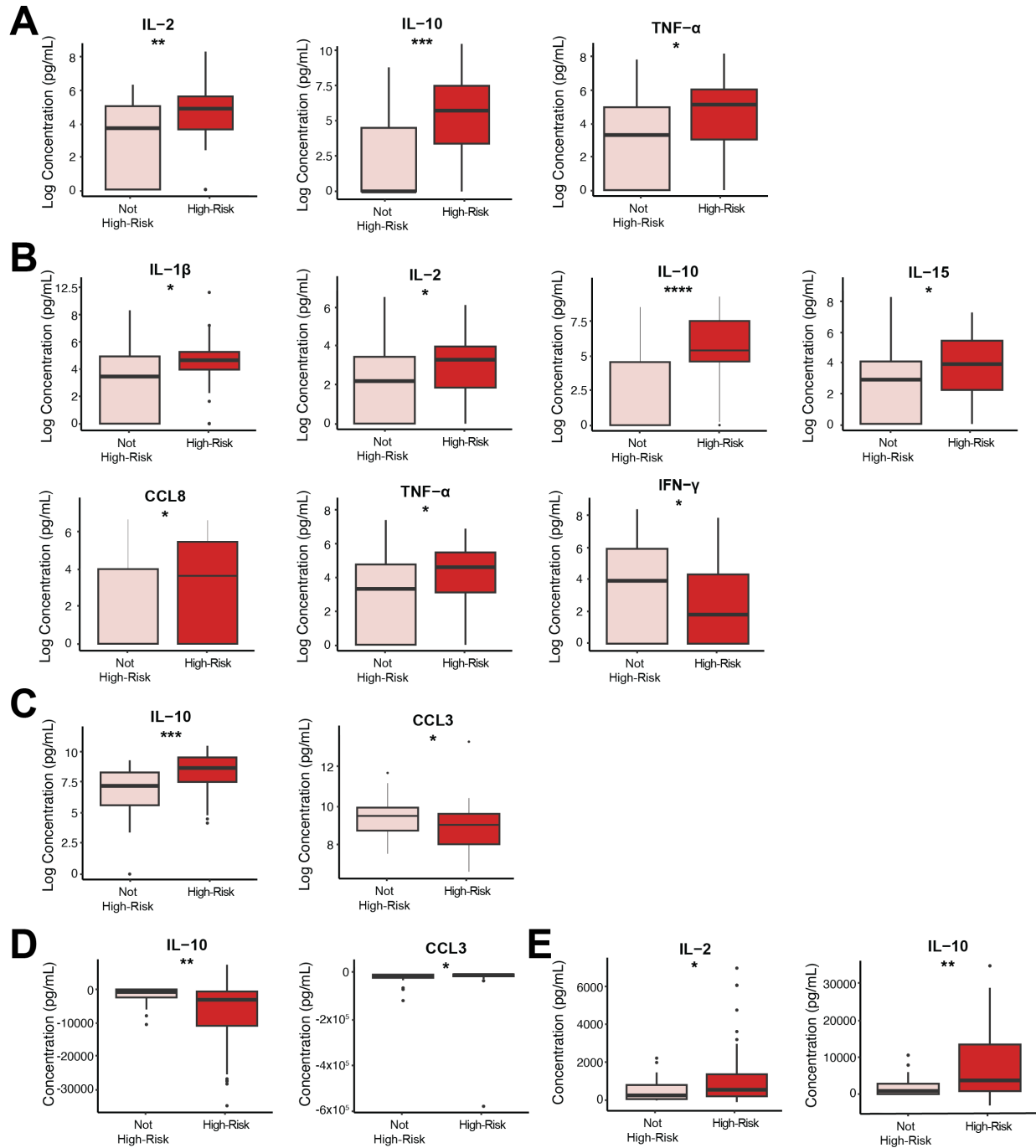


Figure 6.6 Cytokine concentration distribution between high risk and not high-risk populations within LTBI positive subjects. The statistically significant differences between groups for the three QFT stimulations, TB1 (A), NIL (B), and MIT (C), and two normalized conditions, TB1-MIT (D) and MIT-NIL (E) are shown. All other cytokines and all under TB1-NIL normalized condition did not show statistical differences between the high risk and not-high risk populations. Two-sample Mann-Whitney-Wilcox tests were used for comparing the cytokine distributions between clinical designations. * $p \leq 0.05$, ** $p \leq 0.01$, *** $p \leq 0.001$, **** $p \leq 0.0001$

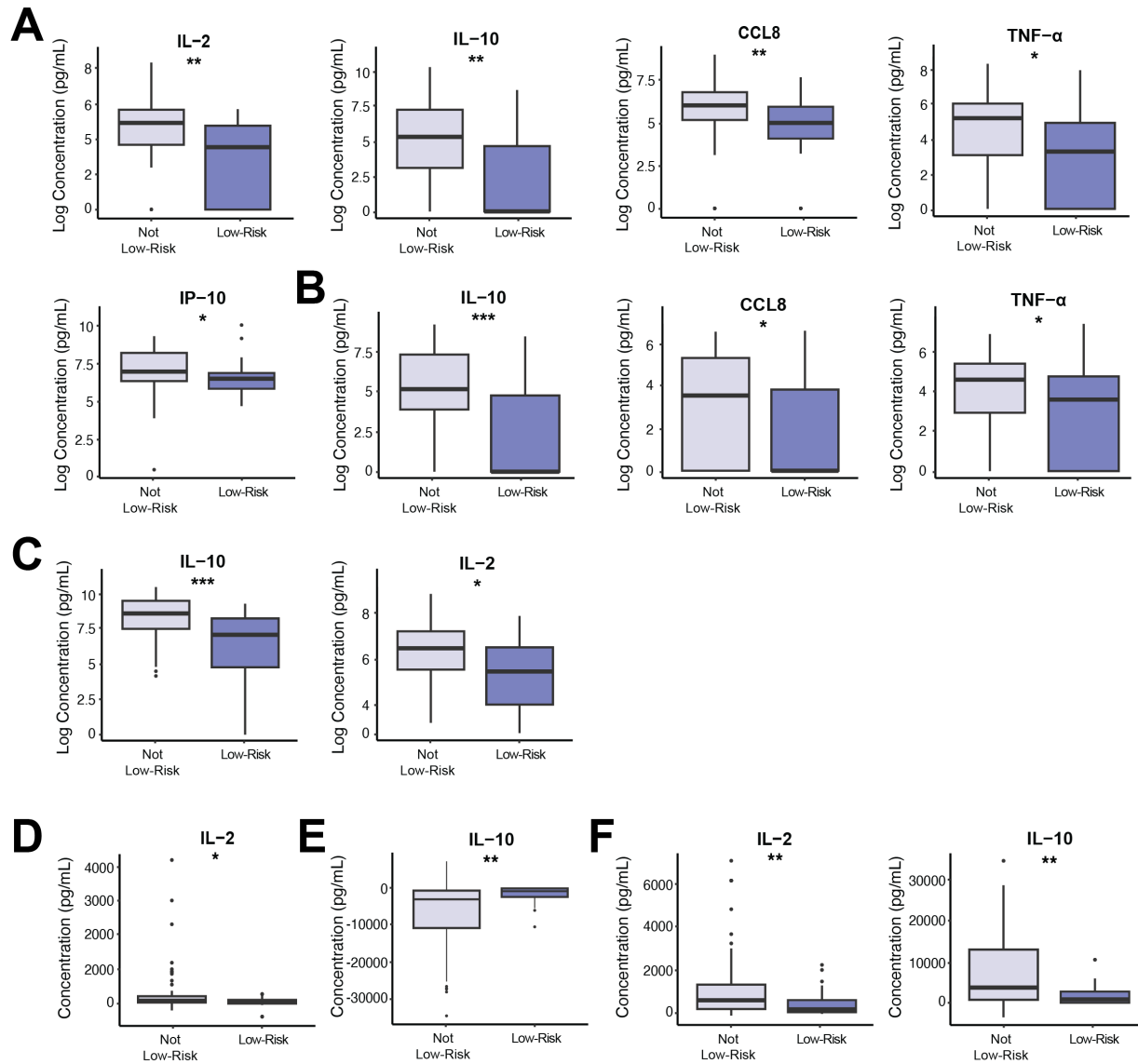


Figure 6.7 Cytokine concentration distribution between low risk and not low-risk populations within LTBI positive subjects. The statistically significant differences between the groups for the three QFT stimulations, TB1 (A), NIL (B), and MIT (C), and the three normalized conditions, TB1-NIL (D), TB1-MIT (E), and MIT-NIL (F) are shown. All other cytokines and all under TB1-NIL normalized condition did not show statistical differences between the low risk and not-low risk populations. Two-sample Mann-Whitney-Wilcoxon tests were used for comparing the cytokine distributions between clinical designations. * $p \leq 0.05$, ** $p \leq 0.01$, *** $p \leq 0.001$, **** $p \leq 0.0001$

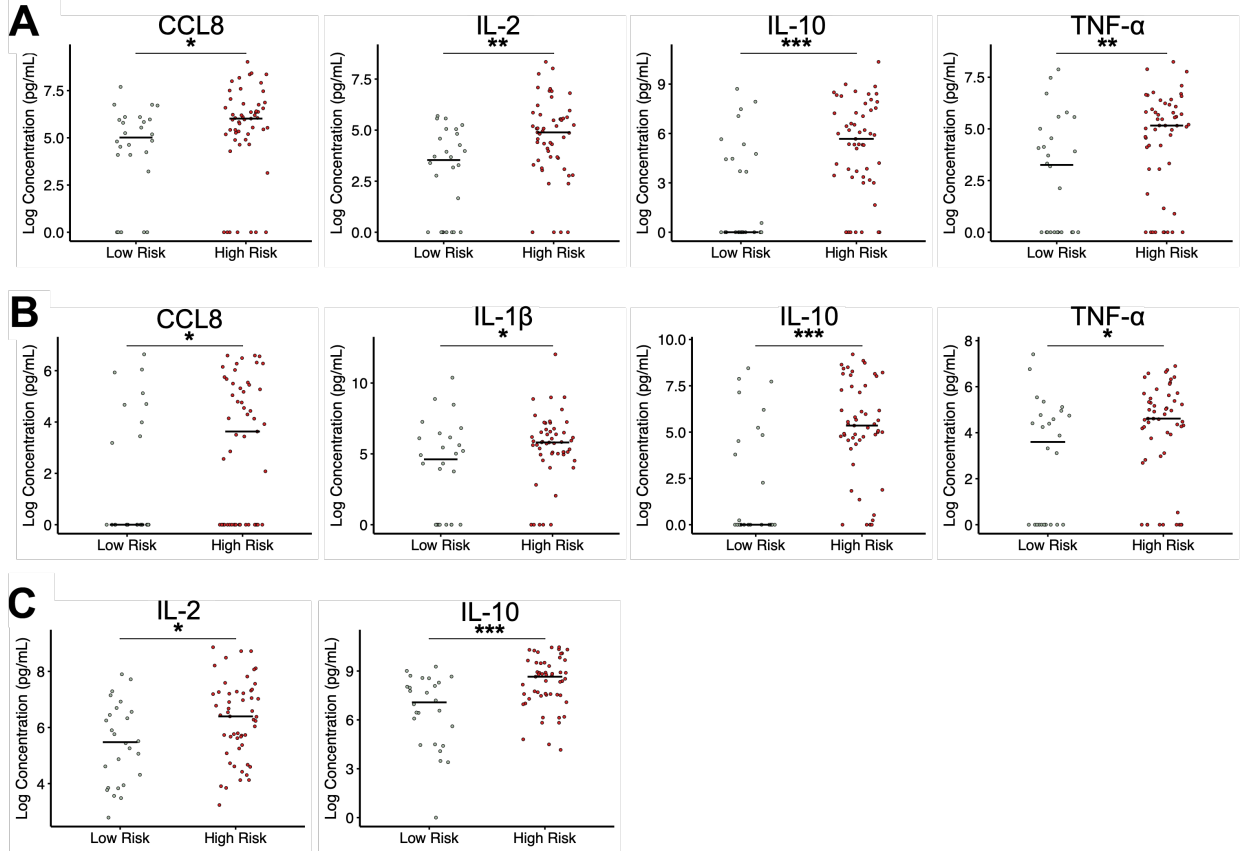


Figure 6.8 Significantly different absolute concentration distributions between high-risk and low-risk LTBI positive patients. Targets under stimulation conditions of TB1 (A), NIL (B), and MIT (C) that were significantly different between clinical populations of high and low risk LTBI+ patients are shown. Median value of clinical population represented as a black line. Data visualized on log scale. Wilcoxon-Mann-Whitney tests were completed to test significant differences in normalized target concentrations between clinical population distributions. * $p \leq 0.05$, ** $p \leq 0.01$, *** $p \leq 0.001$, **** $p \leq 0.0001$

6.8 Tables

Table 6.1 Demographic data of the patients enrolled in the LTBI study.

	Subjects, no. (%)						
	All ^a (n=165)	LTBI- (n= 84)	LTBI+ (n= 78)	P value ^b	High Risk+ (n=50)	Low Risk+ (n=25)	P value ^c
Sex (female)	101 (61.2)	59 (70.2)	42 (53.8)	0.031	22 (29.9)	16 (66.7)	0.050
Age, years							
Mean ± SD	52.32±17.8	57.2±17.4	47.3±16.8	<0.001	46.5±16.7	50.8±17.1	0.331
Range	19 – 84	19 - 84	22 - 81		22 – 81	25 - 78	
Ethnicity							
Caucasian	117 (70.9)	73 (86.9)	43 (55.1)	<0.001	25 (50)	17 (68)	0.379
African American	11 (6.7)	2 (2.4)	8 (10.3)		6 (12)	1 (4)	
Asian Pacific	18 (10.9)	8 (9.5)	10 (12.8)		8 (16)	1 (4)	
Hispanic	7 (4.2)	1 (1.2)	5 (6.4)		3 (6)	3 (6)	
Others	12 (7.3)	0 (0)	12 (15.4)		8 (16)	4 (16)	
Place of Birth ^d							
US Born	111 (67.3)	70 (83.3)	40 (51.3)	<0.001	24 (48)	15 (60)	0.489
Foreign Born (High TB)	5 (3)	3 (3.6)	2 (2.6)		1 (2)	1 (4)	
Foreign Born (Low TB)	49 (29.7)	11 (13.1)	36 (46.2)		50 (25)	9 (36)	
History of BCG vaccination							
Yes	89 (53.9)	50 (59.5)	37 (47.4)	0.063	17 (34.7)	15 (62.5)	0.120
No	25 (15.2)	11 (13.1)	14 (17.9)		12 (24.5)	2 (8)	
Unknown	29 (17.6)	9 (10.7)	19 (24.4)		14 (28.6)	5 (20)	
Probably no	22 (13.3)	14 (16.7)	8 (10.3)		6 (12.2)	2 (8)	
Occupation							
Health care worker, direct patient care	36 (21.8)	16 (19)	20 (25.6)	0.1361	13 (26)	7 (28)	0.975
Health care worker, no direct patient care	34 (20.6)	14 (16.7)	20 (25.6)		13 (26)	6 (24)	
Other	95 (57.6)	54 (64.3)	38 (48.8)		24 (48)	12 (48)	
Predicted cumulative TB risk (%) ^e							
Mean ± SD	4.23±12.15	0.57±1.75	8.24±16.73	<0.001	8.88±15.71	7.17±19.78	0.045
Range	0 – 100	0 – 8.97	0 - 100		0 – 61.25	0 - 100	
Adjusted predicted cumulative TB risk (%) ^f							
Mean ± SD	2.93±8.6	0.25±0.73	5.8±11.82	<0.001	7.87±13.99	2.21±5.05	<0.001
Range	0 – 61.25	0 – 3.81	0 – 61.25		0 – 61.25	0 - 25	
Adjusted predicted annual TB risk (%) ^f							
Mean ± SD	0.09±0.27	0.01±0.03	0.19±0.36	<0.001	0.24±0.41	0.11±0.28	<0.001
Range	0 – 1.99	0 - 0.12	0 – 1.99		0 – 1.99	0 – 1.34	
History of immunosuppression (+) ^g	21 (12)	10 (11.9)	11 (14.1)	0.230	5 (10)	5 (20)	
Tuberculin skin test							
TST (+)	53 (32.1)	18 (21.4)	35 (44.9)	<0.001	24 (48)	11 (44)	0.285
TST mm induration	6.21±8.22	3±6.21	9.64±8.91	0.041	12.88±8.39	6.4±8.79	0.127
Mean ± SD; range	0 – 20	0 - 15	0 - 20		0 - 20	0 - 17	
IGRA test							
QFT (+)	62 (37.6)	0 (0)	50 (76.9)	<0.001	41 (82)	16 (64)	0.064
QFT results (IU/mL)	1.59±2.82	0.02±0.06	3.29±3.31	<0.001	4.33±3.41	1.25±1.92	<0.001
Mean ± SD; range ^h	-0.07 - 10	-0.07 – 0.23	-0.01 - 10		0 – 10	-0.1 – 8.03	

Abbreviations: IGRA = Interferon-gamma release assay; SD = Standard deviation; High TB = High incidence of TB; Low TB = Low incidence of TB; QFT = QuantiFERON TB Gold In-Tube™ or QuantiFERON TB Gold Plus™; TST = Tuberculin skin test. HIV = Human immunodeficiency virus. HCW = healthcare worker.

^a The total sample set analyzed were 165 samples, encompassing 144 unique subjects, including 3 active TB patients, 13 subjects providing 2 separated samples, and 4 subjects providing 3 samples, separated by 5-7 months in testing, representing unique samples.

^b P value for comparison between subjects with LTBI- vs. LTBI+ group designations (Mann–Whitney U test or r x c Exact contingency table).

^c P value for comparison between subjects with High Risk+ group designation (including 3 patients with active TB) vs. Low Risk+ group designation (excluding 3 LTBI subjects with indeterminate Low risk designations). (Mann–Whitney U test or x c Exact contingency table).

- ^d High incidence of TB was defined as a country with ≥ 20 cases per 100,000 population per year. 2023 WHO Global tuberculosis report (http://www.who.int/tb/publications/global_report/en/).
- ^e Estimates for the individual cumulative risk of TB reactivation are based on "The Online TST/IGRA interpreter" prediction modeling that includes TST and IGRA results, risk factors for LTBI and risk factors for progression to active TB (<http://www.tstin3d.com/en/calc.html>).^{49, 50}
- ^f Adjusted estimates for the individual and cumulative risk of TB reactivation are based on "The Online TST/IGRA interpreter" prediction modeling that includes TST and IGRA results, risk factors for LTBI and risk factors for progression to active TB (<http://www.tstin3d.com/en/calc.html>) as previously described.^{49, 50}
- ^g Study subjects included 21 patients with non-HIV immunosuppressed conditions.
- ^h QFT results include Interferon-gamma levels (IU/mL) of antigen tube minus nil from QuantiFERON TB Gold In-Tube™ and TB1 tube from QuantiFERON TB Gold Plus.™.

Table 6.2 Median values of absolute and normalized cytokine levels between LTBI negative and LTBI positive patients.

Target	Condition	LTBI- Median (pg/mL)	LTBI+ Median (pg/mL)	p-value	Significance ^a
CCL2	TB1	7024.0	8386.6	0.14	ns
CCL3	TB1	933.6	1133.6	0.6	ns
CCL4	TB1	2975.0	4294.6	0.36	ns
CCL8	TB1	91.4	341.0	6.10E-06	****
IFN- γ	TB1	37.6	55.8	0.62	ns
IL-10	TB1	769.6	84.6	0.0016	**
IL-15	TB1	103.6	26.6	0.064	ns
IL-17	TB1	0.0	0.0	0.64	ns
IL-1 β	TB1	702.8	703.2	0.79	ns
IL-2	TB1	33.9	96.0	0.00059	***
IL-6	TB1	1469.0	1729.1	0.25	ns
IP-10	TB1	217.5	917.6	9.70E-13	****
TNF- α	TB1	136.0	124.8	0.68	ns
CCL2	NIL	4730.2	3287.5	0.33	ns
CCL3	NIL	1111.2	1357.0	0.45	ns
CCL4	NIL	3421.1	3302.3	0.54	ns
CCL8	NIL	61.2	9.5	0.16	ns
IFN- γ	NIL	26.3	10.8	0.9	ns
IL-10	NIL	715.8	125.6	0.003	**
IL-15	NIL	90.8	33.8	0.065	ns
IL-17	NIL	0.0	0.0	0.37	ns
IL-1 β	NIL	446.7	252.4	0.038	*
IL-2	NIL	29.8	19.7	0.096	ns
IL-6	NIL	1886.0	2027.7	0.35	ns
IP-10	NIL	151.0	174.8	0.41	ns
TNF- α	NIL	134.2	82.8	0.099	ns
CCL2	MIT	10584.4	9352.0	0.29	ns
CCL3	MIT	9038.4	10037.2	0.97	ns
CCL4	MIT	57831.1	43868.5	0.063	ns
CCL8	MIT	700.5	594.2	0.7	ns
IFN- γ	MIT	403.0	742.0	0.06	ns
IL-10	MIT	5029.5	3168.3	0.023	*
IL-15	MIT	150.7	35.6	0.021	*
IL-17	MIT	18.1	0.0	0.37	ns

IL-1β	MIT	3516.0	4194.8	0.75	ns
IL-2	MIT	498.8	524.6	0.44	ns
IL-6	MIT	17640.9	16603.8	0.96	ns
IP-10	MIT	1504.6	1476.7	0.88	ns
TNF-α	MIT	472.4	514.4	0.83	ns
CCL2	TB1_NIL	2869.5	4167.5	0.047	*
CCL3	TB1_NIL	23.1	-217.6	0.18	ns
CCL4	TB1_NIL	0.0	201.0	0.0098	**
CCL8	TB1_NIL	20.9	253.6	1.10E-06	****
IFN-γ	TB1_NIL	4.4	5.0	0.64	ns
IL-10	TB1_NIL	0.0	0.0	0.81	ns
IL-15	TB1_NIL	0.0	0.0	0.43	ns
IL-17	TB1_NIL	0.0	0.0	0.23	ns
IL-1β	TB1_NIL	4.6	169.7	0.028	*
IL-2	TB1_NIL	0.5	54.1	5.70E-07	****
IL-6	TB1_NIL	-55.7	-74.5	0.8	ns
IP-10	TB1_NIL	9.0	603.8	4.70E-13	****
TNF-α	TB1_NIL	0.0	0.0	0.28	ns
CCL2	TB1_MIT	-1725.6	1867.6	0.022	*
CCL3	TB1_MIT	-7775.5	-6327.9	0.45	ns
CCL4	TB1_MIT	-58179.0	-36266.0	0.0071	**
CCL8	TB1_MIT	-462.4	-196.4	0.03	*
IFN-γ	TB1_MIT	-272.3	-557.6	0.071	ns
IL-10	TB1_MIT	-2511.1	-2033.3	0.072	ns
IL-15	TB1_MIT	-34.6	-7.6	0.15	ns
IL-17	TB1_MIT	0.0	0.0	0.14	ns
IL-1β	TB1_MIT	-2656.4	-3795.6	0.91	ns
IL-2	TB1_MIT	-390.6	-243.5	0.47	ns
IL-6	TB1_MIT	-15099.4	-12629.1	0.4	ns
IP-10	TB1_MIT	-976.1	-338.4	9.00E-05	****
TNF-α	TB1_MIT	-268.7	-277.4	0.95	ns
CCL2	MIT_NIL	3655.8	2910.1	0.24	ns
CCL3	MIT_NIL	7807.7	6209.2	0.38	ns
CCL4	MIT_NIL	57095.7	38987.0	0.026	*
CCL8	MIT_NIL	586.6	530.9	0.85	ns
IFN-γ	MIT_NIL	331.5	413.1	0.071	ns
IL-10	MIT_NIL	2650.6	2072.2	0.09	ns
IL-15	MIT_NIL	34.0	0.0	0.057	ns
IL-17	MIT_NIL	0.0	0.0	0.46	ns

IL-1β	MIT_NIL	2741.9	3453.8	0.53	ns
IL-2	MIT_NIL	378.6	354.0	0.33	ns
IL-6	MIT_NIL	14196.5	11895.0	0.54	ns
IP-10	MIT_NIL	1053.9	1158.6	0.82	ns
TNF-α	MIT_NIL	256.3	310.0	0.47	ns
*Wilcoxon-Mann-Whitney tests were completed to test significant differences between clinical population distributions. * $p \leq 0.05$, ** $p \leq 0.01$, *** $p \leq 0.001$, **** $p \leq 0.0001$					

Table 6.3 Median values of absolute and normalized cytokine levels between low-risk and high-risk designated patients within the LTBI+ patient population.

Target	Condition	Low-risk median (pg/mL)	High-risk median (pg/mL)	p-value	Significance ^a
CCL2	TB1	7276.10	8313.55	0.42	ns
CCL3	TB1	1107.28	1090.06	0.81	ns
CCL4	TB1	3999.68	4730.60	0.5	ns
CCL8	TB1	151.72	409.66	0.016	*
IFN- γ	TB1	60.29	49.18	0.49	ns
IL-10	TB1	0.00	289.40	0.00094	***
IL-15	TB1	19.77	80.82	0.11	ns
IL-17	TB1	0.00	0.00	0.49	ns
IL-1 β	TB1	366.90	747.32	0.12	ns
IL-2	TB1	33.63	131.78	0.0022	**
IL-6	TB1	1367.45	1951.91	0.21	ns
IP-10	TB1	658.80	1003.72	0.054	ns
TNF- α	TB1	25.01	173.31	0.0094	**
CCL2	NIL	2636.56	3887.26	0.26	ns
CCL3	NIL	1512.09	1173.34	0.74	ns
CCL4	NIL	2672.44	3533.23	0.45	ns
CCL8	NIL	0.00	36.73	0.036	*
IFN-g	NIL	26.32	5.18	0.11	ns
IL-10	NIL	0.00	210.23	0.00013	***
IL-15	NIL	20.45	50.77	0.13	ns
IL-17	NIL	0.00	0.00	0.85	ns
IL-1 β	NIL	104.47	331.01	0.045	*
IL-2	NIL	11.90	26.20	0.076	ns
IL-6	NIL	1182.50	2413.54	0.084	ns
IP-10	NIL	174.83	189.41	0.54	ns
TNF- α	NIL	36.94	99.76	0.03	*
CCL2	MIT	7988.93	9768.88	0.69	ns
CCL3	MIT	13112.16	8325.17	0.066	ns
CCL4	MIT	46578.76	43588.25	0.88	ns
CCL8	MIT	535.46	863.81	0.97	ns
IFN- γ	MIT	648.63	698.92	0.64	ns
IL-10	MIT	1189.63	5712.88	0.00063	***
IL-15	MIT	37.27	48.09	0.27	ns

IL-17	MIT	0.00	8.74	0.24	ns
IL-1β	MIT	2455.86	4361.65	0.25	ns
IL-2	MIT	238.33	598.45	0.02	*
IL-6	MIT	15372.02	16649.60	0.95	ns
IP-10	MIT	1066.00	1560.32	0.37	ns
TNF-α	MIT	417.80	659.54	0.21	ns
CCL2	TB1_NIL	4750.0	3478.4	0.86	ns
CCL3	TB1_NIL	-290.3	-77.9	0.42	ns
CCL4	TB1_NIL	360.3	0.0	0.94	ns
CCL8	TB1_NIL	111.2	339.5	0.14	ns
IFN-γ	TB1_NIL	8.6	2.8	0.83	ns
IL-10	TB1_NIL	0.0	-5.2	0.39	ns
IL-15	TB1_NIL	0.0	0.0	0.75	ns
IL-17	TB1_NIL	0.0	0.0	0.6	ns
IL-1β	TB1_NIL	161.1	73.7	0.65	ns
IL-2	TB1_NIL	29.3	62.1	0.019	*
IL-6	TB1_NIL	5.8	-104.9	0.68	ns
IP-10	TB1_NIL	503.4	603.8	0.18	ns
TNF-α	TB1_NIL	0.0	20.7	0.47	ns
CCL2	TB1_MIT	1594.7	2026.7	0.48	ns
CCL3	TB1_MIT	-8811.1	-5893.6	0.07	ns
CCL4	TB1_MIT	-35933.7	-36428.4	0.81	ns
CCL8	TB1_MIT	-371.6	-209.8	0.51	ns
IFN-γ	TB1_MIT	-304.2	-605.6	0.083	ns
IL-10	TB1_MIT	-843.1	-3157.7	0.0037	**
IL-15	TB1_MIT	-3.7	-10.6	0.16	ns
IL-17	TB1_MIT	0.0	0.0	0.3	ns
IL-1β	TB1_MIT	-1621.5	-3839.7	0.15	ns
IL-2	TB1_MIT	-94.9	-267.8	0.097	ns
IL-6	TB1_MIT	-12629.1	-12054.7	0.55	ns
IP-10	TB1_MIT	-407.7	-441.3	0.76	ns
TNF-α	TB1_MIT	-154.2	-324.6	0.19	ns
CCL2	MIT_NIL	2051.6	3073.4	0.67	ns
CCL3	MIT_NIL	8942.1	5826.4	0.13	ns
CCL4	MIT_NIL	40636.9	37150.2	0.83	ns
CCL8	MIT_NIL	530.9	572.5	0.95	ns
IFN-γ	MIT_NIL	300.1	459.1	0.11	ns
IL-10	MIT_NIL	925.2	3805.1	0.0025	**
IL-15	MIT_NIL	0.0	0.0	0.31	ns

IL-17	MIT_NIL	0.0	0.0	0.3	ns
IL-1β	MIT_NIL	2418.9	3659.7	0.33	ns
IL-2	MIT_NIL	166.4	532.3	0.007	**
IL-6	MIT_NIL	10889.2	12285.3	0.6	ns
IP-10	MIT_NIL	846.8	1129.1	0.69	ns
TNF-α	MIT_NIL	192.9	458.4	0.15	ns

^aPatients without either high or low risk designations were excluded from analysis. Wilcoxon-Mann-Whitney tests were completed to test significant differences between clinical population distributions. * $p \leq 0.05$, ** $p \leq 0.01$, *** $p \leq 0.001$, **** $p \leq 0.0001$

6.9 References

- (1) *Tuberculosis (TB)*. <https://www.who.int/news-room/fact-sheets/detail/tuberculosis> (accessed 2024-02-19).
- (2) *2.2 TB mortality*. <https://www.who.int/teams/global-tuberculosis-programme/tb-reports/global-tuberculosis-report-2022/tb-disease-burden/2-2-tb-mortality> (accessed 2024-02-19).
- (3) Migliori, G. B.; Ong, C. W. M.; Petrone, L.; D'Ambrosio, L.; Centis, R.; Goletti, D. The Definition of Tuberculosis Infection Based on the Spectrum of Tuberculosis Disease. *Breathe* **2021**, *17* (3), 210079. <https://doi.org/10.1183/20734735.0079-2021>.
- (4) Escalante, P.; Vadiyala, M. R.; Pathakumari, B.; Marty, P. K.; Van Keulen, V. P.; Hilgart, H. R.; Meserve, K.; Theel, E. S.; Peikert, T.; Bailey, R. C.; Laniado-Laborin, R. New Diagnostics for the Spectrum of Asymptomatic TB: From Infection to Subclinical Disease. *Int. J. Tuberc. Lung Dis.* **2023**, *27* (7), 499–505. <https://doi.org/10.5588/ijtld.23.0032>.
- (5) Pai, M.; Behr, M. A.; Dowdy, D.; Dheda, K.; Divangahi, M.; Boehme, C. C.; Ginsberg, A.; Swaminathan, S.; Spigelman, M.; Getahun, H.; Menzies, D.; Raviglione, M. Tuberculosis. *Nat. Rev. Dis. Primer* **2016**, *2* (1), 1–23. <https://doi.org/10.1038/nrdp.2016.76>.
- (6) Ernst, J. D. The Immunological Life Cycle of Tuberculosis. *Nat. Rev. Immunol.* **2012**, *12* (8), 581–591. <https://doi.org/10.1038/nri3259>.
- (7) Flynn, J. L.; Chan, J. Immunology of Tuberculosis. *Annu. Rev. Immunol.* **2001**, *19* (1), 93–129. <https://doi.org/10.1146/annurev.immunol.19.1.93>.
- (8) Mukherjee, S.; Perveen, S.; Negi, A.; Sharma, R. Evolution of Tuberculosis Diagnostics: From Molecular Strategies to Nanodiagnosics. *Tuberculosis* **2023**, *140*, 102340. <https://doi.org/10.1016/j.tube.2023.102340>.
- (9) Houben, R. M. G. J.; Dodd, P. J. The Global Burden of Latent Tuberculosis Infection: A Re-Estimation Using Mathematical Modelling. *PLOS Med.* **2016**, *13* (10), e1002152. <https://doi.org/10.1371/journal.pmed.1002152>.
- (10) Pai, M.; Denlinger, C. M.; Kik, S. V.; Rangaka, M. X.; Zwerling, A.; Oxlade, O.; Metcalfe, J. Z.; Cattamanchi, A.; Dowdy, D. W.; Dheda, K.; Banaei, N. Gamma Interferon Release Assays for Detection of Mycobacterium Tuberculosis Infection. *Clin. Microbiol. Rev.* **2014**, *27* (1), 3–20. <https://doi.org/10.1128/CMR.00034-13>.
- (11) Mack, U.; Migliori, G. B.; Sester, M.; Rieder, H. L.; Ehlers, S.; Goletti, D.; Bossink, A.; Magdorf, K.; Hölscher, C.; Kampmann, B.; Arend, S. M.; Detjen, A.; Bothamley, G.; Zellweger, J. P.; Milburn, H.; Diel, R.; Ravn, P.; Cobelens, F.; Cardona, P. J.; Kan, B.; Solovic, I.; Duarte, R.; Cirillo, D. M.; C. Lange; TBNET. LTBI: Latent Tuberculosis Infection or Lasting Immune Responses to M. Tuberculosis? A TBNET Consensus Statement. *Eur. Respir. J.* **2009**, *33* (5), 956–973. <https://doi.org/10.1183/09031936.00120908>.
- (12) Rangaka, M. X.; Wilkinson, K. A.; Glynn, J. R.; Ling, D.; Menzies, D.; Mwansa-Kambafwile, J.; Fielding, K.; Wilkinson, R. J.; Pai, M. Predictive Value of Interferon- γ Release Assays for Incident Active Tuberculosis: A Systematic Review and Meta-Analysis. *Lancet Infect. Dis.* **2012**, *12* (1), 45–55. [https://doi.org/10.1016/S1473-3099\(11\)70210-9](https://doi.org/10.1016/S1473-3099(11)70210-9).
- (13) Getahun, H.; Matteelli, A.; Chaisson, R. E.; Raviglione, M. Latent Mycobacterium Tuberculosis Infection. *N. Engl. J. Med.* **2015**, *372* (22), 2127–2135. <https://doi.org/10.1056/NEJMra1405427>.

- (14) Diel, R.; Loddenkemper, R.; Nienhaus, A. Predictive Value of Interferon- γ Release Assays and Tuberculin Skin Testing for Progression from Latent TB Infection to Disease State: A Meta-Analysis. *Chest* **2012**, *142* (1), 63–75. <https://doi.org/10.1378/chest.11-3157>.
- (15) Kaforou, M.; Broderick, C.; Vito, O.; Levin, M.; Scriba, T. J.; Seddon, J. A. Transcriptomics for Child and Adolescent Tuberculosis*. *Immunol. Rev.* **2022**, *309* (1), 97–122. <https://doi.org/10.1111/imr.13116>.
- (16) Suliman, S.; Thompson, E. G.; Sutherland, J.; Weiner, J.; Ota, M. O. C.; Shankar, S.; Penn-Nicholson, A.; Thiel, B.; Erasmus, M.; Maertzdorf, J.; Duffy, F. J.; Hill, P. C.; Hughes, E. J.; Stanley, K.; Downing, K.; Fisher, M. L.; Valvo, J.; Parida, S. K.; van der Spuy, G.; Tromp, G.; Adetifa, I. M. O.; Donkor, S.; Howe, R.; Mayanja-Kizza, H.; Boom, W. H.; Dockrell, H. M.; Ottenhoff, T. H. M.; Hatherill, M.; Aderem, A.; Hanekom, W. A.; Scriba, T. J.; Kaufmann, S. H. E.; Zak, D. E.; Walzl, G.; Walzl, G.; Black, G. F.; van der Spuy, G.; Stanley, K.; Kriel, M.; Du Plessis, N.; Nene, N.; Roberts, T.; Kleynhans, L.; Gutschmidt, A.; Smith, B.; Nene, N.; Loxton, A. G.; Chegou, N. N.; Tromp, G.; Tabb, D.; Ottenhoff, T. H. M.; Klein, M. R.; Haks, M. C.; Franken, K. L. M. C.; Geluk, A.; van Meijgaarden, K. E.; Joosten, S. A.; Boom, W. H.; Thiel, B.; Mayanja-Kizza, H.; Joloba, M.; Zalwango, S.; Nsereko, M.; Okwera, B.; Kisingo, H.; Kaufmann, S. H. E.; Parida, S. K.; Golinski, R.; Maertzdorf, J.; Weiner, J.; Jacobson, M.; Dockrell, H.; Smith, S.; Gorak-Stolinska, P.; Hur, Y.-G.; Lalor, M.; Lee, J.-S.; Crampin, A. C.; French, N.; Ngwira, B.; Ben-Smith, A.; Watkins, K.; Ambrose, L.; Simukonda, F.; Mvula, H.; Chilongo, F.; Saul, J.; Branson, K.; Suliman, S.; Scriba, T. J.; Mahomed, H.; Hughes, E. J.; Bilek, N.; Erasmus, M.; Xasa, O.; Veldsman, A.; Downing, K.; Fisher, M.; Penn-Nicholson, A.; Mulenga, H.; Abel, B.; Bowmaker, M.; Kagina, B.; Chung, W. K.; Hanekom, W. A.; Sadoff, J.; Sizemore, D.; Ramachandran, S.; Barker, L.; Brennan, M.; Weichold, F.; Muller, S.; Geiter, L.; Kassa, D.; Abebe, A.; Mesele, T.; Tegbaru, B.; Baarle, D. van; Miedema, F.; Howe, R.; Mihret, A.; Aseffa, A.; Bekele, Y.; Iwnetu, R.; Tafesse, M.; Yamuah, L.; Ota, M.; Sutherland, J.; Hill, P.; Adegbola, R.; Corrah, T.; Antonio, M.; Togun, T.; Adetifa, I.; Donkor, S.; Andersen, P.; Rosenkrands, I.; Doherty, M.; Weldingh, K.; Schoolnik, G.; Dolganov, G.; Van, T.; Kafaar, F.; Workman, L.; Mulenga, H.; Scriba, T. J.; Hughes, E. J.; Bilek, N.; Erasmus, M.; Xasa, O.; Veldsman, A.; Cloete, Y.; Abrahams, D.; Moyo, S.; Gelderbloem, S.; Tameris, M.; Geldenhuys, H.; Hanekom, W.; Hussey, G.; Ehrlich, R.; Verver, S.; Geiter, L. Four-Gene Pan-African Blood Signature Predicts Progression to Tuberculosis. *Am. J. Respir. Crit. Care Med.* **2018**, *197* (9), 1198–1208. <https://doi.org/10.1164/rccm.201711-2340OC>.
- (17) Leong, S.; Zhao, Y.; Ribeiro-Rodrigues, R.; Jones-López, E. C.; Acuña-Villaorduña, C.; Rodrigues, P. M.; Palaci, M.; Alland, D.; Dietze, R.; Ellner, J. J.; Johnson, W. E.; Salgame, P. Cross-Validation of Existing Signatures and Derivation of a Novel 29-Gene Transcriptomic Signature Predictive of Progression to TB in a Brazilian Cohort of Household Contacts of Pulmonary TB. *Tuberculosis* **2020**, *120*, 101898. <https://doi.org/10.1016/j.tube.2020.101898>.
- (18) Zak, D. E.; Penn-Nicholson, A.; Scriba, T. J.; Thompson, E.; Suliman, S.; Amon, L. M.; Mahomed, H.; Erasmus, M.; Whatney, W.; Hussey, G. D.; Abrahams, D.; Kafaar, F.; Hawkrigde, T.; Verver, S.; Hughes, E. J.; Ota, M.; Sutherland, J.; Howe, R.; Dockrell, H. M.; Boom, W. H.; Thiel, B.; Ottenhoff, T. H. M.; Mayanja-Kizza, H.; Crampin, A. C.; Downing, K.; Hatherill, M.; Valvo, J.; Shankar, S.; Parida, S. K.; Kaufmann, S. H. E.; Walzl, G.; Aderem, A.; Hanekom, W. A. A Blood RNA Signature for Tuberculosis Disease Risk: A Prospective Cohort Study. *The Lancet* **2016**, *387* (10035), 2312–2322. [https://doi.org/10.1016/S0140-6736\(15\)01316-1](https://doi.org/10.1016/S0140-6736(15)01316-1).

- (19) Xi, X.; Li, T.; Huang, Y.; Sun, J.; Zhu, Y.; Yang, Y.; Lu, Z. J. RNA Biomarkers: Frontier of Precision Medicine for Cancer. *Non-Coding RNA* **2017**, *3* (1), 9. <https://doi.org/10.3390/ncrna3010009>.
- (20) Porter, B. W.; Venkatappa, T. K. Uncloaking an Ancient Adversary: Can Pathogen Biomarker Elicitors Play a Role in Confirming Extrapulmonary TB and Latent TB Infection? *Tuberc. Edinb. Scotl.* **2018**, *113*, 30–37. <https://doi.org/10.1016/j.tube.2018.08.014>.
- (21) Essone, P. N.; Leboueny, M.; Maloupazoa Siawaya, A. C.; Alame-Emane, A. K.; Aboumegone Biyogo, O. C.; Dapnet Tadatsin, P. H.; Mveang Nzoghe, A.; Essamazokou, D. U.; Mvoundza Ndjindji, O.; Padzys, G.-S.; Agnandji, S. T.; Takiff, H.; Gicquel, B.; Djoba Siawaya, J. F. M. Tuberculosis Infection and Antigen Specific Cytokine Response in Healthcare Workers Frequently Exposed to Tuberculosis. *Sci. Rep.* **2019**, *9* (1), 8201. <https://doi.org/10.1038/s41598-019-44294-0>.
- (22) Kim, S. Y.; Park, M. S.; Kim, Y. S.; Kim, S. K.; Chang, J.; Lee, H. J.; Cho, S.-N.; Kang, Y. A. The Responses of Multiple Cytokines Following Incubation of Whole Blood from TB Patients, Latently Infected Individuals and Controls with the TB Antigens ESAT-6, CFP-10 and TB7.7. *Scand. J. Immunol.* **2012**, *76* (6), 580–586. <https://doi.org/10.1111/j.1365-3083.2012.02776.x>.
- (23) Kellar, K. L.; Gehrke, J.; Weis, S. E.; Mahmutovic-Mayhew, A.; Davila, B.; Zajdowicz, M. J.; Scarborough, R.; LoBue, P. A.; Lardizabal, A. A.; Daley, C. L.; Reves, R. R.; Bernardo, J.; Campbell, B. H.; Whitworth, W. C.; Mazurek, G. H. Multiple Cytokines Are Released When Blood from Patients with Tuberculosis Is Stimulated with Mycobacterium Tuberculosis Antigens. *PLOS ONE* **2011**, *6* (11), e26545. <https://doi.org/10.1371/journal.pone.0026545>.
- (24) Chegou, N. N.; Heyckendorf, J.; Walzl, G.; Lange, C.; Ruhwald, M. Beyond the IFN- γ Horizon: Biomarkers for Immunodiagnosis of Infection with Mycobacterium Tuberculosis. *Eur. Respir. J.* **2014**, *43* (5), 1472–1486. <https://doi.org/10.1183/09031936.00151413>.
- (25) Wang, X.; Jiang, J.; Cao, Z.; Yang, B.; Zhang, J.; Cheng, X. Diagnostic Performance of Multiplex Cytokine and Chemokine Assay for Tuberculosis. *Tuberc. Edinb. Scotl.* **2012**, *92* (6), 513–520. <https://doi.org/10.1016/j.tube.2012.06.005>.
- (26) Lu, L. L.; Smith, M. T.; Yu, K. K. Q.; Luedemann, C.; Suscovich, T. J.; Grace, P. S.; Cain, A.; Yu, W. H.; McKittrick, T. R.; Lauffenburger, D.; Cummings, R. D.; Mayanja-Kizza, H.; Hawn, T. R.; Boom, W. H.; Stein, C. M.; Fortune, S. M.; Seshadri, C.; Alter, G. IFN- γ -Independent Immune Markers of Mycobacterium Tuberculosis Exposure. *Nat. Med.* **2019**, *25* (6), 977–987. <https://doi.org/10.1038/s41591-019-0441-3>.
- (27) MacLean, E.; Broger, T.; Yerlikaya, S.; Fernandez-Carballo, B. L.; Pai, M.; Denking, C. M. A Systematic Review of Biomarkers to Detect Active Tuberculosis. *Nat. Microbiol.* **2019**, *4* (5), 748–758. <https://doi.org/10.1038/s41564-019-0380-2>.
- (28) Chegou, N. N.; Sutherland, J. S.; Malherbe, S.; Crampin, A. C.; Corstjens, P. L. A. M.; Geluk, A.; Mayanja-Kizza, H.; Loxton, A. G.; Van Der Spuy, G.; Stanley, K.; Kotzé, L. A.; Van Der Vyver, M.; Rosenkrands, I.; Kidd, M.; Van Helden, P. D.; Dockrell, H. M.; Ottenhoff, T. H. M.; Kaufmann, S. H. E.; Walzl, G. Diagnostic Performance of a Seven-Marker Serum Protein Biosignature for the Diagnosis of Active TB Disease in African Primary Healthcare Clinic Attendees with Signs and Symptoms Suggestive of TB. *Thorax* **2016**, *71* (9), 785–794. <https://doi.org/10.1136/thoraxjnl-2015-207999>.
- (29) Chegou, N. N.; Sutherland, J. S.; Namuganga, A.-R.; Corstjens, P. L.; Geluk, A.; Gebremichael, G.; Mendy, J.; Malherbe, S.; Stanley, K.; van der Spuy, G. D.; Kriel, M.; Loxton, A. G.; Kriel, B.; Simukonda, F.; Bekele, Y.; Sheehama, J. A.; Nelongo, J.; van der

- Vyver, M.; Gebrexabher, A.; Hailu, H.; Esterhuyse, M. M.; Rosenkrands, I.; Aagard, C.; Kidd, M.; Kassa, D.; Mihret, A.; Howe, R.; Cliff, J. M.; Crampin, A. C.; Mayanja-Kizza, H.; Kaufmann, S. H. E.; Dockrell, H. M.; Ottenhoff, T. H. M.; Walzl, G. Africa-Wide Evaluation of Host Biomarkers in QuantiFERON Supernatants for the Diagnosis of Pulmonary Tuberculosis. *Sci. Rep.* **2018**, *8* (1), 2675. <https://doi.org/10.1038/s41598-018-20855-7>.
- (30) Manngo, P. M.; Gutschmidt, A.; Snyders, C. I.; Mutavhatsindi, H.; Manyelo, C. M.; Makhoba, N. S.; Ahlers, P.; Hiemstra, A.; Stanley, K.; McAnda, S.; Kidd, M.; Malherbe, S. T.; Walzl, G.; Chegou, N. N. Prospective Evaluation of Host Biomarkers Other than Interferon Gamma in QuantiFERON Plus Supernatants as Candidates for the Diagnosis of Tuberculosis in Symptomatic Individuals. *J. Infect.* **2019**, *79* (3), 228–235. <https://doi.org/10.1016/j.jinf.2019.07.007>.
- (31) Jacobs, R.; Malherbe, S.; Loxton, A. G.; Stanley, K.; van der Spuy, G.; Walzl, G.; Chegou, N. N. Identification of Novel Host Biomarkers in Plasma as Candidates for the Immunodiagnosis of Tuberculosis Disease and Monitoring of Tuberculosis Treatment Response. *Oncotarget* **2016**, *7* (36), 57581–57592. <https://doi.org/10.18632/oncotarget.11420>.
- (32) Nogueira, B. M. F.; Krishnan, S.; Barreto-Duarte, B.; Araújo-Pereira, M.; Queiroz, A. T. L.; Ellner, J. J.; Salgame, P.; Scriba, T. J.; Sterling, T. R.; Gupta, A.; Andrade, B. B. Diagnostic Biomarkers for Active Tuberculosis: Progress and Challenges. *EMBO Mol. Med.* **2022**, *14* (12), e14088. <https://doi.org/10.15252/emmm.202114088>.
- (33) Mihret, A.; Bekele, Y.; Bobosha, K.; Kidd, M.; Aseffa, A.; Howe, R.; Walzl, G. Plasma Cytokines and Chemokines Differentiate between Active Disease and Non-Active Tuberculosis Infection. *J. Infect.* **2013**, *66* (4), 357–365. <https://doi.org/10.1016/j.jinf.2012.11.005>.
- (34) Qiu, B.; Liu, Q.; Li, Z.; Song, H.; Xu, D.; Ji, Y.; Jiang, Y.; Tian, D.; Wang, J. Evaluation of Cytokines as a Biomarker to Distinguish Active Tuberculosis from Latent Tuberculosis Infection: A Diagnostic Meta-Analysis. *BMJ Open* **2020**, *10* (10), e039501. <https://doi.org/10.1136/bmjopen-2020-039501>.
- (35) Awoniyi, D. O.; Teuchert, A.; Sutherland, J. S.; Mayanja-Kizza, H.; Howe, R.; Mihret, A.; Loxton, A. G.; Sheehama, J.; Kassa, D.; Crampin, A. C.; Dockrell, H. M.; Kidd, M.; Rosenkrands, I.; Geluk, A.; Ottenhoff, T. H. M.; Corstjens, P. L. A. M.; Chegou, N. N.; Walzl, G.; Walzl, G.; Chegou, N. N.; Kriel, M.; van der Spuy, G.; Loxton, A. G.; Stanley, K.; Malherbe, S.; Mcanda, S.; Kriel, B.; Phalane, K. G.; Essone, P.; Sutherland, J. S.; Owolabi, O.; Sillah, A.; Mendy, J.; Gindeh, A.; Donkor, S.; Togun, T.; Ota, M.; Crampin, A. C.; Simukonda, F.; Amberbir, A.; Chilongo, F.; Houben, R.; Kassa, D.; Gebrezgeabher, A.; Mesfin, G.; Belay, Y.; Gebremichael, G.; Alemayehu, Y.; van der Vyver, M.; Amutenya, F. N.; Nelongo, J. N.; Monye, L.; Sheehama, J. A.; Iiping, S.; Mayanja-Kizza, H.; Namuganga, A. R.; Muzanye, G.; Nsereko, M.; Peters, P.; Howe, R.; Mihret, A.; Bekele, Y.; Tessema, B.; Yamuah, L.; Ottenhoff, T. H. M.; Geluk, A.; Franken, K.; Corstjens, P. L. A. M.; Tjon Kon Fat, E. M.; de Dood, C. J.; van der Ploeg-van Schip, J. J.; Rosenkrands, I.; Aagaard, C.; Kaufmann, S. H. E.; Esterhuyse, M. M.; Cliff, J. M.; Dockrell, H. M. Evaluation of Cytokine Responses against Novel Mtb Antigens as Diagnostic Markers for TB Disease. *J. Infect.* **2016**, *73* (3), 219–230. <https://doi.org/10.1016/j.jinf.2016.04.036>.
- (36) Won, E.-J.; Choi, J.-H.; Cho, Y.-N.; Jin, H.-M.; Kee, H. J.; Park, Y.-W.; Kwon, Y.-S.; Kee, S.-J. Biomarkers for Discrimination between Latent Tuberculosis Infection and Active Tuberculosis Disease. *J. Infect.* **2017**, *74* (3), 281–293. <https://doi.org/10.1016/j.jinf.2016.11.010>.

- (37) Wang, S.; Li, Y.; Shen, Y.; Wu, J.; Gao, Y.; Zhang, S.; Shao, L.; Jin, J.; Zhang, Y.; Zhang, W. Screening and Identification of a Six-Cytokine Biosignature for Detecting TB Infection and Discriminating Active from Latent TB. *J. Transl. Med.* **2018**, *16* (1), 206. <https://doi.org/10.1186/s12967-018-1572-x>.
- (38) Manna, M. P. L.; Orlando, V.; Donni, P. L.; Sireci, G.; Carlo, P. D.; Cascio, A.; Dieli, F.; Caccamo, N. Identification of Plasma Biomarkers for Discrimination between Tuberculosis Infection/Disease and Pulmonary Non Tuberculosis Disease. *PLOS ONE* **2018**, *13* (3), e0192664. <https://doi.org/10.1371/journal.pone.0192664>.
- (39) Stepanovich, G. E.; Chapman, C. A.; Meserve, K. L.; Sturza, J. M.; Ellsworth, L. A.; Bailey, R. C.; Bermick, J. R. Chorioamnionitis-Exposure Alters Serum Cytokine Trends in Premature Neonates. *J. Perinatol.* **2023**, *43* (6), 758–765. <https://doi.org/10.1038/s41372-022-01584-2>.
- (40) Qavi, A. J. Rapid Detection of an Ebola Biomarker with Optical Microring Resonators. *OPEN ACCESS* **2022**, *22*.
- (41) Graybill, R. M.; Cardenosa-Rubio, M. C.; Yang, H.; Johnson, M. D.; Bailey, R. C. Multiplexed microRNA Expression Profiling by Combined Asymmetric PCR and Label-Free Detection Using Silicon Photonic Sensor Arrays. *Anal. Methods* **2018**, *10* (14), 1618–1623. <https://doi.org/10.1039/C8AY00190A>.
- (42) Wade, J. H.; Alsop, A. T.; Vertin, N. R.; Yang, H.; Johnson, M. D.; Bailey, R. C. Rapid, Multiplexed Phosphoprotein Profiling Using Silicon Photonic Sensor Arrays. *ACS Cent. Sci.* **2015**, *1* (7), 374–382. <https://doi.org/10.1021/acscentsci.5b00250>.
- (43) Washburn, A. L.; Shia, W. W.; Lenkeit, K. A.; Lee, S.-H.; Bailey, R. C. Multiplexed Cancer Biomarker Detection Using Chip-Integrated Silicon Photonic Sensor Arrays. *Analyst* **2016**, *141* (18), 5358–5365. <https://doi.org/10.1039/C6AN01076H>.
- (44) Robison, H. M.; Escalante, P.; Valera, E.; Erskine, C. L.; Auvil, L.; Sasieta, H. C.; Bushell, C.; Welge, M.; Bailey, R. C. Precision Immunoprofiling to Reveal Diagnostic Signatures for Latent Tuberculosis Infection and Reactivation Risk Stratification. *Integr. Biol.* **2019**, *11* (1), 16–25. <https://doi.org/10.1093/intbio/zyz001>.
- (45) Robison, H. M.; Chapman, C. A.; Zhou, H.; Erskine, C. L.; Theel, E.; Peikert, T.; Lindestam Arlehamn, C. S.; Sette, A.; Bushell, C.; Welge, M.; Zhu, R.; Bailey, R. C.; Escalante, P. Risk Assessment of Latent Tuberculosis Infection through a Multiplexed Cytokine Biosensor Assay and Machine Learning Feature Selection. *Sci. Rep.* **2021**, *11* (1), 20544. <https://doi.org/10.1038/s41598-021-99754-3>.
- (46) Arlehamn, C. S. L.; McKinney, D. M.; Carpenter, C.; Paul, S.; Rozot, V.; Makgotlho, E.; Gregg, Y.; Rooyen, M. van; Ernst, J. D.; Hatherill, M.; Hanekom, W. A.; Peters, B.; Scriba, T. J.; Sette, A. A Quantitative Analysis of Complexity of Human Pathogen-Specific CD4 T Cell Responses in Healthy M. Tuberculosis Infected South Africans. *PLOS Pathog.* **2016**, *12* (7), e1005760. <https://doi.org/10.1371/journal.ppat.1005760>.
- (47) El Sahly, H. M.; Adams, G. J.; Soini, H.; Teeter, L.; Musser, J. M.; Graviss, E. A. Epidemiologic Differences between United States- and Foreign-Born Tuberculosis Patients in Houston, Texas. *J. Infect. Dis.* **2001**, *183* (3), 461–468. <https://doi.org/10.1086/318079>.
- (48) Lewinsohn, D. M.; Leonard, M. K.; LoBue, P. A.; Cohn, D. L.; Daley, C. L.; Desmond, E.; Keane, J.; Lewinsohn, D. A.; Loeffler, A. M.; Mazurek, G. H.; O’Brien, R. J.; Pai, M.; Richeldi, L.; Salfinger, M.; Shinnick, T. M.; Sterling, T. R.; Warshauer, D. M.; Woods, G. L. Official American Thoracic Society/Infectious Diseases Society of America/Centers for Disease Control and Prevention Clinical Practice Guidelines: Diagnosis of Tuberculosis in

- Adults and Children. *Clin. Infect. Dis. Off. Publ. Infect. Dis. Soc. Am.* **2017**, *64* (2), 111–115. <https://doi.org/10.1093/cid/ciw778>.
- (49) Escalante, P.; Peikert, T.; Van Keulen, V. P.; Erskine, C. L.; Bornhorst, C. L.; Andrist, B. R.; McCoy, K.; Pease, L. R.; Abraham, R. S.; Knutson, K. L.; Kita, H.; Schrum, A. G.; Limper, A. H. Combinatorial Immunoprofiling in Latent Tuberculosis Infection. Toward Better Risk Stratification. *Am. J. Respir. Crit. Care Med.* **2015**, *192* (5), 605–617. <https://doi.org/10.1164/rccm.201412-2141OC>.
- (50) Menzies, D.; Gardiner, G.; Farhat, M.; Greenaway, C.; Pai, M. Thinking in Three Dimensions: A Web-Based Algorithm to Aid the Interpretation of Tuberculin Skin Test Results. *Int. J. Tuberc. Lung Dis. Off. J. Int. Union Tuberc. Lung Dis.* **2008**, *12* (5), 498–505.
- (51) QuantiFERON-TB Gold (QFT) ELISA Package Insert.
- (52) *QuantiFERON-TB Gold Plus ELISA Kit Package Insert - QIAGEN*. <https://www.qiagen.com/us/resources/resourcedetail?id=ac068fc7-a994-4443-ac7c-dda43ce2bc5e&lang=en> (accessed 2024-02-19).
- (53) Theel, E. S.; Hilgart, H.; Breen-Lyles, M.; McCoy, K.; Flury, R.; Breeher, L. E.; Wilson, J.; Sia, I. G.; Whitaker, J. A.; Clain, J.; Aksamit, T. R.; Escalante, P. Comparison of the QuantiFERON-TB Gold Plus and QuantiFERON-TB Gold In-Tube Interferon Gamma Release Assays in Patients at Risk for Tuberculosis and in Health Care Workers. *J. Clin. Microbiol.* **2018**, *56* (7), e00614-18. <https://doi.org/10.1128/JCM.00614-18>.
- (54) Yu, D.; Humar, M.; Meserve, K.; Bailey, R. C.; Chormaic, S. N.; Vollmer, F. Whispering-Gallery-Mode Sensors for Biological and Physical Sensing. *Nat. Rev. Methods Primer* **2021**, *1* (1), 83. <https://doi.org/10.1038/s43586-021-00079-2>.
- (55) Iqbal, M.; Gleeson, M. A.; Spaugh, B.; Tybor, F.; Gunn, W. G.; Hochberg, M.; Baehr-Jones, T.; Bailey, R. C.; Gunn, L. C. Label-Free Biosensor Arrays Based on Silicon Ring Resonators and High-Speed Optical Scanning Instrumentation. *IEEE J. Sel. Top. Quantum Electron.* **2010**, *16* (3), 654–661. <https://doi.org/10.1109/JSTQE.2009.2032510>.
- (56) Bailey, R. C.; Washburn, A. L.; Qavi, A. J.; Iqbal, M.; Gleeson, M.; Tybor, F.; Gunn, L. C. A Robust Silicon Photonic Platform for Multiparameter Biological Analysis; Kubby, J. A., Reed, G. T., Eds.; San Jose, CA, 2009; p 72200N. <https://doi.org/10.1117/12.809819>.
- (57) Robison, H. M.; Bailey, R. C. A Guide to Quantitative Biomarker Assay Development Using Whispering Gallery Mode Biosensors: Whispering Gallery Mode Biosensors. *Curr. Protoc. Chem. Biol.* **2017**, *9* (3), 158–173. <https://doi.org/10.1002/cpch.23>.
- (58) Meserve, K.; Qavi, A. J.; Aman, M. J.; Vu, H.; Zeitlin, L.; Dye, J. M.; Froude, J. W.; Leung, D. W.; Yang, L.; Holtsberg, F. W.; Amarasinghe, G. K.; Bailey, R. C. Detection of Biomarkers for Filoviral Infection with a Silicon Photonic Resonator Platform. *STAR Protoc.* **2022**, *3* (4), 101719. <https://doi.org/10.1016/j.xpro.2022.101719>.
- (59) *Move Data, not Blood - 30 Minutes Results - Onsite Lab Automation*. <https://www.genalyte.com/> (accessed 2024-02-19).
- (60) Aydin, S. A Short History, Principles, and Types of ELISA, and Our Laboratory Experience with Peptide/Protein Analyses Using ELISA. *Peptides* **2015**, *72*, 4–15. <https://doi.org/10.1016/j.peptides.2015.04.012>.
- (61) Cerda-Kipper, A. S.; Montiel, B. E.; Hosseini, S. Immunoassays | Radioimmunoassays and Enzyme-Linked Immunosorbent Assay☆. In *Encyclopedia of Analytical Science (Third Edition)*; Worsfold, P., Poole, C., Townshend, A., Miró, M., Eds.; Academic Press: Oxford, 2019; pp 55–75. <https://doi.org/10.1016/B978-0-12-409547-2.14510-X>.

- (62) Alhadj, M.; Zubair, M.; Farhana, A. Enzyme Linked Immunosorbent Assay. In *StatPearls*; StatPearls Publishing: Treasure Island (FL), 2023.
- (63) Mann, H. B.; Whitney, D. R. On a Test of Whether One of Two Random Variables Is Stochastically Larger than the Other. *Ann. Math. Stat.* **1947**, *18* (1), 50–60.
- (64) McKnight, P. E.; Najab, J. Mann-Whitney U Test. In *The Corsini Encyclopedia of Psychology*; John Wiley & Sons, Ltd, 2010; pp 1–1.
<https://doi.org/10.1002/9780470479216.corpsy0524>.
- (65) Breiman, L. Random Forests. *Mach. Learn.* **2001**, *45* (1), 5–32.
<https://doi.org/10.1023/A:1010933404324>.
- (66) Zhu, R.; Zeng, D.; Kosorok, M. R. Reinforcement Learning Trees. *J. Am. Stat. Assoc.* **2015**, *110* (512), 1770–1784. <https://doi.org/10.1080/01621459.2015.1036994>.
- (67) Archer, K. J.; Kimes, R. V. Empirical Characterization of Random Forest Variable Importance Measures. *Comput. Stat. Data Anal.* **2008**, *52* (4), 2249–2260.
<https://doi.org/10.1016/j.csda.2007.08.015>.

Chapter 7 Analytical Considerations for Future Development of Longitudinal, Multi-Biomarker Assays: Dilution Effects, Combination Assays, and Stability Studies

7.1 Author Contributions and Acknowledgements

This chapter contains unpublished work. The content of this chapter was conceived and written, all analysis was completed, and all figures were designed by the thesis author, Krista Meserve. Data used in figures 7.9 and 7.10 was collected by Bailey Lab member Manik Reddy and data used in figure 7.11 was collected by Bailey Lab member Hanyu Zheng.

This chapter contains a grouping of projects I initiated in various assay development and validation spaces. These projects provided me the opportunity to train and mentor three graduate rotation students who later joined the Bailey Lab. Thank you to Manik Reddy for his initial work in assay designs for shifting the IL-8 calibration and Hanyu Zheng for his work on developing the SA-bead-based assay. I'd like to thank Anusha Vajrala for her ongoing work in the stability study and calibration variation that has continued beyond what I present in this chapter. Thank you to Ryan Bailey for his project guidance and to Hanyu and Hayley Herderschee for their time and efforts in editing this chapter.

7.2 Introduction

Bioanalytical assays are critical techniques to quantitatively measure metabolites in biologically relevant matrices, such as blood, plasma, or serum.¹ Bioanalytical methods are developed for many purposes ranging from drug and biomarker discovery, pharmacokinetic studies, and clinical research to forensic science and sports drug testing. In drug discovery and

pharmaceutical research, the analyte of interest is commonly a small molecule, and the standard detection method is mass spectrometry. High-performance liquid chromatography coupled with tandem mass spectrometry and triple quadrupole mass spectrometry using selected reaction monitoring are regarded as the best for quantitation of the biomolecules.¹ When the analyte of interest is a macromolecule, a ligand binding assay (LBA), such as an enzyme-linked immunosorbent assay (ELISA), is the leading detection method for quantitation of the specific target.²

7.2.1 ELISA methods

ELISA methods are widely used in biochemical, pharmaceutical, and clinical laboratories to detect proteins, antibodies (Abs), or other ligands. The assays involve an antigen or antigen recognition element bound to a solid surface, such as a microwell plate, that encounters a series of blockers, detection reagents, and buffer washes and ends with an enzymatic reaction to produce a signal proportional to the analyte concentration.³ The ELISA version selected is dependent on the detection goal. Direct ELISAs coat the plate with a sample containing the antigen of interest and detect using an enzyme-conjugated primary detection Ab and substrate.⁴ Direct ELISAs are faster than other ELISAs, but have low sensitivity, non-specific binding, and are prone to false positives. Indirect ELISAs also coat the plate with a sample containing the antigen of interest followed by a detection Ab but employ a secondary enzyme-conjugated Ab that recognizes the detection Ab and turns over the substrate.⁵ Indirect ELISAs increase the sensitivity but are still prone to low specificity due to other proteins in the sample binding to the plate surface and cross-reactivity between the secondary detection Abs. These methods can also be used for Ab detection. In this case, antigen standards are adhered to the plate, followed by a

blood sample containing an Ab of interest. An enzyme-conjugated secondary detection Ab is employed to detect the presence and concentration of bound Ab.

Competitive ELISAs use a biotin (Bt) tagged antigen structurally similar to the antigen of interest to compete with the principal antigen in the sample for binding sites on the plate-bound Abs.⁵ Signal generation takes advantage of the Bt tag and an enzyme-linked streptavidin (SA) substrate. The signal is inversely proportional to the sample analyte concentration, with a high signal indicating no competition occurred and only the Bt-antigen mimic is present. Low signal indicates that the principal antigen in the sample outcompeted the Bt-antigen mimic for binding sites. This method can be flipped for Ab analysis, with antigen coating the surface and a Bt-Ab present to compete with the Ab of interest.³ This assay style can measure an extensive range of small antigens and has low variability, however, it still suffers from low specificity and has high limits of detection.

The final widely used version, and that which is relevant to the data collected in this chapter, is the sandwich ELISA. Sandwich ELISAs coat the plates with an antigen-specific Ab and the sample containing the antigen of interest is added, followed by the antigen-specific detection Ab, a secondary enzyme-conjugated Ab, and substrate. Although this method increases the number of steps and time (18 hours just in incubation time)⁶ and requires a matched pair of two antigen-specific Abs, the sandwich ELISA has the highest sensitivity and accuracy among versions, reduces background signal, drastically improves the specificity, and does not require a 'clean' antigen containing sample.⁵ These improvements are extremely important in qualifying and validating assays for patient diagnostics, drug discovery, and other applications. An inherent drawback of ELISAs is the single-plex nature of the assay. Each well can be optimized to detect just one target, so if multiple analytes need to be detected, sample volume needs to be increased

because more wells will need to be filled. Additionally, calibrations for each target assessed and quality controls must be conducted on each plate to get the most accurate results. The need for on-plate standard calibrations reduces the number of targets that can be analyzed on one plate.

Optimization can occur at any step in the assay to improve the detection of analytes of interest. Altering the concentration or identity of the target-specific Abs, enzyme-conjugated recognition element, and substrate can all change the assay outcomes. Rigorous assay optimization and validation are critical before assays are used for drug efficacy or commercialized for home use. The development of new biosensors commonly takes advantage of the sensing principles of ELISAs, specifically sandwich ELISAs, and aims to increase the speed and throughput of the assay.

7.2.2 Assay validation parameters for assay implementation

For use in the pharmaceutical industry, small molecule assays must meet specific validation parameter requirements related to selectivity, specificity, stability, calibration, limit of quantification, reproducibility, and robustness.¹ Biomarker assays should aim to address these same parameters during development. However, the Food and Drug Administration (FDA) recognizes that other considerations may need to be addressed and some may not apply.⁷ Much of the work presented in this chapter aims to connect these requirements to the multiplexed sandwich-style protein biomarker assays we conduct on our microring resonator sensor platform and begins to establish internal guidelines for assay qualification. The requirements and optimization parameters discussed in this chapter include calibrations, dilutions, robustness, and long-term assay assessment.

7.2.2.1 Calibration

Calibrating or standardizing an assay allows for users to correlate the assay signal to the relevant concentration of analyte in an unknown sample. Calibrations must be completed for each analyte of interest and each new method used. According to the US FDA guidelines for bioanalytical method validation, the calibration curve should consist of a blank sample and six to eight non-zero samples that cover the expected range of detection, be continuous, be reproducible, and be completed in the same biological matrix as the intended samples. For LBAs specifically, the curve should include anchor points outside of the quantifiable range to help with the fitting of the curve.⁷

The accepted fits for concentration-response relationships of LBAs are most often four- or five-parameter logistic fits. LBAs depend on protein-protein (antigen-Ab) interaction equilibriums, which result in non-linear responses, necessitating the logistic fits.⁸ The standard curve for an LBA is typically plotted on a semi-log scale to transform the curve into an ‘S-shaped’ profile. It is deemed inappropriate to apply a linear fit to a sigmoidal curve or to force the inherent non-linear relationship into a linear one using a log-log transformation.^{8,9} Additional good practices^{7,8,10} vary by regulatory body but include even spacing of calibration points along a logarithmic scale, identification of a maximum ratio of upper to lower limit of quantitation to ensure robustness, and a minimum of two replicates averaged for a final calibration curve.

A four-parametric logistic fit curve is utilized in the work presented in this thesis; therefore, the anatomy of this curve is relevant. The y-axis is the net shift calculated as the difference in the relative shift from immediately before the signal amplification step in our assay to the end of the final buffer rinse. The x-axis is the standard concentration of analyte, plotted on a log scale. The eight-point calibration curve includes a matrix blank and seven additional points

ranging from the concentration previously determined to elicit the maximum signal down to below the limit of quantitation.

The S-shaped curve consists of four main regions: the upper and lower asymptotes, the midpoint, and the dynamic range. The upper horizontal asymptote is the saturating region, referring to all the capture Ab receptors being partnered to the antigen. Concentrations in this range will not illicit a higher signal proportional to higher concentration. Net shifts of unknown samples that fall in this non-sensitive region should not be used quantitatively. Including calibration standards or analyzing samples with the analyte well above the saturating point can lead to the prozone, or hook, effect.¹¹ The prozone effect is when an overabundance of antigen present in solution leads to oversaturation of the capture Abs or protein aggregation. Steric effects can lead to fewer strongly bound antigen-Ab pairs, and the subsequent buffer rinses remove the protein analytes that are not strongly bound, resulting in a final signal lower than expected. Including these high concentration points in a calibration curve results in the saturating region plateau having more of a 'hooked' profile than a flat asymptotic profile. In samples, the reduced signal could lead to lower analyte quantitation and result in a false negative outcome. False negative outcomes occurred in many rapid Ab tests of patients infected with syphilis and led to increased awareness of testing undiluted sera in this patient population.^{12,13} The hook effect is mitigated by introducing the analyte and recognition Ab in subsequent steps instead of simultaneously and by analyzing samples at multiple dilutions.

The baseline signal is the lower horizontal asymptote in the 'S-shaped' LBA calibration curve. This region denotes the signal expected from the assay method when no analyte, or analyte at concentrations below the detection limit, is present. The baseline signal will not be zero for most assays, as background noise is present from the other reagent steps in the assay.

Concentrations that fall within this non-sensitive range should not be calculated and should be denoted as being below the limit of detection. Most work, including ours, will artificially convert this data point to zero even though the analyte may just be undetectable by the chosen method. The midpoint of the calibration curve, also known as the inflection point or center point, is the point at which the curve transitions from concave up to concave down and is the area of greatest change, so the highest sensitivity. Assays should aim to have the unknown target fall as close to the midpoint of the calibration curve as possible for the most sensitive results. Finally, the dynamic range is the region surrounding the midpoint, above the limit of detection and below the saturating region. When not plotted on a log scale, this region may appear linear and is the region for which the assay is optimized for. The ideal sample would always fall within the dynamic range of the assay. As advancements in bioanalytical technologies have continued to improve the limits of detection, more analytes high in concentration will produce signals in saturating regions, leading to a greater need to dilute high-concentration analytes.

7.2.2.2 Dilutions

Dilution of a sample in a running buffer compatible with the analyte and sample matrix, such as phosphate-buffered saline (PBS), is common. There are many reasons for using diluted samples, such as optimizing the expected concentration range to fall within the calibration's dynamic range, minimizing clogging or other assay impairment in 100% matrix, lowering required sample volume, or identifying if the prozone effect is present.⁸ For LBAs, the FDA guidelines for bioanalytical method validation recommend completing quality controls and calibrations for each dilution used and demonstrating that the prozone effect is not present.⁷

Diluting samples is particularly relevant to multiplexed assays, or assays in which multiple analytes are detected in one sample. As mentioned above, ELISAs can only detect one

target per well, and each target is commonly analyzed at multiple dilutions in duplicate or triplicate. In multiplexed assays, the concentrations at which analytes are present can span over ten orders of magnitude, necessitating either lengthy optimization of tuning the calibration ranges or multiple dilutions that aim to place all analytes into the dynamic range of their respective calibrations.^{14,15}

A drawback of dilution is the non-linearity of analyte concentrations in complex matrices.^{15,16} The non-linear phenomenon can occur in protein biomarkers when samples are diluted into complex matrices and the resulting concentration is not proportional to signal output, with higher dilutions tending to have greater non-linear trends.^{17,18} There are multiple methods to test for non-linearity and ways to account for this phenomenon.¹⁹ Dilution linearity testing can be completed by spiking a high concentration of analyte into the matrix and diluting it into the working range to create dose-response curves to determine percent recovery and accuracy of the diluted measurement.^{20,21} Alternatively, results can be reported as relative intensity or signal, rather than concentration to mitigate the effects of dilutions on the absolute value of calculated analyte concentration.¹⁶ Dilution is an effective way to adjust analyte concentration within the dynamic range, especially in multiplexed assays, but monitoring the effects of dilution across targets and patients is important for ensuring robust measurements and results.

7.2.2.3 Target robustness

The robustness, or ruggedness, of an assay is a measure of the ability of the method to remain unaffected by minor variations in the operating procedure or parameters.²⁰ Parameters can include timing, temperature, reagent lots, or operating personnel or labs. Testing the robustness of an assay is a long-term assessment and is not characterized by one lone test. Changing each parameter one at a time (prospectively or retrospectively) and evaluating the

assay outcome can give a sense of the robustness of the assay. In pharmaceutical assay development, intentional changes are made, such as adding three minutes to each assay step until the outcome is affected.²² The ranges of acceptable times or other tested parameters are then included in the assay report as a measure of assay robustness. Small changes in assay procedures should not significantly change the outcome of a robust assay, and continually monitoring an assay's robustness over time is extremely important for any bioanalytical assay application.²³

7.2.2.4 Reproducibility and variability

Reproducibility and variability are central parts of analytical chemistry, and an assay cannot be robust if it is not reproducible with low variability. Accuracy and precision testing is the umbrella component of these metrics in the US FDA guidelines for bioanalytical method validation and the idea of reproducibility and variability is additionally housed within all other validation components. Each validation component (calibration curves, quality controls, selectivity, accuracy, etc.) listed in the FDA guidelines has acceptance criteria that quantify accepted metrics based on reproducibility or variability in the test results. One example is in the calibration curve criteria.⁷ For LBAs, non-zero calibration standards should be within 20% of the theoretical concentration but up to 25% closer to the saturating or baseline regions. These are the same acceptance levels as the accuracy and precision tests that must include at least six independent runs of five analyte concentrations spanning the calibration range, with three replicates each. For LBAs, intra-batch (within run) variability is generally lower than inter-batch (between run) variability.²⁴ In summary, bioanalytical assays must demonstrate high robustness and reproducibility with low variability through numerous points of analysis, such as calibration curves, parameter alteration, longitudinal testing, and accuracy measurements.

7.2.3 Connections to this chapter

This chapter discusses four topics spanning the various assay validation measures discussed above. The results and discussion section opens with an analysis of inter- and intra-batch variation in the multiplexed calibrations for our latent tuberculosis infection (LTBI) assay panel and a comparison of the two biologic matrices of sample analysis (10% and 50% plasma). The intra-batch variability is lower than the inter-batch variability and inter-batch variability is heavily target dependent. Some targets, such as CCL3 and IL-6, are identified as having the lowest variability in calibration parameters (midpoint value, saturating and baseline signals) and could be used as benchmark targets for qualifying new chip batches. On the other hand, targets such as IL-1 β and IFN- γ have demonstrated high variability between chip batch calibrations and should not be used to qualify chip batches. There is greater variation in the 50% plasma matrix, but over half of the targets exhibit very low variation between the matrix calibrations. The second results and discussion section regards the sample dilution. In the LTBI project, each sample is analyzed at two dilutions, and the absolute dilution is selected using proximity to the midpoint of the calibration curve. Analysis of the selected dilution revealed that all stimulation conditions and targets use the 2 \times and 10 \times dilutions, but the 2 \times dilution is slightly favored and would be the chosen dilution to analyze if the clinical sample volume is low. The third section focuses on a long-term, intra-batch stability study of the sensor chips that, to date, provides information on the three-month stability of the antibodies on the sensor chip. The net shifts are more consistent within a time point than within a chip deck, but the variation between chip decks and time does not show trends of stability loss. Finally, we explore a new assay method that would optimize the calibration curve of a specific target to quantify analytes at higher concentrations. Ultimately, no assay was identified for use, but important optimization data was gained.

This chapter aims to aggregate various observations and analyses that set the foundation for more formal multiplexed assay validation measurements and documentation. The results might not be pertinent to a larger audience but will serve as legacy documentation for future Bailey Lab members working on the longitudinal LTBI project and on other clinical biomarker-based projects. The ability to replicate the inter-batch calibration curves was hindered by the low number of sensor chip batches acquired from Genalyte, Inc. during my Ph.D., but the data and trends can serve as a starting point for more formal studies to determine acceptance ranges of our specific assay targets. The IL-8 assay optimization project can also be used to train new graduate student rotators in the relevant techniques and principles needed to grasp long-term clinical projects.

7.3 Methods

7.3.1 Microring resonator technology

All data in this chapter was collected using silicon photonic microring resonator instrumentation. This whispering-gallery-mode technology tracks binding events through the refractive index (RI) changes within the evanescent field emanating from each microring waveguide.²⁵⁻²⁹ Briefly, light traveling down an on-chip linear waveguide couples into and resonates within the circular waveguide at a wavelength specific to the effective RI within the sensing region, according to the following equation:

$$\lambda = \frac{2\pi r}{m} n_{eff}$$

where λ is the wavelength, m is an integer, r is the radius of the circular waveguide, and n_{eff} is the effective RI of the optical mode. Capture probes covalently attached to the microring resonator attract specific target molecules to the sensor surface, altering the sensing region's RI.

The altered RI gives rise to a change in the resonant wavelength and results in a measurable shift in non-transmitted wavelength. Resonance shift is tracked throughout an entire binding experiment and, using calibration curves, can be converted to concentration of an unknown target in solution.

The sensing chips were fabricated by Genalyte, Inc.³⁰ and contained 128 individual microring sensors, spatially arrayed in sixteen clusters of four across two distinct microfluidic channels. The chips also contain unexposed, cladding-covered rings that serve as thermal controls. This technology allows for thermally controlled measurements of up to 16 different targets, each with four technical replicates, in two samples simultaneously.

The instruments were from Genalyte, Inc. Data from this chapter was collected using two different instrument versions. Data related to samples and calibrations (dilution analysis, calibration comparisons, and stability studies) were collected on the Matchbox instrument, as previously described in **Chapter 2**.³¹ The IL-8 alternate assay experiments, and any other optimization work, were completed on the M1 instrument, as previously described in the literature.³² Both instruments process samples using the same sensor chip design and automate fluidic handling at 30 $\mu\text{L}/\text{min}$ across both microfluidic channels. The main difference between the Matchbox and M1 instruments is the sensor chip holder mechanism. In the Matchbox, plastic injection-molded cartridges from Genalyte, Inc. house the chips in a plug-and-play fashion and are discarded after use. This instrument setup is generally used for plasma- and serum-containing experiments, and the disposable cartridge eliminates potential carryover from prior samples and reduces clogging. In the M1, the chips are layered with a gasket and cartridge top, then manually screwed down to secure the set-up. The M1 chip holder is reused from experiment to experiment

and is, therefore, mainly for optimization and testing assays with running buffer as the experimental matrix.

7.3.2 Sensor chip spotting and preparation

For the IL-8 assay development projects, the preparation of the sensor chips was completed by hand and a detailed protocol is described in **Chapter 2**. Briefly, sensor chips were silanized with (3-aminopropyl)triethoxysilane (APTES), followed by introduction of a homo-bifunctional linker, bis(sulfosuccinimidyl)suberate (BS3), and functionalized with the capture Ab of interest. The BS3 covalently links the amine group on the silane to the amine group on the capture Ab. Various capture reagents were spatially arrayed across both microfluidic channels, with two to three ring groups, or eight to twelve rings, covered per target using the hand spotting method. The capture agents were incubated on-chip for one hour, followed by a one-hour incubation with a BSA-containing blocking buffer to blanket any unreacted BS3 and prevent a reaction between target proteins and surface-linked BS3. Finally, the spotted chips were dried with nitrogen and coated with dry coat, a sugar-based solution to protect the Abs until use. For the data collected in the other sections of this chapter, a 14-plex array (IL-1 β , IL-2, IL-6, IL-8, IL-10, IL-15, IL-17, CCL2, CCL3, CCL4, CCL8, IP-10, TNF- α , IFN- γ) was functionalized using microspotting techniques by Genalyte, Inc. Each antibody capture covered one ring cluster of four rings per channel. The functionalization reagents and steps are identical to the hand-spotting method.

7.3.3 Microring resonator immunoassay, calibrations, and sample analysis

The assays completed for data discussed in relation to dilution factors, calibration comparisons, and many of the IL-8 alternate assay sections were standard immunoassays

discussed in the previous chapters. In brief, the running buffer (1X-PBS with 5% BSA) was flowed across the chip to equilibrate the surface for five minutes. The data collection began with running buffer flowing consistently for five minutes to collect the baseline signal. This was followed by diluted sample or standard solution (various concentrations, 10 mins), a buffer rinse (2 mins), biotinylated tracer antibody (Bt-Ab) mixture for all targets in the sample (various concentrations, 10 mins), a buffer rinse (2 mins), streptavidin horse-radish peroxidase (SA-HRP, 4 µg/mL, 10 min), a buffer rinse (2 mins), 4-chloro-1-naphthol (4CN, stock concentration, 8 mins), and a final buffer rinse (3 mins), for a total assay time of 52 minutes using the M1 instrument. The same assay completed on the Matchbox instrument reduces reagent steps from 10 to 7 minutes, resulting in a 40-minute assay. The protein of interest and Bt-Ab form the sandwich complex that is tagged with the SA-HRP recognition reagent through strong Bt-SA interactions. The 4CN initiates a catalytic precipitation with the localized HRP and forms an insoluble byproduct within the evanescent field, amplifying the resonant wavelength and resulting in lower detection limits and broader sensing regions.

Calibrations were conducted for each set of sensor chips acquired from Genalyte, Inc. Sensor chip batches varied in volume from 200 to 450 chips. Two calibrations for each sample matrix (50% plasma and 10% plasma) were conducted immediately upon receipt of a chip batch. Samples were then analyzed with that chip batch. After ~150-200 chips or two months, whichever came first, another set of calibrations was completed. This continued until all chips in the chip batch were used. Conducting calibrations over the course of running samples, rather than all at the beginning or end, accounts for any variation over time in the sensor chips. At least three calibrations were completed for smaller chip batches (n=200-300 chips) for each matrix.

For larger chip batches (n=300-450), at least four calibrations were completed over the time of running samples.

Calibration curves consisted of eight data points ranging from a concentration that achieves a saturating signal to a matrix blank, with six five-fold dilutions in between, as described in Chapter 2. All targets in a multiplexed panel were calibrated simultaneously, with all relevant targets as a standard mixture in the matrix of interest (50% plasma or 10% plasma) and all relevant Bt-Abs as a tracer mixture in buffer. Each of the eight standards was analyzed using the same assay method described above. Resulting net shifts from each standard were fit to a four parametric logistic function:

$$y = \frac{A_1 - A_2}{1 + \left(\frac{x}{x_0}\right)^p} + A_2$$

where y is the net shift (Δpm) of the sample with concentration x (pg/mL), A_1 is the minimum net shift (Δpm), A_2 is the maximum net shift (Δpm), x_0 is the center value (pg/mL), and p is the power parameter affecting the slope around the inflection point, using R programming.^{31,32} The fit parameters (A_1 , A_2 , x_0 , and p) were exported as CSV files and plotted, as seen in the figures of this chapter. Once multiple calibrations had been completed within a chip batch, the net shifts for each standard concentration were averaged and used to construct a final calibration curve that was subsequently used to quantify the targets analyzed with that chip batch. New calibrations were constructed for each new sensor chip batch in both matrices (50% and 10% plasma) and used only for samples analyzed with that chip batch.

Samples were analyzed at two dilutions, 2 \times and 10 \times . Prior to analysis, plasma samples were thawed at 4°C and centrifuged in a benchtop centrifuge for 3-5 seconds to pellet any solid particles that could clog the system. The supernatant was diluted two-fold and ten-fold into the

running buffer at a total volume of 330 μL . The sample was analyzed using the same assay method described above, with a cocktail mixture of all Bt-Abs in the panel.

7.3.4 Immunoassay data work-up

The data from each assay was analyzed by in-house codes using R programming. The detailed data analysis steps are described in Chapter 2 and the work-up relevant to the data in this chapter is further described in the opening of the “Results and Discussion” section. Each microring sensor outputs the relative shift at specific times in a CSV file. The code aggregated all the raw data, labeled the rings with the respective capture antibody name, subtracted thermal controls, and averaged the net shifts across the technical replicates. Various data plots, including a trace of the relative shift for each ring throughout the full assay and a bar graph of the final net shift for each ring, were output for quality control and analysis.

Once all samples had been analyzed for a given chip batch, an in-house R programming code was used to convert from net shifts to target concentrations. All data from analyzed samples was aggregated and the net shifts were converted to concentrations using each target’s respective calibration curve fit. At this point, each analyzed target in every sample had two associated concentrations: one from the two-fold dilution and one from the ten-fold dilution. The code compared the resulting concentrations from each dilution and selected the one that resulted in a concentration closer to the midpoint, or x_0 value, of the dilution’s calibration curve. If both dilutions resulted in a concentration of zero, the 10 \times dilution was selected as a placeholder. If both dilutions resulted in a concentration above the upper limit of the calibration, that data point was removed. The selected concentrations were multiplied by the respective dilution factor and used for further analysis.

7.3.5 Calibration comparisons analysis

Calibration curves across multiple chip batches were plotted as overlays using an in-house R programming code. The calibrations explored in this chapter came from the four different multiplexed sensor chip batches spotted by Genalyte, Inc. obtained during my time in the Bailey Lab. The first was received in June 2021 and primarily used to finish analyzing the neonate samples (Chapter 4). Approximately sixty sensor chips were allocated to analyze the first ten LTBI subjects (Chapter 5 and Chapter 6), which is equivalent to forty samples. All samples were analyzed in a week; therefore, only two LTBI calibrations per matrix were deemed necessary for this chip batch. The second set of sensor chips was received in February 2022, with approximately 200 chips fully allocated for the LTBI project. Three calibrations per matrix were constructed: two in the middle of February upon receipt of chips and one at the end of March when samples were almost fully analyzed. The third set of sensor chips was received at the end of June 2022, with approximately 200 chips fully allocated for the LTBI project. Three calibrations per matrix were constructed, two in July and one at the end of August. Finally, the fourth set of sensor chips was received at the end of November 2023, with approximately 450 chips fully allocated for the LTBI project. One calibration has been constructed, with more to come in the early months of 2024. The calibrations were conducted on the Matchbox instrument.

7.3.6 Intra-batch, long-term assay stability study

The long-term assay stability study data was collected using the November 2023 sensor chip batch. Upon receipt of the sensor chip batch, there were four storage boxes, or decks, with ~113-115 chips each. Quality control precision experiments that included a full amplification assay with a set group of biomarkers that spatially span across the flow channel were completed. These markers include IL-2, IL-6, IL-8, IL-15, CCL4, and IFN- γ . The targets IL-6, IL-15, CCL4, and IFN- γ were selected as they span from one end of the chip to the other, allowing us to see if

there is variation specific to the time BS3 was left on-chip before Ab functionalization. IL-2 and IL-8 were added because of the capture Ab volume-related issues discussed in this chapter. The Mouse (Ms) IgG negative control spotted rings on either end of the chip were also assessed for variation. To complete these quality control experiments, the protein standards at 10 ng/mL were analyzed using the standard immunoassay method.

For the stability study, the same experiment to test this group of six targets was completed every month in a sample matrix of 1X PBS-BSA buffer. The first time point was upon receipt of the chip batch in early December. Two chips from each deck, eight chips in total, were tested. The remaining time points tested one chip from each deck and occurred every month for the first three months. It is planned to continue with a time point each month until at least six months since receipt and potentially out to one year.

7.3.7 Dilution selection data analysis

Data from the LTBI project was used to explore if any conditions or targets favored the 2× or 10× dilutions. No clinical data or concentration of cytokines were assessed, as the interest was related to stimulation, target, and dilution selected. Any net shifts that resulted in a zero concentration (n=459 out of 4,852 concentrations) were removed from the data set, as the code uses the 10× dilution as the placeholder for targets resulting in a zero concentration. Keeping the data present would artificially increase the number of targets perceived to select the 10× dilution. The data points removed included: 2 from CCL2, 3 from CCL3, 8 from CCL4, 72 from CCL8, 70 from IFN- γ , 7 from IL-15, 230 from IL-17, 8 from IL-1 β , 11 from IL-2, 3 from IL-6, 32 from IP-10, and 26 from TNF- α . Looking at the removed data from the stimulation condition perspective, 51 data points were removed from MIT conditions, 160 from NIL, 119 from TB1, and 142 from TB2. Alluvial diagrams were chosen for visualization due to their ability to show

two data splits from a central node (selected dilution). The diagrams were made by inputting the CSV file into the RawGraphs 2.0 web interface, assigning nodes, and setting design preferences.³³

7.3.8 Various IL-8 assay designs

Various assay methods were employed to shift the IL-8 assay to the right, allowing for more samples to have an IL-8 concentration within the linear dynamic range of the curve. Unless otherwise stated, the Bt-Ab tracers used in the following assays were anti-IL-8 antibodies. All experiments were conducted on the M1 instrument with hand-spotted chips. IL-8 standards at relevant concentrations were made using 100 µg/mL stock IL-8 protein diluted into 1X PBS-0.5% BSA buffer (PBS-BSA).

7.3.8.1 Non- Biotinylated tracer Ab

In this assay design, the steps were identical to the standard microring immunoassay method, as described in the “Microring resonator immunoassay, calibrations, and sample analysis” section above, and included sample introduction, followed by the Bt-Ab, SA-HRP, and 4CN. However, instead of the Bt-Ab tracer being deployed at a running concentration of 2 µg/mL, a mixture of Bt-Ab and non-biotinylated tracer antibody (non-Bt-Ab) was deployed at various concentrations and ratios in standard PBS-BSA buffer. The non-Bt-Ab was functionally identical to the Bt-Ab, meaning they bound to the same spot on the IL-8 protein but did not contain the biotin tag.

7.3.8.2 Capture Ab dilution

In this assay design, the steps were identical to the standard microring immunoassay method, as described in the “Microring resonator immunoassay, calibrations, and sample

analysis” section above, and included sample introduction, followed by the Bt-Ab, SA-HRP, and 4CN. The alteration in this assay design is not in the assay itself but in the spotted capture Abs. The capture is spotted at 0.25 mg/mL (stock = 0.5 mg/mL) with 10% glycerol in 1X PBS for standard sensor chip spotting. In this assay design, concentrations of spotted IL-8 capture Ab included 0.45 mg/mL, 0.25 mg/mL, 25 µg/mL, 20 µg/mL, 10 µg/mL, 2.5 µg/mL, and 0.25 µg/mL, with 10% glycerol in 1X PBS. In addition, mixtures of IL-8 capture Ab and mouse control IgG Ab were tested for spotted IL-8 capture Ab at 0.25 mg/mL, 25 µg /mL, 20 µg/mL, 10 µg/mL, 2.5 µg/mL, and 0.25 µg/mL with IgG Ab held constant at 0.25 mg/mL and 10% glycerol in 1X PBS. The chip functionalization protocol described in the “Sensor chip spotting and preparation” section above was followed for all capture dilutions.

7.3.8.3 Streptavidin bead-based assay

Additional preparation for this assay design included constructing SA-bead calibrations and washing the streptavidin (SA) coated 100 nm magnetic beads. The calibration was constructed using four two-fold dilutions, ranging from 250 µg/mL to 31.25 µg/mL. The beads (stock concentration = 1 mg/mL) were diluted in PBS with 0.05% tween-20 (PBST) to a total volume of 10 µL. The absorbance of the standards was measured at 286 nm with a nanodrop blanked with PBST.

The washing procedure was adapted from Luchanksy, M.S. et al.³⁴ First, 37.5 µL of 1 mg/mL SA-beads were diluted to 150 µg /mL in an Eppendorf tube using PBS-T and centrifuged at 10,000 rcf for four minutes. Using a magnet, the bead pellet was held at the bottom of the tube while the supernatant was removed, leaving approximately 30-40 µL of bead solution. The beads were resuspended in 250 µL of PBST, pipetted up and down approximately 50 times, and subsequently centrifuged at 10,000 rcf for four minutes. This washing procedure was repeated

for a total of four exchanges. After the final supernatant removal, the beads were resuspended in 250 μL of PBST, and the absorbance was measured at 286 nm using the nanodrop; a final concentration was obtained using the constructed calibration, and the beads were diluted to the running concentration of 50 $\mu\text{g}/\text{mL}$. For this assay design, the standard assay method was altered. The sample introduction was followed by biotinylated tracer Ab (2 $\mu\text{g}/\text{mL}$, 10 mins) and SA-beads (50 $\mu\text{g}/\text{mL}$, 10 mins), with a final 10-minute buffer rinse.

7.3.8.4 HRP-linked tracer Ab

Additional preparation for this assay design included conjugating horse radish peroxidase (HRP) to the unmodified IL-8 tracer Ab. An HRP conjugation kit was purchased from Abcam, and the protocol was followed.³⁵ All steps took place under a fume hood. First, the HRP and modifier reagent from the kit were thawed from the -20°C freezer and 8 μL of modifier reagent was added directly to 80 μL of unmodified IL-8 Ab and inverted to mix. The entire mixture was added to the lyophilized HRP vial and mixed by pipetting. The resulting reddish solution was transferred to a black Eppendorf tube to protect from light and left to react at room temperature for three hours. Finally, the quencher was thawed and 8 μL was added to the black Eppendorf to stop the reaction. The resulting solution was used in subsequent assays, as directed by the manufacturer. For this assay design, the standard assay method was altered. The sample introduction was followed by the HRP-tracer Ab (2 $\mu\text{g}/\text{mL}$, 10 mins) and 4CN (stock, 8 mins).

7.4 Results and Discussion

This chapter aims to aggregate various observations and analyses stemming from the LTBI project data collection and from projects initiated for our graduate student rotators to complete. While the results may not be pertinent to a larger audience, this will be useful documentation for future Bailey Lab members working with the microring resonator platforms,

specifically those working on the longitudinal LTBI project. This chapter includes four different topics: (1) variations in calibrations for each target across sensor chip batches and plasma matrices, (2) trends in dilution selection for LTBI samples, (3) stability of sensor chip decks over time, and (4) development of an alternate assay for a specific target, IL-8. A general background of data collection workflow is needed to understand these topics.

The current data collection workflow from microring resonator assay to data processing for clinical samples is depicted in **Figure 7.1** and has been developed and employed for many years in the Bailey Lab. The workflow starts with a multiplexed immunoassay that includes up to fifteen target-specific capture Abs and mouse IgG negative controls (**Figure 7.1A**). The standard assay steps include analyte introduction, sandwich complex formation with a biotinylated tracer antibody (Bt-Ab) specific to each target, enzymatic labeling of each sandwich with streptavidin horse radish peroxidase (SA-HRP), and signal amplification with 4CN. The 4CN amplification reagent reacts with the localized HRP to form a precipitate in the sensing region, drastically altering the RI within the evanescent field, shifting the resonant wavelength, and resulting in lower limits of detection and broader sensing regions, in comparison to using the shifts from the intermediate assay steps for quantitation. All fluid is handled with automated microfluidics and 1X-PBS-BSA buffer rinses occur between each step.

Each sample for clinical projects is analyzed at two dilutions, 2× and 10×, aiming to achieve a concentration for each target within the dynamic range of the calibration curve (**Figure 7.1B**). For samples high in concentration, the 2× dilution may result in a net shift in the saturating range (upper horizontal asymptote) of the assay, but the 10× dilution would result in a net shift closer to the inflection point of the calibration curve, where it is most sensitive. Conversely, for samples low in concentration, the 10× dilution would be too dilute and reside

below the limit of detection; however, the 2× dilution would result in a net shift closer to the curve's inflection point.

Once the samples are analyzed on the multiplexed assay at two dilutions, the constructed calibration curves convert the net shifts for each target to its associated concentration at both the 2× and 10× dilutions (**Figure 7.1C**). However, one dilution must be selected as the overall value used in bioinformatics analysis. The standard method we employed to keep selection uniform across samples and projects is to select the dilution that resulted in a concentration closest to the midpoint, x_0 , of the respective calibration curve. The selected dilution is then multiplied by the dilution factor of the selected dilution: two for the 2× dilution and ten for the 10× dilution. In the example depicted in **Figure 7.1C**, the 'grey' target was higher in concentration comparatively to the 'blue' target. The 'grey' target's 2× dilution fell within the saturating range of the 50% plasma calibration curve, but the 10× dilution fell within the dynamic range of the 10% plasma calibration curve. Therefore, the 10× dilution was selected. Conversely, the 'blue' target's 2× and 10× dilution fell within the dynamic range of the respective calibration curves, but the 2× dilution resulted in a net shift closer to the inflection point of the 50% calibration curve. Therefore, the 2× dilution was selected for the 'blue' target. This selection process is done for each target in each sample. For the LTBI project, approximately 360 samples were analyzed with a 14-plex assay at two dilutions, resulting in 10,080 individual concentrations, which were reduced to 5,040 lines of data after dilution selection.

In this chapter, I discuss four different topics that tangentially relate to analytical considerations for longitudinal projects and assay design. The first project direction assesses variations in calibrations for each target across sensor chip batches and seeks to qualitatively and quantitatively identify which targets are most robust, leading to trends in expected variation for

future sensor chip batches. The second project direction identified trends in which dilution (2× or 10×) was selected as the final concentration for LTBI samples, leading to relevant information regarding sample process reduction for future LTBI project study plans. The third project generates data to quantitatively assess the stability of antibody spotted multiplexed sensor chip decks over time, data we currently do not have and can be used to determine optimal timeframes for using the Genalyte, Inc. spotted sensor chips. The final project direction, inspired by the results from the second project, was pursued by graduate student rotators under my supervision and direction. This project aimed to alter the IL-8 assay in a way that would shift the calibration curve to the right, an attempt to reduce the number of assays that resulted in saturating responses, with implications in future assay design projects.

7.4.1 Analyzing calibrations across multiple chip batches to identify expected variation

7.4.1.1 Logistical changes in chip batch spotting runs can result in shifted calibration curves that are still usable.

There is a level of expected variation between assays analyzed by different chip batches. Variability can result from reagents (spotting or assay reagents) aging over time, changes in reagent lots or manufacturers, or inherent variation in the spotting procedure. The nine calibrations I have completed for all fourteen measured targets (IL-1 β , IL-2, IL-6, IL-8, IL-10, IL-15, IL-17, CCL2, CCL3, CCL4, CCL8, IP-10, TNF- α , and IFN- γ) in 10% and 50% plasma matrices are presented in **Figure 7.2** and **Figure 7.3**, respectively. The calibrations are grouped by variation in the midpoint (x_0 value), with the four least variable in **Figure 7.2A** and **Figure 7.3A**, the four most variable in **Figure 7.2C** and **Figure 7.3C**, and the remaining grouped in **Figure 7.2B** and **Figure 7.3B**.

Nine calibrations are plotted in each graph across four sensor chip batches. The June 2021 chip batch stands apart from the other three in many targets at both dilutions. For example, the green lines in **Figure 7.2** for IL-6, IL-10, CCL2, TNF- α , IL-1 β , and CCL4 and in **Figure 7.3** for IL-6, IL-2, IL-10, CCL4, TNF- α , IL-1 β , IL-17, CCL2, and IFN- γ are significantly shifted right or truncated in dynamic range. The calibrations were still usable for that chip batch, but with subsequent chip batches, the calibrations were noticeably of better quality. The difference between the June 2021 chip batch and the others could be due to updated spotting procedures or the age of the capture antibodies. However, all reagents were tested for quality before sending to Genalyte, Inc. for sensor chip spotting.

Additionally, the IL-2 calibrations in blue lines in **Figure 7.2** were heavily shifted right. These calibrations were completed with a new lot of IL-2 protein standard that degraded rapidly after thawing. This led to further investigation with nanodrop and gel electrophoresis experiments to compare the new protein lot with an older one. Ultimately, a new company was identified to provide us with the IL-2 protein standard. These two noted blue calibrations were not used for quantifying the IL-2 in patient samples; instead, new calibrations were constructed with the viable protein standard. These lines were kept in this figure to highlight how understanding what calibrations have looked like in past chip batches can help to identify irregularities in reagent behavior.

The most recent chip batch, November 2023, only has one calibration to date (grey line) and is the largest chip batch we have ordered. The more chips spotted in a sensor chip spotting run, the longer the BS3 linker sits on-chip before Ab introduction, which could result in more degradation and less efficiency in linking Abs to the silanized surface. On average, each target probe takes about 7 minutes to spot 484 chips and 5.5 minutes to spot 242 chips, as four minutes

are required to switch out probes and wash the nozzle, which does not change based on chip number. Across sixteen capture agents being spotted (the fourteen targets and two clusters of mouse IgG controls on either end of the flow channel), it would take roughly 112 minutes to spot 484 chips and 88 minutes for 242 chips. All previous batches had around 200 chips spotted at a time; however, the November 2023 batch was doubled, allowing us to establish the effect of an extra 30 minutes of spotting time. Another complication for this chip batch was loss of antibody stock solution after shipping that will be mitigated with parafilm vials in the future. The CCL2 and IL-17 antibodies were slightly lower in volume but close to what is needed for spotting at 0.25 mg/mL. However, IL-2 and IL-8 had very little volume, about one-third to one-half of what was needed. It is unclear if the liquid in these samples evaporated, leaving a more concentrated solution, or if volume leaked out of the closed Eppendorf in transit.

For most targets, there is little difference in the November 2023 batch compared to previous chip batches. However, the grey line in **Figure 7.2** for IP-10, IL-2, IL-8, IL-15, IL-1 β and CCL4 and in **Figure 7.3** for IL-8, IL-2, IP-10, and CCL2 are shifted right, more so like the June 2021 calibrations. The shifts to the right may be an artifact of lower coupling efficiency, as fewer antibodies successfully spotted would result in lower net shifts. The lower-than-expected antibody volume for chip spotting can explain the IL-2, IL-8, and CCL2 variation. The IL-1 β and CCL4 targets are the most variable across calibrations (discussed more below). The most concerning target here is the truncation and shift of IP-10, especially considering the influence of the IP-10 target for the LTBI diagnostic assays (Chapter 5 and Chapter 6). Further testing of IP-10 will include buying fresh reagents and recalibrating. While there are noted differences in comparison to the February 2022 and June 2022 chip batches, the November 2023 chip batch is

still usable for all targets. At least two to three additional calibrations will be completed and averaged before converting the net shifts of samples analyzed to analyte concentrations.

7.4.1.2 There is more variability in the 50% plasma matrix and specific targets can be identified as low or high calibration variability, regardless of the sensor chip batch.

Comparing calibrations from multiple chip batches can provide insight into which targets are most robust because most chip batches are analyzed with different lots of assay reagents (capture Abs, protein standards, tracer Abs). The comparison can also determine which targets have an expected variation in inter- and intra-chip batch calibrations and how the matrix affects each target's calibration. The variation between the calibrations was measured by calculating the average and standard deviation of the midpoint, x_0 value, of the calibration curve. The June 2021 chip batch was excluded from these calculations due to the inherent differences in some of the targets that we believe to be due to spotting procedure changes and reagent differences, as well as the two July 2022 calibrations for IL-2 in the 10% plasma. The calibration parameters of interest are the x_0 value in pg/mL (**Table 7.1**) and the maximum and minimum shift in picometers (**Table 7.2**).

The calibrations completed in the 50% plasma matrix have greater variation in the midpoint value than in the 10% plasma matrix. This could be due to over blocking of the chip surface from exogenous proteins in the matrix, preventing binding of the analyte to its antibody and increasing the variation calibration to calibration.

In the 10% plasma matrix, IL-6, CCL3, CCL8, and IP-10 have the lowest standard deviation in x_0 value between the February 2022, July 2022, and November 2023 chip batches (**Table 7.1, Figure 7.2A**) and IL-1 β , IL-17, CCL4, and IFN- γ have the highest variation (**Figure 7.2C**), with the rest of the six targets in between (**Figure 7.2B**). The calibration overlays show

that inter-chip batch calibrations are more similar than intra-chip batch calibrations, meaning the deviation in x_0 value is associated more with batch -to- batch variability than calibration-to-calibration variability.²⁴ Lower inter-chip batch deviation is preferred, as calibrations of a chip batch are used for the samples analyzed with the same chip batch. These results highlight the importance of calibrating for every chip batch, with multiple calibrations for each.

In the 50% plasma matrix, IL-6, IL-8, CCL3, and CCL8 have the lowest standard deviation in x_0 value between the February 2022, July 2022, and November 2023 chip batches (**Figure 7.3A, Table 7.1,**) and IL-1 β , IL-17, CCL2, and IFN- γ have the highest variation (**Figure 7.3C**), with the rest of the six targets in between (**Figure 7.3B**). These results are extremely similar to the grouping in the 10% plasma calibrations. Three of the four targets identified as the lowest variation (IL-6, CCL3, and CCL8) and three of the four targets identified as the highest variation (IL-1 β , IL-17, and IFN- γ) are the same across the 10% and 50% plasma calibrations. This overlap and consistency in low/high variation between chip batches means the variation is more likely due to functional variability in the antibodies or the assays themselves rather than in the sensor chips that have been previously demonstrated to have low batch-to-batch variation or in the preparation of the reagents and calibration standards.

Targets like IL-6 and CCL3 that have both inter- and intra-chip batch calibration curves overlaid almost directly on top of each other can be used as quality controls, as large shifts or differences in profiles in these targets can be signals of faulty chip spotting, reagents, or standard generation. They also demonstrate the reproducibility in spotting procedures and calibration construction. Targets such as IL-1 β and CCL4 should be less likely to qualify chip batches or calibration constructions as faulty, as this evidence suggests there is expected variation in these

specific targets. Even still, there is less variation in intra- batch calibrations, validating the need for calibrations of every chip batch.

The patterns identified and quantified between the nine most recent calibrations can be used to notice extreme differences in chip batches. Future calibrations from the November 2023 and subsequent sensor chip batches should be aggregated. After five different sensor chip batches have been fully calibrated, reference ranges for x_0 values, maximum shifts, and minimum shifts can be calculated and used for future sensor chip batch qualification. Set ranges will provide students working on these long-term projects with a benchmark of where the calibrations should fall for new sensor chip batches. Additionally, normal ranges for x_0 values, maximum shifts, and minimum shifts within one chip batch can be calculated to standardize expected changes within individual chip batches over time. These benchmarks can then be used to qualify new chip batches, helping to keep the patient data high quality through the longitudinal clinical projects.

7.4.1.3 Inter-matrix comparisons show the majority of targets result in comparable calibrations between the 10% and 50% plasma matrices.

The February 2022 sensor chip batch calibrations were averaged within the matrix and used for converting net shifts to analyte concentrations in patient samples. Additionally, the averaged calibrations for the 50% and 10% plasma matrices were plotted together to assess similarities or differences in how the targets calibrate in the different matrices (Figure 7.4). This subsection will separate the targets by qualitative and quantitative similarities in the profiles of the 10% and 50% plasma calibrations. Half of the studied targets, IL-6, IL-8, IL-10, IL-17, CCL3, CCL8, and IP-10, are generally very similar between the two matrix calibrations in x_0 values and in curve profiles (**Figure 7.4A**). Four of the fourteen studied targets, IL-2, IL-15,

CCL4, and TNF- α , are similar in profile but the 50% matrix has a slight right shift compared to the 10% matrix (**Figure 7.4B**). The remaining three targets, IL-1 β , CCL2, and IFN- γ , have different profiles, or shapes of the curves, between the two matrices (**Figure 7.4C**).

The targets most similar across both matrices when assessing the averaged calibrations in the February 2022 chip batch were IL-6, IL-8, IL-10, IL-17, CCL3, CCL8, and IP-10. In all of these calibrations, the range between the two horizontal asymptotes is directly overlaid onto each other, and the x_0 values differ by less than 0.62 ng/mL. This is the critical part of the calibration curve, as it is where the assay sensitivity is generated. The greatest variation within these targets is in the saturating or baseline signals. IL-6 and IL-8 differ in baseline net shifts by an average of 210 pm and in saturating net shifts by an average of 430 pm. These are relatively low differences in net shifts but result in noticeable differences in profiles as compared to IL-10 and IL-17. Both dilutions have the same baseline shift for CCL3, but the 50% matrix results in a saturating shift of 517 pm greater than the 10% matrix. Similarly, but on the opposite end of the curve, IP-10 and CCL8 matrices result in very similar saturating shifts, but the 50% matrix baseline shift is 401 pm and 375 pm greater than the 10% matrix, respectively. However, even with these slight differences in one or both horizontal asymptotes of the curve, the most sensitive regions of the curve and the midpoint values are highly similar between matrices. These specific targets highlight that some sandwich assay reagents do not change with a changing sample matrix and there is potential for generating just one calibration curve to be used for both analyzed dilutions.

Four targets, IL-2, IL-15, CCL4, and TNF- α , have similarities between the matrices in the fit profile and one or both of the horizontal asymptotes, but the 50% plasma matrix has a right shift in the midpoint, and therefore the central region of the curve is shifted to the right by an average value of 1.18 ng/mL. Three targets, IL-2, IL-15, and TNF- α , result in baseline and

saturating shifts with less than 118 pm and 197 pm difference between the matrices, respectively. CCL4 resulted in a baseline difference of just 17 pm but 647 pm between the two saturating regions. This difference did not drastically change the midpoint value to any greater extent than the other targets in this classification. The shift right in the 50% plasma calibration indicates a slightly less effective assay, as lower concentrations do not result in as measurable of a shift as the 10% calibration, likely a consequence of higher exogenous protein content in 50% plasma than in 10%. The protein and other waste in the plasma matrix may temporarily block the binding sites due to non-covalent forces or slow down the binding kinetics in the analyte introduction step. These targets must be further studied to entertain the ability to use one calibration curve for both matrices.

The final grouping of three targets, IL-1 β , CCL2, and IFN- γ , have the most differences in midpoint value, saturating shift values, and overall profiles, but all vary in different ways. The 50% matrix calibration for IL-1 β has a saturating shift of 920 pm higher, a baseline shift of 125 pm higher, and a midpoint 4.9 ng/mL higher than the 10% matrix. However, the profiles of the two curves are generally the same. The 50% matrix calibration for CCL2 has a saturating shift of 1136 pm higher, a baseline shift of 150 pm higher, and a midpoint 2.3 ng/mL higher than the 10% matrix. Additionally, the profiles of the curves are different. The 10% matrix has a steeper middle region of the curve, resulting in a higher sensitivity and more of a signal off/on assay reminiscent of CCL3. The 50% matrix is less steep, but provides a greater dynamic range, similar to IL-10. The IFN- γ calibration curves are almost identical in midpoint value (0.02 pg/mL difference), but the 50% plasma matrix had a higher baseline shift by 247 pm and a lower saturating shift by 1045 pm when compared to the 10% matrix. The profiles are slightly different, with the 10% matrix providing a greater detection range, but they are not as distinctly

different as the CCL2 curves. While these three targets demonstrated the greatest variation between 10% and 50% plasma matrices, they varied for different reasons. These targets would not be suitable for reducing the calibrations to one matrix due to the high variation in the fit parameters and the profiles.

These inter-matrix groupings overlap heavily with the calibration variation across chip batches (**Figure 7.2** and **Figure 7.3**) discussed in the previous subsection. The targets with the least variable x_0 values in inter- and intra-chip batch calibrations for both 50% and 10% matrices were IL-6, IL-8, CCL3, CCL8, and IP-10, all of which are classified as similar between the two matrices. Furthermore, the targets with the most variability in x_0 values for multi-chip batch calibrations were IL-1 β , IL-17, CCL2, CCL4, and IFN- γ , three of which (IL-1 β , CCL2, and IFN- γ) were classified as the most different between the two matrices. These overlaps support the individual results of each subsection, furthering the conclusion that variation results from the functional variation in the antibody sandwich pairs.

Most of the measured targets were highly similar in all parameter values and profiles or in some parameter values and fit profiles, indicating the excellent robustness of the assay. These targets could potentially rely on one matrix calibration curve for all sample dilutions. However, a few targets need further analysis or optimization to allow for this. Each calibration uses four sensor chips and four equivalents of detection reagents and each matrix in a study requires at least three calibrations to be completed for a full chip batch; therefore, reducing the number of calibration matrices required to analyze samples would be advantageous to save time, money, sensor chips, and reagents, if doing so would not compromise the accuracy and integrity of the assay.

7.4.2 Dilution analysis identifies 2 \times as the more important dilution for LTBI samples

Moving away from calibration curves, this section explores trends in post-sample processing. The human plasma samples for the LTBI project are analyzed using the standard multiplexed assay method and then converted to analyte concentrations based on calibration curves. As described in the “Dilution selection data analysis” section above, the in-house code uses the 50% plasma calibration to convert the net shifts in the 2× dilution to analyte concentration and the 10% plasma calibration to convert the net shifts in the 10× dilution to analyte concentration. The code calculates the distance the resulting analyte concentration is from the x_0 value of the respective curve, selects the closest dilution, and then adjusts the concentration for the dilution effect. One research direction initiated by this analysis process was to investigate what sample dilution tends to be selected and whether the sample type (QFT stimulation) or target tends to select a specific dilution. The implication of these results is to identify if one dilution should be prioritized if sample volumes provided are lower than required to analyze both dilutions or if just one dilution can be used to analyze all the samples in future LTBI projects, cutting costs and analysis time in half.

Alluvial diagrams are typically used to show the flow of data counts between bins, or nodes. The diagram in **Figure 7.5** centers the selected dilution between the LTBI stimulation sample type and the specific targets. The data used here originated from the patient samples I analyzed for the projects presented in **Chapter 5** and **Chapter 6**. The 87 patient sample sets included four samples per patient (NIL=negative stimulation, MIT= positive stimulation, TB1 and TB2 = TB specific peptide stimulations) and fourteen targets (IL-1 β , IL2, IL6, IL8, IL10, IL15, IL17, CCL2, CCL3, CCL4, CCL8, IP-10, IFN- γ and TNF- α) per sample. After removing any failed assays, the study resulted in 4,872 individual concentrations. Any net shifts that resulted in a zero concentration (n=459) were removed. The 10× dilution is arbitrarily selected

as the dilution placeholder for target net shifts below the baseline threshold and keeping them in the data set would artificially increase the number of times the 10× dilution was perceived to be selected.

The dilutions were selected relatively evenly (57% for 2× and 43% for 10×) with a slight preference towards the 2× dilution, validating that the dilutions we use for this project are appropriate for the targets of interest. If the split between 10× and 2× was highly different, we may have reconsidered the dilutions we use in sample analysis. All four stimulation conditions had a preference, albeit small, towards the 2× dilution, with 51.4% of MIT, 60.8% of NIL, 54.8% of TB1, and 61.3% of TB2 stimulation-associated pieces of data selecting the 2× dilution. The MIT and TB1 stimulations are more evenly split between dilutions in comparison to the NIL and TB2 stimulations. This intuitively makes sense for the NIL stimulation, as the media blank is expected not to cause high responses and some targets will be at lower concentrations, resulting in lower dilution (2×) preference.

The two most surprising findings are the MIT and TB2 splits. Opposite of the NIL condition reasoning, it was expected that the MIT, or positive stimulation control, would prefer the 10× dilution, as many of the targets would be higher in concentration. It may be that the target concentrations are high in both the 10× and 2× but are just closer to the midpoint of the 50% calibration than the 10% calibration. The finding that the TB2 stimulation relies more on the 2× dilution than the TB1 stimulation is interesting, given the discussion in Chapter 5 regarding the similarities in the TB1 and TB2 stimulation tubes. There may be target concentrations in the TB1 stimulation that lay close to the midpoint of one calibration, while the concentration in the TB2 stimulation lies close to both calibration midpoints. After account for dilution factors, this would lead to different dilution selections but still result in similar

concentrations. Overall, there is no major reliance on one dilution when looking at overall dilution selection or stimulation condition, but evidence suggests a slight preference towards the 2× dilution. If volume becomes a limitation in the LTBI samples, the 2× dilution should be completed before the 10× dilution.

Splitting the data between the nodes of selected dilution and target led to disparities. Over half of the targets (CCL3, CCL4, IL-1 β , IL-2, IL-10, IL-15, IL-17, IP-10, IFN- γ , and TNF- α) select the 2× dilution over 50% of the time. Specifically, targets CCL4, IL-10, IL-2, and TNF- α rely on the 2× dilution for over 70% of samples. This highly preferential 2× selection indicates that these targets are generally lower in concentration than the other targets. Three of the four remaining targets (CCL2, CCL8, and IL-6) select the 2× dilution 40-50% of the time, which is still close to an even split between the dilutions. The last target, IL-8, selects the 2× dilution only 12% of the time, a finding that led to the project discussed in **section 7.4.4**. The data splits at the target nodes suggest that since more targets preferentially select the 2× dilution, and only one target is highly preferential to the 10× dilution, the 2× dilution should be prioritized over the 10× dilution if needed. Taken together, the data from all LTBI subjects plotted using an alluvial diagram suggests that while both dilutions are used relatively evenly, the 2× dilution is preferentially selected more of the time in all stimulation conditions and most targets and should be prioritized if sample volume does not warrant analyzing both dilutions.

7.4.3 Intra-batch, long-term assay stability study

A longitudinal study was planned and started with a goal to acquire data pertaining to stability of the sensor chips spotted with capture antibodies. The study was started using the November 2023 sensor chip batch and, to date, four time points have been completed: one upon sensor batch receipt, and three spanning almost three months post receipt. The same cocktail of

standard proteins was run in both channels on each chip and the average net shift across both channels was taken as the net shift of the target for each deck. The average net shifts of the six targets and Ms IgG controls were plotted for each of the four chip decks within this sensor chip batch over four time points (**Figure 7.6**).

There is some variation across the time points, but there is no definitive fall-off over the first three months in any target or chip deck. The net shifts are most similar within time points than within decks. However, within the decks the time point one net shift and time point four net shifts are highly similar with overlapping standard deviations across almost all targets. The least variable targets showing the most consistent shift across decks, within decks, and across time are IL-2, IL-6, and IL-8. IL-15 has little intra-deck variation in decks one and two, but more variation in decks three and four. The deck dependency could be related to the time the chips are waiting for spotting, as the chips within a deck are spotted closer together than those in other decks. CCL4 has slight variability between time points, with time point four having a slightly higher average across all decks. A time point dependent difference across all decks, but only for one target, is likely due to reagent preparation. If all targets demonstrated a related difference, it may be more apt that it's related to deck or stability. However, time point four is only different in this way for CCL4 and, in addition, the net shift is still within standard deviations of various other time points. The next tested time point will reflect if the time four data is sustained.

IFN- γ is the most interesting, in that there is a consistent decrease in shift across all decks starting at time point three, and not rebounding or further decreasing at time point four but staying consistent. However, IFN- γ net shift is very consistent between deck within each time point. Finally, the control rings show the greatest variability. It is known that IFN- γ protein exhibits non-specific binding when analyzed in buffer, rather than serum or plasma. Decks three

and four are very consistent in control ring response. However, decks one and two are variable, with high up ticks being sustained in deck one. One reason for highest variability in deck one is that the deck one chip has been the first to be analyzed immediately after reagent preparation for all time points. The reagents for all four chips are made simultaneously and the mixture may be more homogenous after sitting. Future changes to test this and potentially mitigate the high variation in deck one is to let the protein standard sit for an hour before analysis. A second reason for this high variability is that the spotting of chip deck one is different than chip deck four, such as it may be the first or last to be spotted. It is clear in the target-specific spotted rings that there is little effect across decks, within time points. To note, chips from deck one and deck two were the chips used to analyze some latent tuberculosis project samples in early 2024 and controls were not consistently decreased to the levels seen in this study. This could point to the high net shifts being due to the absence of biologic matrix, as in plasma samples they are more stable.

The data from the first four data points in this sensor chip batch stability study show the antibodies spotted on these sensors are generally stable for at least three months from receipt. Traditionally, we have aimed to use spotted chips within six months of receipt but have no data from these antibodies to support this timeline. Testing the same assay for the next six to nine months in one-month intervals will provide data supporting the anecdotal timeframe and possibly data supporting lengthening or shortening the usable range. The compiled data will be analyzed for variation within and across chip decks and time points. Along with chip use timelines, the data will allow us to better understand when in the lifetime of chip batches calibrations should be ran to account for slight signal drop-off, how antibody stability is similar or different target-to-target, and the ideal number of chips we should be ordering in chip batches moving forward.

7.4.4 Alternate assays for IL-8 can shift the curve, but at the cost of the detection range

Analysis of dilution selection in **section 7.4.2** revealed that target IL-8 selects the 10× dilution in 88% of the samples. Furthermore, 56% of the pieces of data noted as being above the upper bound of the calibration curve are from IL-8 alone. This means that the concentration of IL-8 in the samples we are analyzing is very high. Ideally, the concentration needs to be adjusted to be closer to the midpoint of the calibration curve rather than in the saturating region. To meet this goal, either the sample needs to be further diluted or the assay needs to be adjusted to capture a higher analyte concentration. The former solution is not amenable to the current workflow, as a third dilution would need to be analyzed, increasing cost, time, and required volume from each patient sample. Therefore, we set out to optimize the IL-8 assay to capture a higher concentration.

Detecting a higher concentration of analyte is the opposite of what most assay optimization aims to do. The ideal assay in this scenario would shift the IL-8 calibration to the right, as visualized in **Figure 7.7**. The midpoint x_0 value would shift to a higher analyte concentration while keeping the same saturating and baseline shift values. This would allow the assay to measure higher concentrations more accurately without compromising its dynamic range.

This section covers four different assay methods that aimed to shift the IL-8 calibration curve while maintaining the dynamic range. The current biocatalytic precipitation-based assay method using 4CN sequentially flows analyte, Bt-Ab, SA-HRP, and 4CN across capture antibodies specific to the analyte of interest, as depicted in **Figure 7.8A**. Two assay methods modified the IL-8 specific reagents in the current assay design, making them easy to integrate in a multiplexed panel. The first used a non-biotinylated tracer Ab (non-Bt-Ab) to block some of

the binding sites of the Bt-Ab (**Figure 7.8B**). The second diluted the concentration of IL-8 capture antibodies on the chip, keeping the assay steps the same as the current method (**Figure 7.8C**). The other two assay methods modified the assay steps, with one replacing SA-HRP and 4CN with SA-coated magnetic beads (**Figure 7.8D**) and one replacing the Bt-Ab and SA-HRP with HRP directly conjugated to IL-8 tracer Ab (**Figure 7.8E**). In this section, the results and challenges of each method are discussed.

7.4.4.1 Mixing in non-Bt-Ab with Bt-Ab shifted the midpoint of the curve but truncated the dynamic region.

One modified assay method tested was using a non-Bt-Ab for IL-8 (**Figure 7.8B**). The hypothesis was that the non-Bt-Ab would occupy the binding site on the IL-8 protein and prevent the Bt-Ab from binding, effectively reducing the signal at the same analyte concentration. The fewer biotinylated sandwich assays localized to the surface would decrease the precipitation of 4CN, reducing the amount of precipitate covering other sandwich motifs, allowing more biocatalytic turnover, and facilitating higher concentrations being detected. A similar method for adjusting the calibration curve of a proximity-based ligation assay called this type of scheme ‘epitope depletion’ and was used in conjunction with a second tuning method, ‘probe loading’, to quantitate target proteins at physiologic concentrations spanning multiple orders of magnitude.¹⁵

First, to ensure the non-Bt-Ab was working as expected, an assay with the current saturating protein concentration for IL-8 of 50 ng/mL was completed with the standard method of 2 µg/mL Bt-Ab (**Figure 7.9A**) and with the same concentration of non-Bt-Ab (**Figure 7.9B**). The binding traces in the figures show that both tracers bind the protein (~17 minutes into the assay) but the subsequent SA-HRP reagent only binds the Bt-Ab (~30 minutes into the assay). The assay with Bt-Ab continued to a saturating net shift (8400 ± 200 pm) for the IL-8 spotted

rings, and the assay with non-Bt-Ab continued to produce a response negligible from the Ms IgG control spotted rings (60 ± 10 pm), as displayed in the first two bars of **Figure 7.9C**. These results validated that the non-Bt-Ab was still binding the IL-8 protein but did not result in a significant net shift after the completion of all assay steps.

Varying combinations of Bt-Ab and non-Bt-Ab were tested in the full assay format to detect 50 ng/mL of IL-8 protein (**Figure 7.9C**). The net shift did not substantially decrease (7500 ± 300 pm) compared to the standard assay when both Abs were mixed at 1 μ g/mL, likely due to the overcompensation in typical Bt-Ab concentration. A 4-fold decrease to 250 ng/mL Bt-Ab did not substantially decrease the net shift (6880 ± 80 pm). A 40-fold decrease of Bt-Ab to 25 ng/mL with 2 μ g/mL of non-Bt-Ab led to a drop off in the signal (3000 ± 300 pm) produced by the 50 ng/mL of IL-8 standard. However, when the non-Bt-Ab was removed, the shift produced by the assay with 25 ng/mL Bt-Ab alone increased back to 6800 ± 200 pm, highlighting both that the high running concentrations we typically use could be decreased if needed and that the non-bt-Ab needs to be present for the signal to decrease. Together, these preliminary experiments to detect 50 ng/mL IL-8 protein narrowed down the range of Bt-Ab concentrations that should be tested at higher IL-8 standard concentrations to between 25 and 250 ng/mL. Furthermore, the net shifts at 25 ng/mL Bt-Ab with and without the non-Bt-Ab present indicate that the two antibodies compete for protein binding sites, and the non-Bt-Ab prevents the Bt-Ab from binding to the target analyte. This illustrates the importance of including the non-Bt-Ab at a higher concentration than the Bt-Ab to successfully decrease the resulting net shift instead of simply diluting out the Bt-Ab alone.

The assay with varying concentrations of Bt-Ab and non-Bt-Ab at 2 μ g/mL was completed at an increased concentration of IL-8 protein standard, 300 ng/mL (**Figure 7.9D**). As

expected, decreasing the Bt-Ab content decreased the resulting net shift. The 25 ng/mL Bt-Ab condition reached a net shift of approximately 3600 ± 200 pm, just 600 pm higher than the shift resulting from 50 ng/mL of IL-8 standard protein. This difference in shift is lower than desired for a six-fold change in protein standard concentration. Therefore, concentrations of Bt-Ab above 25 ng/mL but below 250 ng/mL were analyzed in a full calibration curve to understand directly if the curve could be shifted to the right.

Three concentrations of Bt-Ab mixed with 2 μ g/mL of non-Bt-Ab were used as the tracer step in an eight-point calibration curve that ranged from 19 pg/mL to 300 ng/mL of IL-8 protein (**Figure 7.9E**). The decrease of Bt-Ab content with non-Bt-Ab present successfully shifted the midpoint, x_0 , value to higher concentrations. However, the dynamic range and assay sensitivity suffer just as systematically. As higher concentrations of Bt-Ab were tested, the curve transitioned back to the original 2 μ g/mL Bt-Ab curve. To note, the 200 ng/mL and 100 ng/mL Bt-Ab calibration curves are flipped in expected order for midpoint value and profile, and the 100 ng/mL calibration resulted in a higher baseline shift than the other conditions. Additional replications would need to be completed to understand if this was due to user variation or if there is an underlying cause for this switch at these concentrations.

The non-Bt-Ab method was validated using the assay trace profiles and the importance of adding the non-Bt-Ab counterpart to a diluted concentration of Bt-Ab was highlighted in net shift results. The modified assay successfully shifted the x_0 value of the calibration curve to the right. However, due to the truncation in dynamic range and sensitivity, this assay method was deemed unusable for further optimization and use with patient samples. We next moved to the other IL-8 specific component in the standard assay design: the capture antibody.

7.4.4.2 Diluting the capture antibody did not change the net shift for higher concentrations of IL-8 protein.

The capture antibodies on the surface of the sensor chip are one of the two target-specific components of the assays; therefore, modifying their concentration would not affect other targets in a multiplexed assay (**Figure 7.8C**). The standard spotting concentration of each capture antibody is 0.25 mg/mL, or 250 µg/mL, with 10% glycerol in 1X PBS. Similar to the non-Bt-Ab method hypothesis, we hypothesized that lower concentrations of IL-8 capture Ab would result in less biocatalytic precipitation for a given standard concentration, reducing precipitate coverage of the remaining sandwich motifs, allowing for detection of higher concentrations. Intuitively, we hypothesized that as capture Ab concentration decreased, the signal would follow. **Figure 7.10A** shows that the lower spotting concentrations of 10 and 2.5 µg/mL result in a significant drop off in signal.

A complication when diluting the capture Ab was decreased steric hindrance, a similar issue encountered with the dilution of Bt-Ab. In the tracer experiments, this was countered with non-Bt-Ab to increase hindrance and prevent the Bt-Ab from binding to the protein. In the capture dilution experiments, lower steric hindrance increases the possibility for the capture antibody to simultaneously bind to the multiple BS3 linker motifs. Tethering the Ab in multiple sites increases the chances of obscuring the pertinent binding sites on the Ab. To increase the steric hindrance, mouse IgG Ab were mixed with diluted IL-8 capture Ab at a constant concentration of 250 µg/mL. At the normal Ab spotting concentration (250 µg/mL), the addition of IgG did not result in a different shift; however, at diluted IL-8 capture Ab concentrations, the mixtures containing IgG increased the net shift in comparison to no IgG (**Figure 7.10A**) when detecting 50 ng/mL of IL-8 standard protein. The data here indicate that including an exogenous

control capture Ab in the spotting solution increases the number of IL-8 capture antibodies tethered to the microring surface in the correct orientation to detect the IL-8 standard.

The optimal concentration of capture Ab that reduced the signal at 50 ng/mL IL-8 protein was determined by spotting multiple dilutions of capture Ab mixed with 250 μ g/mL IgG Ab on a chip and running a standard assay over the captures. In **Figure 7.10B**, the resulting signal for 50 ng/mL protein standard decreased, as expected, with decreased capture Ab. However, the results in **Figure 7.10C** reveal that the net shifts do not significantly fluctuate with increasing concentrations of IL-8 protein across any capture condition. Similar to the non-Bt-Ab method, the assay still saturates around 50 ng/mL protein and would not be a viable method for shifting the IL-8 calibration curve while retaining the dynamic region.

These two assay methods made changes centered on the idea that the 4CN precipitation coats the sandwich motifs before all HRP molecules can be converted. By reducing the total number of analytes binding (capture dilution) or the number of sandwich motifs made (non-Bt-Ab), the 4CN precipitation would not reach saturation until higher analyte concentrations. Eliciting these theories did not solve the challenges in the way we intended, which would have allowed us to integrate these changes into the existing multiplexed assay easily. To continue the work towards shifting the IL-8 calibration curve, we shifted focus to implementing assays with similar steps but different reagents. This could present complications when trying to integrate into the current multiplexed assay, but there were avenues for each explored method to work for IL-8 without compromising the other targets.

7.4.4.3 Implementing a bead-based assay to detect IL-8 standard did not increase the detection range and introduced additional steps to the current workflow.

Streptavidin-coated beads (SA-beads) were previously used as the amplification reagent in early versions of immunoassays using the microring resonators.³⁴ Using the previously applied procedure as a starting point, we employed the SA-bead assay to detect IL-8 (**Figure 7.8D**). The steps to form the sandwich motif were identical to the standard assay. However, instead of SA-HRP and 4CN reagents deployed to tag the sandwich motif and amplify the signal, SA-beads served both functions. These reagents have size differences: streptavidin is ~60 kDa and HRP is ~44 kDa, with diameters in a low nanometer scale. The beads themselves were 100 nm and coated with ~60 kDa streptavidin. We hypothesized that the size of the bead would act as the lone amplification reagent, eliminating the coverage of sandwich motifs by 4CN precipitation and allowing for higher analyte concentrations to be detected.

The bead-based assay required preparation of the beads before running the assay, which increased the preparation time at the start of each experiment. The beads needed to be washed to remove unbound SA, and the final concentration was determined using absorbance at 286 nm and a fresh calibration curve (**Figure 7.11A**). The washing procedure included three buffer exchanges and centrifugation steps in the recommended buffer of 1X PBS with 0.05% Tween-20 (PBST). The washing step resulted in different bead loss each time, ranging from 0% to 30% loss in expected concentration. The variation in the washing method, the requirement to wash the beads each day, and the reconstruction of the calibration curve for each wash would not be ideal for implementing this method into the existing clinical sample workflow, but the detection of IL-8 using this method was still tested.

The trace of the assay blank and the assay to detect 50 ng/mL IL-8 protein are presented in **Figure 7.11B** and **C**, respectively. The decrease in resonant wavelength at the 30-minute mark corresponds to the introduction of the bead solution. The beads were diluted half-fold from their post-wash concentration into the running buffer of PBS-BSA, meaning that half of the buffer introduced at the 30-minute mark contained tween-20. The method was reattempted after substituting all the running buffer steps with PBST, but the removal of BSA led to a steady decrease in the baseline signal throughout the assay, as BSA was not present to continue blocking the microring surface. The method was also attempted in a complex matrix of 10% serum acting as the blocking agent. The negative control rings improved, but the IL-8 capture spotted rings significantly increased to a net shift of 500 ± 100 pm in the blank (no protein standard) experiment. The assay successfully detects 50 ng/mL of IL-8 protein with a net shift of 970 ± 90 pm; however, similar to previous methods, introducing higher IL-8 protein concentrations did not increase the final net shift (**Figure 7.11D**).

The preparation required for the beads, the negative shift in the negative control rings, no increase in net shift with increasing IL-8 standard concentrations, and signal increase in a 10% serum blank experiment together did not make this a viable method to shift the curve or to integrate into the existing workflow. Moving forward, a final method change was attempted that would more readily integrate into the existing workflow.

7.4.4.4 HRP-conjugated IL-8 Abs combines two assay steps into one and shifts the curve, but still truncates the dynamic range.

Exploring alternate assay methods led to the discovery of sandwich assay method that directly conjugates the HRP enzyme to the detection antibody, eliminating the biotin-streptavidin interaction step.³⁶ Translating the assay method to our existing setup would be simple, as the IL-

8 HRP conjugated tracer Ab (HRP-Ab) could be mixed with the other target's Bt-Ab. The SA-HRP step would occur for the other targets but would not affect the IL-8 target sandwich. The 4CN would then turn over the HRP on all targets and the amplification would occur as usual (**Figure 7.8E**). The hypothesis was that fewer HRP molecules (44 kDa) than biotin molecules (0.2 kDa) on each tracer Ab would lead to fewer HRP enzymes localized to the surface, again decreasing the amount of coverage by 4CN precipitation product, allowing for higher concentrations to be analyzed.

The preparation for the HRP-Ab assay only required HRP conjugation to the tracer Ab using a commercialized kit and protocol, similar to biotin conjugation. The assay using 2 $\mu\text{g/mL}$ HRP-Ab was conducted at various concentrations of IL-8 protein standard, just as had been done with the previous assays (**Figure 7.12A**). However, after 50 ng/mL of IL-8 protein, the shift did not increase. An eight-point calibration curve from 3.2 pg/mL to 50 ng/mL IL-8 protein showed the assay method was successful at shifting the x_0 value of the calibration curve but truncated the more sensitive region of the curve (**Figure 7.12B**), like many of the other tested assays.

Many of the tested assay methods successfully shifted the x_0 value of the calibration curve to higher concentrations of IL-8 standard. This 'worse' assay would allow for higher concentrations of IL-8 protein that are found in the LTBI samples to be more accurately measured. However, the shift in the midpoint came with the truncation of the dynamic, and most sensitive, range, potentially increasing the number of samples over the saturation limit even with the shift. In addition, different capture and tracer antibodies and catalytic amplification reagents were tested but did not provide evidence of reaching the goal. None of the tested assays were selected to pursue for further use with patient samples. An assay method that can be tested in the future is inspired by Schulte et al. and is amplification by hybridization chain reaction, which

uses an initiator linked tracer antibody that triggers self-assembly of a labeled polymer and is followed by binding of anti-label reporter antibody.³⁷ The polymerization may be enough amplification for the assay, but the anti-label antibodies can be employed to improve signal. A second assay method that could be tested is inspired by Hou et al. and is amplification using tyramine-HRP repeats, followed by the current biocatalytic precipitation.³⁸ This takes advantage of the current amplification step but may shift the calibration due to steric bulk. In the meantime, the standard assay has proven to be very well optimized for detecting protein targets.

7.5 Limitations and Future Directions

The analysis of calibrations, plasma matrices, and dilution selection described in this chapter is intended to document observed patterns in the LTBI project. These were not formal studies and would benefit from more calibrations of future chip batches. The variation described is mainly between two chip batches (February 2022 and July 2022) and just one calibration with the latest chip batch that had noted logistical differences in the spotting process. More full chip batch calibrations are needed to make more formal ranges for each target's x_0 value, saturation value, and baseline value. It would be interesting to further characterize the calibrations within chip batches and set acceptable reference ranges for both inter- and intra-chip batch calibrations. Additionally, analyzing the 10% and 50% plasma calibrations within each target for more than the July 2022 chip batch presented here would allow for more decisive conclusions on target-specific variation.

The limitation of the IL-8 shifting experiments was that none of the tested methods sufficiently shifted the sensitive region while maintaining the dynamic range. Most of the methods relied on the hypothesis that the limiting factor was 4CN precipitate saturating the signal. By reducing the amount of 4CN that could precipitate at a set concentration, there would

be less 4CN coverage, allowing for higher concentrations to increase 4CN turnover. If this were the case, higher concentrations would have led to a higher signal, keeping the saturating signal around 7000 pm but increasing the concentration at which that occurs. Future directions for the IL-8 shifting project include trying other amplification reagents, such as TMB substrate, rather than 4CN, and testing more abstract assay methods, such as adapting a silver nanoparticle, non-enzyme aggregation method or using a polymerization scheme to amplify the signal for IL-8.^{37,39,40} However, the current method for IL-8 is still relevant to our studies and can continue to be used successfully if no alternate assay method can be identified.

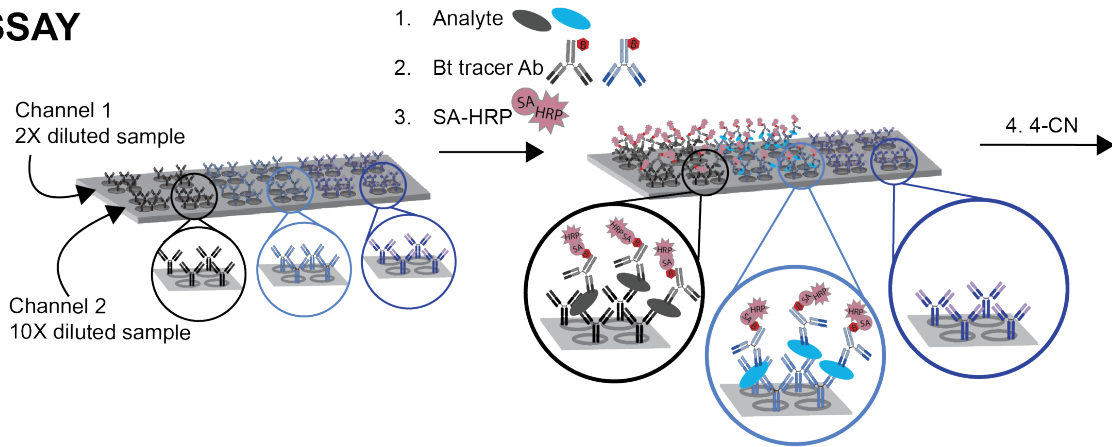
7.6 Conclusion

The analysis of these pieces of data collected as part of more extensive studies has provided insight into what can be deemed as ‘regular’ variation for each target. Passing on this information will help future students have a starting point for evaluating each new chip batch. Within the calibration comparisons and dilution selection data, there are smaller conclusions regarding how some targets are more robust, while some are more variable, that the 50% plasma calibrations have higher variability in x_0 value than the 10% plasma calibrations, and that there is a slight preference towards the 2× dilution in all stimulation conditions and in most targets. However, the large conclusion that stems from all this analysis is that the assay method we currently use as our gold standard and the workflow for sample analysis was very well optimized by the prior project team members. My work here shows that the foundations laid on these projects can stand the test of time and generations of graduate students conducting the work. I am the first to document the data this way, as my time on the LTBI project was the first to use multiple chip batches, necessitating understanding how different the chip batches could be. By implementing the analysis of calibration comparisons and stability studies, I have further

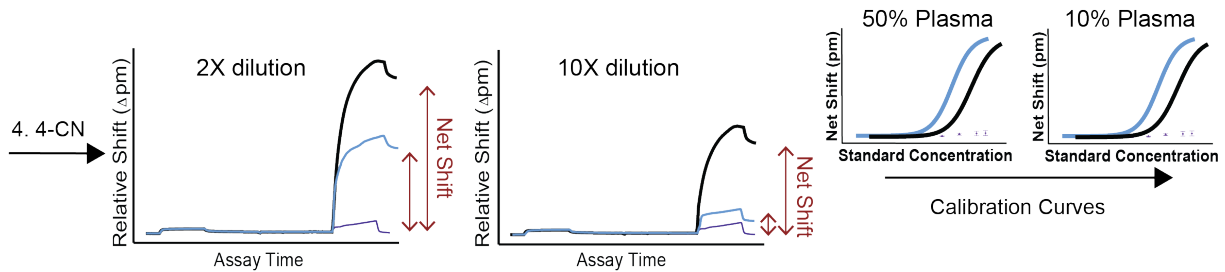
improved the workflow to better identify when targets or chip batches are faulty. While we were unsuccessful in developing a better (or 'worse') assay for IL-8, it highlights the robust design of the current biocatalytic precipitation assay we employ. Overall, this work aims to provide documentation of various analytical considerations and patterns that should be taken and compared for future chip batches and sample results within the Bailey Lab.

7.7 Figures

A. ASSAY



B. RESULTS



C. DATA WORK-UP

Calibration Curves	Target	Dilution	Concentration		Target	Dilution	Concentration	Adjusted Conc.	
→	Grey	2X	1000	→	Grey	10X	280	2800	→ Analysis
	Grey	10X	280						
	Blue	2X	500						
	Blue	10X	80						

Figure 7.1 Diagram of a data collection workflow relevant to LTBI sample processing. The assay is conducted on a functionalized, multiplexed chip (A) that contains target-specific capture antibodies (blue and black) and mouse IgG negative antibody spotted negative control rings (purple). Each assay step happens in succession using all automated microfluidics. The negative control rings are spotted with Mouse IgG antibodies. Each sample is analyzed at two dilutions (2× and 10×), resulting in two measurements of each target (B) per sample. The net shifts are converted to analyte concentration in a sample using the respective calibration curves for each target and dilution (C). Reduction of the data to one concentration associated with each analyte occurs by selecting the dilution that results in a concentration with the lowest distance from the mid-point of the calibration curve. This constitutes the final data set for further analysis.

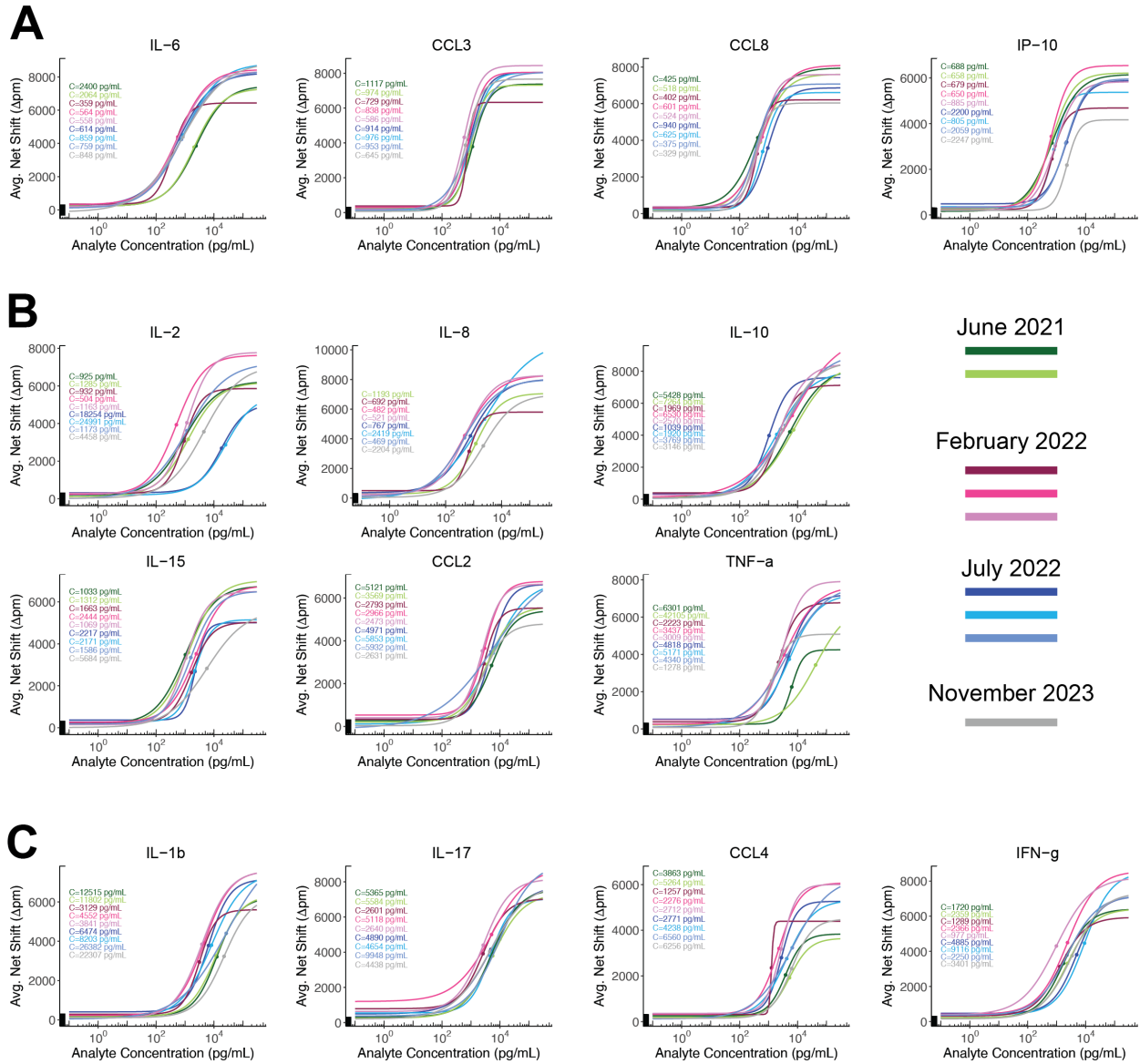


Figure 7.2 Variation in the 10% plasma calibration between sensor chip decks. The individual calibrations were overlaid and color-matched to calibrations conducted on the same chip deck to visualize both variations between chip decks and variations over time within a single chip deck. Targets IL-6, CCL2, CCL3, and CCL8 have the lowest variability between chip decks (A), targets IL-2, IL-8, IL-10, IL-15, CCL2, and TNF- α have some variation between chip decks (B), and targets IL-1 β , IL-17, CCL4, and IFN- γ have the greatest variation between chip decks.

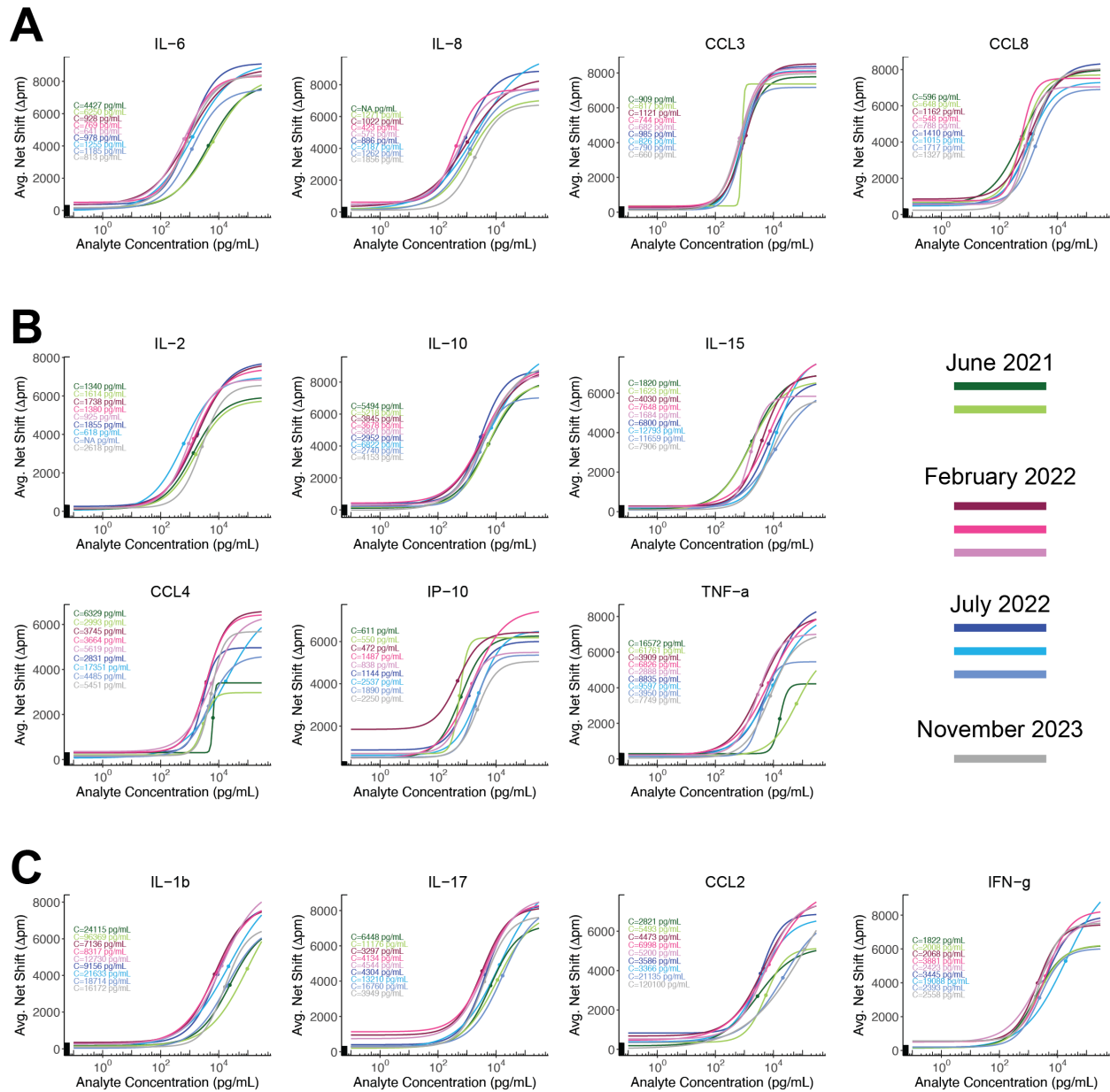


Figure 7.3 Variation in the 50% plasma calibration between sensor chip decks. The individual calibrations were overlaid and color-matched to calibrations conducted on the same chip deck to visualize both variations between chip decks (A), targets IL-2, IL-10, IL-15, CCL4, IP-10, and TNF- α have some variation between chip decks (B), and targets IL-1 β , IL-17, CCL2, and IFN- γ have the greatest variation between chip decks.

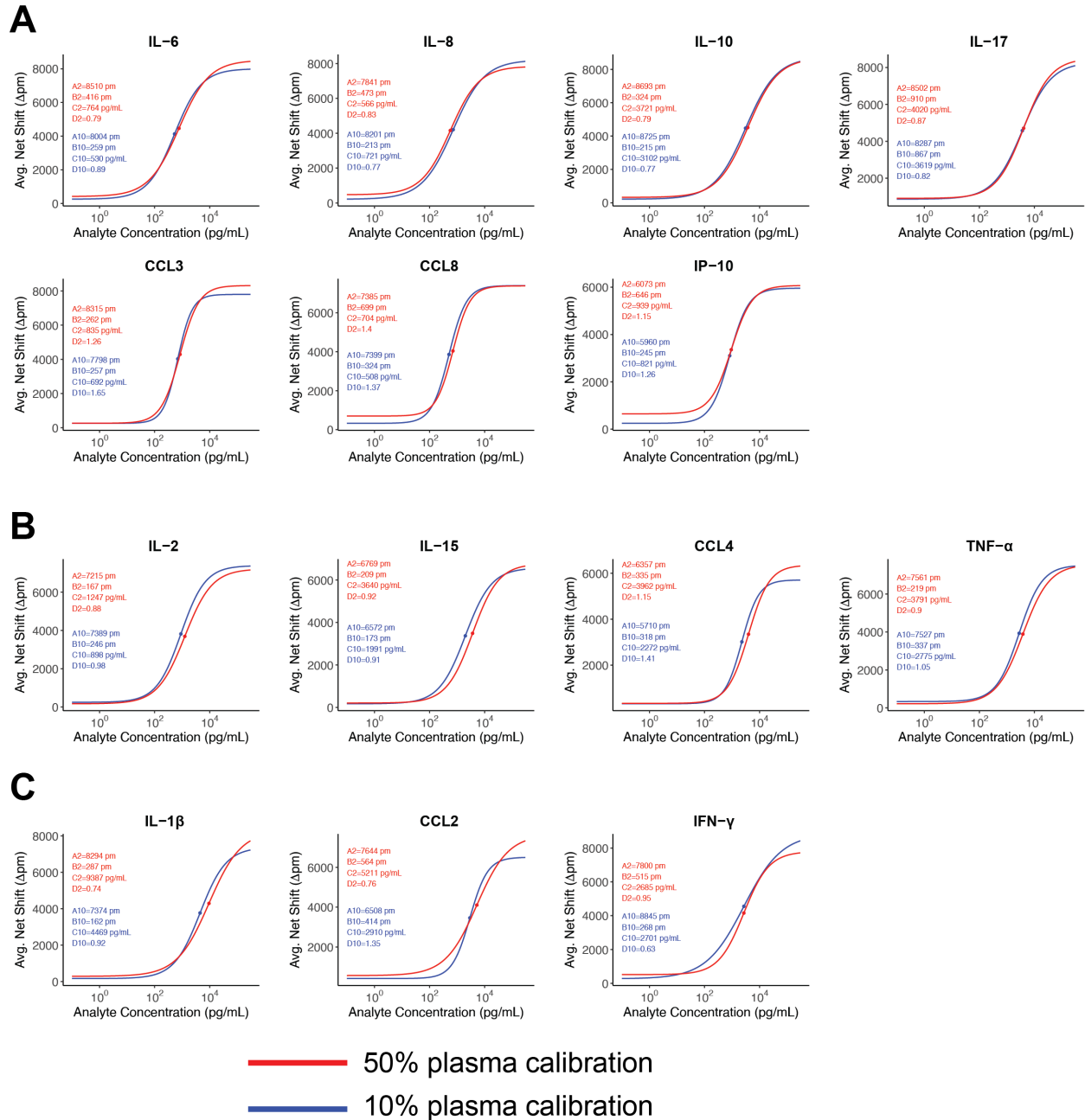


Figure 7.4 Comparing calibrations for both matrix calibrations. The variation between dilutions can be assessed per target using the average calibrations from the July 2022 chip deck. Targets IL-6, IL-8, IL-10, IL-17, CCL3, CCL8, and IP-10 (A) are similar in midpoint value between the two dilutions. Targets IL-2, IL-15, CCL4, and TNF-α (B) are similar in profile but the 50% calibration is slightly shifted to the right. Targets IL-1β, CCL2, and IFN-γ (C) have the most difference in midpoint and profile between matrix calibrations.

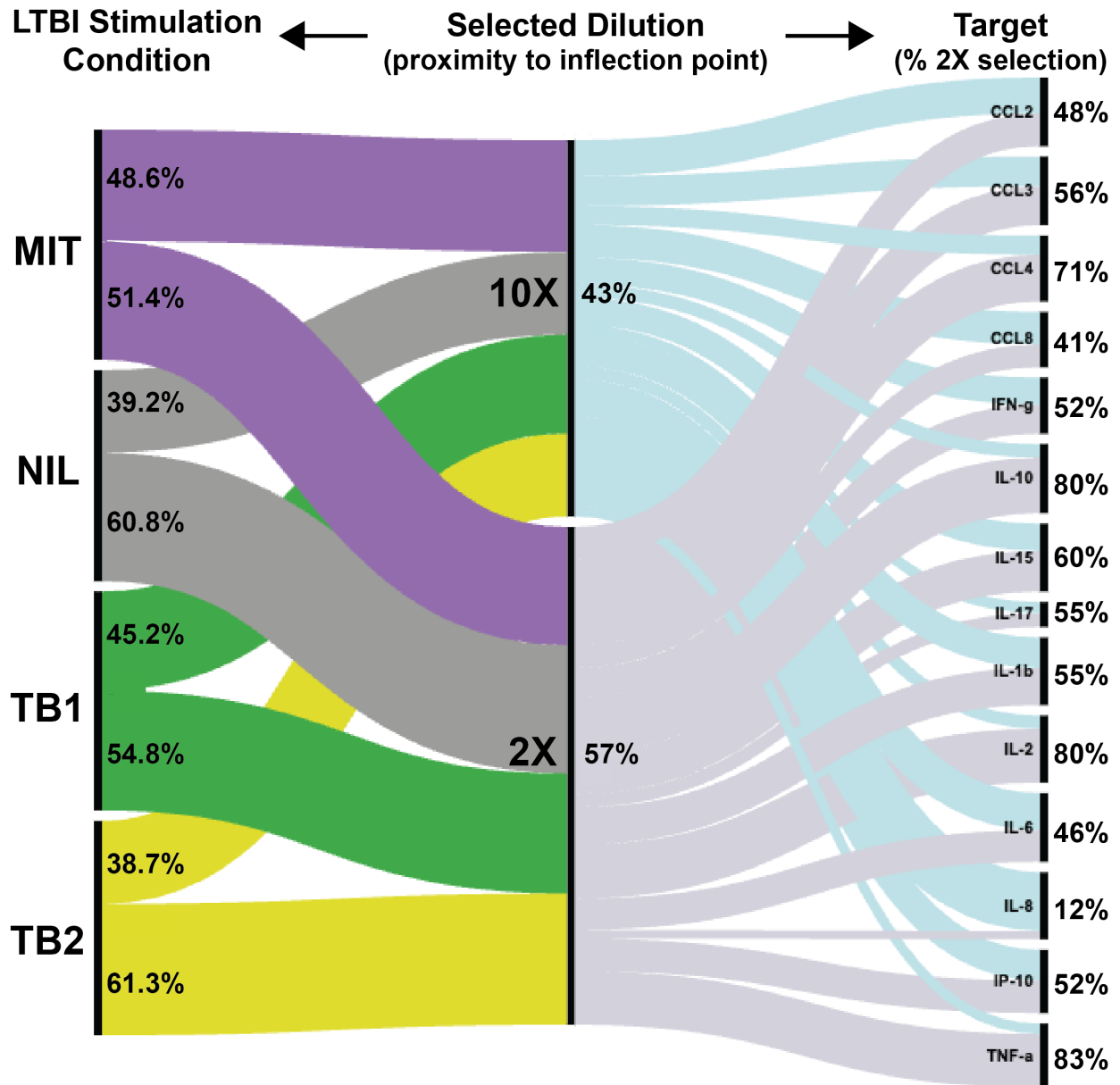


Figure 7.5 Alluvial diagram to visualize dilution selection across the LTBI patient sample set. This type of flow diagram is used to visualize changes in group composition between various states. From the center, the data flows from selected dilution to QuantiFERON stimulation on the left and to individual targets on the right. The height of the stripes indicates of number of samples connecting two nodes.

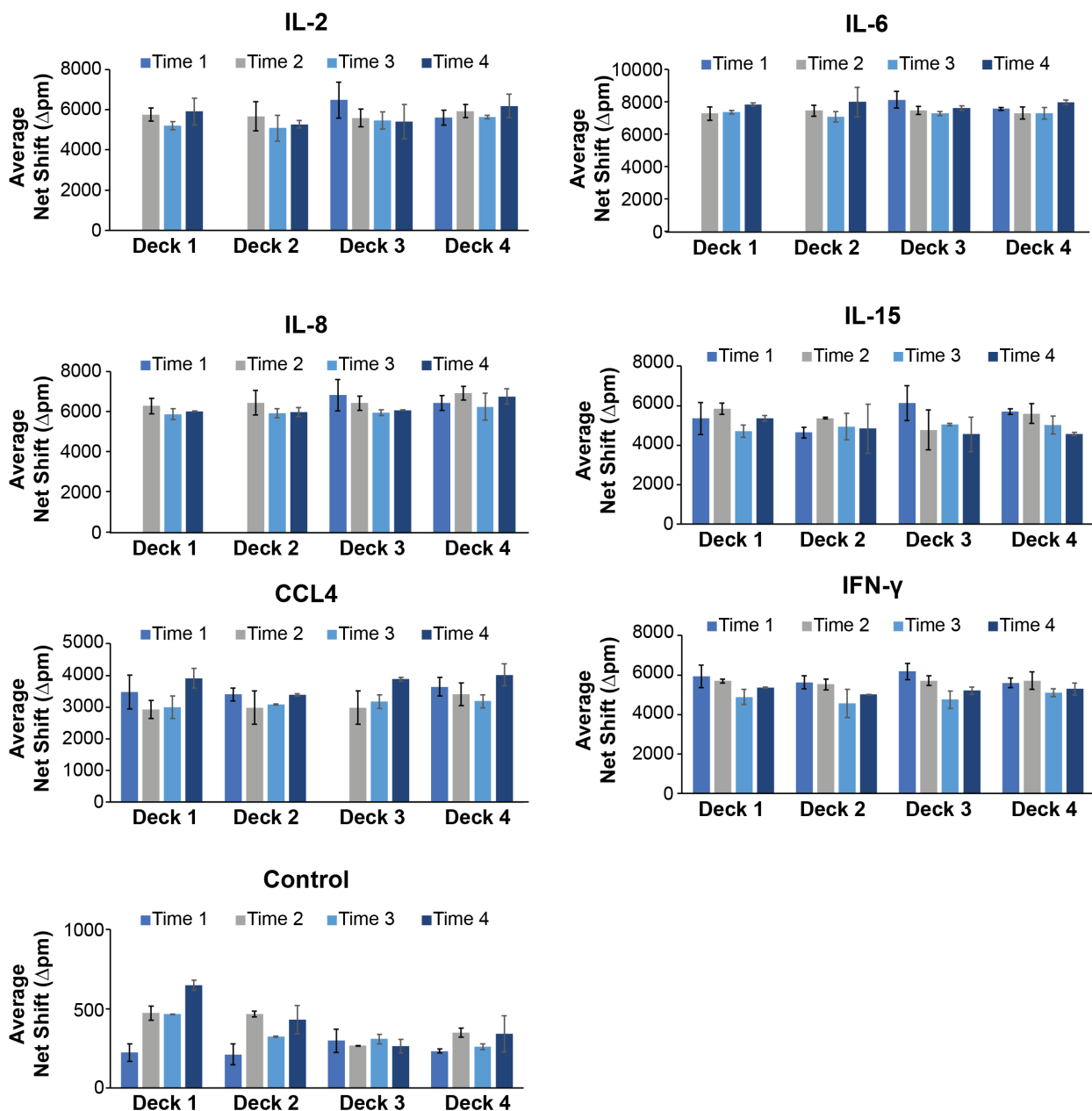


Figure 7.6 Intra-chip batch stability. Six targets ranging spatially across the chip were selected and analyzed at 10 ng/mL through three months post receipt. Time one was the day the chips were received from Genalyte, Inc. Time two was three weeks after receipt, time three was one month after time two and time three was one month later. The different deck numbers refer the box number (1-4) that the chips were housed in, as four decks contained ~115 chips each. If a target was not measured at a time point, it was left blank.

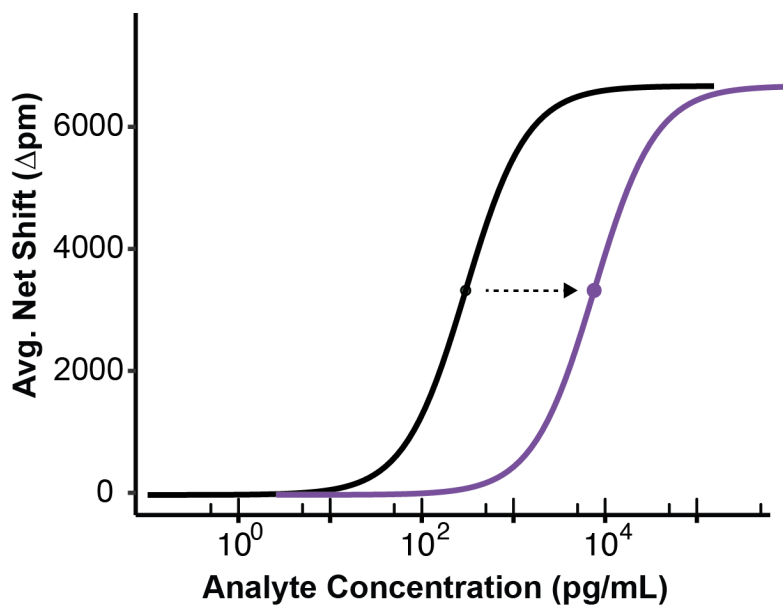


Figure 7.7 Example of shifted calibration curve. The ideal shift (purple) would increase the concentration at which the midpoint of the original calibration curve (black) lies while not compromising the dynamic range.

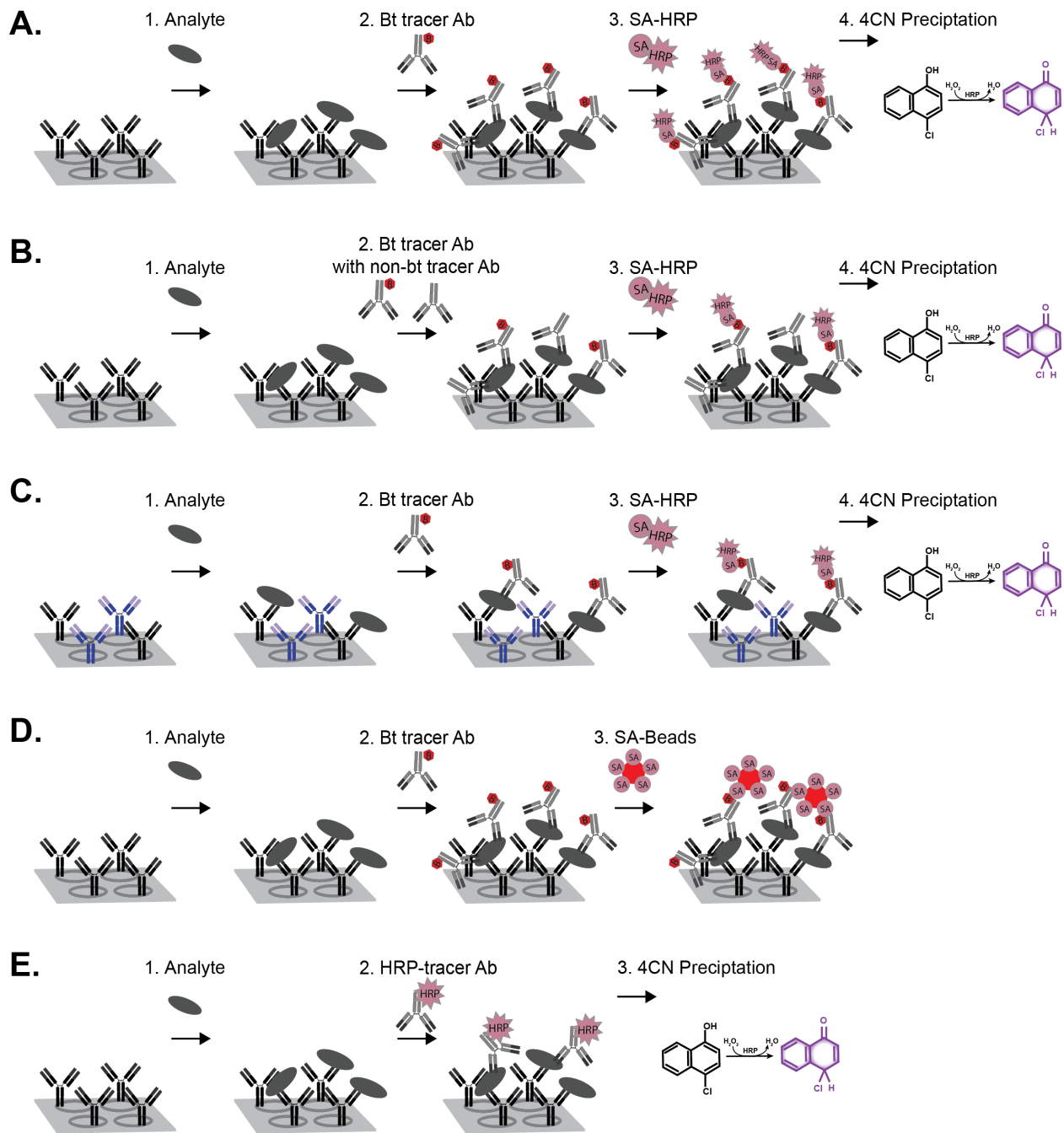


Figure 7.8 Diagrams of different assay designs tested to shift the IL-8 calibration curve. The standard method (A) includes analyte introduction, biotinylated tracer antibody, streptavidin horse radish peroxidase (SA-HRP), and the 4CN amplification step. The non-biotinylated tracer assay (B) includes the same steps, but the concentration of biotinylated tracer is decreased and supplemented with non-biotinylated tracer. The diluted capture assay (C) again uses the same steps as the standard method, but the capture antibody is spotted at a lower concentration and supplemented with mouse IgG control antibodies. The SA bead assay (D) includes analyte introduction and biotinylated tracer antibody, followed by SA-coated beads as both the recognition and amplification step, eliminating SA-HRP and 4CN steps. Finally, the HRP-conjugated tracer assay (E) includes analyte introduction, followed by an HRP-conjugated tracer, and ends with the 4CN amplification.

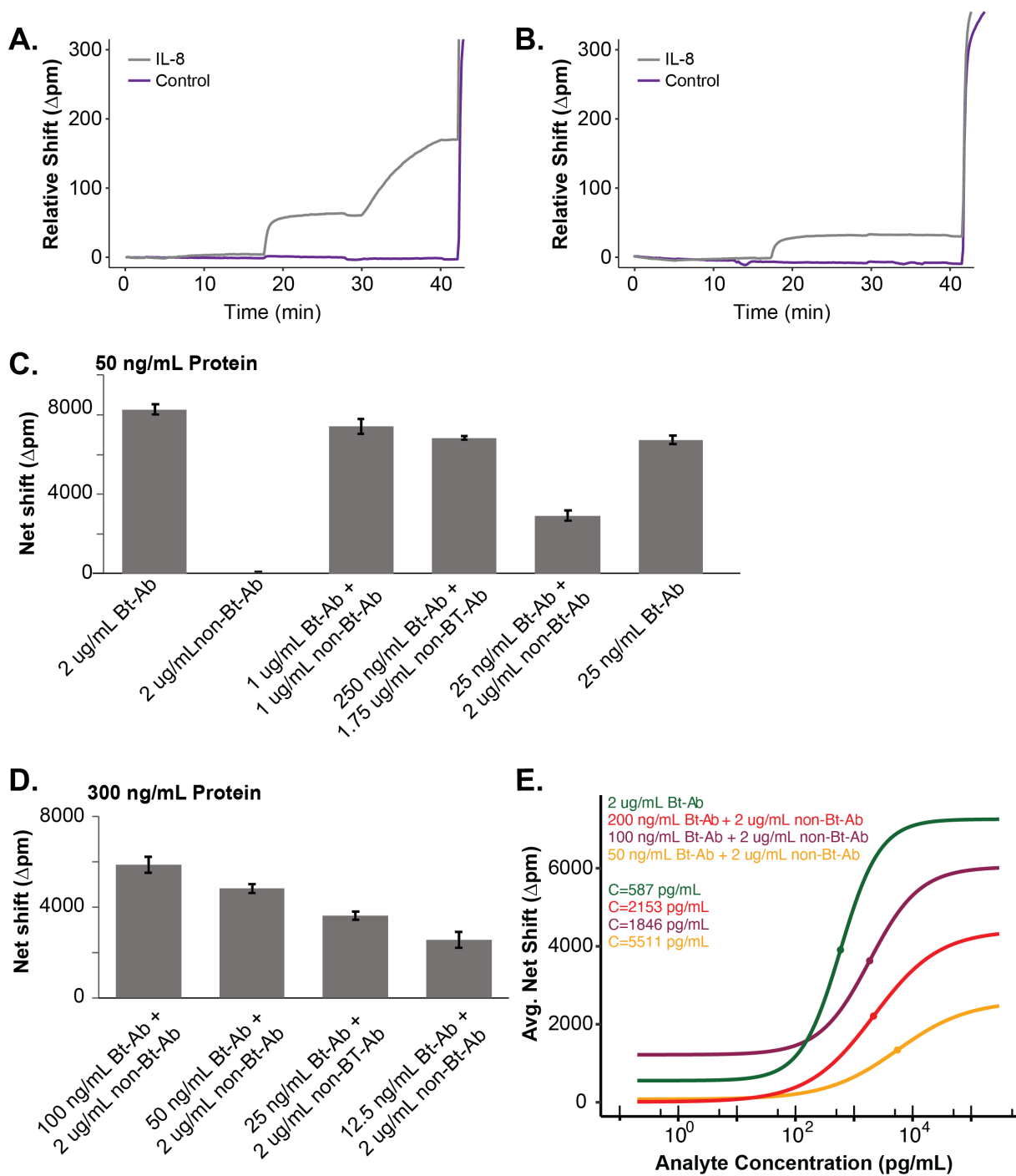


Figure 7.9 Shifting IL-8 calibration using the non-biotinylated tracer assay design. The zoomed-in trace of the assay to detect 50 ng/mL of IL-8 standard protein with only biotinylated tracer Ab (A) and only non-biotinylated tracer Ab (B) highlights the differences between the same assay completed with the two tracer antibodies. The net shifts of the assay to detect 50 ng/mL of standard protein are plotted (C) to showcase changes when various combinations of Bt-Ab and non-Bt-Ab were used. The net shifts of the assay using a higher standard concentration (300 ng/mL) are plotted (D) to determine optimal Bt-Ab concentration when non-Bt-Ab concentration is held consistent. Calibration curves for IL-8 (E) using various concentrations of Bt-Ab at a set non-Bt-Ab concentration show a shift in x_0 accompanied by a truncation of the dynamic range.

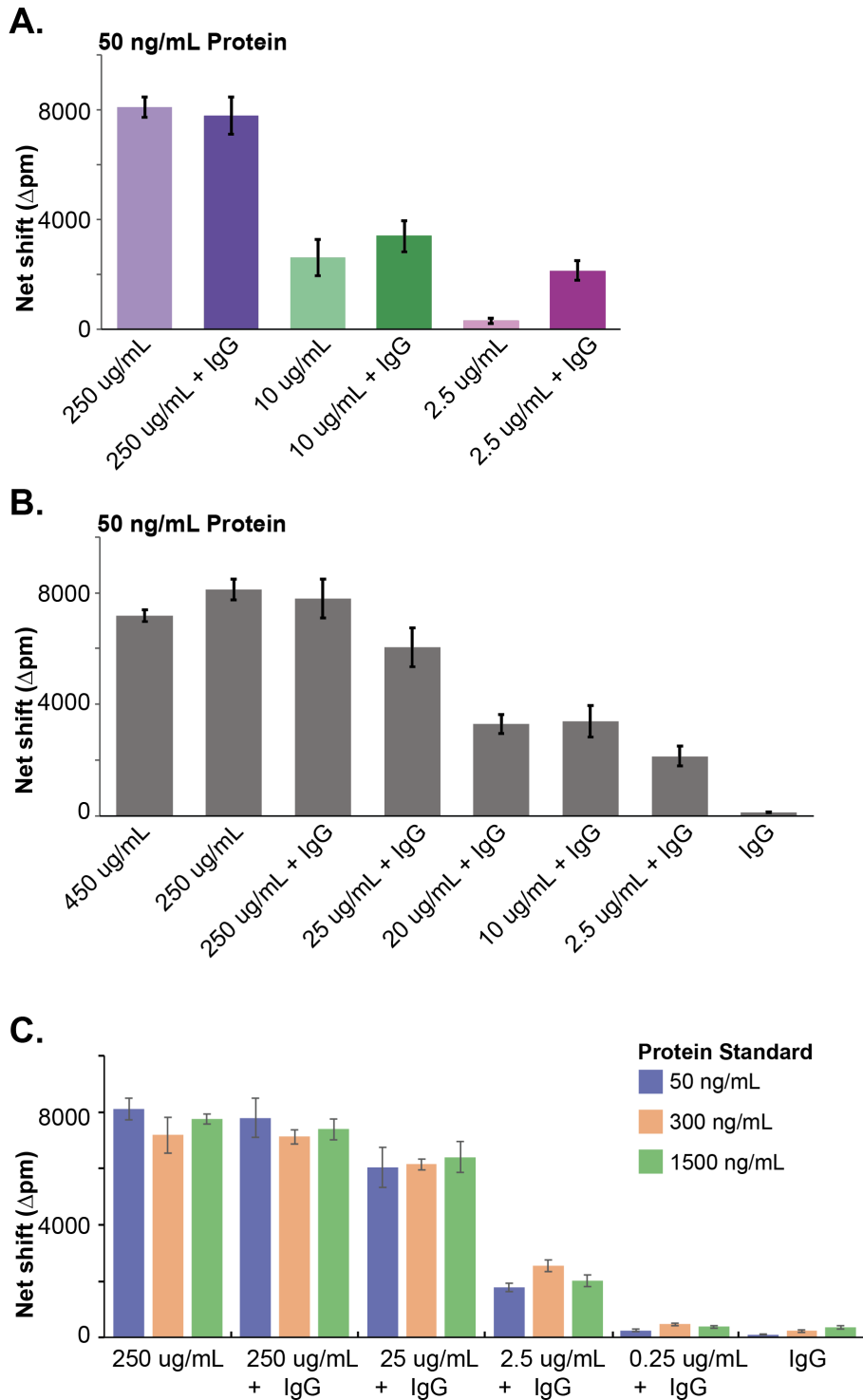


Figure 7.10 Shifting IL-8 calibration by altering spotting concentration of capture Ab. The net shifts of completed assays are plotted to highlight the effect of adding 2 ug/mL of mouse IgG control Ab to varying concentrations of IL-8 capture Ab (A), show the signal decrease as IL-8 capture Ab concentration decreases at a set concentration of mouse IgG (B), and visualize the minimal change in shift between 50 and 1500 ng/mL of protein standard for all capture dilution combinations (C). IgG= 2 ug/mL mouse IgG control antibody.

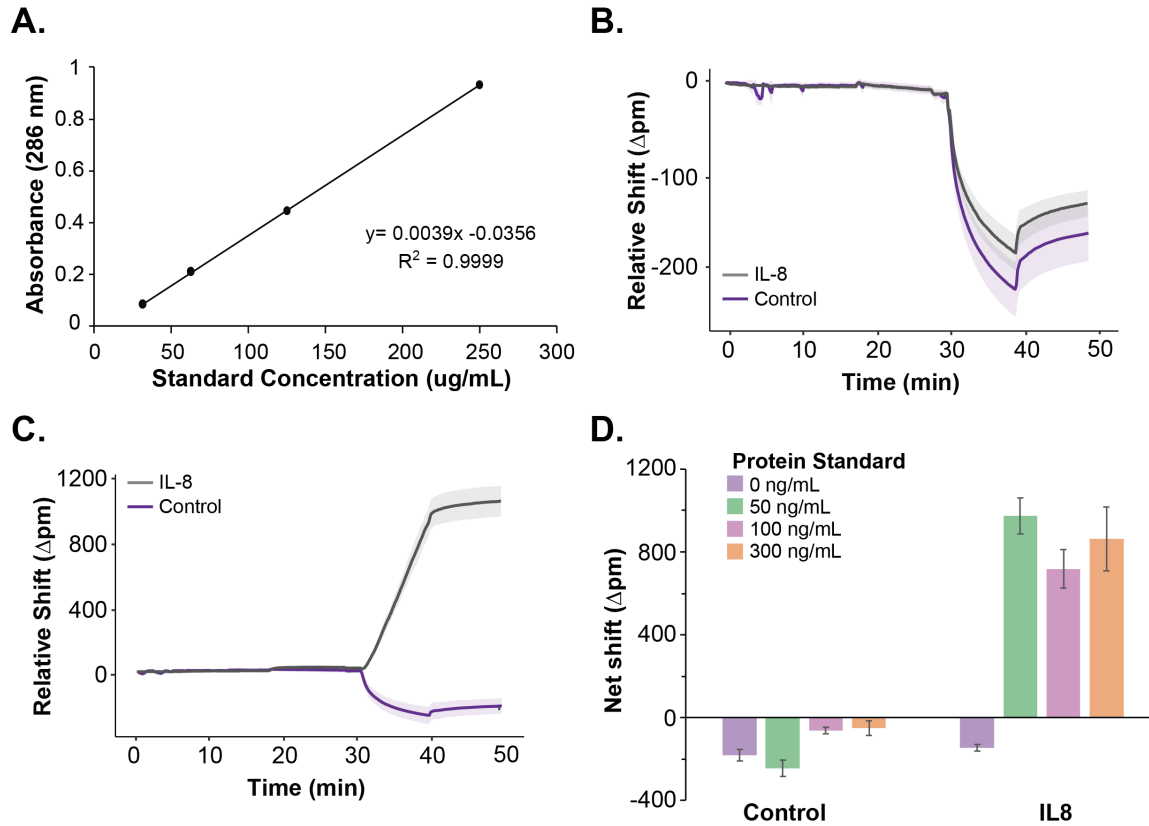


Figure 7.11 Shifting IL-8 calibration by altering the assay format with streptavidin (SA) coated beads. The beads require washing before use and the post-washed bead concentration must be calculated from a SA-bead standard calibration curve (A). The assay trace for a blank, no protein, experiment (A) and 50 ng/mL protein (B) are plotted, showing a negative shift upon the addition of beads. The net shifts for control spotted rings and IL-8 capture spotted rings are plotted (D) across varying concentrations of IL-8 protein standard, with minimal differences.

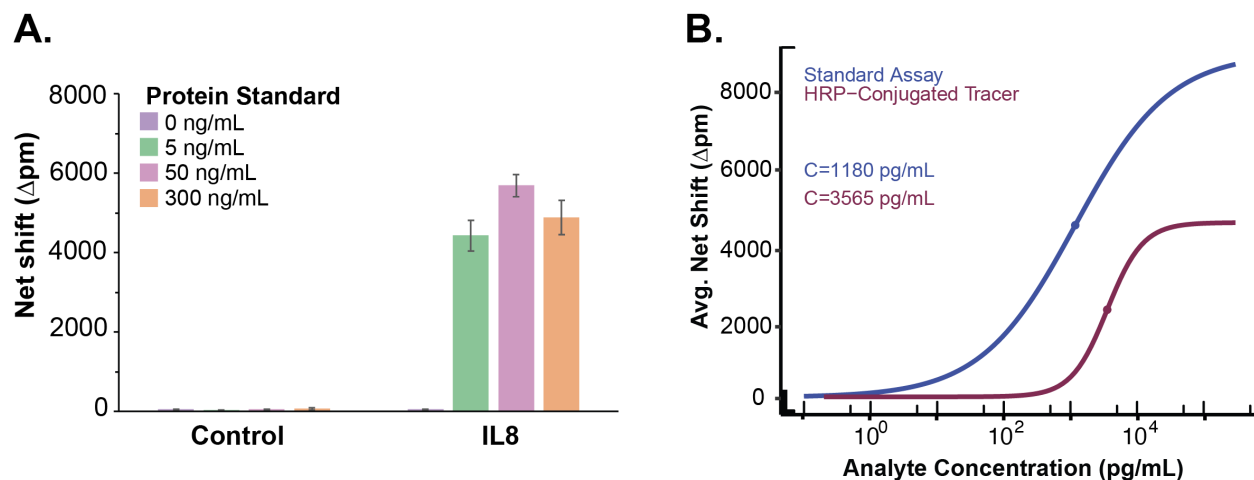


Figure 7.12 Shifting IL-8 calibration by altering the assay design with HRP-conjugated tracer antibodies. The net shifts of completed assays for control spotted rings and IL-8 capture spotted rings were plotted (A) across varying concentrations of IL-8 protein standard, with minimal change. The calibration curve constructed with this method (purple) is overlaid with a typical IL-8 calibration curve (blue), showing a shift in x_0 but a truncation of the dynamic range (B).

7.8 Tables

Table 7.1 Average and standard deviation (pg/mL) in the x_0 value of the calibration curves for 50% plasma and 10% plasma calibrations.

Target	Average x_0 value ^a 50% plasma	Standard Deviation 50% plasma	Average x_0 value ^a 10% plasma	Standard Deviation 10% plasma
CCL2	7460	6827	3946	1572
CCL3	7460	6827	806	155
CCL4	830	168	3724	2035
CCL8	6164	5033	542	209
IFN- γ	1138	394	3469	2816
IL-10	5122	6192	2992	1795
IL-15	4002	1344	2405	1519
IL-17	7503	3913	4898	2456
IL-1 β	7171	5449	10698	9547
IL-2	13408	5587	1646	1595
IL-6	1522	715	651	181
IL-8	939	222	1079	851
IP-10	1173	649	1361	762
TNF- α	1517	754	3468	1417

^aThe averages include the three February 2022, the three July 2022, and one November 2023 calibrations, but not the two June 2021 calibrations.

Table 7.2 Average and standard deviation of the maximum value (A) and minimum value (B) in picometers of the calibration curves for 50% plasma and 10% plasma calibrations.

Target	Parameter	Average value ^a 50% plasma	Standard Deviation 50% plasma	Average value ^a 10% plasma	Standard Deviation 10% plasma
CCL2	A	7273	560	6372	890
	B	539	182	238	223
CCL3	A	8074	440	7805	688
	B	211	85	203	113
CCL4	A	5935	872	5416	772
	B	242	117	255	101
CCL8	A	7610	556	6922	734
	B	572	200	258	89
IFN- γ	A	7928	1322	7565	947
	B	375	191	358	103
IL-10	A	8759	934	8485	1065
	B	233	164	183	147
IL-15	A	6719	889	5803	778
	B	195	79	212	114
IL-17	A	8468	590	7982	798
	B	572	365	608	320
IL-1 β	A	7835	873	7218	1007
	B	199	119	189	128
IL-2	A	14756	19958	6603	1099

	B	155	61	192	132
IL-6	A	8534	558	8227	830
	B	268	186	186	163
IL-8	A	8175	1014	8024	1502
	B	338	202	190	200
IP-10	A	6053	844	5491	819
	B	793	482	307	101
TNF- α	A	7542	1117	7101	972
	B	165	81	292	173
^a The averages include three February 2022, three July 2022, and one November 2023 calibrations, but not the two June 2021 calibrations.					

7.9 References

- (1) Pandey, S.; Pandey, P.; Tiwari, G.; Tiwari, R. Bioanalysis in Drug Discovery and Development. *Pharm. Methods* **2010**, *1* (1), 14–24. <https://doi.org/10.4103/2229-4708.72223>.
- (2) Tabatabaei, M. S.; Ahmed, M. Enzyme-Linked Immunosorbent Assay (ELISA). In *Cancer Cell Biology: Methods and Protocols*; Christian, S. L., Ed.; Methods in Molecular Biology; Springer US: New York, NY, 2022; pp 115–134. https://doi.org/10.1007/978-1-0716-2376-3_10.
- (3) Aydin, S. A Short History, Principles, and Types of ELISA, and Our Laboratory Experience with Peptide/Protein Analyses Using ELISA. *Peptides* **2015**, *72*, 4–15. <https://doi.org/10.1016/j.peptides.2015.04.012>.
- (4) Alhaji, M.; Zubair, M.; Farhana, A. Enzyme Linked Immunosorbent Assay. In *StatPearls*; StatPearls Publishing: Treasure Island (FL), 2023.
- (5) Cerda-Kipper, A. S.; Montiel, B. E.; Hosseini, S. Immunoassays | Radioimmunoassays and Enzyme-Linked Immunosorbent Assay☆. In *Encyclopedia of Analytical Science (Third Edition)*; Worsfold, P., Poole, C., Townshend, A., Miró, M., Eds.; Academic Press: Oxford, 2019; pp 55–75. <https://doi.org/10.1016/B978-0-12-409547-2.14510-X>.
- (6) *Sandwich ELISA protocol* | Abcam. <https://www.abcam.com/protocols/sandwich-elisa-protocol-1> (accessed 2024-02-20).
- (7) *Bioanalytical Method Validation Guidance for Industry*. <https://www.fda.gov/regulatory-information/search-fda-guidance-documents/bioanalytical-method-validation-guidance-industry> (accessed 2023-12-15).
- (8) Azadeh, M.; Gorovits, B.; Kamerud, J.; MacMannis, S.; Safavi, A.; Sailstad, J.; Sondag, P. Calibration Curves in Quantitative Ligand Binding Assays: Recommendations and Best Practices for Preparation, Design, and Editing of Calibration Curves. *AAPS J.* **2017**, *20* (1), 22. <https://doi.org/10.1208/s12248-017-0159-4>.
- (9) Hong, Q.; Shen, Y.; Liu, S.; Zhang, Y. Re-Examination of Plotting Analytical Response against Different Forms of Concentration. *Anal. Chem.* **2021**, *acs.analchem.1c02683*. <https://doi.org/10.1021/acs.analchem.1c02683>.
- (10) *Bioanalytical method validation - Scientific guideline* | European Medicines Agency. <https://www.ema.europa.eu/en/bioanalytical-method-validation-scientific-guideline> (accessed 2024-01-04).
- (11) Jacobs, J. F. M.; van der Molen, R. G.; Bossuyt, X.; Damoiseaux, J. Antigen Excess in Modern Immunoassays: To Anticipate on the Unexpected. *Autoimmun. Rev.* **2015**, *14* (2), 160–167. <https://doi.org/10.1016/j.autrev.2014.10.018>.
- (12) Liu, L.-L.; Lin, L.-R.; Tong, M.-L.; Zhang, H.-L.; Huang, S.-J.; Chen, Y.-Y.; Guo, X.-J.; Xi, Y.; Liu, L.; Chen, F.-Y.; Zhang, Y.-F.; Zhang, Q.; Yang, T.-C. Incidence and Risk Factors for the Prozone Phenomenon in Serologic Testing for Syphilis in a Large Cohort. *Clin. Infect. Dis.* **2014**, *59* (3), 384–389. <https://doi.org/10.1093/cid/ciu325>.
- (13) Berkowitz, K.; Baxi, L.; Fox, H. E. False-Negative Syphilis Screening: The Prozone Phenomenon, Nonimmune Hydrops, and Diagnosis of Syphilis during Pregnancy. *Am. J. Obstet. Gynecol.* **1990**, *163* (3), 975–977. [https://doi.org/10.1016/0002-9378\(90\)91107-N](https://doi.org/10.1016/0002-9378(90)91107-N).
- (14) Anderson, N. L.; Anderson, N. G. The Human Plasma Proteome: History, Character, and Diagnostic Prospects *. *Mol. Cell. Proteomics* **2002**, *1* (11), 845–867. <https://doi.org/10.1074/mcp.R200007-MCP200>.

- (15) Newman, S. S.; Wilson, B. D.; Mamerow, D.; Wollant, B. C.; Nyein, H.; Rosenberg-Hasson, Y.; Maecker, H. T.; Eisenstein, M.; Soh, H. T. Extending the Dynamic Range of Biomarker Quantification through Molecular Equalization. *Nat. Commun.* **2023**, *14* (1), 4192. <https://doi.org/10.1038/s41467-023-39772-z>.
- (16) Rosenberg-Hasson, Y.; Hansmann, L.; Liedtke, M.; Herschmann, I.; Maecker, H. T. Effects of Serum and Plasma Matrices on Multiplex Immunoassays. *Immunol. Res.* **2014**, *58* (2), 224–233. <https://doi.org/10.1007/s12026-014-8491-6>.
- (17) Button, E. B.; Cheng, W. H.; Barron, C.; Cheung, H.; Bashir, A.; Cooper, J.; Gill, J.; Stukas, S.; Baron, D. C.; Robert, J.; Rowe, E. M.; Crompton, P. A.; Wellington, C. L. Development of a Novel, Sensitive Translational Immunoassay to Detect Plasma Glial Fibrillary Acidic Protein (GFAP) after Murine Traumatic Brain Injury. *Alzheimers Res. Ther.* **2021**, *13* (1), 58. <https://doi.org/10.1186/s13195-021-00793-9>.
- (18) Liu, L.; Kwak, H.; Lawton, T. L.; Jin, S.-X.; Meunier, A. L.; Dang, Y.; Ostaszewski, B.; Pietras, A. C.; Stern, A. M.; Selkoe, D. J. An Ultra-Sensitive Immunoassay Detects and Quantifies Soluble A β Oligomers in Human Plasma. *Alzheimers Dement.* **2022**, *18* (6), 1186–1202. <https://doi.org/10.1002/alz.12457>.
- (19) Gottschalk, P. G.; Dunn, J. R. Measuring Parallelism, Linearity, and Relative Potency in Bioassay and Immunoassay Data. *J. Biopharm. Stat.* **2005**, *15* (3), 437–463. <https://doi.org/10.1081/BIP-200056532>.
- (20) Andreasson, U.; Perret-Liaudet, A.; van Waalwijk van Doorn, L. J. C.; Blennow, K.; Chiasserini, D.; Engelborghs, S.; Fladby, T.; Genc, S.; Kruse, N.; Kuiperij, H. B.; Kulic, L.; Lewczuk, P.; Mollenhauer, B.; Mroczko, B.; Parnetti, L.; Vanmechelen, E.; Verbeek, M. M.; Winblad, B.; Zetterberg, H.; Koel-Simmelink, M.; Teunissen, C. E. A Practical Guide to Immunoassay Method Validation. *Front. Neurol.* **2015**, *6*.
- (21) McDade, T. W.; Miller, A.; Tran, T. T.; Borders, A. E. B.; Miller, G. A Highly Sensitive Multiplex Immunoassay for Inflammatory Cytokines in Dried Blood Spots. *Am. J. Hum. Biol.* **2021**, *33* (6), e23558. <https://doi.org/10.1002/ajhb.23558>.
- (22) Dejaegher, B.; Heyden, Y. V. Ruggedness and Robustness Testing. *J. Chromatogr. A* **2007**, *1158* (1), 138–157. <https://doi.org/10.1016/j.chroma.2007.02.086>.
- (23) White, S.; Dunn, J.; Summerfield, S. The Quest for Assay Robustness across the Life Cycle of a Bioanalytical Method. *Bioanalysis* **2015**, *7* (7), 815–824. <https://doi.org/10.4155/bio.15.25>.
- (24) Viswanathan, C. T.; Bansal, S.; Booth, B.; DeStefano, A. J.; Rose, M. J.; Sailstad, J.; Shah, V. P.; Skelly, J. P.; Swann, P. G.; Weiner, R. Quantitative Bioanalytical Methods Validation and Implementation: Best Practices for Chromatographic and Ligand Binding Assays. *Pharm. Res.* **2007**, *24* (10), 1962–1973. <https://doi.org/10.1007/s11095-007-9291-7>.
- (25) Iqbal, M.; Gleeson, M. A.; Spaugh, B.; Tybor, F.; Gunn, W. G.; Hochberg, M.; Baehr-Jones, T.; Bailey, R. C.; Gunn, L. C. Label-Free Biosensor Arrays Based on Silicon Ring Resonators and High-Speed Optical Scanning Instrumentation. *IEEE J. Sel. Top. Quantum Electron.* **2010**, *16* (3), 654–661. <https://doi.org/10.1109/JSTQE.2009.2032510>.
- (26) Yu, D.; Humar, M.; Meserve, K.; Bailey, R. C.; Chormaic, S. N.; Vollmer, F. Whispering-Gallery-Mode Sensors for Biological and Physical Sensing. *Nat. Rev. Methods Primer* **2021**, *1* (1), 83. <https://doi.org/10.1038/s43586-021-00079-2>.
- (27) Wade, J. H.; Bailey, R. C. Applications of Optical Microcavity Resonators in Analytical Chemistry. *Annu. Rev. Anal. Chem.* **2016**, *9* (1), 1–25. <https://doi.org/10.1146/annurev-anchem-071015-041742>.

- (28) Bailey, R. C.; Washburn, A. L.; Qavi, A. J.; Iqbal, M.; Gleeson, M.; Tybor, F.; Gunn, L. C. A Robust Silicon Photonic Platform for Multiparameter Biological Analysis; Kubby, J. A., Reed, G. T., Eds.; San Jose, CA, 2009; p 72200N. <https://doi.org/10.1117/12.809819>.
- (29) Luchansky, M. S.; Washburn, A. L.; Martin, T. A.; Iqbal, M.; Gunn, L. C.; Bailey, R. C. Characterization of the Evanescent Field Profile and Bound Mass Sensitivity of a Label-Free Silicon Photonic Microring Resonator Biosensing Platform. *Biosens. Bioelectron.* **2010**, *26* (4), 1283–1291. <https://doi.org/10.1016/j.bios.2010.07.010>.
- (30) *Move Data, not Blood - 30 Minutes Results - Onsite Lab Automation.* <https://www.genalyte.com/> (accessed 2024-02-19).
- (31) Meserve, K.; Qavi, A. J.; Aman, M. J.; Vu, H.; Zeitlin, L.; Dye, J. M.; Froude, J. W.; Leung, D. W.; Yang, L.; Holtsberg, F. W.; Amarasinghe, G. K.; Bailey, R. C. Detection of Biomarkers for Filoviral Infection with a Silicon Photonic Resonator Platform. *STAR Protoc.* **2022**, *3* (4), 101719. <https://doi.org/10.1016/j.xpro.2022.101719>.
- (32) Robison, H. M.; Bailey, R. C. A Guide to Quantitative Biomarker Assay Development Using Whispering Gallery Mode Biosensors: Whispering Gallery Mode Biosensors. *Curr. Protoc. Chem. Biol.* **2017**, *9* (3), 158–173. <https://doi.org/10.1002/cpch.23>.
- (33) *RAWGraphs 2.0.* <https://app.rawgraphs.io/> (accessed 2024-02-20).
- (34) Luchansky, M. S.; Washburn, A. L.; McClellan, M. S.; Bailey, R. C. Sensitive On-Chip Detection of a Protein Biomarker in Human Serum and Plasma over an Extended Dynamic Range Using Silicon Photonic Microring Resonators and Sub-Micron Beads. *Lab. Chip* **2011**, *11* (12), 2042. <https://doi.org/10.1039/c1lc20231f>.
- (35) HRP Conjugation Kit - Lightning-Link® (Ab102890). <https://www.abcam.com/products/conjugation-kits/hrp-conjugation-kit-lightning-link-ab102890.html>.
- (36) Zhao, W.-W.; Ma, Z.-Y.; Yu, P.-P.; Dong, X.-Y.; Xu, J.-J.; Chen, H.-Y. Highly Sensitive Photoelectrochemical Immunoassay with Enhanced Amplification Using Horseradish Peroxidase Induced Biocatalytic Precipitation on a CdS Quantum Dots Multilayer Electrode. *Anal. Chem.* **2012**, *84* (2), 917–923. <https://doi.org/10.1021/ac203184g>.
- (37) Schulte, S. J.; Huang, J.; Pierce, N. A. Hybridization Chain Reaction Lateral Flow Assays for Amplified Instrument-Free At-Home SARS-CoV-2 Testing. *ACS Infect. Dis.* **2023**, *acsinfecdis.2c00472*. <https://doi.org/10.1021/acsinfecdis.2c00472>.
- (38) Hou, L.; Tang, Y.; Xu, M.; Gao, Z.; Tang, D. Tyramine-Based Enzymatic Conjugate Repeats for Ultrasensitive Immunoassay Accompanying Tyramine Signal Amplification with Enzymatic Biocatalytic Precipitation. *Anal. Chem.* **2014**, *86* (16), 8352–8358. <https://doi.org/10.1021/ac501898t>.
- (39) Peng, W.; Qin, Y.; Li, W.; Chen, M.; Zhou, D.; Li, H.; Cui, J.; Chang, J.; Xie, S.; Gong, X.; Tang, B. Nonenzyme Cascaded Amplification Biosensor Based on Effective Aggregation Luminescence Caused by Disintegration of Silver Nanoparticles. *ACS Sens.* **2020**, *5* (7), 1912–1920. <https://doi.org/10.1021/acssensors.9b02355>.
- (40) Wang, J. R.; Xia, C.; Yang, L.; Li, Y. F.; Li, C. M.; Huang, C. Z. DNA Nanofirecrackers Assembled through Hybridization Chain Reaction for Ultrasensitive SERS Immunoassay of Prostate Specific Antigen. *Anal. Chem.* **2020**, *92* (5), 4046–4052. <https://doi.org/10.1021/acs.analchem.9b05648>.

Chapter 8 Dissertation Summary, Side Projects, and Future Directions (oh my!)

8.1 Author Contributions and Acknowledgements

This chapter contains unpublished work. The content of this chapter was conceived and written, and all figures were designed by the thesis author, Krista Meserve. Dr. Cole Chapman aided in data collection and analysis of the work presented in figures 8.1 and 8.2, and Dr. Nico Mesyngier contributed to data collection and analysis of the work presented in figure 8.3.

I would like to thank the collaborators on the side projects mentioned here for their expertise, reagents, and thoughtful conversations. Thank you to Dr. Tobias Peikert and Dr. Patricio Escalante from the Mayo Clinic who provided the COVID samples analyzed by myself and Dr. Cole Chapman for the data in figure 8.1. Thank you to Dr. Brian Kay and Christina Miller from Tango Bioscience for providing the reagents used for the monobody work presented in figure 8.2. Thank you to Dr. Nico Mesyngier from the Bailey Lab for collaborating on the ring-drops project presented in figure 8.3 and for providing the knowledge and expertise in microfluidics. Thank you to Dr. Ryan Bailey for project guidance and providing many collaborative opportunities during my time here. I would additionally like to thank all my previous lab mates for always being willing to discuss current research problems and future research ideas. I would like to acknowledge my current lab mates Ayush Chitrakar and Lindsay Heagle for their feedback and edits towards this chapter.

8.2 Dissertation Summary

The body of work presented in this thesis summarizes multiple projects tied together with the goal of developing and applying robust sandwich-style immunoassays to various disease states to identify or deploy diagnostic, prognostic, or monitoring protein biomarkers. **Chapter 1** weaves together the various projects I worked on through discussion of biomarker classifications, cytokines, and commercialized multiplexed cytokine assays. The basic protocol using the microring resonators to measure the concentration of chosen analytes in clinical samples was described in detail in **Chapter 2**, with specifications for the Ebola Virus project. The same method and analytical considerations discussed in this protocol chapter were employed across all clinical projects, with the only difference being the plexity and targets employed.

A two-plex assay I developed for applications in Ebola virus diagnosis and prognosis is discussed in **Chapter 3**. We developed and validated an assay for detection of Ebola and Sudan virus soluble glycoproteins, an early biomarker of infection. The assay was applied to non-human primate samples and was successful in detecting the Ebola virus glycoprotein, providing evidence that our assay could be used to diagnose infection. **Chapter 4** employed a seven-plex immunoprofiling assay applied to the clinical population of preterm neonates. We explored the inflammatory protein levels between neonates exposed and unexposed to a maternal inflammation. We reported that exposure resulted in an unpredictable immune response in the early days of life, compared to those unexposed. Additionally, we noted patterns in the longitudinal profiles, acquired through multiple temporally distinct samples, in patients who underwent treatment for various infections during the study. The proof-of-concept results showed promise towards using a longitudinal profiling approach to identify monitoring biomarkers in this population.

The third main disease state studied in this dissertation is latent tuberculosis infection and is the focus of **Chapter 5** and **Chapter 6**. In **Chapter 5**, we compare results from two clinically distinct data sets. Both data sets were comprised of non-specific protein immunoprofiles from stimulated plasma patient samples, which were employed in machine learning to differentiate patients by latent tuberculosis status and by risk of reactivation to active tuberculosis status. The machine learning results, and important biomarkers identified by the model, were similar between both cohorts, validating the separate sets of results. In **Chapter 6**, the two data sets were aggregated to increase the population size and analysis was repeated. In this combined cohort, we achieved latent tuberculosis classification with 87% accuracy and stratified latently infected patients at both high and low risks of reactivation. The results indicate the risk of reactivation can be thought of as a linear spectrum with levels of IL-10 and IL-2 being the distinguishing biomarkers. These projects represent years of data collection across two Bailey Lab members in collaboration with multiple external research groups. The main impact of this project is identification of the most predictive protein biomarkers that should be considered for future development of latent tuberculosis and risk stratification protein-based assays.

The final data-focused chapter (**Chapter 7**) discusses analytical topics related to biomarker assays, including variation, dilutions, stability, and optimization. The chapter mainly uses data generated as part of the clinical-based chapters to begin quantitatively and qualitatively understanding variation in the multiplexed calibration curves. I discuss target-specific variation and conclude based on the inter- and intra-sensor chip deck and plasma matrix calibration comparisons that CCL3, IL-6, and CCL8 are least variable and can be used to qualify new sensor chip decks and method success. Additionally, I present data related to the temporal stability of the sensor chip deck towards understanding how long the sensor chips can be used after antibody

spotting. Finally, the chapter concludes with the different assay methods we used in attempts to optimize one of the specific biomarkers in our panel. This chapter will be useful for future Bailey Lab members working on long-term clinical projects including defining more quality control and analytical metrics.

I take this final chapter to summarize a few side projects and discuss ideas of future directions in each of the main projects presented in this thesis. Two of the three side projects relate to the COVID-19 pandemic that led to the infamous shutdown of campus (and the world) during my first year of graduate school. The third discussed side project is an internal Bailey Lab collaboration that aimed to combine two of the lab's techniques: droplet microfluidics and microring resonators. While these projects were not substantial enough to include in data chapters, they were instrumental in learning assay design and device engineering principles. The second section of the chapter will delve into future project directions related to each of my projects, as well as projects relevant to the Bailey Lab that I've enjoyed tangentially helping troubleshoot over the years.

8.3 Short-lived side projects

8.3.1 Covid Immunoprofiling: the highest plexity panel for the lowest sample count

Coronavirus disease 2019 (COVID-19) is a disease caused by infection with severe acute respiratory syndrome coronavirus 2 (SARS-CoV-2). The respiratory-based infection led to total shutdowns of the country, and much of the world, in March 2020. To date, (January 2024), there have been over 700 million COVID-19 cases around the world and nearly 7 million deaths attributed to the effects of the disease.¹ A large focus in the early part of the pandemic was development of rapid diagnostics to identify those who were infected and begin quarantine procedures. Polymerase chain reaction (PCR) assays were common at the dystopian mass testing

centers due to their sensitivity, but antigen-based tests, such as lateral flow assays or biosensor-based diagnostics, became popular for cheap, at-home testing. Most antigen tests aimed to detect the SARS-CoV-2 nucleocapsid or spike proteins on the viral surface.

Rather than focusing on diagnosing infection, as was being done by numerous companies in the industry, our lab moved to immunoprofiling non-specific inflammatory cytokine and chemokine biomarkers to understand the inflammatory dysregulation in COVID patients. Our collaborators, Dr. Tobias Peikart and Dr. Patricio Escalante at the Mayo Clinic, collected blood from 22 patients, 16 with COVID and 6 healthy controls. The peripheral blood mononuclear cells (PBMCs) were stimulated for forty hours with COVID specific (SS1 and SS2), positive controls (SAR, CD3, MYO, TET), and negative control (MED) antigens. SS1 and SS2 were recombinant subunits of the SARS-CoV-2 spike protein, SAR was the SARS-CoV-1 spike protein, TET was the tetanus toxoid, MYO was myoglobin, CD3 was anti-CD3 peptides, and MED was cell media. The stimulated supernatant was collected and frozen prior to analysis. The seven different stimulations per patient led to a total of 154 samples analyzed for this project.

The assay steps utilized heavily throughout this thesis (buffer, sample/standard, buffer, biotinylated tracer antibodies, buffer, streptavidin horse radish peroxidase, buffer, 4-chloro-1-naphthol amplification, buffer) was used over a 15-plex Genalyte, Inc. spotted sensor chip. The targets on the panel were selected for both precedent in our existing assay panels and the current understanding of coronavirus infections, and included: IL-1 β , IL-2, IL-6, IL-7, IL-10, CCL2, CCL3, CCL4, CCL7, IP-10, TNF- α , TGF- α , IFN- γ , IFN- λ 1, and GM-CSF. Once researchers working on COVID-19 related projects were allowed back on campus, my Bailey Lab mentor, Dr. Cole Chapman, and I began validating and optimizing the reagents for targets that had not been previously employed on our platform (IL-7, CCL7, TGF- α , IFN- λ 1, and GM-CSF). After

successful individual optimization, the antibodies were tested for cross-reactivity and then sent for spotting. The spotted sensor chip deck was calibrated in 0.5% and 5% serum (**Figure 8.1A**) and the raw concentrations of all 15 targets was measured in the 154 samples (example sample in **Figure 8.1B**).

The data was worked up in the same method described in all previous chapters of this dissertation and normalization within each target and each subject was calculated under the following conditions: COVID specific minus negative control (SS1-MED, SS2- MED) and COVID specific minus positive control (SS1-CD3, SS1-MYO, SS1-SAR, SS1-TET, SS2-CD3, SS2-MYO, SS2-SAR, SS2-TET).

The statistical tests between COVID negative and COVID positive groups was the Mann-Whitney U test (Wilcoxon-Mann-Whitney, WMW, discussed in **Chapter 5**) due to the non-normal concentration distribution, low sample counts, ordinal responses, and independence between the two groups. Across the 105 combinations of targets and raw conditions, only eight comparisons were statistically different in data distribution between COVID status (**Figure 8.1C**) and across the 120 combinations of targets and normalized conditions, eight were significantly different between COVID status (**Figure 8.1D**).

Of note, most of the significant comparisons showed the COVID negative group having higher concentrations of respective biomarker, indicating a suppression in the COVID positive patients. CCL3 under two of the positive control stimulations was higher in the COVID positive population. This could indicate CCL3 was an indicator of an immune response, rather than specific to COVID. There were significant differences between COVID populations for IL-2, IL-7, and GM-CSF after stimulation with covid-specific antigen, SS2. The SS2 antigen stimulated sample is heavily present in the significant differences in the normalized conditions, with seven

of the eight resulting from a control stimulation subtracted from SS2 stimulation. The SS2 antigen is related to the SARS-CoV-2 spike protein, therefore, these significant differences are due to COVID-specific responses. Many of the same targets that were significant in the raw condition were significant in the normalized condition and would have been targets to continue to monitor over more patient samples.

This project showcased the ability to prepare and validate new targets for our platform, with the new targets IL-7, CCL7, TGF- α , IFN- λ 1, and GM-CSF being optimized in a rapid timeframe (~1 month of half-week shift work). It also was the highest-plexity panel developed in the Bailey Lab, with all sixteen microring clusters functionalized with a different antibody (fifteen target-specific spotted clusters and one IgG negative cluster). However, the study was sample limited, especially for healthy controls, resulting in poor statistical power. This proof-of-concept pilot study was used in a grant application with a respiratory based clinical team at the Mayo Clinic that was ultimately not awarded, and thus no further samples were sent for us to analyze and potentially improve the limitations of this small cohort study.

8.3.2 Monobody based assay designs: it takes two reagents to tango

This short-lived project involved the use of a type of new recognition element that has not been previously described in this thesis: monobodies (Mbs). A Mb is a synthetic binding protein using a fibronectin type III domain scaffold and is structurally similar to the variable region of an antibody's heavy chain.^{2,3} The smaller size of Mbs make them advantageous as therapeutics for small binding pocket targets and for development of multi-valent recognition molecules, as multiple Mbs can be linked to a single carrier molecule. Tango Bioscience, whose slogan is, "*It takes two to tango*", is a Chicago-based biotech company using phage display techniques to evolve Mbs towards specific binding domains with the goal of creating monobody

sandwich style assays.^{4,5} Our collaboration centered around screening monobody pairs for their ability to bind the receptor binding domain (RBD) protein of SARS-CoV-2.

The company sent four untagged Mbs and an RBD-Fc fusion as the analyte standard.⁶ Half of each Mb was left untagged for use as the capture Mb, while the second half was biotinylated for use as the tracer Mb. The proposed assay design is similar to the standard assay design used in this thesis, with a pair of Mbs replacing the antibody pair (**Figure 8.2A**). The initial set of four Mbs sent from Tango Bioscience crashed out of solution upon thawing. After adjusting storage buffers, they sent a fresh set of four Mbs that was tested using a multiplexed format. We tested all sixteen possible combinations of capture and tracer Mbs, with the hypothesis that unique pairs (i.e. A-B, A-C, C-D) would have a greater chance of eliciting a signal than matched pairs (i.e. A-A, C-C) due to the expected binding sites. However, every microring resulted in the same final shift, including the Ms IgG negative control rings and blank, unspotted, microrings (**Figure 8.2B**) for all tested Mb tracers.

After these initial results, Tango Bioscience provided biotinylated RBD (Bt-RBD) and c-tagged RBD rather than the Fc fusion. A truncated assay using Bt-RBD as the analyte eliminates the need for a Bt-tracer and was used to test analyte binding to capture Mbs. The results indicated that there was a difference in ability of Mbs to capture the RBD analyte, with Mb B having the same result as the controls, Mb A having a shift greater than the controls, and Mb C and D having the greatest shift (~5000 pm) and greatest differentiation from the controls. These results indicated that the Mbs were acting differently and that they were able to bind the target analyte. However, when moving back to the sandwich assay design, the omnipresent signal returned when detecting 2 µg/mL of RBD-c (**Figure 8.2C**). The Ms IgG spotted rings did result in a slightly lower net shift but were still very high. Additionally, when a blank assay containing

no protein was tested, the results were almost identical to the assay with protein present (**Figure 8.2D**).

Taken together, these results indicate the Mbs acting as the tracer are extremely prone to non-specific binding, as there is similar, amplified signal with and without analyte present. We attempted to resolve the non-specific binding by having a tween additive in the running buffer and using a biologic matrix, but the non-specific binding of the tracer Mb could not be mitigated. In a conventional ELISA, this result would be seen as having a high background signal, which was exactly what Tango Bioscience was seeing in their ELISA tests with these four Mbs, validating that the issue was with the specificity of the evolved Mbs rather than the assay design. Our platform was able to identify the issue was specifically with the tracer Mb because the real time trace indicated the RBD analyte was specifically binding to the Mb spotted rings, with all rings only increasing after the Mb tracer step. Due to the high blanks and background signal, we were unable to identify a pair of Mbs that would work in the sandwich assay format and Tango Bioscience discontinued work with this method.

This project showcased the ability to switch around potential reagents for assay development and screening related projects. With better optimized reagents, our method could have provided information regarding strongest binding partners and binding kinetics and could have quickly tested various reagent concentrations and Mb mixtures. The results we obtained for this project matched what the collaborators were seeing in plate based ELISAs, further validating that the issues stemmed from reagents, rather than the assay itself.

8.3.3 Ring-Drops: two Bailey Lab techniques are better than one

The third short-lived project, and final one discussed here, was an internal Bailey Lab collaboration between team microrings and team microfluidics (Dr. Nico Mesyngier).⁷ The

project concept was developed by Nico and had been a project on his mind for years, but no previous microring lab member had been interested in embracing the project. Luckily for Nico, I had a logistical hold up on my main projects that left me with some time to entertain our mutual side project. The aim of this project was to (1) simply combine two Bailey Lab techniques into one method and (2) detect a single aqueous droplet on the microring sensors.

The two lab techniques we aimed to combine were the microring resonators (heavily discussed through this dissertation) and droplet microfluidics. Droplet microfluidics is a technique that generates small, nanoliter to picoliter scale, aqueous droplets housed in and separated by an immiscible oil phase.⁸ The oil prevents the aqueous droplets from merging, generating hundreds of individual microscale reactors each second, and provides a constant flow in direction from inlet to outlet. The droplets are generated at rates of hundreds per minute using in-house fabricated polydimethylsiloxane (PDMS) devices.⁹ Typically, droplet generation projects center around using the droplets as mini reaction vessels for automating bioassay steps, detecting analytes with thousands of replicates, or continuous monitoring. The set up includes two syringe pumps set to push an aqueous or oil phase onto the droplet generator microfluidic device at set, constant rates. On chip, the droplets are generated, and the aqueous droplets are carried by the oil phase to the outlet tubing. Visualization of the droplets is done using an optical microscope located over the microfluidic device. More complex systems can include magnetic plates, pulse electrodes, and laser setups for advanced detection. For this work, a flow focusing droplet generator with 150 μm by 150 μm square cross section channels was used with syringe pumps for liquid flow and optical camera for visualizing what was happening on the microfluidic device.

Integrating the droplet generator with the microring resonator instrument was the first engineering challenge we tackled. Variables such as ferrule sizes, flow rates, and the effects of gravity due to the droplets being generated lower than the microring sensors needed to be optimized before flowing droplets across the microring chip. These variables were optimized and the final set up of the microfluidics equipment and connection of the droplet generator to the microring sensors can be seen in **Figure 8.3A** and **B**. After the appropriate connections were fitted and oil was able to consistently flow from the syringe, through the droplet generator, and across the microring chip, we started the water-containing syringe pump to begin the flow of the droplets through the system. Droplets containing NaCl had previously shown that the microrings were able to detect the change in refractive index (RI) between water- and NaCl-containing droplets, as the decrease in relative shift for NaCl droplets indicated that the evanescent field was reaching through the oil layer and into the passing droplets (**Figure 8.3C**). However, the rapidly passing droplets were not able to be interrogated individually and resulted in a characteristic bulk shift. The change in resonant wavelength shift based on droplet content was promising and led to the challenge of separating the droplets from each other to potentially detect one droplet.

We varied the flow rates administered by the syringe pumps (1-30 $\mu\text{L}/\text{min}$ range) in attempts to space out the drops to no avail (**Figure 8.3D**). With the droplet generator, even with low aqueous flow rate, the droplets are still generated at hundreds per second.⁹ Additionally, the outlet tubing (ID= 0.3 mm) was larger than the dimension of the PDMS device, causing the droplets to expand and decrease the oil volume in between droplets. This forms a droplet train, rather than individual droplets. The presence of the camera over the droplet generator led us to noticing that after the aqueous phase syringe pump was stopped, droplets were still forming consistently for 3-4 minutes due to the pressure buildup in the PDMS device and tubing.

Thereafter, the droplets began forming in irregular patterns (ie packets of droplets, group of three droplets, single droplets) at irregular time intervals. We continued data collection during this time and began to notice spikes in the microring signal shortly after seeing the individual droplets moving out of the droplet generator (**Figure 8.3D**).

We intentionally used this observation to connect groups of, and individual, droplets to peaks in the resonators. We used the logged timestamp we visually saw these small clusters of droplets escape from the droplet generator and, after accounting for the delay time for the droplet to traverse from the droplet generator to the resonator sensors, tabulated which resonator peak corresponded to visual droplets (**Figure 8.3E and F**). These results demonstrate the ability of the sensors to detect single aqueous droplets, with a lower shift in signal compared to groups of droplets. However, this ‘wait for pressure to decrease to get individual droplets’ method was not a feasible approach to continue this project.

In addition to the results outlined here, we worked to visualize the droplets as they moved past the microring chip surface to understand the effects of surface treatments on keeping the droplets separated. This involved 3-D printing microring cartridge tops that included a window over the flow channels. While this project offered us a technically challenging engineering focused project, there were no identified applications in which using the microring resonators as a sensing mechanism would be beneficial in a droplet microfluidics setting. The cost aspect of the microrings instrumentation would be prohibitive and even if used for a droplet microfluidics assay format, the capture antibodies would saturate before single droplets could be made. Therefore, after proving to the previous lab members that you can, in fact, detect one aqueous droplet with the microring resonators, this internal collaboration concluded. This side project led us to better understandings of projects in the lab, allowed us to be creative engineers, and led to

the finding that we can detect a single droplet of fluid flowing across unfunctionalized microring resonators.

8.4 Future Directions

8.4.1 Future directions of hemorrhagic fever diagnostic panels

8.4.1.1 Expanding to higher plexity assays to include disease specific and non-specific biomarkers for greater diagnostic and clinical efficiency

The future direction of the Ebola virus (EBOV) diagnostic and prognostic panel discussed in **Chapter 2** and **Chapter 3** is to take advantage of the multiplexing capabilities of the microring platform and expand the panel of biomarkers to increase clinical utility. There are two proposed ways to increase the panel: with biomarkers specific to other hemorrhagic/endemic diseases or with non-specific inflammatory markers.

The current work duplexed the EBOV soluble glycoprotein (sGP) with Sudan virus (SUDV) sGP, both specific biomarkers of their respective infections. Biomarkers specific to an additional ebolavirus strain that has infected humans, Bundibugyo ebolavirus (BDBV), or biomarkers indicative of filoviral family infections, including Marburgvirus (MARV), could build out a panel specific to filoviral hemorrhagic fever infections. The BDBV strain produces sGP, but there are minimal commercially available antibody (Ab) pairs for detection. Therefore, partnering with an Ab development company to generate BDBV sGP specific Abs or using another target of viral infection, such as the glycoprotein that coats the viral surface, would be needed. Furthermore, MARV is in the filoviral family but is a genus separate from ebolavirus and does not produce sGP. Commonly explored targets of MARV infection include the surface

glycoprotein, the virus matrix protein (VP40), virus like particles (VLP), or nucleoprotein (NP). These can also be targets for any of the ebolavirus strains if needed.¹⁰

Other endemic diseases with similar symptom onset to filoviral infections could be addressed in a differential diagnostic platform. Possible targets could include the non-structural protein biomarkers for flaviviruses (yellow fever virus, Dengue virus, and zika virus)^{11,12} or novel protein biomarkers for malaria (glyceraldehyde 3-phosphate dehydrogenase and dihydrofolate reductase-thymidylate synthase)¹³ and leishmania (elongation factor 1-a).¹⁴ Published work regarding multiplexed diagnostic panels in this clinical space are currently focused within ebolavirus strains or are serology-based Ab detection platforms.^{11,15-17} Multiplexed syndromic approaches to infectious disease diagnostics is critical for efficient surveillance and differential diagnosis.¹⁸ I propose to use the microring resonator platform to build a novel, protein-based, immunoassay that could differentially diagnose multiple ebolavirus strains (EBOV, SUDV, BDBV), Marburgvirus, yellow fever virus, dengue virus, zika virus, malaria, and leishmania. The implications of a cross-species multiplexed infectious disease tool would be desirable from an analytical capability standpoint and from a public health and outbreak control view.

A secondary method of EBOV-focused panel expansion can move us towards researching diagnostic, prognostic, monitoring, or response biomarkers by multiplexing the EBOV sGP diagnostic biomarker with non-specific inflammatory protein biomarkers. Cytokines are the key players in immune cell signaling and, thus, play a large role in response to infection and are notable targets for building immunodiagnostics of infectious diseases.¹⁹ Early immunoprofiling of EBOV disease focused on determining differences in cytokines or chemokine levels in various disease populations. Comparisons included infected subjects

(humans or non-human primates (NHP)) versus non-infected subjects, infected and symptomatic subjects versus infected and asymptomatic subjects, and infected survivors versus infected non-survivors. Hutchinson et al. found elevated levels of CCL2, CCL4, CCL5, and IL-1 β in serum of EBOV infected NHP compared to healthy controls.²⁰ A follow up study with SUDV as the exposure found CCL4, IL-6, IL-8, and IL-10 to be higher in non-surviving patients, while IFN- α was higher in survivors.²¹ Leroy et al. similarly found higher levels of CCL2, CCL3, CCL4, IL-1 β , IL-6, and TNF- α in plasma of EBOV infected asymptomatic human patients when compared to unexposed controls and non-survivors.²² The increased levels peaked 4-6 days post infection and rapidly waned in under three days, which avoided excessive fever and organ damage as was seen in non-survivors. The increased concentration with rapid decrease was hypothesized to be the reason that some individuals remained asymptomatic and survived the infection compared to others. Research focusing on identifying fatality associated biomarkers reported hypersecretion of IL-1 β , IL-1ra, IL-6, IL-8, IL-15, IL-16, CCL2, CCL3, CCL4, IP-10 and MCSF was associated with fatal outcomes.²³ A multi time-point study compared acute phase (0-11 days post infection) cytokine levels to convalescent phase (35-64 days post infection) and found IL-1a, IL-1 β , IL-6, and TNF- α are suppressed in acute phase compared to convalescent phase and IFN- α 2, IFN- γ , and IL-10 are higher in non-survivors than in survivors within the acute phase.²⁴

More recent work has changed focus towards identifying response biomarkers and biomarkers associated with post-infection complications. Viode et al. employed a proteomic workflow to identify differences in the acute response of survivors and non-survivors of EBOV infection and reported multiple response biomarkers of an IFN- β -1a treatment.²⁵ Large cohort studies in the last five years have attempted to shed light on long lasting effects within survivors of EBOV infection, including musculoskeletal, neurologic, auditory, and visual

complications.^{26,27} Tozay et al. reported logistic regression correlations of higher IFN- γ concentration to patients with increased muscle pain, higher CRP and lower IL-8 levels to patients with vision problems, lower CCL3 concentrations in those with lower body numbness, lower TNF- α in those with chronic headaches, and lower IL-6 in those with hearing loss.²⁷ Although, these weak correlations were not significant after applying multiple comparisons. Finally, Wiedemann et al. reported that up to two years post infection, EBOV survivors have elevated inflammatory markers of IL-8 and TNF- α and chronic immune activation markers of CCL5, and sCD40L.²⁸ These increases could be causing some of the chronic post-infection symptoms.

Using the multiplexed microring panel, we could potentially complete a study similar to the tuberculosis immunoprofiling work in that a large cohort of patient samples under various clinical bins (healthy controls, EBOV infected asymptomatic, EBOV infected survivor, EBOV infected non-survivor) and at various time points (acute, convalescent, 1+ year post infection) are assessed. Many of the studies reported above include samples at multiple time points, which we have employed in the neonatal immunoprofiling work discussed in **Chapter 4**. The panel would include the EBOV and SUDV specific soluble glycoprotein antigens and an assortment of cytokines and chemokines with literature precedent (IL-1 β , IL-1ra, IL-6, IL-8, IL-10, IL-15, CCL2, CCL3, CCL4, CCL5, IP-10, TNF- α , and sCD40L). With the exception of IL-1ra, CCL5, and sCD40L, all of these specific and non-specific biomarkers have been previously validated and applied on our platform. The three new targets would need to be tested and validated individually, and everything would need to be tested for cross-reactivity of the new reagents and of the EBOV-specific reagents.

Bioinformatic machine learning analysis would be done between the various clinical bins to associate the biomarkers with either a specific outcome or disease phase. Unlike previous studies, this multiplexed panel includes both specific and non-specific protein targets that can be used in conjunction as any one of either diagnostic, prognostic, monitoring, or response biomarkers. There is a possibility that the infection specific targets provide the best diagnostic information, while a subset of inflammatory markers provide prognostic (or other) information. Reporting this combination specific and non-specific assay and the set of biomarkers that could make the most concrete decisions could inform future development of protein-based rapid detection assays with implications in outbreak control and resource allocation.

8.4.1.2 Increasing the portability of designed assays to improve accessibility

An additional area of work orthogonal to the continued assay development for this project can include projects related to portability of the instrumentation and/or assay. The current technology we use, as well as what has been developed by Genalyte, Inc., are aimed at clinical laboratory use and are rather bulky. Our instrument fits on a benchtop but is still too large and requires a power source to operate. To implement any developed assay into an underserved environment requires a higher level of portability than is currently possible with our instrumentation and can be improved upon in multiple ways, one being development of smaller instrumentation and another being development of point-of-care assays.

The development of smaller instrumentation would likely be outside the scope of our lab specifically but could be completed in collaboration with Genalyte, Inc. or another engineering focused group. The ideal instrumentation would be small, require minimal sample and instrumental input, run with a battery pack, and provide a quick and actionable response. There is

a possibility to miniaturize aspects of the current system with extensive engineering design and optimization.

Within the realm of our lab work, smaller point-of-care tools could be developed for deployment in endemic areas. Current technologies, such as lateral flow assays, could be developed using specific biomarkers found as important in diagnosis or prognosis of disease using the previously described method. Development would need to include multiplexed printing of capture antibodies onto nitrocellulose paper, optimizing a multi-step (likely bead-based) assay, and identifying an appropriate visualization method. Once the portable assay is developed, many samples would need to be analyzed to determine response levels and correspond response to outcome. It is likely that the method would not be quantitative and ratios of response between various capture lanes would be used for diagnosis or prognosis. The implications of this work include an improved access to important diagnostic testing and creation of rapid testing for outbreak response and resource allocation.

8.4.2 Future directions in pediatric profiling

8.4.2.1 Longitudinal profiling for prognostic biomarker identification and monitoring assays

The neonatal project presented in **Chapter 4** discussed the unpublished investigation into the longitudinal profiles of the subjects who provided multiple samples over their time in the neonatal intensive care unit (NICU). It is clear through these profiles that the cytokines increase in concentration during clinically indicated treatment time points. These highlighted time points were not included in the statistical tests completed for the publication and were defined as timepoints that blood samples were taken while the subject was undergoing treatment for a known infection. The limitation of the current work was the low number of patients with similar

adverse events. However, a potential future research project can better take advantage of the longitudinal profiling towards identifying prognostic, diagnostic, and/or monitoring biomarkers for various infections.

A study focused on a singular disease state that can be analyzed longitudinally would be an ideal case for employing this method. Multiple patients providing samples before, after, and during an infection or treatment would allow for machine learning analysis of the biomarker profiles as a use for diagnosis or onset of disease. Potentially, rather than raw biomarker levels, the rate of change or a ratio of biomarker levels from one time point to the next, could be used to make the desired evaluation. If there are similar profiles or ratios of biomarkers that peak or change before disease onset, they could be used as prognostic markers. If there are similar profiles or ratio of biomarkers that are present in groups of patients in which a treatment works that are different from that in groups of patients in which a treatment does not work, those markers could be used as response or treatment monitoring biomarkers.

Applications for a longitudinal profiling project with goals of biomarker identification could span from health care impacts to public health epidemiological focused projects. In a health setting, patients who are hospitalized in long term care or who must visit a clinic repeatedly for a treatment would be advantageous populations for a longitudinal profiling study of a specific population. It is likely these patients are already receiving routine blood draws, and our platform has frequently used 'waste' sample, or leftover plasma or serum after clinical testing. Patient populations and research goals that would fit this project could include pediatric ICU stays for a specific disease (flu, RSV, pneumonia, etc.) to identify prognostic markers for infection outcome, ICU patients being monitored before and after a specific surgery (transplant, heart surgery, medical device implant, etc.) to identify response biomarkers, or patients

undergoing treatments for a specific cancer type to identify monitoring biomarkers for treatment effects or prognostic biomarkers for patient outcomes. An epidemiological project could entail monitoring people who live near a specific exposure (production plant, construction site, commercial farmland, etc.) to correlate exposures with biomarker levels over time with a goal of identifying monitoring, response, or susceptibility biomarkers. With a well-defined, specific subject population, a longitudinal study would have more power than when it was a secondary observation in a larger project.

8.4.2.2 The newest clinical project in the lab: pediatric sepsis biomarker discovery

The current future direction in a pediatric immunoprofiling context is the start of a pediatric sepsis-based project in collaboration with emergency medicine doctors at the Mott Children's Hospital. The immunoprofiling panel will include many of the non-specific cytokine targets (IL-1 β , IL-2, IL-6, IL-8, IL-10, CCL3, IFN- γ , TNF- α , and IP-10) and new targets (PCT, MMP8, PAI-1, and CRP) pending their optimization on our platform. Taken together, these targets will provide information on inflammatory dysregulation in the pediatric population.

The study design aims to collect blood samples from the subjects at time of presentation to the emergency department (ED) and twenty-four hours later. The samples will be tested in clinical laboratories for clinically indicated tests and nucleic acid profiling. Serum samples will be stored and analyzed by our team for the inflammatory protein concentrations. The RNA signatures, cytokine and protein concentrations, and electronic health record data will be analyzed with machine learning with the overarching goal of predicting the onset of sepsis upon initial ED presentation. Additionally, various diagnostic, prognostic, monitoring, or response biomarkers could be identified using the data generated from this study. The implications of this

work include better health outcomes, improved resource allocation, and decreased cost of treatment.

While the overarching predictive analysis will include machine learning analysis done by collaborators, there are in-house statistical tests and analysis with the Bailey Lab generated data that can be completed. Similar to the LTBI biomarker panel, the new targets can be monitored for variation in inter- and intra- sensor chip deck calibrations. The overlapping targets can initially be used for spotting and method validation, as the variation in calibrations of these specific targets has been characterized in **Chapter 7**. The resulting concentrations of the thirteen biomarkers can be binned between subjects who did get sepsis versus those who did not and by timepoint (ED presentation vs 24 hours later), ideally age and gender matched between bins. Wilcoxon-Mann-Whitney analysis can be completed between the bins to identify statistical differences between disease groups, as well as between time points. The significant differences could indicate potential prognostic biomarkers. Additionally, ratios of biomarker concentrations between the two timepoints can be tested between disease groups to determine specifically if temporal changes of target concentrations are significant, identifying potential monitoring biomarkers. Overall, future work in pediatric or immunoprofiling projects will be an advantageous use for our developed assay platform and clinical workflow with implications in diagnostic, prognostic, and monitoring biomarker discovery.

8.4.3 Future directions in latent tuberculosis diagnostic projects

8.4.3.1 Moving into a new study cohort in Tijuana, Mexico and the logistic hurdle of establishing an international study site.

The latent tuberculosis infection (LTBI) project discussed in **Chapter 5** and **Chapter 6** is part of an ongoing multi-institute project funded by the NIH. After finishing the proof-of-concept

work showcased here, we aim to repeat the method in a population where TB is highly prevalent and there are many reactivation events. The initial work was completed in Rochester, Minnesota, with our collaborators in respiratory medicine at the Mayo Clinic. While still present, TB is not generally widespread in the United States; therefore, we aim to implement this workflow in Tijuana, Mexico, which has a greater prevalence of TB infection. Our microring team and the Mayo Clinic team partnered with Dr. Rafael Laniado-Laborin of the tuberculosis clinic in Tijuana to longitudinally immunoprofile health care workers. The plan is to collect QuantiFERON (QFT) stimulated plasma waste from around 300 patients (mix of LTBI, active TB, non-TB respiratory infected, healthy controls, and case contacts) at four different time points across two to three years.

One aspect of the study will be to assess differences in biomarker levels and predictive modeling results between the already analyzed Mayo Clinic population and this new cohort. Boxplots to visualize measured and normalized cytokine levels. Wilcoxon-Mann-Whitney statistical tests will be used to determine significant differences between cohorts when stratified by disease state. Results similar to the Mayo Clinic cohort in important predictive biomarkers would indicate we have identified a more generalizable trend, as it holds across cohorts from multiple locations. Dissimilar results would suggest the results are location- or demographic-specific and more comparisons of the population statistics would be required.

A second aspect of the study will be longitudinal profiling of the patients, making healthcare workers an ideal population due to their proximity to the TB clinic and general requirement to be in the area long term. Analyzing multiple time points, similar to the longitudinal profiling work in **Chapter 4**, will lead to cytokine profiles spanning multiple years, and possibly multiple disease states within one patient. Take, for example, a patient at time point

one who is clinically classified as a healthy control (LTBI negative and low risk of reactivation). At time point two, the QFT test indicates infection with TB, and further testing confirms an LTBI diagnosis with a high risk of reactivation. The patient would receive isoniazid treatment. The next time point may conclude the patient is still LTBI positive but now at a low risk of reactivation due to treatment. The final timepoint could be after the infection has cleared and they are LTBI negative, with prior infection and low risk of reactivation. The temporal change of each cytokine, or combinations thereof, within patients similar to this description can lead to information to predict reactivation preemptively rather than relying on cytokine levels at one time point.

A third aspect of this study is the inclusion of close contacts. For the health care worker patients that result in a positive QFT test, their family members or people they live with will be contacted for enrollment in the study. The mode of transmission is respiratory droplets, and it is reasonable to presume that transmission occurs in the household. Including the close contact population in the study will provide insight into potentially protective biomarkers, especially if the study subjects display different immunoprofiles depending on whether they later have a presenting infection.

This study was initially funded during my rotation with the Bailey Lab in the Fall of 2019 which initiated conversations between our team and the Mayo Clinic team. In March 2020, the study at both the Mayo Clinic site and early implementation at the Mexico site were put on hold. In the middle of 2021, the Mayo Clinic restarted recruiting patients for this study and initial plans were made for equipment needed at the Mexico study site. The study site needed everything, including QFT supplies, lab consumables, a -80°C freezer, and specialized instrumentation.

In winter 2022, I was tasked with procuring the appropriate equipment and getting it to the study site. Coordinating with suppliers, our collaborators, and the wonderful procurement team at UM, led to a full-size standing -80°C freezer and a DYNEX fully automated ELISA system arriving at the study site in Tijuana in June. Unfortunately, the DYNEX instrument delivered was incorrect and the correct one was exchanged two months later. From there, everything from pipette tips, conical tubes, and pH meters to PBS buffer and QFT test kits needed to be purchased for the study site. Working closely with Dr. Laniado-Laborin, we identified multiple companies that could provide the supplies, but only a few could provide the materials with consistent communication and in appropriate delivery time frames. Despite the additional questions and paperwork from the UM procurement team, we determined it was easier, faster, and cheaper to buy materials from suppliers in Mexico rather than procuring from US-based sites, arranging transport, and paying import fees. Another of the many hurdles was that nobody at the study site had experience with these specific processes and tests, meaning each practice run held between the Mayo Clinic and the Tijuana study site would be cut short due to missing materials or reagents. We would then place the order through UM procurement and the item would arrive anytime between two weeks and three months later.

After almost a full year of obtaining the consumable supplies and training the Mexico site study team, healthcare worker enrollment began in the fall of 2023. The (hopefully) final hurdle in the sample workflow was transport of the human samples across the border. We were able to make a connection with Professor Steffanie Strathadee at UCSD, who has a transport team that travels biweekly to Tijuana and brings back samples for processing. I set up the payment for the transport team, who will pick up the packaged samples at Dr. Laniado-Laborin's lab, work with border patrol to transport human samples across the border, and then drop off the package at

UPS. The package will be sent to the Mayo Clinic, who will save the PBMCs for flow cytometry studies and forward the frozen QFT plasma samples to UM. The first transport finally occurred in January 2024. Unfortunately, it turned out that the ‘plasma samples’ that the Mexico team had saved and shipped to the Mayo Clinic was the plasma from the ficoll cell separation protocol and was not the leftover QFT test plasma. The QFT plasma from the patients enrolled in the study for cytokine profiling had been thrown away. Currently, new patients are being enrolled and the QFT plasma will be saved for our studies.

This two-year period from when I began managing the set-up of the Mexico site to getting some samples across the border was filled with a lot of emails, stress, and many (many, many) hold ups. However, the opportunity to manage this large scale, international purchase and laboratory set-up was an invaluable experience in organization and effective communication between multiple stakeholders. While I’m disappointed that the preparation of the study site was drawn out, and I will not be part of the sample analysis for the Mexico site study, I’m glad to have played a role in this project and hope that this study can continue successfully in the years to come.

8.4.3.2 Expanding the clinical designations bins to develop more specific diagnostic tools.

Future studies to improve LTBI diagnostics need to include more samples spread across clinical bins of interest. One limitation of our completed studies was that we focused only on the LTBI phase of infection. This can be improved by expanding enrollment beyond those with latent infection. Clinical designations can also expand to identify TB infected individuals beyond active and latent to include incipient and subclinical infection. Differences between positive and negative subjects within these clinical designations, as well as across the different designations,

can then be assessed to provide more specific diagnostic or predictor biomarkers. In addition, including subpopulations of patients with other respiratory infections (i.e. pneumonia) or other bacterial infections (i.e. non-tuberculosis mycobacteria) would improve the specificity and decrease false positives of the diagnostic tool by accounting for immunological differences caused by non-TB/LTBI infections.

Bringing attention to ensuring true homogeneity in machine learning separation bins can ultimately improve generalizability of the results within the target population. The ideal diagnostic would assess all patients who had suspected TB infection (all those who received QFT testing) and classify them as LTBI, active TB, or other. These results would confirm the QFT findings (for active TB) and provide additional separation between LTBI and other. From there, the profiles of those classified only as LTBI would be further identified as being high risk or low risk. Therefore, models using only the LTBI positive subpopulation to differentiate high and low risk would be ideal. It is a limitation of early studies (Chapter 5) that we were unable to do the high and low risk classifications within just LTBI+ bins but the aggregated data in Chapter 6 removed this limitation.

8.4.3.3 Including multidrug resistant TB infected subjects

An interesting direction for future development of the tuberculosis project is in multidrug resistant TB (MDR-TB).²⁹ MDR-TB is a strain that is resistant to isoniazid and rifampin and can result from misuse of antibiotics, incorrect dosage, poor quality drugs, or incorrect treatment. The spread of MDR-TB strains is even more damaging than non MDR strains, as treatment is more complicated. Additionally, continued antibiotic resistance could lead to superbug strains of infection that are extremely difficult to treat. Early detection is one strategy to mitigate transmission of all TB and is especially essential for MDR-TB strains.³⁰ Various biosensor

technologies have been employed to detect MDR-TB including gold nanoparticle derivatized oligonucleotides that detect single base mutations in resistant strains, a loop-mediated isothermal amplification method to detect resistance using gold nanoprobess with perfect specificity and sensitivity, and a nucleic acid lateral flow immunoassay using gold nanoparticles for rapid detection of both isoniazid and rifampin resistance after PCR.³¹

We could potentially include a subject population within our study of those with active TB from MDR strains. Subjects would have to be pre-identified as having an MDR strain to allow for the clinical designation. However, we could potentially identify specific host cytokine signatures associated with MDR-TB that are not associated with, or associated at different levels with, active TB, LTBI, or other respiratory infected individuals. We could implement identification of MDR strain infected individuals using the same panel and workflow as LTBI diagnosis and risk assessment, adding to the utility and impact of our method.

8.4.3.4 Including social determinants of health to improve diagnostic predictions

A final direction to consider for future work, especially when expanding the project into a geographic area with different socioeconomic factors, is to consider the social determinants of health (SDOH) of the study participants. SDOH are non-medical factors and conditions of a person's environment, including where they were born, live, learn, work, and worship, that have studied effects on health and quality-of-life outcomes and risks.³² Additionally, a person's relationship with various systems, such as economic policies, development agendas, social policies, and political systems, have important influence on health incomes. My interest in the public health aspect of diagnostics and disease intervention developed in a public policy course I took as part of the precision health certificate program where we explored various public health

systems, health care organizations, health disparities, and public policy advocacy strategies at local, state, and federal levels.

There are five domains of SDOH that could each, in some way, be deployed in our study.^{32,33} These include: (1) economic stability (poverty levels, employment opportunities, wages, and food or housing stability), (2) education access and quality (degree achieved, general literacy, and language proficiency), (3) health care access and quality (primary care options, health insurance, proximity to medical care, and health literacy), (4) neighborhood and built environment (housing quality and availability, access to transportation, and local crime rates), and (5) social and community context (familial dynamics and responsibilities, discrimination, incarceration, mental health, systemic inequity, community cohesion, and workplace conditions). Many governmental (CDC, WHO) and local programs are working to understand the SDOH in global and regional contexts and address the social and structural conditions through policy, data collection and surveillance, evaluation, partnership and collaborations, community engagement, and infrastructure.^{34,35} Addressing the SDOH in a public health context will be one of the many methods to improve health equity, in the US and globally.

The connection of public health to tuberculosis is clear. A contagious pathogen is readily spread through close contacts and diagnosis and treatment can be hard to obtain in low-income areas where prevalence is high. Addressing the SDOH relevant to TB requires structural interventions in the upstream determinants of TB, such as unhealthy behaviors, living conditions, and community disease prevalence.³⁶⁻³⁸ Studies have concluded that along with co-morbidities (HIV, diabetes, rheumatoid arthritis), factors such as malnutrition, alcoholism, and tobacco abuse lead to an increased disease susceptibility.³⁹ Many studies focus on determining the connection

between SDOH and infection, treatment outcomes, or health outcomes.^{40,41} There is a gap in the literature relating SDOH variables to LTBI reactivation events.⁴²

Work in other clinical areas, such as premature mortality, sepsis, and cardiovascular disease, have noted inclusion of SDOH increased the predictive modeling accuracy of the machine learning models and the results facilitated efforts in identifying patients who would benefit from more targeted services.^{43–47} Including SDOH in TB predictive modeling, specifically in predicting reactivation risk, could help save resources and provide targeted treatment to specific sub populations of patients. In our projects, the SDOH identified as important could be recorded in the clinical data set and then used as variables, alongside the biomarker concentrations, in the predictive models. Another method could entail using only the biologic variables to classify subjects into high or low risk bins, as we have done in the past, but then correlating subjects classified within a specific bin to their SDOH to identify patterns in SDOH associated with the high-risk clinical bins. These methods could help to identify which SDOH should be a focus for public health interventions and increase equitable outcomes in TB diagnostics.

8.4.4 Future expansion of analytical metrics: Calculation of acceptance intervals for inter and intra chip deck validation

The work presented in the first section of **Chapter 7** regarding comparison for calibration curves across and within sensor chip deck lots can be further expanded with subsequent sensor chip decks from Genalyte, Inc. The average and standard deviation of the midpoint value, baseline shift, and saturating shift calculated for the chapter represented an aggregation of four sensor chip decks and nine calibrations. Future calibrations done on the current chip deck, and with future chip decks, should be added to the data set and new averages, standard deviations,

and ranges should then be calculated. These calibration metrics should continue to be investigated across all chip decks (as was discussed in the chapter), as well as within individual chip decks. Variation mainly emanates from functional variation in target specific antibodies, rather than from the sensors or analytical methods employed.

With an aggregated data set across five or more chip decks, or approximately fifteen calibrations, we can begin to record calibration metrics and ranges for each individual target to qualify future chip decks. In January 2022, I had received a sensor chip deck that, after initial cross-reactivity and amplification tests, was clearly malfunctioning. There was little binding and the amplification result for tested targets was low and highly variable across the different storage decks. After discussing the issues with the chip spotting team, we determined the issue and the chip deck received in February 2022 was significantly improved. I had only validated one chip deck at this time and decided that, moving forward, more formal validation of the chip decks was required. I implemented a cross-deck validation test where we measure the response of a handful of the targets across all storage boxes within the chip lot. Additionally, I began comparing the calibrations to the previous chip decks. These steps should continue to be implemented into the sensor chip deck validation workflow to ensure quality of the sensor chips before they are employed for patient sample analysis.

The inter- chip deck validation ranges should be used within the lab to ensure any observed variation is within an expected range and to check reagent quality for new chip decks. Using the identified robust target reagents (CCL3, CCL8, IL-6), the spotting process, chip quality, and the method implementation by the researcher can be tested, as the new calibration curves for these targets should be very similar to previous calibrations. If a new calibration still looks (visually) appropriate, but quantitatively does not fall within the expected variation ranges

of more than one metric, care should be taken to understand why before use in samples. Was the capture antibody from a new supplier? Are the protein standards or the tracer antibody nearing their expiration dates? New reagents can be purchased and used for the next calibration. However, as long as the calibration curves are able to be constructed, the chip deck can be used. Intra-deck metrics should begin to be calculated to understand expected variation of the calibrations within an individual chip deck. This will provide information on the change in response from individual targets over time, as calibrations are conducted on the sensor chip decks over the lifetime of sample analysis. Traditionally, the net shifts from the same standard protein concentration are averaged across the calibrations from a chip deck and a four parametric curve is fit to those averaged values. However, no work has been done to characterize the variability in the intra-chip deck calibrations and how the variation in the metrics affects the fit of the average values. Investigation into this data analysis will be beneficial moving forward into procuring larger scale sensor chip decks.

8.4.5 Future assay development towards more efficient assays

8.4.5.1 Stop flow assay design

A method that could be tested on the microring resonators that could potentially use less reagents is a stop-flow method. Currently, we use continuous flow of each reagent housed in a 96-well plate over the capture antibodies at 30 $\mu\text{L}/\text{min}$ for seven to ten minutes, using 210-300 μL of sample. The continuous flow helps prevent nonspecific binding events from occurring but could potentially hinder lower-affinity or slower kinetic specific interactions, resulting in no binding events. Thinking of the reagent like a giant droplet housed between blocking buffer rinses could allow additional time for the specific interactions to occur.

Logistically, this would look like drawing the reagent from the well, stopping the flow, or slowing to <5 $\mu\text{L}/\text{min}$ if stopping is not possible, and letting the reagent sit on the chip for an optimized time. The pumps would then turn back on for a blocking buffer rinse. This could be repeated for all the reagent steps or could just be done for the sample step if optimal. This change would then use less than 35-50 μL of sample or reagent, leading to lower volume requirement and decreased cost, which would increase the efficiency of our assays.

8.4.5.2 Multi-biomarker multiplexed assay development

A way to increase the efficiency of our assays and broaden the applicable disease states is to combine different types of molecular biomarkers into one assay. An early project in the Bailey Lab using the microring resonators was detection of microRNAs (miRNA).^{48,49} ssDNA was spotted as a capture agent on the microring sensor chips, the complementary miRNA standard was flowed across the microring surface, and the complex was detected with anti-DNA:RNA antibodies. Moving into clinical samples, the projects mainly transitioned to signaling protein targets due to stability, commercialized reagents, and applicability. However, an interesting research direction would be returning to miRNA detection, multiplexed with protein targets in one assay.

There have been significant updates in assay methods, chip preparation, and instrumentation since the time of the miRNA work. At the time, a different spotting process was being used to link capture agents to the surface of the microrings, so initial work would need to determine if the updated spotting process would be sufficient for linking the modified ssDNA onto the surface. The miRNA standards were analyzed in a hybridization buffer that contained formamide, saline-sodium phosphate-EDTA, Denhardt's solution (mixture of various blocking reagents), and sodium dodecyl sulfate. For multiplexing, the protein-specific antibody captures

would need to be tested for activity following exposure to this buffer. Additionally, the miRNA detection assay steps were on a much longer time scale (40–60-minute steps) compared to our current methods (7-10-minute steps). Finally, the detection scheme ended with the anti-DNA:RNA antibody and further amplification (biotinylation of the DNA:RNA antibody, SA-HRP, and 4CN steps) was not employed at the time. Therefore, the process of biotinylating the antibodies and using the biocatalytic precipitation step would have to be tested.

If the modifications to our current assay design can be optimized for detection of the miRNA and appropriate limits of detection are able to be achieved, there is potential to multiplex the current protein targets with various miRNA. Due to the hybridization buffer requirement for the miRNA samples, there may have to be two separate sample steps, first a subset of the sample in hybridization buffer and a second without. However, if the protein targets are still viable and able to bind the antibody captures in the presence of the hybridization buffer, then a single step could still be feasible. Even with two sample steps, the additional 7-10 minutes of the assay would be minimal considering the implications of multiple target analytes being detected in one assay.

An initial multi-marker assay could be multiplexing miRNA from the let-7 family with cytokine protein biomarkers, such as IL-2, IL-6, and IL-10. The let-7 family of miRNA have been linked as pathologic biomarkers of numerous viruses and diseases, such as hepatitis, herpesvirus, human immunodeficiency virus, respiratory syncytial virus, flu and sepsis infections, and have been detected in serum and blood samples.⁵⁰ Let-7c was an initial target tested on the microrings, which would provide a starting point for comparing the current method to results from the previous method. Additionally, let-7a has been linked to sepsis infections and interactions with cytokines, such as IL-2, IL-6, IL-1 β , and TNF- α .⁵¹

The application to sepsis diagnostic and prognostic work would fit into the future directions discussed above and current work being done in our lab. Multi-target multiplexing would increase the applicability and efficiency of our microring resonator platform and detection method. There is expected to be a lot of optimization and analytical work needed to evaluate the ability of multiplexing the different markers together, but it is an interesting possibility to move our work and platform into a novel diagnostic space.

8.4.6 Additional Bailey Lab future project idea: Double emulsion microfluidics for multiplexed sensing

During my time in the lab, I have become familiar with many of the projects housed in the other domains through many troubleshooting conversations with my lab mates, attending interdisciplinary talks and luncheons, and getting to work with some technologies first-hand (**Section 8.3.3**). Herein, I will briefly describe a potential future direction in the microfluidics space that was inspired by a departmental seminar and discussions with lab mates. A caveat: There may be logistical factors for this project that are not feasible or realistic, which I would be unaware of due to not working in the microfluidics development space. However, cool science can still come from a naïve mind!

One of the microfluidics projects in our lab is ionic or polyionic sensing via droplet microfluidics and fluorescence-based sensing. There are various sensing components optimized for specific targets that facilitate the target of interest being drawn from an aqueous sample droplet (e.g. blood) into an oil carrier phase. A recent research direction for these specific projects revolves around multiplexed sensing, which currently involves spatial separation of droplets in different microfluidic channels, each with a different target-specific set of recognition

reagents in the oil phase. However, this spatial separation will require more sample than multiplexing within a single droplet.

To multiplex temporally, rather than spatially, a research direction for the droplet microfluidics team could be using double emulsion techniques to swap oils with different target-specific sensing components around a single aqueous droplet. This direction was inspired by Dr. Hee-Sun Han's departmental lecture in 2023. The Han group has written a protocol paper for making double emulsion (DE) microfluidics devices that could be used as a starting point for the application of interest.⁵² In our current work, single emulsions (SE) are used, as the aqueous droplets are segmented emulsions in a continuous oil phase. In DE, the aqueous droplet is segmented by an oil shell within an aqueous continuous phase. Using various structures in the microfluidic device, the oil shell can be removed, coalescing the droplet back into the aqueous phase. I envision this technique used for multiplexing of ionic sensing by segmenting the aqueous sample with an initial oil mixture containing sensing reagents for a specific target (i.e. potassium). The DE would continue down a channel to allow for reagent mixing and pass through a detection space to measure the fluorescence in the oil shell. After detection, the oil would be removed through microstructures in the device, coalescing the droplet with the continuous, aqueous sample stream. A second oil mixture containing reagents for a second specific target (i.e. sodium) would then come in and re-form the DE shell. Similar to before, there would be mixing time and fluorescence detection in the oil shell. This process of moving from DE to SE and back to DE could be repeated for all targets of interest.

The process of coalescing the aqueous droplet with the continuous stream between different sensing oil regimes would allow for remixing of the sample between sensing phases. In addition to detecting multiple analytes in one sample in an automated on-chip method, the

resulting fluorescence signal would be concentrated to the area around the shell. Current methods lack a concentrated fluorescence signal, as using the whole area of the carrier oil phase dilutes out the fluorescence response. Centralizing and concentrating the response to a ring around the droplet could improve signal to noise ratios. Furthermore, the oil shell would be in contact with the same sample in its inner and outer core surfaces. This would spatially increase the ways the target of interest could relocate into the oil phase, potentially increasing signal and lowering limits of detection. A limitation of this method would be that the continuous phase is the sample, rather than oil, and therefore, more sample volume would be needed than a SE method. However, running the current devices for over five hours uses only ~1 mL of continuous phase, which is feasible sample volume for a biologic sample and five hours represents an excessively long experiment. Overall, development of this method could provide a unique engineering, biosensing, and fluid dynamics project that could expand the technology toolbox and sensing techniques within the Bailey Lab.

8.5 Concluding Remarks

In this dissertation I have contributed research in diagnostic and prognostic profiling in multiple diseases and conditions, including latent tuberculosis, Ebola virus, and chorioamnionitis. The work I completed and presented in this thesis have increased the disease states in which microring resonators have been employed as the sensing platform and furthered their compatibility in clinical workflows. I have introduced a new analytical method to the field of multiplexed filoviral sGP detection, single-plex as detection had previously been done through ELISAs or lateral flow assays.^{53,54} Take together, I used silicon photonic microring resonators as the sensing platform and analyzed over 700 patient samples with multiplexed protein biomarker detection panels. The panels ranged from a two-plex assay for disease specific protein

biomarkers to seven-, fourteen-, and fifteen-plex nonspecific cytokine and chemokine protein biomarker panels. The data generated from the cytokine profiling clinical projects provided insight into host immune response to infection and allowed for calculation of various analytical metrics towards defining quality control values of our assays. Expansion of the viral diagnostic panel to include host cytokine profiling and including social determinants of health within the latent tuberculosis reactivation risk assessments will propel these projects into exciting clinical spaces for infectious disease management and risk intervention.

8.6 Figures

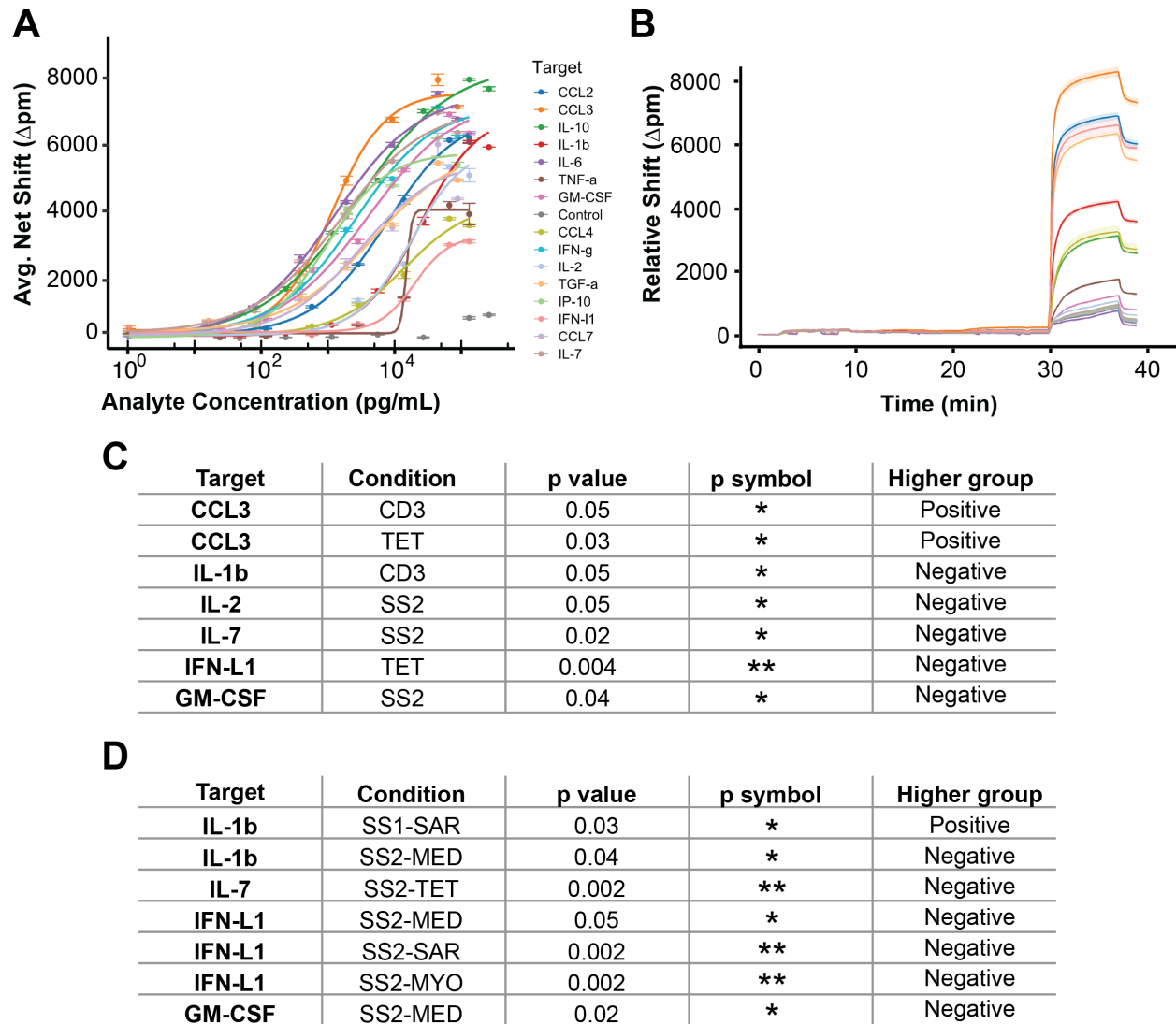


Figure 8.1 COVID-19 immunoprofiling project summary. The project profiled 15 different cytokine and chemokine biomarkers (A) in 5% serum, with an example sample trace in (B). The legend in between the calibration and example trace is for both plots. Minimal statistical significances were found between COVID positive and COVID negative subject populations for both raw (C) and normalized (D) concentrations.

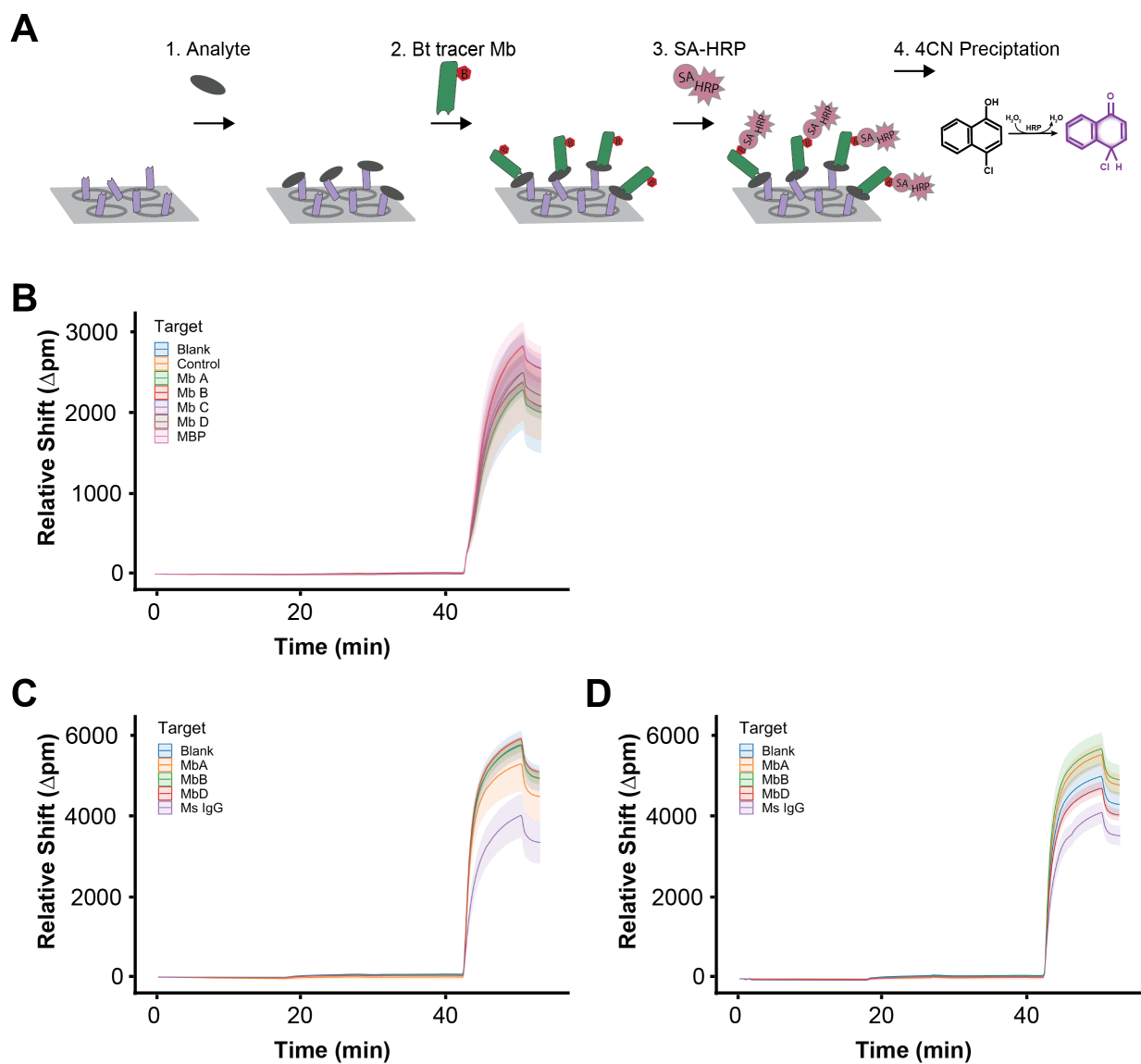


Figure 8.2 Tango monobody project summary. The proposed assay design (A) has one Mb linked to the microring surface that captures the analyte of interested (RBD of SARS-CoV-2. A separate biotinylated Mb would then detect the analyte, followed by SA-HRP and 4CN for signal amplification. Initial screening resulted in low relative shifts and non-specific binding (B) when detecting 2 μ g/mL of RBD analyte. Optimizing reagent concentrations and buffer conditions allow for some separation between the rings spotted with Mb captures and Ms IgG spotted rings (C) when detecting 2 μ g/mL of RBD with Mb C but is still plagued with non-specific binding to unspotted rings and there is little variation between the protein detection assay and the blank (D), indicating tracer Mb non-specific binding.

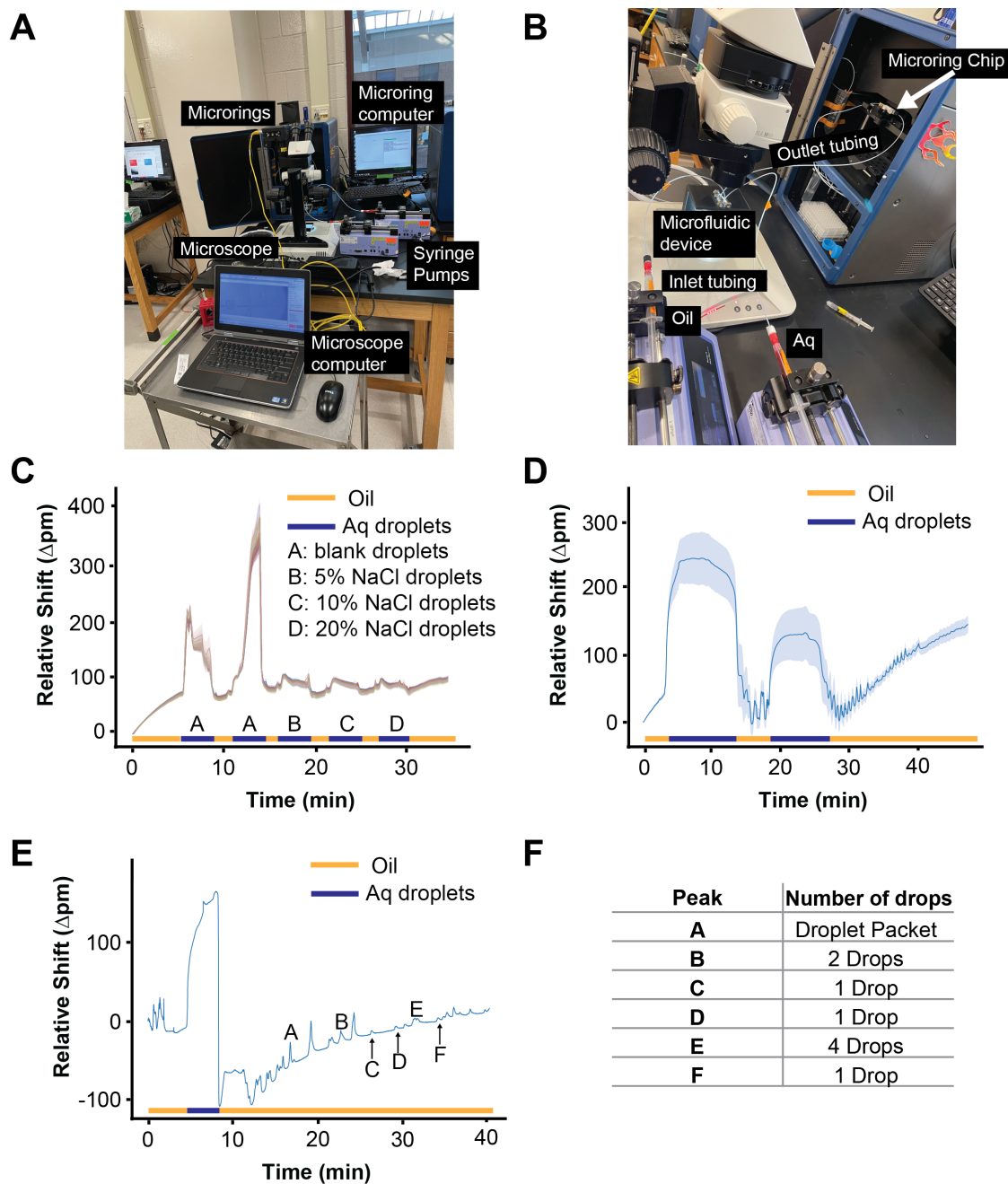


Figure 8.3 Ring-drops project summary. The necessary equipment for the droplet generator (computer, microscope, syringe pumps) was placed on a movable table (A) and moved into proximity with the microring instrument. The droplets were generated on the PDMS device using syringe pumps into a T-junction device, with the outlet tubing interfacing with the microring resonators (B). Initial experiments with bulk droplets flowing across the microrings showed a decrease in signal when NaCl solution replaced the aqueous solution (C). The constant droplet generation resulted in bulk shifts but stopping the Aq syringe pump resulted in smaller droplet packets able to be detected outside of bulk shifts (D). Using this pulsed packet method, we were able to detect small packets of droplets (E, F).

8.7 References

- (1) *COVID - Coronavirus Statistics - Worldometer*.
<https://www.worldometers.info/coronavirus/> (accessed 2024-02-20).
- (2) Koide, A.; Bailey, C. W.; Huang, X.; Koide, S. The Fibronectin Type III Domain as a Scaffold for Novel Binding Proteins. *J. Mol. Biol.* **1998**, *284* (4), 1141–1151.
<https://doi.org/10.1006/jmbi.1998.2238>.
- (3) Koide, A.; Wojcik, J.; Gilbreth, R. N.; Hoey, R. J.; Koide, S. Teaching an Old Scaffold New Tricks: Monobodies Constructed Using Alternative Surfaces of the FN3 Scaffold. *J. Mol. Biol.* **2012**, *415* (2), 393–405. <https://doi.org/10.1016/j.jmb.2011.12.019>.
- (4) *Home Page*. Tango Biosciences. <https://tangobio.com/> (accessed 2024-01-15).
- (5) Gorman, K. T.; Roby, L. C.; Giuffre, A.; Huang, R.; Kay, B. K. Tandem Phage-Display for the Identification of Non-Overlapping Binding Pairs of Recombinant Affinity Reagents. *Nucleic Acids Res.* **2017**, *45* (18), e158. <https://doi.org/10.1093/nar/gkx688>.
- (6) Miller, C. J.; McGinnis, J. E.; Martinez, M. J.; Wang, G.; Zhou, J.; Simmons, E.; Amet, T.; Abdeen, S. J.; Van Huysse, J. W.; Bowsher, R. R.; Kay, B. K. FN3-Based Monobodies Selective for the Receptor Binding Domain of the SARS-CoV-2 Spike Protein. *New Biotechnol.* **2021**, *62*, 79–85. <https://doi.org/10.1016/j.nbt.2021.01.010>.
- (7) Mesyngier, N. Developing a Droplet-Based Phase Grating for Use as a Label-Free, High-Throughput Analytical Platform. Ph.D. Dissertation, University of Michigan, Ann Arbor, Michigan, 2023.
- (8) Lagus, T. P.; Edd, J. F. A Review of the Theory, Methods and Recent Applications of High-Throughput Single-Cell Droplet Microfluidics. *J. Phys. Appl. Phys.* **2013**, *46* (11), 114005. <https://doi.org/10.1088/0022-3727/46/11/114005>.
- (9) Yobas, L.; Martens, S.; Ong, W.-L.; Ranganathan, N. High-Performance Flow-Focusing Geometry for Spontaneous Generation of Monodispersed Droplets. *Lab. Chip* **2006**, *6* (8), 1073. <https://doi.org/10.1039/b602240e>.
- (10) *Factsheet about Marburg virus disease*. <https://www.ecdc.europa.eu/en/infectious-disease-topics/z-disease-list/ebola-virus-disease/facts/factsheet-about-marburg-virus> (accessed 2024-01-15).
- (11) Yen, C.-W.; Puig, H. de; O. Tam, J.; Gómez-Márquez, J.; Bosch, I.; Hamad-Schifferli, K.; Gehrke, L. Multicolored Silver Nanoparticles for Multiplexed Disease Diagnostics: Distinguishing Dengue, Yellow Fever, and Ebola Viruses. *Lab. Chip* **2015**, *15* (7), 1638–1641. <https://doi.org/10.1039/C5LC00055F>.
- (12) Bailey, M. J.; Tan, G. S. Chapter 35 - The Zika Virus NS1 Protein as a Vaccine Target. In *Zika Virus Impact, Diagnosis, Control, and Models*; Martin, C. R., Hollins Martin, C. J., Preedy, V. R., Rajendram, R., Eds.; Academic Press, 2021; pp 367–376.
<https://doi.org/10.1016/B978-0-12-820267-8.00035-2>.
- (13) Yerlikaya, S.; Owusu, E. D. A.; Frimpong, A.; DeLisle, R. K.; Ding, X. C. A Dual, Systematic Approach to Malaria Diagnostic Biomarker Discovery. *Clin. Infect. Dis. Off. Publ. Infect. Dis. Soc. Am.* **2021**, *74* (1), 40–51. <https://doi.org/10.1093/cid/ciab251>.
- (14) Kamran, M.; Ejazi, S. A.; Bhattacharyya, A.; Didwania, N.; Ali, N. A Native 51 kDa Leishmania Membrane Protein Revealed as a Novel Antigenic Candidate for Immuno-Diagnosis of Human VL and PKDL Diseases. *J. Cell. Immunol.* **2020**, *Volume 2* (Issue 6), 301–307. <https://doi.org/10.33696/immunology.2.059>.

- (15) Yoshida, R.; Muramatsu, S.; Akita, H.; Saito, Y.; Kuwahara, M.; Kato, D.; Changua, K.; Miyamoto, H.; Kajihara, M.; Manzoor, R.; Furuyama, W.; Marzi, A.; Feldmann, H.; Mweene, A.; Masumu, J.; Kapeteshi, J.; Muyembe-Tamfum, J.-J.; Takada, A. Development of an Immunochromatography Assay (QuickNavi-Ebola) to Detect Multiple Species of Ebolaviruses. *J. Infect. Dis.* **2016**, *214* (Suppl 3), S185–S191. <https://doi.org/10.1093/infdis/jiw252>.
- (16) Raulino, R.; Thaurignac, G.; Butel, C.; Villabona-Arenas, C. J.; Foe, T.; Loul, S.; Ndimbo-Kumugo, S.-P.; Mbala-Kingebeni, P.; Makiala-Mandanda, S.; Ahuka-Mundeke, S.; Kerkhof, K.; Delaporte, E.; Ariën, K. K.; Foulongne, V.; Ngole, E. M.; Peeters, M.; Ayoub, A. Multiplex Detection of Antibodies to Chikungunya, O'nyong-Nyong, Zika, Dengue, West Nile and Usutu Viruses in Diverse Non-Human Primate Species from Cameroon and the Democratic Republic of Congo. *PLoS Negl. Trop. Dis.* **2021**, *15* (1), e0009028. <https://doi.org/10.1371/journal.pntd.0009028>.
- (17) Boisen, M. L.; Oottamasathien, D.; Jones, A. B.; Millett, M. M.; Nelson, D. S.; Bornholdt, Z. A.; Fusco, M. L.; Abelson, D. M.; Oda, S.; Hartnett, J. N.; Rowland, M. M.; Heinrich, M. L.; Akdag, M.; Goba, A.; Momoh, M.; Fullah, M.; Baimba, F.; Gbakie, M.; Safa, S.; Fonnies, R.; Kanneh, L.; Cross, R. W.; Geisbert, J. B.; Geisbert, T. W.; Kulakosky, P. C.; Grant, D. S.; Shaffer, J. G.; Schieffelin, J. S.; Wilson, R. B.; Saphire, E. O.; Branco, L. M.; Garry, R. F.; Khan, S. H.; Pitts, K. R. Development of Prototype Filovirus Recombinant Antigen Immunoassays. *J. Infect. Dis.* **2015**, *212* (suppl_2), S359–S367. <https://doi.org/10.1093/infdis/jiv353>.
- (18) Emperador, D. M.; Mazzola, L. T.; Wonderly Trainor, B.; Chua, A.; Kelly-Cirino, C. Diagnostics for Filovirus Detection: Impact of Recent Outbreaks on the Diagnostic Landscape. *BMJ Glob. Health* **2019**, *4* (Suppl 2), e001112. <https://doi.org/10.1136/bmjgh-2018-001112>.
- (19) Engin, E. D. The Use of Multiplexing Technology in the Immunodiagnosis of Infectious Agents. *J. Immunoassay Immunochem.* **2019**, *40* (1), 109–122. <https://doi.org/10.1080/15321819.2018.1563551>.
- (20) Hutchinson, K. L.; Villinger, F.; Miranda, M. E.; Ksiazek, T. G.; Peters, C. J.; Rollin, P. E. Multiplex Analysis of Cytokines in the Blood of Cynomolgus Macaques Naturally Infected with Ebola Virus (Reston Serotype)*. *J. Med. Virol.* **2001**, *65* (3), 561–566. <https://doi.org/10.1002/jmv.2073>.
- (21) Hutchinson, K. L.; Rollin, P. E. Cytokine and Chemokine Expression in Humans Infected with Sudan Ebola Virus. *J. Infect. Dis.* **2007**, *196*, S357–S363.
- (22) Leroy, E.; Baize, S.; Volchkov, V.; Fisher-Hoch, S.; Georges-Courbot, M.-C.; Lansoud-Soukate, J.; Capron, M.; Debré, P.; Georges, A.; McCormick, J. Human Asymptomatic Ebola Infection and Strong Inflammatory Response. *The Lancet* **2000**, *355* (9222), 2210–2215. [https://doi.org/10.1016/S0140-6736\(00\)02405-3](https://doi.org/10.1016/S0140-6736(00)02405-3).
- (23) McElroy, A. K.; Erickson, B. R.; Flietstra, T. D.; Rollin, P. E.; Nichol, S. T.; Towner, J. S.; Spiropoulou, C. F. Ebola Hemorrhagic Fever: Novel Biomarker Correlates of Clinical Outcome. *J. Infect. Dis.* **2014**, *210* (4), 558–566.
- (24) Gupta, M.; MacNeil, A.; Reed, Z. D.; Rollin, P. E.; Spiropoulou, C. F. Serology and Cytokine Profiles in Patients Infected with the Newly Discovered Bundibugyo Ebolavirus. *Virology* **2012**, *423* (2), 119–124. <https://doi.org/10.1016/j.virol.2011.11.027>.
- (25) Viodé, A.; Smolen, K. K.; Fatou, B.; Wurie, Z.; Van Zalm, P.; Konde, M. K.; Keita, B. M.; Ablam, R. A.; Fish, E. N.; Steen, H. Plasma Proteomic Analysis Distinguishes Severity

- Outcomes of Human Ebola Virus Disease. *mBio* **2022**, *13* (3), e00567-22.
<https://doi.org/10.1128/mbio.00567-22>.
- (26) A Longitudinal Study of Ebola Sequelae in Liberia. *N. Engl. J. Med.* **2019**, *380* (10), 924–934. <https://doi.org/10.1056/NEJMoa1805435>.
- (27) Tozay, S.; Fischer, W. A., II; Wohl, D. A.; Kilpatrick, K.; Zou, F.; Reeves, E.; Pewu, K.; DeMarco, J.; Loftis, A. J.; King, K.; Grant, D.; Schieffelin, J.; Gorvego, G.; Johnson, H.; Conneh, T.; Williams, G.; Nelson, J. A. E.; Hoover, D.; McMillian, D.; Merenbloom, C.; Hawks, D.; Dube, K.; Brown, J. Long-Term Complications of Ebola Virus Disease: Prevalence and Predictors of Major Symptoms and the Role of Inflammation. *Clin. Infect. Dis.* **2020**, *71* (7), 1749–1755. <https://doi.org/10.1093/cid/ciz1062>.
- (28) Wiedemann, A.; Foucat, E.; Hocini, H.; Lefebvre, C.; Hejblum, B. P.; Durand, M.; Krüger, M.; Keita, A. K.; Ayouba, A.; Mély, S.; Fernandez, J.-C.; Touré, A.; Fourati, S.; Lévy-Marchal, C.; Raoul, H.; Delaporte, E.; Koivogui, L.; Thiébaud, R.; Lacabaratz, C.; Lévy, Y. Long-Lasting Severe Immune Dysfunction in Ebola Virus Disease Survivors. *Nat. Commun.* **2020**, *11* (1), 3730. <https://doi.org/10.1038/s41467-020-17489-7>.
- (29) CDCTB. *MDRTB Factsheet*. Centers for Disease Control and Prevention. <https://www.cdc.gov/tb/publications/factsheets/drtb/mdrtb.htm> (accessed 2024-02-20).
- (30) Espindola, A. L.; Varughese, M.; Laskowski, M.; Shoukat, A.; Heffernan, J. M.; Moghadas, S. M. Strategies for Halting the Rise of Multidrug Resistant TB Epidemics: Assessing the Effect of Early Case Detection and Isolation. *Int. Health* **2017**, *9* (2), 80–90. <https://doi.org/10.1093/inthealth/ihw059>.
- (31) Muthukrishnan, L. Multidrug Resistant Tuberculosis – Diagnostic Challenges and Its Conquering by Nanotechnology Approach – An Overview. *Chem. Biol. Interact.* **2021**, *337*, 109397. <https://doi.org/10.1016/j.cbi.2021.109397>.
- (32) *Social Determinants of Health - Healthy People 2030*. <https://health.gov/healthypeople/priority-areas/social-determinants-health> (accessed 2024-01-20).
- (33) *Economic Stability | Prepare Your Health*. <https://www.cdc.gov/prepyourhealth/discussionguides/economicstability.htm> (accessed 2024-01-20).
- (34) *Action on Social Determinants of Health Equity*. <https://www.who.int/initiatives/action-on-the-social-determinants-of-health-for-advancing-equity> (accessed 2024-01-20).
- (35) CDC. *Social Determinants of Health*. Centers for Disease Control and Prevention. <https://www.cdc.gov/about/sdoh/index.html> (accessed 2024-01-20).
- (36) Lönnroth, K.; Jaramillo, E.; Williams, B. G.; Dye, C.; Ravigliione, M. Drivers of Tuberculosis Epidemics: The Role of Risk Factors and Social Determinants. *Soc. Sci. Med.* **1982** **2009**, *68* (12), 2240–2246. <https://doi.org/10.1016/j.socscimed.2009.03.041>.
- (37) Hargreaves, J. R.; Boccia, D.; Evans, C. A.; Adato, M.; Petticrew, M.; Porter, J. D. H. The Social Determinants of Tuberculosis: From Evidence to Action. *Am. J. Public Health* **2011**, *101* (4), 654–662. <https://doi.org/10.2105/AJPH.2010.199505>.
- (38) Noppert, G. A.; Malosh, R. E.; Moran, E. B.; Ahuja, S. D.; Zelner, J. Contemporary Social Disparities in TB Infection and Disease in the USA: A Review. *Curr. Epidemiol. Rep.* **2018**, *5* (4), 442–449. <https://doi.org/10.1007/s40471-018-0171-y>.
- (39) Duarte, R.; Lönnroth, K.; Carvalho, C.; Lima, F.; Carvalho, A. C. C.; Muñoz-Torrico, M.; Centis, R. Tuberculosis, Social Determinants and Co-Morbidities (Including HIV). *Pulmonology* **2018**, *24* (2), 115–119. <https://doi.org/10.1016/j.rppnen.2017.11.003>.

- (40) Choi, H.; Lee, M.; Chen, R. Y.; Kim, Y.; Yoon, S.; Joh, J. S.; Park, S. K.; Dodd, L. E.; Lee, J.; Song, T.; Cai, Y.; Goldfeder, L. C.; Via, L. E.; Carroll, M. W.; Barry, C. E.; Cho, S.-N. Predictors of Pulmonary Tuberculosis Treatment Outcomes in South Korea: A Prospective Cohort Study, 2005-2012. *BMC Infect. Dis.* **2014**, *14* (1), 360. <https://doi.org/10.1186/1471-2334-14-360>.
- (41) Naidoo, P.; Peltzer, K.; Louw, J.; Matseke, G.; Mchunu, G.; Tutshana, B. Predictors of Tuberculosis (TB) and Antiretroviral (ARV) Medication Non-Adherence in Public Primary Care Patients in South Africa: A Cross Sectional Study. *BMC Public Health* **2013**, *13* (1), 396. <https://doi.org/10.1186/1471-2458-13-396>.
- (42) Pedrazzoli, D.; Boccia, D.; Dodd, P. J.; Lönnroth, K.; Dowdy, D. W.; Siroka, A.; Kimerling, M. E.; White, R. G.; Houben, R. M. G. J. Modelling the Social and Structural Determinants of Tuberculosis: Opportunities and Challenges. *Int. J. Tuberc. Lung Dis.* **2017**, *21* (9), 957–964. <https://doi.org/10.5588/ijtld.16.0906>.
- (43) Amrollahi, F.; Shashikumar, S. P.; Meier, A.; Ohno-Machado, L.; Nemati, S.; Wardi, G. Inclusion of Social Determinants of Health Improves Sepsis Readmission Prediction Models. *J. Am. Med. Inform. Assoc.* **2022**, *29* (7), 1263–1270. <https://doi.org/10.1093/jamia/ocac060>.
- (44) Zhao, Y.; Wood, E. P.; Mirin, N.; Cook, S. H.; Chunara, R. Social Determinants in Machine Learning Cardiovascular Disease Prediction Models: A Systematic Review. *Am. J. Prev. Med.* **2021**, *61* (4), 596–605. <https://doi.org/10.1016/j.amepre.2021.04.016>.
- (45) Galea, S.; Tracy, M.; Hoggatt, K. J.; DiMaggio, C.; Karpati, A. Estimated Deaths Attributable to Social Factors in the United States. *Am. J. Public Health* **2011**, *101* (8), 1456–1465. <https://doi.org/10.2105/AJPH.2010.300086>.
- (46) Stabellini, N.; Cullen, J.; Moore, J. X.; Dent, S.; Sutton, A. L.; Shanahan, J.; Montero, A. J.; Guha, A. Social Determinants of Health Data Improve the Prediction of Cardiac Outcomes in Females with Breast Cancer. *Cancers* **2023**, *15* (18), 4630. <https://doi.org/10.3390/cancers15184630>.
- (47) Tan, M.; Hatef, E.; Taghipour, D.; Vyas, K.; Kharrazi, H.; Gottlieb, L.; Weiner, J. Including Social and Behavioral Determinants in Predictive Models: Trends, Challenges, and Opportunities. *JMIR Med. Inform.* **2020**, *8* (9), e18084. <https://doi.org/10.2196/18084>.
- (48) Qavi, A. J.; Bailey, R. C. Multiplexed Detection and Label-Free Quantitation of MicroRNAs Using Arrays of Silicon Photonic Microring Resonators. *Angew. Chem. Int. Ed.* **2010**, *49* (27), 4608–4611. <https://doi.org/10.1002/anie.201001712>.
- (49) Qavi, A. J.; Kindt, J. T.; Gleeson, M. A.; Bailey, R. C. Anti-DNA:RNA Antibodies and Silicon Photonic Microring Resonators: Increased Sensitivity for Multiplexed microRNA Detection. *Anal. Chem.* **2011**, *83* (15), 5949–5956. <https://doi.org/10.1021/ac201340s>.
- (50) Letafati, A.; Najafi, S.; Mottahedi, M.; Karimzadeh, M.; Shahini, A.; Garousi, S.; Abbasi-Kolli, M.; Sadri Nahand, J.; Tamehri Zadeh, S. S.; Hamblin, M. R.; Rahimian, N.; Taghizadieh, M.; Mirzaei, H. MicroRNA Let-7 and Viral Infections: Focus on Mechanisms of Action. *Cell. Mol. Biol. Lett.* **2022**, *27*, 14. <https://doi.org/10.1186/s11658-022-00317-9>.
- (51) How, C.-K.; Hou, S.-K.; Shih, H.-C.; Huang, M.-S.; Chiou, S.-H.; Lee, C.-H.; Juan, C.-C. Expression Profile of MicroRNAs in Gram-Negative Bacterial Sepsis. *Shock Augusta Ga* **2015**, *43* (2), 121–127. <https://doi.org/10.1097/SHK.0000000000000282>.
- (52) Cowell, T.; Han, H.-S. Double Emulsion Flow Cytometry for Rapid Single Genome Detection. In *Single-Cell Assays: Microfluidics, Genomics, and Drug Discovery*; Li, P. C. H., Wu, A. R., Eds.; Methods in Molecular Biology; Springer US: New York, NY, 2023; pp 155–167. https://doi.org/10.1007/978-1-0716-3323-6_12.

- (53) Furuyama, W.; Marzi, A. Development of an Enzyme-Linked Immunosorbent Assay to Determine the Expression Dynamics of Ebola Virus Soluble Glycoprotein during Infection. *Microorganisms* **2020**, *8* (10), 1535. <https://doi.org/10.3390/microorganisms8101535>.
- (54) Couturier, C.; Wada, A.; Louis, K.; Mistretta, M.; Beitz, B.; Povogui, M.; Ripaux, M.; Mignon, C.; Werle, B.; Lugari, A.; Pannetier, D.; Godard, S.; Bocquin, A.; Mely, S.; Béavogui, I.; Hébélamou, J.; Leuenberger, D.; Leissner, P.; Yamamoto, T.; Lécine, P.; Védrine, C.; Chaix, J. Characterization and Analytical Validation of a New Antigenic Rapid Diagnostic Test for Ebola Virus Disease Detection. *PLOS Neglected Tropical Diseases* **2020**, *14* (1), e0007965. <https://doi.org/10.1371/journal.pntd.0007965>.

Appendices

Appendix A: Chemistry Instructional Coaching: Adapting a Peer-Led Professional Development Program for Chemistry Graduate Teaching Assistants

A.1 Author Contributions and Acknowledgements

This appendix chapter is from the published article: Fantone, R.C.*, Zaimi, I.*, Meserve, K.*, Geragosian, E.K., Álvarez-Sánchez, C.O., Spencer, J.L., Shultz, G.V. [Chemistry Instructional Coaching: Adapting a Peer-Led Professional Development Program for Chemistry Graduate Teaching Assistants](#), *Journal of Chemical Education*, **2023**. Dr. Ginger Shultz and Dr. Jeff Spencer conceived the program and initial iterations were co-led by Dr. Jeff Spencer, Dr. Eleni Geragosian, and Christian Álvarez-Sánchez. Program adaptations and recent program iterations were co-led by Rebecca Fantone, Ina Zaimi, and the thesis author, Krista Meserve. The structure of the manuscript, data analysis, all figures and tables, and revisions were equally contributed to by the thesis author, Rebecca, and Ina. All authors contributed initial drafts of various sections and aided in manuscript editing.

I have been a coach in the program since Summer 2020 and have been an administrator since Fall 2021. As an administrator, I worked on developing and implementing the adaptations discussed in the manuscript, particularly restructuring the KTI resources for a GTA context, spearheading the monthly coaches meetings, and editing and advising the team-developed resources. In addition, I have co-led coach training during summer 2022 and 2023 and have planned and led the monthly coaching meetings for two years. This program has had a huge impact on my time in Michigan by providing a space to improve the teaching culture in the department and to continue developing and practicing mentorship skills. I would like to thank

my co-first authors, Rebecca and Ina, for making a great team. We spent many hours of brainstorming, writing, editing, and revising together and learned how to merge three (very) different writing styles! I would like to thank the co-authors, Eleni, Jeff, and Christian, for their work in starting this program here at Michigan, training me as a coach, and for being great mentors themselves. I'd like to thank Professor Ginger Shultz, and the rest of the Shultz Group, for their support on this project and publication.

A.2 Abstract

Graduate teaching assistants (GTAs) are crucial facilitators of undergraduate education, yet many begin their teaching appointments with minimal knowledge of teaching practices. Chemistry Instructional Coaching offers GTAs at the University of Michigan an opportunity to develop their instructional practice through a collaborative, non-evaluative, and reflective coaching program. We implemented an instructional coaching program designed in collaboration with Knowles Teacher Initiative to meet the needs of GTAs teaching in a postsecondary setting. In a coaching cycle, a trained GTA (the coach) guides a recruited GTA (the coachee) through conversations that allow the coachee to develop a teaching-related goal, plan how to implement changes to their instruction, and reflect on the measurable outcomes. This iterative cycle builds on itself over the course of one or two semesters, with new goals being identified for each cycle. Through adapting the program in our department over time, we utilized feedback from coaches and coachees to adjust the structure of the coaching program and develop relevant materials to support knowledge of instructional practice. Herein, we report on the program design, enrollment, and current structure, and we discuss the main adaptations we implemented to develop a sustainable program within the chemistry department. We believe that this graduate

student-led instructional coaching program has the potential to be integrated into other departments or postsecondary settings.

A.3 Introduction

GTAs Learning to Teach. Graduate teaching assistants (GTAs) are assets to chemistry undergraduate education because they teach laboratory and discussion sections with 20-30 undergraduate students and, accordingly, provide one-on-one contact with them. However, many GTAs begin their teaching appointments with minimal teaching experience and professional development opportunities.^{1,2} GTAs may rely on their content knowledge, but content knowledge alone is not sufficient for teaching.³ Teaching also requires pedagogical knowledge and pedagogical content knowledge.⁴ Because of minimal teaching experience and professional development, chemistry GTAs often describe feeling unprepared to teach and exhausted from teaching.⁵ Additionally, they feel isolated in their teaching roles^{2,6} and view their teaching roles to be a “link,” a “supplement,” or a “manager,” not an instructor.⁵ Consequently, professional development opportunities for GTAs learning to teach must be expanded, and they must address the challenges GTAs face when learning to teach.

Professional Development Opportunities for GTAs Learning to Teach. Scholars have designed, implemented, and evaluated a variety of chemistry GTA trainings. These published trainings vary in length, from a few days⁷ to a whole year.⁸ These trainings also vary in depth, including course specific,⁷ laboratory specific,⁹⁻¹² or generalized for both laboratory and discussion sections.^{8,13-18}

For example, Marbach-Ad et al. developed a six-week unit that modeled teaching and emphasized teaching roles and a teaching community.¹³ Faculty, experienced GTAs, and, eventually, new GTAs shared stories of their teaching experiences. GTAs reported feeling

supported as a result of the training. Student evaluations of GTAs who participated in the training were higher on measures of effective teaching, being prepared, and respecting students than evaluations of GTAs who did not participate. Similarly, Lang et al. developed an eight-week training that introduced laboratory and discussion GTAs to teaching practices and supported GTAs in implementing them in their classrooms.¹⁷ The training involved observations, reflections, and discussions with experienced GTAs. GTAs felt the training supported them; however, they desired more support in implementing teaching practices in their classrooms and more opportunities to observe their peers' classrooms. These are just two of several examples of a structured approach to supporting GTAs learning to teach.

In both cases, despite participating in long-term trainings, GTAs requested more specified and sustained support. Social teacher-learning structures, such as instructional coaching,¹⁹⁻²¹ could address GTAs' requests. Instructional coaching structures reflections between the instructor and an experienced instructor around the instructor's problem of practice,^{22,23} and student data.^{24,25} Because of its structure, instructional coaching provides specified, contextualized support (e.g., to the instructor's problem of practice) and sustained support (e.g., with an experienced instructor). While instructional coaching is present in primary and secondary settings it is rare in postsecondary settings.²⁶⁻³⁰

To support this process, we partnered with the Knowles Teacher Initiative (KTI) (knowlesteachers.org), which designs and implements instructional coaching in primary and secondary settings. Together, we designed, implemented, and adapted instructional coaching for the postsecondary setting. Here, we present Chemistry Instructional Coaching, including its structure, development, and the themes that we learned from its adaptation. We aim to show how

a teaching community can be constructed that addresses the challenges in GTAs learning how to teach.

A.4 Chemistry Instructional Coaching

We define Chemistry Instructional Coaching (coaching) as a mentorship program where mentors (coaches) support mentees (coachees) in developing their teaching. We value and commit ourselves to creating a reciprocal, collaborative, empathetic, reflective, and non-evaluative coaching community. In this peer mentored program, coaches tend to be second-, third-, or fourth-year graduate students with teaching experience, and coachees tend to be first-year GTAs (**Appendix Table A-1**). However, coachees can be and have been second-, third-, fourth-, or fifth year GTAs, as we emphasize the practice of teaching and growth throughout all stages of a GTAs development.

The program is independent from the Chemistry Department it is situated in and is funded through internal institutional grants. Thus, it is entirely run and supported by a graduate advisor (GVS) and graduate student leaders. The program is primarily led by the graduate student leadership team (the leadership team), a small group of graduate students who are facilitators and administrators in addition to coaches. Their responsibilities include developing recruitment materials and recruiting for, planning, and implementing a yearly coaching training, creating coaching resources, pairing coachees with coaches, and planning and implementing monthly coaching meetings. Moreover, the leadership team maintains an audit trail of notes, memos, documents (and their versions), coaching artifacts, and surveys. We used these to provide the examples in this report.

Coaching Cycle. At the start of the process, the leadership team pairs a coachee with a coach, and the coach initiates the coaching cycle (**Appendix Figure A-1**). The coaching cycle is a

three-stage cycle, consisting of a “planning” or a pre-instruction stage, an “implementation” stage with observations and data collection, and a “reflecting” or post-instruction stage.^{19–21,24,25} During the planning stage, the coach and coachee identify the coachee’s problem of practice, and the coachee sets a goal.^{22,23} Related studies have shown that instructors set goals related to their teaching practices, their adaptation of teaching resources, and their alignment of teaching resources with their teaching context.^{26,27,29} We have found that, similar to secondary instructors, GTAs set goals related to their teaching practices (e.g., supporting student engagement or differentiating instruction). However, GTAs also set goals related to their classroom management (e.g., time management or providing directions) and their classroom environment (e.g., building confidence when communicating with students or setting boundaries with student contact) (**Appendix Table A-2**). During the implementation stage, the coach observes the coachee and collects the data that they planned during the planning stage. Student surveys, student work, or GTA reflective journals are examples of data collected in a coaching cycle. Finally, during the reflection stage, the coach compiles the data and presents the data to the coachee, allowing the coachee to interpret the data, incorporate the coach’s interpretation, and reflect. Ideally, the coaching cycle is iterative with at least two cycles completed over the course of a semester, where discussion and reflection spurs adaptation of the goal into the next coaching cycle (**Appendix Table A-3**). Across the semester, coaches and coachees tend to meet for a total of 4 hours—a relatively low time commitment outside of a GTA’s teaching responsibilities.

As an example, we present a cycle with a coachee, who was a fifth-year organic chemistry graduate student teaching discussion sections for a second-semester organic chemistry course. During the planning stage in the first cycle, the coachee wanted to learn how to plan, implement, and adapt a lesson as part of the lesson planning process. The coach provided the

coachee with resources on lesson planning, and the coachee drafted and edited two lesson plans with the coach's feedback. During the implementation stage, the coach observed the lessons, noting where the lesson plans aligned and misaligned with the coachee's enactment of the lessons. During the reflection stage, the coachee noticed that they lectured more than they planned to, and, because of that, they interpreted that students did not have the time to engage in their small-group problem-solving activities. Therefore, for the second coaching cycle, the coachee shifted their goal to improve student engagement during the planning stage. In this case, the coachee's first goal exposed a problem that could be scaffolded into their second goal and might otherwise have gone unnoticed.

Recruiting Coaches. The leadership team trains coaches in the summer, so they recruit graduate students to be coaches at the end of the spring semester. Coaches do not have to be active GTAs, but we do recruit graduate students who have taught at least two semesters. For recruitment, the leadership team use a variety of recruitment materials (**Appendix Figure A-2**) and approaches: posts on the Chemistry Department's Twitter; emails to the Chemistry Department's listservs; posters on the Chemistry Department's boards; and slides in course staff meetings. Moreover, the leadership team asks instructors to nominate GTAs who may be in their research group, who have taught with them, who have served on committees with them, or who they have worked with in departmental activities. These recruitment materials direct GTAs to the coaching website, where they can complete the application. The application collects contact information (e.g., name, email, and year) and asks, "Why do you want to be a coach?" Since 2019, we have recruited 17 GTAs (**Appendix Table A-1**), and all 17 GTAs have become coaches.

Coaching Training. Coaching training is implemented in six, one-and-a-half-hour, in-person sessions (9 hours) with at-home work (3 hours) (**Appendix Table A-4**). The leadership team

leads the sessions and lectures on important concepts (e.g., the coaching cycle, coaching stances, teaching strategies), and they plan small-group activities, small-group discussions, and whole-group discussions. Additionally, the leadership team invites, but does not require, trained coaches to participate in order to contribute various perspectives, experiences, and questions to the discussions.

Recruiting Coachees. The leadership team recruits GTAs to be coached at the start of the fall and spring semesters. Similar to recruiting coaches, they recruit with a variety of recruitment materials and approaches. These recruitment materials direct GTAs to the coaching website, where GTAs can complete the application. The application collects contact information (e.g., name, email, and year) and asks, “What class will you be teaching?” In contrast to recruiting coaches, recruiting coachees is ongoing. The leadership team monitors the application and pairs coachees with coaches as soon as possible. Since 2019, we have recruited 28 GTAs (**Appendix Table A-1**), and all 28 GTAs have become coachees.

Pairing Coachees with Coaches. While the focus of coaching is not content knowledge, the leadership team aims to pair coachees with coaches who have taught the same or similar courses. As of Fall 2022, 54% of coachees have been paired with a coach who has taught the same course, and 86% of coachees have been paired with a coach who has taught a similar course. This ensures that the coach has an understanding of the coachee’s course, including the content knowledge and curricular saliency for the course and the GTA’s role and responsibilities in the course. Approximately, half of the coachees continue with coaching at the start of our spring semester. Sometimes, the coach-coachee pair continues; other times, the coach-coachee pair changes.

Program Enrollment. The ratio of trained coaches to recruited coachees has varied (**Appendix Table A-5**). Initially, the number of coaches was kept small to pilot the program and assess feasibility. In the first year, we recruited six GTAs to be coaches, and the leadership team recruited eight GTAs to be coachees, allowing all coaches to be paired with at least one coachee. With positive trends in participation, the program expanded and seven new coaches were trained the following year, leading to a total of ten active coaches. However, this expansion in coaches occurred during the COVID-19 Pandemic, in which the coachee participation decreased to three. We suspect that coachee recruitment dropped because of the COVID-19 Pandemic and the demands of online teaching. Coaching – as well as teaching – pivoted from in-person meetings to online meetings. While the leadership team advertised that coaching is low-effort with four hours scheduled throughout the semester, it is likely that GTAs were experiencing “Zoom fatigue” and other external factors and were not able to join more Zoom meetings. Three coaches were paired with the enrolled coachees and conducted coaching cycles. The remaining seven trained coaches paired up, practicing coaching cycles with each other. While this arrangement was unplanned, it was helpful because coaches gained practice and the coach who became the coachee experienced the coaching cycle from the coachee perspective. Due to the low engagement from coachees during this period, we did not recruit and train more coaches. In the third year, teaching pivoted back to in-person meetings, and we recruited thirteen GTAs to be coachees, allowing all eight active coaches to be paired with one coachee and five of the eight to be paired with two coachees. Due to the high engagement from coachees, we recruited four GTAs to be coaches, resulting in eight active coaches in the fourth year. Some coaches expressed being able to balance two coachees while others wished to keep it to one due to additional graduate responsibilities. Therefore, we aim to maintain a 1:1 ratio where coaches can participate

meaningfully, feeling neither underwhelmed without a coachee nor overwhelmed with many coachees.

A.5 Program Evaluation

Our evaluation was designed to understand the experiences of coachees within the coaching program and to describe the retention and reach of the program within the department. Furthermore, throughout the implementation of the program, we used our evaluation to make further adaptations to address challenges coaches and coachees faced (discussed in the next section). We guided our evaluation by taking extensive notes during administrative meetings and monthly coaching meetings about coaches' experiences, soliciting coaches' feedback on coaching training, and surveying coachees on their experiences in the coaching program.

We surveyed coachees via Qualtrics, a survey management system, at the end of each semester. Coachees' anonymous responses are only accessible to the leadership team. The survey presents a series of multiple-choice, multiple-check, and short-response questions. Some questions solicit feedback on the coachee's coach (e.g., "How was your coach helpful or unhelpful?"), and other questions solicit feedback on the coachee's coaching experience (e.g., "What did you or didn't you learn about your teaching?"). A few questions solicit information on the coachee's goals (e.g., "What goal did you set for your first coaching cycle?"), allowing us not only to catalog goals but also group them into teaching practice, classroom management, or classroom environment goals (**Appendix Table A-2**). The survey is voluntary, and coachees are not required to answer the questions, whether they cannot answer them, or they do not want to answer them. In this section we report on the retention and reach of the coaching program, coaching goals established within coaching cycles, and coachees' experiences as reported in their end-of-term surveys.

Retaining GTAs. The retention of coaches is critical to sustain the coaching program within the Department. As of 2023, we have recruited and trained 17 GTAs to be coaches (**Appendix Table A-1**). On average, GTAs have remained coaches for 3.7 ± 1.3 semesters. Coaches who serve for multiple semesters are able to build on their coaching experience and provide excellent coaching services to GTAs. Furthermore, experienced coaches have contributed to the development of the program by drawing on their diverse experiences as coaches over multiple semesters.

Retention of coachees in the program is also important because it encourages sustained growth of GTAs. Since 2019, we have recruited 28 GTAs to be coachees (**Appendix Table A-1**). On average, GTAs have remained coachees for 1.5 ± 0.5 semesters. Approximately, half of GTAs stop being coached at the end of fall semester while half of them continue being coached at the start of the spring semester. Most coachees are first-year GTAs, and we notice that we recruit more coachees at the start of the fall semester than we do at the start of the spring semester. Coaching is introduced to GTAs in the Chemistry Department's first-year orientation. Therefore, GTAs may be less confident before they have taught the first semester and may become more confident after they have taught that first semester. However, we still recruit at the start of both semesters because GTAs teaching roles and confidence can change. GTAs may use the coaching program as an initial support system because they are beginning many new activities during the start of their teaching experience. However, once they have completed their first semester, teaching may become more familiar, and they may be less apt to participate.

Serving Introductory, Large-Enrollment Courses. Most GTAs who participate have taught introductory, large-enrollment courses. 64.3% of coachees have taught general chemistry or organic chemistry laboratory sections and 21.4% of coachees have taught general chemistry or

organic chemistry discussions sections. The remaining coachees have taught small-enrollment, upper-level courses. These introductory courses not only have the highest numbers of first-time GTAs but also the highest numbers of first- and second-year undergraduate students, both important populations to serve. These results emphasize the potential reach of the coaching program on GTA teaching and student learning.

Coachee Experiences. Coachee experiences were captured in their responses to short response questions in the survey. In response to the question “How was your experience being coached on teaching this term?” coachees overwhelmingly reported positive experiences within the coaching program and described multiple benefits they received from the program, such as developing teaching skills, having access to a knowledgeable and skilled GTA, and experiencing positive social and communal interactions with their coach and students.

For example, some coachees reported how coaching helped them learn new teaching skills, *“This coaching experience helped me develop new sets of skills and improve on them, since this was my first official teaching experience.”*

Other coachees described how having a coach offered an additional perspective and guidance that they would otherwise not have had access to led to meaningful student experiences, *“I enjoyed the insights and guidance to make my efforts more meaningful for student learning experience. The pattern allowed me to have some control over the kinds of goals I wanted to work toward, while providing an adequate amount of guidance to make those goals more refined and meaningful.”* Many coachees described positive experiences of having another person to talk to their teaching about. One coachee described, *“I enjoyed the helpful guidance from [my coach]. It was good to have a sounding board for ideas on how to improve as an*

instructor.” Another coachee described the benefit of having a source of feedback about their teaching, “[*It was*] *good to have feedback on specific concerns I had about the course.*”

Coachees further expanded upon the helpfulness of talking about teaching in response to the question “What was the most helpful part of having a coach this semester?” Some coachees benefited from hearing about their coach’s teaching experiences, “*The most helpful part of having a coach was hear[ing] their experiences teaching and how they have dealt with unique situation[s].*” Other coachees wrote about the benefits of having a peer to discuss shared experiences and challenges of teaching, “*The most helpful part of having a coach this semester was being able to talk to someone about my struggles as a [GTA] for [Organic Chemistry II].*” Indeed, having a proactive and compassionate coach is essential to the coaching process and are traits we encourage and instill in our training. By “*having someone kind and proactive listen to my teaching struggles and want to help,*” as one coachee wrote, our coachees feel supported and report positive teaching experiences.

Finally, coachees were asked, “What was the least helpful/useful?” in a short response. The majority of coachees did not report aspects of the program they did not find helpful. However, a few coachees described challenges related to their lack of knowledge and experience. For example, one coachee reported struggling to find a problem of practice due to their limited teaching experience, “*I felt like I struggled with coming up with ideas in the coaching cycle, because as [a] first year there is so much going on that I just don't know what I am looking for. I think maybe once I get a bit more teaching experience, I would have a better idea of what I wanted to work on, especially since I would have more to reflect on.*” Another coachee suggested that the program provide more professional development resources on teacher learning, especially when skill development is essential for reaching their coaching goal, “*The*

lack of concrete guidance on resources for learning new skills was hard, especially when those new skills came up as part of a goal.” Both of these examples exemplified the need to provide additional structures and support within the coaching program to address GTA specific needs. The leadership team used these responses along with coaches’ experiences to further adapt the program and to prepare coaching resources to address GTA needs.

A.6 Designing, Adapting, and Sustaining Coaching

The Chemistry Instructional Coaching program originated from conversations on social teacher-learning structures at the post-secondary level between co-authors GVS, a chemistry education researcher, and JLS, a chemistry education graduate student and high school science teacher. GVS and JLS thought that instructional coaching could address the challenges in chemistry GTAs learning how to teach. Mainly, instructional coaching could provide sustained support that would be semester- or year-long, flexible support that would be respectful of GTAs’ schedules and responsibilities, and contextualized support that would be responsive to an individual GTAs’ wants, needs, and constraints. JLS and co-author EKG attended their training, and GVS, JLS, and EKG worked with KTI to adapt KTI’s training and its materials from a secondary setting to a postsecondary setting. Adaptation is a part of implementation,³¹ and through anticipated changes of the program over time, we report on three of these: (1) coaches needed collaborative, reflective meetings; (2) the coaching cycle needed to be modified; and (3) our resources needed to support coaches’ teaching practice in addition to their coaching practice. Herein, we describe the challenges we faced while adapting instructional coaching to a postsecondary setting and the solutions used to address them in later iterations.

Collaborating and Reflecting on Coaching Practice During Monthly Coaching Meetings.

We found routine one-hour monthly coaching meetings with the coaches throughout the

academic year was an essential practice for facilitating learning within the program. For the leadership team, these meetings fostered conversations that led to necessary changes to the coaching format; for the coaches, they provided a platform for improving coaching and teaching practice and problem solving within their own coaching cycles. For example, during the first year's monthly meetings, the leadership team provided logistical reminders to coaches on the coaching cycle and the program structure, and the coaches debriefed about their own coaching cycles. During the coaches debriefs, coaches noted that coachees struggled to identify a problem of practice or how to set a goal. Coaches reflected that they themselves struggled to support coachees in identifying a problem of practice and setting goals. From this, the leadership team created team-developed resources (described below) to support coaches and coachees finding a problem of practice and setting attainable goals during the planning meetings. In Year 2, the leadership team planned small-group activities in the monthly meetings to facilitate further discussions about their coaching practice. The coaches chose the topics (e.g., the coaching cycle and coaching practice) and the activities (e.g., discussion on articles and videos on coaching) for the meetings. This reflection and collaboration aligned with coaches' coaching practice and their personal goals, such as developing transferable professional skills. Notably, coaches chose one topic to discuss month after month – their coaching experiences and how their teaching experiences affected that. Coaches expressed difficulty in supporting coachees' teaching practice when they themselves have limited teaching practice. In response, the leadership team created additional team-developed resources to support coaches' teacher learning (discussed in next section).

Over the course of the program, we found our routine coaching meetings focused on creating opportunities for coaches to discuss the status of their coaching cycle and providing a

platform to share stories of their experiences, successes, and challenges faced in their coaching cycles. These discussions equip the leadership team with ways to better support our coaches. The leadership team was able to facilitate these discussions by utilizing small-group activities and by giving the coaches agency to select coaching-related professional development topics to center the meetings around. Furthermore, these monthly coaching meetings create a space where coaches can reflect on their coaching practice and can collaborate on challenges, which, in turn, creates a sustainable coaching and teacher-learning community.

Bending, Not Breaking, the Coaching Cycle. To address the finding that many GTAs found setting an initial goal to be challenging, we added the option for a pre-planning meeting and observation component to help the coach and coachee build trust and provide additional time to identify a goal for the first cycle. The pre-planning meeting is intended for the coach to understand the coachee as “a whole person,” keeping in mind their personal commitments, institutional constraints, and salient identities in addition to “teacher” or “researcher.” This knowledge, in conjunction with data from a classroom observation, helps the coach suggest or guide the coachee to set a goal and begins a long-term relationship that is essential to building a teaching community.

Creating Team-Developed Resources and Adapting KTI Resources to Support Coaches’ Coaching and Teaching Practice. To facilitate sustained development of coaches’ coaching practice and teacher-learning, we found that more GTA-specific and context specific resources were needed. From Year 1 to Year 3, we trained coaches with KTI resources, such as their conversation maps and coaching stances, which are documents that guide the coach on how to navigate a coaching conversation through an organized list of prompts. In this context, GTAs rely on a two-day teaching training that is offered by the Chemistry Department and, as a result,

coaches found that first-year GTAs had limited knowledge of their teaching practice. For example, during the planning meeting, GTAs could not answer the prompt “What would you like to understand about your teaching practice?” from the KTI planning conversation map, constraining coaching conversations. Therefore, we adapted KTI resources for a first-time GTA audience. For example, we adapted the KTI planning conversation map to ask questions about GTAs’ past learning experiences and their current teaching experiences before it asks about their teaching practices. These questions include but are not limited to: “What have been the most challenging moments as a GTA?” “What have been your aha or uh-oh moments?” “What do you like about teaching?” “What do you dislike about teaching?” and “Is there a teacher who you enjoyed or would like to emulate?” Thus, our KTI-adapted resources direct coaches to learn about their coachees, so they can better support developing GTA’s knowledge of their teaching practices. In addition, we created team-developed resources (e.g., example coaching goals and example data collection methodologies; **Appendix Figure A-3**). These materials were used in conjunction with the KTI-adapted materials with the goal of providing inspiration and examples of coaching cycles to the coachee, as well as acknowledging their minimal teaching experiences.

Furthermore, we found that coachees expected their coaches to be expert teachers or experts in teaching. Although coaches have more teaching experience than coachees do, coaches and coachees are peers, and both rely on the two-day teacher training from the Chemistry Department. We knew that building teaching knowledge was influential for developing teaching practices and, therefore, important for both coaches and coachees. We created a “teaching terms” resource, which defines and provides examples for common teaching terms along with links to literature on the terms. Moreover, we created “grading,” “lesson planning,” “balancing students’ access and your time,” “supporting students’ engagement,” and “guiding students’ knowledge”

resources, as these topics have been common teaching practice goals in our program. These teaching resources are educational, providing definitions, examples, and links. The teaching resources are also practical, including prompts, sentence stems, and spaces for both coaches and coachees to use during their meetings.

Over the course of piloting and implementing the program, we faced multiple challenges in adapting coaching to our GTA context, including practically implementing coaching cycles with respect to our coachees responsibilities and teaching experiences and supporting our coaches in addressing these challenges in their cycles. We addressed these challenges by creating sustained support for our coaches with routine monthly meetings and adapting and developing various resources that consider the GTA as a whole person, with different teaching, class work, research, and personal responsibilities. The resources and adaptations we made continue to support coaches and their coachees. The lessons we learned can be used by others to inform their own GTA development program.

A.7 Conclusions and Implications

Graduate students play an outsized role in undergraduate teaching at many institutions. However, supporting their professional development as educators is challenging because of the many demands of graduate programs. Instructional coaching, which has been widely used at the K-12 level, is a promising approach to support graduate teaching because it is flexible, requires a relatively low time commitment, and, therefore, can work within the constraints of graduate programs. We built an instructional coaching program for chemistry graduate students at the University of Michigan and demonstrated that instructional coaching can be applied at the post-secondary level to support GTAs from within their classroom.

To develop the program, we began by working with coaching experts from the Knowles Teacher Initiative. A group of graduate students first learned how to be coaches and later became coach leaders, training new coaches, collecting evaluation data, and using that data to improve the coaching structures. Specifically, we found that graduate students who participated as coaches and coachees needed additional resources in order to participate meaningfully in the coaching cycle. We developed resources that provided inspiration for coaching goals and educated both coaches and coachees on teaching practice. Both coaches and coachees self-reported a benefit to participation, and their ongoing participation in the program reinforces this perspective.

We believe that instructional coaching is transferable to other settings. The description of the program and the materials provided in the supporting information demonstrate how the program was adapted for our context. We encourage the uptake of instructional coaching by others. However, we strongly recommend involving an experienced coach or program at the onset to ensure that it is implemented as intended.

A.8 Future Directions

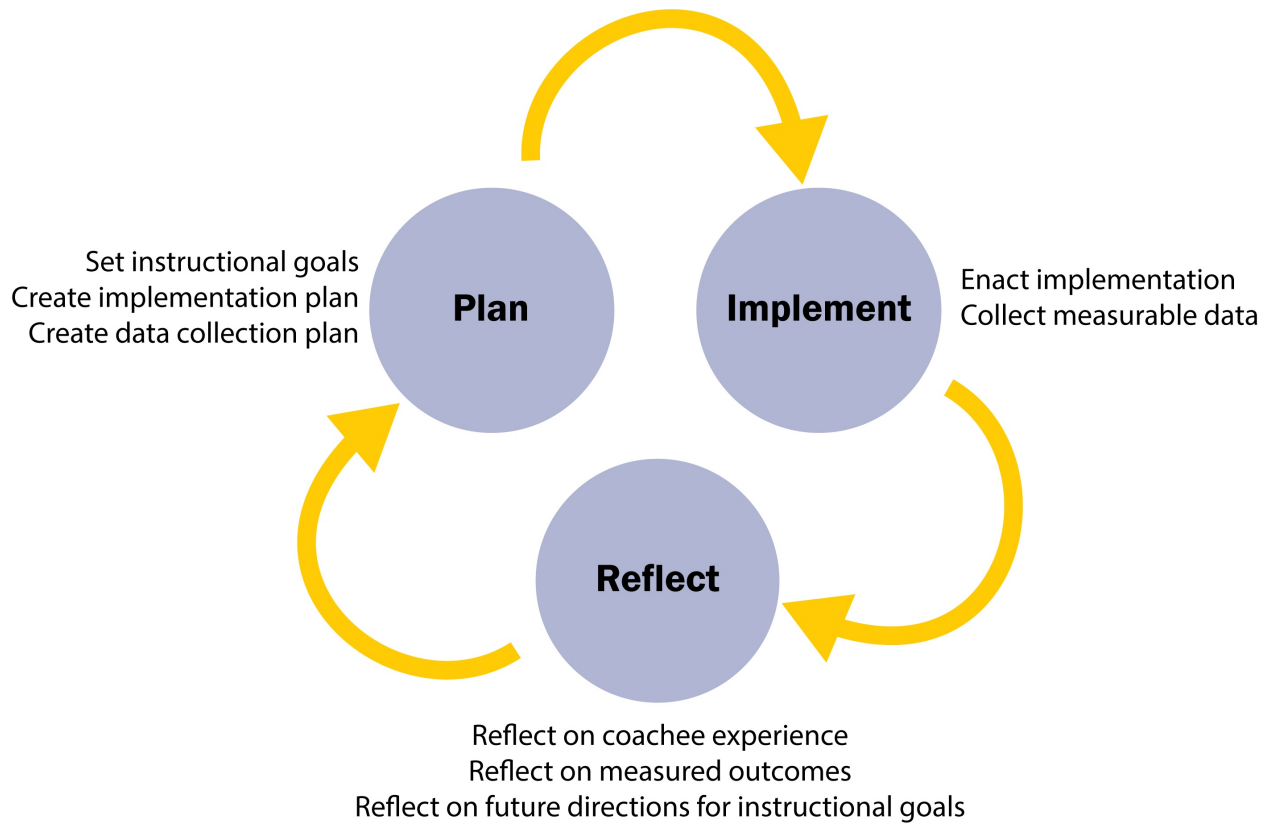
In this manuscript, we discussed how a coaching program was adapted to fit the needs of GTAs at our institution leading to the current state of the program. A natural next step will be to investigate coaches and coachees participation patterns and professional growth. For example, the program is “opt-in” and thus we are interested in how this may affect access to the program and more particularly why some GTAs elect to participate while others do not. Similarly, it would be helpful to better understand why some GTAs continue with coaching after a single term while others do not. Other fruitful lines of inquiry could include longitudinally tracking coachees attitudes toward teaching and the evolution of their teaching practice while being

coached. Further study could improve our understanding of how coaching functions in this setting and provide information for adapting the program to GTA's evolving needs.

Coach specific development would also be a productive direction for inquiry that could inform program adaptations. For example, investigating how coaches develop coaching ability could be conducted using a more holistic approach that would complement our current experience-based evaluations. This investigation focus would inform whether approaches to coach training improve coaching ability. For example, we have tried a coaching tiered coaching system, where trained coaches could opt into being coached by more experienced coaches. Coach specific investigations would inform whether this or other strategies are productive.

Overall, this report focused on the initial adaptation of an instructional coaching program to a chemistry GTA context. Our next step is to expand the program to both increase participation of coaches and coachees and increase the impact of coaching within the department. The data and program changes we propose in this section will provide a more concrete look into the impact of the coaching program on GTAs through coachee participation, the growth of our coaches, and the reach of the program.

A.9 Figures



Appendix Figure A-1 Coaching Cycle. The coaching cycle is a three-stage cycle, consisting of a “planning” or a pre-instruction stage, an “implementation” stage with observations and data collection, and a “reflecting” or post-instruction stage. Figure adapted from Knowles Teacher Initiative.

A

WE'RE RECRUITING

Chemistry Instructional Coaching is recruiting Chemistry Graduate Students to be Coaches. Coaching is a reflective, reiterative, and non-evaluative mentorship where coaches support coachees in developing their teaching.

Coaches aren't "perfect" or "expert" Graduate Student Instructors.

- Coaches will develop communication, collaboration, reflection, and mentorship skills.
- Coaches will learn teaching strategies.
- Coaches will learn how to support coachees in developing teaching practices.



Coaching training runs from July to August with weekly, in-person sessions.

If you are Chemistry Graduate Student who is interested in being a coach, fill out this form by **Wednesday, June 22.**


B


WE'RE RECRUITING

Chemistry Instructional Coaching is recruiting Graduate Student Instructors (GSIs) to be Coachees. Coaching is a reflective, reiterative, and non-evaluative mentorship where coaches support coachees in developing their teaching.


Coaching is low effort (4 hours / 1 semester) and high impact:

- Coachees will set teaching goals and learn teaching strategies.
- Coachees will gain a teacher mentor and a teaching community.

Coachees must teach a chemistry course but can range from beginner GSIs to experienced GSIs.



If you are GSI who is interested in being a coachee, fill out this form by **Wednesday, September 14.**



Appendix Figure A-2 Example recruitment materials. The coaching team used printed and digital flyers with QR codes that directed students to the sign up for both (A) coach and (B) coachee recruitment.

A

Potential Coaching Goals

Your coach aims to support you in your teaching, whatever that may mean for you. Your coach will help you reflect on your teaching experiences, so **you choose** what you'd like to focus on. If you and your coach are struggling to define a goal, see the list below for various topics GSIs have focused on in the past.

Time Management skills:

- Balancing time spent in full group discussions and break out rooms
- Managing time in the classroom (pacing, allowing time for questions, etc.)
- Managing time outside of the classroom (grading, preparing for sessions, etc.)
- Finishing up lab activities on time

Teaching skills:

- Increasing active communication in virtual or in-person discussions
- Refining PPT presentations, using the whiteboard, etc.
- Learning to use/create lesson plans, grading rubrics, etc.
- Improving instructor follow-up questions that may:
 - Redirect student reasoning
 - Model correct reasoning

Student/Teacher dynamics:

- Increasing students' comfortability with stopping you or asking you questions
- Increasing your accessibility to students
- Responding to student questions or conversations to promote their engagement and learning
- Listening to and talking with students

Providing feedback to students:

- Developing and using grading rubrics
- Midterm feedback

Student Focused Goals:

- Increasing student participation/engagement in the classroom/lab
- Increase student motivation
- Increase student conceptual understanding

Questions you might ask yourself:

- Do students feel comfortable with stopping you or asking questions?
- What are ways to make yourself accessible to the students?
- How to respond well to student questions or conversations?
- Are you listening to students? How are you talking to students?

B

Chemistry Instructional Coaching Data Collection

Adapted from the Knowles Teaching Initiative

Role of Data in the Coaching Cycle: The Coaching Cycle encourages the use of data in order to determine the success of the work the Coach and GSI do together. The source of data chosen will be tailored to the goals of the GSI and be used to stimulate discussion of those goals during the Reflect portion of the Coaching Cycle. Below is a list of possible data sources.

Quantitative Sources of Data

- 1) Checklists
- 2) Quantitative Surveys
- 3) Records: Cumulative files, tests, attendance
- 4) Observation/Field Notes:
 - a) Event Count
 - b) Duration (i.e. time stamping events)
 - c) Verbal Flow

Qualitative Sources of Data

- | | |
|--|---------------------------------------|
| 1) GSI Data Sources | 2) Observation/Field Notes: |
| a) GSI Journals | a) Anecdotal Record |
| b) Emails from the GSI | b) Verbal Behaviors |
| c) Meeting or Task Notes | c) Recording student questions |
| d) Self-Assessment | d) Recording student participation |
| e) Task Analysis of GSI materials (e.g., lesson plans, activities, etc.) | e) Time stamping events |
| | f) Photos/Drawings of Classroom |
| 3) Student Data Sources | 4) Qualitative Questionnaires/Surveys |
| a) Emails to the GSI | a) Google forms |
| b) Student work, projects, performances | b) Midterm Feedback |

Adapted from Knowles Teaching Initiative

Appendix Figure A-3 Examples of team developed resources. To help coaches facilitate conversations with their coachees, we developed a range of resources specific to GTA context, included (A) potential goals for a coaching cycle and (B) data collection methods.

A.10 Tables

Appendix Table A-1 Recruitment of Coaches and Coachees.

	Year in Graduate School					
	First Year	Second Year	Third Year	Fourth Year	Fifth Year	Total
Coaches	0	6	6	4	1	17
Coachees	24	3	0	0	1	28

As of Fall 2022. For coaches, the year in graduate school corresponds to the year that they have completed their coaching training and are conducting their first coaching cycle. For coachees, it is the year in graduate school that coachees are in during their first coaching cycle. On average, there are approximately 100 active GTAs teaching in the department each year.

Appendix Table A-2 Summary of Coachee’s goals by program year and retrospective theme categorization.

Year	Theme	Goals
Year 1	Classroom Management	Preparing for the lesson Time management concerning enacting the lesson Providing directions and commanding students’ attention
	Classroom Environment	n/a*
	Teaching Practices	Supporting students’ learning Facilitating students’ discussions Supporting students’ engagement
Year 2	Classroom Management	Lesson planning Grading efficiently and consistently
	Classroom Environment	n/a*
	Teaching Practices	Supporting students’ engagement
Year 3	Classroom Management	Planning lectures Delivering lectures Providing directions and commanding students’ attention Time management concerning grading
	Classroom Environment	Building confidence when planning and delivering lessons Building confidence when communicating with students
	Teaching Practices	Supporting students’ engagement Minimizing power dynamics in groups for small-group work
Year 4	Classroom Management	Time management concerning preparing for the lesson Time management concerning enacting the lesson Providing directions and commanding students’ attention Grading lab reports efficiently
	Classroom Environment	Building confidence when teaching in English Setting boundaries with student contact Questioning role as a teacher
	Teaching Practices	Asking students questions Differentiating instruction

*n/a – No goals were identified for this category during this year.

Coaches help coachees with a wide range of goals that can be classified by three main themes: classroom management, classroom environment, and teaching practices.

Appendix Table A-3 Recommended coaching schedule throughout the semester.

	September	October	November	December
Week 1		Observing and Collecting Data 1	Observing and Collecting Data 2	Conclusion Meeting
Week 2	Introduction Meeting	Analyzing Data 1	Analyzing Data 2	
Week 3	Planning Meeting 1	Reflecting Meeting 1	Reflecting Meeting 2	
Week 4		Planning Meeting 2		
<p>The leadership team recommends this coaching schedule for the Fall semester. However, flexibility is important for both coach and coachee so the leadership team encourages the coaching pair to meet in adapted timelines that work for their goal.</p>				

Appendix Table A-4 Timeline of coaching training and description of content discussed in each session.

Timeline	Description of Sessions
Meeting 1	<p>Defining Coaching and the Coaching Cycle</p> <ul style="list-style-type: none"> • Community building activity and establish meeting norms • Individually and group define what coaching means • Learn parts of the coaching cycle and anticipated semester timeline
Meeting 2	<p>Coaching Stances, Planning Meetings, and Reflecting Meetings</p> <ul style="list-style-type: none"> • Learn and identify differences in the three stances (cognitive, collaborative, and consultive) and pivoting between them • Introduction to conversation maps • Introduction and description of planning and reflection meetings
Meeting 3	<p>Implementation and Collecting Data</p> <ul style="list-style-type: none"> • Define components of a SMART goal • Explore quantitative and qualitative methods of data collection and which types of goals each method is appropriate for • Discuss how to share collected data with a coachee, while allowing them to reach their own conclusions
Meeting 4	<p>Anticipating Challenges</p> <ul style="list-style-type: none"> • Discuss how to use the ‘Facets of Trust’³² to build and maintain trust in the coaching relationship • Use ‘Mind the Gap’ framework³³ to identify differences between desired and current abilities of a coachee • Discuss potential challenges in a coaching relationship
Meeting 5	<p>Coaching Goals and Teaching Resources</p> <ul style="list-style-type: none"> • Review the various coaching and teaching related team-developed worksheets • Evaluation of the worksheets and how to put them into practice • Practice planning meeting conversations in pairs
Meeting 6	<p>Wrap-up and Practice Coaching</p> <ul style="list-style-type: none"> • Review coaching definitions from meeting 1 and reflect on any changes individuals would make after finishing the workshop • Practice full coaching cycles in pairs and provide feedback
<p>The coaching training sessions are a mix of leadership team lectures, independent thinking, small group activities with discussions, and large group sharing and discussions.</p>	

Appendix Table A-5 Recruitment of coaches and coachees by year.

	Recruited Coaches	Active Coaches	Recruited Coachees
Year 1	6	6	8
Year 2	7	10	3
Year 3	0	8	13
Year 4	4	8	5

As of Fall 2022. Recruited coaches represent the number of GSIs trained in the respective year. Active coaches represent the number of coaches actively coaching in the respective year. This number accounts for the newly trained coaches, continuing coaches from previous training years, and for coaches who left the program.

A.11 References

- (1) Sunal, D. W.; Hodges, J.; Sunal, C. S.; Whitaker, K. W.; Freeman, L. M.; Edwards, L.; Johnston, R. A.; Odell, M. Teaching Science in Higher Education: Faculty Professional Development and Barriers to Change. *Sch. Sci. Math.* **2001**, *101* (5), 246–257. <https://doi.org/10.1111/j.1949-8594.2001.tb18027.x>.
- (2) Luft, J. A.; Kurdziel, J. P.; Roehrig, G. H.; Turner, J. Growing a Garden without Water: Graduate Teaching Assistants in Introductory Science Laboratories at a Doctoral/Research University. *J. Res. Sci. Teach.* **2004**, *41* (3), 211–233. <https://doi.org/10.1002/tea.20004>.
- (3) Seymour, E. *Partners in Innovation: Teaching Assistants in College Science Courses. 2005 Boulder, CO: Rowman and Littlefield.*; 2005.
- (4) Andrews, T. C.; Speer, N. M.; Shultz, G. V. Building Bridges: A Review and Synthesis of Research on Teaching Knowledge for Undergraduate Instruction in Science, Engineering, and Mathematics. *Int. J. STEM Educ.* **2022**, *9* (1), 66. <https://doi.org/10.1186/s40594-022-00380-w>.
- (5) Zotos, E. K.; Moon, A. C.; Shultz, G. V. Investigation of Chemistry Graduate Teaching Assistants' Teacher Knowledge and Teacher Identity. *J. Res. Sci. Teach.* **2020**, *57* (6), 943–967. <https://doi.org/10.1002/tea.21618>.
- (6) Lane, A.; Hardison, C.; Simon, A.; Andrews, T. A Model of the Factors Influencing Teaching Identity among Life Sciences Doctoral Students. *J. Res. Sci. Teach.* **2018**, *56*. <https://doi.org/10.1002/tea.21473>.
- (7) Pentecost, T. C.; Langdon, L. S.; Asirvatham, M.; Robus, H.; Parson, R. Graduate Teaching Assistant Training That Fosters Student-Centered Instruction and Professional Development. *J. Coll. Sci. Teach.* **2012**, *41*, 68–75.
- (8) Dragisich, V.; Keller, V.; Zhao, M. An Intensive Training Program for Effective Teaching Assistants in Chemistry. *J. Chem. Educ.* **2016**, *93* (7), 1204–1210. <https://doi.org/10.1021/acs.jchemed.5b00577>.
- (9) Bond-Robinson, J.; Rodrigues, R. A. B. Catalyzing Graduate Teaching Assistants' Laboratory Teaching through Design Research. *J. Chem. Educ.* **2006**, *83* (2), 313. <https://doi.org/10.1021/ed083p313>.
- (10) Flaherty, A.; O'Dwyer, A.; Mannix-McNamara, P.; Leahy, J. Aligning Perceptions of Laboratory Demonstrators' Responsibilities To Inform the Design of a Laboratory Teacher Development Program. *J. Chem. Educ.* **2017**, *94* (8), 1007–1018. <https://doi.org/10.1021/acs.jchemed.7b00210>.
- (11) Flaherty, A.; O'Dwyer, A.; Mannix-McNamara, P.; Leahy, J. J. The Influence of Psychological Empowerment on the Enhancement of Chemistry Laboratory Demonstrators' Perceived Teaching Self-Image and Behaviours as Graduate Teaching Assistants. *Chem. Educ. Res. Pract.* **2017**, *18* (4), 710–736. <https://doi.org/10.1039/C7RP00051K>.
- (12) Mutambuki, J. M.; Schwartz, R. We Don't Get Any Training: The Impact of a Professional Development Model on Teaching Practices of Chemistry and Biology Graduate Teaching Assistants. *Chem. Educ. Res. Pract.* **2018**, *19* (1), 106–121. <https://doi.org/10.1039/C7RP00133A>.
- (13) Marbach-Ad, G.; Schaefer, K. L.; Kumi, B. C.; Friedman, L. A.; Thompson, K. V.; Doyle, M. P. Development and Evaluation of a Prep Course for Chemistry Graduate Teaching Assistants at a Research University. *J. Chem. Educ.* **2012**, *89* (7), 865–872. <https://doi.org/10.1021/ed200563b>.

- (14) Richards-Babb, M.; Penn, J. H.; Withers, M. Results of a Practicum Offering Teaching-Focused Graduate Student Professional Development. *J. Chem. Educ.* **2014**, *91* (11), 1867–1873. <https://doi.org/10.1021/ed500134d>.
- (15) Dragisich, V.; Keller, V.; Black, R.; Heaps, C. W.; Kamm, J. M.; Olechnowicz, F.; Raybin, J.; Rombola, M.; Zhao, M. Development of an Advanced Training Course for Teachers and Researchers in Chemistry. *J. Chem. Educ.* **2016**, *93* (7), 1211–1216. <https://doi.org/10.1021/acs.jchemed.5b00578>.
- (16) Dragisich, V. Wellness and Community Modules in a Graduate Teaching Assistant Training Course in the Time of Pandemic. *J. Chem. Educ.* **2020**, *97* (9), 3341–3345. <https://doi.org/10.1021/acs.jchemed.0c00652>.
- (17) Lang, F. K.; Randles, C. A.; Jeffery, K. A. Developing and Evaluating a Graduate Student Teaching Assistant Training Course in the Chemistry Department of a Large American University. *J. Chem. Educ.* **2020**, *97* (6), 1515–1529. <https://doi.org/10.1021/acs.jchemed.9b00686>.
- (18) Corrales, A.; Komperda, R. Characterizing Graduate Student Identity Development in the Context of an Integrated Research and Teaching Graduate Student Training Course. *J. Chem. Educ.* **2022**, *99* (4), 1747–1757. <https://doi.org/10.1021/acs.jchemed.1c00927>.
- (19) Costa, A. L.; Garmston, R. J. *Cognitive Coaching: A Foundation for Renaissance Schools. Second Edition*; Christopher-Gordon Publishers, Inc, 2002.
- (20) Loucks-Horsley, S.; Stiles, K. E.; Mundry, S.; Love, N.; Hewson, P. W. *Designing Professional Development for Teachers of Science and Mathematics*; Corwin Press, 2009.
- (21) Desimone, L. M.; Pak, K. Instructional Coaching as High-Quality Professional Development. *Theory Pract.* **2017**, *56* (1), 3–12. <https://doi.org/10.1080/00405841.2016.1241947>.
- (22) Horn, I. S.; Little, J. W. Attending to Problems of Practice: Routines and Resources for Professional Learning in Teachers' Workplace Interactions. *Am. Educ. Res. J.* **2010**, *47* (1), 181–217. <https://doi.org/10.3102/0002831209345158>.
- (23) COCHRAN-SMITH, M.; LYTLE, S. L. Chapter 8: Relationships of Knowledge and Practice: Teacher Learning in Communities. *Rev. Res. Educ.* **1999**, *24* (1), 249–305. <https://doi.org/10.3102/0091732X024001249>.
- (24) Knight, J. *Instructional Coaching: A Partnership Approach to Improving Instruction*; Corwin Press, 2007.
- (25) Aguilar, E. *The Art of Coaching: Effective Strategies for School Transformation*; John Wiley & Sons, 2013.
- (26) Joyce, B.; Showers, B. The Coaching of Teaching. *Educ. Leadersh.* **1982**, *40* (1), 4.
- (27) Showers, B.; Joyce, B. The Evolution of Peer Coaching. *Educ. Leadership* **1996**, *53* (6), 12–17.
- (28) Emerson, J. D.; Mosteller, F. Development Programs for College Faculty: Preparing for the Twenty-First Century. *Educ. Media Technol. Yearb.* **2000**, *25*, 26–42.
- (29) Neufeld, B.; Roper, D. *Growing Instructional Capacity in Two San Diego Middle Schools*; 2003. <https://eric.ed.gov/?id=ED481055> (accessed 2024-02-20).
- (30) Tucker, M. S. *Surpassing Shanghai: An Agenda for American Education Built on the World's Leading Systems*; Harvard Education Press, 2011.
- (31) Penuel, W. R.; Fishman, B. J. Large-Scale Science Education Intervention Research We Can Use. *J. Res. Sci. Teach.* **2012**, *49* (3), 281–304. <https://doi.org/10.1002/tea.21001>.

- (32) Hoy, W. K.; Tschannen-Moran, M. Five Faces of Trust: An Empirical Confirmation in Urban Elementary Schools. *J. Sch. Leadersh.* **1999**, *9* (3), 184–208. <https://doi.org/10.1177/105268469900900301>.
- (33) Aguilar, E. The Key to Working With Adult Learners: Mind the Gap. *Education Week*. February 28, 2018. <https://www.edweek.org/education/opinion-the-key-to-working-with-adult-learners-mind-the-gap/2018/02> (accessed 2023-08-30).

Appendix B: Record of Sandwich-Style Microring Assay Reagents Used in this Thesis

B.1 Antibody Reagent Information

Appendix Table B-1 Documented information for the antibody and standard reagents used in this thesis.

Target	Assay Context	Storage/stock Concentration	Running Concentration	Supplier	Item Number and most recent Lot
CCL2	Capture Ab	0.5 mg/mL	0.25 mg/mL	Thermo	14-7099 2493163
	Standard Protein	100 µg/mL	300 ng/mL	Thermo	RP8648 WK3434642
	Detection Ab	0.5 mg/mL	2 µg/mL	Thermo	13-7096 2373788
CCL3	Capture Ab	0.5 mg/mL	0.25 mg/mL	RnD	MAB670 HJ1119071
	Standard Protein	100 µg/mL	100 ng/mL	RnD	270-LD CG132041
	Detection Ab (Bt in house)	0.5 mg/mL	1 µg/mL	RnD	MAB270 DS00519101
CCL4	Capture Ab	0.5 mg/mL	0.25 mg/mL	RnD	MAB271 KH0621051
	Standard Protein	100 µg/mL	150 ng/mL	RnD	270-LD CG132041
	Detection Ab (Bt in house)	0.5 mg/mL	2 µg/mL	RnD *Custom order	CUST01702 AZY022203A
CCL7	Capture Ab	0.5 mg/mL	0.25 mg/mL	RnD	MAB282 ZF012006A
	Standard Protein	100 µg/mL	50 ng/mL	RnD	282-P3
	Detection Ab (Bt in house)	0.2 mg/mL	1 µg/mL	RnD	BAF282 AOP0718071
CCL8	Capture Ab	0.5 mg/mL	0.25 mg/mL	RnD	MAB281 ZE0421112
	Standard Protein	100 µg/mL	100 ng/mL	RnD	281-CP NS0223091
	Detection Ab (Bt in house)	0.2 mg/mL	2 µg/mL	RnD	BAF281 ANM072209A

GM-CSF	Capture Ab	0.5 mg/mL	0.25 mg/mL	RnD	MAB615 ASX282006A
	Standard Protein	100 µg/mL	150 ng/mL	RnD	7954-GM MAP2220041
	Detection Ab	0.5 mg/mL	1 µg/mL	RnD	BAM215 ALG1619031
IFN-γ	Capture Ab	1 mg/mL	0.25 mg/mL	Mabtech	3420-3 116.3
	Standard Protein	100 µg/mL	100 ng/mL	Thermo	RIFNGSO XJ361814
	Detection Ab	1 mg/mL	1 µg/mL	Mabtech	3420-6
IFN-λ1	Capture Ab	0.5 mg/mL	0.25 mg/mL	RnD	BAF1598 KL60717091
	Standard Protein	100 µg/mL	150 ng/mL	RnD	1598-IL IVI0619111
	Detection Ab	0.2 mg/mL	1 µg/mL	RnD	BAF1598 KL60717091
IL-1β	Capture Ab	0.5 mg/mL	0.25 mg/mL	Thermo	14-7018 2355028
	Standard Protein	100 µg/mL	300 ng/mL	Thermo	RIL1BI XF343615
	Detection Ab	0.5 mg/mL	2 µg/mL	Thermo	13-7016 2252056
IL-2	Capture Ab	0.5 mg/mL	0.25 mg/mL	BD Bioscience	555051 0156598
	Standard Protein	100 µg/mL	150 ng/mL	BD Bioscience	554603 2301093
	Detection Ab	0.5 mg/mL	2 µg/mL	BD Bioscience	555040 2021656
IL-6	Capture Ab	1 mg/mL	0.25 mg/mL	Thermo	16-7069 2432586
	Standard Protein	100 µg/mL	100 ng/mL	Thermo	RP8619
	Detection Ab	0.5 mg/mL	2 µg/mL	Thermo	13-7068 2748779
IL-7	Capture Ab	0.5 mg/mL	0.25 mg/mL	RnD	MAB207 HE072006A
	Standard Protein	100 µg/mL	100 ng/mL	RnD	207-IL AY1420013
	Detection Ab	0.2 mg/mL	1 µg/mL	RnD	BAF207 AUM1019041
IL-8	Capture Ab	0.5 mg/mL	0.25 mg/mL	BD Bioscience	554716 9014561
	Standard Protein	100 µg/mL	50 ng/mL	BD Bioscience	554609 2237354

	Detection Ab	0.5 mg/mL	2 µg/mL	BD Bioscience	554718 0286237
IL-10	Capture Ab	1 mg/mL	0.25 mg/mL	Thermo	16-7108 2612963
	Standard Protein	100 µg/mL	300 ng/mL	Thermo	PHC0105 2421697
	Detection Ab	0.5 mg/mL	2 µg/mL	Thermo	13-7109 2399963
IL-15	Capture Ab	0.5 mg/mL	0.25 mg/mL	Biolegend	515001 B362395
	Standard Protein	100 µg/mL	100 ng/mL	RnD	247ILB TLM1723091
	Detection Ab	0.5 mg/mL	2 µg/mL	Biolegend	515104 B362226
IL-17	Capture Ab	0.5 mg/mL	0.25 mg/mL	Mabtech	3520-3 mABMT44.6
	Standard Protein	100 µg/mL	150 ng/mL	Biolegend	570502 B370981
	Detection Ab	0.5 mg/mL	2 µg/mL	Mabtech	3520-6 mAbMT504
IP-10	Capture Ab	0.5 mg/mL	0.25 mg/mL	BD Bioscience	555046 9346140
	Standard Protein	100 µg/mL	50 ng/mL	BD Bioscience	551130 2061779
	Detection Ab	0.2 mg/mL	0.5 µg/mL	RnD	BAF266 AAP192203A
TGF-α	Capture Ab	0.5 mg/mL	0.25 mg/mL	RnD	AF-239-NA ANR0519091
	Standard Protein	100 µg/mL	100 ng/mL	RnD	239-A CWW1319021
	Detection Ab	0.2 mg/mL	1 µg/mL	RnD	BAF239 A001318101
TNF-α	Capture Ab	0.5 mg/mL	0.25 mg/mL	Biolegend	502801 B369417
	Standard Protein	100 µg/mL	300 ng/mL	Biolegend	570102 B344486
	Detection Ab	0.5 mg/mL	2 µg/mL	Biolegend	502904 B353934
EBOV	Capture Ab	0.5 mg/mL	0.25 mg/mL	IBT	0365-001
	Standard Protein	100 µg/mL	2.4 µg/mL	IBT	0565-001
	EBOV/SUDV pan tracer	0.5 mg/mL	2 µg/mL	IBT	N/A
SUDV	Capture Ab	0.5 mg/mL	0.25 mg/mL	IBT	0302-030
	Standard Protein	100 µg/mL	2.4 µg/mL	IBT	0570-001

	EBOV/SUDV pan tracer	0.5 mg/mL	2 µg/mL	IBT	N/A
--	----------------------	-----------	---------	-----	-----

B.2 Assay Reagent Information

Appendix Table B-2 Documented information for the assay reagents used in this thesis.

Reagent	Storage Concentration	Running Concentration	Supplier	Item Number and most recent Lot
Mouse IgG control capture antibodies	5 mg/mL	0.25 mg/mL	Invitrogen	0031903 WG3344432
Streptavidin horse radish peroxidase (SA-HRP)	1 mg/mL	2-4 µg/mL	Thermo	21130 YB3837133
4-chloro-1-naphthol (4CN)	Stock	Stock	Thermo	0034012 WG330477
Plasma matrix: Human Plasma Apherisis Derived with Li Heparin anticoagulant	Stock	Stock	Innovative Research	IPALIH50ML 34376
Serum matrix: Human Serum Off the Clot	Stock	Stock	Innovative Research	ISER50ML 36670
Non-Bt IL8 detection antibody	0.5 mg/mL	Various concentrations	BD Bioscience	55717 2101159

B.3 Storage Conditions

Most capture antibodies were stored as received at 4°C. Capture antibodies for CCL3, CCL4, CCL7, CCL8, GM-CSF, IFN-λ1, IL-7, and TGF-α were reconstituted to respective storage concentration, aliquoted into small volumes, and stored at -80°C. Capture antibodies for EBOV and SUDV targets were desalted, diluted to 0.5 mg/mL, aliquoted, and stored at -80°C. All protein standards were reconstituted to 100 µg/mL, aliquoted into small volumes, and stored at -80°C. Most biotinylated detection antibodies were stored as received at 4°C. Tracer antibodies for CCL3, CCL4, CCL8, IP-10, CCL7, GM-CSF, IFN-λ1, IL-7, TGF-α, and EBOV/SUDV were reconstituted to respective storage concentration, aliquoted into small

volumes, and stored at -80°C . Mouse IgG capture antibodies, SA-HRP, 4CN, and non-bt IL8 antibodies were stored as received at 4°C . Plasma and serum matrices were aliquoted and stored at -20°C . Human and non-human primate specimen were stored at -80°C .